Dissertation

submitted to the
Combined Faculties of Natural Sciences and Mathematics
of the Ruperto-Carola-University of Heidelberg, Germany,
for the degree of
Doctor of Natural Sciences

Put forward by
Sepideh Sadegi
born in Tehran, Iran

Oral examination: 26.07.2023

Investigating the Activity of M Dwarfs: Spectroscopic, Photometric, and Modelling Analyses

Referees:

Prof. Dr. rer. nat. Andreas Quirrenbach
Prof. Dr. rer. nat. Cornelis Dullemond

"I may not have gone where I intended to go, but I think I have ended up where I needed to be."

Douglas Adams
The Long Dark Tea-Time of the Soul

Abstract

Stellar activity, characterised by various phenomena such as active regions, flares, coronal mass ejections (CME), etc., can be observed in low-mass stars, such as M-dwarfs. Understanding the activity of M-dwarfs is of paramount importance due to their suitability as hosts for exoplanets, including potentially habitable ones. By comprehending the activity of these stars, we not only enhance the accuracy of exoplanet detection but also gain crucial insights into the habitability of these associated exoplanets. Furthermore, studying activity in low-mass stars provides invaluable knowledge about their internal structure and sheds light on the dynamo processes that generate their magnetic fields. The primary objective of this PhD dissertation is to examine the impact of stellar activity on high-precision spectroscopic and photometric data. In pursuit of this goal, I utilised data from two highly successful exoplanet surveys, namely CARMENES and TESS.

For the first project, a sample of 58 highly active M dwarfs was carefully selected from the CARMENES survey. The aim was to examine the effect of active regions on the radial velocity (RV) measurements in these stars, using the chromatic index (CRX) as a robust parameter capable of capturing the wavelength-dependent RV signatures. The first part of this research focused on assessing the significance of the CRX-RV correlation in these stars, and its potential relationship with key stellar parameters such as mass, rotation period, $v \sin i$, and others. In the second part, the investigation delved into the identification and analysis of periodic RV signals associated with the rotation period (or its harmonics) across the échelle orders of the visible-light (VIS) and near-infrared (NIR) channels of the CARMENES spectrograph.

The second project focused on studying the TESS light curves of the same group of stars, if available, to explore the potential correlation between their flare properties, stellar parameters, and chromospheric activity indices obtained from CARMENES. Given the well-established association between sunspots and flares, it was important to investigate whether a similar relationship exists among these magnetically connected phenomena on other stars. To achieve this, a semi-automated flare detection algorithm was developed to extract key flare characteristics such as amplitude, equivalent duration, and bolometric energy. To investigate the distribution of flares emitted at different energy levels, flare frequency diagrams (FFDs) were generated and parameterised to facilitate the observation of potential relationships.

The final project involved a comprehensive case study that focused on the detailed modelling of the stellar surface of V388 Cas. This was achieved by utilising high-resolution spectra obtained from CARMENES in conjunction with simultaneous TESS photometry. To accomplish this, we employed the powerful modelling tool, `StarSim`, to effectively simulate a rotating photosphere with spotted regions. The first step involved using the inverse method to retrieve the active regions of the star based on the simultaneous observations. Subsequently, we predicted the RV values across different wavelength ranges, matching the echelle spectrographs' orders, and compared them to the observed RV values. This comparison allowed us to identify wavelength regions that were more susceptible to spot-induced signals in the absence of atmospheric and instrumental noise. In addition to this analysis, the TESS observations of V388 Cas were leveraged to conduct a study on the evolution of flares. Furthermore, we explored the possibility of a CME occurrence on the star by examining a blue asymmetry in the chromospheric lines of a spectroscopic observation taken 12 hours after a superflare event.

Zusammenfassung

Stellare Aktivität, gekennzeichnet durch verschiedene Phänomene wie aktive Regionen, Flares, koronale Massenauswürfe usw., kann bei massearmen Sternen wie M-Zwergen beobachtet werden. Das Verständnis der Aktivität von M-Zwergen ist von größter Bedeutung aufgrund ihrer Eignung als Gastgeber für Exoplaneten, einschließlich potenziell bewohnbarer. Durch das Erfassen der Aktivität dieser Sterne verbessern wir nicht nur die Genauigkeit der Exoplanetenerkennung, sondern gewinnen auch entscheidende Erkenntnisse über die Bewohnbarkeit dieser damit verbundenen Exoplaneten. Darüber hinaus liefert die Untersuchung der Aktivität in massearmen Sternen unschätzbares Wissen über deren interne Struktur und wirft Licht auf die Dynamo-Prozesse, die ihre magnetischen Felder erzeugen. Das Hauptziel dieser Doktorarbeit ist es, den Einfluss der stellaren Aktivität auf hochpräzise spektroskopische und photometrische Daten zu untersuchen. Um dieses Ziel zu erreichen, wurden Daten von zwei äußerst erfolgreichen Exoplaneten-Umfragen verwendet, nämlich CARMENES und TESS.

Für das erste Projekt wurde eine Stichprobe von 58 stark aktiven M-Zwergen sorgfältig aus der CARMENES-Umfrage ausgewählt. Das Ziel war es, den Einfluss aktiver Regionen auf die Radialgeschwindigkeitsmessungen (RV) in diesen Sternen zu untersuchen, wobei der chromatische Index (CRX) als robuster Parameter verwendet wurde, der in der Lage ist, die wellenlängenabhängigen RV-Signaturen zu erfassen. Der erste Teil dieser Forschung konzentrierte sich darauf, die Bedeutung der CRX-RV-Korrelation in diesen Sternen und ihre potenzielle Beziehung zu wichtigen stellaren Parametern wie Masse, Rotationsperiode, $v \sin i$ und anderen zu bewerten. Im zweiten Teil beschäftigte sich die Untersuchung mit der Identifizierung und Analyse periodischer RV-Signale, die mit der Rotationsperiode (oder ihren Harmonischen) in den Echelle-Ordnungen der sichtbaren (VIS) und nahen Infrarot (NIR) Kanäle des CARMENES-Spektrographen zusammenhängen.

Das zweite Projekt konzentrierte sich darauf, die TESS-Lichtkurven derselben Gruppe von Sternen zu untersuchen, sofern verfügbar, um die potenzielle Korrelation zwischen ihren Flare-Eigenschaften, stellaren Parametern und chromosphärischen Aktivitätsindizes, die von CARMENES erhalten wurden, zu erforschen. Angesichts der etablierten Verbindung zwischen Sonnenflecken und Flares war es wichtig zu untersuchen, ob eine ähnliche Beziehung zwischen diesen magnetisch verbundenen Phänomenen auch bei anderen Sternen besteht. Zu diesem Zweck wurde ein halbautomatischer Flare-Erkennungsalgorithmus entwickelt, um wichtige Flare-Eigenschaften wie Amplitude, äquivalente Dauer und bolometrische Energie zu extrahieren. Um die Verteilung von Flares unterschiedlicher Energiepegel zu untersuchen, wurden Flare-Frequenzdiagramme (FFDs) generiert und parameterisiert, um die Beobachtung potenzieller Zusammenhänge zu erleichtern.

Das abschließende Projekt umfasste eine umfassende Fallstudie, die sich auf die detaillierte Modellierung der stellaren Oberfläche von V388Cas konzentrierte. Dies wurde durch die Verwendung von hochauflösenden Spektren, die von CARMENES in Verbindung mit simultaner TESS-Photometrie erhalten wurden, erreicht. Um dies zu erreichen, haben wir das leistungsstarke Modellierungswerkzeug `StarSim` eingesetzt, um eine rotierende Photosphäre mit Fleckenzonen effektiv zu simulieren. Der erste Schritt bestand darin, die aktiven Regionen des Sterns mithilfe der inversen Methode basierend auf den simultanen Beobachtungen zu

ermitteln. Anschließend haben wir die Radialgeschwindigkeitswerte für verschiedene Wellenlängenbereiche vorhergesagt, die den Ordnungen der Echelle-Spektrographen entsprechen, und mit den beobachteten Radialgeschwindigkeitswerten verglichen. Dieser Vergleich ermöglichte es uns, Wellenlängenbereiche zu identifizieren, die anfälliger für von Flecken verursachte Signale sind, selbst in Abwesenheit von atmosphärischem und instrumentellem Rauschen. Zusätzlich zu dieser Analyse wurden die TESS-Beobachtungen von V388Cas genutzt, um eine Studie über die Entwicklung von Flares durchzuführen. Darüber hinaus haben wir die Möglichkeit des Auftretens einer koronalen Massenauswurfes (CME) auf dem Stern untersucht, indem wir eine blaue Asymmetrie in den chromosphärischen Linien einer spektroskopischen Beobachtung 12 Stunden nach einem Superflare-Ereignis untersucht haben.

Contents

List of Figures

List of Tables

List of Abbreviations

2MASS	**Two** **M**icron **A**ll-**S**ky **S**urvey
AU	**A**stronomical **U**nit
BB	**B**lack **B**ody
CARMENES	**C**alar **A**lto high-**R**esolution search for **M** dwarfs with **E**xoearths with **N**ear-infrared and optical **E**chelle **S**pectrographs
CCD	**C**harge-**C**oupled **D**evice
CCF	**C**ross-**C**orrelation **F**unction
CRIRES	**CR**yogenic high-resolution **I**nfra-**R**ed **E**chelle **S**pectrograph
CRX	**Ch****R**omatic **I**ndex
ESO	**E**uropean **S**outhern **O**bservatory
ESPRESSO	**E**chelle **S**pectrograph for **R**ocky **E**xoplanets and **S**table **S**pectroscopic **O**bservations
EW	**E**quivalent **W**idth
FWHM	**F**ull **W**idth at **H**alf-**M**aximum
GLS	**G**eneralized **L**omb-**S**cargle (periodogram)
HARPS	**H**igh **A**ccuracy **R**adial **V**elocity **P**lanet **S**earcher
HITRAN	**HI**gh-resolution **TRAN**smission molecular absorption database
HRD	**H**ertzsprung-**R**ussell **D**iagram
ISM	**I**nter**s**tellar **M**edium
JWST	**J**ames **W**ebb **S**pace **T**elescope
LSW	**L**andessternwarte **H**eidelberg
MS	**M**ain **S**equence
NIR	**N**ear **I**nfrared
RG	**R**ed **G**iant
RGB	**R**ed **G**iant **B**ranch
RV	**R**adial **V**elocity
SERVAL	**S**pectrum **R**adial **V**elocity **A**nalyser
TESS	**T**ransiting **E**xoplanet **S**urvey **S**atellite

To Parvaneh,
my mother, my rock,
for her unwavering support
and unconditional love
throughout my life.

Chapter 1

Introduction

Know Thy Star, Know Thy Planet.

NASA

Humanity has long cast its gaze skyward, engaging in speculation about the existence of other worlds and contemplating the possibility of life thriving beyond our own planet within the vast expanse of the universe. This topic was considered a philosophical matter for millennia. Among the philosophers, Aristotle (384–322 B.C.E.) believed that the universe was finite and contained a limited number of celestial bodies that he knew of. He reasoned that the universe could not be infinite since an infinite number of things could not exist. His notion of Earth being at the centre of the universe resulted in the conclusion that the Earth was one-of-a-kind and that humanity was alone in the universe (Campbell, 2016). On the other hand, philosophers like Epicurus (341–270 B.C.E.) held a more optimistic view on the notion of infinite worlds. Epicurus posited that the universe was composed of an infinite number of atoms, making it conceivable that an endless number of worlds or universes might exist. In his Letter to Herodotus, Epicurus states: "There are infinite worlds both like and unlike this world of ours. For the atoms being infinite in number, as was proved already, are borne on far out into space. For those atoms, which are of such nature that a world could be created out of them or made by them, have not been used up either on one world or on a limited number of worlds, nor again on all the worlds which are alike, or on those which are different from these. So that there nowhere exists an obstacle to the infinite number of the worlds." (Bakker, 2018). Epicurus' belief in the idea of worlds being unlimited in multitude made him more convinced that there were other worlds similar to our own, which might harbour beings similar to humans. However, it is crucial to recognise that Epicurus' ideas and beliefs should be interpreted within the historical context of ancient Greece and the philosophical traditions that prevailed at the time. It is worth

noting that these views may not necessarily align with contemporary scientific knowledge and understanding of the universe.

Science began to get hold of this topic during the scientific revolution in the 16th and 17th centuries. In the early 16th century, Nicholas Copernicus (1473–1543) proposed a heliocentric model of the solar system, which challenged the prevailing idea of our system's uniqueness. Copernicus's theory proposed that the Sun, rather than the Earth, was at the centre of the solar system, and that the planets, including Earth, revolved around it in circular orbits. Other scientists, such as Johannes Kepler (1571-1630) and Galileo Galilei (1564-1642), continued to develop and refine this model. Kepler's laws of planetary motion, which describe how planets orbit the Sun, provided a significantly more accurate description of the solar system than the geocentric model and lent strong support to the heliocentric model. Galileo's independent observations of the planets, made possible by the telescope he built, provided further confirmation of the accuracy of the heliocentric model.

The discovery that the Sun is indeed a star by Angelo Secchi (1818–1878), based on his comparison of the Sun's spectral features with those of other stars (Secchi, 1875), was a major breakthrough in the 19th century. This groundbreaking discovery supported the hypothesis that other stars might have planetary systems of their own. Nevertheless, it would take another century for astronomers to gather the first significant evidence of a planetary system beyond our own. The discovery of two planetary-mass bodies orbiting the millisecond pulsar PSR B1257+12, using the pulsar timing method, was announced in 1992 by Wolszczan and Frail (1992). However, the first confirmed detection of an exoplanet orbiting a solar-type star was made three years later by Mayor and Queloz (1995) using high-accuracy radial velocity (Doppler) measurements. Located in the constellation Pegasus about 50 light-years from Earth, the planet 51 Pegasi b (a.k.a. Dimidium) orbits a G2 IV star. Its discovery in 1995 marked a major breakthrough in exoplanet research and opened up new possibilities for studying planetary systems beyond our own. Since then, over 5300 exoplanets have been detected and confirmed using a range of methods[1], demonstrating that planetary systems are common in the Milky Way and throughout the universe.

The field of exoplanetary science has achieved numerous significant breakthroughs to date, but among the most important is the discovery of multiple Earth-sized exoplanets with similar compositions to the Earth. Some of these exoplanets orbit in the habitable zone of their stars, where conditions may support the presence of liquid water on the planet's surface and potentially foster life. Kepler-186f (Quintana et al., 2014), Kepler-438b (Torres et al., 2015), and TRAPPIST-1e (Gillon et al., 2017) are among the most notable Earth-like exoplanets discovered to date. These discoveries are of great significance in the search for extraterrestrial life. Exoplanet research has also uncovered an array of planet types that have no equivalent in our own solar system, including hot Jupiters, mini-Neptunes, rogue planets, and Super-Earths. This remarkable diversity underscores the vastness and complexity of the universe, and the potential for discovering a wide variety of worlds beyond our own. Studying the composition and characterisation of exoplanetary atmospheres has greatly improved our understanding of these distant worlds. Moreover, the detection of biomarkers, such as oxygen and methane, could be crucial indicators of life-sustaining conditions on these planets. Finally, the discovery of exoplanetary systems has expanded our understanding of the formation and evolution of planetary systems, further deepening our knowledge of the universe. Furthermore, the discovery of a diverse array of planetary systems has revealed

[1] https://exoplanetarchive.ipac.caltech.edu/

that the solar system's arrangement of rocky planets in the inner regions and gas giants in the outer regions is not a typical configuration. This suggests that the unique layout of our solar system may have played a crucial role in the emergence and evolution of life on Earth (Raymond, 2011).

While the discoveries in the field of exoplanetary science are undeniably fascinating, it's important to recognise that they have far-reaching implications beyond simply satisfying our curiosity about the universe. The study of exoplanets has opened up new avenues for answering fundamental questions in physics, such as those related to planet formation. Furthermore, the technical challenges associated with detecting minuscule planetary signals amidst vast amounts of noise have motivated researchers to develop innovative solutions that have had applications beyond exoplanet research. Thanks to today's state-of-the-art instruments, it is now possible to achieve sub $1\,\mathrm{m\,s^{-1}}$ uncertainties in exoplanet detection (e.g., the ESPRESSO spectrograph has an error budget of approximately $\sim$10 $\mathrm{cm\,s^{-1}}$; Pepe et al., 2010). As a result, the detection of exoplanets is no longer limited by instrumental precision alone, but instead is primarily limited by astrophysical jitter. The development of numerous ground-based telescopes equipped with advanced instruments (such as ESO's HARPS spectrograph) as well as several space missions dedicated to exoplanetary research (including Kepler, K2, TESS, and JWST) has created unprecedented opportunities for scientists to investigate and address some of the most challenging questions in this field. One such question, which is crucial for confirming exoplanet detections, is determining whether a given signal is caused by a planet or some other astrophysical phenomenon, such as activity on the host star. Today, the phrase, *Planet, or activity, that is the question*, more than anything else echoes in the minds of exoplanet astronomers as they work to uncover the mysteries of these distant worlds.

I began my PhD work in the exoplanetary group at Landessternwarte (LSW), the public observatory at the University of Heidelberg, with a passion for finding exoplanets and studying their potential habitability. LSW is one of eleven institutes that comprise the CARMENES consortium, which is dedicated to finding exoplanets around low-mass M stars using the radial velocity method. However, early in my PhD research, I faced one of the most challenging obstacles in the search for exoplanets: understanding the activity of the host star. This encounter ultimately redirected my research path from searching for exoplanets to investigating the activity of M dwarf stars.

Stellar activity can cause variations in astronomical data that can mask or mimic planetary signals, leading to false detections. To address this issue, astronomers have developed various methods to distinguish between activity-induced signals and genuine planetary signals. These include analysing data at different wavelengths or using high-precision observations to identify and remove noise. Another approach is to exploit the effect of stellar activity on certain spectral lines, known as activity indicators, and use these activity indices to model the host star's activity. General techniques for detecting and treating periodic signals, such as Fourier analysis and pre-whitening, can also be used, assuming that activity-induced variations are correlated with the stellar rotation period (P_{rot}) or its higher harmonics ($\frac{1}{2}P_{\mathrm{rot}}$, $\frac{1}{3}P_{\mathrm{rot}}$, etc.). Statistical methods, such as Gaussian Process Regression (GP), have also proven to be very effective for treating stellar activity as a quasi-periodic signal. While many of my colleagues in the CARMENES consortium have employed one or a combination of the methods described above to detect exoplanets (e.g., Sarkis et al., 2018; Perger et al., 2019; Bauer et al., 2020; Kossakowski et al., 2022), my focus is on understanding the impact of

activity on spectroscopic and photometric data of the most active M dwarfs observed in the CARMENES survey. This task is not straightforward, largely because stellar activity is a stochastic phenomenon and what we observe is the collective effect of several physical processes occurring on the star with different timescales. However challenging it may be, understanding stellar activity is not only crucial for exoplanetary research, but also serves as a reliable proxy for the internal magnetic dynamo mechanism of stars. Through this study, we can potentially unravel the interdependent effects of stellar mass, age, and rotation rate. Therefore, delving into the complex nature of stellar activity is an essential step towards a more comprehensive understanding of the Universe. I firmly believe that every step forward in understanding the elusive effects of stellar activity on astronomical data is crucial. In my own work, I strive to contribute to this ongoing effort and hope that my endeavours will prove beneficial to the wider scientific community.

Although my PhD work has primarily focused on M dwarf stars, I feel it is important to begin this introductory chapter with a brief review of the Sun as a main-sequence star, its internal structure, dynamo mechanism, and activity cycles. My reasoning is that the Sun is the nearest star to us, and as such, it is the best known star in terms of its properties and behaviour. The Sun is also unique in that it is the only star that we can study in situ by sending probes and making close-up observations. With powerful solar telescopes such as the Daniel K. Inouye Solar Telescope (DKIST) [2], we are able to resolve even the smallest features on its surface. Therefore, the Sun serves as the benchmark for understanding the characteristics and behaviour of other stars in the universe.

In the following sections, I will provide an overview of M dwarf stars, which are the main targets of my study, and discuss various activity diagnostics. This will set the stage for the remainder of the thesis.

1.1 The Sun as a star

The Sun, much like all other stars, is essentially a massive sphere composed of hot plasma. Assuming that the star is isolated, spherically symmetric and in a steady state, the four equations of stellar structure govern how matter, pressure, luminosity, and temperature vary with respect to the star's radius:

$$\frac{\mathrm{d}M}{\mathrm{d}r} = 4\pi r^2 \rho(r), \tag{1.1}$$

$$\frac{\mathrm{d}P}{\mathrm{d}r} = -G\frac{M(r)\rho(r)}{r^2}, \tag{1.2}$$

$$\frac{\mathrm{d}L}{\mathrm{d}r} = 4\pi r^2 \rho(r)\epsilon(r), \tag{1.3}$$

$$\begin{cases} \frac{\mathrm{d}T}{\mathrm{d}r} = -\frac{3}{4ac}\frac{\kappa(r)\rho(r)}{T^3(r)}\frac{L(r)}{4\pi r^2}, & \text{radiative transport} \\ \frac{\mathrm{d}T}{\mathrm{d}r} = \left(1-\frac{1}{\gamma}\right)\frac{T}{P}\frac{\mathrm{d}P}{\mathrm{d}r}, & \text{convective transport} \end{cases} \tag{1.4}$$

[2] https://phys.org/news/2020-12-solar-telescope-image-sunspot.html

where M is the mass, ρ is the density, P is the pressure, G is the gravitational constant, L is the luminosity, ϵ is the energy generation rate per unit mass, T is the temperature, a is the radiation density constant, c is the speed of light, κ is the Rosseland mean opacity of the matter, and $\gamma = c_p/c_v$ is the adiabatic index. All the parameters are given at the distance r from the centre of the star.

Equation 1.1, also known as the mass conservation law or the mass continuity equation, describes the cumulative mass distribution within the star. Equation 1.2 is the hydrostatic equilibrium that states the thermal pressure caused by the hot plasma of particles and radiation within the star and the gravitational force caused by the stellar mass balance one another. Equation 1.3, which is designated as the energy conservation law, explains how the energy radiating from the stellar surface into space is equivalent to the energy produced inside the stellar core. Finally, the last set of equations, namely Equations 1.4 which describe radiative transport and convective transport, explain how the stellar energy is transported within the star towards its surface. Main-sequence stars generate energy through the fusion of hydrogen into helium. However, the specific fusion process used by different types of main-sequence stars varies depending on their mass and temperature. Hot, early-type dwarfs primarily use the CNO (carbon-nitrogen-oxygen) cycle, while solar-type and later-type dwarfs use the p-p (proton-proton) chain. The mechanism of energy transport, whether it be convection or radiation, depends on the type of star and the location within the star. As a result, the energy transport equation differs accordingly. Convection is most efficient when there is a large temperature difference between adjacent layers of the star's material, whereas radiation is most effective when the material through which it propagates is not highly opaque, irrespective of the temperature gradient. Figure 1.1 illustrates the internal structure of high-mass, intermediate-mass and low-mass main-sequence stars and how the transport mechanisms can change between the core and the envelope. For stars with masses exceeding 1.5 $M_\odot$, energy production occurs mainly in a small inner core due to the strong temperature and pressure dependencies of the CNO cycle. This generates a sharp temperature gradient above the inner core, which leads to convection becoming the dominant energy transport mechanism in the inner part of the star. Conversely, in the outer regions of these stars, the temperature gradient is less steep, which facilitates the transfer of energy predominantly through radiation. For stars with masses between 0.5 and 1.5 $M_\odot$, such as the Sun, energy production through the p-p chain is more uniformly distributed and does not create a significant temperature gradient to support effective convection. As a result, radiation is the primary mode of energy transport in the inner region of these stars. However, in the outer region where the temperature is lower, hydrogen atoms can recombine, increasing the material's opacity. This makes convection more effective than radiation for transferring energy. Section 1.1.1 provides a more detailed description of the internal structures of the Sun-like stars. For stars with masses below 0.5 $M_\odot$, the outer convection zone expands while the inner radiation zone contracts until it vanishes completely at around 0.35 $M_\odot$, resulting in fully convective stars. More information on this type of star can be found in Section 1.2. The equations governing energy transport in stars (Equations 1.4) highlight the crucial role of mass in determining a star's structure and evolutionary path. Other fundamental properties, such as temperature, pressure, gravity, and age, are also intrinsically tied to stellar mass.

The **mass of the Sun** has been known since the 18th century. As the Earth orbits the Sun in an elliptical path, it is possible to determine the Sun's mass through the use of

[3] https://www.sun.org/uploads/images/Heat_Transfer_in_Stars.png

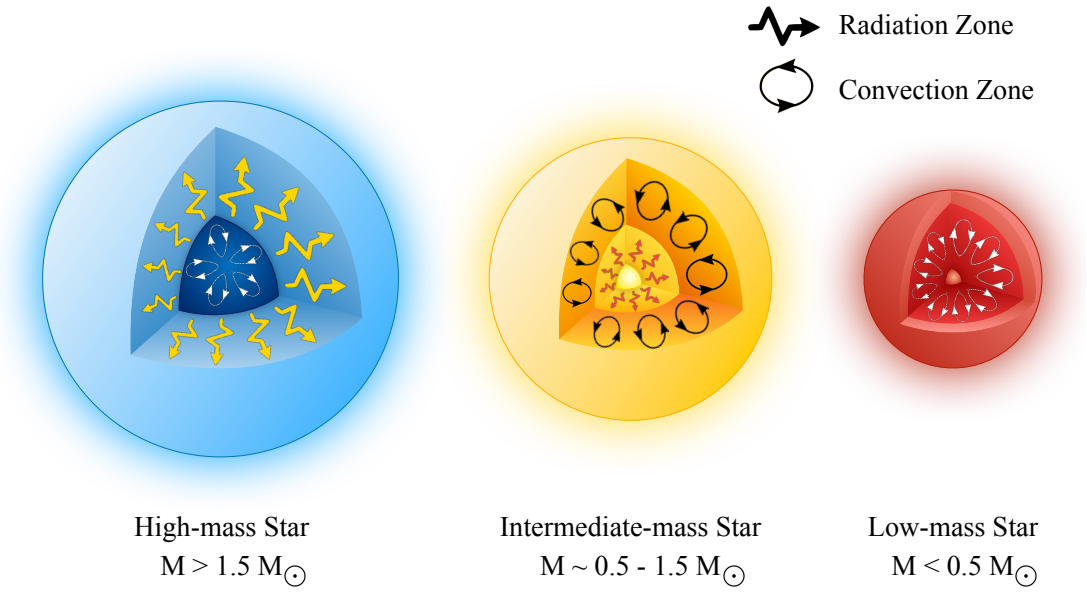

FIGURE 1.1: Illustration of energy transfer mechanisms in main-sequence stars of varying masses and spectral types. Massive early-type stars have a convective core and an outer radiation zone, Sunlike stars have a radiative core and an outer convection zone, and low-mass late M dwarfs are fully convective.
(Image credit: recreated and modified from Sun.org[3])

Kepler's third law of planetary motion (Kepler, 1619), which can be expressed as:

$$\mathrm{M}_\odot = \frac{4\pi^2}{G}\frac{(1\mathrm{AU})^3}{(1\mathrm{yr})^2} \tag{1.5}$$

At the time, the length of a year was already well known, and the distance between the Earth and Sun had recently been determined during the Venus transits of 1761 and 1769. Hornsby (1771) calculated the Earth-Sun distance to be approximately 93, 726, 900 miles (150.839×10^9 meters), which has only a 0.8% discrepancy from the current definition of 1 astronomical unit (AU), equal to 149, 597, 870, 700 meters. Henry Cavendish determined the value of the Gravitational constant G in 1798 to be 6.74×10^{-11} m^3 kg^{-1} s^{-2}, which was accurate to within 1% of the modern accepted value of $G = 6.67408 \pm 0.00031 \times 10^{-11}$ m^3 kg^{-1} s^{-2}. Utilizing the more precise measurements, the current estimation of the Sun's mass is $1.98847 \pm 0.00007 \times 10^{30}$ kg (Prša et al., 2016), which is referred to as one solar mass ($\mathrm{M}_\odot$) and serves as the standard unit for measuring the masses of other stars. The mass range of most stars typically falls between 0.08 and 100 $\mathrm{M}_\odot$. Objects with a mass below this range cannot reach the required temperature in their core to initiate hydrogen fusion, and are classified as substellar objects such as brown dwarfs and planets. Conversely, objects with a mass above this range become unstable as their radiation pressure exceeds their gravitational force, resulting in a massive outflow. This upper limit is known as the Eddington limit or Eddington luminosity and is given by

$$L_{Edd} = \frac{4\pi G M m_\mathrm{p} c}{\sigma_\mathrm{T}} \cong 1.26 \;.\; 10^3 \left(\frac{M}{\mathrm{M}_\odot}\right) W = 3.2 \;.\; 10^4 \left(\frac{M}{\mathrm{M}_\odot}\right) L_\odot, \tag{1.6}$$

where σ_T is the Thomson cross-section for the electron, m_p is the mass of a proton, and $L_\odot$ is the luminosity of the Sun.

In terms of stellar masses, the Sun is quite unremarkable as it falls within the average range and is neither particularly high nor low mass. However, compared to the typical mass of stars in the galaxy, the Sun can be considered a relatively high mass star as it ranks in the top 10% of stars in terms of mass distribution.

The **solar radius** is another important astrophysical unit of measure used to express the size of stars. Several measurements of the solar radius have been made over the years, resulting in slightly varying values. Using helioseismology, Schou et al. (1997) measured the solar radius to be $6.9598 \pm 0.0007 \times 10^{10}$ cm. Alternatively, Brown and Christensen-Dalsgaard (1998) calculated a value of $6.9551 \pm 0.026 \times 10^{10}$ cm by observing solar meridian transits during 1981 and 1987. More recent measurements by Emilio et al. (2012) and Hauchecorne et al. (2014) using the transits of Mercury in 2003 and 2006, and the transit of Venus in 2012 resulted in a slightly larger value of 6.96342×10^{10} cm. Currently, the International Astronomical Union recommends a nominal value of the solar radius of $R_\odot^N = 6.95700 \times 10^{10}$ cm for quoting stellar radii in units of the solar radius (Prša et al., 2016).

The **solar luminosity**, denoted by $L_\odot$, is another fundamental parameter that is widely used to measure the brightness of other celestial objects. It represents the intrinsic brightness of the Sun and can be determined from measurements of the solar radiation reaching the Earth, known as solar irradiance or solar constant, denoted by $I_\odot$. The solar constant is defined as the amount of radiation per unit area at a distance of 1 astronomical unit (AU) from the Sun. The solar luminosity is then given by

$$L_\odot = 4\pi k I_\odot A^2, \tag{1.7}$$

where A is the distance from the Earth to the Sun in meters (1 AU), and k is a constant that accounts for the fact that the mean Earth-Sun distance is not exactly 1 AU. According to Lang (1999), the modern estimate for the Sun's luminosity is $L_\odot = 3.85 \pm 0.01 \times 10^{26}$ W. The International Astronomical Union recommends a nominal solar luminosity of $L_\odot^N = 3.828 \times 1026$ W (Prša et al., 2016).

The magnitude system, invented by Hipparchus, an ancient Greek astronomer, about 2000 years ago, is another way of describing the brightness of celestial objects. The system is based on comparing the brightness of stars to one another using the naked eye, the only tool available in that era. The brightest stars visible from Greece were assigned a magnitude of "first magnitude", and the faintest ones observable to an unaided eye were assigned a magnitude of "sixth magnitude". Hipparchus set the ratio of brightness between the 1^{st} and 6^{th} magnitude stars to be about 100:1, and each magnitude group was set to be 2.5 times fainter than the previous brighter one. Because the human eye was the only tool for measuring the brightness of stars, the magnitude system is based on a logarithmic scale (roughly similar to the eye). Additionally, due to the peculiar convention adopted by the ancient Greeks, fainter objects have larger magnitudes, while the brightest objects have negative magnitudes. In modern times, the magnitude scale has been calibrated using a constant proposed by Pogson (1856). This constant, $10^{2/5} \approx 2.512$, is used to relate differences in magnitudes to differences in brightness such that a difference of five magnitudes corresponds precisely to a factor of 100 in brightness. The **apparent magnitude** of a celestial object is a measure of its brightness as seen from Earth. The apparent magnitude m of a star relative to a reference star with magnitude m_{ref} is given by

$$m - m_{\text{ref}} = -2.512 \log_{10} \left(\frac{I}{I_{\text{ref}}} \right), \tag{1.8}$$

where I and I_{ref} are the corresponding observed irradiances or luminosities of the target star and reference star, respectively. The constant -2.512 in Equation 1.8 reflects the logarithmic nature of the magnitude scale. The star Polaris, with a magnitude of 2, was initially chosen as the zero point of the magnitude scale (Pogson, 1856). However, after discovering that Polaris is a variable star, Vega with a magnitude of 0 was selected as the comparison star. It's important to note that the apparent magnitude of a star or any celestial object only indicates how bright it appears to an observer on Earth. Since the apparent magnitude depends on both the object's intrinsic luminosity and its distance from Earth, it's not a good measure for comparing the luminosity of astronomical objects.

To compare the intrinsic brightness of celestial objects on the scale of magnitude, one approach is to hypothetically place them all at a standard reference distance from the observer. This method was first proposed by Kapteyn (1902) in the early 1900s and was later standardised by the International Astronomical Union (Fowler and Union, 1922). The **absolute magnitude** M of an astronomical object is defined as its apparent magnitude if it were located at a distance of 10 parsecs (pc). The relation between absolute magnitude and apparent magnitude is given by

$$M = m - 5 \left(1 - \log_{10} d\right), \tag{1.9}$$

where M and m are the absolute and apparent magnitudes, respectively, and d is the distance to the object in in pc.

The apparent and absolute magnitudes of astronomical objects are dependent on the wavelengths at which they are measured. By observing an object through different filters and comparing the resulting magnitudes, it is possible to determine its **colour index**. In the case of stars, this colour value is closely related to the star's temperature. Hotter stars have a smaller colour index, indicating that they emit more light in the blue portion of the spectrum, while cooler stars have a larger colour index and appear brighter when viewed through a red filter. The most commonly used system of filters is the UBV system, which consists of filters centred at mean wavelengths of 3650, 4400, and 5500 Å (Lang, 1999). The bolometric magnitude is another way to measure the brightness of an object, which considers the total amount of radiation emitted across all wavelengths. This is determined by measuring the total radiant flux integrated over all wavelengths. To convert from an absolute or apparent magnitude measured in a specific filter to its bolometric magnitude, a bolometric correction (BC) is required, which is given by the difference between the magnitudes:

$$\text{BC} = M_{\text{V}} - M_{\text{bol}} = m_{\text{V}} - m_{\text{bol}}. \tag{1.10}$$

Here, M_{V} and m_{V} are the absolute and apparent magnitudes, respectively, measured in the visual band, while M_{bol} and m_{bol} are measured over all wavelengths.

As the Sun emits most of its energy in the visual wavelength range, its bolometric correction is marginal, estimated to be only about $+0.17$ mag (Lang, 1999). The Sun appears very bright with a visual apparent magnitude of $M_{\text{V}\odot} = -26.74$ mainly due to its proximity to us, but its actual absolute magnitude is only $m_{\text{V}\odot} = +4.83$ (Cox, 2000). The Sun's colour index is measured to be $\text{B} - \text{V} = 0.656 \pm 0.005$ (Gray, 1992).

The **effective temperature** T_{eff} of a star can be determined from its total (bolometric) luminosity, which is approximated by a black body emission with the same overall radiative power as the star. The effective temperature is defined according to the Stefan–Boltzmann law:

$$T_{\text{eff}} = \sqrt[4]{\frac{L}{4\pi\sigma R^2}} \tag{1.11}$$

where σ is the Stefan–Boltzmann constant. For the Sun, its effective temperature is approximately 5780 K (Lang, 1999), while the recommended value by the International Astronomical Union is $T^N_{\text{eff},\odot} = 5772 \pm 0.8$ K (Prša et al., 2016). The effective temperature serves as the basis for the spectral classification of stars, which indicates their spectral characteristics.

The classification scheme for stars was first proposed by Angelo Secchi, who observed the differences in the spectra of stars with varying colours and grouped them based on their spectral features (Secchi, 1868). As the number of observed stars grew, Edward C. Pickering, together with Williamina Fleming, introduced a wider range of stellar groups, assigning the letters A, B, C, etc., to denote the stars from hydrogen-rich to hydrogen-poor (Pickering, 1890; Pickering and Fleming, 1897). Later, Annie Jump Cannon reordered the spectral sequence based on specific spectral features that became stronger or weaker, resulting in a smooth transition between stellar classes. She also reduced the number of the previously defined groups to seven: O, B, A, F, G, K, and M (Cannon and Pickering, 1901). It is now understood that this classification is based on the effective temperature of stars, with the hottest and bluest stars labelled O, and the coolest and reddest labelled M. Cannon further refined the classification of stars by introducing a numerical sub-classification system that uses digits 0-9 to indicate the temperature within a given **spectral type**. Specifically, 0 denotes the hottest stars within a given type, while 9 represents the coolest. Her system, known as the Harvard spectral classification, was published in the Henry Draper Catalogue between 1918 and 1924 (Cannon and Pickering, 1918–1924), and remains the most widely used classification system to date.

About a decade after the introduction of the Harvard spectral classification scheme, Henry Norris Russell developed a specialised diagram based on the work of Ejnar Hertzsprung on stellar luminosity (Hertzsprung, 1905). This diagram, now known as the Hertzsprung-Russell Diagram (HRD), plots stars by their absolute magnitude or luminosity versus their spectral type or effective temperature (Russell, 1914). The HRD has become an essential tool in modern astronomy, providing significant insights into the structure and evolution of stars. Nowadays, there are different versions of the HRD, some using spectral classes, others using effective temperatures or colours as a proxy for effective temperature. However, they all rely on the same fundamental principle that stars of a particular type and colour possess a specific effective temperature.

The structure of the HRD is straightforward, with luminosity increasing upward in the ordinate and effective temperature increasing to the left in the abscissa. Stars tend to cluster in certain regions of the diagram. The majority fall in a long strip running from the hot, luminous upper left to the cooler, less luminous lower right, known as the Main Sequence (MS). The second largest group occupies a region towards the top right, called the Red Giant Branch (RGB). Figure 1.2 shows a version of the HRD for nearby stars in the Milky Way, with the Sun's position marked with a yellow dot.

[4] https://www.astronexus.com/hyg

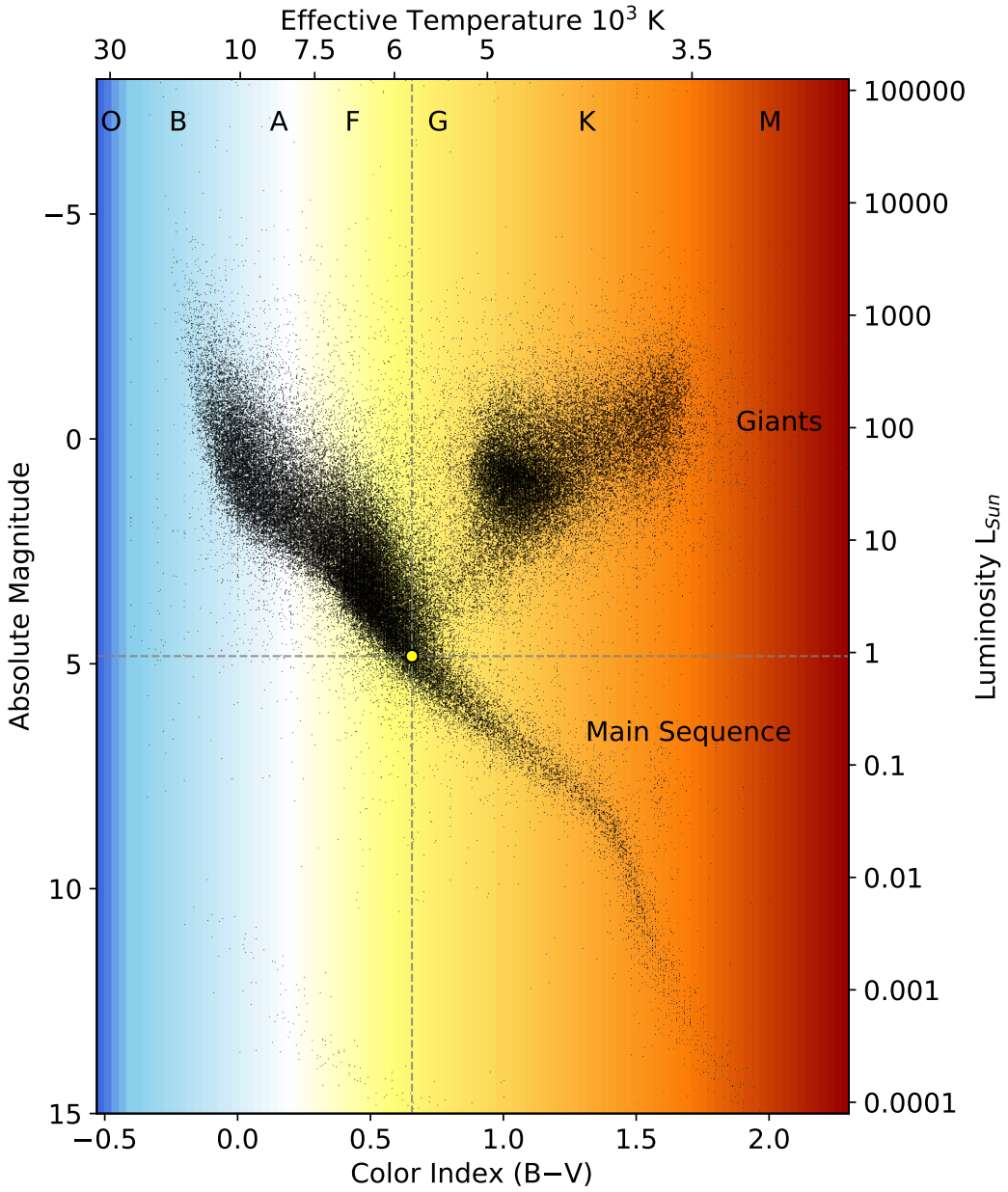

FIGURE 1.2: The HR diagram of nearby stars, with the position of the Sun marked prominently. The data points for this plot are obtained from the HYG star database archive[4], which includes approximately 120,000 stars from the Hipparcos, Yale Bright Star, and Gliese Catalogues. It should be noted that this diagram is not based on a volume-limited sample; thus, the relative number of stars is not representative. There are significantly more stars at the lower mass end relative to the higher masses, which is not adequately reflected in this plot. The diagram plots the absolute magnitude and luminosity against the (B–V) colour, spectral type, or effective temperature.

The HRD demonstrates that the spectral class alone is insufficient for a full classification of a star, particularly for cooler types G–M, where being part of the MS or the RGB can make a substantial difference in the star's absolute magnitude. Thus, in the 1940s, the Harvard classification was revised to include the luminosity class by assigning a Roman numeral between 0 and VI to the star's spectral type, with hypergiants (0), supergiants (I), bright giants (II), giants (III), sub-giants (IV), dwarfs (V), and sub-dwarfs (VI) defined as the various classes. According to this classification, the Sun is a G2.0 V star, indicating that it is a relatively cool MS star, but a hotter one within the G spectral class.

Stellar **age** is a crucial parameter, but its estimation is a challenging task, and it cannot be directly measured for individual stars. There are two types of methods to estimate stellar age: model-dependent and empirical. Although the stellar age is not directly related to my work, I will briefly mention some of the most common methods. For a more comprehensive overview, readers can refer to Soderblom (2010).

One approach to estimating stellar age is kinematic ages, which involves tracing back the motions of a group of stars to a point in the past where their spatial dispersion was at a minimum, assumed to be the time of formation. Such groups are called "moving groups", and all members are assumed to have the same age. Although this method is widely used, it requires precise astrometry, which can be challenging to obtain.

Stellar isochrones are another method used to determine the age of a star. These are theoretical models that predict the position of a group of stars with the same chemical composition on the HRD. By comparing the observed properties of a star to a set of isochrones, we can estimate the age of the star. However, isochronal ages are notoriously difficult to determine because stars change little in brightness or temperature during their hydrogen-burning lifetimes.

Another method to determine the age of a star is the Lithium depletion boundary. In this method, the equivalent width of the lithium I spectral line at around 6708 Å is calculated. The EW of this spectral line is a good age indicator (Wallerstein and Conti, 1969). Traces of lithium were produced during the Big Bang and is present in the interstellar matter from which a star is formed. If the star's initial mass is greater than 0.06 $M_\odot$, it undergoes lithium burning which converts lithium and hydrogen into helium. The reaction rates of this process depend on the star's age, mass, and effective temperature. Younger stars tend to retain more lithium than older stars, leading to a larger equivalent width (EW) of the Li I spectral line. This makes the Li I EW a useful indicator for determining the age of a star.

The age of the Sun is known with exceptional precision and accuracy, unlike any other star. It is determined through radioactive chronology of the solar system material such as meteorites and asteroids in laboratory settings. According to Chaussidon (2007), the Sun is $4,567 \pm 1 \pm 5$ million years old, where the first uncertainty of 1 Myr represents the measurement error, and the second uncertainty of 5 Myr is due to uncertainty over the exact sequence of events during the early years of the Solar System's history.

The surface **composition** of the Sun presumably reflects the composition of the molecular cloud from which it formed 4.567 billion years ago. According to the Big Bang model, hydrogen was formed in the first few minutes, along with helium and traces of light elements like lithium. The primordial mass fractions are roughly $X \approx 0.75$ (hydrogen fraction), $Y \approx 0.25$ (helium fraction), and $Z = 10^{-8}$ (all other elements, called "metals"). Since then, the interstellar medium (ISM) has been polluted by a small fraction ($\approx 2\%$) of metals

produced by stars in their core and blown into the ISM through supernovae, planetary nebulae, or mass loss outflows. Therefore, the composition of the ISM had changed significantly from the Big Bang values by the time the Sun formed. Based on precise atomic data and 3D modelling, the current estimation for the solar composition is $X = 0.738$, $Y = 0.249$ and $Z = 0.013$ (Asplund et al., 2009). These values correspond to the composition of the photosphere, which is the only region that can be analysed directly through spectroscopy.

Measuring the elemental abundances in stars other than the Sun with the same precision is challenging. Therefore, the term "metallicity" is frequently used to describe the abundance of heavy elements in other stars, and iron is often employed as a proxy due to its strong spectral features in Sun-like stars. The definition of metallicity is as follows:

$$[\mathrm{Fe/H}] = \log_{10}\left(\frac{\mathrm{N_{Fe}}}{\mathrm{N_H}}\right)_{\star} - \log_{10}\left(\frac{\mathrm{N_{Fe}}}{\mathrm{N_H}}\right)_{\odot}, \tag{1.12}$$

where N_{X} (X = Fe, H) represents the number of atoms of element X in the star per unit volume. Metallicity is a logarithmic ratio and therefore does not have a unit, but it is conventionally expressed in units of "dex" (short for decimal exponent). By definition, the solar metallicity is 0 on this logarithmic scale. Stars with $[\mathrm{Fe/H}] > 0$ have higher metallicity than the Sun, while those with $[\mathrm{Fe/H}] < 0$ have lower metallicity.

The **rotation period** of the Sun is one of its most important properties, and it has been found to vary with latitude, radius, and time (Schou et al., 1998; Beck, 2000). As early as 1630, Christoph Scheiner noted that sunspots near the equator cross the solar surface faster than those near the poles, revealing the differential rotation of the Sun (Beck, 2000). The non-uniform rotation of the Sun is a result of its composition; since the Sun is made primarily of plasma, it cannot rotate as a solid body. The details of this phenomenon are not yet fully understood and are an active area of research in solar astronomy.

In the mid-19th century, Carrington (1863) made the first measurement of solar differential rotation by tracking thousands of sunspots across the solar disk. Since then, advances in technology have allowed for more precise measurements of the solar rotation period using techniques such as Doppler shifts and helioseismology (Beck, 2000). The sidereal rotation period, which measures the rotation relative to the distant stars, is 24.47 days at the equator and approximately 38 days at the pole. On the other hand, the synodic rotation period measures the time it takes for a fixed solar feature to appear at the same position as viewed from the Earth, and it is 26.24 days at the equator. This value is slightly longer than the sidereal period because it takes into account the Earth's orbital motion around the Sun. The Carrington sidereal and synodic rotation periods are 25.38 and 27.2753 days, respectively. However, there is no universally accepted value for the solar rotation period. The most commonly used value is 27 days, but it is important to note that this value is an approximation and that the rotation period of the Sun is not a constant.

The Sun's magnetic activity has been known for over a century and has been the subject of extensive research (e.g., Carrington, 1863; Spörer, 1879; Hale, 1908; Hale et al., 1919). Since the generation and manifestations of solar magnetic activity are discussed in detail in Sections 1.1.3 and 1.1.4, respectively, I will not delve into those topics here and refer readers to those sections for more information. In the following sections, I will focus on the solar interior and atmosphere.

1.1.1 The Solar Interior

Since the interior of the Sun is opaque, it can only be studied indirectly. One of the most successful methods for investigating the inside of the Sun is helioseismology, which involves observing how oscillation modes propagate inside the Sun to reveal information about its structure and dynamics. These findings have been found to be in spectacular agreement with standard models (Christensen-Dalsgaard, 2002). The interior of the Sun is composed of four distinct regions, as shown in Figure 1.3.

The innermost region of the Sun is known as the **core**, which extends from the centre to about one-quarter of the solar radius (García et al., 2007; Basu et al., 2009). This is where the gravitational pressures of the upper layers compress and heat the gas, raising the local temperature to around 15.7 million degrees Kelvin and the density to up to $150\,\mathrm{g\,cm^{-3}}$. Under these conditions, the ionised hydrogen atoms collide so vigorously that some hydrogen nuclei fuse together, producing helium through a process called the proton-proton or pp chain. This process dominates in the Sun and in stars with masses about or less than 1 $M_\odot$, and it involves three steps:

$$\begin{cases} & {}^1\mathrm{H} + {}^1\mathrm{H} \longrightarrow {}^2\mathrm{D} + \mathrm{e}^+ + \nu_\mathrm{e} \\ \text{then} & {}^2\mathrm{D} + {}^1\mathrm{H} \longrightarrow {}^3\mathrm{He} + \gamma \\ \text{then} & {}^3\mathrm{He} + {}^3\mathrm{He} \longrightarrow {}^4\mathrm{He} + {}^1\mathrm{H} + {}^1\mathrm{H} \end{cases}$$

First, two protons collide to produce deuterium, a positron, and a neutrino. Second, a proton collides with the deuterium to produce a ^{3}He nucleus and a gamma-ray. Finally, two ^{3}He nuclei collide to produce a ^{4}He nucleus with the release of two protons (Salpeter, 1952). In these fusion reactions, the net mass of the resultant particles is about 0.7% less than the combined mass of the particles that went into the reaction. The missing mass is converted to pure radiant energy in accordance with Einstein's famous mass-energy equivalence formula, $E = mc^2$. In this equation, E represents the energy released, m represents the lost mass, and c represents the speed of light.

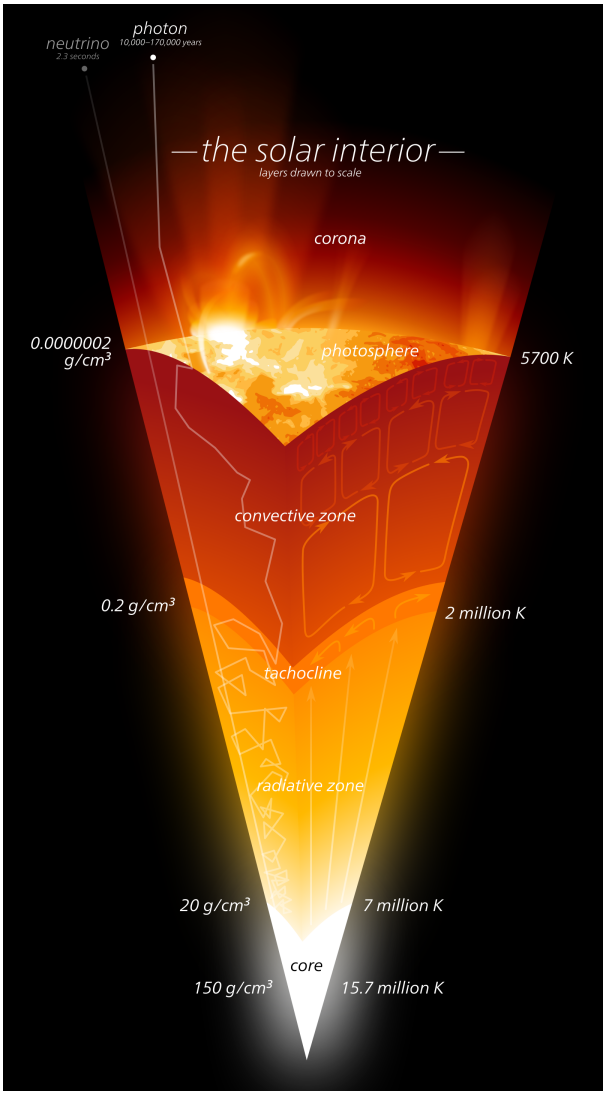

FIGURE 1.3: Cross-section cut of the solar interior structure, depicting the path of energetic photons generated in the core as a by-product of nuclear fusion. The photons become trapped in the radiative zone for an extended period before reaching the tachocline. In contrast, neutrinos pass through the overlying layers of the Sun without interacting in a matter of seconds.
(Image credit: Kelvinsong.)

During the fusion process, a portion of the energy produced generates outward pressure that counterbalances gravity, supporting the Sun and preventing its inner layers from collapsing. The remaining energy diffuses outward as radiation through the upper layers of the Sun, eventually reaching the solar surface and propagating into space. Almost all of the fusion process, about 99%, occurs within 0.24 $R_\odot$, and by 0.3 $R_\odot$, thermonuclear reactions cease almost entirely. The initial composition of the core, by mass, was similar to that of the rest of the Sun. However, over time nuclear fusion has gradually converted the core's contents, resulting in a depletion of hydrogen and an enrichment of helium.

Surrounding the solar core and extending to approximately 0.7 $R_\odot$ is the **radiative zone**, where the density gradually decreases from $20\,\mathrm{g\,cm^{-3}}$ at the core's outer edge to $0.2\,\mathrm{g\,cm^{-3}}$ at the interface with the convection zone. The temperature similarly drops from 7 MK to 2 MK across this distance. In the radiative zone, energy is transferred primarily through radiation (see the top equation in 1.4). Photons produced by the core's nuclear fusion process scatter off ions and electrons so frequently that their journey through this dense layer of ionised gas takes tens or even hundreds of thousands of years. Upon reaching the upper edge of the radiative zone, these photons encounter the interface layer. Since there are no thermonuclear reactions in the radiative zone, the composition of its elements has remained relatively constant since the Sun's formation.

In the early 1900s, helioseismic observations of the Sun revealed that the outer convective zone of the Sun undergoes differential rotation, similar to fluid motions. In contrast, the inner radiative zone exhibits rigid and uniform rotation, similar to a solid body. This led to the discovery of a thin interface layer between these two regions, where a sharp transition between the different rotational laws results in a great shear profile, causing successive horizontal layers to slide past one another (Spiegel and Zahn, 1992). This shear layer is called the **tachocline** and is believed to play an important role in forming the large-scale solar magnetic field (for more details, see Section 1.1.3).

The thickness and centre of the radius of the tachocline at the solar equator were determined by Charbonneau et al. (1999) to be $w = 0.039 \pm 0.013$ $R_\odot$ and $r_c = 0.693 \pm 0.002$ $R_\odot$, respectively. According to helioseismic measurements, this region is slightly prolate, with the centre of the radius being closer to the surface by approximately $\sim 0.024 \pm 0.004$ $R_\odot$ at a latitude of 60° compared to the equator (Charbonneau et al., 1999).

The outermost layer of the solar interior is known as the **convection zone**, which spans from about 0.7 $R_\odot$ to near the visible surface. At the base of this zone, the temperature is approximately 2 MK, and the density is only around $0.2\,\mathrm{g\,cm^{-3}}$. This relatively low temperature and density allow ions to recombine with their electrons, producing neutral atoms that make the plasma more opaque to high-energy photons. Consequently, radiation becomes an inefficient method to transfer heat energy outward. As a result, the trapped heat makes low-density plasma buoyant, leading to the formation of circular convection currents.

The heated plasma at the base of the convection zone expands, causing it to decrease in density and rise upward toward the photospheric surface. Once it reaches the surface, it cools down through radiation and diffusion and then sinks back down into the interior to heat up again, thus continuing the convective cycle. The mass movement of the plasma makes the convection zone highly turbulent and allows it to rapidly transport heat to the surface, where the temperature drops to 5,700 K and the density approaches zero. The effect of this convective motion is visible on the solar surface in the form of granulation, which will be discussed in more detail in Section 1.1.4.3. The convection zone is also essential

in generating phenomena like active regions and flares by twisting the magnetic field as it passes through this region. (For further details, see Section 1.1.3).

1.1.2 The Solar Atmosphere

The atmosphere of the Sun is composed of four distinct layers: the photosphere, the chromosphere, the transition region and the corona. Each layer exhibits unique characteristics and leaves a distinct fingerprint on the solar spectra. However, these layers are not a set of static planes but rather highly inhomogeneous and dynamic that constantly moving and changing in temperature and density. As a result, it is impossible to consider the effects of these atmospheric layers on solar phenomena in isolation, as they are interconnected to varying degrees. Figure 1.4 is a schematic plot for the average temperature and density of the solar atmosphere layers as a function of the height from the photosphere surface.

The **photosphere** is the visible surface of the Sun and is the layer that emits light and heat. It is the lowest layer of the Sun's atmosphere and has a temperature of around 5,500 degrees Celsius. The photosphere is also the region where most of the Sun's visible light is emitted, and its density is around $10^{-7} kg\ m^{-3}$. The photosphere is composed of granules that are created by the convective motion of hot gas rising from the Sun's interior and cooler gas sinking back down. These granules can be observed as small, bright, and dark areas when the Sun is observed with a telescope. The photosphere is also the region where sunspots appear, which are darker areas that are cooler than the surrounding gas. The photosphere is a critical layer of the Sun's atmosphere as it is the region where the energy produced in the Sun's core is released into space. The photosphere is generally considered to be a thin layer, only a few hundred kilometres thick, located at the top of the Sun's convective zone where the temperature and pressure are low enough for atoms to recombine into neutral atoms and photons to escape freely. it is typically considered to be at a height of around 500 kilometres above the Sun's surface.

The **Chromosphere** is located above the photosphere and has a height range of about 2 Mm. Its temperature varies from 5,800 K at the photosphere to 25,000 K at the edge. The Chromosphere has two main characteristics: an increase in temperature with height and a constantly changing complex structure. Hydrogen emits Hα at high temperatures, which can be observed using spectrograph filters. Hα absorption reveals features of the Chromosphere such as spicules, which are plasma jet-like protrusions that can extend up to 10,000 km and have short lifetimes ranging from 1 to 15 minutes. Approximately 30,000 spicules exist at any given time, covering 2-3% of the Sun's surface. The Chromosphere is important because flares release most of their energy in this layer.

The region that follows the Chromosphere is called the **Transition Region** and it is approximately 100 km deep. This region experiences a rapid increase in temperature, reaching between 2 $\times$ 105 - 106 K. As we move further away from the Sun, the gas pressure drops off quickly while the magnetic pressure drops off more slowly. This means that the ratio of gas pressure to magnetic pressure, called plasma beta (β), becomes $\beta < 1$, and the plasma is shaped by the magnetic field. As a result, the structures we observe, such as coronal loops and spicules, are defined by the magnetic field. Flows and dynamic activity dominate in this region due to the magnetic field shaping the plasma.

The **Corona** is the final layer in the solar atmosphere and can be seen as a white halo surrounding the Sun during a total solar eclipse. The temperature in this layer ranges

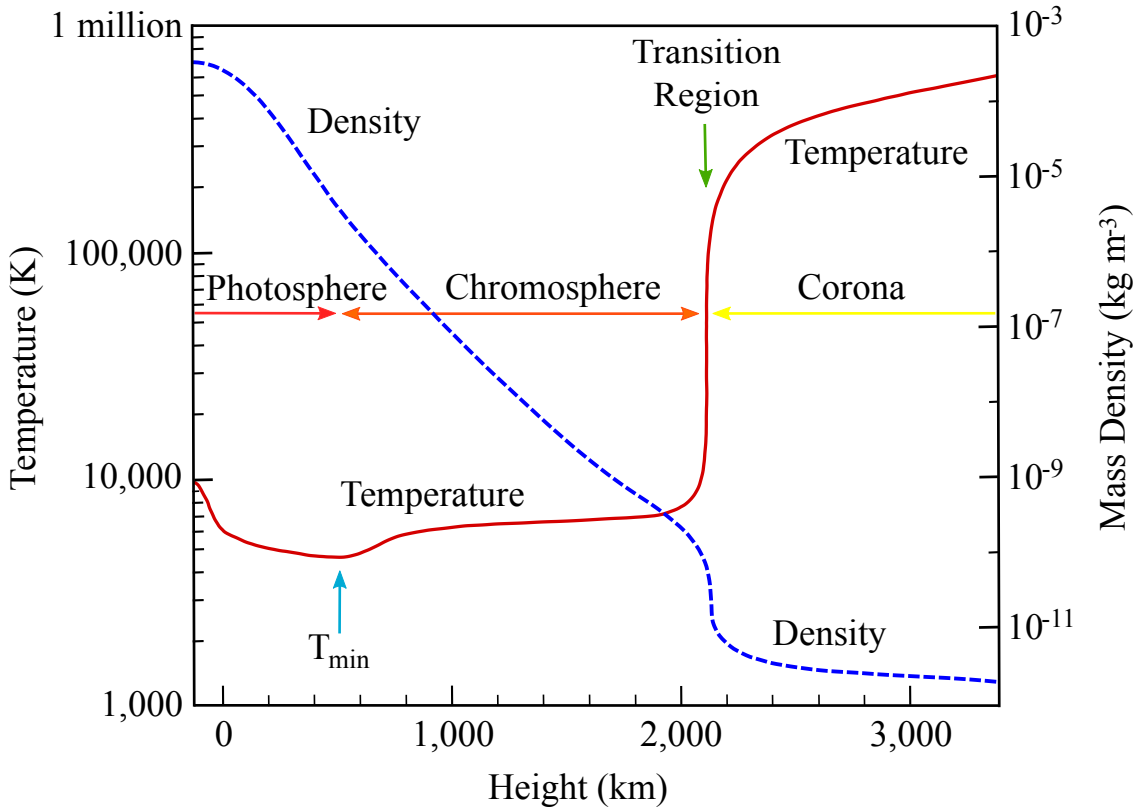

FIGURE 1.4: The profiles of temperature (solid red line) and mass density (dashed blue line) with respect to the height in the solar atmosphere according to the VAL model (Vernazza, Avrett, and Loeser, 1981).
(Image credit: adapted from Original Figure by Eugene Avrett, Smithsonian Astrophysical Observatory, with modification.)

from a few million Kelvin and the corona's visible extent extends out to several million kilometers, although its effects can be seen as far as the edge of the heliosphere at 100 AU. The corona emits radiation in a wide range of wavelengths, including X-rays, Extreme Ultraviolet (EUV), and radio. It has a very low density near the Sun, typically 108 - 109 particles cm^{-3}, making it essentially transparent to most electromagnetic radiation and not in local thermal equilibrium. The Coronal Heating Problem is a major unsolved issue in solar physics as it is still unclear how magnetic energy dissipates within the corona to heat the plasma to such high temperatures. The solar wind originates from the corona and its effects can be seen throughout the entire solar system. The slow solar wind is made up of streams of ions and electrons which flow outwards from the Sun at a speed of 440 km/s and a temperature of 83,000 K. The speed of the solar wind can reach thousands of km/s at 1 AU in regions where the magnetic flux is open (coronal holes).

1.1.3 The Solar Dynamos

The first evidence for the presence of magnetic fields on the Sun came from the studies of sunspots by Hale (1908). This discovery led to the question of why magnetic fields should even exist on the surface of a rotating body such as the Sun (Larmor, 1919). Furthermore, long-term solar observations have revealed that the large-scale magnetic activity of the Sun

is remarkably organised, exhibiting a periodic cycle of approximately eleven years. During each cycle, the Sun exhibits a range of magnetic phenomena, collectively referred to as "solar activity", which vary in spatial and energy scales (for more information, see Section 1.1.4). The variation in activity level during each cycle suggests that the Sun's magnetic field is continuously being regenerated.

The solar dynamo is the leading theory that provides a reasonable scientific explanation for the mechanisms behind cyclic magnetic fields and their manifestations on the Sun. This theory originates from a field in physics known as magnetohydrodynamics (MHD), which studies the magnetic properties of electrically conducting fluids. The solar dynamo theory explains the process in which the mechanical energy of the plasma flow inside the Sun can be converted into magnetic energy by stretching and twisting the magnetic field lines. It demonstrates that the interactions of the flow with the magnetic field maintain the field against Ohmic dissipation.

While understanding the solar dynamo theory is crucial for explaining stellar activity and dynamo models in other active stars, the technical details of this complex theory are beyond the scope of this thesis. For the sake of simplicity, I will only present a simplified version of the theory and avoid delving into technical terms.

As explained earlier, the convection zone of the Sun contains turbulent streams of ionised plasma. The flow of these charged particles generates electric currents, which in turn create magnetic fields through Ampère's law:

$$\nabla \times B = \mu_0 J, \tag{1.13}$$

where B represents the magnetic field, μ_0 is the magnetic permeability constant, and J is the electric current density.

The change in the magnetic fields, in turn, induces electric currents, as described by Faraday's law of induction:

$$\nabla \times E = -\frac{\partial B}{\partial t}, \tag{1.14}$$

where E represents the electric field.

The electric field and the current density can be related using Ohm's law:

$$J = \sigma \left(E + v \times B \right), \tag{1.15}$$

where v is the velocity of a fluid element of the plasma, and σ is the electric conductivity of the fluid.

By combining these three equations, it is possible to eliminate E and J and derive a simplified equation known as the MHD induction equation (see, e.g., Davidson, 2001):

$$\frac{\partial B}{\partial t} = \frac{1}{\mu_0 \sigma} \nabla^2 B + \nabla \times \left(v \times B \right). \tag{1.16}$$

The term $1/\mu_0\sigma$, usually expressed as η, is known as the magnetic diffusivity in plasma physics and has SI units of $\mathrm{m\,s^{-2}}$.

The MHD induction equation describes the dynamics and evolution of the magnetic field in plasma under some initial conditions and assumptions that the theory entails. For instance, for the solar dynamo problem: (i) the flow must be turbulent, not just like a stream.

(ii) It has to exhibit a certain degree of helicity (Seehafer, 1996). (iii) It is required to be three-dimensional, which implies that it must have components in the radial, meridional (north-south), and latitudinal (azimuthal) directions. (iv) The dynamo mechanism must be sufficiently complex. This is because Cowling's anti-dynamo theorem states that a purely axisymmetric magnetic field, which vanishes at infinity, cannot be maintained through dynamo action (Cowling, 1933). Therefore, dynamo models that rely heavily on symmetrical configurations are not viable. (v) Effective differential rotation is necessary for the dynamo process Schou et al. (1997). This is because the motion of plasma can convert a north-south oriented (poloidal) magnetic field into an azimuthal (toroidal) magnetic field, and vice versa. (vi) The tachocline as a narrow region where a rapid change between constant and differential rotations takes place and creates an extremely sheared plasma flow must be presented. (vii) Finally, the meridional circulation of the Sun is needed to explain irregularities in the solar cycle. The meridional flow is observed via helioseismology to be along meridian lines from the equator toward the poles at the surface and from the poles to the equator at some depth. The poleward flow near the surface is slow, of the order of $20\,\mathrm{m\,s^{-1}}$, while the equatorward return below the surface is even slower, with speeds of the order of 1 to $2\,\mathrm{m\,s^{-1}}$, as it carries the material in much higher density.

Under these prerequisites, Equation (1.16) describes the operation and evolution of the dynamo as follows: There are two contributors to the variation of the magnetic field. The first term on the right side of the equation represents an Ohmic diffusion process due to the plasma's conductivity. The second term represents an advection due to the bulk plasma motion with velocity v. The relative effect of these two terms, diffusion or advection of a magnetic field, can be estimated by the magnetic Reynolds number, a dimensionless parameter denoted by $\mathrm{R_m}$:

$$\mathrm{R_m} = \mu_0 \sigma L V = \frac{LV}{\eta}, \tag{1.17}$$

where V and L represent values for typical velocity and length scales of the flow, respectively.

If the magnetic Reynolds number is much larger than 1, advection dominates. In the opposite limit, if $\mathrm{R_m}$ is much smaller than 1, then diffusion dominates. For the solar dynamo action, where L is on the order of the solar radius, $\mathrm{R_m}$ is consistently much larger than 1. Therefore, Ohmic diffusion is highly ineffective over such a large spatial scale, and there is no problem in maintaining a solar magnetic field against diffusion. Under this condition, Alfvén's theorem, also known as the frozen-in flux theorem, can be applied. This theorem implies that the magnetic field lines are frozen into the plasma and have to move along with it (Alfvén, 1942). As a result, the magnetic field can be amplified by stretching a field line when $\mathrm{R_m} \gg 1$. A helpful analogy is to think of flux tubes as rubber bands. In the same manner that stretching, twisting, and folding rubber bands would increase their tension and pressure, stretching out, folding, and twisting magnetic field lines by the plasma flow can strengthen the field and, at specific points, even change its direction.

All the above-mentioned physical laws, theorems and assumptions of the solar dynamo model can be summarised in a two-step model called alpha-omega ($\alpha\Omega$) dynamo. The first step, known as the Ω effect, states that if we start with a poloidal magnetic field, the differential rotation of the Sun would deform and twist this field around the Sun. The stretching effect is stronger at the equator than at the poles, resulting in the transformation of the original poloidal magnetic field into a toroidal one near the equator after several rotations (as shown in the upper section of Figure 1.5). The Ω effect is driven by a combination of a

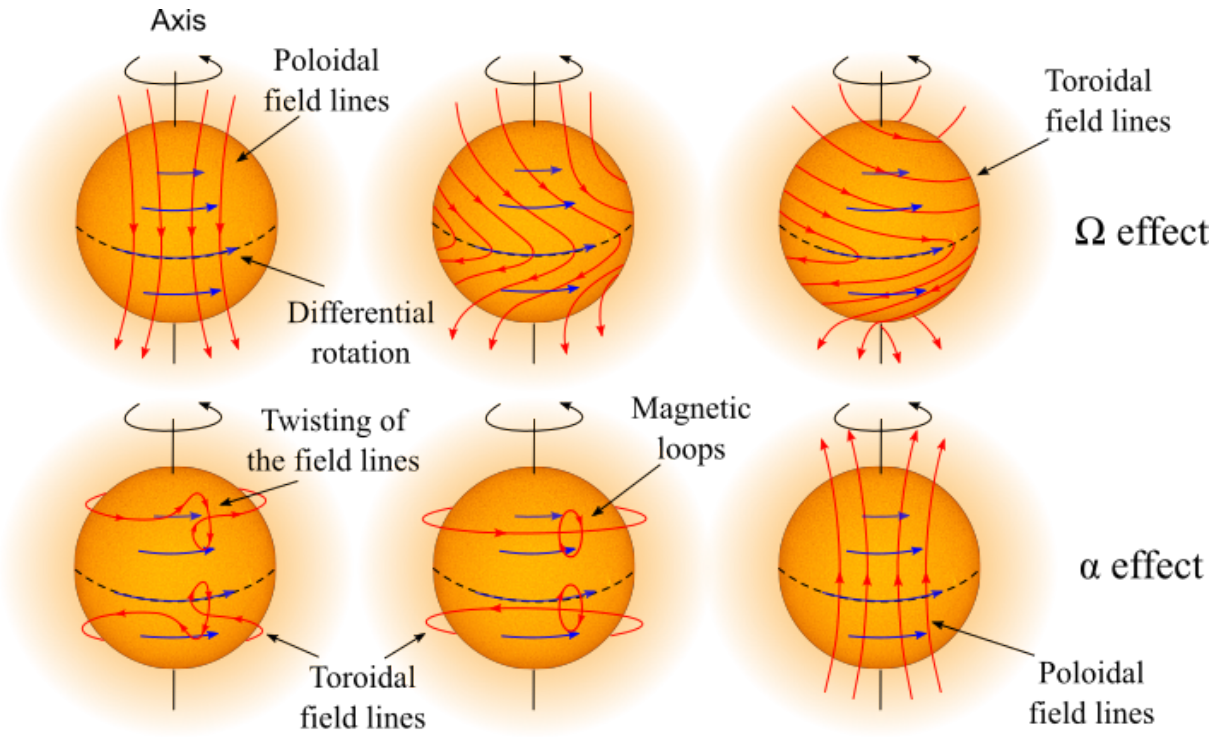

FIGURE 1.5: Magnetic field structure of the Sun: Ω effect converts poloidal field to toroidal field via differential rotation. α effect twists toroidal field as it rises with convection cells.

large magnetic Reynolds number (R_m) and a sheared toroidal rotation around the equator, which transform the poloidal magnetic field into a toroidal magnetic field with opposite directions in the Northern and Southern hemispheres. Furthermore, the magnetic field lines are intensified as a result of the frozen-in flux theorem.

The second step of the $\alpha\Omega$ dynamo model, known as the α effect, explains the conversion of a toroidal magnetic field into a poloidal one through the twisting of the magnetic flux strands that are lying in the toroidal (azimuthal) direction (see the lower section of Figure 1.5). In this process, magnetic flux tubes located in shallow depths and low latitudes in the convection zone come together to form concentrated magnetic ropes. These ropes rise to the surface via magnetic buoyancy and produce the bipolar magnetic fields associated with a pair of sunspots when they break through the solar surface (Parker, 1955b). At this stage, the Coriolis effect comes into play and starts to twist and expand the rising flux tubes, leading to the twisting of the magnetic field lines as well. The reversed sign of both the Coriolis force and the toroidal magnetic field in the northern and southern hemispheres results in the formation of small-scale magnetic field loops of the same polarity in both hemispheres (Coriolis, 1835). Over time, these small-scale loops gradually coalesce due to magnetic diffusivity, resulting in the generation of a large-scale poloidal magnetic field (Parker, 1955a). This completes the two-step alpha-omega dynamo model, which explains how the Sun's magnetic field constantly regenerates by transforming from poloidal to toroidal and vice versa. During solar maxima, toroidal magnetic fields generate sunspots and other activity-related phenomena, while poloidal fields predominate during solar minima. The solar cycle repeats every approximately 11 years, with the associated magnetic fields switching polarity from

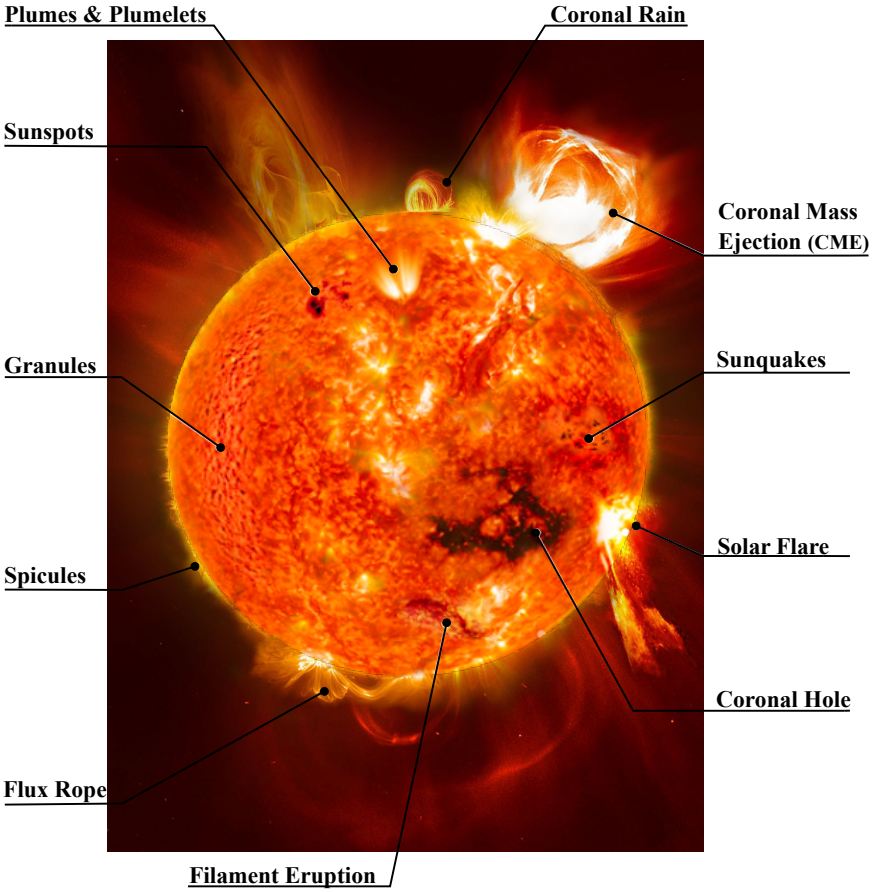

FIGURE 1.6: View of Solar surface features and emission phenomena. (Image credit: adapted from Original Figure by NASA/Mary Pat Hrybyk-Keith, with modifications.)

one cycle to the next. This results in the observed 22-year solar cycle (Babcock, 1961).

1.1.4 The Solar Activity

As stated earlier in the previous section, the Sun's large-scale magnetic field undergoes constant regeneration, resulting in a dynamic and active star. Simultaneously, the solar atmosphere exhibits a plethora of variability phenomena that constantly change and evolve over timescales ranging from minutes to years. These phenomena appear to be closely bound to the Sun's magnetic field and occur mostly in groups. Examples of these phenomena include *sunspots, faculae, spicules, plages, solar flares, coronal mass ejections* (CMEs), *filaments*, and *coronal holes*, among others. Figure 1.6 provides a visual representation of some of the fascinating features of the Sun's activity. Since these phenomena can only be observed with high spatial resolution on the Sun, observations of other stars, which are often disc-integrated, are usually interpreted in the context of solar activity. In this section, I will focus on the activity features that are most relevant to the phenomena observed on other stars studied in this thesis and discussed in later chapters. For the remaining phenomena, a brief description will be provided for completeness.

1.1.4.1 Sunspots

Sunspots are dark regions on the surface of the Sun that form when intense bundles of magnetic field lines from the solar interior break through the photosphere, creating tube-like structures and inhibiting the onset of convection (See Figure 1.7). The presence of the flux tubes prevents hot plasma from rising immediately from the deeper layers of the convection zone and replenishing the material within the forming spot. Additionally, the convective inhibition delays the transport of material from within the sunspot back into the stellar interior, allowing the material to cool at the surface for a longer duration. As a result, the cooler material within the sunspot appears as a dark feature amidst the hotter and brighter surroundings, making it easily observable. For an in-depth review of the general properties of sunspots, refer to Solanki (2003).

Telescopic observations of sunspots have been recorded by astronomers since the early 1600s, but evidence exists that sunspots have been observed with the naked eye for even longer, dating back as far as 800 BC (Mossman, 1989; Stephenson, 1990; Hetherington, 1996). Astronomers have observed that sunspots appear in cycles lasting approximately 11 years. Additionally, they noticed that sunspots tend to initially emerge in pairs or groups located at about 30 to 35 degrees above and below the solar equator. As the cycle progresses, the mean latitudes of subsequently appearing sunspots migrate towards the solar equator. This phenomenon is known as Spörer's Law, named after the German astronomer Gustav Spörer who first described it in 1879 (Spörer, 1879; Solanki, 2003). Early observations of sunspots by astronomers such as Richard Carrington in the mid-19th century also contributed to a better understanding of this phenomenon (Carrington, 1863). Closely related to Spörer's Law is Joy's Law, which describes the tendency for sunspots to be tilted such that the leading spots are closer to the solar equator than the following spots. The degree of tilt increases as the latitude of the sunspot region increases (Hale et al., 1919). Plotting the pattern of sunspot emergence over time forms the famous "butterfly diagram" (See Figure 1.8).

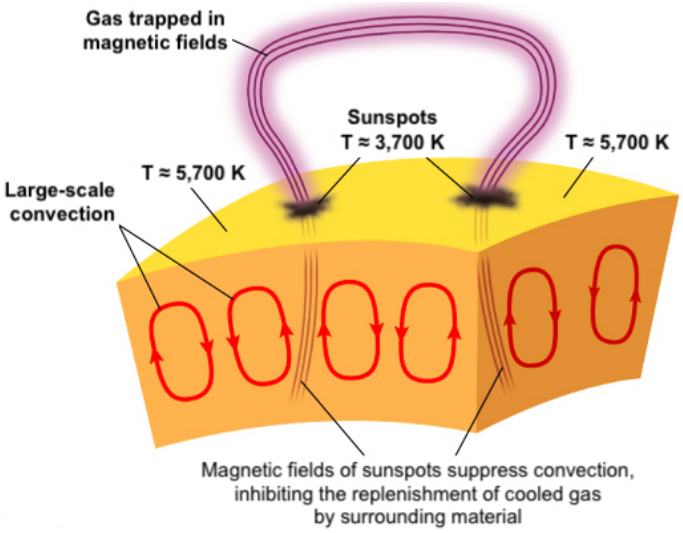

FIGURE 1.7: Schematic formation of a sunspot, where the convective motion of plasma is inhibited by magnetic fields, leading to a localised cooling of the Sun's surface.
(Image credit: adapted from an illustration © Addison Wesley, with modifications.)

In the early 20th century, George Hale made a breakthrough discovery when he observed the Zeeman splitting of spectral lines from sunlight. This observation provided evidence for the existence of magnetic field lines at the surface of the Sun (Hale, 1908). Subsequently, Hale and other astronomers deduced that sunspots were regions of particularly strong magnetic fields, which appeared dark in contrast to their surroundings because they were cooler, with temperatures around 3,700 K compared to about 5,700 K for the surrounding areas. They also realised that sunspots typically emerge in regions of bipolar magnetic fields, where pairs

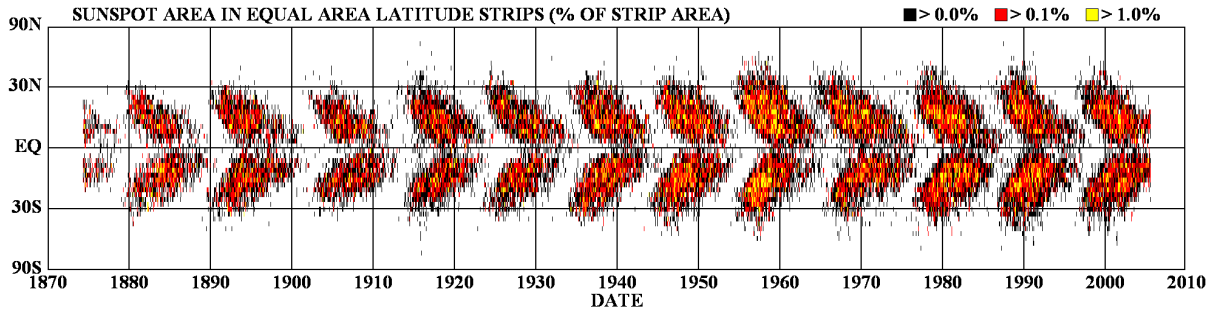

FIGURE 1.8: The butterfly diagram, a visualization of sunspot emergence over time and latitude, with sunspot area represented by colour intensity. (Image credit: Hathaway, 2010)

of sunspots with opposite magnetic polarities are observed at the North and South ends of the bipolar region (Hale, 1915). Moreover, they discovered that the 11-year sunspot cycle was actually part of a larger 22-year cycle, where the polarity of the magnetic fields in sunspots reversed after the first 11 years. This phenomenon is known as Hale's Polarity Law (Hale, 1924).

The size distribution of sunspots can vary widely during a solar cycle, with some spots as small as 1,500 km in diameter and others reaching sizes up to 20,000 km. However, even the largest sunspots cover only a small fraction of the solar surface, typically less than 1% (Strassmeier, 2009). The distribution of sunspot sizes across the solar surface follows a log-normal function, meaning that there are many more small sunspots than large ones (Bogdan et al., 1988). The average coverage of sunspots on the Sun also depends on the phase of the solar cycle and ranges from 0.0001% to 0.1% (Strassmeier, 2009). Sunspots can last from a few days to several weeks, with an average lifetime of about two to four weeks. The lifespan of a sunspot depends on various factors such as its size, magnetic complexity, and location on the Sun's surface (Solanki, 2003). McIntosh (1990) has developed a classification system for sunspots based on their morphological characteristics, including their size, shape, and complexity. This system expands on the Zurich classes and produces 60 different types of sunspot groups.

1.1.4.2 Solar Flares

Solar flares have been studied for over a century, with the first observation recorded by Richard Carrington in 1859. While studying sunspots on the solar surface, Carrington noticed brightenings in the same area, which we now call a white light flare. These observations coincided with telegraph disruptions globally and Northern Lights visible as far south as Cuba, marking the first-ever recorded space weather event. This event opened the door for solar flare research, which has since become a thriving field of study. Solar flares are of great significance not only for their effects on Earth, but also for their applications to exoplanets.

Solar flares are sudden and intense brightenings in the solar corona that can be seen across all wavelengths. They result from the rapid reconfiguration of the magnetic field and often accompany a mass motion of fast-moving high-energy particles known as Coronal

Mass Ejections (CMEs). Solar flares are powerful events that can release energy outputs of up to 10^{32} ergs. Prior to a flare, the magnetic field becomes stressed and twisted, causing a build-up of magnetic energy in the form of current. When the magnetic field structure simplifies through magnetic reconnection, this energy is converted into kinetic, thermal, and particle acceleration.

Magnetic reconnection is a process that causes a change in the topology of an almost ideal plasma's magnetic field (i.e., $E + v \times B = 0$). Prior to a solar flare, the magnetic field becomes twisted, which generates a buildup of magnetic energy. Imagine this scenario in a set of coronal loops where the fully ionized plasma of the corona is guided by a magnetic field. If the topology of the magnetic field changes, the path that particles and plasma follow must also change. This change occurs within a region called the diffusion region, a boundary layer where disconnection and reconnection take place. Within this layer, dissipation causes changes in the magnetic field topology (Shibata and Magara, 2011). The increase in diffusivity is due to large gradients in the magnetic field, B. As a result, plasma particles can switch to different parts of the magnetic field, which can then reconnect. This process releases energy from the system, followed by the relaxation of the magnetic field to a lower energy state. This liberated energy is responsible for many of the phenomena observed on the Sun's surface and other events that occur in the solar system.

Solar flares typically originate from active regions on the Sun, which are often associated with sunspots. However, flares are often accompanied by other observable phenomena that occur in or around the active region. For instance, two or more footpoints are always present during a flare release, which appear as bright patches within the active region in the lower atmosphere. These footpoints form the ends of coronal loops with one positive and one negative polarity, connecting the loop to the photosphere.

Footpoints, which appear as bright patches within an active region in the lower atmosphere, are always present during a flare release. These footpoints form the ends of coronal loops with one positive and one negative polarity, connecting the loop to the photosphere. Footpoints are also connected to another important feature of flares called flare ribbons, which are the most prominent feature of a solar flare and result from particle beams accelerated via magnetic reconnection. Flare ribbons can be observed in Hα and ultraviolet (UV) wavelengths and occur at the same time as the flare release. They can be observed to separate from each other as the flare progresses, brighten briefly, and then dissipate and disappear. Flare ribbons represent the footpoints of coronal loops within the chromosphere that have reconnected. During the reconnection, accelerated particles flow down from the site of reconnection along the magnetic field producing bright ribbon-shaped features in the lower chromosphere. Flare ribbons are important for providing details about the topology of the magnetic field during the reconnection process, as they can reveal information about the way in which the magnetic field reconnects.

1.1.4.3 Other Magnetic Phenomena

To provide a more comprehensive understanding of the solar activity, this section will present a concise overview of several noteworthy phenomena, which are illustrated in Figure 1.6.

Coronal Hole

A coronal hole is a fascinating and enigmatic feature of the Sun's outer atmosphere, the corona. It is a region characterised by significantly lower levels of temperature and density compared to its surroundings. These dark, cooler regions appear as vast, open areas when observed in ultraviolet or X-ray wavelengths. Coronal holes are important as they are sources of high-speed solar wind particles that escape into space, creating disturbances in the magnetosphere and influencing space weather.

Coronal mass ejection (CME)

Coronal mass ejections (CMEs) are colossal eruptions of plasma and magnetic fields from the Sun's corona. They involve the expulsion of a massive amount of charged particles, mainly protons and electrons, into space at high speeds. CMEs are often associated with solar flares and occur due to the sudden release of magnetic energy stored in the Sun's corona. When the magnetic field lines undergo a magnetic reconnection, the rearrangements of the magnetic field lines release a tremendous amount of energy and propel the plasma and magnetic field outward. As a result of a CME, a vast cloud of magnetised plasma, known as a CME cloud, is ejected into space. These CME clouds can expand over millions of kilometres and travel at speeds ranging from a few hundred to thousands of kilometres per second. They carry an enormous amount of energy and can release billions of tons of matter into space. CMEs have the potential to cause significant impacts on Earth and other planets in the solar system. When a CME cloud reaches the Earth, it interacts with the planet's magnetic field, leading to geomagnetic storms. These storms can disrupt satellite communications, power grids, and navigation systems. Additionally, CMEs can trigger stunning auroras when the charged particles interact with the Earth's upper atmosphere.

Coronal Rain

Coronal rain also occurs in the Sun's corona. It refers to the sight of hot plasma raining back down onto the Sun's surface in the form of cool, dense droplets. These droplets are made up of ionised gas, and they appear like fiery tongues gracefully descending before fading away. Coronal rain is primarily observed near sunspots or regions of intense magnetic activity. The underlying cause of this mesmerising spectacle is the interplay between magnetic fields and plasma dynamics. As magnetic loops in the corona get twisted and stressed, they can become unstable and release the trapped plasma, which then falls back to the Sun along the loops due to gravity.

Faculae & plages

Faculae are bright, luminous areas on the surface of the Sun associated with the presence of strong magnetic fields (Spruit, 1976). They are typically small, bright spots or patches that are brighter than the surrounding photosphere, with temperatures around 100 K hotter than the rest of the photosphere (Thomas and Weiss, 2008). These areas are commonly found in the intergranular lanes and are often seen near sunspots. In fact, sunspots are almost always surrounded by faculae and plages. Faculae, however, can exist on their own and are often grouped together into large networks. Due to their shape as thin flux tubes with bright walls, they are most visible near the edge of the sun. Faculae have lifetimes of

a few hours, but groups of faculae can remain on the surface of the sun for several weeks and even several cycles (Hirayama, 1978). They always appear before sunspots and can outlive them as well. Since faculae are not noticeably brighter than the surrounding quiet photosphere and are uniformly distributed across the solar disc, their photometric effect is usually negligible. Nonetheless, due to their strong magnetic fields, faculae, like sunspots, can induce a significant signature in spectroscopic observations. It is worth mentioning that these two types of magnetic features are often referred to as "active regions" in the field of solar and stellar astronomy.

Filaments

Filaments, also known as prominences when observed at the limb, are long-lived, stable features in the solar atmosphere that appear as long, thin, dark structures against the solar disk (Engvold, 2015, and references therein). However, filaments within active regions tend to be shorter in length, lower in height, and have shorter timescales than those in the quiet Sun (Parenti, 2014). They consist of relatively cool, dense plasma suspended against gravity by the magnetic field in the corona, forming along a polarity inversion line (PIL) in photospheric magnetic fields (Parenti, 2014; Chen, 2017). In force balance, filaments have outward magnetic pressure in the filament channel balanced by the downward tension of the strapping field above.

Filament eruption occurs when the force balance is catastrophically lost via resistive processes such as breakout reconnection (Antiochos, 1998; Antiochos, DeVore, and Klimchuk, 1999) and tether-cutting (Moore et al., 2001), or via an ideal instability such as the kink (Török and Kliem, 2005) and torus (Kliem and Török, 2006) instabilities (Chen, 2011, and references therein). Active region filaments are often associated with magnetic flux emergence, which can destabilize the filament and trigger an eruption (Schrijver and Siscoe, 2011).

Flux Rope

A flux rope is a magnetic structure that is thought to be at the heart of many of the Sun's eruptions. It is characterised by a twisted magnetic field configuration resembling a helical rope. The formation of a flux rope arises from the interplay between magnetic fields and plasma dynamics. As magnetic fields become twisted and stressed, they can undergo a magnetic reconnection process, which rearranges the field lines and leads to the formation of a rope-like structure. Flux ropes are of significant interest as they play a crucial role in various phenomena, such as solar flares, coronal mass ejections, and geomagnetic storms.

Granules & supergranules

Granules are small-scale convective cells that cover the solar photosphere, the visible surface of the Sun. They appear as bright, grain-like structures and are typically around 1,000 kilometers in diameter. Granules form due to the convective motion of plasma beneath the photosphere. Hot plasma rises to the surface, creating bright regions, while cooler plasma sinks back down, creating darker regions. Granules have an average lifespan of a few minutes and are constantly in motion, contributing to the overall dynamics of the solar surface. Supergranules, on the other hand, are larger-scale convective cells that span approximately

30,000 kilometers in diameter. They are composed of multiple granules and are characterized by slower and longer-lasting flows compared to granules. Supergranules have an average lifetime of around 24 to 48 hours. These structures are important in redistributing heat and magnetic fields across the solar surface, playing a significant role in the overall energy transport of the Sun.

Plumes & Plumelets

Plumes, also known as chromospheric plumes or spicules, are narrow, jet-like structures that extend vertically from the solar surface into the chromosphere. They are typically observed as dark features against the bright background of the chromosphere. Plumes can reach heights of several thousand kilometres and have lifetimes ranging from a few minutes to tens of minutes. They are believed to be caused by the interaction of convective motions and magnetic fields in the solar atmosphere. Plumes play a role in the transfer of energy and mass between the Sun's surface and the outer layers of the solar atmosphere.

Plumelets are smaller and more short-lived variations of plumes. They are often seen as smaller, fleeting spikes or protrusions on the edges of larger plumes. Plumelets exhibit similar behaviour as plumes but at smaller spatial scales, as a result, they are thought to be associated with the same underlying processes of convective motions and magnetic fields.

Spicules

Spicules are narrow, jet-like structures that extend vertically from the solar surface into the chromosphere. They are characterised by their rapid and dynamic nature, shooting up from the solar surface at speeds of around 20 kilometres per second and reaching heights of several thousand kilometres. They typically have a lifespan of a few minutes to tens of minutes. When observed, they appear as dark, elongated structures against the brighter background of the chromosphere. These structures are believed to be caused by the interaction of convective motions and magnetic fields in the solar atmosphere. It is thought that spicules result from the rapid upward motion of plasma along magnetic field lines. As plasma is propelled upwards, it cools and condenses, giving the spicules their dark appearance. Spicules play a significant role in the transfer of energy and mass within the Sun's atmosphere. They contribute to the heating of the chromosphere and the outer layers of the solar atmosphere. Spicules also participate in the replenishment of material in the corona and the solar wind, influencing space weather and the dynamics of the Sun-Earth system.

Sunquakes

Sunquakes are seismic events, analogous to earthquakes on Earth, that occur on the Sun but on a much larger scale. They are essentially vibrations or seismic waves that ripple through the solar interior and are triggered by powerful solar flares or eruptive events. When a solar flare or eruption releases a tremendous amount of energy, it generates intense shockwaves that propagate through the Sun's interior. These shockwaves can cause the Sun's surface to oscillate, resulting in the formation of sunquakes, which can travel through the different layers of the Sun, including the photosphere, chromosphere, and into the solar interior.

1.2 Low Mass Stars

Low-mass stars, particularly M dwarfs, are the most abundant stars in the Milky Way galaxy (Henry et al., 2006; Henry et al., 2018). They constitute around two-thirds of the stars in the solar neighbourhood (Winters et al., 2015). Despite their ubiquity, M dwarfs have received relatively little attention until recently due to their small size and intrinsic faintness. With an apparent magnitude greater than 6.7, M dwarfs are too dim to be visible with the naked eye and can only be observed in the solar neighbourhood, even with modern technology.

M dwarfs are the most common product of the star formation process and dominate the stellar mass function. However, with a low mass range of only 0.077 to 0.622 $M_{\odot}$, M dwarfs are just massive enough to initiate and sustain hydrogen fusion in their core, which puts them right on the verge of being a star. They have radii ranging from 0.096 to 0.613 $R\odot$, luminosities between 0.000235 to 0.0757 $L\odot$, and effective temperatures ($T_{\rm eff}$) ranging from 2300 to 3900 K (Cifuentes et al., 2020). Table 1.1 presents a summary of the key stellar properties of M dwarf subtypes as provided by Cifuentes et al. (2020). With these values of luminosity and temperature, M dwarfs occupy the low and dim end of the main sequence on the HR diagram.

Table 1.1: Key stellar parameters of M Dwarf subtypes, compiled from Cifuentes et al. (2020)

Spectral Type	Mass $[M_{\odot}]$	Radius $[R_{\odot}]$	Luminosity $[10^{-4}L_{\odot}]$	$T_{\rm eff}$ K
M0.0	0.622	0.613	757	3900
M0.5	0.578	0.571	585	3800
M1.0	0.556	0.550	496	3700
M1.5	0.524	0.519	409	3600
M2.0	0.475	0.473	306	3500
M2.5	0.432	0.433	228	3400
M3.0	0.386	0.389	161	3300
M3.5	0.338	0.343	111	3300
M4.0	0.302	0.309	87	3200
M4.5	0.253	0.263	50	3100
M5.0	0.195	0.207	28	3100
M5.5	0.159	0.173	20.1	3000
M6.0	0.121	0.138	11.1	2900
M6.5	0.106	0.123	7.2	2750
M7.0	0.101	0.119	3.6	2700
M7.5	0.104	0.121	5.8	2500
M8.0	0.104	0.121	5.1	2500
M8.5	0.088	0.107	3.4	2400
M9.0	0.077	0.096	2.69	2350
M9.5	0.077	0.096	2.35	2300

Due to their low $T_{\rm eff}$, M dwarfs emit most of their radiation in the infrared wavelength regime, which is why they are commonly referred to as "red dwarfs". To illustrate the spectral radiance of M dwarfs over a given range of wavelengths, I used the values for

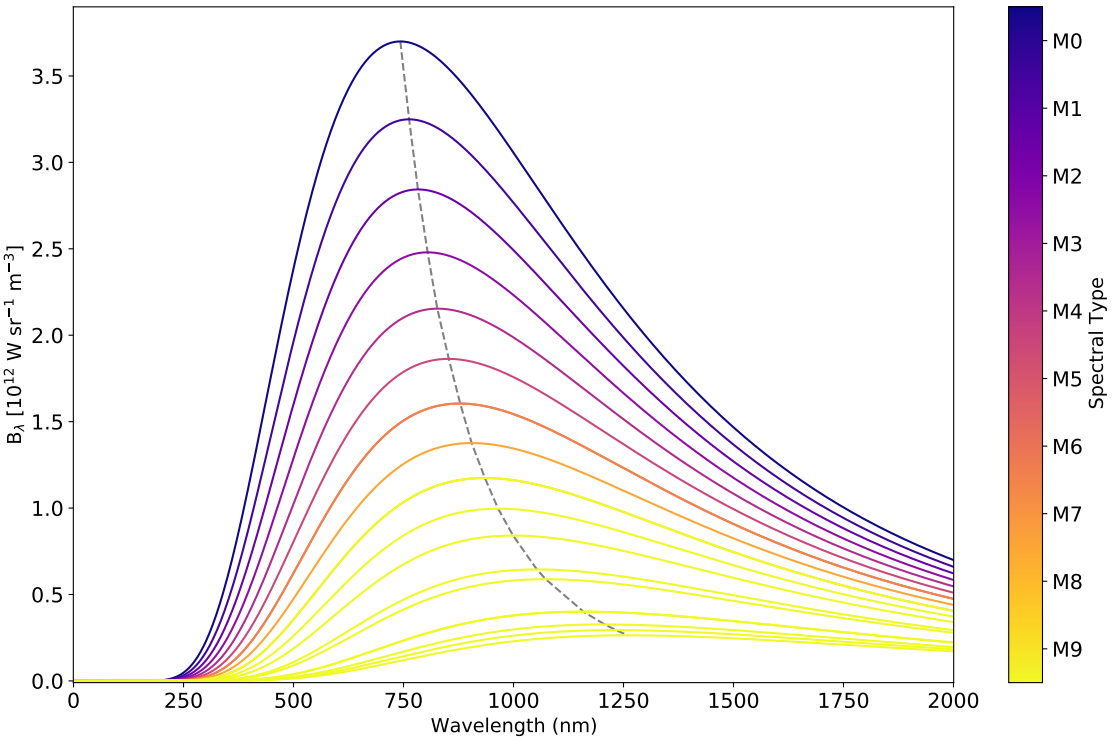

FIGURE 1.9: Blackbody spectral radiance per unit wavelength for different M dwarf subtypes, corresponding to the effective temperatures listed in Table 1.1 and calculated using Equation 1.18. The grey dashed line connects the peaks of the curves at the wavelengths given by Equation 1.19. The graph demonstrates how the peak of the emission curve shifts towards longer (redder) wavelengths as the temperature decreases.

effective temperature from Table 1.1 and Planck's law for black body radiation:

$$B_\lambda(\lambda, T) = \frac{2hc^2}{\lambda^5} \frac{1}{exp(\frac{hc}{\lambda k_B T}) - 1}, \tag{1.18}$$

where $B_\lambda(\lambda, T)$ is the spectral radiance density at a given wavelength λ and temperature T, and h, c, and k_B are Planck's constant, the speed of light in a vacuum, and the Boltzmann constant, respectively. Figure 1.9 displays the resulting spectra that illustrate how the spectral radiance of M dwarfs varies with effective temperature and wavelength. The graph highlights that as the effective temperature decreases, the peak of the emission curve (λ_{max}) shifts towards longer (near-infrared) wavelengths, as indicated by a grey dashed line. This shift follows Wien's displacement law

$$\lambda_{\text{max}} = \frac{b}{T} \tag{1.19}$$

with Wien's displacement constant $b = 2.8977721 \times 10^{-3}$ mK.

Due to their cool surface temperatures, red dwarfs are able to form oxide molecules such as titanium oxide (TiO), vanadium(II) oxide (VO), as well as water (H_2O), methane (CH_4), and other neutral metals in their atmospheres. These molecules are the primary

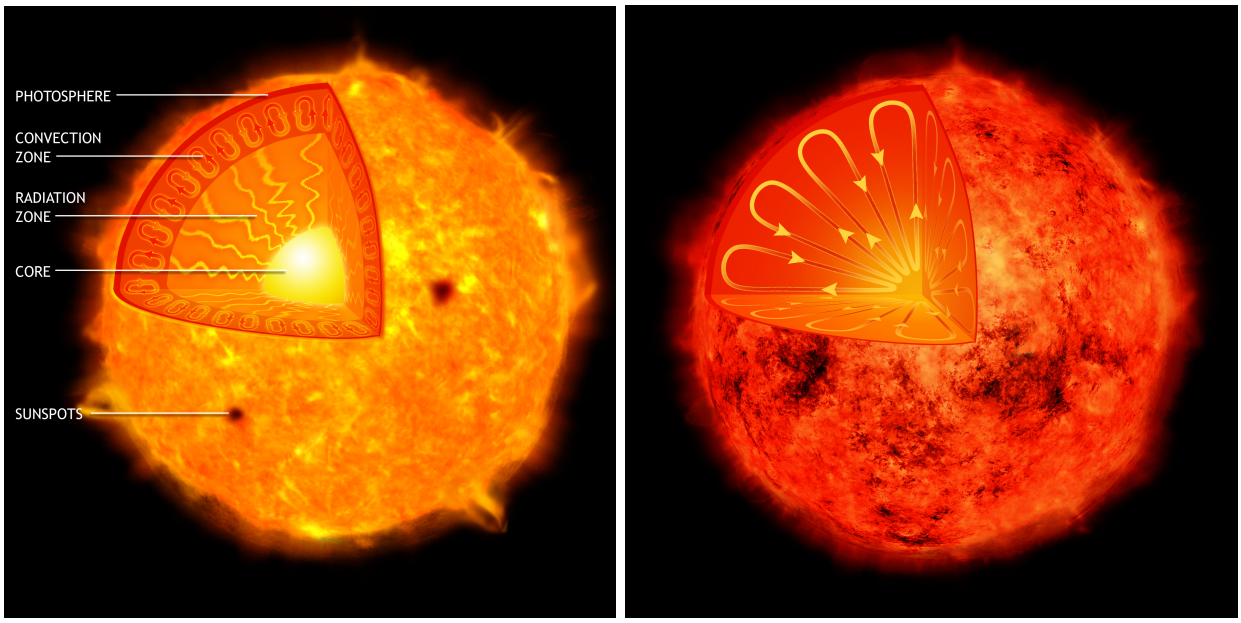

FIGURE 1.10: An artistic representation of the internal structure comparison between a Sun-like star (on the left) and a fully convective star (on the right). (Image credit: NASA/CXC/M.Weiss.)

source of opacity in the cool star's atmosphere, forming dense forests of molecular lines on the stellar spectrum. These prominent features make it challenging to accurately determine atmospheric parameters for M dwarfs, especially when compared to Sun-like stars.

M dwarfs have an estimated lifespan of between 1 and 10 trillion years, which far exceeds the current age of the universe. As a result, no M dwarf has yet reached the advanced stages of evolution and moved off the main sequence. This remarkable longevity is mainly due to the lower mass and internal structure of these stars, which consume their hydrogen fuel at a much slower rate than more massive stars. This is because the lower mass of M dwarfs exerts less pressure on their cores, resulting in a lower fusion rate. Moreover, M dwarfs with spectral type later than M4 and mass < 0.3 $M_{\odot}$ are believed to be fully convective throughout most of their structure (Hawley et al., 2014). This means that they have access to their entire reserve of hydrogen, in contrast to solar-type stars, which have a radiative zone that isolates the core and restricts access to their hydrogen fuel. Full convection also continuously mixes the helium and hydrogen throughout the interior of M dwarfs, preventing the buildup of heavier elements in the core. As heavier elements sink back towards the core, they carry fresh hydrogen with them, facilitating the fusion process and prolonging the lifespan of the star. Figure 1.10 provides a visual comparison between the internal structure of a Sun-like star (on the left) and a fully convective red dwarf (on the right).

Although fully convective M dwarfs lack a tachocline, which might suggest that they would have a negligible magnetic field, the presence of active regions and strong flaring activity indicates otherwise. As low-mass stars have become increasingly popular targets for exoplanet surveys, understanding the mechanisms that generate activity and the strength of activity manifestations in these stars is crucial, particularly with regard to the potential habitability of their exoplanets. In the following sections, we first review the dynamo processes of fully convective stars in Section 1.2.1, and then compare solar and stellar activity

in Section 1.2.2.

1.2.1 Fully Convective Dynamos

Early M dwarfs have an internal structure similar to that of the Sun and other solar-type stars. Therefore, it's theoretically possible for these stars to generate a large-scale magnetic field through the $\alpha\Omega$ dynamo mechanism, which requires a differential rotation and a tachocline. However, M dwarfs with masses below about 0.35 $M_\odot$ are fully convective and lack a tachocline, which suggests that they cannot host a solar-type dynamo (Chabrier and Baraffe, 1997). Despite that, many late M dwarfs exhibit strong activity and follow the typical rotation-activity relationship (Delfosse et al., 1998; West et al., 2004; Reiners and Basri, 2007). The mechanism responsible for generating the complex, large-scale magnetic fields observed in fully convective M dwarfs remains uncertain. However, these stars exhibit a high-order multipole magnetic field topology that differs from the aligned dipole field produced by the $\alpha\Omega$ dynamo (Chabrier and Küker, 2006). This suggests that the conventional $\alpha\Omega$ dynamo may not be able to account for the observed magnetic fields in M dwarfs.

Durney, De Young, and Roxburgh (1993) proposed an alternative process for fully convective stars, which involves a turbulent velocity field generating a chaotic magnetic field, even in the absence of rotation. This process can generate a small-scale magnetic field that is sustained if the magnetic Reynolds number is high enough. However, the resulting magnetic fields are limited to small scales, with length and time scales comparable to that of turbulence. While rotation is not essential in this scenario, it does slightly increase the generation rate of the field. Despite this, the small-scale magnetic field produced cannot account for the high levels of magnetic activity observed in M stars and brown dwarfs. Therefore, Chabrier and Küker (2006) investigated the possibility of generating a large-scale magnetic field using a pure α^2 dynamo process.

According to the α^2 dynamo model, the strength of the field depends on the stellar parameters, such as the rotation rate, with a larger Coriolis force yielding a stronger field. The Coriolis force arises from the movement of matter within a rotating system and acts perpendicularly to the direction of motion and axis of rotation. The α^2 dynamo requires a high Rossby number, which means that the inertial force is much larger than the Coriolis force, resulting in strong Coriolis forces. These forces act on the plasma within the star, generating helical motions that rise from the convective core, leading to the creation of a stable large-scale magnetic field. The rotation of the star can also affect the field, as a faster rotation rate will cause the fields to become more stressed and twisted, leading to a greater number of flares with higher energies (Chabrier and Küker, 2006).

Despite considerable efforts to explain the mechanism(s) responsible for generating magnetic fields in low-mass stars, there remain several unanswered questions and mismatches with observations. For example, Donati et al. (2006) used a combination of spectropolarimetry and tomographic imaging techniques, referred to as Zeeman-Doppler Imaging (ZDI), to construct the magnetic topologies of the fully convective and rapidly rotating M4.0 V dwarf V374 Peg. This study reported the detection of a strong axisymmetric large-scale poloidal field with a very low level of differential rotation. This finding poses a significant challenge to the current theoretical models since both the turbulent dynamo and α^2 dynamo models predict non-axisymmetric large-scale magnetic field configurations for fully convective stars. After this discovery, subsequent studies on early and mid-M dwarfs revealed that

partly convective stars possess a weak non-axisymmetric magnetic field with a significant toroidal component, while fully convective stars exhibit strong poloidal axisymmetric dipole-like topologies. Additionally, the differential rotation drops by an order of magnitude across the theoretical full convection threshold, and the fully convective stars observed so far exhibit nearly solid body rotation (Donati et al., 2008; Morin et al., 2008).

The study by Pipin and Yokoi (2018) proposed a new dynamo mechanism based on cross-helicity that can generate both axisymmetric and non-axisymmetric magnetic fields in rotating stars with convective envelopes. This mechanism, called the γ^2-dynamo, can produce large-scale magnetic fields solely due to turbulent cross-helicity. The researchers compared the properties of the large-scale magnetic field generated by the γ^2-dynamo and the α^2-dynamo using mean-field models. Both generation mechanisms can maintain large-scale dynamos, even for fully convective stars with a solid body rotation law. When the cross-helicity and the α-effect work independently of each other, non-axisymmetric magnetic configurations become more desirable. This situation arises in purely γ^2 or α^2 dynamos. However, a combination of these scenarios, known as the $\gamma^2\alpha^2$-dynamo, can generate axisymmetric, dipole-like magnetic fields with strengths of several kGs.

1.2.2 Stellar Activity

Stellar activity is typically observed in stars that possess an outer convective shell and strong magnetic fields. Several factors influence the strength of a star's activity, including its mass, age, rotation rate, and the strength and complexity of its magnetic field. In particular, M dwarfs are known for their high levels of activity and can exhibit a variety of activity manifestations.

In this section, I will provide a brief overview of two common forms of stellar activity: spots and flares. It will be discussed how these phenomena differ from those observed on the Sun, highlighting the unique characteristics of stellar activity in other stars. Additionally, I will explain how spectroscopic and photometric observations can be utilized to detect and measure these phenomena.

1.2.2.1 Spots and Rotation

Observations of dark features and magnetic structures on the surfaces of other stars have led to the concept that starspots exist and are likely equivalent to sunspots on our own star. While the two phenomena share many similarities, there are also some notable differences worth exploring. In this review, I will discuss the differences between starspots and sunspots in terms of temperature, size, lifespan, and location. Furthermore, I will explain the impact of starspots on spectral line profiles and how we can study them.

Spots always appear darker due to their lower temperature compared to the surrounding photosphere. The magnitude of this temperature difference (ΔT) can vary depending on the type of star and the size of the spot. Studies using molecular diagnostics have revealed that starspot temperatures are typically 500 to 2,000 K lower than the photospheric temperature. This range is quite similar to sunspots, which typically have a temperature range of about 600 to 1,800 K less than the photosphere (Schrijver, 2002). According to Berdyugina (2005), ΔT between starspots and the surrounding photosphere appears to be larger for hotter stars.

Late F and early G stars, on average, show values near 2,000 K for ΔT, while for late M stars, this value drops to around 200 K.

Sunspots typically have sizes ranging from 1,500 to 20,000 km, covering up to 1% of the solar surface during solar maximum (Strassmeier, 2009, see Subsection 1.1.4.1). Measuring the size of starspots is more challenging due to the lack of high-resolution surface observations. The amplitude of photometric variations depends not only on the size of the spot or group of spots present at a given longitude but also on the brightness contrast of the spot group. This brightness contrast, in turn, is determined by the temperature contrast. Numerous studies utilizing various techniques have been conducted to address this complex issue. Doppler imaging has uncovered starspots spanning from 0.1% to 22% of the stellar surface (Strassmeier, 2009). TiO absorption bands have demonstrated that young K dwarfs can exhibit 20-40% starspot coverage (O'Neal et al., 2004), whereas young M dwarfs can have a starspot coverage of $40 \pm 10\%$ (Jackson and Jeffries, 2013). The larger and more complex starspots observed on M dwarfs may be attributed to their slower rotation rates, which allow these starspots to persist for longer periods and become more developed over time.

Sunspots and small starspots typically last from a few days to several weeks (Schrijver, 2002). The lifetime of a spot is generally proportional to its size, with larger spots lasting longer (Berdyugina, 2005). This is because spots decay by diffusing out into the surrounding photosphere, and spots with a larger area-to-perimeter ratio take more time to disappear (Solanki, 2003). Theoretical models of spot decay suggest that turbulent diffusion is responsible for eating away at the edges of the spots (Simon and Leighton, 1964; Litvinenko and Wheatland, 2015; Litvinenko and Wheatland, 2017). The idea that diffusive mechanisms cause starspot decay has also been supported by observational research. For instance, a study by Giles, Collier Cameron, and Haywood (2017) analysed a sample of stars from Kepler, using the sinusoidal amplitude of Kepler light curves as a proxy for starspot size. The study investigated the correlation between the amplitude of the light curves and the decay timescale of starspots, as well as the dependence of these correlations on the effective temperature of the star. The results revealed a correlation between the decay time of starspots and their inferred size, with larger spots generally surviving longer. Furthermore, the decay time was found to depend strongly on the temperature of the star, with cooler stars exhibiting longer-lived spots, particularly for stars with longer rotational periods.

On the Sun, sunspots are typically found between latitudes of $\pm 35°$ and migrate closer to the equator as the solar cycle progresses (as discussed in Subsection 1.1.4.1). Starspots exhibit a behaviour comparable to that of sunspots, although they may appear at much higher latitudes. In some cases, there have been observations of massive polar spots on certain stars (Schrijver, 2002; Strassmeier, 2009, and references therein). Sunspots are known to occur more frequently at specific longitudes on the Sun known as "active longitudes". These regions exhibit heightened magnetic activity, which can lead to the recurrent appearance of sunspots in the same area (Berdyugina and Usoskin, 2003). Similar active longitudes have also been observed on other stars, as reported in studies such as those by Olah et al. (1989), Berdyugina and Tuominen (1998), and Lanza et al. (2009). They rotate in phase with the star's rotation and could account for the persistent, coherent signal of starspots.

The light curves of solar-type and low-mass stars can exhibit significant amplitude variations, which are often attributed to the presence of large, dominant starspots on the stellar surface that move in and out of view as the star rotates. As these spots grow and decay,

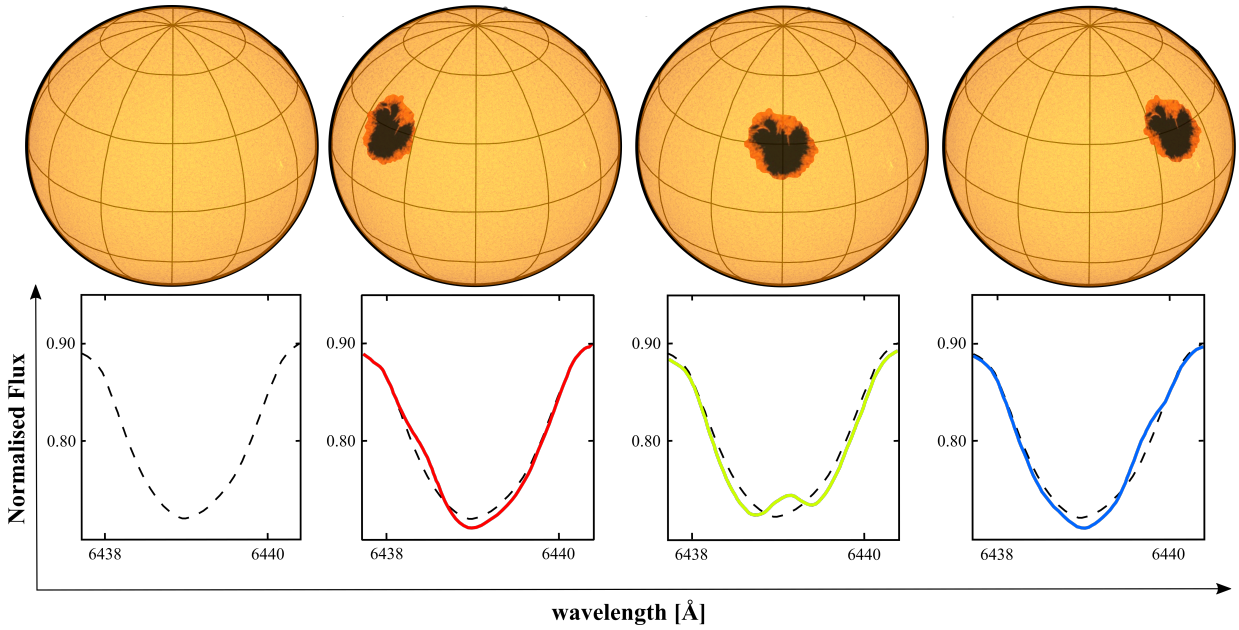

FIGURE 1.11: Spectral line profiles for a simulated starspot on a fast-rotating star. The dashed line represents the profile with no spots, while the solid lines represent the profile with a spot moving across the disc as the star rotates. The presence of the starspot causes distortions in the shape of the spectral line profile, which can result in RV variations with respect to the observer. (Image credit: adapted from Berdyugina (2005), with modification.)

they induce variations in the star's photometry that are modulated by its rotation. As a star rotates, one half of its disc moves towards us and the other half moves away. Consequently, the flux emitted by the approaching half is blueshifted, while the receding half is redshifted. If the stellar surface is featureless, the Doppler shifts from both halves of the star cancel each other out, and the spectral line profile remains undisturbed, as depicted in the left diagram of Figure 1.11. If a starspot passes into and out of view as the star rotates, as illustrated in the subsequent diagrams of Figure 1.11, it blocks some of the star's flux. This leads to an imbalance between the redshifted and blueshifted halves of the star, which causes dumps or dips in the shape of the spectral line profiles. The magnitude of these asymmetries depends on the properties of the lines themselves. As a result of these small perturbations to the line profile, the centroid of the line profile shifts slightly, which can translate into radial velocity (RV) variations of about 1 $\mathrm{m\,s^{-1}}$ for sunspots (Lagrange et al., 2011). However, for more active and rapidly rotating stars, starspot-induced RV variations can be much larger (Makarov et al., 2009).

As rotation is believed to play a key role in the generation of magnetic fields in stars, determining their rotation periods has become an increasingly popular topic. This is particularly important for low-mass stars, as their magnetic activity is closely related to their rotation. For instance, Stelzer et al. (2016) analysed K2 observations of 134 M dwarfs to investigate the relation between magnetic activity and stellar rotation. They found that slow and fast-rotating M dwarfs exhibit a notable difference in activity, with a sharp transition occurring for periods greater than approximately 10 days.

Rotation plays a crucial role not only in determining the age of low-mass stars, but

also in their magnetic activity. Rapidly rotating stars of this type are expected to exhibit higher levels of activity, as rotation strongly influences their dynamo mechanism (Hartmann and Noyes, 1987). This relationship between rotation and activity, known as the rotation-activity-age relation, is a key concept that underpins much of the discussion in this thesis.

1.2.2.2 Stellar Flares

Stellar flares, occurring on other stars, are equivalent to solar flares. While sharing similarities in nature, they often unleash significantly greater energy releases, owing to the larger size and stronger magnetic fields of many stars compared to the Sun. In fact, flares observed on M dwarfs can be hundreds or even thousands of times more powerful than solar flares, emitting a broad spectrum of electromagnetic radiation that includes X-rays and ultraviolet light.

Stellar flares have been a subject of study for over a century, with pioneering observations shedding light on their nature. Early in this pursuit, Bopp and Moffett (1973) and Gershberg and Shakhovskaia (1983) conducted detailed optical observations of stellar flares on M dwarfs, providing valuable insights. In terms of X-ray observations, Heise et al. (1975) made significant contributions using EXOSAT, detecting an X-ray flare from the M4.5V star YZ CMi. Since then, the physics of stellar flares have been extensively investigated by numerous researchers across the electromagnetic spectrum, spanning from γ-rays to radio frequencies.

The Kepler mission (Borucki et al., 2010) revolutionised stellar observations, providing nearly uninterrupted monitoring of stars over extended periods, ranging from months to years. This invaluable dataset enabled numerous studies on the properties of stellar flares. Among the stars that garnered significant interest was the M dwarf star GJ 1243, renowned for its frequent flaring events captured in its lightcurve. With a spectral type of M4, GJ 1243 serves as an excellent example of a star featuring a fully convective core (Davenport et al., 2014; Davenport, Mendoza, and Hawley, 2020). Noteworthy research, such as that conducted by Ramsay et al. (2013), explored this star, unveiling a multitude of short-duration, low-energy flares using high-cadence Kepler data. Further analysis by Hawley et al. (2014) on the same dataset delved into classical and complex flares, establishing correlations between flare energy, amplitude, duration, and decay time. The wealth of findings from these studies adds to our understanding of stellar flares and their diverse characteristics.

In a related study, Stelzer et al. (2016) delved into the intricate relationship between magnetic activity and stellar rotation. They utilised K2 data of 134 M dwarfs, distinguishing between slow and fast-rotating M dwarfs. Notably, they observed an abrupt change in activity after a period of approximately 10 days, suggesting a compelling link between stellar activity and rotation. However, due to the majority of targets having only long cadence (30 min) data, the analysis of flare statistics may be incomplete, as short-duration flares (which can have timescales in the range of minutes to hours) may have been missed. To address this limitation, Davenport (2016) conducted an inclusive investigation by utilising every available Kepler light curve to search for and catalogue stellar flares across all spectral types.

Classical stellar flares display a distinctive profile characterised by a rapid rise and an exponential decay, while complex profiles exhibit multiple peaks. These flaring events can endure from a few minutes to several hours, encompassing energies that greatly exceed the largest flares observed on the Sun, which are approximately 10^{32} erg.

1.3 Motivation and thesis outline

The primary purpose of this thesis is to thoroughly examine the impact of surface magnetic activity on the observed data from a group of highly active M dwarfs located in the solar neighbourhood. To gain a comprehensive understanding, I conducted a versatile analysis of these stars using high-precision spectroscopic and photometric data obtained from dedicated exoplanet research surveys, namely CARMENES and TESS. To enhance the overall understanding, a sophisticated stellar activity model code was also employed to replicate the influence of active regions on RV measurements in the absence of systematics.

Chapter 2

provides a comprehensive review of the surveys utilised in this study, focusing on the data they provide. It offers a succinct overview of the exoplanet detection methods employed by each survey and discusses the potential impact of stellar activity on the accuracy of planet detection. Additionally, an overview of the available activity indicators is presented, along with their efficacy in tracking stellar activity.

Chapter 3

focuses on spectroscopic analysis of active M dwarfs, leveraging the wavelength-dependence of activity effects in stellar spectra. The study examines the level of wavelength dependence in target stars and explores potential correlations with key stellar parameters. Furthermore, a subgroup of six stars is selected for a thorough investigation of periodic signals associated with their rotation periods, using order-by-order RV measurements.

Chapter 4

aims to analyse the TESS light curves of the same stars to examine the possible connection between their flare properties, stellar parameters, and chromospheric activity indices acquired from CARMENES. A semi-automated flare detection algorithm was created to identify important flare features including amplitude, equivalent duration, and bolometric energy. To understand the distribution of flares emitted at various energy levels, flare frequency diagrams were created and characterized to aid in identifying potential associations.

Chapter 5

presents the detailed modelling of active M dwarf, V388 Cas. I utilised simultaneous observations from CARMENES and TESS to retrieve active regions on the stellar photosphere using the inverse method with the modelling tool `StarSim`. The resulting surface map was then used to predict RV per order in the absence of external noise. Additionally, the project explored the flare evolution of V388 Cas and investigated the possibility of a CME event on the star.

Chapter 6

presents a discussion and summary of the main findings of this thesis, along with an outline of future research directions.

Chapter 2

Data Sample

> Errors using inadequate data are much less than those using no data at all.
>
> *Charles Babbage*

The research presented in this thesis is based on observational data collected from two surveys: CARMENES and TESS, both of which are dedicated to the discovery of exoplanets in the solar neighbourhood using two of the most successful techniques for detecting them to date. While CARMENES utilizes ground-based spectroscopy, TESS provides space-based photometry, allowing for a more comprehensive understanding of the targets studied.

This chapter provides an introduction to each survey, outlining the specifics of the telescopes and instruments, explaining the detection methods used to discover exoplanets, and describing how stellar activity can affect the data and falsely resemble a planet.

2.1 Spectroscopy method

Spectroscopy is a powerful technique used in astronomy to study the physical properties of celestial objects by analysing the light they emit or absorb. It relies on the use of a spectrograph, which separates the incoming light into its component wavelengths or colours and records the resulting spectrum. The three main components of a spectrograph are an entrance slit, a dispersive element, and a detector. There are two main types of dispersive elements used in spectrographs: prisms and gratings. A prism spectrograph uses the property of glass to separate white light into various wavelengths by refracting different wavelengths into different directions. A grating spectrograph operates on similar principles as a prism spectrograph, but instead of using a prism, it uses a diffraction grating as a dispersive element. A diffraction grating is a thin, flat piece of glass or metal that contains a series of closely spaced parallel lines or grooves on its surface. The choice between a prism spectrograph or a grating spectrograph depends on the specific requirements of the observation being carried out. Factors such as wavelength range, spectral resolution, and efficiency should all be considered when selecting which type of spectrograph to use. Prisms are simpler and easier to use than gratings, but they typically produce lower-resolution spectra and are limited to a narrower wavelength range. In modern spectroscopy, Gratings, particularly blazed gratings, have become the preferred choice over prisms due to their superior performance. However, prisms have made a comeback in the form of grisms, which combine the functions

of both gratings and prisms to create a hybrid optical element. Grisms have found a wide range of applications in spectroscopy due to their compact size and high efficiency (Muslimov et al., 2023). A comprehensive theoretical understanding of the optical characteristics of spectroscopic instruments is available in Eversberg and Vollmann (2015).

Spectroscopy enables the determination of various physical properties of celestial objects, including their chemical composition, temperature, density, and velocity. This is accomplished by analysing the spectral lines produced by the atoms and molecules within the object. Each element or molecule produces a distinct set of spectral lines that can be used to identify its presence and quantify its abundance. By analysing the intensity, width, and shape of these spectral lines, we can infer a wealth of information about the properties of the object being studied. One application of spectroscopy in modern astrophysics, specifically in the exoplanetary domain, is to study the motion of stars by measuring the Doppler shift of spectral lines, which allows for determining the object's radial velocity. This can be used to infer the presence of planets, binary stars, or other companions in orbit around a star. For additional information on this topic, refer to Section 2.1.3.

2.1.1 Échelle Spectrograph

Spectrographs used for detecting exoplanets require a combination of high resolving power and a broad wavelength range. The unique design of Échelle spectrographs enables these two essential features to be met. In this context, it is worth providing a brief overview of important elements of such instruments, as they are the type of spectrograph used in CARMENES.

Spectral resolving power, R, is a crucial metric in spectroscopy that refers to an instrument's ability to distinguish between spectral features that are very close together in wavelength. The higher the resolving power of a spectroscopic instrument, the better it is at resolving narrow spectral features. This quantity is defined as

$$R = \frac{\lambda}{\Delta\lambda}, \tag{2.1}$$

where λ is the observed wavelength and $\Delta\lambda$ is the spectral resolution, which is the minimum wavelength difference between two resolved features.

For a spectrograph that uses a grating as the main dispersive element, the grating equation determines the conditions under which light of a certain wavelength λ is dispersed by the grating at a given angle of incidence α and angle of diffraction β in accordance with the interference condition. The grating equation is given by

$$n\lambda = d(\sin\alpha + \sin\beta), \tag{2.2}$$

where n refers to the order of diffraction, and d is the groove width of the grating. For a blazed grating, which features a specific blaze angle Θ_B, the angles of incidence and diffraction are given $\alpha = \Theta_B + \theta$ and $\beta = \Theta_B - \theta$, respectively. In modern spectrographs, a quasi-Littrow configuration is commonly used, in which the blaze angle is selected to ensure that the incidence and diffraction angles are perpendicular to the surfaces of the grating grooves and are nearly equal, i.e., $\Theta_B = \alpha \approx \beta$.

RV spectrographs necessitate high-precision measurements of individual spectral features to minimize combined uncertainty, which calls for both high resolutions and broad spectral

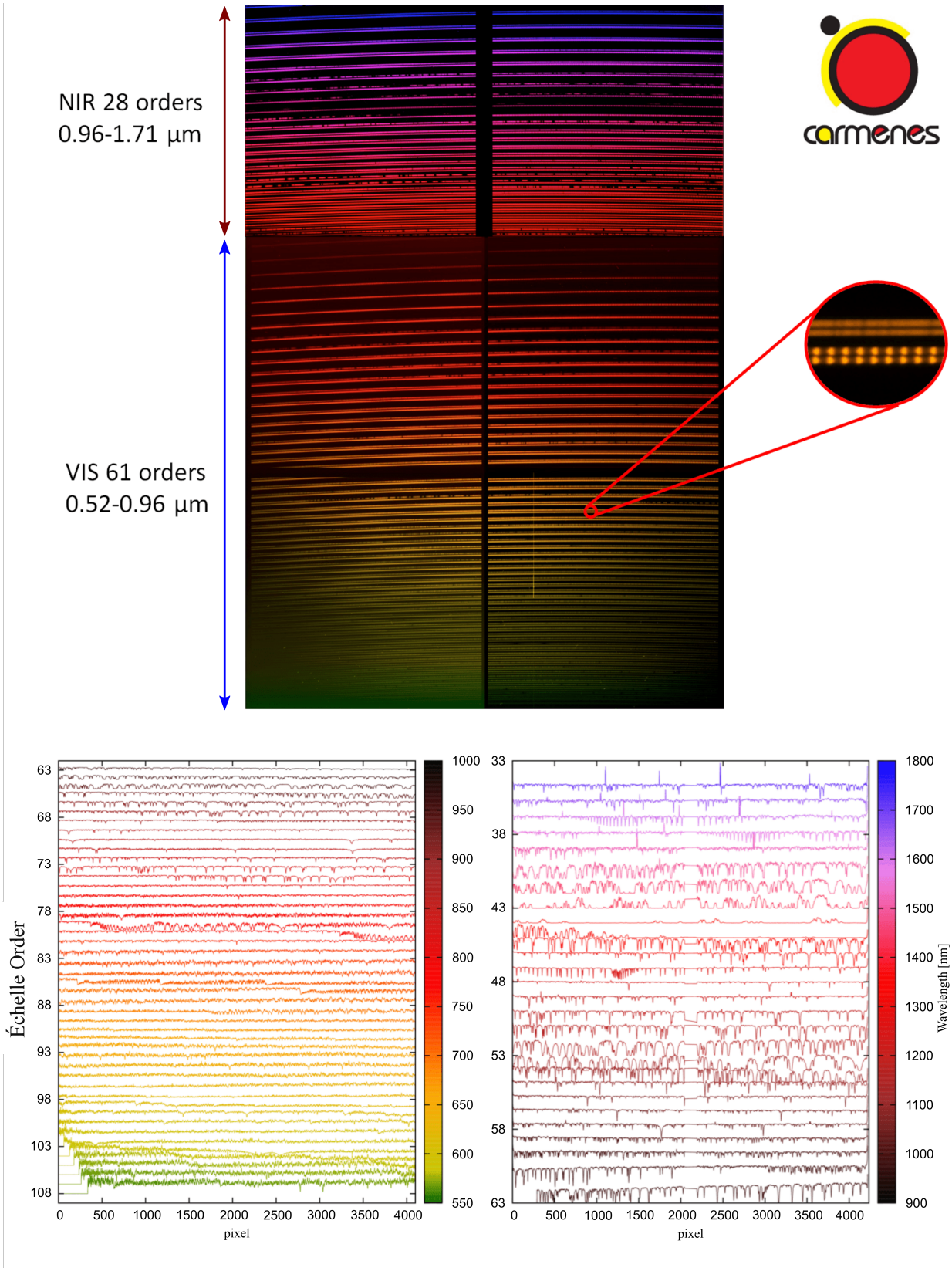

FIGURE 2.1: CARMENES 2D spectrum of an M dwarf star. The upper third of the top panel corresponds to orders produced by the NIR channel, while the two bottom thirds show orders generated by the VIS channel. The bottom panel shows the complete extracted spectrum of the VIS (left) and NIR (right) channels, separated into individual orders. (Image credit: Adapted from Amado and Consortium (2016), with modifications).

wavelength ranges. This can be achieved by using a form of blazed grating known as an Échelle grating as the primary dispersive element. Échelle gratings are designed with a large blaze angle ($\Theta_B > 45°$) and large groove widths, typically ranging from 3 to 50 μm. Spectrographs that operate in the visible wavelength range reach their peak efficiencies at high order numbers, typically $n = 60$ to 130, where the orders strongly overlap. This overlap implies that two consecutive orders are separated by a very small angle $\Delta\beta$. For near-infrared spectrographs, lower order numbers are usually used. To separate the overlapping orders, a second dispersion element known as a cross-disperser is placed perpendicular to the grating diffraction axis. Cross-dispersers can be made of prisms, gratings, grisms, or Volume Phased Holographic (VPH) gratings. When the dispersed light is detected by a CCD chip, it produces a typical two-dimentional spectrum, where wavelengths vary across orders and within each order, as shown in the upper panel of Figure 2.1.

Extracting radial velocities from a 2D Échelle spectrum involves several steps. First, the acquired spectrum frames must be pre-processed, followed by the extraction of Échelle orders from the 2D frames. Next, the extracted orders must undergo wavelength calibration. Finally, radial velocities can be determined from the calibrated spectra. The bottom panel of Figure 2.1 shows the CARMENES spectrum separated into orders, extracted from the raw data of the VIS (left) and NIR (right) spectrographs.

2.1.2 The CARMENES survey

CARMENES, which stands for Calar Alto high-Resolution search for M dwarfs with Exoearths with Near-infrared and optical Échelle Spectrographs, is a groundbreaking project that has been utilising the RV method to survey a sample of over 350 stars since January 2016. Its primary objective is to detect Earth-like planets with temperate conditions (Quirrenbach2016). CARMENES simultaneously refers to an instrument, a survey and a consortium. The instrument is comprised of a pair of high-resolution cross-dispersed Échelle spectrographs that are mounted on the Cassegrain focus of the 3.5 m telescope at Calar Alto Observatory in Granada, southern Spain. The visual (VIS) channel of the spectrograph operates in the wavelength range of 0.52–0.96 μm with a spectral resolution of R = 94,600, and the near-infrared (NIR) channel covers the wavelength range of 0.96–1.71 μm with R = 80,400 (Quirrenbach et al., 2014; Quirrenbach et al., 2018). The broad wavelength coverage of the CARMENES spectrograph is an unprecedented feature that allows investigating stellar activity and safer detection of planetary companions. The instrument was constructed for Doppler measurements with high long-term stability and can achieve a precision of the order of $\sim 1\,\mathrm{m\,s^{-1}}$ in VIS and $\sim 3\,\mathrm{m\,s^{-1}}$ in NIR.

2.1.3 The radial velocity method

When a star is accompanied by a planet, both objects engage in a shared motion around their common centre of mass. If the orbital plane is not perpendicular to the observer's line of sight, the radial component of the star's velocity towards or away from the observer undergoes periodic changes, as depicted in Figure 2.2. This modulation in velocity is known as the radial velocity (RV) and can be determined by measuring the Doppler shift of spectral lines:

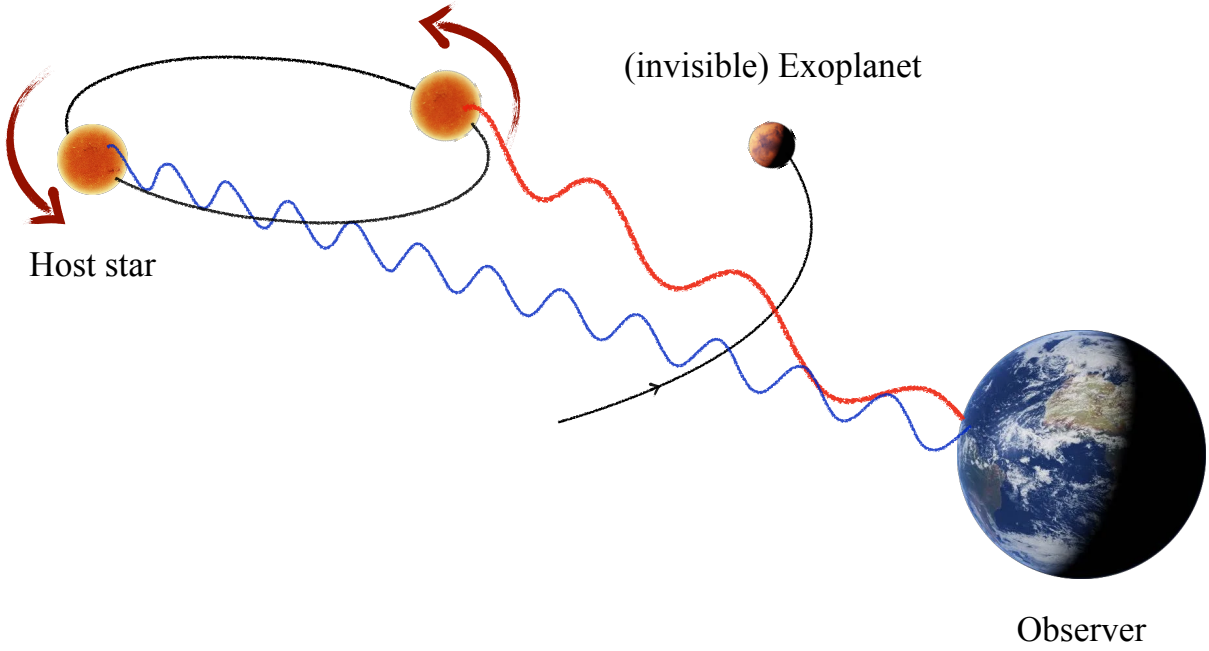

FIGURE 2.2: Radial-velocity method illustration: this method detects exoplanets by measuring variations in the velocity of a star as it is influenced by the gravitational pull of its orbiting planet. Spectral shifts occur as the star moves towards or away from the observer; red-shifted when receding, and blue-shifted when approaching. (Image credit: inspired by ESO [1]).

$$\frac{\Delta\lambda}{\lambda} \equiv \frac{\lambda_{\text{obs}} - \lambda}{\lambda} = \frac{\text{RV}}{c} \tag{2.3}$$

where λ_{obs} is the observed wavelength, λ is the rest wavelength, and c is the speed of light.

When the star moves towards the observer, the RV is negative ($\lambda_{\text{obs}} < \lambda$), resulting in a blue-shifted spectrum. Conversely, when the star moves away from the observer, the RV is positive ($\lambda_{\text{obs}} > \lambda$), resulting in a red-shifted spectrum. In the case of a planet orbiting a star with mass $M_\star$ and a period P on an orbit with numerical eccentricity e, the semi-amplitude K of the RV modulation can be determined by

$$K = \left(\frac{2\pi G}{P}\right)^{\frac{1}{3}} \frac{M_{\text{P}} \sin i}{(M_\star + M_{\text{P}})^{\frac{2}{3}}} \frac{1}{\sqrt{1-e^2}}, \tag{2.4}$$

where G is the gravitational constant, M_{P} is the mass of the planet, and i is the inclination angle, which represents the angle between the orbital plane and a plane perpendicular to the line of sight. Typically, this angle is unknown, which limits the derivation of an exact mass for the planet from the RV modulation. However, when combined with transit, direct imaging, or astrometric methods, it becomes possible to obtain a mass estimation for the planet.

[1] https://www.eso.org/public/images/eso0722e/

2.2 Photometry method

Photometry is a widely used method in astronomy for studying celestial objects by measuring their brightness. The technique involves collecting and accumulating light emitted by an object and analysing it to determine its properties. In astronomical observations, the most common type of detector used to measure the intensity of light in the optical band is a CCD (charge-coupled device) camera, which can be used to detect and measure the light emitted by celestial objects. A CCD camera comprises an array of pixels that can detect and record light, making it a powerful tool for measuring brightness. By analysing the pattern of light intensity across the pixels, it is possible to measure the brightness of a star or other object with high precision. Depending on the telescope size and CCD used, photometry can measure the brightness of multiple objects within a wide field of view, allowing for the independent measurement of each object's brightness. These properties make photometry a quick and effective technique in modern astronomy that is generally cheaper than spectroscopy.

Photometry is a versatile technique in astronomy that can be used to study a wide range of celestial objects by applying different types of filters, including broad-band and narrow-band filters. By measuring the intensity of light emitted by these objects, we can classify them, determine their magnitudes, colour indices, effective temperatures, and even metallicity. Photometry is also useful for studying variable stars, planets, and their atmospheres.

In recent years, one of the most significant applications of photometry in astronomy has been in the field of "transit photometry", which enables the detection of exoplanets. By measuring the slight changes in a star's brightness during transit, we can learn about the composition and structure of exoplanet atmospheres and gain valuable insights into the nature of these distant worlds. Additionally, photometry can be used to study the physical properties of exoplanets, such as their size, mass, and atmosphere.

2.2.1 The TESS survey

The Transiting Exoplanet Survey Satellite (TESS; Ricker et al., 2015) is a cutting-edge space-based telescope designed to survey over 200,000 of the brightest main-sequence stars in the solar neighbourhood, with the aim of discovering transiting planets. Launched in April 2018, TESS began its primary mission by observing the Southern Ecliptic Hemisphere until July 2019. It then turned its attention to the Northern Ecliptic Hemisphere until July 2020. Following the success of its primary mission, TESS's mission was extended for another 27 months until mid-2022 to gather additional data. Currently, TESS is set to embark on a Second Extended mission that will last approximately three years.

TESS stands out from its predecessors, CoRoT and Kepler/K2, in terms of its field of view. While the earlier missions monitored only a small fraction of the sky, TESS surveys nearly the entire sky in the solar vicinity. TESS features four wide-angle telescopes, each equipped with a low-noise CCD camera with a field of view of $24° \times 24°$. The four telescopes operate together as a $1, \times, 4$ array, providing a total field of view of $24° \times 96°$ (see Figure 2.3). With this setup, the primary survey is conveniently divided into 26 sectors, 13 in the Northern Hemisphere and 13 in the Southern Hemisphere, each spanning $24° \times 96°$ with overlapping regions at the ecliptic poles. TESS spent approximately 27 days, or two orbits, observing each sector, while the overlapped areas received up to $\sim$ 350 days of observation. This long-term monitoring of stars in the region, which would be in the continuous viewing zones

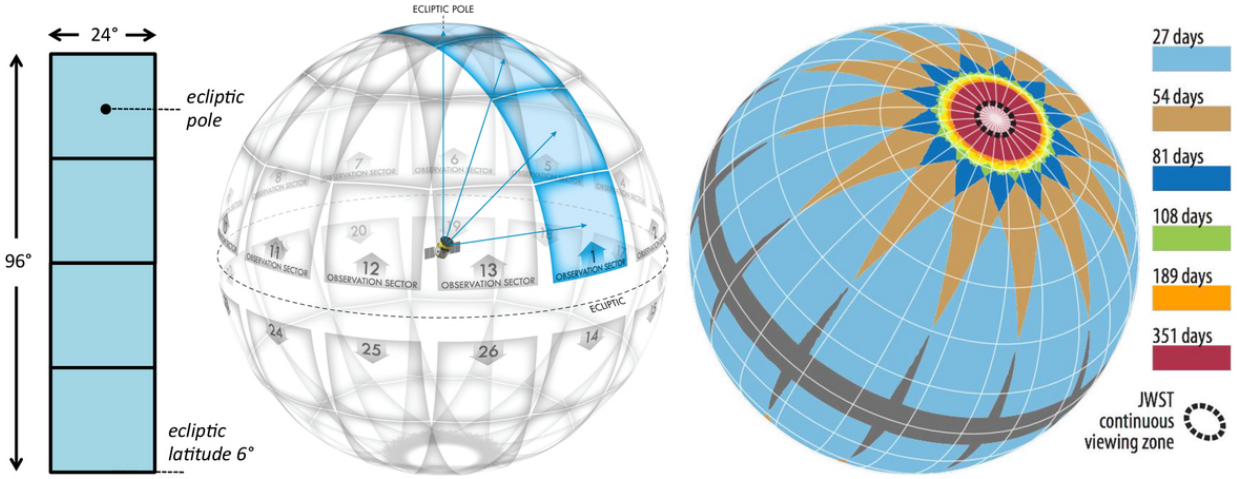

FIGURE 2.3: Map of TESS overlapping observing sectors in ecliptic coordinates. Includes primary mission observation duration and JWST continuous viewing zone.
(Image credit: NASA).

(CVZs) of the James Webb Space Telescope (JWST; Gardner et al., 2006) would increase the chances of discovering smaller, rocky planets with longer orbital periods. Any suitable exoplanet candidates identified by TESS would have the opportunity for atmospheric studies by JWST.

Since the nearby G, K, and specifically M dwarfs are the main objective of TESS, its photometric bandpass has been set in the range of 600–1000 nm (Ricker et al., 2015), which is more suitable for studying red dwarfs. Moreover, the similarity of the TESS bandpass with the Gaia G_{rp} band (630–1050nm) (Gaia DR2; Gaia Collaboration et al., 2018b) would allow for the possible contaminated source evaluation, which is highly probable in the TESS photometry due to its large pixel size of $\sim 21''$.

During the primary mission, the 200,000 selected targets were read out every 2 min as postage stamps and released as target pixel files (TPFs) and calibrated lightcurves. In addition, the precise photometric information of approximately 100 million objects with an apparent magnitude brighter than I = +16 was obtained at a cadence of 30 minutes and made available to the community as Full Frame Images (FFIs). These FFIs allow conducting photometry on any target within the 2300 square degree field of view of the TESS. During the extended mission, TESS has increased its operating power by accelerating the cadence for the FFIs from 30 to 10 minutes and adding a new 20-second cadence observation mode for the postage stamps.

All the TESS calibrated data is archived to the Mikulski Archive for Space Telescopes (MAST) site[2] and is available for download conveniently. The TESS science pipeline, developed by the Science Processing Operations Center (SPOC) at NASA, provides two versions of the light curve for the 2-min cadence data, Simple Aperture Photometry (SAP flux) and Presearch Data Conditioning algorithm (PDCSAP flux), where the latter is corrected for systematics and trends presented in the data and is more suited for planet transit search (Jenkins et al., 2016). Each photometric data point is also assigned a QUALITY flag indicating whether the data point has been affected by instrumental or other types of anomalies.

[2] https://mast.stsci.edu/portal/Mashup/Clients/Mast/Portal.html

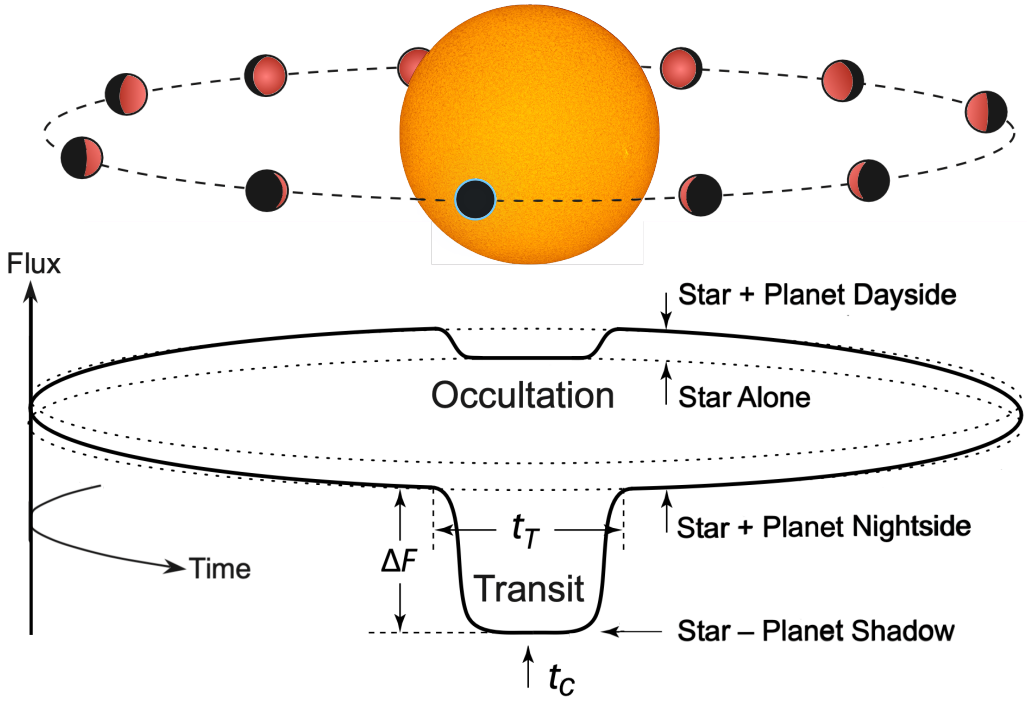

FIGURE 2.4: Illustration of transits and occultation.
After Perryman (2018); Winn (2010).

The description of the QUALITY flags is available on the TESS Data Product Overview page[3], allowing further treatment of the data based on the nature of the scientific study.

Although the core mission goal of TESS is finding smaller transiting exoplanets orbiting nearby bright cool dwarfs, the great precision and the time coverage of data (with a 2-min cadence) provided the means to study the signs of magnetic activity in these types of stars. In the following section, we discuss the effect of stellar variability on the TESS light curves.

2.2.2 The transit method

Transit photometry is undoubtedly one of the highly effective detection methods for hunting exoplanets. From the first successful detection of a transiting planet, HD 209458 b[4] in 1999 up until May 2023, 3,988 transiting planets have been detected by ground- and space-based observatories[5], which make up $\sim$74.6% of all the confirmed planets to date.

The basic principle of this method is founded on eclipses. In the case of suitable alignment of the planetary orbital plane with respect to the line of sight from the Earth, the planet blocks a small portion of the stellar light periodically as it passes in front of the stellar disk. This event is called a primary eclipse or, more commonly, a transit. Depending on the geometry of the system (mainly its eccentricity), each transit might be followed by a secondary eclipse, when the planet passes behind the stellar disk in an event known as occultation (see Figure 2.4).

[3] https://outerspace.stsci.edu/display/TESS/2.0+-+Data+Product+Overview

[4] HD 209458b was detected simultaneously but independently by Henry et al. (1999) and Charbonneau et al. (2000)

[5] https://exoplanetarchive.ipac.caltech.edu/index.html

In order to detect a planetary transit, the photometric light curve of a star is obtained and searched for such dimming events. The main observables that can be directly derived from a transit light curve are the period of the planet, transit depth, and duration. If the stellar mass and radius can be estimated from, say, spectral classification, spectroscopy, or asteroseismic observations, then the planetary radius, semi-major axis, and the inclination of the orbital plane can be derived from transit observations. To derive the planetary mass, however, complementary measurements by the radial velocity method are required.

The length of time between two successive mid-transit times (marked by t_c in Figure 2.4) on the stellar light curve provides the orbital period of the planet P. Obviously, the transit method works best for planets in closer orbits since, for example, more than a year of uninterrupted observations are needed to find an Earth-type planet at 1 AU, while for HD 209458 b, which is a typical "hot Jupiter" planet with an orbital distance of 0.04747 AU, the orbital period is only 3.52 days.

The fraction by which the star gets dimmer, a.k.a. transit depth ΔF, is directly proportional to the ratio of the projected area of the planetary and the stellar surface and is given by

$$\Delta F \simeq \left(\frac{R_\mathrm{p}}{R_\star}\right)^2 \simeq 0.01 \left(\frac{R_\mathrm{p}}{R_\mathrm{J}}\right)^2 \left(\frac{R_\star}{R_\odot}\right)^{-2}, \tag{2.5}$$

where ΔF is the transit depth, and R_p and $R_\star$ are the planetary and stellar radii, respectively. Equation (2.5) yields an estimate of the planetary size in terms of the size of its host star. It also displays how the transit method is more effective for detecting planets in systems with higher planet-to-star radius ratios. Therefore, a low-mass star is more favourable for detecting an Earth-sized planet, as the effect would be very puny for a Sun-like star. For instance, HD 209458 b, which is orbiting around a G0 V star with a mass of 1.148 $\mathrm{M}_\odot$, would cause an eclipse depth of 1.32%. Similarly, a Jupiter-size planet would block $\sim$1% of the light of a Sun-like star. For an Earth-like planet orbiting around a solar-like star, the transit depth would be only 5×10^{-5}, less than a 0.01% effect. In comparison, a transit depth of the order $\sim$7% could happen for lower mass stars, M dwarfs (Haghighipour et al., 2010).

The effect of a secondary eclipse on the flux received from the system is even weaker. During the occultation, the total light belongs to the star alone, in the absence of the contribution from the dayside of the planet. As a result, this depth corresponds to the thermal emission of the planet's heated face. Charbonneau (2003) showed that in the Rayleigh-Jeans limit and the absence of limb-darkening, the depth of the occultation is given by

$$\Delta F \simeq \frac{T_\mathrm{p}}{T_\star} \left(\frac{R_\mathrm{p}}{R_\star}\right)^2, \tag{2.6}$$

where T_p and $T_\star$ are the temperatures of the planet and star, respectively. Equation (2.6) also provides an estimate of the planetary temperature (Charbonneau, 2003).

The transit duration t_T is the time it takes for the planet to cross over the stellar disk. It depends on the stellar size, the speed of the planet in its orbit, the orbital distance, and the inclination of the orbital plane or the exact path the planet takes across the star. For a circular orbit, the transit duration is given by, (e.g., Winn, 2010; Perryman, 2018),

$$t_\mathrm{T} \simeq \frac{P R_\star}{\pi a} \simeq 13 \left(\frac{M_\star}{M_\odot}\right)^{-1/2} \left(\frac{a}{1\ \mathrm{AU}}\right)^{1/2} \left(\frac{R_\star}{R_\odot}\right), \tag{2.7}$$

where P is the orbital period, a is the semi-major axis of the planet's orbit, and $M_\star$ and $R_\star$ are the stellar mass and radius, respectively. For a hot Jupiter, such as HD 209458 b, with the orbital distance of ~ 0.05 AU, going right across the equator of its solar-like star, the length of transit would be about three hours. For a planet similar to Earth at 1 AU, an equatorial transit would last about 13 hours, and for a Jupiter-size planet at a distance of 5.2 AU, an equatorial transit length would be ~ 30 hours.

There are a few obstacles that make the transit technique a bit challenging. The main drawback is the slim chance of a planetary orbital plane being oriented sufficiently close to the observer's line of sight to see transits. For a randomly-oriented orbital plane in the case of zero eccentricity, $e = 0$, and a negligible radius of the planet compared to its host star, $R_\mathrm{p} \ll R_\star$, the transit probability is given by, (e.g., Borucki and Summers, 1984; Winn, 2010; Perryman, 2018),

$$P_\mathrm{tra} = P_\mathrm{occ} = \frac{R_\star + R_\mathrm{p}}{a} \simeq \frac{R_\star}{a} \simeq 0.005 \left(\frac{R_\star}{R_\odot}\right) \left(\frac{a}{1\ \mathrm{AU}}\right)^{-1}. \tag{2.8}$$

For a circular orbit, the probability value is the same for transits P_tra and occultations P_occ as shown in Equation (2.8), but for an eccentric orbit, a factor of $\frac{1}{1-e}$ would be added to the equation, and there is a possibility that only one of the two events, either transit or occultation, would be visible. The probability of observing the transit of any of the Solar System's planets except Mercury is less than 1%, and at 1 AU, it would be less than 0.5%, but for a hot Jupiter around a Sun-like star, it is as high as 10%.

In spite of the low transit probability, the presence of numerous dedicated ground- and space-based surveys, which can continuously scan large areas of the sky at once, made the transit method such a lucrative technique. For example, the most successful transit survey to date, NASA's Kepler mission, from its launch in 2009 until August 2013, when its mission was halted by NASA due to the reaction wheel issues, provided extensive photometric data for more than 150,000 main sequence stars (Borucki et al., 2010). Kepler alone has revolutionised the field of exoplanets by discovering 2,709 transiting exoplanets and another 2,057 candidates that are yet to be confirmed[6]. The Kepler mission was repurposed as K2 in 2014 and discovered another 537 exoplanets and more than 950 to be confirmed[6]. The Kepler/K2 space telescope was retired on 30th October 2018 after nine years of observations, leaving a wealth of data for the astrophysics community. The Kepler/K2 retirement paved the way for its successor TESS to continue its legacy.

2.3 Challenges on the way

Current state-of-the-art spectrographs are breaking the sub-1 $\mathrm{m\,s^{-1}}$ precision limit, a remarkable achievement that allows the detection of smaller planetary signals in the data. Instrumental noise is no longer the limiting factor at this level of precision, as atmospheric and stellar noise become the primary barriers that need to be addressed. In this section, I will discuss how these noise sources manifest in the data and what techniques can be employed to mitigate their effects.

[6] https://exoplanetarchive.ipac.caltech.edu/docs/counts_detail.html

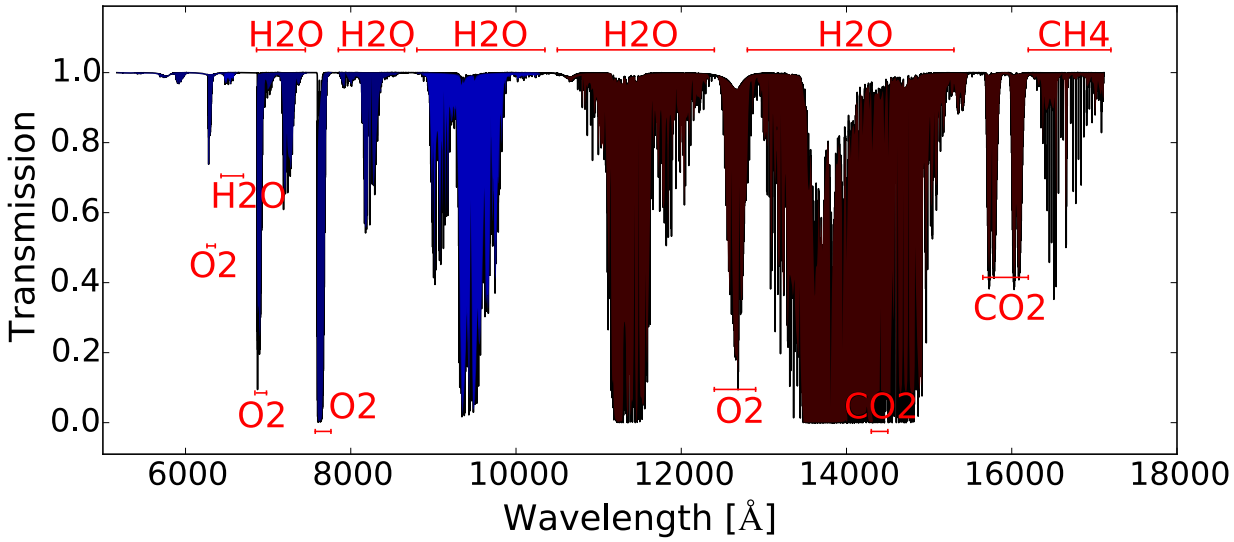

FIGURE 2.5: Synthetic transmission model of the Earth's atmosphere across the full wavelength range of CARMENES, including the VIS (blue) and NIR (red) channels. The model takes into account the major atmospheric absorbers, which include H_2O, O_2, CO_2, and CH_4.
After Nagel (2019).

2.3.1 Earth's atmosphere

Telluric lines are molecular absorption features caused by Earth's atmosphere that can interfere with ground-based astronomical observations. The major molecules responsible for these absorptions are H_2O, O_2, CO_2, and CH_4, which absorb specific wavelengths of light, producing dark lines in the spectrum that are known as telluric contamination. This phenomenon can severely affect spectroscopic analyses, particularly at redder and near-infrared wavelengths, where telluric contamination becomes more prominent. Figure 2.5 illustrates the telluric bands within the wavelength range of CARMENES.

Although telluric contamination is typically not problematic for spectrographs that operate in the bluer wavelength range, as regions containing telluric lines can often be avoided, it can pose a significant challenge for instruments optimised to observe M dwarfs, which primarily emit at redder visual and near-infrared wavelengths. To minimise the effects of telluric contamination, astronomers have developed sophisticated correction techniques.

One commonly used and effective method for correcting telluric contamination in astronomical spectra is to observe a telluric standard star that is taken at a similar time and airmass to the science target. Typically, bright hot stars of O-, B-, or A-type are selected as telluric standards, as their high temperatures result in spectra with a clean continuum and few metal lines. To further minimise intrinsic features in the spectrum, rapidly rotating standard stars are preferred. Since the rotational broadening results in a spectrum that more adequately fits the atmospheric transmission. The telluric corrected spectrum then can be obtained by dividing the target spectrum with the telluric standard spectrum. However, using telluric standard stars in the NIR wavelength regime, such as the I, z, Y, or H bands, can be quite challenging, as these stars exhibit strong photospheric hydrogen absorption lines, particularly in those bands (Vacca, Cushing, and Rayner, 2003).

A potential solution to the problem of finding suitable telluric standard stars is to use solar-like G-type stars as telluric standards. This approach was suggested by Maiolino, Rieke, and Rieke (1996) who used a high-resolution solar FTS spectrum as a reference and modified it to match the characteristics of the telluric standard and created a template spectrum. This template is then used to correct the target observation for telluric contamination and intrinsic features of the standard star. The success of this approach strongly depends on the extent to which the spectral lines in the standard star spectrum match those in the solar spectrum. Any deviations in the stellar parameters, such as effective temperature or metallicity, can introduce artefacts into the corrected spectrum. Moreover, this method may be limited by the availability of bright G-type stars that are at similar airmass and time as the target observation. The process can also be costly in terms of telescope time as in the infrared spectral range, the integration time required for standard star observations can be similar to, or even longer than, the integration time required for the science target.

Another practical method to obtain a telluric-free science spectrum involves using synthetic transmission models that are calculated with radiative transfer codes. Lallement et al. (1993) made the first development in this method, creating a synthetic H_2O transmission spectrum in the wavelength range of the sodium doublet at 589.5 nm. Widemann et al. (1994) subsequently extended this approach to the near-infrared by using a synthetic atmospheric H_2O absorption spectrum around 931-948nm. This allowed them to distinguish between stellar lines of cool K and M stars and telluric lines, thereby identifying absorption lines in the star's spectrum. Although synthetic transmission models have been available for several years, they were not commonly used as a standard method because of the poorly accessible radiative transfer codes and incomplete molecular databases. However, recent years have seen significant progress in the development of telluric correction using synthetic transmission spectra. For instance, Seifahrt et al. (2010) used a line-by-line radiative transfer model (LBLRTM; Clough et al., 2005) incorporating a standard atmosphere and the HITRAN database (Gordon, Rothman, and Toon, 2011; Rothman et al., 2009) to simulate the transmission and emission of light in the Earth's atmosphere. They generated theoretical transmission spectra covering H_2O, CO_2, CH_4, N_2O, O_3, and CO absorption bands for a wide wavelength range and fitted them to a series of B- and A-type stars observed at various airmasses. Using this approach, they were able to reproduce telluric absorption features with an accuracy of approximately 2%. This development has led to the creation of several publicly available codes such as TelFit (Gullikson, Dodson-Robinson, and Kraus, 2014), `molecfit` (Kausch et al., 2015; Smette et al., 2015), and `tellrem` (Rudolf et al., 2016), which have further improved the accuracy and accessibility of synthetic transmission models.

In addition to traditional methods, novel techniques have also been developed for tackling the telluric contamination problem. One approach involves compiling a library of telluric standard star spectra observed under different atmospheric conditions, using Principal Component Analysis (PCA) to identify independent absorbers, and creating a synthetic transmission spectrum by combining these absorption patterns and subtracting it from observations (Artigau et al., 2014). Another approach is to use machine-learning algorithms to simultaneously infer the stellar spectra, telluric spectra, and radial velocities of a series of high-resolution, high signal-to-noise ratio spectra without external information about the source or atmospheric conditions. This method is implemented in the open-source Python package, wobble (Bedell et al., 2019).

2.3.2 Stellar activity

As mentioned previously, stellar activity gives rise to observable variations in spectroscopic and photometric measurements, which are quantified using activity indicators. These indicators serve the purpose of assessing the activity level of a star, identifying its rotation period, and differentiating between an RV signal caused by a planet and one induced by stellar activity. The efficacy of activity indicators in detecting stellar activity is contingent upon factors such as the star's mass and activity level (Lafarga et al., 2021). In the subsequent paragraphs, we provide an overview of commonly employed activity indicators.

2.3.2.1 Activity indicators

Chromospheric lines serve as indicators by measuring the flux of activity-sensitive chromospheric lines. They provide valuable information about the activity level of the star and can be utilised to determine rotation periods. Examples of commonly used chromospheric lines include the Ca ii H&K doublet, the Hα line, the Na i D doublet, and the Ca ii IRT triplet (Wilson, 1968; West et al., 2004). In the case of M dwarfs, photospheric molecular bands such as the TiO and VO bands are frequently employed as indicators (Schöfer et al., 2019). These indicators offer insights into the activity and rotational behaviour of stars.

CCF parameters: The CCF profile, which represents the average profile of all the lines in the spectra, contains valuable information about the star's activity. Its shape can be characterised by a Gaussian function, and the width at half maximum altitude (FWHM) and contrast of the CCF are commonly employed as activity indicators. Additionally, the bisector inverse slope (BIS), which measures the asymmetry of the CCF, is often utilised for this purpose (Queloz et al., 2001; Lafarga et al., 2020). These parameters provide insights into the activity level and characteristics of the star.

Chromatic index: Zechmeister et al. (2018) introduced the chromatic index (CRX) as an activity indicator, which utilises the wavelength-dependent flux contrast between the photosphere, spots, and faculae. The CRX measures the variation of RV with respect to wavelength. Specifically, it is calculated as the slope of a linear fit to the RV values plotted against the central wavelength of each order in a cross-dispersed échelle spectrum at each time step. This index provides valuable information about the wavelength dependence of the RV variations and contributes to the understanding of stellar activity dynamics.

Differential line width (dLW): This activity indicator, introduced by Zechmeister et al. (2018), quantifies the differential variations in line width between the observed spectrum and a reference template. It is similar to the FWHM (Full Width at Half Maximum), but it is specifically associated with the least-squares fitting method used to measure the RVs.

Chapter 3

The effect of active regions on radial velocity variations

Details of authorship: *The content of this is based entirely on the work that will soon be submitted to the A&A journal. I am the lead author of this paper and was responsible for conducting the scientific work, calculations, analysis, and interpretation of the results. Additionally, I wrote the text and produced all the figures myself.*

3.1 Motivation

Reliable detection of an Earth-mass planet with the radial velocity (RV) technique requires identifying and, in some cases, modelling out the intrinsic activity of the host star, specifically for M dwarfs, which are known to be particularly affected by magnetically active regions. The effect of these active regions, e.g. cool spots and hot faculae, on the stellar spectra is wavelength dependent. There were attempts to measure RVs of Sun-like stars using only a subset of activity-insensitive spectral lines. This line selection approach cannot be easily applied to M dwarfs as their atomic lines are heavily blended amongst each other and with molecular bands. However, the chromatic index (CRX) is an activity indicator that can effectively detect asymmetric inhomogeneities on the stellar surface by tracing the wavelength dependence of the RV shifts. Our goal is to get an in-depth understanding of CRX by investigating its correlation with major stellar parameters and tracking down activity-induced signals across the échelle orders of the visible-light (VIS) and near-infrared (NIR) channels of the CARMENES spectrograph. We exploit the fact that the inhomogeneous distribution of magnetic active regions on the stellar surface leads to RV variations with the stellar rotational period.

We divided a selection of 56 highly active M dwarfs in the CARMENES sample into three subcategories: 'chromatic', 'suggestive' and 'achromatic' based on the degree of CRX-RV correlation and analysed their stellar properties. Furthermore, we calculated generalised Lomb-Scargle periodograms (GLS) of RVs across the orders of the échelle spectrograph for six selected stars. We studied the presence and significance of periodicities in the rotational modulation of the star and measured how the signal semi-amplitude and the GLS power change over orders.

3.2 Context

The radial velocity (RV) method has substantially contributed to the field of exoplanet research as a detection method as well as a follow-up technique for transit discoveries to spot false positives and determine the planetary mass and bulk density. Periodic Doppler shifts in the spectra of a host star, if registered above some high significance level in a periodogram analysis, can indicate the presence of a planetary companion responsible for the orbital reflex motion of the star. However, RV modulation of a star's spectra is not always due to orbiting companions. Several other factors can introduce spurious periodic variations in stellar RV measurements, including instrumental systematics, time sampling effects, and intrinsic stellar variability. Obtaining data from stabilised high-resolution spectrographs and optimising observing strategies could potentially resolve the first two issues to a high degree. However, stellar activity has remained the primary obstacle in detecting and characterising low mass exoplanets. There are several examples in the literature where a signal that was first interpreted as being caused by a planet turned out to be due to stellar activity or is still under debate (Queloz et al., 2001; Robertson et al., 2014; Robertson, Roy, and Mahadevan, 2015; Anglada-Escudé et al., 2014; Anglada-Escudé and Tuomi, 2015; Anglada-Escudé et al., 2016; Tuomi et al., 2018; Sarkis et al., 2018; Kossakowski et al., 2022). In fact, distinguishing between genuine planetary signals and those induced by intrinsic stellar activity has the highest priority in today's RV searches for small exoplanets (Boisse et al., 2011; Davis et al., 2017).

Stellar activity arises in the presence of strong magnetic fields and a convection zone. Different forms of stellar surface activity, e.g. granulation, active regions, and magnetic cycles, vary with timescales that can range from a few minutes to several years, and they impose RV variations with amplitudes ranging from $\mathrm{cm\,s^{-1}}$ to $\mathrm{km\,s^{-1}}$, depending on the activity level of the star (e.g., Kjeldsen and Bedding, 1995; Desort et al., 2007; Lovis et al., 2011; Cegla et al., 2019).

The stellar spectrum is sensitive to the strength of magnetic fields, convection velocity, and surface temperature. The appearance of active regions, i.e. dark spots and bright faculae, on the stellar surface distorts the shape of rotationally broadened spectral line profiles. The distortion is due to the temperature contrast between the unperturbed photosphere and active regions, and the amount of it depends on the sensitivity of the lines to temperature. When attempting to measure the RV of a spectrum through cross-correlation with a template or binary mask (e.g., Baranne et al., 1996), the changes in the shapes of the spectral lines can then be misinterpreted as a velocity shift of the peak of the cross-correlation function (CCF), which can introduce spurious RV variations over time. As these asymmetries shift within the line profile with co-rotating active regions, the resulting RV variations can modulate by the stellar rotation period, P_{rot} or its higher harmonics ($\frac{1}{2}P_{\mathrm{rot}}$, $\frac{1}{3}P_{\mathrm{rot}}$, etc.). However, in the case of stars that exhibit differential rotation, periods other than the harmonics of the rotational period may be generated (Boisse et al., 2011).

There are a variety of methods for identifying activity-induced RV variations. The most straightforward and widely used approach is to search for correlations between RV measurements and various "activity indicators". These indicators can be divided into two categories, namely chromospheric and photospheric ones. The former are based on measurements of the flux in the core of lines originating in the stellar chromosphere. For example, the Ca II H&K index has been routinely studied for solar-type stars (Wilson, 1968; Vaughan, Preston, and

Wilson, 1978; Noyes et al., 1984; Baliunas et al., 1995; Saar, Butler, and Marcy, 1998; Wright et al., 2004; Lovis et al., 2011), while hydrogen Balmer lines, like Hα, have been explored in more depth for M dwarfs (Delfosse et al., 1998; Gizis et al., 2000; Mohanty and Basri, 2003a; West et al., 2004; West et al., 2008; Schöfer et al., 2019). The photospheric indicators, in turn, attempt to quantify variations of the average photospheric absorption line shapes in order to compare them with any RV signal that may be present. Parameters derived from the CCF fall into this category and are commonly used to probe activity (Queloz et al., 2001; Boisse et al., 2009; Boisse et al., 2011; Figueira et al., 2013; Lanza et al., 2018; Simola, Dumusque, and Cisewski-Kehe, 2019; Lafarga et al., 2020).

In addition to the classical activity indicators, a novel and highly effective index has been developed within the CARMENES survey, known as the chromatic index (CRX; Zechmeister et al., 2018). The CRX is defined as the gradient of a straight line fitted to the RVs measured for the individual échelle orders as a function of the natural logarithm of the wavelengths of the orders (lnλ). It captures the wavelength dependence of the RVs, and its unit is velocity per wavelength ratio e (Neper, symbol Np[1]). The correlation of the CRX with the RV is generally referred to as chromaticity, which can be positive in the case of correlations or negative for anti-correlations.

If variations in any of these activity indicators correlate with an RV signal, it is a sign that the signal is probably caused by stellar activity. The same is true if periodograms of some of the indicators and the RVs show peaks at similar periods or harmonics of each other (e.g., Queloz et al., 2001; Bonfils et al., 2007; Kane et al., 2016; Sarkis et al., 2018; Toledo-Padrón et al., 2019). The caveat of this approach is that the affinity between stellar activity and RV might be disregarded in cases where the activity features do not leave a measurable trace on the activity indices or where the RV and activity signals are incoherent due to the complexity and variation of the active regions or the presence of a differential rotation. A recent study carried out by Lafarga et al. (2021) on the activity-related periodicities of RVs and nine simultaneously measured spectroscopic activity indicators for 98 M dwarfs in the CARMENES sample revealed that the activity indicators exhibit a diverse performance depending on the specific mass and activity level of the star. The authors showed that even for highly active stars, the signal might not reach a statistically significant false-alarm probability (FAP) in periodograms of certain activity indicators. In fact, there is no activity indicator that can effectively assess the significance of activity signals for all types of stars.

Modelling the activity-induced RV variations for Sun-like stars (Desort et al., 2007) and M dwarfs (e.g., Reiners et al., 2010; Andersen and Korhonen, 2015) has shown that the impact of the stellar magnetic activity on the spectral lines is not the same throughout VIS and NIR regimes (see, e.g. Figure 12. in Reiners et al., 2010). Following that, several studies investigated the behaviour of different spectral lines in response to activity and, more specifically, how their depth and equivalent width (EW) correlate with stellar activity (Davis et al., 2017; Thompson et al., 2017; Wise et al., 2018). In a new approach, Dumusque (2018) employed a line-by-line analysis to measure the RV of individual spectral lines independently. The authors carefully find activity-sensitive spectral lines and harness activity jitters by considering only a subset of lines that are shown to be insensitive to activity. This approach successfully mitigated the stellar activity signal of the Sun-like star αCen B by a factor of

[1]The unit of the CRX index is [m s^{-1} per Np]. Np is dimensionless and exactly one if the corresponding wavelength ratios are equal to e.

two, for which brightness and signal-to-noise (S/N) allow line-by-line RV measurements to reach the same precision as standard techniques.

Although the line selection method looks promising for bright Sun-like stars, it is not easily applicable to M dwarfs. The major complication is that the spectrum of cool stars is composed of a dense forest of spectral lines, while atomic lines all over are blended with molecular bands such that individual absorption lines can hardly be found. Besides, due to the intrinsic faintness of M dwarfs, measuring the RVs of selected individual lines increases the impact of the photon noise and renders the line selection technique impracticable.

CARMENES is a high-precision radial velocity survey with the chief goal of detecting exoplanets orbiting nearby M dwarfs. In the CARMENES survey, measurements of various activity indicators allow the identification and subsequent consideration of stellar activity, mainly through Gaussian process (GP) regression modelling, to validate planet discoveries (e.g., Perger et al., 2019; Bauer et al., 2020; Stock et al., 2020). At the same time, this survey provides a wealth of resources for advanced activity studies: e.g., computing specific chromospheric and photospheric indices and studying their features (Fuhrmeister et al., 2018; Fuhrmeister et al., 2019; Fuhrmeister et al., 2020; Fuhrmeister et al., 2022), or correlations of activity indicators through the entire M subclasses (Schöfer et al., 2019; Lafarga et al., 2021), as well as in-depth analyses and modelling of single active stars (Baroch et al., 2020; Jeffers et al., 2022).

The first study on the behaviour of the CRX was carried out by Tal-Or et al. (2018) on a group of 31 stars with large RV scatter ($\mathrm{std(RV)} > 10\ \mathrm{m\,s^{-1}}$) and moderate to fast projected rotational velocity ($v \sin i > 2\ \mathrm{km\,s^{-1}}$), known as the 'active RV-loud' sample. About 30% of the RV-loud stars showed a significant linear anti-correlation between their RVs and CRXs, and for another 20% of the stars, a marginal anti-correlation was detected. The lack of correlation for the remaining targets was attributed to an intricate spot pattern, high spot-to-photosphere temperature contrast, and/or the presence of a strong magnetic field. Since the Tal-Or et al. (2018) analysis, the number of targets that meet the criteria of the active RV-loud sample has almost doubled, and more measurements for some of the former targets are available. Hence, we apply Tal-Or et al. (2018) criteria to the CARMENES sample to detect new cases and investigate CRX potentials and limitations in more depth. The goal is to investigate whether specific stellar parameters can influence the chromatic behaviour of stars. Furthermore, we investigate periodic changes in the RVs of the échelle orders of the CARMENES spectrograph for a selection of stars, in order to identify regions susceptible to activity variations and compare these regions across stars. The chapter is organised as follows: In Section 3.3, we introduce our sample of stars and the selection criteria used in this study. The methods employed to analyse our data, considering the limitations posed by the small number of data points for most targets in our sample, are presented in Section 3.4. In Section 3.5, we discuss our findings regarding potential relationships between the chromaticity of RV measurements and stellar parameters. We delve into the activity behaviour across the spectral orders for six selected targets in Section 3.6. Finally, in Section 3.7, we provide a discussion of our results and summarise the main conclusions derived from this study.

3.3 Sample and observations

Our sample is selected from the CARMENES main survey (guaranteed-time observations; GTO program) that monitored about 370 M dwarfs between January 2016 and March 2022. The CARMENES instrument is mounted on the 3.5 m Zeiss telescope at the Observatorio de Calar Alto in Almería, Spain, and consists of a pair of red-optical (VIS) and near-infrared (NIR) échelle spectrographs that cover the wavelength ranges 5200–9600 Å and 9600–17 100 Å at spectral resolutions of $R = 94\,600$ and $R = 80\,400$, respectively (Quirrenbach et al., 2016; Quirrenbach et al., 2018).

The spectra were processed, wavelength calibrated, and reduced by the `caracal` pipeline (CARMENES reduction and calibration software; Caballero et al., 2016) using flat-relative optimal extraction (Zechmeister, Anglada-Escudé, and Reiners, 2014). The RVs were then derived from the spectra with the `serval`[2] package (Spectrum radial-velocity analyser; Zechmeister et al., 2018). The RV datasets were corrected for barycentric motions, secular acceleration, instrumental drifts, and nightly zero-point offsets as described in Trifonov et al., 2018 and Tal-Or et al., 2019.

Our sample consists of stars that passed the following selection criteria as defined by Tal-Or et al. (2018):

- $\mathrm{std}\,(\mathrm{RV}) = 1.4826\ \mathrm{MAD}\,(\mathrm{RV}) > 10\ \mathrm{m\,s^{-1}}$
- $v \sin i > 2\ \mathrm{km\,s^{-1}}$
- no known or suspected companion

Considering the median absolute deviation ($\mathrm{MAD} = \mathrm{median}\,\{|x_i - \tilde{x}|\}$) instead of regular standard deviation (std) minimises possible biases due to outliers and small-number statistics (e.g., Tal-Or et al., 2018, and references therein). A projected rotation velocity larger than 2 $\mathrm{km\,s^{-1}}$ ensures that stellar activity plays a significant role in the RV variation of these stars (Reiners, 2007). Finally, excluding targets with known or suspected companions secures that the scatter in RVs is not influenced by stellar reflex motions.

The 56 targets that met the selection criteria made up the updated active RV-loud sample that we analysed in this work. The designations of the targets, alongside their main stellar parameters, are listed in Table A.1. These stars have spectral types in the range M0.0–M9.0 V, stellar masses from 0.07 to 0.6 $\mathrm{M_\odot}$, J magnitudes between 5 and 12 mag, $v \sin i$ values that are by definition $> 2\ \mathrm{km\,s^{-1}}$ (with a maximum of 59.8 $\mathrm{km\,s^{-1}}$), rotation periods ranging from 0.1 to 23.6 days, and activity levels, as measured by the logarithm of the normalised Hα luminosity ($\log L_{\mathrm{H}\alpha}/L_{\mathrm{bol}}$), ranging from $\sim$ -4.9 to -3.3.

The sample's distribution of spectral types is shown in Figure 3.1 as a fraction of all CARMENES stars in each spectral type bin; their absolute number is indicated on the top of each bar. The fraction of the active RV-loud stars in the CARMENES survey is increasing towards later spectral types, from about 4% of RV-loud stars for spectral classes M0–M2 to 40% of RV-loud stars for spectral classes M5 and later.

For our sample, we have a total of 1739 spectra taken in the VIS, as opposed to 649 spectra used by Tal-Or et al. (2018), which is an increase of about 168%. The present study also employs 1733 spectra taken in the NIR, which were not included in the work by Tal-Or

[2] https://github.com/mzechmeister/serval

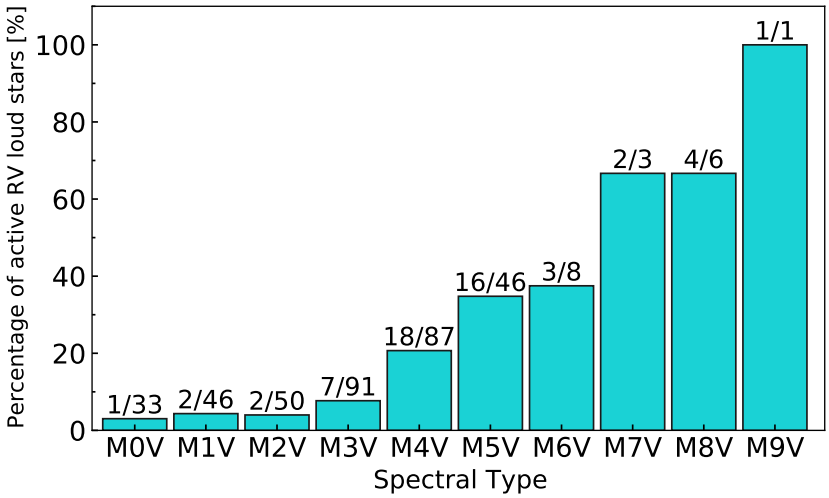

FIGURE 3.1: Percentage of RV-loud stars in the whole CARMENES sample as a function of spectral subtype. The number on the top of each bar indicates the fraction of RV-loud stars of the absolute number of CARMENES stars in the full sample in each bin.

et al. (2018). Information about the number of observations for each star, the time span of the measurements and the median S/N around $\lambda = 7460\,\text{Å}$ (order 82), along with further statistical analysis (for details, see Section 3.4), are provided in Tables A.2 and A.3 for the VIS and NIR channels, respectively.

3.4 Data analysis

3.4.1 Tests for correlations and trends

We performed several statistical tests to identify correlations and trends in our sample. Prior to that, in order to cleanse the data, we discarded observations with S/N < 5 in the reference orders 82 (around $\lambda = 7460\,\text{Å}$) in VIS and 49 (around $\lambda = 12400\,\text{Å}$) in NIR. Furthermore, we applied the modified Z-score method (Iglewicz, 1993) to the measured RVs and their uncertainties to reject outliers and data points with large error bars. The modified Z-score method uses the median and the deviation from the median to detect outliers and hence is more robust compared to the more common σ clipping method. The modified Z-score of observations is defined as

$$\mathrm{M}_i = \frac{0.6745\ (x_i - \tilde{x})}{\mathrm{MAD}}$$

where $\tilde{x}$ is the sample median, and the constant 0.6745 is the 75% confidence level of the standard normal distribution, to which the MAD converges. Observations with Z-scores above the cut-off value are labelled as potential outliers ($|\mathrm{M}_i| > \mathrm{D}$). We adopted D = 3.5 in this analysis, as Iglewicz (1993) suggested this value as the cut-off value relying on a simulation study with 10,000 replications of n pseudo-normal observations for sample sizes

TABLE 3.1: RV-Loud Star Subsample Categorisation Based on CRX-RV Correlation

Category	Criterion	Number of Stars	
		VIS	NIR
Chromatic	log(p-value) < -2.3	19	14
Suggestive	-2.3 < log(p-value) < -1.3	11	10
Achromatic	log(p-value) > -1.3	26	32

equal to 10, 20, and 40. On average, the modified Z-score method removed less than 5 data points for each star in our sample. However, due to the instrumental change in the NIR channel (see, e.g., Bauer et al., 2020), only data after 30 October 2016 has been considered, and hence more data points have been discarded for some stars in this regime. Tables A.2 and A.3 present the number of the used data points after the cleaning procedure ($n_{\rm RV}$) for the VIS and NIR channels. We have also listed std(RV) values used for sample selection, as well as the median RV uncertainties ($\overline{\delta \rm RV}$) of the stars' cleaned RVs. We calculated the std(RV) uncertainty using std(RV)$(2\ n_{\rm RV})^{-0.5}$ following Tal-Or et al. (2018). A larger $\overline{\delta \rm RV}$ compared to std(RV) for RX J0447.2+2038 (J04472+206) in VIS and Barta 161 12 (J01352-072) and GT Peg (J22518+317) in NIR indicates that the observed scatter for these targets could be dominated by the measurement error rather than other trends.

In order to determine the wavelength dependence of RVs for a given star, we used the F-statistic and its p-value (Fisher, 1925). We considered a linear regression model between RV and CRX as opposed to the constant model as the null hypothesis. We performed the F-statistic as follows

$$F_{\rm lin} = (N-2)\,\frac{\chi^2_{\rm const} - \chi^2_{\rm lin}}{\chi^2_{\rm lin}}.$$

where 'lin' and 'const' identify whether the model used was the linear fit or constant[3], respectively, and N is the number of data points. We then determined the p-value by comparing the F-statistic to the F-distribution with appropriate degrees of freedom for each model. The P-value represents the probability of obtaining the calculated F-statistic by chance if the null hypothesis (that the linear regression model is not preferred over the constant model) is true. If the p-value is less than a predetermined significance level (e.g. <0.01, i.e. 99% confidence), the null hypothesis is rejected, meaning that the linear regression model is preferred over the constant model, and the correlation between the RV and CRX is considered statistically significant. Following the criteria outlined by Tal-Or et al. (2018), we adopt p-values of 0.005 and 0.05 as a measure for a significant and a marginal correlation between RV and CRX, respectively. Accordingly, we categorised our sample into three subsamples as follows: stars with p-values < 0.005 (or log(p-value) < -2.3) as 'chromatic', those with p-values > 0.05 (log(p-value) > -1.3) as 'achromatic', and targets that fall between these values (0.005 <p-values < 0.05) are marked as 'suggestive'. Table 3.1 summarises the criteria and lists the number of stars that fall in each category.

[3]The χ^2 used for a constant model is

$$\chi^2_{\rm constant} = \frac{\sum (RV_i - \overline{RV})^2}{\sigma^2_{\rm RV}}.$$

A challenge to the statistical analysis of our sample is the large difference in the number of RV measurements for stars, which varies between 11 to 123 data points in VIS and goes as low as 4 data points in NIR. Since statistical methods, such as the p-value, are highly affected by the sample size, directly comparing the p-value of targets with such a large discrepancy in the sample size is unreliable. To prevent the difference in the sampling from affecting the p-value, we apply a bootstrapping method with 10,000 iterations to the RV measurements of each star, selecting each time a random subsample of 11 data points with replacement for the p-value estimation. The final p-value is estimated as the median of these 10,000 iterations. The resulting p-values are listed in Tables A.2 and A.3.

For comparison, we also measured the Pearson correlation coefficient $\mathscr{R}$ using a bootstrapping method with 10,000 iterations, similar to the calculation of the p-values. The median of $|\mathscr{R}|$ for chromatic targets in VIS and NIR is 0.89 and 0.82, respectively. For suggestive targets, $|\mathscr{R}| = 0.61$ for both VIS and NIR, and for the achromatic subsamples, $|\mathscr{R}|$ is 0.19 and 0.26 in VIS and NIR, respectively. These values are in good agreement with the p-value estimates. The bootstrapped $\mathscr{R}$s are presented in Tables A.2 and A.3.

In Figure A.1, we show the order-by-order RV measurements together with the slope of the best fit line to the RVs over order, which leads to the CRX values and the corresponding CRX-RV correlations in VIS and NIR for the active RV-loud sample. The stellar rotation period and the category, as well as the log(p-value) and the CRX-RV correlation slope, are indicated in the legends for each target. We colour-coded the plots with the rotation phase of the stars to detect possible dependencies of observations on the rotational phase, and for targets with unknown photometric rotation periods, the data points are coloured with the number of observations.

As shown in Figure A.1, for many stars the CRX-RV plots displays a cloud of points with no structures or certainly no linear correlations. Therefore, to quantify the goodness of the CRX-RV regression slope, we use $|m/\sigma_m|$, with σ_m being the error bar on the fitted slope. The values for the CRX-RV slope (m), χ^2_m, and $|m/\sigma_m|$ are tabulated in Tables A.2 and A.3.

3.4.2 Periodogram analysis

To detect periodic signals in the data, we computed Generalised Lomb-Scargle periodograms (GLS; Zechmeister and Kürster, 2009) of the RV and CRX time series in both spectrograph channels. We restricted ourselves to targets with a sufficient sampling rate (at least 20 data points) and $\overline{\mathrm{S/N}}$ above $\sim$20 at order 82 ($\sim$750 nm) and $\sim$40 at order 49 ($\sim$1250 nm) for the VIS and NIR channels, respectively. For stars with a known rotation period $>$ 1 d, we sampled frequencies from 0.001 d^{-1} to an upper limit of 1 d^{-1}, with an oversampling factor of the frequency grid of 100 points to ensure the recovery of all significant peaks. For targets with sub-day rotation periods, we considered a frequency grid from 0.01 d^{-1} to 10 d^{-1}, with an oversampling factor of 10 to save computing time. The daily and yearly aliases result from nightly observations for ground-based observations and must be taken into account. Therefore, we also calculated the 1-day alias frequency of the selected signals with frequency f as $f_{\mathrm{alias}} = 1\mathrm{d}^{-1} - f$. Signals corresponding to (known) stellar rotation periods (or harmonics thereof) are considered activity-related signals. In the case of targets with unknown rotation periods, common signals in RV and CRX which are smaller than the upper limit calculated from stellar radius and projected rotational velocity are assumed

activity signals. To obtain the significance of a given periodogram peak, we calculated the false alarm probability (FAP) of the signal through the analytical formula presented in Zechmeister and Kürster (2009). The periods and FAPs of the significant peaks that we identified as being attributed to stellar activity are presented in Tables A.2 and A.3. In addition, activity-related periods identified through the periodogram analysis, even if found to be statistically insignificant, are included in the tables along with their corresponding FAP values. In cases where the 1-day alias of the activity-related signals showed a higher power, we mention that period and its alias and significance in the table notes. We ignored yearly aliases and insignificant peaks at periods other than $P_{\rm rot}$ or its harmonics.

The results of the periodogram analysis support the categorisation we performed based on the degree of CRX-RV correlation: For chromatic and suggestive targets, the periodograms both of RVs and CRXs show (mostly significant) peaks at the $P_{\rm rot}$, $\frac{1}{2}P_{\rm rot}$, or 1-day aliases thereof. For achromatic targets, in contrast, the periodograms either show a peak only in RVs or no peak at all. There are two exceptions to the consonance between the categorisation and periodogram results, both of which appear in the NIR channel. The first one is AD Leo (J10196+198), the well-known active star with $P_{\rm rot}$ = 2.24 d that was analysed in great detail by Kossakowski et al. (2022). While AD Leo is chromatic in the VIS channel, it was categorised as achromatic in NIR, with a log(p-value) of -1.0 and Pearson $\mathscr{R} = -0.33$. However, the periodograms of $\rm RV_{NIR}$ and $\rm CRX_{NIR}$ show significant peaks at $\sim$ 2.2 d with FAP $\leq$ 0.1% and $\sim$ 0.24%, respectively. The other target is V1216 Sgr (J18498-238), with $P_{\rm rot}$ = 2.85 d, that is classified as a suggestive target in both VIS and NIR channels. V1216 Sgr is one of the three stars in our sample that show signals at both $P_{\rm rot}$ and $\frac{1}{2}P_{\rm rot}$ in $\rm RV_{VIS}$. The $\rm CRX_{VIS}$ of V1216 Sgr shows a less significant signal (FAP $\sim$ 18.19%) at $\frac{1}{2}P_{\rm rot}$, whereas $\rm RV_{NIR}$ and $\rm CRX_{NIR}$ do not show any signal related to the activity. The other stars with peaks in $P_{\rm rot}$ and $\frac{1}{2}P_{\rm rot}$, J22468+443 and J18174+483, are discussed in detail in Section 3.6.1 and 3.6.2.

3.4.2.1 New Rotation Period Measurements

Among the targets with an unknown or previously unknown rotational period, there are cases with significant peaks in their periodograms that we attributed to the stellar rotation period. For example, J10584-107 is a mid-M dwarf (M5.0 V) with a $v \sin i$ of 3.2 $\rm km\,s^{-1}$categorised as a suggestive target. The $\rm RV_{VIS}$ and $\rm CRX_{VIS}$ periodograms show significant peaks at 1.27 d and its 1d alias, around 4.6 d. We calculated the upper limit on the maximum $P_{\rm rot}$ from the stellar radius and $v \sin i$ to be 6.56 d and concluded that the 4.6 d peak is most likely the rotational period of the star. In NIR, where this target is categorised as achromatic, the periodograms do not show any significant period other than the daily and yearly aliases. Another target is the late-type M7.0 V star, VB 8 (J16555-083), which has no rotation period available in the literature. We retrieved the photometric light curves from the MEarth-South survey[4] (Irwin et al., 2009; Irwin et al., 2015), performed the periodogram analysis, and found the highest peak at 10.94 d with FAP$\leq$ 0.1. This period shows a 1-day alias signal at 1.1 d with a FAP$\sim$0.37%. Since the upper limit on $P_{\rm rot}$ for this target is about 1.587 d, we consider the 1.1 d signal as the rotation period of the star. The periodograms of $\rm RV_{VIS}$ and $\rm RV_{NIR}$ show significant peaks at 1.09 d and a 1-day alias at 11.2 d. Between targets with more than 40 data points in the VIS channel, there are two targets with inconclusive periodogram

[4] https://lweb.cfa.harvard.edu/MEarth/DR10/south2014-2020/index.html

analyses. These are J19169+051S and J19255+096, two M8.0 V dwarfs with $J \geq 9.9$ mag. Their low mass and faintness contribute to less precise radial velocity measurements and inconclusive periodogram results.

3.5 Correlation between chromaticity and stellar parameters

We considered two approaches to investigate how the chromatic behaviour relates to the other stellar parameters and how it changes over the VIS and NIR wavelength regimes. First, we studied the distribution of the three subsamples over the main properties of the stars, that is, the spectral type, stellar mass, apparent brightness, rotational velocity, rotational period, and the activity level as measured by $\log L_{\mathrm{H}\alpha}/L_{\mathrm{bol}}$. Figure 3.2 shows histograms of the mentioned stellar parameters. The fraction of each subsample in VIS and NIR is overplotted with a distinct colour for each category. Moreover, since the RVs of the chromatic and suggestive subsamples are either correlated or anti-correlated with CRX, we distinguished the fraction of the targets with positive and negative correlations in these two categories with // and \\, respectively. By definition, achromatic stars with uncorrelated RVs and CRXs do not allow this distinction. We also included histograms of the number of used RV data points and the RV scatter std(RV) to Figure 3.2, in order to investigate possible relations to these two parameters. The values for stellar parameters are taken from Table A.1, and the number of the data and std(RV) are from Tables A.2 and A.3. The histograms of the rotation period and activity level only include stars with a known P_{rot} and $\log L_{\mathrm{H}\alpha}/L_{\mathrm{bol}}$, and the total number of targets used for each histogram is noted in the respective plots.

The top panels of Figure 3.2 show the histograms of the spectral type. As noted earlier, the active RV-loud sample covers all M spectral subtypes; however, the majority of stars, no matter whether chromatic, suggestive, or achromatic, have mid spectral subtypes (M4.0 V to M5.5 V). The chromatic behaviour of early to mid-type M dwarfs disappears either entirely or becomes less significant in the NIR regime. Also, stars with a positive CRX-RV correlation are clustered between M4.0 V and M5.5 V, and their fraction increases in the NIR domain.

The distribution of stellar masses, in the second row, shows that 82% of stars have a mass below 0.35 $\mathrm{M}_{\odot}$ and are likely fully convective. Chromatic behaviour is present across most mass ranges in the VIS regime, but is more concentrated in higher-mass stars. 50% of stars with $\mathrm{M} > 0.35$ $\mathrm{M}_{\odot}$ are chromatic compared to 30% of stars with lower masses. When considering both chromatic and suggestive stars, the proportions of chromatic behaviour are more balanced between high and low-mass stars (60% vs 52%, respectively). In the NIR regime, only 10% of high-mass stars are categorised as chromatic while 30% of stars display chromaticity overall, representing a 50% decrease compared to the VIS channel. Lower mass stars exhibit more chromatic behaviour in the NIR domain, with 28% being classified as chromatic targets and 46% as both chromatic and suggestive. There is no preferred mass range for stars with CRX-RV positive correlation in the VIS domain, however, in the NIR domain, stars with a significant positive chromaticity tend to have a mass between 0.25 and 0.3 solar $\mathrm{M}_{\odot}$.

The distribution of stars based on their apparent brightness in the third row does not show any particular correlation. In contrast, the histogram of $v \sin i$, shown in the fourth

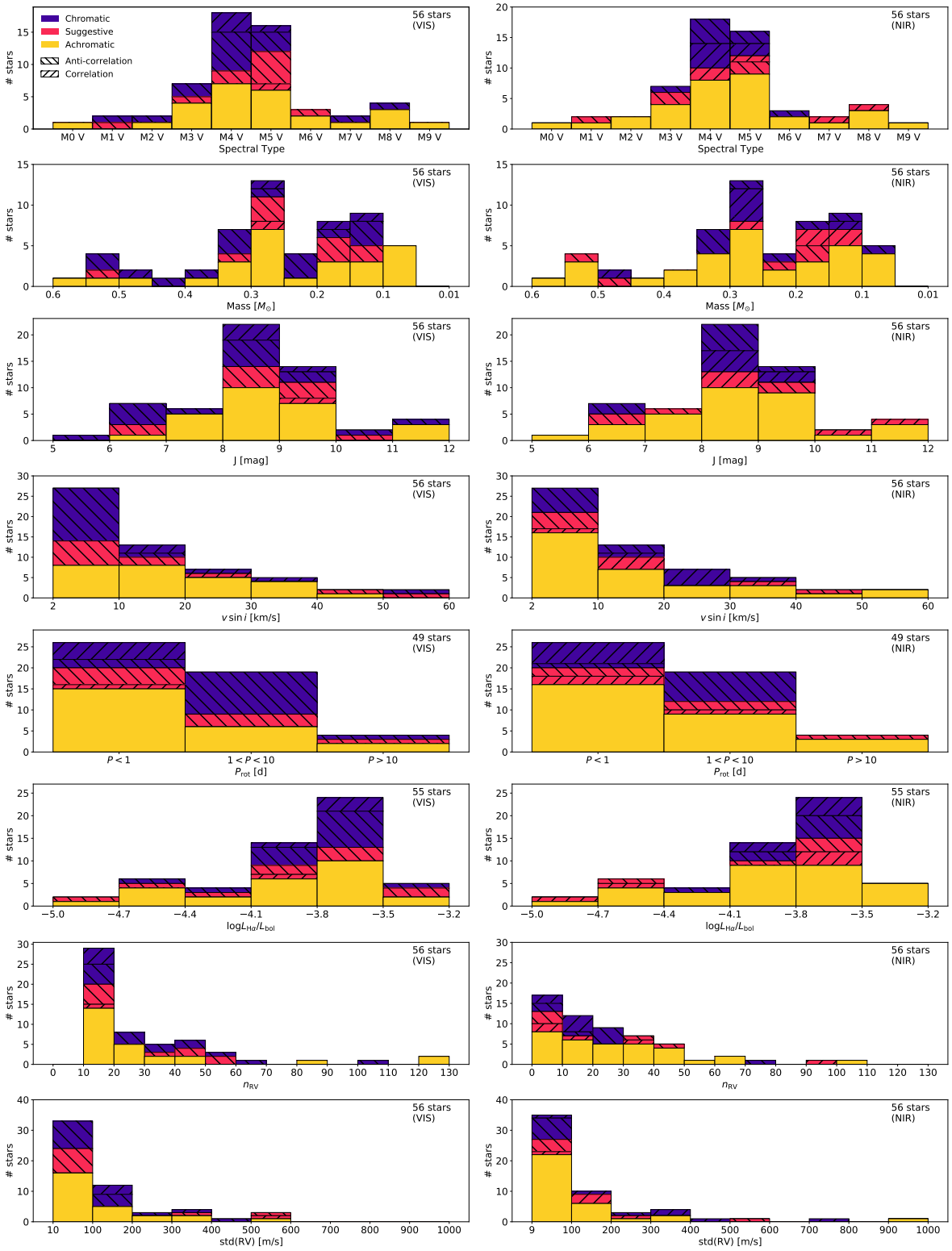

FIGURE 3.2: Histograms of active RV-loud stars. Chromatic, suggestive, and achromatic subsamples are shown in purple, pink and yellow, respectively. The fraction of stars with CRX-RV correlation is shown with //, while anti-correlation is depicted with \\. The histogram plots are made of the whole sample of 56 stars, except for $P_{\rm rot}$ and $\log L_{\rm H\alpha}/L_{\rm bol}$, where these parameters are known for only some of the stars. The number of targets used for making plots with the corresponding channel is noted on each plot. Stellar properties are compiled from Table A.1, and the number of the used RV data points $n_{\rm RV}$, RV scatter $std(RV)$, and the portion of each subsample are collected from Tables A.2 and A.3 for the VIS and NIR data, respectively.

row, conveys that perhaps the rotational velocity is the key factor responsible for the chromatic behaviour of the stars. In the VIS channel, 68% of the chromatic stars and 55% of suggestive ones have $v \sin i < 10$ km s^{-1}. All these stars exhibit CRX-RV anti-correlation. In comparison, only 31% of the achromatic stars have $v \sin i < 10$ km s^{-1}. However, in the NIR domain, the number of the achromatic stars with $v \sin i < 10$ km s^{-1} doubles, which is 50% of all the achromatic stars in this regime. Also, 42% of the combined chromatic and suggestive stars with $v \sin i < 10$ km s^{-1}show a negative CRX-RV correlation, while 42% with $v \sin i > 10$ km s^{-1} show a positive CRX-RV correlation.

Similarly, the histogram of the rotation period, shown in the fifth row, demonstrates that 65% of stars in the VIS regime with sub-day rotation periods are achromatic. Also, all the chromatic and suggestive stars with a positive CRX-RV correlation, which make up ~ 20% of the stars in these two categories, have $P_{\rm rot} < 1$ d. In comparison, 50% of the stars with a negative CRX-RV correlation have a rotation period between 1 and 10 days. Since there are only four stars with $P_{\rm rot} > 10$ d in our sample, it is not easy to draw any reliable conclusions about the chromatic behaviour of slow-rotating stars. In the NIR channel, almost the same proportion of stars as in the VIS channel with $P_{\rm rot} < 1$ d is achromatic, but the number of achromatic targets with $1 < P_{\rm rot} < 10$ d increases from 32% in VIS to 47% in NIR. Similar to the VIS domain, stars with positive CRX-RV correlation mainly bear a sub-day rotation period, and those with anti-correlation have $P_{\rm rot} > 1$ d.

The distribution of stars over the normalised Hα luminosity, provided in the sixth row of Figure 3.2, shows that all stars in our sample are Hα active, and about 70% of them have $\log L_{\rm H\alpha}/L_{\rm bol}$ measurements between -4.1 and -3.5. However, Hα activity does not seem to be directly correlated with the chromatic behaviour of stars, as we can see that both chromatic and achromatic stars are equally spread over a wide range of Hα activity levels in both the VIS and NIR channels.

A major concern about our sample was the small number of RV measurements, which could lead to biases in the reliable tracing of wavelength dependency in our sample. The distributions of RV data points ($n_{\rm RV}$) shown in the seventh row of Figure 3.2 display that for 52% of stars observed in VIS, there are less than 20 data points to use. In NIR, 30% of the stars have even fewer than ten data points since we had to discard data taken before 30 October 2016. Nevertheless, we could detect different degrees of wavelength dependency independent of the number of RV data points in both channels. We note here that all stars with a positive CRX-RV correlation in VIS and all but one in NIR have $n_{\rm RV} < 20$. Finally, in the bottom row of Figure 3.2, we show the distribution of RV scatters for our subsamples. Tal-Or et al. (2018) showed a significant std(RV)–$v \sin i$ correlation in their sample of stars and proved that the RV scatter could be the result of the activity of the star and the loss of RV information due to the rotational line broadening simultaneously. From the histogram of std(RV), it is clear that there is no correlation between the RV scatter and the chromaticity of the star.

As a second approach, we examined how the CRX-RV regression slope and the goodness of fit vary over the above-mentioned stellar properties. In Figure 3.3, we show the CRX-RV slope m over $P_{\rm rot}$ and $v \sin i$, the two stellar parameters that appear to be correlated with the chromatic behaviour in stars. In the top left panel, the regression slopes of the stars over $P_{\rm rot}$ are divided by a black vertical line into two sections. Stars with $P_{\rm rot} < 1$ d are more scattered as compared to those with $P_{\rm rot} > 1$ d, which seem to have more consistent slope values. In addition, the goodness of fit for these stars, shown in the bottom left panel,

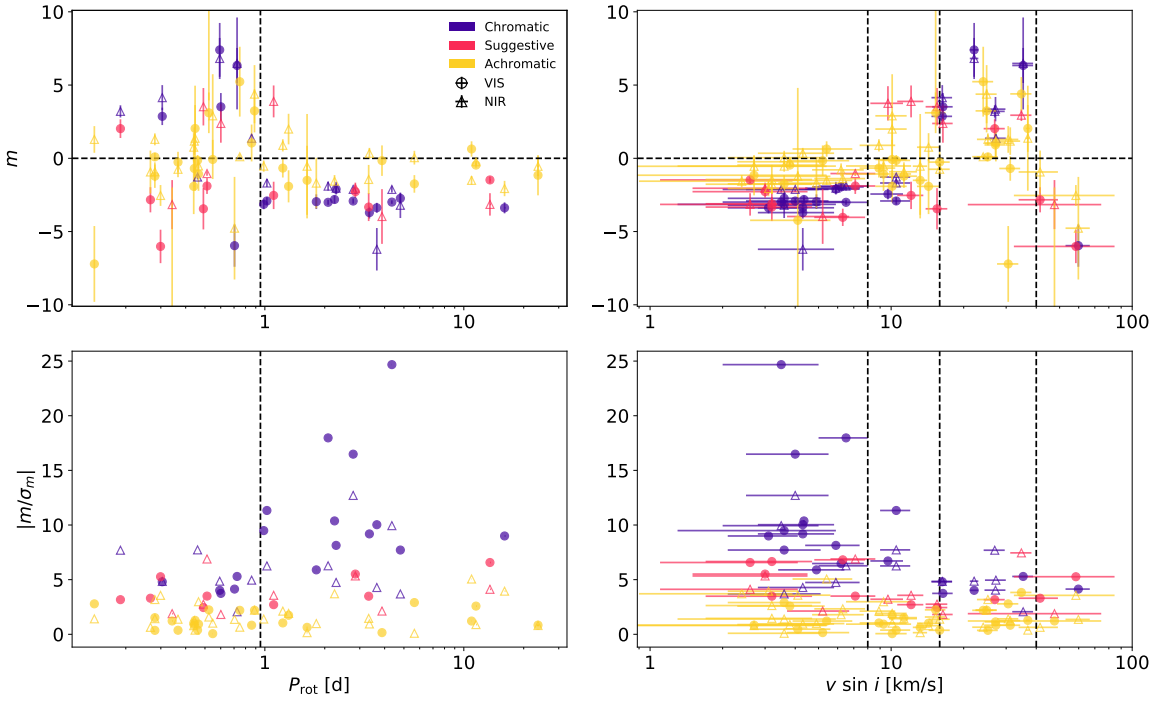

FIGURE 3.3: The CRX-RV regression slopes as a function of the stellar rotation period ($P_{\rm rot}$, *top left*), and rotational velocity (v sin i, *top right*). The goodness of the fit ($|m/\sigma_m|$) corresponds to the slopes from the top panels vs $P_{\rm rot}$ (*bottom left*) and v sin i (*bottom right*). Filled circles represent VIS data, and open triangles correspond NIR data. The black dashed lines are to aid eyes in categorising groups of stars (for details, see Section 3.5).

indicates that the chromatic stars in the latter group have a stronger linear trend than those in the former set, particularly in the VIS channel. In the top right panel, the slope of the regression over v sin i reveals clusters of stars that we divided by black vertical lines into four groups. The first batch contains stars with v sin $i < 8$ km s^{-1} that show a negative slope in both VIS and NIR channels, whereas stars with v sin i between 8 and 16 km s^{-1} exhibit a negative slope in the VIS channel and both negative and positive slopes in NIR. Stars with $16 < v$ sin $i < 40$ km s^{-1} form another batch with nearly only positive slopes in both VIS and NIR channels, while the fast rotating stars with v sin $i > 40$ km s^{-1} display a negative slope in both channels. The bottom right panel shows how the goodness of a linear regression exacerbates for the faster-rotating chromatic stars. These plots indicate that stars may have different activity mechanisms at work depending on their rotational velocity. To further elaborate, for stars with a moderate rotation velocity ($2 < v$ sin $i < 10$ km s^{-1}) within the CARMENES wavelength range, the dominant effect is the temperature contrast which creates negative chromaticity. As the v sin i increases, it is probable that the Zeeman splitting of spectral lines, which also accompanies strong magnetic fields, prevails and counteracts the contrast effect. The displacements of the Zeeman components grow with wavelength hence creating positive chromaticity in the RV measurements (see, e.g. Reiners et al., 2013). Since the effect of temperature contrast is less pronounced in the NIR, the Zeeman effect first mainly impacts NIR observations (for v sin $i \sim 10$ km s^{-1}) and becomes the overall predominant effect for faster-rotating stars ($16 < v$ sin $i < 40$ km s^{-1}). For stars

with $v \sin i > 40$ km s^{-1}, it is hard to verify if the negative regression slope is due to an activity phenomenon or the loss of RV content caused by spectral line broadening. Another possible explanation for the positive slope is the presence of telluric contamination in the red orders of the VIS channel. Probably, the faster-rotating stars are more affected by telluric since their spectral lines are broadened which leads to less RV content and more scattering in the measurements.

We also examined the relations between the CRX-RV regression slope and the other stellar parameters, namely spectral type, stellar mass, apparent brightness, normalised Hα luminosity, number of RV data points, and RV scatter (see Figure A.2); however, we did not find any correlations with these quantities.

3.6 Tracing stellar activity across échelle orders

As already mentioned, achieving an RV precision at the m s^{-1} level demands the use of hundreds or even thousands of spectral lines to reduce the measurement error, especially for intrinsically faint M dwarfs with low S/N. In CARMENES, RVs are measured for individual échelle orders within an observation and then combined into an overall value by taking a weighted average of the order-wise RVs (Zechmeister et al., 2018). The CARMENES VIS channel consists of 61 orders recorded on a 4k × 4k CCD detector. Only 42 orders (wavelength range of $\sim$ 5600 – 9200 Å) are considered for computing RV measurements, as the ten bluest orders do not reach a high enough S/N for M stars, and the last nine orders are affected by telluric contaminations and the beam splitter cutoff (Bauer et al., 2020). The CARMENES NIR channel contains 28 orders expanding over Y, J, and H photometric bands. The spectrum in this regime is recorded on a set of two 2k × 2k CCD detectors placed side by side, with a gap corresponding to about 140 pixels in between them (Bauer et al., 2020). As a result, each half-order is treated separately by `serval`, and RV measurements are calculated for 56 wavelength segments. However, only 19 half-orders are considered for calculating the final RV value as the rest of the orders are affected by telluric contamination, specifically in the J band.

To investigate the contribution of individual orders to the activity-related signals, we computed GLS periodograms for the RVs of each order separately, with a fixed frequency range and sampling factor as described in Section 3.4.2. We then generated a stacked periodogram by plotting the order frequencies, colour-coded by the power of the GLS periodogram. The y-axis of the stacked periodogram shows the order numbers of the échelle spectrograph and tracks the presence and significance of signals vertically over the wavelength range. This type of analysis has been performed in the past, for example, for Teegarden's Star using the maximum likelihood periodogram (Zechmeister et al., 2019). To better quantify the impact of activity on each order, we calculated the semi-amplitude K of the best-fitted sine curve at the desired period (e.g., $P_{\rm rot}$ or $\frac{1}{2}P_{\rm rot}$) for the order-wise RVs as well as the overall RV time series. This approach allows us to compare the activity-induced RV variability between spectral orders for a given star. Moreover, by normalising the order-wise K values by the semi-amplitude K of the overall RVs, we can compare the activity-related RV variations for spectral orders between different stars with different activity levels (see Section 3.7).

We have selected six stars with a high enough sampling rate and significant peaks in the GLS periodogram of their RVs for the detailed periodogram analysis over the individual orders of the CARMENES VIS and NIR spectrographs. All the selected targets have been observed by the the Transiting Exoplanet Survey Satellite (TESS; Ricker et al., 2015) as well, though not simultaneously with the CARMENES observations[5]. Nevertheless, we have obtained their photometric light curves for further comparison with the RV and CRX measurements. The six stars all have spectral types earlier than M4.5 V, and are moderately rotating stars with $2.6 < v \sin i < 4.3$ km s^{-1}, and $P_{\rm rot}$ between 2.8 and 16 days. Among them, four are categorised as chromatic, one as suggestive and one as achromatic. Two of the chromatic stars show one dip per rotation in their photometric light curves, which is attributed to an asymmetric distribution of active regions on the stellar surface (Basri and Shah, 2020), while the other two display a double-dip pattern per rotation, probably due to a more complex surface magnetic field structure and symmetric distribution of the photospheric features (Basri and Shah, 2020; Jeffers et al., 2022).

In the following, we first describe the details of the performed analysis on the selected targets and then compare the results for this diverse set of stars.

3.6.1 J22468+443 (EV Lac)

EV Lac, a mid-M dwarf (M3.5 V) with a high normalised Hα luminosity ($\log L_{\rm H\alpha}/L_{\rm bol} \sim$ -3.65), is one of the most active stars in our sample, showing chromatic behaviour. The photometric light curve of the star, obtained by TESS in sector 16 from 12 September to 6 October 2019, shows a double-dip structure with a periodic variation of $\sim$ 4.35 days. This value is in close agreement with the previously reported value of 4.38 d by Díez Alonso et al. (2019) from the SuperWASP survey (Pollacco et al., 2006). Figure A.3 shows the RV and CRX time series of EV Lac together with the TESS light curve, phase-folded to the rotation period of the star. The double-dip pattern is evident in the RV and CRX time series of both the VIS and NIR channels. The semi-amplitude of the fitted sinusoid model to the RV data is about ten m s^{-1} larger in VIS compared to NIR. Similarly, the semi-amplitude of the fitted sinusoid model to the CRX values, which is anti-correlated to the RV curves, shows $\sim$ 60 m s^{-1} Np^{-1} larger excursion compared to NIR.

The periodograms of EV Lac show multiple activity-related signals at its rotational period, second harmonic, and their 1-day aliases. In the VIS channel, the most significant signals for overall RVs and CRXs are at $\frac{1}{2}P_{\rm rot}$ and its 1-day alias with FAP $< 0.1\%$, and another less significant one at $P_{\rm rot}$ with FAP $\sim 0.83\%$ and $\sim 20\%$, respectively. Similarly, the order-wise periodograms show their highest peak at $\frac{1}{2}P_{\rm rot}$ with FAP $< 0.1\%$ in all orders except for orders #75, #74 (810 – 830 nm) and #68, #67 (890 – 920 nm), which are affected by the atmospheric H_2O absorptions. However, the $P_{\rm rot}$ signal gets more power and becomes significant (FAP $< 0.1\%$) at redder wavelengths between orders #83 and #70 (730 – 881 nm), except for orders #75 and #74 that contain telluric features. Table A.4 presents the periods and FAPs of the significant peaks identified for each order in the VIS channel, together with the FAPs of the peaks at $P_{\rm rot}$ and $\frac{1}{2}P_{\rm rot}$ for EV Lac. The top panel of Figure 3.4 shows the GLS periodogram of the overall RV (black line) and the stacked GLS of the order-wise RVs for EV Lac in the VIS channel. The primary signal is seen at

[5]TESS Web Viewing Tool: https://heasarc.gsfc.nasa.gov/cgi-bin/tess/webtess/wtv.py Accessed 27 September 2022.

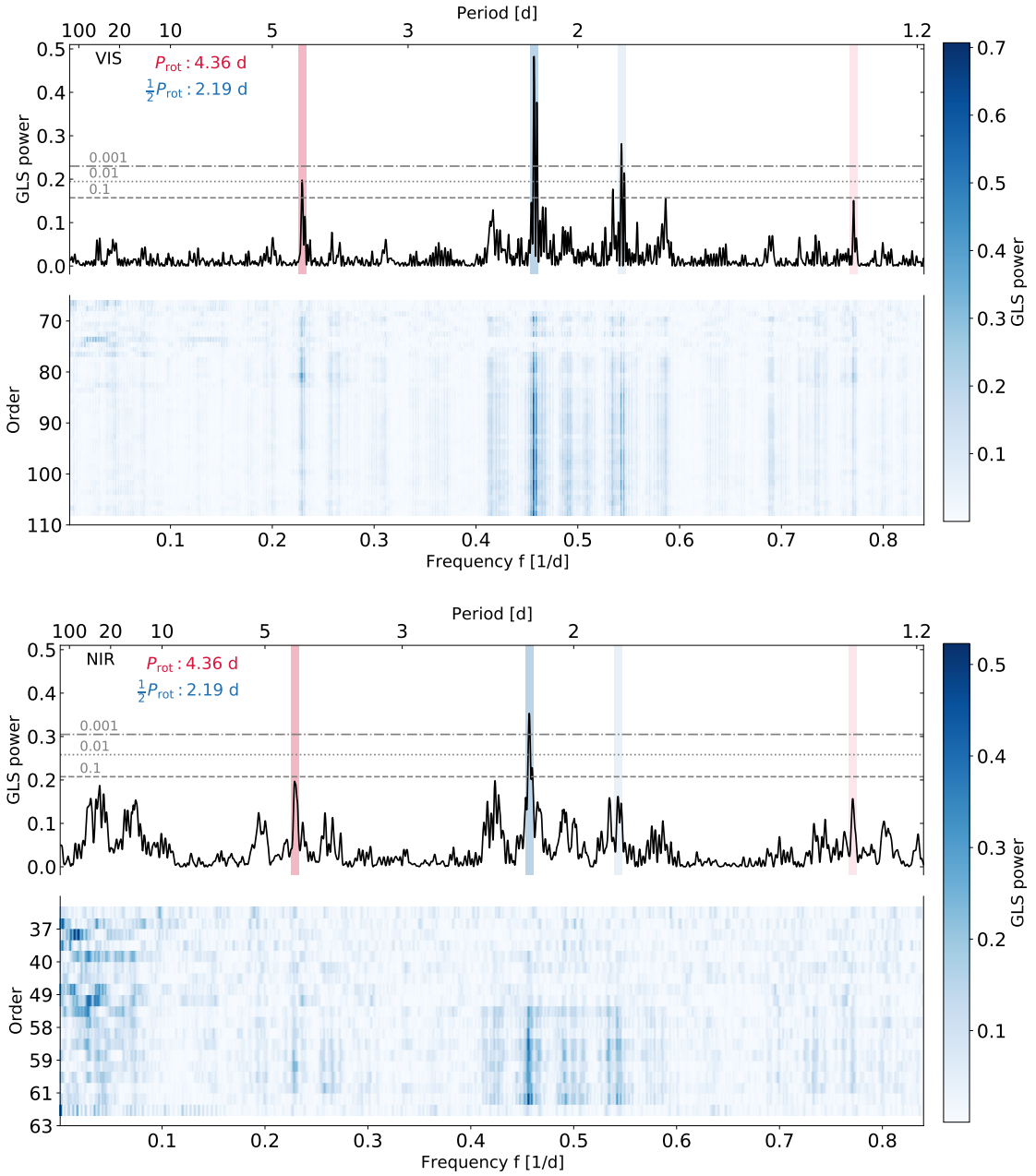

FIGURE 3.4: *Top panel:* The GLS periodogram of the $\mathrm{RV_{VIS}}$ data set (black), as well as the stacked periodogram for the order-wise $\mathrm{RV_{VIS}}$ data of EV Lac (J22468+443). The order-frequency map is colour-coded with the power of the GLS, where darker areas indicate a stronger signal. In the top panel, the horizontal grey lines indicate FAP levels at 10% (dashed), 1% (dotted), and 0.1% (dash-dotted). The red and blue shaded regions correspond to the rotational period of 4.36 d and $\frac{1}{2}P_{\rm rot}$ of 2.19 d, respectively, while the lighter colours represent their 1-day aliases. The exact value for the most significant signals and their corresponding FAP for each order, together with the FAP of the activity-related peaks at $P_{\rm rot}$ and $\frac{1}{2}P_{\rm rot}$, are provided in Table A.4. *Bottom panel:* Same, but for the $\mathrm{RV_{NIR}}$ data set. Due to the telluric contamination, only specific orders are considered in the NIR wavelength regime (see Section 3.6 for details). Selected orders, the values for the highest peaks, their corresponding FAP, and the FAP of the activity-related signals are listed in Table A.5.

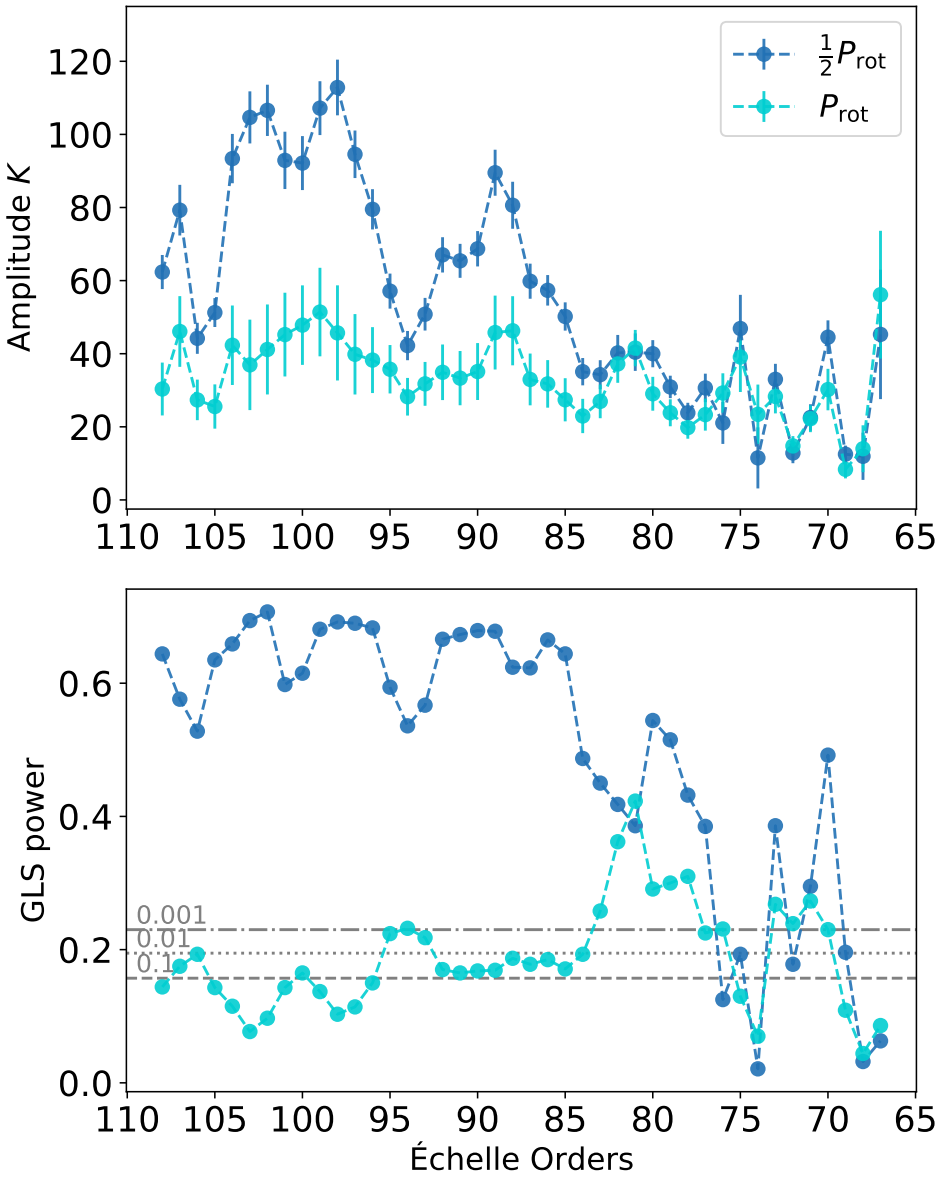

FIGURE 3.5: *Top panel:* A comparison between the order-wise RV semi-amplitude K of the best-fitting sine function at $P_{\rm rot}$ and $\frac{1}{2}P_{\rm rot}$ over the échelle orders of the VIS channel for EV Lac. *Bottom panel:* The corresponding GLS power of the peak at $P_{\rm rot}$ and $\frac{1}{2}P_{\rm rot}$ over échelle orders. The horizontal lines correspond to FAP levels of 10% (dashed), 1% (dotted), and 0.1% (dash-dotted).

2.19 days, corresponding to the $\frac{1}{2}P_{\rm rot}$. When this signal becomes weaker around spectral order #80, another signal at 4.36 days, which corresponds to the rotation period of the star, becomes stronger. Orders affected by telluric contamination show mostly aliases of the daily signals. Figure 3.5 provides a comprehensive comparison between the RV semi-amplitude K calculated per spectral order at $P_{\rm rot}$ and $\frac{1}{2}P_{\rm rot}$ (top panel) and their corresponding GLS periodogram power (bottom panel). The semi-amplitudes at $\frac{1}{2}P_{\rm rot}$ and $P_{\rm rot}$ exhibit a similar modulation, although K at $\frac{1}{2}P_{\rm rot}$ demonstrates a greater excursion in the bluer orders. The GLS powers of the signals at $\frac{1}{2}P_{\rm rot}$ mirror the behaviour of those at $P_{\rm rot}$ in shorter wavelengths. As the GLS power at $\frac{1}{2}P_{\rm rot}$ subsides, it becomes more pronounced at $P_{\rm rot}$, and vice versa. This behaviour persists up to order #77 ($\sim$ 795 nm). In contrast, the redder orders display a more comparable pattern and strength in their GLS powers.

The bottom panel of Figure 3.4 shows the GLS periodogram of the overall RV and the stacked GLS of the order-wise RVs in the NIR channel. Similar to the VIS channel, the periodograms of RV and CRX in the NIR display their highest peaks at $\frac{1}{2}P_{\rm rot}$ with FAP $< 0.1\%$, but no significant power at $P_{\rm rot}$ or the 1-day aliases. The half-order periodograms start showing a significant peak at $\frac{1}{2}P_{\rm rot}$ from the red side of order #62 at 985 nm, where the telluric contaminations subside, to the red side of order #59 at 1048 nm. From this point redward, the peak at $\frac{1}{2}P_{\rm rot}$ becomes much less significant, and the daily and yearly aliases dominate the periodograms. The $P_{\rm rot}$ shows no significant power in almost all half-orders except for the red side of order #61 and both sides of the order # 60 (between 1001 – 1027 nm), with FAPs between 1 and 10%. We can see that activity-related signals are less significant in the NIR channel compared to VIS and only show power in orders over the J photometric band. The most significant period, their FAP and FAP of signals at $P_{\rm rot}$ and $\frac{1}{2}P_{\rm rot}$ are listed in Table A.5, where the half-orders that fall on the blue side of the detector are noted with L and those on the red side with R.

To investigate the origin of the signals observed in different spectral orders, we rely on various chromospheric and photospheric activity indicators provided by `serval`, or computed following Schöfer et al. (2019). The activity indicators examined for EV Lac are provided in Table A.6, including the corresponding spectral order for each indicator. The table presents the most significant periodogram peaks, along with their respective FAP values and the FAPs of the signals at $P_{\rm rot}$ and $\frac{1}{2}P_{\rm rot}$. Our analysis shows that the chromospheric activity indicators in the VIS channel have no or little contribution to the activity signals observed in their corresponding orders. For instance, He I D_3, Na I D_2, and Na I D_1 are located in orders which are dominated by $\frac{1}{2}P_{\rm rot}$ signals, and Hα, Ca II infrared triplet (IRT), and Fe 8691 in orders where both signals at $\frac{1}{2}P_{\rm rot}$ and $P_{\rm rot}$ display significant power. Nevertheless, He I D_3, Na I D_2, Na I D_1, and Fe 8691 do not exhibit any significant peaks in their periodograms, and Hα and Ca II IRT lines show their strongest peaks at signals which are most likely caused by sampling and not stellar activity. It is worth noting that Hα and Ca II IRT exhibit only an insignificant peak around $P_{\rm rot}$ with FAP $> 10\%$.

In contrast, the chromospheric indicators in the NIR regime seem more effective in tracking activity signals for this star. He 10833, although located in the vicinity of the telluric contaminations, shows a significant peak at $\frac{1}{2}P_{\rm rot}$ with FAP $< 1\%$. Paβ, however, shows a less significant but noticeable peak close to the $\frac{1}{2}P_{\rm rot}$ after removing observations that were contaminated by telluric absorptions. The periodograms of the orders where these lines are positioned do not show any signal but daily aliases.

Among photospheric activity indicators, CaH 3 shows periodicities at $\frac{1}{2}P_{\rm rot}$ and $P_{\rm rot}$ with

FAPs ∼ 0.4% and 1.37%, respectively. Of the TiO molecular bands, TiO 7050 shows a very significant signal at $P_{\rm rot}$ and a smaller but still significant signal at $\frac{1}{2}P_{\rm rot}$ (FAP < 0.1%). CaH 3 spreads over orders #88 and #87, and TiO 7050 over orders #87, and #86. All these orders are dominated by strong signals at $\frac{1}{2}P_{\rm rot}$ (FAP < 0.1%) and a smaller signal at $P_{\rm rot}$ (FAP < 1%). TiO 8430 shows a significant peak at $P_{\rm rot}$ with FAP < 1% but no strong signal at $\frac{1}{2}P_{\rm rot}$. This molecular band is located in orders #73 and #72, where the stellar rotation period gets more power and becomes the dominant signal. The TiO 8860 band and FeH Wing-Ford band (hereinafter FeH WFB) both show their highest peak around 9.4 d with FAP < 1%, which seems unrelated to stellar activity. TiO 8860 is located in order #69, where $\frac{1}{2}P_{\rm rot}$ signal is the strongest. Similarly, FeH WFB is positioned on the red side of order #62, which is dominated by $\frac{1}{2}P_{\rm rot}$ signal.

3.6.2 J18174+483 (TYC 3529-1437-1)

TYC 3529-1437-1 (TYC 3529 for short) is an early (M2.0 V) M dwarf, with $\log L_{\rm H\alpha}/L_{\rm bol} \sim$ -4.034, which makes it a moderately active star. The photometric time series of TYC 3529 from SuperWASP shows a periodicity of 15.8 d (Díez Alonso et al., 2019), while earlier available data of the same survey yields the value of 16.26 d (Norton et al., 2007). TYC 3529 was also observed in eight of the TESS sectors, where its $P_{\rm rot}$ fluctuated between 15.40 d and 16.25 d. Figure A.4 presents the TESS light curves of each sector phase-folded to the respective period close to the $P_{\rm rot}$ of the star, as indicated on each panel. The phase-folded plots reveal that the photometric light curve of the star goes through phases of single- and double-dip patterns over the course of three years such that the highest peaks of the periodograms in sectors 14 (observed between 18 July and 14 August 2019) and 52 (19 May to 12 June 2022) are around $\frac{1}{2}P_{\rm rot}$, while for sectors 25 (14 May to 8 June 2020), 26 (9 June to 4 July 2020), 40 (25 June to 23 July 2021), 41 (24 July to 20 August 2021), 53 (13 June 2022 to 8 July 2022), and 54 (9 July 2022 to 8 August 2022), they are close to $P_{\rm rot}$. Furthermore, Figure A.4 displays the range of observed peak-to-peak variation ($R_{\rm var}$) in the rotational modulation for each sector. A comparison of the $R_{\rm var}$ values reveals a significantly greater variation in sectors 40 and 41, almost 1.8 times that of the other sectors. This disparity can be attributed to a larger contrast between the dark and bright areas or a more extensive coverage of dark regions on the stellar surface during these periods. The episodic behavior observed in the photometric light curve of TYC 3529 serves as an indicator of the star's variable nature and substantial changes in its surface features.

The CARMENES observations of TYC 3529 spanned nearly three years, from April 2016 to January 2019, resulting in the collection of 71 data points for this target (69 of which were utilised in our analysis). The GLS analysis of the full RV dataset in the VIS channel reveals two peaks at 16.037 d and 8.1 d, with the FAP∼0.23% and 1.31%, respectively. However, $\rm CRX_{VIS}$ shows only one peak at 7.958 d with FAP∼1.31%. The complete set of $\rm RV_{NIR}$ data shows only a moderately significant peak at 16.13 d with FAP∼5.62%, and the $\rm CRX_{NIR}$ does not show any significant power at $P_{\rm rot}$ or $\frac{1}{2}P_{\rm rot}$.

The results for the order-wise analysis of the complete data set in the VIS channel is presented in Table A.7, and the stacked periodograms for both VIS and NIR channels are shown in the top left panel of Figure 3.6. In the VIS channel, activity-related signals get power at $P_{\rm rot}$ mostly between orders #100 and #85 (∼ 606–725 nm). While orders #90 to #85 show their highest peaks around both $P_{\rm rot}$ and $\frac{1}{2}P_{\rm rot}$, there are orders for which

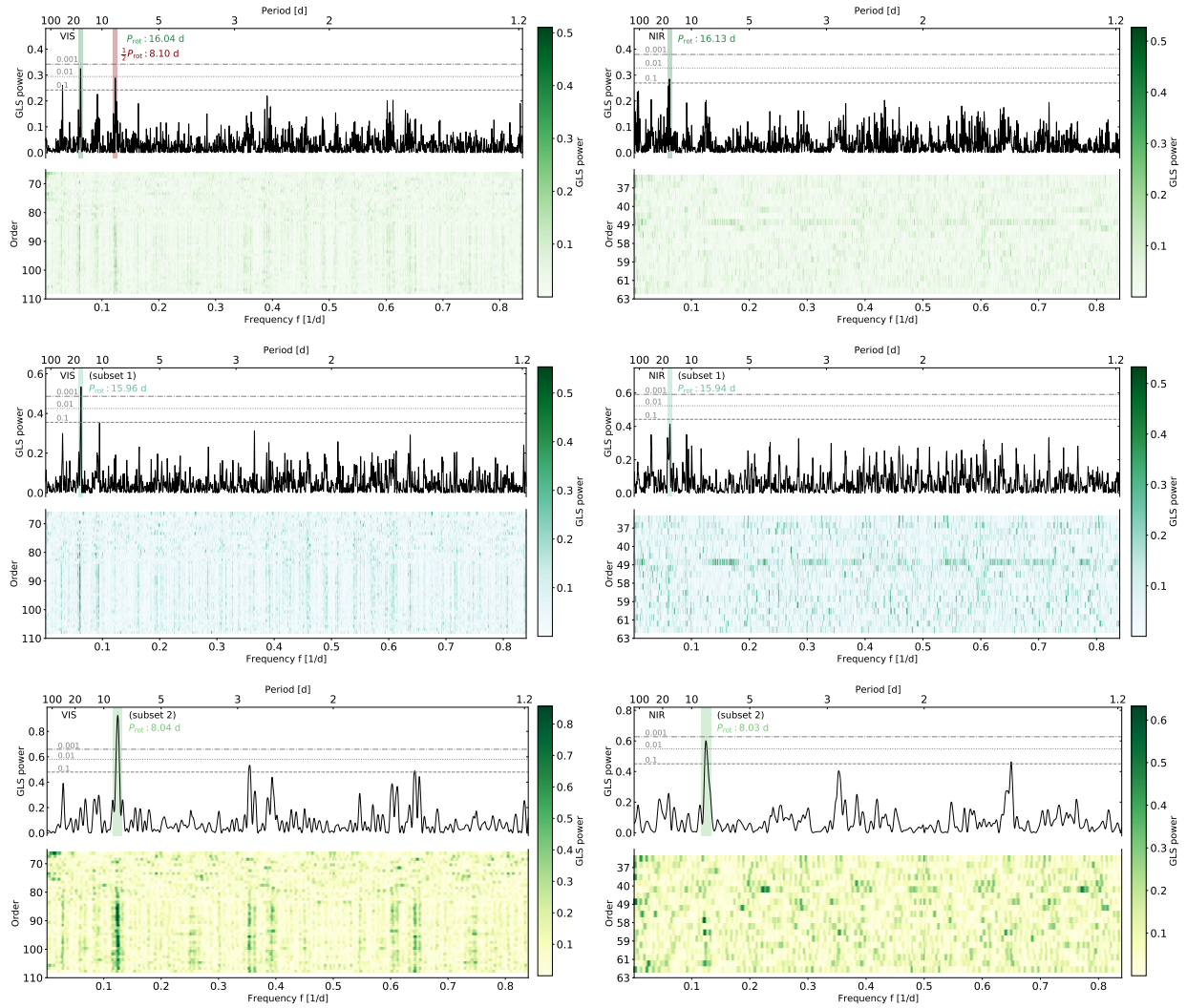

FIGURE 3.6: Same as Figure 3.4, but for TYC 3529-1437-1 (J18174+483). *Top Panel:* Complete dataset of 69 RV data points. *Middle Panel:* First Subset (44 RVs). *Bottom Panel:* Second Subset (25 RVs).

.

only one of the activity signals gets significant power, e.g. orders #101, #99, and #97, with signals close to $\frac{1}{2}P_{\rm rot}$ and orders #81, #78, and #70, with signals at $P_{\rm rot}$. Overall, for TYC 3529, the activity signals are weak at the blue end of the spectra, and similarly, they mostly disappear at orders $<$ #85 ($\lambda > 720$ nm). Observing the RVO over wavelength plot for J18174+483, depicted in Figure A.1, it becomes apparent that the RVOs at both the red and blue spectral ends exhibit increased scattering and larger uncertainties. This observation may help explain the absence of activity signals in those regions. In the NIR channel, the overall RV periodogram reveals a low-significance peak (FAP $< 10\%$) near the $P_{\rm rot}$ of the star. However, curiously, the order-wise RV periodograms do not exhibit any discernible activity-related signals, as demonstrated in the top right panel of Figure 3.6.

Concerning activity indicators, presented in Table A.8, Hα shows a moderately significant signal (FAP $< 10\%$), but not its highest peak at $P_{\rm rot}$. Ca II IRTs all exhibit their highest peak at the 1-day alias of the rotation period (with all FAPs above 5%). Among the molecular

bands, only CaH 3 displays an insignificant signal at $\frac{1}{2}P_{\rm rot}$ (FAP $\sim$ 40%). The rest of the indicators do not show any activity-related signals.

The left panel of Figure A.5 illustrates the phase-folded RV and CRX time series of TYC 3529 using the full dataset, with the period corresponding to the star's rotation period. For $\rm CRX_{VIS}$, the phase-folding is performed with respect to $2P_{\rm rot}$. Observing discrepancies between some of the $\rm RV_{VIS}$ data points and the fitted light curve suggests a possible connection to the star's episodic behaviour. To investigate this further, we conducted a search for periodic signals within the initial 20 data points. Subsequently, we added one data point at a time and reevaluated the GLS, monitoring the strength of the signal as it either intensified or weakened. This approach allowed us to divide our sample into two distinct subsets.

The first set consists of 44 data points, expanded between 21 April 2016 and 28 August 2018. The periodogram of $\rm RV_{VIS}$ shows a clear and significant peak at 15.96 d (FAP $< 0.1\%$) and no signal at $\frac{1}{2}P_{\rm rot}$. Similarly, for $\rm CRX_{VIS}$, there is a less significant but still noticeable peak at 15.95 d with FAP$\sim$6.4% and no signal at $\frac{1}{2}P_{\rm rot}$. The first subset in the NIR channel consists of 33 data points taken in the same timespan as the VIS first dataset considering only those datapoints obtained after the instrumental upgrade in October 2016. The $\rm RV_{NIR}$ displays only an insignificant signal at 15.94 d (FAP $> 10\%$), and $\rm CRX_{NIR}$ shows nothing but a forest of insignificant peaks. The middle panel of Figure A.5 displays the phase-folded RV and CRX time series of TYC 3529 for the first subset. The highest peaks of the order-by-order periodogram analysis for the CARMENES VIS are tabulated in Table A.9. The stacked periodograms for both channels are also shown in the middle panels of Figure 3.6. In the VIS channel, the peak at the $P_{\rm rot}$ gets power in order #106 ($\sim$ 577 nm) and remains significant (with FAP between 0.1% and 10%) up to order #85 ($\sim$ 720 nm) except for orders #104 ($\sim$ 586 nm) and #102 ($\sim$ 600 nm), where the power weakens. On the red side of the spectra, we can find the peak at $P_{\rm rot}$ only in orders #82 to #78 (between 746 and 785 nm) and #70 ($\sim$ 874 nm). In the NIR channel, apart from the blue side of order #58 ($\sim$ 1048 nm) exhibiting a low-significance signal near $P_{\rm rot}$ with a FAP of approximately 8.4%, no other significant signals were observed. Therefore, the results of the periodogram analysis for the NIR channel of subset 1 were not included in the tabulation. Conversely, many of the activity indicators in subset 1 successfully captured a signal near the full $P_{\rm rot}$ value. Table A.10 presents the results of the activity indicators analysis for the first subset. Among the indicators analysed, TiO7050 exhibited the strongest power at $P_{\rm rot}$ (FAP $< 0.1\%$), followed by Hα (FAP $< 0.1\%$), CaIIIRTs (with FAP ranging between approximately 0.2 and 0.8%), and HeI D_3 (FAP $\sim$ 1.7%). However, the remaining indicators did not demonstrate significant activity signals. Figure 3.7 illustrates the comparison between the order-wise RV semi-amplitudes K and their corresponding GLS powers for the first and second subsets. While the amplitudes of the variations (top plot) exhibit comparable magnitudes and patterns, the GLS powers in the second subset are notably more significant than their counterparts in the first subset. In the redder orders, where the telluric contamination dominates the data, the power of the activity-induced signals in both subsets almost entirely diminishes.

The second subset consists of 25 data points observed between 30 August 2018 and 17 January 2019. In this subset, the activity signal at $\frac{1}{2}P_{\rm rot}$ ($\sim$ 8.0 d) exhibits significant power for both $\rm RV_{VIS}$ and $\rm CRX_{VIS}$ (FAP $< 0.1\%$). However, no activity signal is detected near the full rotation period in this subset. Likewise, most of the bluer orders in the VIS channel, up to order #80, exhibit a significant peak at or near $\frac{1}{2}P_{\rm rot}$. However, orders closer to the NIR range suffer from greater uncertainties and noise, likely due to telluric contamination,

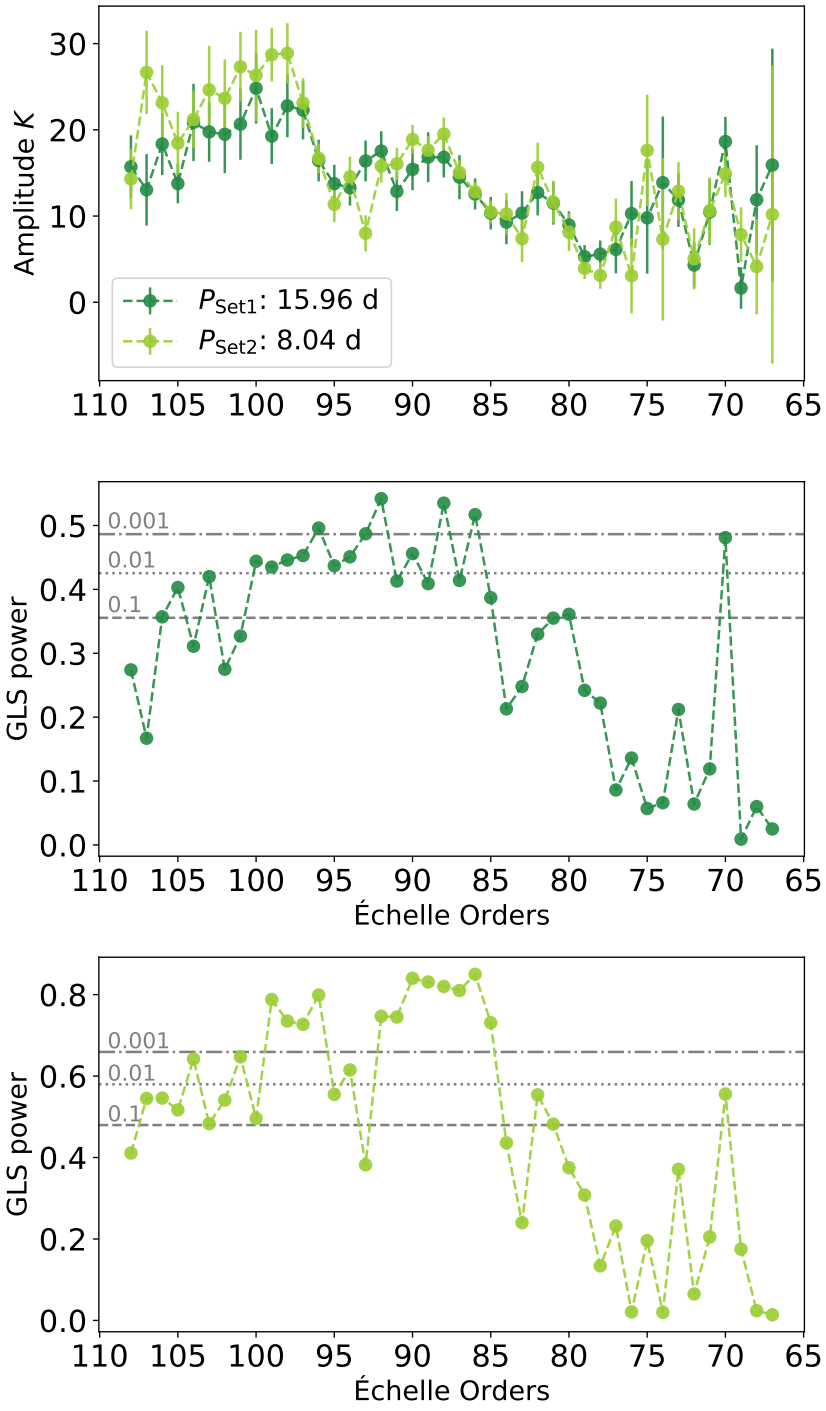

FIGURE 3.7: *Top:* A comparison between the radial velocity amplitude of the best-fitting sine function at the rotation frequency($f_{\rm rot}$) and $2f_{\rm rot}$ over échelle orders for TYC 3529-1437-1. *Bottom:* A comparison between the GLS power of the peak at $P_{\rm rot}$ and $\frac{1}{2}P_{\rm rot}$ over échelle orders. The horizontal lines correspond to FAP levels of 10% (dashed), 1% (dotted), and 0.1% (dash-dotted).

thereby lacking activity-related signals. The right panel of Figure A.5 displays the phase-folded RV and CRX time series of TYC 3529 for the second subset. The results of the order-by-order periodogram analysis for this dataset can be found in Table A.11. In the NIR channel, only the periodograms of overall RV_{NIR} and the blue side of order #58 ($\sim$ 1048 nm) demonstrate relatively significant power at $\frac{1}{2}P_{rot}$ (FAP $\sim$ 0.2%), while CRX_{NIR} still fails to exhibit any significant peak. The periodogram analysis of this channel is prived in Table A.12. In the NIR channel, only the periodograms of overall RV_{NIR} and the blue side of order #58 ($\sim$ 1048 nm) display relatively significant power at $\frac{1}{2}P_{rot}$ (FAP $\sim$ 0.2%). Similarly to the VIS channel, there are no signs of activity near the full rotation period of the star within this subset. Furthermore, CRX_{NIR} does not exhibit any significant peaks. The results of the periodogram analysis for this channel are provided in Table A.12. The GLS analysis of activity indicators for the second subset uncovered that, unlike the first subset, which exhibited significant activity signals in various chromospheric and photospheric indicators, the second subset showed only moderate significance for TiO7050 near $\frac{1}{2}P_{rot}$, with FAP levels of 5%. Table A.13 provides the results of the activity indicators analysis for the second subset.

3.6.3 J15218+209 (OT Ser)

OT Ser is another early M dwarf (M1.5 V) with a relatively high activity level ($\log L_{H\alpha}/L_{bol} \sim$ -3.766) and chromatic behaviour. Díez Alonso et al. (2019) estimates the rotation period of the star to be 3.37 d using the photometric data from the SuperWASP survey. Similarly, Norton et al. (2007) reported the 3.3829 d periodicity for this star and showed the stellar light curve with a single dip per rotation. OT Ser was observed by TESS in sectors 24 and 51, spanning from April to May 2020 and 2022, respectively. The observations in sector 24 confirmed that OT Ser maintained its single-dip light curve and exhibited a rotation period of 3.38 days. Unfortunately, the sector 51 data only yielded a shorter period of 3.33 days. This discrepancy could be attributed to significant gaps in the light curve caused by a high background level and detector saturation. As a result, the TESS data from sector 51 has limited use, and our analysis does not yield a definitive conclusion.

CARMENES obtained 52 data points for OT Ser between May 2016 and February 2019 in the VIS and NIR channels. The GLS periodograms of the RV_{VIS} and CRX_{VIS} data (see the top panel of Figure 3.8 for the periodogram of RV_{VIS}) shows a forest of peaks mainly due to a combination of the high and low cadence sampling. However, the 3.372 d period could be retrieved for both RV and CRX values from the VIS channel. The data from the NIR channel, however, does not show any activity-related signal, and therefore it is excluded from further analysis. Figure A.6 displays the phase-folded plots of the TESS photometric data from sector 24, alongside the RV and CRX time series for both the VIS and NIR channels.

In the order-by-order periodogram analysis of the VIS channel, robust and significant peaks at the rotation period of the star were successfully detected, with a difference only in the thousandth decimal place from the 3.372-day period. These peaks were observed in the bluer orders up to order #81 (around $\lambda \sim 756$ nm). However, the signal at P_{rot} weakened for orders #84 and #83 ($\sim$ 730 nm), with FAP values still above 10%. In the red orders, the activity-related signals completely disappeared, except for orders #73 ($\sim$ 838 nm) and #70 ($\sim$ 874 nm). Order #72 also displayed its highest peak at the 1-day alias of P_{rot}. Although there were substantial RV scatterings in the red orders of OT Ser (as observed in the RV–λ

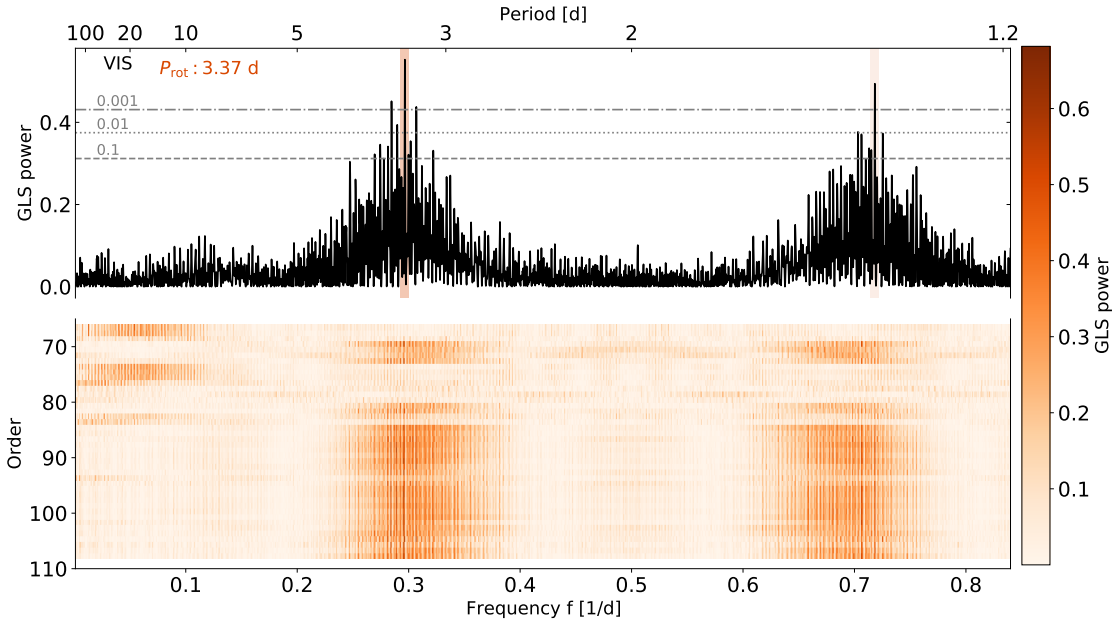

FIGURE 3.8: Same as Figure 3.4, but for OT Ser (J15218+209) RV data from the VIS channel. Activity-related signals are significant in blue orders (between #108 and #81) but disappear in red orders except for orders #73 to #70.

plot for J15218+209 in Figure A.1), we cannot attribute the absence of activity signals in these orders solely to the RV scattering, as the activity signal is also absent in orders that do not exhibit such behaviour (e.g., orders #79 at $\sim$ 775 nm and #78 at $\sim$ 785 nm). The best signals, their FAPs, and the FAPs at $P_{\rm rot}$ for VIS orders are tabulated in Table A.14. The GLS periodogram for overall $\rm RV_{VIS}$ and the stacked GLS for VIS orders are shown in Figure 3.8, while the order-wise RV semi-amplitude K and their corresponding GLS power are depicted in Figure 3.9. The amplitude of the rotation signal exhibits a notable excursion with significant power in the blue orders, extending up to order 85. However, the signal diminishes significantly in the majority of the redder orders.

Among the chromospheric and photospheric activity indicators of OT Ser listed in Table A.15, CaH 3 exhibits a significant peak (FAP $< 0.1\%$) at the 1-day alias of the 3.66-day signal. Similarly, TiO 7050, TiO 8430, and VO 7942 display their highest peak at the 1-day alias of the 3.41-day signal. However, the remaining indicators do not exhibit any significant power in relation to activity-related periods.

3.6.4 J11026+219 (DS Leo)

DS Leo is a moderately active early M dwarf (M1.0 V) with a normalised Hα luminosity of -4.53 and borderline chromatic behaviour. The photometric data from SuperWASP exhibit a 14.6 d periodicity (Díez Alonso et al., 2019), while the more recent observations from TESS sector 22 (obtained between February and March 2020) reveals a value of 13.77 d for the rotation period of the star. CARMENES observed DS Leo from January 2016 to May 2018 and collected 53 and 42 data points with the VIS and NIR channels, respectively.

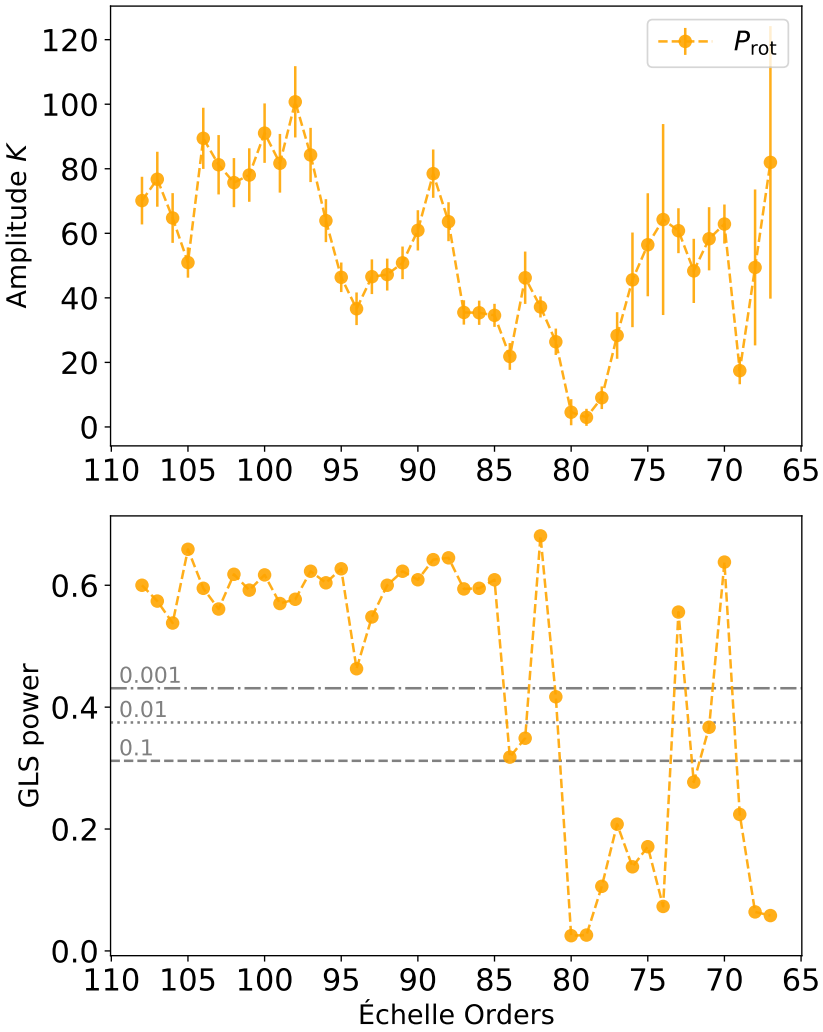

FIGURE 3.9: *Top panel:* Order-wise RV semi-amplitude K of the best-fitting sine function at $P_{\rm rot}$ across the échelle orders of the VIS channel for OT Ser. *Bottom panel:* Corresponding GLS power of the peak at $P_{\rm rot}$. The horizontal lines correspond to FAP levels of 10% (dashed), 1% (dotted), and 0.1% (dash-dotted).

The periodograms of $\mathrm{RV_{VIS}}$ and $\mathrm{CRX_{VIS}}$ show two relatively significant peaks close to the rotational period of the star. While for $\mathrm{RV_{VIS}}$, the highest peak appears at 13.97 d (FAP $< 1.0\%$) and a slightly weaker one at 13.72 d (FAP $\sim 1.0\%$), for CRX, the 13.72 signal gains more power (FAP $< 1.0\%$) and the 13.97 signal (with FAP $< 5.0\%$) becomes only the secondary signal. Figure A.7 illustrates the phase-folded representations of the TESS photometric data obtained from sector 22. Additionally, the figure includes the corresponding radial velocity (RV) and chromaticity (CRX) time series for both the VIS and NIR channels.

The order-wise periodogram analysis of DS Leo, utilising the VIS data, also shows signals around both 13.97 and 13.72 d periods with FAP between ∼0.1 and 10% throughout orders #108 to #86 ($560 < \lambda < 710$ nm), except for order #105 (~ 583 nm), where the periodogram does not show any significant peak, and order #92 (~ 665 nm), where a signal close to the

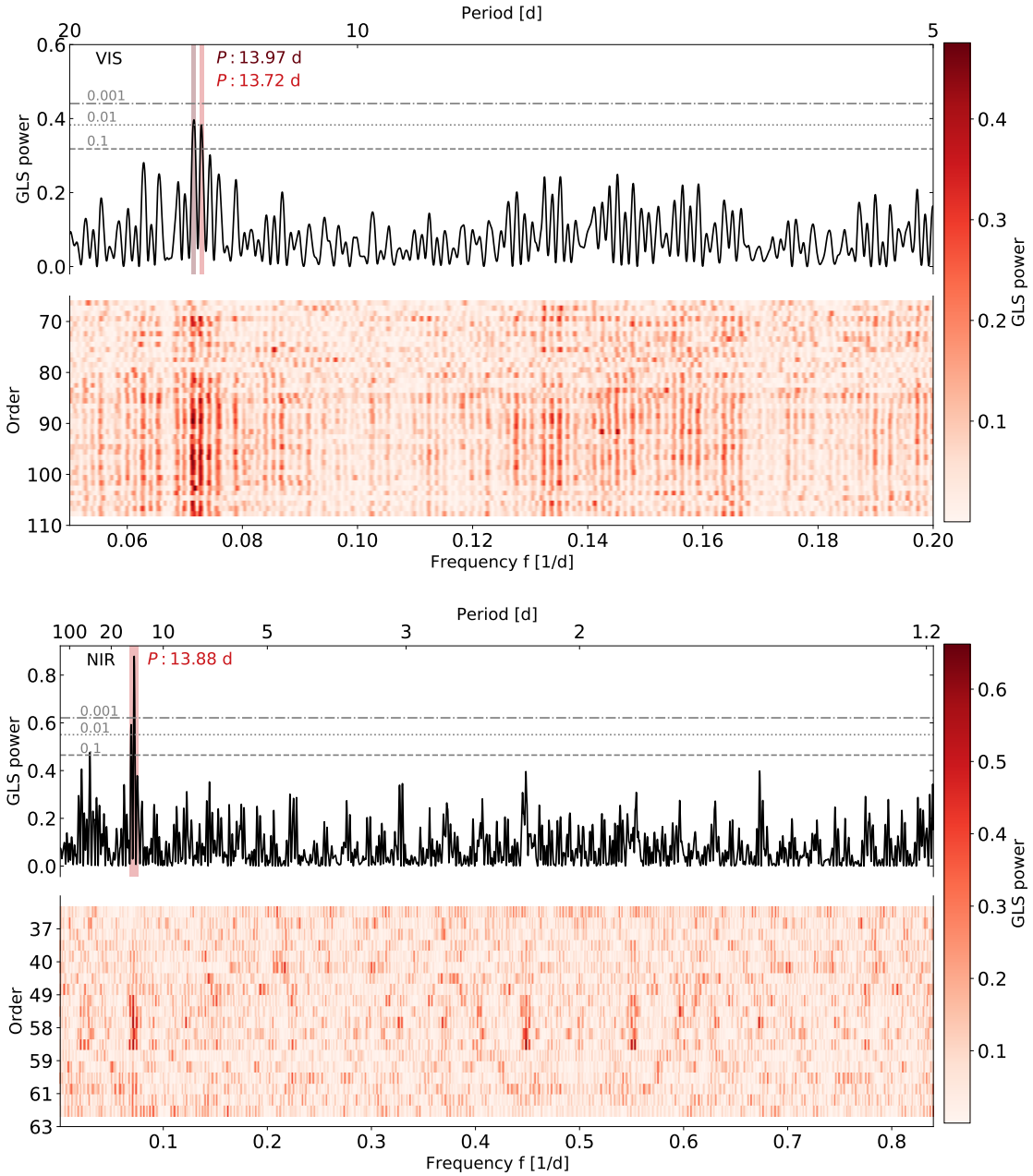

FIGURE 3.10: Same as Figure 3.4, but for DS Leo (J11026+219). *Top panel*: Zoomed-in GLS periodogram and stacked periodogram highlighting the signals of interest for RVs in the VIS channel. *Bottom panel*: GLS periodogram and stacked periodogram for RVs in the NIR channel.

$\frac{1}{2}P_{\rm rot}$ gets power. From order #85 ($\sim$ 720 nm) toward the red end of the spectrograph, the activity-related signals can be located only in orders #82 ($\sim$ 746 nm), #71($\sim$ 862 nm), and #70($\sim$ 874 nm). The absence of the activity signals in other red orders can be attributed to the high uncertainty on the measured RV data points in these orders (see the RV–λ plot for J11026+219 in Figure A.1). Similar to the previous targets, the best signals and their FAP are listed in Table A.16. The top panel of Figure 3.10 exhibits the stacked GLS periodograms for DS Leo. The plot is zoomed in to provide a clearer view of the frequency ranges centred

around 13.97 d and 13.72 d.

As for the NIR channel, DS Leo still maintains marginal chromaticity. Although only 30 data points are good to use after the instrument upgrade in October 2016, the RV_{NIR} periodogram shows a significant peak at 13.883 d (FAP $< 0.1\%$). For CRX_{NIR}, however, the strongest peak at 13.316 d does not reach the significant level (no peaks with FAP $< 10\%$). By examining the stacked periodogram displayed in the bottom panel of Figure 3.10, along with the corresponding best signals listed in Table A.17, it becomes evident that only orders #59 (approximately 1025–1044 nm), #58 (approximately 1043–1062 nm), and the left half of order #56 (approximately 1080–1090 nm) contribute to the activity signal. While the remaining orders do not exhibit any significant peaks.

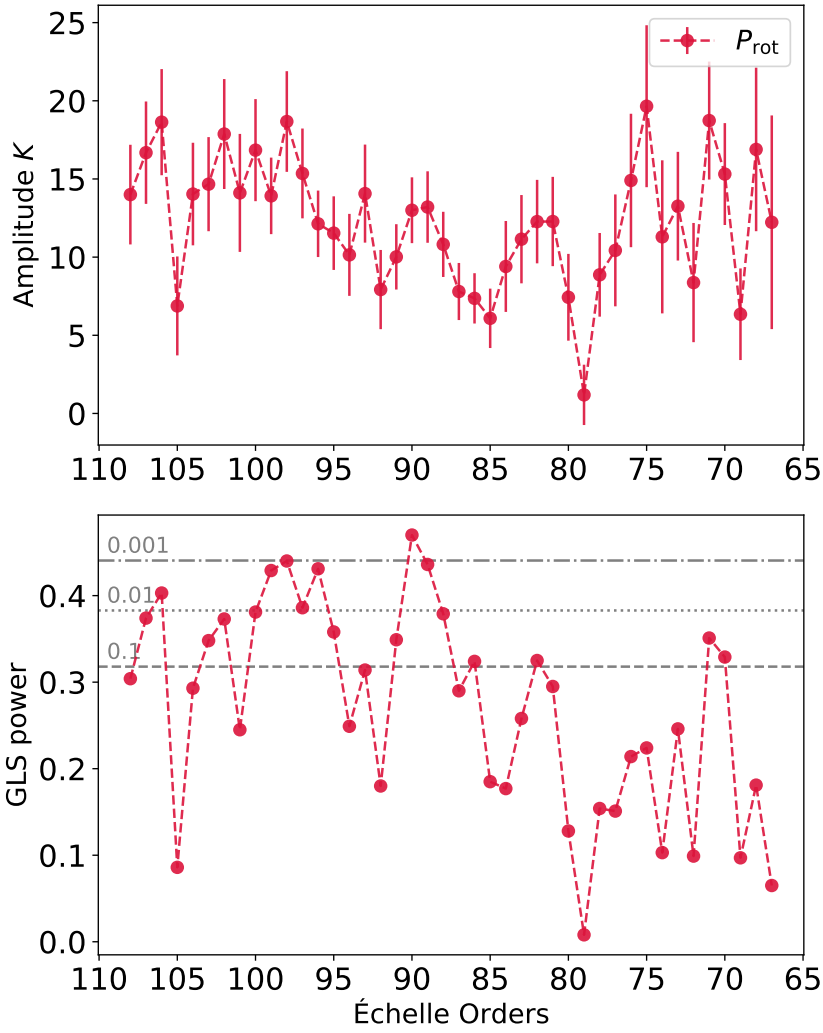

FIGURE 3.11: *Top panel:* Order-wise RV semi-amplitude K of the best-fitting sine function at P_{rot} across the échelle orders of the VIS channel for DS Leo. *Bottom panel:* Corresponding GLS power of the peak at P_{rot}= 13.72 d. The horizontal lines correspond to FAP levels of 10% (dashed), 1% (dotted), and 0.1% (dash-dotted).

Figure 3.11 illustrates the order-wise RV semi-amplitude (K) and their corresponding

GLS power for DS Leo. In contrast to previous stars, the order-wise K values for DS Leo do not exhibit a significant excursion in the blue orders, and the GLS power falls below the 10% significance level for the majority of the orders. The marginal decrease in amplitudes up to order 80 suggests a tentative chromatic behaviour, placing DS Leo in the suggestive target category.

The analysis of spectroscopic activity indicators, provided in Table A.24, indicates very obvious peaks close to $\frac{1}{2}P_{\rm rot}$ of the star ($\sim$ 6.87 d) for Hα, all three Ca II IRT lines, and Paβ with moderate significance levels (0.5 < FAP < 7%). However, none of these indicators shows any power at $P_{\rm rot}$. As for the molecular bands, CaH 3 shows a peak at 14.67 d (FAP $\sim$ 5.4%), and TiO 7050 shows its highest peak at 13.97 d (FAP $\sim$ 0.6) and another slightly less significant peak at 6.9 d (FAP $\sim$ 1.1%). The rest of the activity indicators do not show any significant peak in their periodograms.

3.6.5 J07446+035 (YZ CMi)

YZ CMi is a widely recognised and extensively studied mid-M dwarf (M4.5 V) characterised by its high level of activity. It exhibits a significant Hα luminosity, with $\log L_{\rm H\alpha}/L_{\rm bol} \sim \sim$ -3.61, and a strong chromaticity in its RVs. The $P_{\rm rot}$ of the star was determined by Díez Alonso et al. (2019) to be 2.78 d using the MEarth survey. It has also been observed by TESS in sectors 7 and 34 (between January and February 2019 and 2021, respectively), where it shows a 2.774 d periodicity in each sector. The star's light curve in sector 7 reveals a distinct single dip per rotation. However, in sector 34, a secondary dip begins to emerge, adding complexity to the rotational pattern. Figure A.8 displays the phase-folded time series of the TESS photometry, revealing a clear periodicity at 2.78 d. The figure also includes the CARMENES radial velocity (RV) and chromaticity (CRX) measurements, both of which exhibit a consistent and strong periodicity at the same 2.78 d period in both channels. YZ CMi spectroscopic data is taken from January 2016 to January 2018, providing 49 and 28 high-quality spectra in the VIS and NIR channels, respectively. Similar to the TESS sector 7 data, the CARMENES RV and CRX measurements show a single dip per rotation. The semi-amplitude of the fitted sine model to the RV data shows about 40 m s^{-1} larger modulation in VIS than NIR. Likewise, the semi-amplitude is $\sim$ 200 m s^{-1} larger for CRX$_{\rm VIS}$ compared to CRX$_{\rm NIR}$.

The order-by-order periodogram analysis, shown in Tables A.19 and A.20 and Figure 3.12, indicate that YZ CMi is the unique star in our sample, with the highest number of orders showing significant activity-related signals. In the VIS channel, all orders except orders #74, #68, and #67 exhibit a signal at 2.78 d with FAP < 0.1%. Order #74 shows a smaller but still significant (FAP $\sim$ 0.16%) periodicity at $P_{\rm rot}$, and orders #68 and #67 do not show any significant signal due to telluric contamination. Similarly, in the NIR channel, from the red side of order #62 to order #58 and the blue side of order #56 in the Y band (between 985–1063 nm and around 1085 nm), order #49 in the J band ($\sim$1245 nm), and the blue side of order #37 in the H band ($\sim$ 1640 nm) all show peaks at $P_{\rm rot}$ that is more significant over the Y band (FAP < 0.1%) and less powerful over J and H photometric bands (FAP < 5.0%). Orders that show their highest signal at $P_{\rm rot}$ also show significant peaks at the 1-day alias of the rotation period in both channels.

YZ CMi does not show any significant signals in the chromospheric line indicators, as presented in Table A.21. In contrast, molecular bands CaH 3, TiO 7050, TiO 8430, and

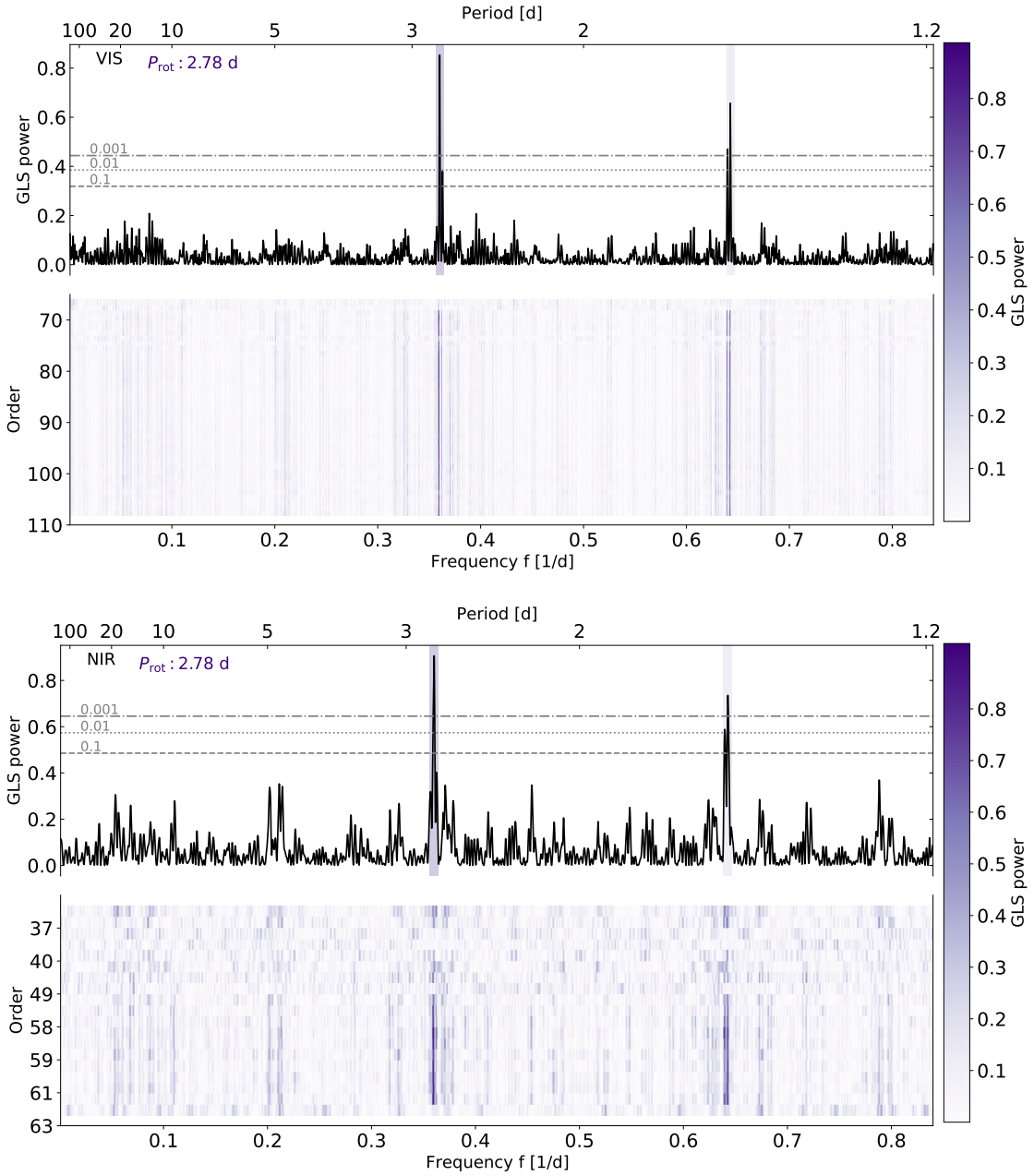

FIGURE 3.12: Same as Figure 3.4, but for YZ CMi (J07446+035). The activity signal, at $P_{\rm rot}$ and its 1-day alias, is significantly strong throughout almost all orders in both channels.

VO 7436 all show significant power with FAP $< 0.1\%$ at $P_{\rm rot}$. In addition, the TiO 8860 band and FeH WFB exhibit a smaller signal (FAP $< 10\%$) close to the $P_{\rm rot}$.

3.6.6 J05365+113 (V2689 Ori)

V2689 Ori is an early M dwarf (M0.0 V) with a mild activity level ($\log L_{\rm H\alpha}/L_{\rm bol} \sim$ -4.5) and lack of RV chromaticity. The rotation period derived from the ASAS photometric data

is about 12.3 d (Díez Alonso et al., 2019). However, TESS observations in sector 6 (taken from December 2018 to January 2019) show a periodic signal at about 11.76 d. This value is similar to the periodicity we get from spectroscopic data taken by the CARMENES VIS channel. CARMENES obtained over 100 spectra for V2689 Ori between January 2016 and January 2019, making it one of the most observed targets in the active RV-loud sample. The periodograms of RV_{VIS} and RV_{NIR} show significant periodicities (FAP $\leq 0.1\%$) close to the P_{rot} precisely at 11.76 d and 11.79 d. Figure A.9 displays the CARMENES RV and CRX data and the TESS light curve folded to the respective periods or the P_{rot} in the case of CRXs.

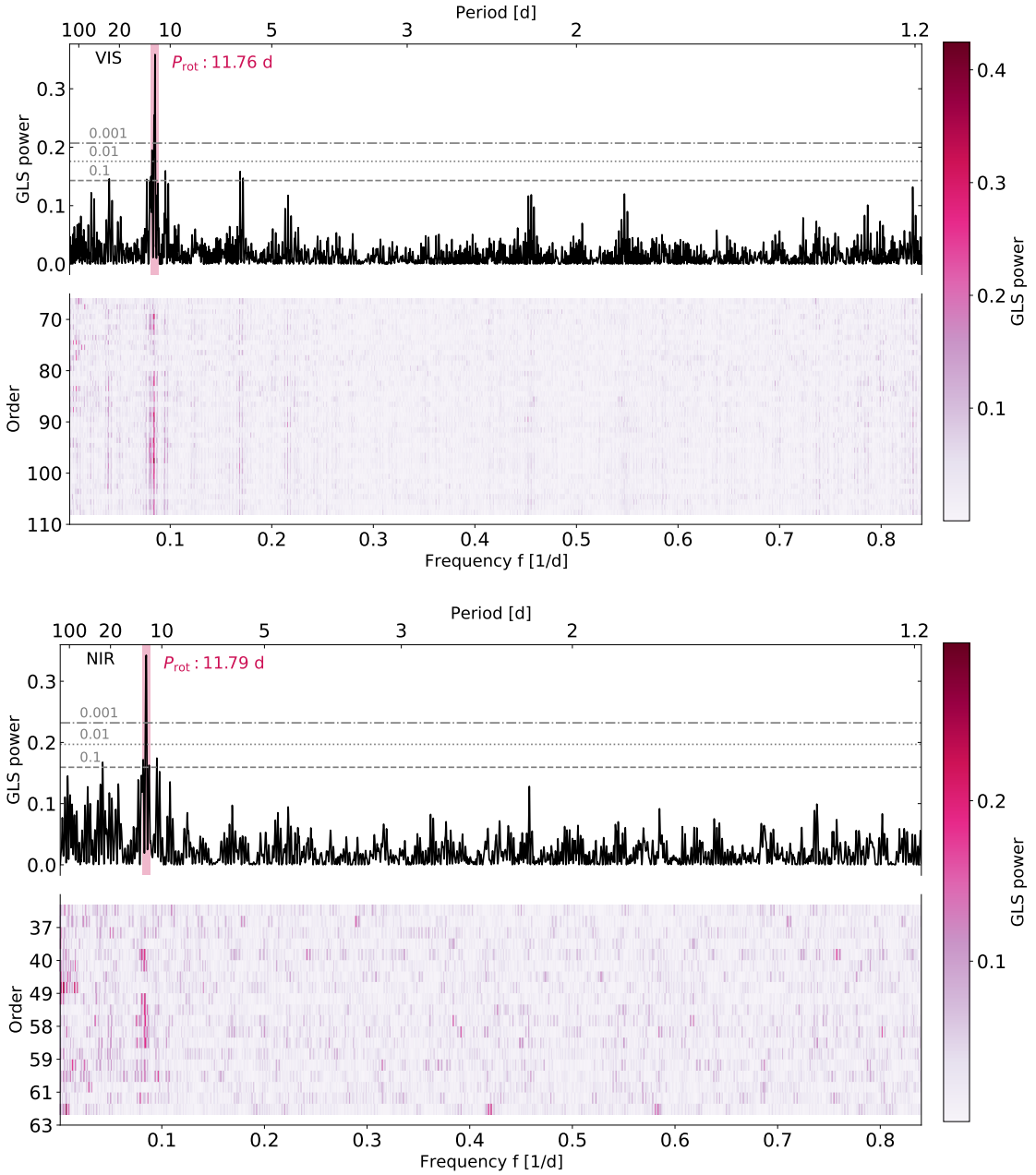

FIGURE 3.13: Same as Figure 3.4, but for V2689 Ori (J05365+113).

This star is classified as achromatic, as evidenced by the absence of any significant chromaticity in both CRX_{VIS} and CRX_{NIR}. However, Lafarga et al. (2021) showed that the chromospheric lines, Hα, and Ca II infrared triplet (IRT) and CCF parameters FWHM and BIS all show a significant peak (FAP $\leq$ 0.1%) at 11.8 d as well. While dLW shows a less significant peak at 11.43 (FAP $\sim$ 8%). This information indicates that V2689 Ori is chromospherically active, and although the rotation period of the star manifested itself in the chromospheric lines and some of the photospheric indicators, it was not captured by CRX.

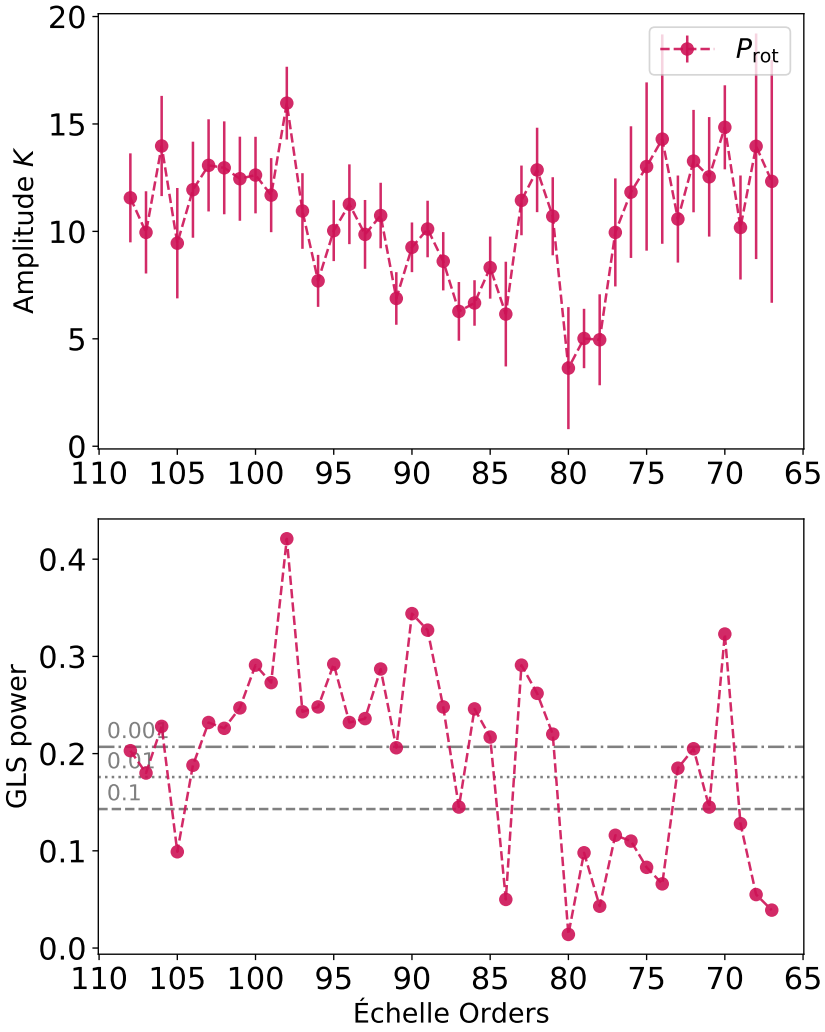

FIGURE 3.14: *Top panel:* Order-wise RV semi-amplitude K of the best-fitting sine function at P_{rot} across the échelle orders of the VIS channel for V2689 Ori. *Bottom panel:* Corresponding GLS power of the peak at P_{rot}. The horizontal lines correspond to FAP levels of 10% (dashed), 1% (dotted), and 0.1% (dash-dotted).

Figure 3.13 presents the stacked GLS periodogram for V2689 Ori. Meanwhile, Figure 3.9 displays the order-wise RV semi-amplitude K values and their corresponding GLS power for this star.

3.7 Discussion and Conclusion

We conducted a comprehensive analysis of a sample consisting of 56 highly active M dwarfs observed by CARMENES in the solar neighbourhood. Our goal was to examine the impact of active regions on the radial velocity (RV) measurements of these stars in both the visual and near-infrared (IR) regimes. To achieve this, we utilised the chromatic index (CRX), a photospheric activity indicator that quantifies the slope of the RV–ln λ relationship. Interestingly, despite all stars in our sample being highly active, some of them did not exhibit significant wavelength dependence in their RV measurements as indicated by CRX. To explore potential factors influencing the wavelength dependence of RVs, we initially categorised the stars in our sample based on the degree of CRX-RV correlation. Subsequently, we compared these stars by analysing the slope of the CRX-RV linear regression fit in conjunction with their key stellar properties.

Stellar rotation and chromaticity

In our investigation, we identified rotation as a key factor influencing the chromatic behaviour observed in stars. Notably, the connection between CRX-RV slope values becomes even more evident when considering the projected rotation velocity ($v \sin i$). Our observations indicate that stars with moderate rotational velocities exhibit a negative CRX-RV slope in both their VIS and NIR data. On the other hand, faster rotators tend to display a positive CRX-RV slope. This characteristic initially manifests in the NIR data of the suggestive subsamples and, for larger $v \sin i$ values, it extends to both the VIS and NIR data of both chromatic and suggestive subsamples.

Negative vs positive chromaticity

The presence of active regions on the stellar surface is indicated by a negative chromaticity. These regions exhibit a temperature difference relative to the photosphere, resulting in a flux-contrast that leads to a greater distortion in RV at shorter wavelengths (Desort et al., 2007; Reiners et al., 2010). As the contrast effect diminishes with longer wavelengths, the CRX-RV anti-correlation should become less significant or possibly nonexistent in the NIR channel. In addition to the reduced contrast in this wavelength regime, the larger errors in RV measurements resulting from the lower resolution of the NIR spectrograph, instrumental systematics, and the presence of telluric contamination contribute to this expectation. Conversely, a positive chromaticity indicates an increase in the amplitude of radial velocity variations for redder wavelengths, suggesting the involvement of mechanisms beyond temperature contrast. One possible physical phenomenon that could lead to an increasing amplitude of RV variations with wavelength is the Zeeman effect. According to Reiners et al. (2013), the Zeeman splitting of spectral lines within the wavelength range of 500–2300 nm could be as significant as the flux-contrast effect, depending on the strength of the accompanying magnetic fields associated with the active regions. We observed a positive chromaticity in our sample, correlating with an increase in $v \sin i$. One plausible explanation for this trend is the dominance of the Zeeman splitting effect in fast rotators, surpassing the impact of flux-contrast. Another potential factor contributing to the positive slope is the presence of telluric contamination specifically in the red orders of the VIS channel. It is likely that

TABLE 3.2: Stellar Properties and Order-by-Order Analysis Summary for Six Selected Stars

Name	SpT	Mass $[M_\odot]$	$\log L_{H\alpha}/L_{bol}$	TiO 7050	TiO 8430	TiO 8860	Orders VIS [%]	Orders NIR [%]
V2689 Ori	M0.0 V	0.58	-4.54	0.89	0.86	0.99	71	32
DS Leo	M1.0 V	0.54	-4.53	0.82	0.85	0.98	60	26
OT Ser	M1.5 V	0.52	-3.77	0.69	0.81	0.96	74	-
TYC 3529 (S1)	M2.0 V	0.52	-4.03	0.67	0.82	0.93	57	-
TYC 3529 (S2)	M2.0 V	0.52	-3.96	0.66	0.82	0.93	60	10
EV Lac	M3.5 V	0.34	-3.65	0.51	0.76	0.89	83	42
YZ CMi	M4.5 V	0.19	-3.61	0.43	0.74	0.82	95	68

faster-rotating stars are more susceptible to telluric effects due to broader spectral lines, resulting in reduced RV content and increased scattering in the measurements.

Achromaticity among active stars

We should note that the presence of achromatic stars within our sample is not confined to a specific range of $v \sin i$ values. This implies that multiple factors might contribute to the lack of chromaticity in these stars. One possible explanation is the presence of complex spot patterns, wherein multiple spots exhibit chromatic contributions that nearly cancel each other out. Another possibility is that the strong magnetic fields associated with active regions counteract the flux-contrast RV chromaticity by means of the Zeeman splitting effect, resulting in an achromatic behaviour. Additionally, these stars may possess higher spot-to-photosphere temperature contrasts, as simulations predict a weaker decrease in RV amplitude with wavelengths for such contrasts (Reiners et al., 2010). Considering the various explanations, it is likely that one or a combination of these factors contributes to the lack of RV chromaticity in achromatic stars, specifically among those with differing $v \sin i$ values.

Tracing activity signals over spectral orders

As previously mentioned, the presence of active regions induces radial velocity (RV) modulations typically associated with the rotation period or its harmonics of the star. To investigate these activity-related periodicities in greater detail, we conducted a comprehensive search for RV variations across individual orders of the CARMENES VIS and NIR spectrograph. Our analysis focused on six early-to-mid-type M dwarfs from our sample, which possess known rotation periods, sufficient data sampling, and significant peaks in the GLS periodogram. Our objective was to identify specific orders within the spectrograph that exhibit a clear rotational (or its higher harmonics) signal. By identifying such orders, we aimed to uncover regions that are particularly sensitive to activity signals, allowing for a more detailed understanding of the underlying phenomena.

In Figure 3.15, we present a comparison of the order-wise RV semi-amplitude (K) obtained from the best-fitting sine function at either the rotation period (P_{rot}) or its harmonic ($\frac{1}{2}P_{rot}$) across the échelle orders of the VIS channel for the selected stars. To facilitate a clearer comparison, the order-wise K values are normalised to the K value calculated for the overall RV, which is derived by taking the weighted average of the order-wise RVs. For

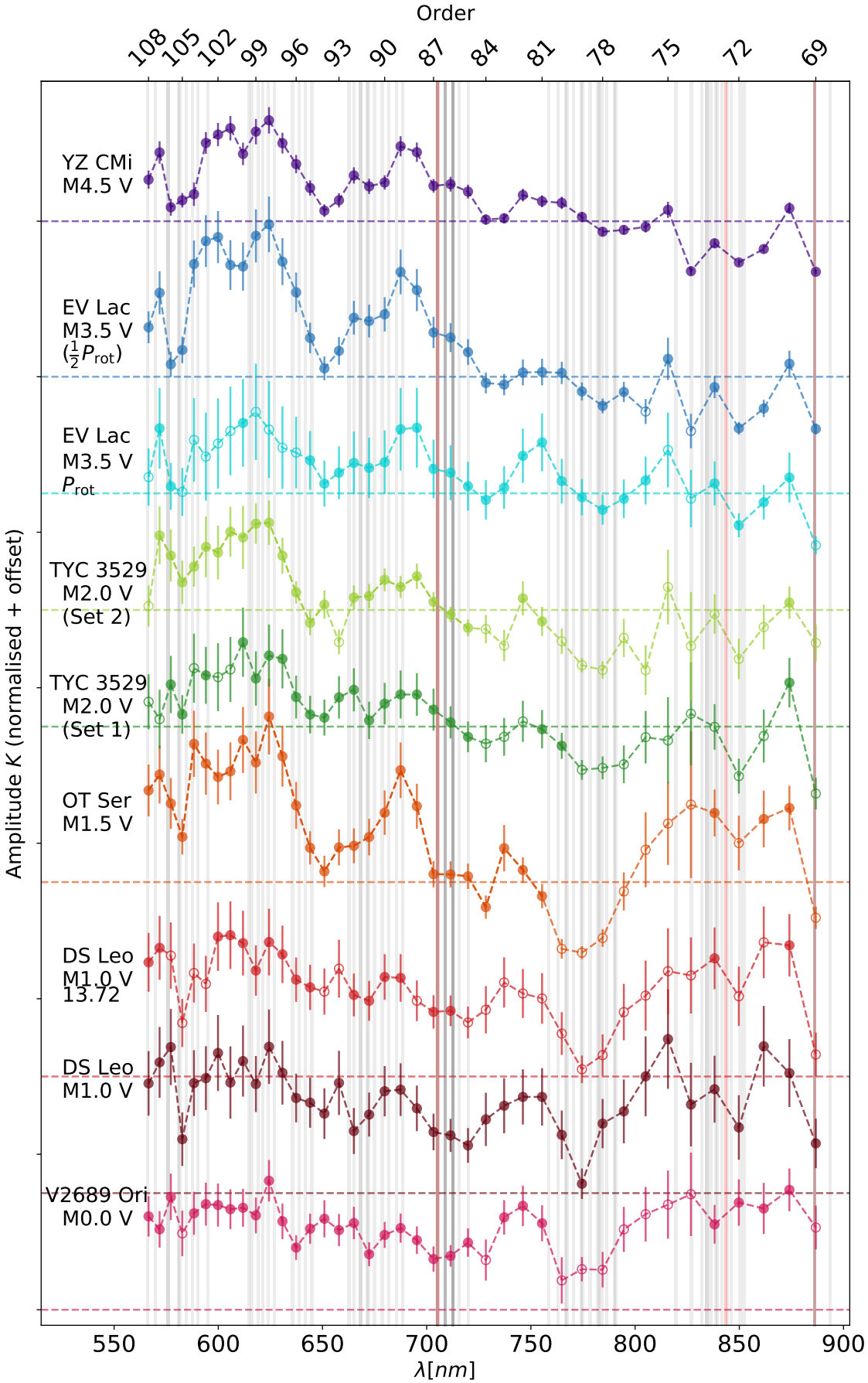

FIGURE 3.15: Comparison of RV Semi-Amplitudes (K) for Rotational Signals in Six Selected Stars

each star, the normalisation value is represented by a horizontal dashed line, which is colour-coded to match the stellar pattern. The boldface K values highlight significant signals in the corresponding orders. It is evident that most active stars, including YZ CMi and EV Lac, exhibit robust and notable activity-related signals across all orders. However, for the remaining stars, the activity signals tend to diminish in the redder wavelengths, specifically between 750 – 850 nm.

Table 3.2 provides a breakdown of the percentage of orders exhibiting significant activity signals for each star. YZ CMi demonstrates the most stable activity signal, with 95% of orders (40 out of 42 available orders) in the VIS channel and 68% of half-orders (13 out of 19) in the NIR channel showing significant signals. Interestingly, V2689 Ori, classified as an achromatic star, still displays a notable signal corresponding to its $P_{\rm rot}$ in 71% of orders in the VIS channel and 32% of orders in the NIR channel. It is noteworthy that despite its achromatic nature, V2689 Ori exhibits a discernible activity signature. On the other hand, TYC 3529, known for its episodic behaviour, demonstrates the least activity among the six selected stars, with rotation signals present in only 57% of the VIS orders during its initial subset and no activity signals detected in the NIR orders.

An additional intriguing trait is that the amplitude of RV variations exhibits greater excursion in the blue orders for stars with later spectral types. This behaviour could be attributed to the presence of various atomic lines and molecular bands, particularly the presence of titanium oxide (TiO) absorption bands in the spectra of these stars. TiO molecular bands are known to serve as effective tracers of active regions (Afram and Berdyugina, 2019). According to Berdyugina and Usoskin (2003), the TiO band head at 7054 Å is considered one of the best molecular diagnostics for the magnetic field in sunspot umbrae and starspots.

To explore this hypothesis further, we quantified the strength of the TiO 7050, TiO 8860, and TiO 8430 indices following the methodology outlined by Schöfer et al. (2019) for our target stars. The median values of these indices are listed in Table 3.2. A smaller index value indicates a stronger presence of TiO in the spectrum. As demonstrated in the table, TiO bands tend to become stronger for later-type M dwarfs. Moreover, it appears that TiO band heads at bluer wavelengths exhibit greater strength, which may explain the larger RV excursion observed in these regions. In Figure 3.15, the grey vertical lines represent the positions of all known TiO lines according to Valenti, Piskunov, and Johns-Krull (1998), while the red vertical lines correspond to the TiO 7050, TiO 8860, and TiO 8430 bands that have already been quantified for CARMENES stars. Quantifying TiO bands in the bluer order remain challenging due to the lower signal-to-noise ratio of M dwarfs in this wavelength range. Nevertheless, it is worth considering this aspect in future studies, as it holds the potential to provide valuable insights into the observed pattern.

Finally, another noteworthy trait observed among these selected stars is that photospheric indicators prove to be more effective in tracing the rotational signals of highly active stars. Conversely, for the less active stars, chromospheric indicators exhibit greater effectiveness in tracing rotational signals. This behaviour is not only observed across different stars but also within the different data sets of TYC 3529. Specifically, in the first subset characterised by weaker activity-related signals in RV values, the chromospheric indicators successfully detected activity. This finding highlights that there is no universal activity indicator applicable to all stars. It underscores the importance of considering both photospheric and chromospheric indicators when studying rotational signals in stars with varying levels of

activity.

The analysis presented in this chapter represents an initial step towards comprehending the influence of activity on RV measurements. Future studies can build upon this foundation by pursuing several avenues. Firstly, expanding the sample size and increasing the number of observations would enable a more extensive and robust statistical analysis. Additionally, using spectra that are meticulously corrected for telluric contaminations would enhance the accuracy of the measurements. Investigating the activity signals in smaller segments of the wavelength range could help identify specific activity-sensitive regions with greater precision. Furthermore, quantifying TiO band heads in bluer wavelengths offers another promising direction for future investigations. Additionally, simulating the effect of activity using synthetic spectra could provide valuable insights. By incorporating these steps into future studies, we can deepen our understanding of the impact of stellar activity on RV measurements and uncover further insights into this intriguing phenomenon.

Chapter 4

Flare study of active M dwarfs

Like a flare on the Sun, my heart ignites
Burning bright with love, a cosmic sight

Details of authorship: *The content of this Chapter is entirely based on the soon-to-be submitted work to the A&A journal. I am the lead author of this paper and carried out the scientific work, calculations, analysis and interpretation of the results. All figures in this work were produced by me. I wrote the text passages, circulated the manuscript to all co-authors, and incorporated the comments and suggestions received.*

4.1 Motivation

Flares are energetic manifestations of magnetic activity in cool stars, which have a significant impact on the evolution and habitability of planets orbiting these stars. The magnetic activity is closely intertwined with stellar mass, age, and rotation period. By examining the relationship between flare rates, stellar mass, rotation period, and indicators of chromospheric activity, we gain valuable insights into the magnetic field and its evolution in low-mass stars. Our research focuses on exploring the most active M dwarfs in the CARMENES catalogue, which are also observed by TESS, in order to establish potential connections between their flare properties, stellar parameters, and chromospheric activity indices. To achieve this, we have developed a semi-automated flare detection algorithm that enables us to determine key flare characteristics, including amplitude, duration, bolometric energy, and occurrence rates. We have also created flare energy distributions and flare frequency diagrams (FFDs) for stars in our sample. Using the FFD, we determined the flare rate specific to different energy levels for each star. This analysis enabled us to compare the flare activity among stars with varying stellar properties, including masses, rotation periods, and levels of chromospheric activity. Additionally, we have investigated whether there is a correlation between the rotational phase of the stars and the occurrence rate and energy of flares, specifically in stars exhibiting similar light curve morphology within our sample.

4.2 Context

Stellar activity encompasses a diverse array of phenomena intricately linked to the presence and dynamic configurations of magnetic fields in late-type stars. This magnetic activity profoundly influences various layers of the stellar atmosphere, manifesting in observable phenomena such as flares, active regions characterised by cool spots and hot faculae, plages, chromospheric and coronal emissions, and more. Despite extensive research on solar and stellar activity, the fundamental physical processes governing these phenomena continue to harbour some ambiguity. Hence, ongoing investigations using ever more precise instruments are imperative to unravel the enigmatic puzzle of stellar activity and gain a deeper understanding of its underlying mechanisms.

The prevailing consensus in the field acknowledges that stars possessing outer convective envelopes generate a large-scale magnetic field through the self-excited dynamo process. This remarkable mechanism converts kinetic energy into magnetic energy, with the stellar differential rotation playing a pivotal role in its operation (e.g., Wilson, 1966; Kraft, 1967; Parker, 1975; Charbonneau, 2014). The rotation rate of a star, on the other hand, is intrinsically tied to its age. Upon entering the main sequence, stars exhibit rapid initial rotation, gradually decelerating over time as they transfer angular momentum to their magnetized stellar winds (e.g., Skumanich, 1972; Barry, 1988; Baliunas et al., 1995).

The activity-rotation-age paradigm is further complicated by an additional factor: stellar mass. When stars have masses below 0.35 $M_{\odot}$, they undergo a complete structural transformation as they become fully convective (e.g., Chabrier and Baraffe, 1997; Rudolf Kippenhahn, 2012). Consequently, there is a notable decrease in the radii of stars at the boundary of complete convection. This variation leads to smaller stars, specifically those with spectral types M4.0 V and beyond, exhibiting a slower rate of spin-down compared to their early-M dwarf counterparts with spectral types ranging from M0.0 V to M3.0 V. Consequently, mid- and late-M dwarfs tend to possess longer activity lifetimes and higher activity levels in contrast to typically slowly rotating and less active early-M dwarfs (Mohanty and Basri, 2003a; Reiners and Mohanty, 2012). Importantly, these characteristics manifest independently of the changes occurring in the internal dynamo process of fully convective stars, which are expected to occur concurrently (Durney, De Young, and Roxburgh, 1993; Chabrier and Küker, 2006).

Although fully convective stars are expected to exhibit distinct magnetic dynamo behaviour, theoretical models suggest that their activity remains closely tied to rotation rate (Dobler, Stix, and Brandenburg, 2006; Browning, 2008). However, observational evidence indicates a saturation-type relationship between rotation and activity in this regime (Mohanty and Basri, 2003b; Browning et al., 2010). The interplay between stellar mass and rotation rate in low-mass dwarfs necessitates the utilisation of the Rossby number (RO) as a parameterisation for activity indicators and rotation period (Noyes et al., 1984; Micela et al., 1985; Maggio et al., 1987; Stepien, 1994; Randich, 2000; Medina et al., 2020). The Rossby number, which is independent of stellar mass, helps mitigate or alleviate the degeneracy between the rotational period and stellar mass. Furthermore, observations indicate the presence of saturated behaviour in chromospheric and coronal activity indicators (e.g., Ca II H + K, Hα, and $L_{\mathrm{x}}/L_{\mathrm{bol}}$) for Rossby numbers below a critical value (Douglas et al., 2014; Newton et al., 2017; Vilhu and Walter, 1987; Pizzolato et al., 2003; Wright et al., 2011; Wright and Drake, 2016; Wright et al., 2018).

Flares are transient and stochastic events observed in cool stars with outer convection zones. The interaction between the magnetic fields generated in the depths of the convective zone and the photospheric motions, caused by stellar rotation, entangles the magnetic field lines, resulting in their reconnection above and near active regions where the magnetic field lines are concentrated (Benz and Güdel, 2010). These events release substantial amounts of energy, which affect the stellar chromosphere. They heat and evaporate dense plasma into the corona, generating emissions that can be observed across a wide range of wavelengths. Flares observed in visible wavelengths, also known as white-light flares, are characterised by sudden and intense increases in stellar brightness, as seen in the photometric light curve of stars. Detecting flares is generally easier in lower mass stars compared to their solar-type counterparts. This is primarily due to the higher contrast between the flare and quiescent state fluxes in M dwarfs, as well as the lower photospheric luminosity of these stars relative to solar-type stars. As a result, detectable flares occur more frequently in M dwarfs. The impact of flares can also be observed in the stellar spectra, which exhibit shifts, enhancements, and broadening of chromospheric emission lines, as well as wing asymmetries in the Balmer lines, the Ca II K line, and the He I line in more intense cases (Fuhrmeister et al., 2008; Reiners, 2009; Fuhrmeister et al., 2011; Fuhrmeister et al., 2018; Johnson et al., 2021).

The properties of flares, such as their rate and energy, in M dwarfs hold significant importance due to their impact on the atmospheres and surface conditions of potentially habitable exoplanets orbiting in close proximity to these stars. Multiple studies have shown that M dwarfs exhibit a higher frequency of energetic flares compared to the Sun (Vida et al., 2017; Vida et al., 2019a; Howard et al., 2019; Günther et al., 2020). Superflares, characterised by their high energy ranging from 10^{33} to 10^{36} erg, have the potential to significantly impact and deplete planetary atmospheres (Lammer et al., 2007; Venot et al., 2016), creating an inhospitable environment for thriving life forms. However, it is worth noting that an appropriate level of ultraviolet (UV) radiation emitted by flares could have a beneficial effect on prebiotic chemical processes essential for abiogenesis, and in some cases, even initiate surface photosynthesis on planets (Buccino, Lemarchand, and Mauas, 2006; Björn, 2015; Airapetian et al., 2016; Skrutskie et al., 2006; Ranjan, Wordsworth, and Sasselov, 2017; Mullan and Bais, 2018; Rimmer et al., 2018). Therefore, the investigation of flare activity and its correlation with stellar parameters and other activity indicators in low-mass stars is of utmost importance. This research is crucial not only for advancing our understanding of stellar atmospheres but also for the field of exoplanetary science.

With the advent of space-based precision photometry missions such as Kepler/K2 (Borucki et al., 2010) and the Transiting Exoplanet Survey Satellite (TESS; Ricker et al., 2015), the scientific community now has easy access to tens of thousands of high-precision, fast cadence, and long-baseline stellar photometric data. These missions have paved the way for comprehensive studies of flares on a large scale, encompassing various spectral types, stellar rotation rates, and ages (Walkowicz et al., 2011; Candelaresi et al., 2014; Davenport, 2016; Van Doorsselaere, Shariati, and Debosscher, 2017; Davenport et al., 2019; Günther et al., 2020; Feinstein et al., 2020). Furthermore, these missions have facilitated in-depth investigations of the evolution of flares over extended periods for individual active stars, (such as GJ 1243; Hawley et al., 2014; Davenport et al., 2014; Davenport, Mendoza, and Hawley, 2020). Consequently, numerous studies have been conducted to explore the correlation between flare rate and energy with stellar rotation phase, serving as a distinctive signature

of active regions (Hawley et al., 2014; Davenport et al., 2014; Doyle et al., 2018; Roettenbacher and Vida, 2018; Doyle et al., 2019; Doyle, Ramsay, and Doyle, 2020). However, the investigation of the correlation between flare properties and other magnetic activity indicators, such as chromospheric and photospheric activity tracers, which require high-resolution spectroscopic observations, has been conducted infrequently. The limited number of studies can be attributed to the general faintness of M dwarfs in the optical regime and the challenges associated with acquiring high signal-to-noise spectra for these stars. In a notable study conducted by Medina et al. (2020), high-resolution spectra obtained from the Tillinghast Reflector Échelle Spectrograph (TRES) and CTIO HIgh ResolutiON (CHIRON) spectrographs, along with photometric observations from MEarth (Nutzman and Charbonneau, 2008; Irwin et al., 2015) and TESS, were utilised to examine flares in 125 mid-to-late M dwarfs. The researchers reported an intriguing distinction between two groups of stars based on their flare rate and Hα emission. Specifically, they observed a separation between the group of stars exhibiting a saturated flare rate and Hα emission, and those with a low flare rate and no Hα emission. However, no similar differentiation was found between flare rate and two other chromospheric activity indices, namely He I D3 and the Ca II infrared triplet line at 8542.09 Å.

CARMENES[1] (Quirrenbach et al., 2016; Quirrenbach et al., 2018; Quirrenbach et al., 2020) is a precision-driven radial-velocity survey explicitly designed to detect low-mass exoplanets within the habitable zone of nearby M dwarfs. However, the high-resolution spectra obtained by CARMENES, simultaneously captured in visible and near-infrared wavelengths, offer a rich source of data for investigating the intricate details of activity phenomena exhibited by M dwarfs. Numerous studies have already explored various aspects of M dwarf activity using these spectra (e.g., Tal-Or et al., 2018; Fuhrmeister et al., 2018; Fuhrmeister et al., 2019; Schöfer et al., 2019; Baroch et al., 2020; Hintz et al., 2020; Lafarga et al., 2021; Johnson et al., 2021). In our study, we conducted a comprehensive investigation into the flare activity of a sample of M dwarfs observed by CARMENES and TESS. This sample is particularly noteworthy as it consists of some of the brightest active M dwarfs in the solar neighbourhood. This unique selection presents an exceptional opportunity to explore correlations between flare activity, photometric variability, and spectroscopic activity indicators derived from CARMENES data. Our primary objective in this analysis is to identify general trends in flare rates and energies with respect to stellar parameters and chromospheric indicators. Additionally, we aim to deepen our understanding of how flare rates and energies correspond to the observed minima and maxima in the light curves.

This chapter is structured as follows: Section 4.3 introduces the stellar sample and presents the updated properties of the stars. In Section 4.4, we describe the CARMENES spectroscopic observations and the derived chromospheric activity indicators. The TESS photometric observations, rotation period measurements, and the methods used for processing the light curves are outlined in Section 4.5. Our approach for identifying flares and estimating their energies is detailed in Section 4.7. The results of our analysis are presented in Section 4.8, followed by a discussion and outlook in Section 4.9.

[1]Calar Alto high-Resolution search for M dwarfs with Exo-earths with Near-infrared and optical 'Echelle Spectrographs; https://carmenes.caha.es/

4.3 Stellar sample

The targets for this study are nearby active M dwarfs that were observed both by CARMENES during its guaranteed-time observations (GTO program) between 2016 and 2020, and by TESS during its two-year primary mission, using 2-minute short-cadence integrations. The classification of stars based on their activity level followed the criteria established by Tal-Or et al., 2018, which require a radial velocity scatter (RV standard deviation) greater than 10 $\mathrm{m\,s^{-1}}$ and projected rotation velocities, $v \sin i$, larger than 2 $\mathrm{km\,s^{-1}}$.

TABLE 4.1: Stellar sample list including their designations, CARMENES VIS channel spectra count, observation time span, median S/N in order 93, and corresponding TESS sectors of observation.

SIMBAD Designation	Karmn	# Spectra VIS	T_{span} [d]	median S/N (order 93)	TIC	TESS Sectors
G 218-020	J01019+541	21	604	23.5	252110114	17,18
V388 Cas	J01033+623	27	1213	32.2	52183206	18,24
Barta 161 12	J01352-072	11	141	38.9	29853348	3
G 173-039	J02088+494	17	366	56.1	250602194	18
G 80-021	J03473-019	11	136	66.3	333680372	5
LSR J0419+4233	J04198+425	36	1390	1.9	347994537	19
1RXS J050156.7+010845	J05019+011	29	1243	36.8	269077806	5
RX J0506.2+0439	J05062+046	13	524	31.1	455029978	5
2MASS J05082729-2101444	J05084-210	26	745	14.9	146539195	5
V2689 Ori	J05365+113	130	1105	126.6	436248822	6
(LSR J0539+4038)	J05394+406	21	1416	2.7	239097694	19
G 99-049	J06000+027	14	315	53.6	282501711	6
LP 205-044	J06318+414	37	1448	...	144282456	20
(2MASS J06572616+7405265)	J06574+740	13	643	50.4	141476700	19, 20, 26
YZ CMi	J07446+035	51	725	50.6	266744225	7
2MASS J07471385+5020386	J07472+503	16	1247	50.5	309661100	20
GJ 1101	J07558+833	14	445	45.4	289972535	19, 20, 26
DX Cnc	J08298+267	35	1768	23.5	3664898	21
LP 666-009	J08536-034	42	1474	...	7975441	8
(NLTT 20861)	J09033+056	32	1442	...	270511002	8
G 161-071	J09449-123	11	168	26.7	289706625	8
(LP 731-076)	J10584-107	53	1161	21.3	148563078	9
DS Leo	J11026+219	54	848	103.3	97488127	22
LP 733-099	J11201-104	29	1423	76.7	453465810	9
1RXS J114728.8+664405	J11474+667	42	1412	17.3	142878895	14, 15, 21
StKM 2-809	J12156+526	13	369	50.7	416538839	22
FN Vir	J13005+056	12	884	38.6	411248800	23
RX J1353.6+7737	J13536+776	25	1435	48.2	219463771	14, 15, 20, 21, 26
LP 799-007	J13591-198	17	1416	27.6	125421413	11
RX J1417.3+4525	J14173+454	12	410	27.3	168747450	16,23
OT Ser	J15218+209	54	1002	83.2	355793860	24
LP 022-420	J15499+796	15	192	21.6	159398282	14, 15, 19, 20, 21, 25, 26
G 180-060	J16313+408	13	350	21.5	255932726	24,25
1RXS J173353.5+165515	J17338+169	12	334	23.0	400361232	26
LP 071-082	J18022+642	29	861	39.6	233068870	14, 15, 16, 17, 18, 19, 20, 21, 22, 24, 25
LP 390-16	J18131+260	16	1399	43.6	313988572	26
TYC 3529-1437-1	J18174+483	71	1001	88.6	289726188	14, 25, 26
LP 71-165	J18189+661	13	301	42.9	406857100	14, 15, 17, 18, 20, 21, 23, 24, 25, 26
G 208-042	J19511+464	14	325	47.0	273589987	14,15
V374 Peg	J22012+283	12	209	44.6	283410775	15
EV Lac	J22468+443	107	701	66.8	154101678	16
RX J2354.8+3831	J23548+385	13	170	29.0	291689873	17

Notes. Stars in this table are sorted according to their right ascension,i.e., Karmn ID.
Stars that have a SIMBAD designation in parentheses have been excluded from the study (for more information, refer to 4.5.1).

Initially, forty-two stars met these selection criteria. However, we excluded four stars from the analysis due to featureless TESS light curves that lacked any discernible modulation, likely resulting from contamination by nearby stars (see Sect.4.5.1 for more information). The remaining stars that constitute our sample, along with their CARMENES designations (Karmn) and TIC Identifiers, are listed in Table 4.1.

4.4 CARMENES spectroscopy

CARMENES (Quirrenbach et al., 2014) is a high-resolution spectrograph installed at the Observatorio de Calar Alto in Almería, Spain. It is situated on the 3.5 m Zeiss telescope and comprises both a visual (VIS) and a near-infrared (NIR) spectrograph. The VIS covers a wavelength range of 520–960 nm, while the NIR covers 960–1710 nm. The spectral resolution of the VIS and NIR spectrographs is 94,600 and 80,400, respectively. The CARMENES survey focuses on monitoring the brightest M dwarfs in the solar neighbourhood, spanning all spectral subtypes in the J-band. The main survey operation was conducted from 2016 to 2020. In this period, approximately 365 M dwarfs were observed. Each star in our sample has been observed at least 11 times, with a median number of observations of 17. The observations span a period of 136 to 1768 days, with a median value of 735 days. To process the obtained spectra, we utilised the CARMENES standard pipeline, `caracal` (CARMENES reduction and calibration software; Zechmeister, Anglada-Escudé, and Reiners, 2014), for extraction. Subsequently, we computed the radial velocities (RVs) using the `serval`[2] (Spectrum radial-velocity analyzer; Zechmeister et al., 2018) pipeline. For stars in our sample, we provide the median signal-to-noise ratios (S/N) of the extracted spectra at spectral order 93, which corresponds to the Hα line at approximately $\sim$6565 Å. Additionally, we include the number of observations and the time span in days in Table 1 (see Table 4.1).

The `serval` code offers spectroscopic activity indicators, represented by the I index, for several critical photospheric and chromospheric lines, such as Hα, Na I D, and Ca II IRT. These indicators enable us to examine the correlation between RV variations and the temporal behaviour of these indices, allowing us to assess the activity level of the stars. The I index is calculated by determining the ratio of the mean flux within the selected interval around the line to the mean flux of the reference bandpasses located on both sides of the line, as defined by Kürster et al. (2003). Additionally, we performed pseudo-equivalent width (pEW) measurements for chromospheric emission lines and photospheric absorption bands sensitive to magnetic activity. These measurements include Hα, He D_3, Na I D, Ca II IRT, Fe 8691, He 10833, Paβ, Ca H2, Ca H3, TiO 7050, TiO 8430, TiO 8860, VO 7436, and VO 7942. The calculation of pEW values for our targets follows the methodology outlined by Schöfer et al. (2019).

4.5 TESS photometry

The Transiting Exoplanet Survey Satellite (TESS; Ricker et al., 2015) conducted its primary mission from August 2018 to July 2020, observing both the southern and northern hemispheres of the sky. The mission comprised monitoring 26 segments (sector 1 to sector

[2] https://github.com/mzechmeister/serval

26), each lasting approximately 27 days. To analyse the stars in our sample, we retrieved two-minute cadence data from the Mikulski Archive for Space Telescopes (MAST) website[3]. These data were used to determine stellar rotation periods and identify flares.

For each star, we evaluated both the Simple Aperture Photometry (SAP) and Pre-search Data Conditioning (PDC) light curves. We selected the light curves with minimal impact from systematics and trends. Notably, we observed systematic issues, particularly in the PDC data of stars with longer rotation periods. Since the corrections applied to PDC light curves are primarily optimised for transit searches, we prioritised the use of SAP light curves whenever possible. In some instances, we observed that the PDC data flagged and removed certain segments corresponding to significant flare events. For instance, in sector 24, the star G 180-060 (J16313+408, TIC 255932726) exhibited a prominent flare peaking at Barycentric Julian dates (BJD) 2458957.07 (refer to Figure B.30 for the flare located at 1957.07) that was entirely eliminated from the PDC data, prompting us to rely on the SAP light curve instead. However, if the SAP light curve was heavily influenced by instrumental systematics or trends and no discernible flare was impacted by the applied corrections, we opted to use PDCSAP data instead.

Furthermore, in multiple sectors, we encountered data gaps or technical issues that affected the quality of the observations. For instance, in sector eight, there was a disconnection between the instrument and spacecraft, leading to an instrument turn-off and missing data for approximately three days between BJD 2458531.74288 and 2458535.00264. This resulted in a total data gap of around six days, as the pause required for satellite data downlink further contributed to the duration of the gap. Similarly, in sector 18, an instrument turn-off occurred when the spacecraft passed through the Earth's shadow, causing a loss of data for approximately six hours between BJD 2458791.1115 and 2458791.3699. The instrument turn-off caused a change in the spacecraft's thermal state, leading to a trend in the SAP data of all five observed stars in sector 18. Hence, for these stars, we opted for the PDCSAP data if it successfully eliminated the trend in the SAP data without introducing any new anomalies in the star's light curve. In cases where the trend removal resulted in anomalies, we resorted to using SAP data while removing the affected data from the light curve.

Fortunately, the TESS Data Release Notes (DRN) available at the Science Processing Operations Center (SPOC) at NASA Ames Research Center in the MAST site[4] provide comprehensive information on data products, including details about instrumental problems for each sector. To identify any anomalies in the light curve of each star, we cross-referenced the information in the DRNs and measured the observation duration for each star after removing any affected areas, if present. The type of light curve utilised for each target, along with the observation log containing information about the corresponding sectors, cameras, and CCDs, is listed in Table B.1. Please note that the TIC number of the stars in this table is arranged in chronological order based on their first observation time.

As the final step of correction, we excluded data points flagged with quality indicators that signalled issues in the light curves, following the guidance provided by the TESS Data Product Overview[5]. However, we retained data points marked as impulsive outliers (quality flag 512) since they were predominantly associated with flare events, ensuring that flare

[3] https://mast.stsci.edu/portal/Mashup/Clients/Mast/Portal.html
[4] https://archive.stsci.edu/tess/tess_drn.html
[5] https://outerspace.stsci.edu/display/TESS/2.0+-+Data+Product+Overview

energies were not underestimated. Additionally, if there was a flare event present, we retained data points labelled as scattered light (quality flag 4096).

4.5.1 Flux Contamination and discarded stars

One significant challenge associated with TESS photometry is the potential dilution of stellar flux caused by nearby contaminant sources. TESS utilises a relatively large pixel size of $21'' \, \mathrm{px}^{-1}$, indicating that approximately 90% of the ensquared energy is concentrated within a 4×4 pixel area or equivalent to $42''$ in diameter (Ricker et al., 2015). This dilution issue primarily affects the search for exoplanet transits, leading to inaccurate estimation of planetary parameters and the possibility of false-positive detections, where a nearby eclipsing binary spills light over the pixels of the target of interest. Furthermore, it can result in the underestimation of flare energies, making it challenging to detect low-energy flares, as well as causing the misidentification of flares originating from a neighbouring star. This issue has been addressed in studies conducted by Doyle et al. (2019) and Tu et al. (2020) using TESS data. Doyle et al. (2019) effectively identified and flagged stars within their sample that had neighbouring stars up to 1.5 magnitudes fainter than the main target within distances of $42''$. They acknowledged that a fraction of the observed flare events in these stars might actually originate from nearby sources. Similarly, Tu et al. (2020) also detected and removed contaminated stars from their dataset, addressing this issue. This phenomenon of neighbouring star contamination has also been observed in the Kepler data. To mitigate this problem, a combination of manual validation of flare events and thorough target vetting has been suggested as a viable workaround. For instance, Shibayama et al. (2013) specifically focused on stars without any neighbouring sources within a $12''$ radius and manually excluded events where the flare originated from a different star within the aperture. In a study, Jackman, Shkolnik, and Loyd (2021) utilised 'discarded contaminated flares' from the Kepler short cadence data and reported the highest measured M dwarf flare recorded by Kepler. Remarkably, their investigation also revealed that in wide binary systems, the lower mass companion tends to exhibit a higher frequency of flaring at a given energy. These findings underscore the significance of examining blended flares in TESS data, where an even greater occurrence of blending is anticipated due to the larger pixel size of TESS in comparison to that of Kepler (approximately $4'' \, \mathrm{px}^{-1}$).

To examine the potential presence of contaminated sources within our sample, we retrieved the target pixel file (TPF) for each star and conducted a search for these sources within the aperture masks using the Gaia DR2 catalogue DR2 catalogue (Gaia Collaboration et al., 2018b). The TPFs, displayed in Figure B.1, were generated utilising the `tpfplotter`[6] tool (Aller et al., 2020). Each subplot corresponds to an individual star in our sample, with separate plots for stars observed in multiple sectors. In each TPF plot, the primary target is denoted by a white cross and labelled as number 1. Additionally, sources from the Gaia DR2 catalogue are superimposed as red circles and labelled based on their proximity to the main star. The size of the red circles indicates the magnitude of each star. To assess the degree of contamination from nearby stars within each aperture mask, we utilised the Gaia G-band flux measurements. Moreover, we carefully noted the presence of sources located within a $42''$ radius of our targets, situated outside the aperture masks, and exhibiting greater brightness than the main target. These sources have the potential to contribute additional flux into

[6] https://github.com/jlillo/tpfplotter

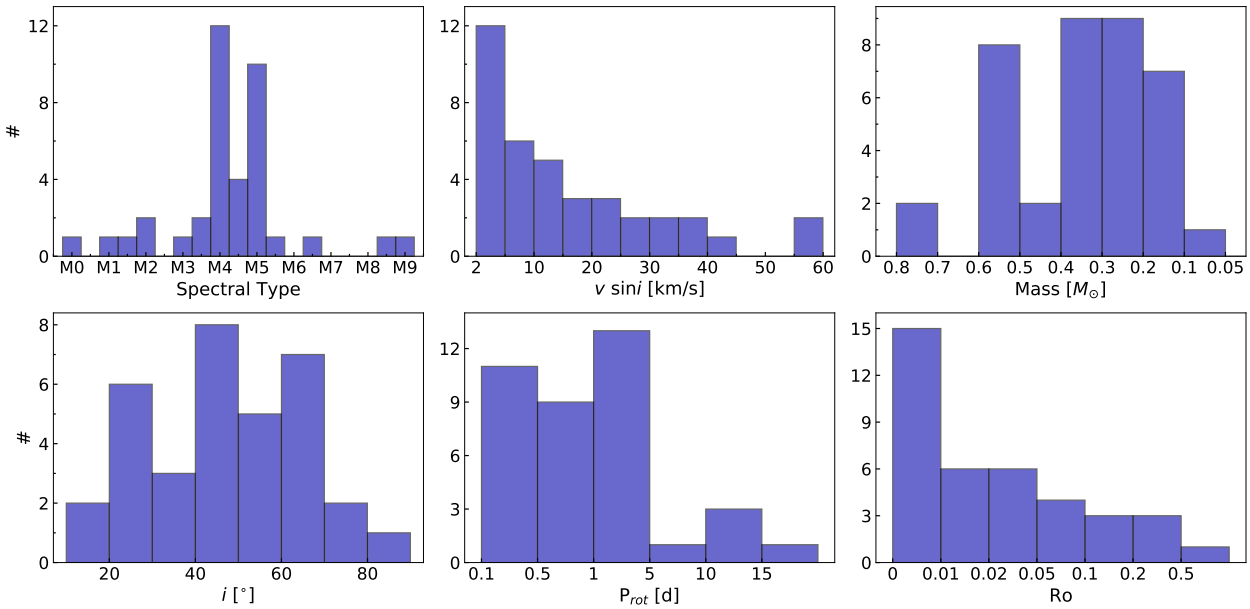

FIGURE 4.1: Comprehensive distribution of the sample across stellar parameters: spectral type, projected rotational velocity $(v, \sin, i)$, stellar mass, inclination in the line of sight (i), rotation period $(P_{\rm rot})$, and Rossby number (Ro). The corresponding values can be found in Table B.2 and Table B.4.

the aperture. We compiled a comprehensive record in Table B.1, which includes the number of stars within the aperture (including the main target), the corresponding percentage of contamination attributed to them, and the count of bright stars neighbouring the main target but located outside the aperture. In Table B.4, which presents a summary of our flare analysis findings, we marked stars with over 25% flux contamination by placing an asterisk next to their corresponding Karmn designations.

Four stars had to be excluded from our original dataset due to severe contamination and the absence of discernible features in their light curves. These stars are NLTT 20861 (J09033+056, TIC 270511002), an M7.0 V dwarf observed by TESS in sector 8, and LP 731-076 (J10584-107, TIC 148563078), with has a spectral type of M5.0 V and was observed in sector 9. Both stars were found to have a bright star located outside their aperture masks. Furthermore, LSR J0539+4038 (J05394+406, TIC 239097694), an M8.0 V star, and 2MASS J06572616+7405265 (J06574+740, TIC 141476700), an M4.0 V dwarf, were observed in sector 19 within an extremely crowded region. Please refer to Figure B.1 for the corresponding TPF plots of these stars.

4.6 Stellar parameters

Figure 4.1 illustrates the distribution of the sample stars across various stellar properties, including spectral type, rotational velocity $(v \sin i)$, stellar mass, spin axis inclination (i), rotational period $(P_{\rm rot})$, and Rossby number (Ro). The stellar parameter values were sourced from the Carmencita database (Alonso-Floriano et al., 2015a; Caballero et al., 2016), with the exception of $P_{\rm rot}$, stellar inclination, and Rossby numbers, which were derived in this study (see Section 4.6.1 for $P_{\rm rot}$ and i calculations, and Section 4.6.2 for Rossby numbers).

The stars in our sample exhibit a wide range of spectral types, spanning from M0.0 V to M9.0 V. The majority of stars are concentrated between M4.0 V and M5.5 V, a range where a transition into the fully convective regime is anticipated. Regarding rotational velocities ($v \sin i$), the values range from > 2 km s^{-1} (by definition) to a maximum of 59.8 km s^{-1}. The stellar masses range from 0.06 to 0.75 $M_\odot$, with 23 fully convective stars having masses below 0.35 $M_\odot$. In terms of magnitude, the G_{RP} values span a range of 7.3 to 14.3 mag, corresponding to distances of up to approximately 50 pc. When it comes to rotation, the majority of stars in our sample exhibit rapid rotation, with periods ranging from 0.139 to 15.188 days. Notably, there are 20 stars with sub-day periods, while only five stars have periods longer than five days. Considering the inclination of the stars in our sample, their values range from 10 to 80 degrees. Additionally, the Rossby numbers span from 0.001 to 0.507.

4.6.1 Stellar rotation periods and spin axis inclinations

We utilised the generalised Lomb-Scargle (GLS) periodogram[7] method (Zechmeister and Kürster, 2009) on the stars in our sample to determine their rotation periods and corresponding false-alarm probabilities. This analysis yielded eleven new rotation periods, ranging from 0.188 to 13.847 days. Among these, eight out of eleven rotation periods measured were less than one day, while the remaining three were 3.346, 5.704, and 13.847 days.

To validate the obtained rotation periods, we calculated the upper limits on $P_{\rm rot}$ for each star using stellar radius R, $v \sin i$, and their associated uncertainties. These upper limits were found to be less than 14 days for all stars. Furthermore, we verified the consistency between our calculated values and the previously published rotation periods by Díez Alonso et al. (2019) and Kiraga (2012) for the 27 stars with known rotation periods. This comparison is illustrated in Figure B.2. The $P_{\rm rot}$ values are listed in Table B.4, and their distribution is illustrated in Figure 4.1.

Following the calculation of rotation periods, we proceeded to estimate the inclination of the rotation axis, denoted as i. To accomplish this, we employed 10^6 Markov Chain Monte Carlo (MCMC) realisations, utilising the TESS photometry-derived $P_{\rm rot}$, stellar radius ($R_{\rm star}$), and the $v \sin i$value available in the stellar parameters table (Table B.2). The inclination was estimated using the relationship:

$$i = \arcsin(P_{\rm rot}\ v \sin i / 2\pi\ R_{\rm star}), \tag{4.1}$$

where i represents the angle measured along the observer's line of sight. In this context, a value of 90° indicates that the stellar rotation axis is perpendicular to the line of sight, while 0° implies a pole-on orientation of the star. It is important to acknowledge that the inclination determined from this relationship carries a significant degree of uncertainty, primarily due to the considerable uncertainty associated with the measured $v \sin i$. The estimated inclinations, along with their corresponding uncertainties, have been included in Table B.2. The distribution of these inclination estimates is visualised in Fig. 4.1.

[7] https://github.com/mzechmeister/GLS

4.6.2 Rossby number

To facilitate a comparison of the flare rate independent of the stellar mass, we computed the Rossby number (Ro) for our sample using the rotation periods and stellar masses ($M_\star$) provided in Table B.2. The Rossby number, denoted as $Ro = P_{\rm rot}/\tau$, is defined as the ratio of $P_{\rm rot}$ to the mass-dependent convective turnover time (τ), which can be empirically determined using Equation (11) from Wright et al. (2011):

$$\log \tau = 1.16 - 1.49 \log \left(\frac{M}{M_\odot} \right) - 0.54 \log^2 \left(\frac{M}{M_\odot} \right). \tag{4.2}$$

Uncertainties in the Ro were estimated through 10^6 MCMC realisations incorporating the stellar mass and rotation period. The calculated Ro values are listed in Table B.4, and their distribution is depicted in Fig. 4.1.

4.6.3 Activity indicators

The equivalent width (EW) serves as a common measure of the strength of a spectral line. It is defined as the width of a hypothetical rectangular absorption feature that covers the same area as the spectral line, normalised to the surrounding continuum. This allows for a consistent comparison of spectral lines with varying shapes. Notably, emission lines can be viewed as negative absorption lines, resulting in negative values for EWs.

In M dwarf spectra, it is often challenging to establish a true continuum. Consequently, the spectrum is typically normalised to a pseudo-continuum (PC), and the EW is measured with respect to the PC, referred to as a pseudo-equivalent width (pEW). For our analysis of correlation with flare features, we compiled all available line indices and pEWs for the sample. Since we observed a similar behaviour between the I indices and pEWs, we solely included the results for the pEWs in this study.

Table B.3 presents the number of spectroscopic observations for each star, along with the median values of the normalised Hα luminosities ($\log L_{\rm H\alpha}/L_{\rm bol}$) and the following pseudo-equivalent widths: pEW(Hα), pEW(He D_3), pEW(Na D_2), pEW(Na D_1), pEW(Na D), pEW(Ca IRT-a), pEW(Ca IRT-b), pEW(Ca IRT-c), and pEW(Fe 8691). Negative values for the equivalent width indicate emission lines.

4.7 Flare analysis

4.7.1 Detection method

To identify flares, detrending the light curve is essential to remove modulation caused by stellar rotation. We utilized the SciPy module's Savitzky-Golay (SavGol) filter independently for each sector, accounting for data gaps during spacecraft re-orientations. Parameter optimisation of the SavGol filter was performed considering stellar rotation period and the occurrence of large flares with extended durations. Additionally, iterative 3 σ clipping of outliers above the local median flux was applied within each window to mitigate flare impact on the fitting process. The number of iterations was tailored to the flare duration in each window, emphasizing the significance of a proper fitting procedure to accurately estimate

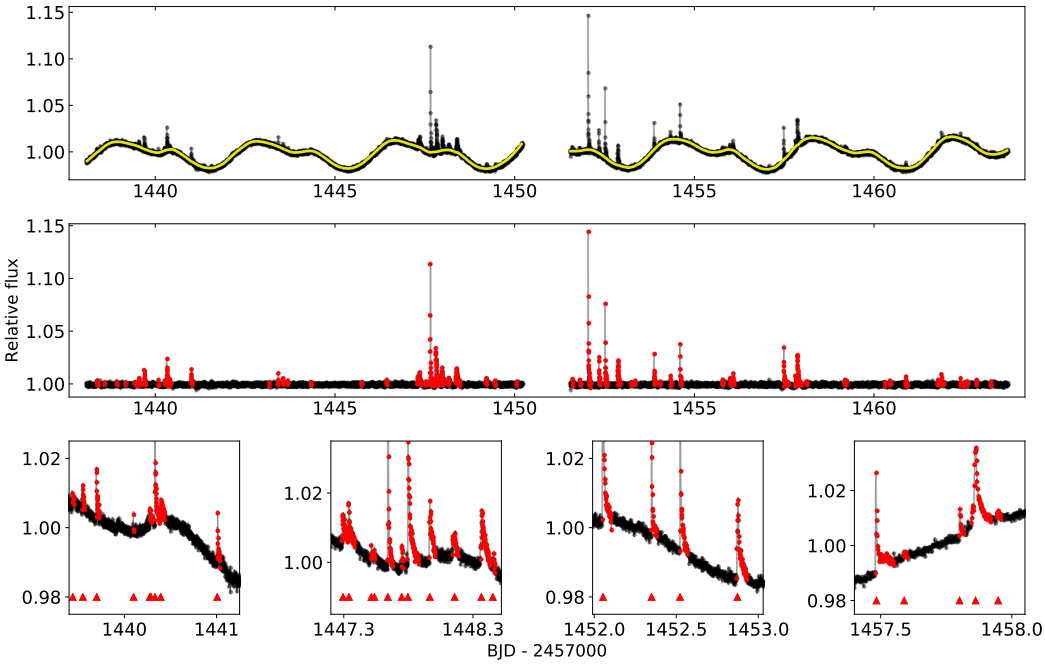

FIGURE 4.2: Flare detection example using the light curve of G 80-021 (TIC 333680372). The graph displays observation time (x-axis) in Barycentric Julian Date (BJD) and normalized TESS SAP flux (y-axis). Black data points represent TESS 2-minute cadence measurements. Top panel: Trend line obtained with Savitzky-Golay filter. Middle panel: Detrended flux with marked flare candidates (red). Lower panels: Zoomed views of regions with detected flares. Flare peaks indicated by triangle marks.

flare energies. After detrending the light curve, flare candidates were identified using the following criteria:

(i) Data points were required to be at least 2.5 σ above the local median of the smoothed light curve.

(ii) Two or more consecutive points should exceed the detection thresholds.

(iii) The flare's rise time (duration between flare start and peak) was expected to be shorter than the decay time (duration between peak and end).

Finally, we conducted a visual inspection to validate each flare candidate. As necessary, we adjusted the assigned start and end times for individual flare candidates and re-evaluated them against the third criterion. In cases where flares exhibited multiple peaks, we treated them as distinct events only if they returned to the quiescent flux level before rising to the subsequent peak. Figure 4.2 showcases an illustrative example of TESS data processed with a SavGol filter for smoothing and subsequent flare detection. The x-axis represents the observation time in Barycentric Julian Date (BJD), while the y-axis shows the TESS SAP flux normalized by the median flux. Black data points correspond to TESS 2-minute cadence measurements. In the top panel, a yellow line illustrates the trend in the light curve obtained by applying the Savitzky-Golay filter. In the middle panel, the detrended flux is presented,

with any detected flare candidates clearly marked in red. For closer examination, the lower panels provide zoomed views of specific regions from the original light curve, focusing on areas where flares have been detected. To highlight the positions of the identified flare peaks, triangle marks are used throughout the graph.

4.7.2 Determination of flare parameters

Each candidate flare event was assessed based on multiple statistics, allowing for in-depth analysis and facilitating comparisons among different stars. For example, we derived the flare duration by determining the time interval between the start and stop times of the flare. To gauge the flare's peak amplitude, we calculated the difference between the flare peak and the local median flux, divided by the local median flux. This metric is measured relative to the quiescent stellar flux and provides a quantification of the excess emission above the median value of flux in the local region. In order to determine the flare energies, we initially evaluated the equivalent duration (ED). The ED represents the duration over which the quiescent star emits the same energy as that emitted by the flare (Gershberg, 1972; Walkowicz et al., 2011; Hunt-Walker et al., 2012; Hawley et al., 2014; Chang, Byun, and Hartman, 2015; Davenport, 2016). Practically, the ED is computed by integrating the area under the flare in the residual light curve, obtained by subtracting the quiescent stellar flux. Measured in units of time (here, seconds), the ED is indicative of the flare's energy.

We estimated flare energies using quiescent stellar luminosity ($L_\star$) and ED, following the methodology outlined in Shibayama et al. (2013) and Günther et al. (2020). The stellar luminosity ($L_\star$), radius ($R_\star$), and effective temperature ($T_{\rm eff}$) were obtained from Schweitzer et al. (2019). To calculate the bolometric flare luminosity ($L_{\rm flare}$), we made the assumption that the spectrum of white-light flares can be approximated by black-body radiation with an effective temperature of 9000±500 K, following a conservative lower limit proposed by Günther et al. (2020). $L_{\rm flare}$ is then calculated using the Stefan–Boltzmann equation:

$$L_{\rm flare} = \sigma_{\rm SB}\ T_{\rm flare}^4\ A_{\rm flare}, \tag{4.3}$$

where $\sigma_{\rm SB}$ represents the Stefan–Boltzmann constant and $A_{\rm flare}$ corresponds to the area of the flare. To estimate $A_{\rm flare}$, we require the luminosities of the star and the flare within the observing bandpass, denoted as $L'_\star$ and $L'_{\rm flare}$, respectively. These luminosities are given as

$$L'_\star = \pi\ R_\star^2 \int R_\lambda B_{\lambda(T_{\rm eff})} d\lambda, \tag{4.4}$$

$$L'_{\rm flare} = A_{\rm flare} \int R_\lambda B_{\lambda(T_{\rm flare})} d\lambda. \tag{4.5}$$

Here, R_λ represents the spectral response function of the TESS instrument [8]. It is worth noting that the normalisation of R_λ is inconsequential since it cancels out in the subsequent calculations. $B_{\lambda(T_{\rm eff})}$ and $B_{\lambda(T_{\rm flare})}$ represent the Planck functions evaluated at the effective temperature of the star and the temperature of the flare, respectively. It's important to note that these calculations are based on the assumption of a consistent flare temperature. Since the flare amplitude of the detrended light curve can be estimated as $L'_{\rm flare}/L'_\star$, we can solve

[8] defined as the product of the long-pass filter transmission and the detector quantum efficiency; available at https://heasarc.gsfc.nasa.gov/docs/tess/data/tess-response-function-v1.0.csv

equations 4.4 and 4.5 to calculate $A_{\rm flare}$:

$$A_{\rm flare} = (L'_{\rm flare}/L'_{\star})\ \pi\ R_{\star}^2 \frac{\int R_{\lambda} B_{\lambda(T_{\rm eff})} d\lambda}{\int R_{\lambda} B_{\lambda(T_{\rm flare})} d\lambda} \tag{4.6}$$

The total bolometric energy of the flare, denoted as $E_{\rm flare}$ is then given by

$$E_{\rm flare} = \int L_{\rm flare}(t)\ dt = \sigma_{\rm SB}\ T_{\rm flare}^4 \int A_{\rm flare}(t)\ dt \tag{4.7}$$

This integral can be further simplified by substituting $\int (L'_{\rm flare}/L'_{\star})$ with the term ED.

4.7.3 Flare Frequency Distributions

Flare rates are commonly analysed using the cumulative Flare Frequency Distribution (FFD; e.g., Lacy, Moffett, and Evans, 1976), which provides a comprehensive understanding of flare rate as a function of energy levels. The FFD follows a probability distribution expressed by the equation:

$$N(E)dE = \Omega E^{-\alpha} dE, \tag{4.8}$$

where $N(E)$ represents the rate of flares as a function of energy, E. The parameter α corresponds to the slope of the power law, while Ω is a normalisation constant.

The FFD is a preferred method of analysis due to the stochastic nature of flare occurrences, which span a wide range of energy levels and durations. By utilising the FFD, it becomes possible to estimate the flare rate across multiple orders of magnitude, even in cases where flares have not been directly observed (Lacy, Moffett, and Evans, 1976; Hawley et al., 2014; Davenport, 2016; Howard et al., 2019; Günther et al., 2020). FFD diagrams serve as valuable tools for comparing the occurrence rates of flares on different stars as a function of flare energy.

The slope of the power law, α, carries valuable information. In a study utilising K2 light curves of K and M stars, Ilin et al. (2019) proposed that α might be consistent across all stars, suggesting a value of approximately 2. If $\alpha \geq 2$, it indicates a substantial abundance of flares, particularly those at lower energies ($10^{24} - 10^{25}$ ergs), capable of heating the quiescent corona (Audard et al., 2000; Güdel et al., 2002). On the other hand, if $\alpha < 2$, the energy supplied to the corona depends on the most energetic events, and low-energy flares do not occur frequently enough to contribute significantly to coronal heating (Hudson, 1991).

4.7.4 TESS Light curve variability range ($R_{\rm var}$)

The variability range ($R_{\rm var}$) provides an assessment of the amplitude of brightness modulations caused by rotating active regions (Basri et al., 2010; Basri et al., 2011). In the original definition by Basri et al. (2010), $R_{\rm var}$ for solar-type stars is determined as the interval between the 5^{th} and 95^{th} flux percentiles of the normalised light curves. In our study, we optimised the definition for our targets by calculating $R_{\rm var}$ as the difference between the 1^{st} and 99^{th} flux percentiles of the sorted flux values after removing the flare events from the light curve.

4.8 Results

A comprehensive summary of our flare analysis results, including the total observation time, flare frequency, duration range, amplitude, ED, log(E), estimated α, $R_{\rm var}$, $P_{\rm rot}$, and Ro for each star in our sample is provided in Table B.4. In addition, we present a comprehensive diagram that showcases various aspects of our flare analysis for each star in our sample. Here, we provide an example of such a diagram for G 80-021 (J03473-019, TIC 333680372). This diagram includes the stellar light curve (normalised by its median) with marked recovered flares (panel *a*), the photometric variability range (R_{var}) (panel *b*), the phase-folded light curve of the rotational modulation (panel *c*), the cumulative flare frequency distribution (FFD) with a power-law fit to flares with energy larger than the median flare energy of the star (panel *d*), the flare frequency as a function of the rotation phase, with the number of flares in each 0.1-sized rotational phase bin normalised by the stellar rotation period (panel *e*), the histograms of flare energy distribution (panel *f*), and finally the flare energy as a function of the rotation phase (panel *g*). Similar diagrams for the remaining targets can be found in Appendix B.

In the following, we present the results of our analysis, focusing on the correlations between flare properties and various stellar parameters, including mass, rotation period, Rossby number, spectroscopic activity indicators, stellar magnetic field, and rotation phase. We then highlight some notable cases within our sample.

4.8.1 Distribution of flare energies

We identified a total of 2,434 flares across 38 stars in our sample, observed collectively for approximately 1,823.31 days spanning 20 sectors of TESS. The individual flare energy distributions for each star are depicted in panel f of Figure B.3 –B.39. Figure 4.4 presents the combined flare energy distribution, encompassing all 2,434 flares from our sample. The histogram exhibits a slight positive skew, indicating a prevalence of lower energy flares. Notably, the decline in the number of flares with energy below 10^{31} erg is attributed to noise in the light curves, limiting the reliable detection of low energy events.

The star exhibiting the highest number of high-energy flares, surpassing the 10^{32} erg threshold, is StKM 2-809 (J12156+526, TIC 416538839), with an impressive average of 2.5 energetic flares per day. StKM 2-809 is a fast rotating M4.0 V star with a measured $v \sin i$ of 35.3 $\pm$ 3.5 km,s^{-1} and a period of 0.725 d. It belongs to the Ursa Major moving group (Cortés-Contreras, 2016) and is estimated to have an age between 300 and 500 Ma according to (King et al., 2003). The light curve of StKM 2-809 is visually presented in Figure B.23.

4.8.2 Comparing flare frequency distributions

As mentioned earlier, flares are inherently stochastic events, exhibiting a wide range of energy and duration spanning several orders of magnitude. Therefore, the cumulative Flare Frequency Distribution (FFD) serves as the optimal tool for assessing and comparing flare rates at specific energy levels across stars. A standard approach involves measuring the frequency of flare occurrences at a given energy, such as 10^{32} erg, utilising the vertical axis of the cumulative FFD plot (e.g., panel d of Figure 4.3).

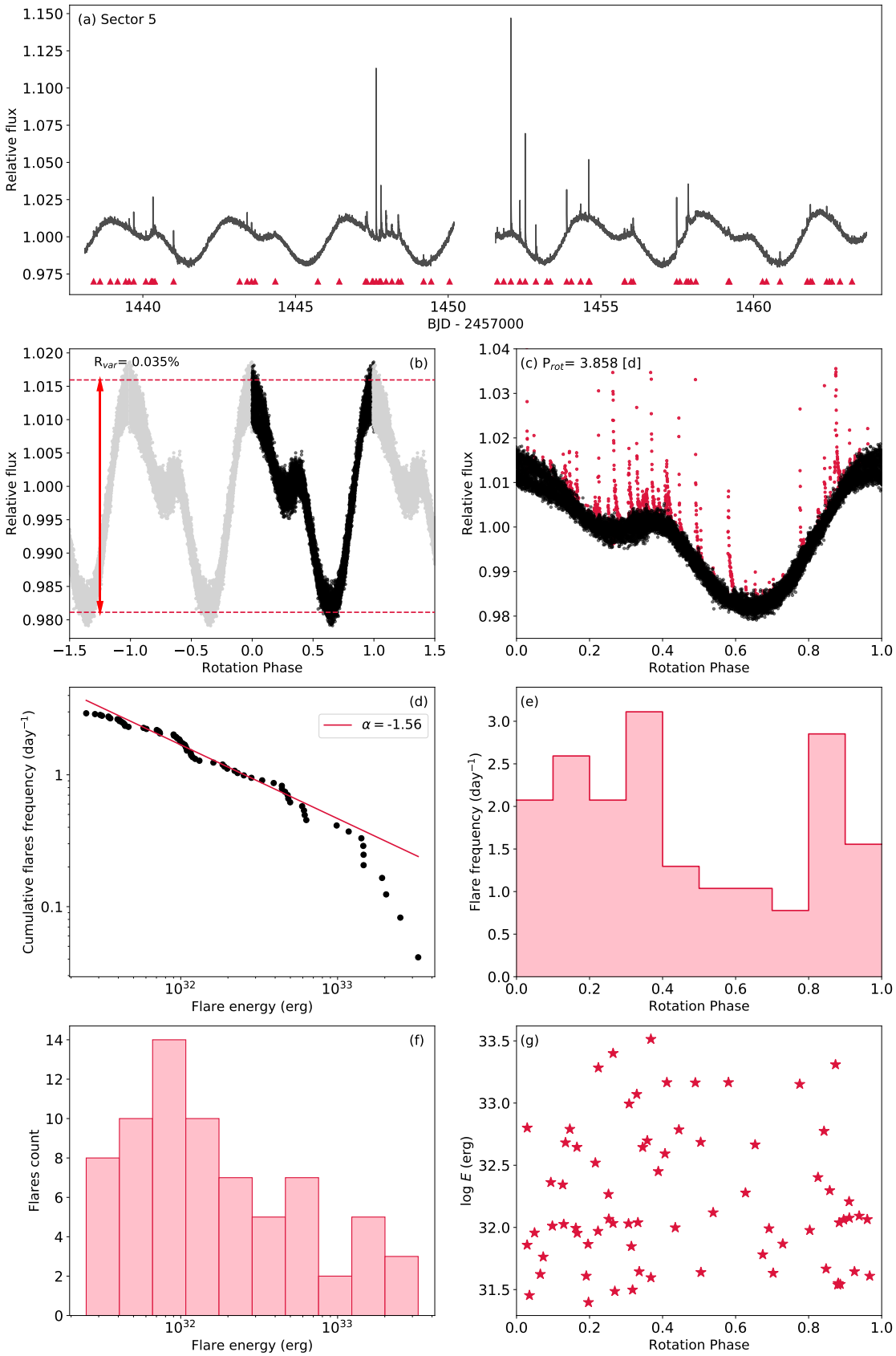

FIGURE 4.3: Flare analysis results for G 80-021 (J03473-019, TIC 333680372). (a) TESS light curve displaying the observed variability and detected flares. (b) Variability range of the light curve after removing flares. (c) Phase-folded light curve illustrating rotational variations. (d) Cumulative FFD based on energy. (e) Frequency of flares plotted against rotation phase. (f) Flare count plotted against flare energy. (g) Bolometric energy of each flare plotted against rotation phase.

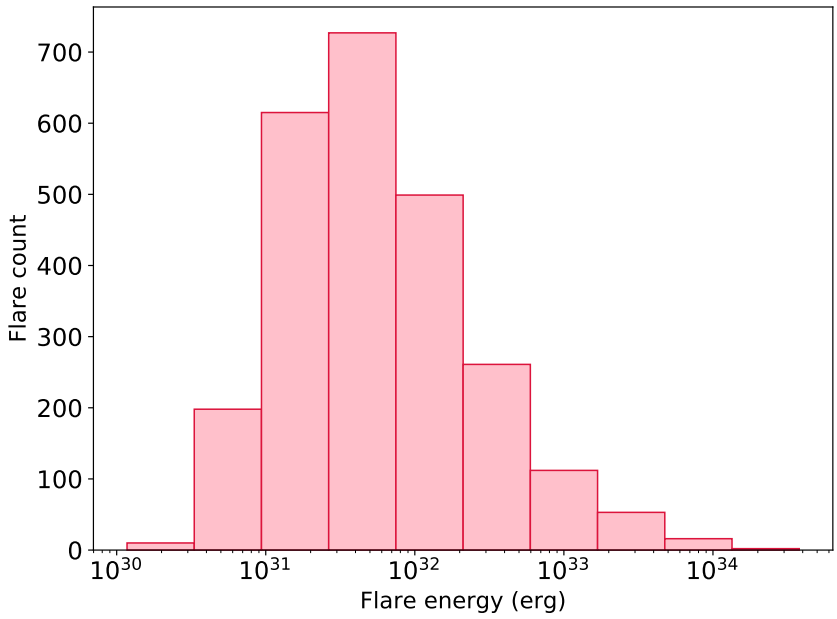

FIGURE 4.4: Energy distribution of 2,434 flares across 38 stars in our sample.

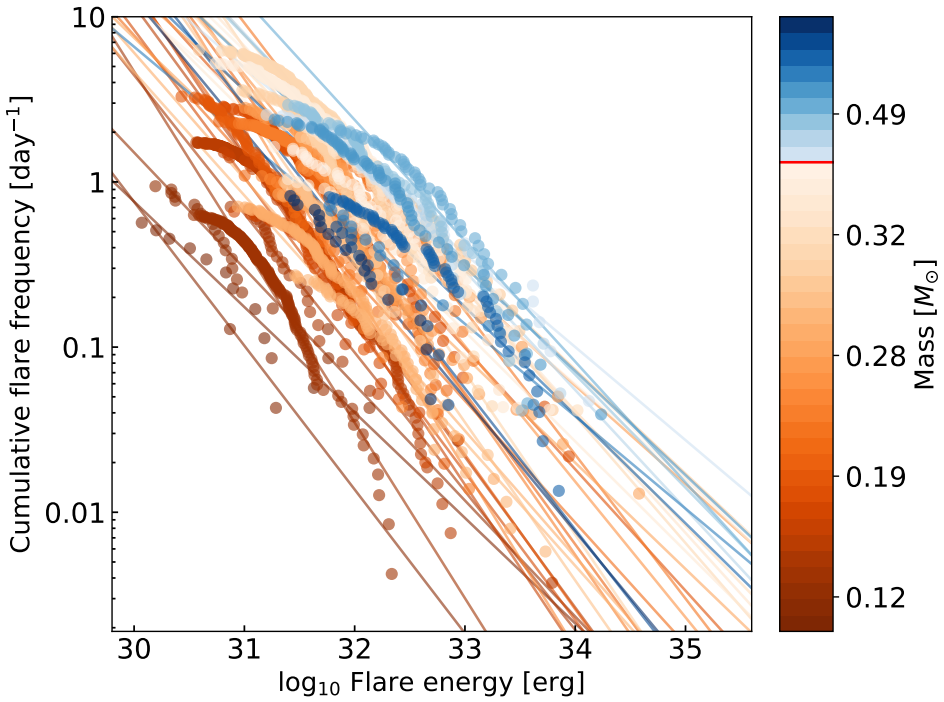

FIGURE 4.5: Cumulative flare frequency diagram for our sample of 38 stars, displaying the overlaid power law fit and colour-coded representation based on stellar mass. Flare rates have been sampled using logarithmic energy bins.

In cases where the desired flare energy surpasses the observed range of flares for a particular star, extrapolation becomes necessary by employing a power-law fit to estimate the flare rate at that specific energy. However, caution must be exercised as the accuracy of the power-law fit may be compromised due to several factors. These factors include discontinuities in the FFD, particularly at higher energies (e.g., Figure B.4, or Figure B.6), an insufficient number of detected flares (e.g., Figure B.10, Figure B.7, Figure B.20), or underestimation of the cumulative number of flare frequencies at lower energies due to detection biases, similar to what has been observed in flare studies utilising Kepler data (Hawley et al., 2014). Therefore, it is crucial to recognise that employing this technique for deriving flare rates may lead to inaccurate estimations.

Figure 4.5 displays the FFDs for our sample of 38 stars. Each star is represented by a distinct FFD, colour-coded based on its mass and accompanied by an overlaid power law fit. To differentiate between stars with a radiative zone and potentially exhibiting a solar-type dynamo from fully convective stars with a turbulent dynamo, two different colour ranges are assigned for masses below and above 0.35 $M_{\odot}$. The threshold of 0.35 $M_{\odot}$ is demarcated by a red marker on the corresponding colour bar. When examining the range of flare energies in our sample using this plot, a notable trend emerges: massive stars exhibit a higher frequency of energetic events compared to their lower-mass counterparts, while low-energy flares are relatively less common. However, it is highly probable that the reduced detection of low-energy flares in these stars can be attributed to their inherent brightness and the resulting diminished contrast between flare events and the background photosphere.

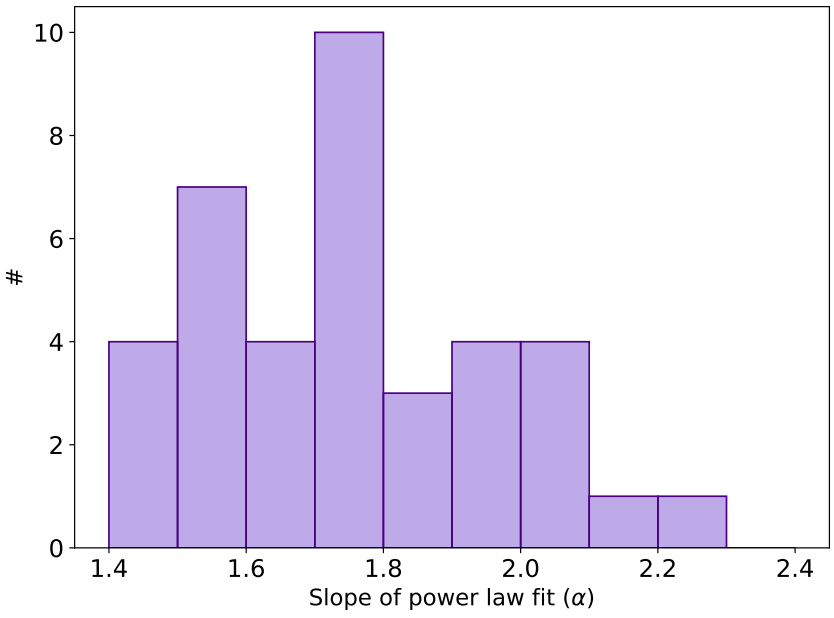

FIGURE 4.6: Distribution of α values, representing the slope of the power law fit to the Flare Frequency Distributions (FFDs) of stars.

We compared the values of α, the slope of the fitted power laws for these FFDs, and presented their distribution in Figure 4.6. The median α value was found to be 1.75, consistent with measurements reported in previous studies for M dwarfs (Lacy, Moffett, and Evans, 1976; Hawley et al., 2014; Silverberg et al., 2016; Maehara et al., 2021). Around 26% stars in

our sample exhibited an α value around 1.75, further supporting this alignment with existing findings. Notably, six stars in our sample exhibited an α value equal to or greater than 2, meeting the minimum threshold necessary to account for coronal heating. These stars include LSR J0419+4233 (J04198+425, TIC 347994537), 2MASS J07471385+5020386 (J07472+503, TIC 309661100), GJ 1101 (J07558+833, TIC 289972535), LP 071-082 (J18022+642, TIC 233068870), LP 71-165 (J18189+661, TIC 406857100), and V374 Peg (J22012+283, TIC 283410775). However, it is important to note that LSR J0419+4233, being a faint M8.5,V star, has only three detected flares, rendering the power law fit and the corresponding alpha value less reliable. On the other hand, the remaining stars encompass spectral types ranging from M4.0 V to M5.0 V, and it is plausible that they generate a sufficient number of lower energy flares to supply the required energy for coronal heating.

4.8.2.1 Correlation between flare energies and stellar masses

To provide a thorough overview of the correlation between flare energy and stellar mass, we plotted the flare energy value at which the FFD of each star reaches 0.1/day as a function of mass. This insightful plot, presented in Figure 4.7, clearly reveals a correlation between stellar mass and flare energies.

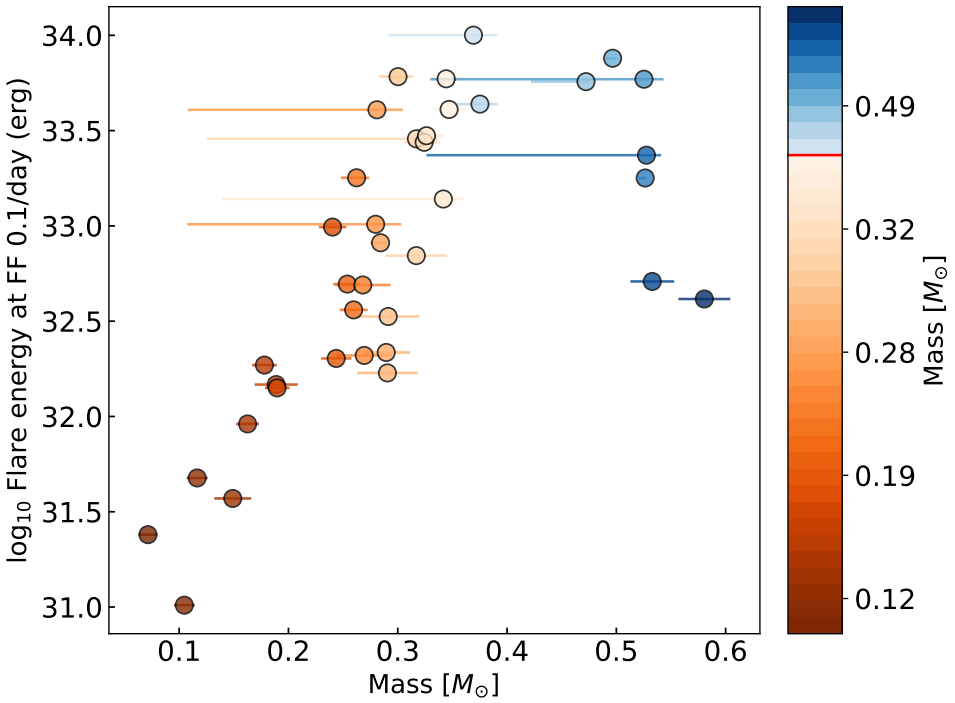

FIGURE 4.7: Correlation between flare energies (@ 0.1/day) and stellar mass. The plot reveals that stars with a mass of approximately 0.35 to 0.5 $M_\odot$ exhibit the highest energy flares at this rate, coinciding with the transition region between $\alpha\Omega$ and α^2 dynamos.

Notably, more massive stars exhibit a higher production of energetic flares at a certain rate, up until a stellar mass range of approximately 0.35 to 0.5 $M_\odot$. Beyond this threshold, there is a decline in the energy of the flares. The distribution of flare energies over the mass

range appears to be continuous, with a peak occurring around the transition region between the dominant types of dynamos in the star. This suggests that the generation of high-energy flares is not exclusively associated with a specific type of dynamo but rather linked to the boundary where complete convection occurs.

Although our study explores a narrower range of stellar masses compared to Lacy, Moffett, and Evans (1976), our findings align well with their results, which indicate that the flare rate at a given energy is dependent on stellar luminosity. Specifically, low-mass stars tend to produce lower energy flares compared to higher mass stars.

Nevertheless, it is important to acknowledge the presence of a significant level of uncertainty associated with the masses of young stars in our sample, including those associated with young associations or young moving groups, as evidenced in Figure 4.7. Estimating the mass of these young objects is a complex and challenging task due to various contributing factors. For a comprehensive understanding of the methodologies employed for mass determination and the associated limitations, we recommend referring to Schweitzer et al. (2019). Additionally, it is worth considering the possibility that these stars may have unknown binary companions, leading to potentially inaccurate mass estimates that mistakenly place them within our sample. All these uncertainties have the potential to influence our results.

4.8.2.2 Correlation between flare energies and rotation periods and Rossby numbers

To examine the potential impact of the rotation period on the occurrence of flares, we generated a plot comparing the distribution of flare energy at a frequency of 0.1/day as a function of rotation period. However, considering the strong degeneracy between the $P_{\rm rot}$ and stellar mass, we also created a similar plot using the Rossby number. Figure 4.8 displays both of these plots, shedding light on the relationship between the rotation and the production of flares in active M dwarfs.

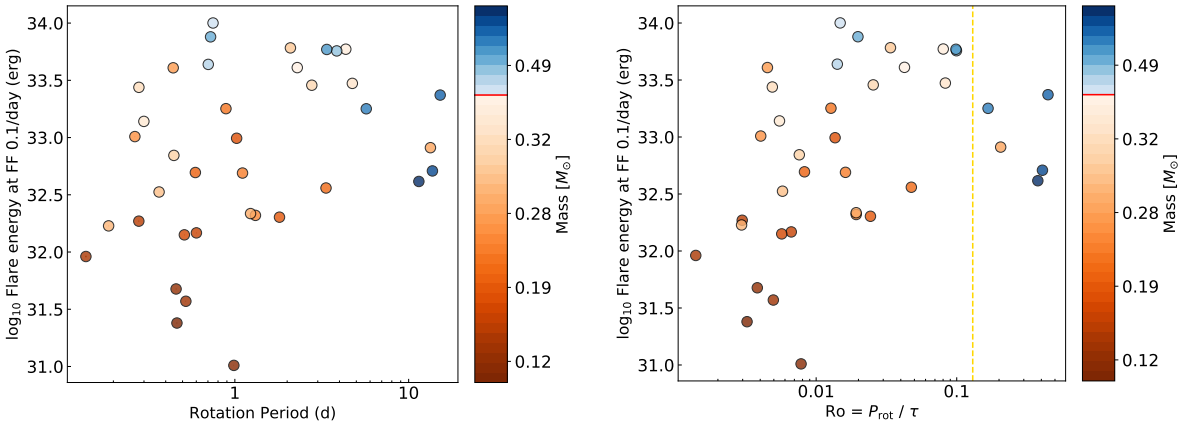

FIGURE 4.8: Correlation between flare energies (@ 0.1/day) and rotation periods (left) and Rossby numbers (right). The vertical yellow dashed line marks the empirical saturation threshold (Ro $\approx$ 0.13). While no significant correlation is observed between flare energies and $P_{\rm rot}$s, a slight indication of increasing flare energy with Rossby numbers can be observed up to Ro $\approx$ 0.13.

Contrary to stellar mass, our findings indicate no dependence of the flare rate on the stellar rotation period or Rossby number within our sample. This contrasts with previous studies that have suggested such correlations. For instance, in a study of 125 single stars with masses ranging from 0.1 to 0.3 $M_{\odot}$ observed during the first year of the TESS mission, Medina et al. (2020) identified a relationship between the flare rate and rotation period or Rossby number. They observed a saturation effect in the flare rate below a critical Rossby number, similar to what has been observed in studies of coronal X-ray emission, chromospheric Ca II H + K, and Hα emission (e.g., Wright et al., 2011). Specifically, Medina et al. (2020) determined a critical Rossby number of Ro = 0.1. Below this value, the flare rate exhibited a constant value of log -1.30 $\pm$ 0.08 flares per day, followed by a rapid decline as the Rossby number increased above Ro = 0.5.

The lack of correlation between flare energies and rotation period in our sample can likely be attributed to the relatively narrow range of rotation observed. It is important to note that all of our stars are fast rotators, which may contribute to the absence of a clear relationship between flare energies and rotation period. However, taking into account the empirical saturation threshold proposed by Wright et al. (2011) at Ro = 0.13, we observed that our sample contains only five stars in the unsaturated regime, and there is a slight hint of an increase in the flare energy in the saturated regime. Expanding the stellar sample to include a greater number of stars with a wider range of rotation periods and masses would provide a more comprehensive understanding of potential correlations.

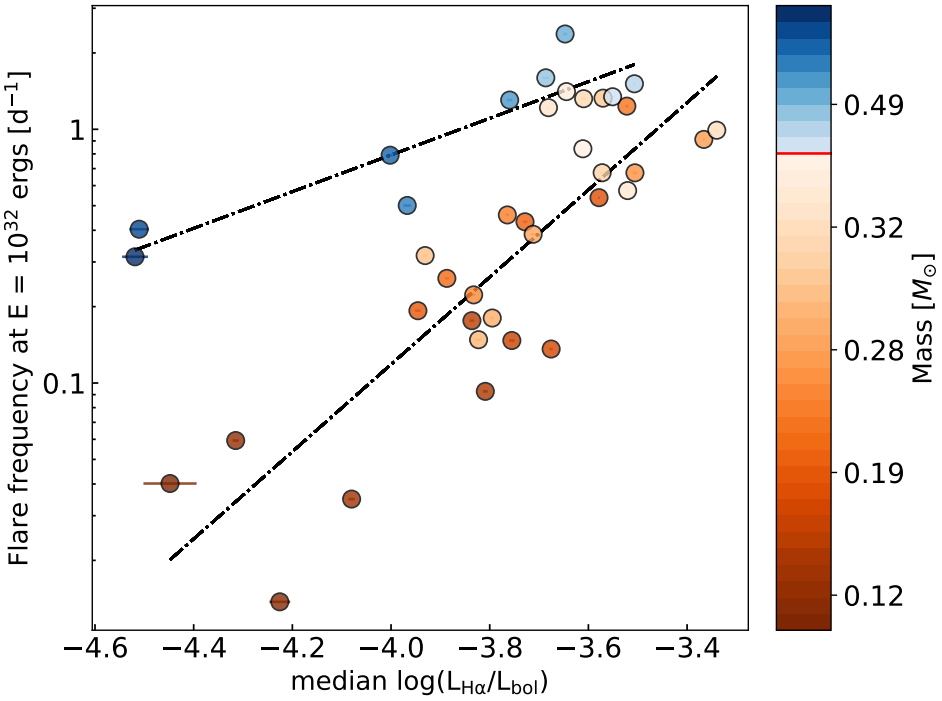

FIGURE 4.9: Flare frequency at E = 10^{32} ergs[d^{-1}] as a function of the normalised Hα luminosity.

4.8.2.3 Correlation between flare rate and normalised Hα luminosity

Flare activity and chromospheric indicators are both proxies for the behaviour of the magnetic dynamo. Therefore, one might expect a relation between these parameters in active M Dwarfs. To investigate the potential relationship between flare rate and spectroscopic indicators, we computed the specific rate of flares emitted at an energy of E = 10^{32} erg using the FFD diagrams. We then examined the correlation between these values and the median of various activity indicators listed in Table B.3.

Among the spectroscopic indicators, the normalised Hα luminosity ($\log L_{\mathrm{H}\alpha}/L_{\mathrm{bol}}$) demonstrated the strongest correlation with the flare rate, as illustrated in Figure 4.9. By incorporating stellar mass as a colour code in this plot, we observed a clear distinction between stars with masses above and below 0.35 $M_{\odot}$. Two distinct regression lines with slopes of 0.72 and 1.72 were fitted to the stars in these two mass groups. Notably, in both mass groups, stars with the highest flare rates also exhibited the highest Hα emission.

4.8.2.4 Correlation between flare energies and magnetic fields

To explore the potential relationship between flare energies, specifically at a rate of 0.1 per day, and the strength of magnetic fields, we compiled the average surface magnetic field (<B>) measurements for the CARMENES sample. These measurements were obtained by comparing spectral absorption lines to radiative transfer calculations, as provided by Shulyak et al. (2019) and Reiners et al. (2022). Figure 4.10 depicts the correlation between flare energies and <B>, with the stellar mass serving as a colour-coded parameter.

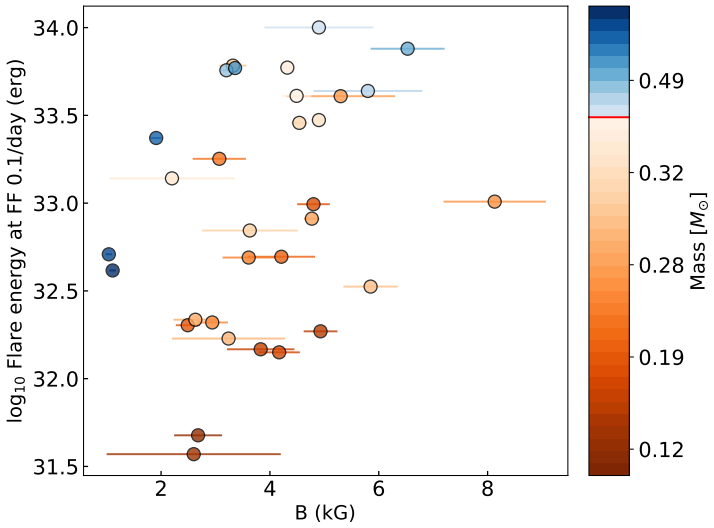

FIGURE 4.10: Correlation between flare energies (@ 0.1/day) and the averaged surface magnetic field <B>. The data points are colour-coded with the stellar mass. Magnetic fields values adopted from Shulyak et al. (2019) and Reiners et al. (2022).

The lack of correlation between flare rates and the averaged magnetic field strength (<B>) can be attributed to several factors. Flares are primarily associated with localized

magnetic fields in active regions, whereas the magnetic field measurements provided by Shulyak et al. (2019) and Reiners et al. (2022) represent the averaged surface fields. This disparity in scale and representation may contribute to the absence of a direct relationship. Furthermore, it is important to consider potential measurement limitations and observational biases when examining both the $<B>$ values and flare energies. The precise determination of magnetic field strength and accurate characterisation of flare energies are complex tasks, influenced by various factors such as instrument sensitivity, observational techniques, and analysis methods. These factors can introduce uncertainties and biases that may obscure or mask any underlying correlation. Therefore, the absence of a clear correlation between flare rates and averaged magnetic field strength may stem from the difference in the spatial scales of the magnetic fields, as well as potential measurement limitations and observational biases inherent in both the magnetic field measurements and flare energy assessments.

4.8.3 Correlation between flares and rotation phase

The pursuit of identifying any preferential rotation phase for the occurrence and energy of flares has been the focus of numerous case studies and statistical analyses involving hundreds of stars. In a study by Hunt-Walker et al. (2012), over 8500 observations of AD Leo from the MOST satellite were analysed, revealing 19 flare events that showed no correlation with the star's rotation period of $2.23^{+0.36}_{-0.27}$ days. Another investigation conducted by Ramsay et al. (2013) examined the flare rate and energy of two M4.0 V stars, namely KIC 5474065 and KIC 9726699, utilising Kepler short cadence observations. The study found that the most energetic flares of KIC 5474065 occurred in the phase intervals $\phi = 0.74 - 0.79$, while for KIC 9726699, they appeared in the phase interval $\phi = 0.84 - 0.85$. However, it should be noted that low-energy flares were observed at various rotational phases for both of these stars. In a study focused on the benchmark planet host TRAPPIST-1, Vida et al. (2017) examined K2 data and found no significant relationship between the flare rate and the rotational modulation of the star. Another notable example is GJ 1243 (G 208-042, J19511+464, TIC 273589987), which is a fully convective M4.0 V dwarf. Both Hawley et al. (2014) and Davenport et al. (2014) independently investigated this star and reported no correlation between the rotation phase and either flare occurrence or energy. In studies encompassing larger samples of stars, Doyle et al. (2018) examined K2 short cadence data for 34 M dwarfs and reported no discernible correlation between rotation phase and flare rate. Expanding their investigation, Doyle et al. (2019) further analysed TESS data from sectors 1–3 for 167 M dwarfs and included 209 solar-type stars from sectors 1–13 in a subsequent study (Doyle, Ramsay, and Doyle, 2020). Yet, in both cases, no preferential rotational phase for flares was identified across the sampled stars. Additionally, Feinstein et al. (2020) conducted a recent study involving 3200 young stars observed by TESS in sectors 1–20, where they similarly found no significant correlation between flare rates and the stellar rotational phase. The lack of correlation observed in these studies is attributed to either a uniform distribution of flare-producing regions across the star or the presence of a large, asymmetric circumpolar spot (or spot groups) that remains consistently visible (Hawley et al., 2014; Davenport et al., 2014; Doyle et al., 2018; Doyle et al., 2019).

However, it is worth noting that in a study involving 119 main-sequence stars observed by Kepler, a correlation was reported between low-energy flares and active regions (Roettenbacher and Vida, 2018). These findings suggest that correlations between flares and active

regions may vary on a case-by-case basis, highlighting the need for individual investigations and analyses of specific samples.

The distribution of flare occurrence across different rotation phases for individual stars in our sample exhibits some hints of rotational phase dependency, as illustrated in panels c, e, and g of Figure B.6, B.24, B.28, and B.37. However, it should be noted that the morphological characteristics of the light curves resulting from active regions are not always consistent. Therefore, we have grouped together stars exhibiting similar light curve features to facilitate meaningful comparisons.

Following the terminology defined by Basri and Nguyen (2018), stars with active regions located relatively close to each other display a single dip (SD) in their light curves, while those with active regions situated on opposite sides of the stellar disk exhibit a double dip (DD) per rotation. We adopt this classification scheme to investigate the potential dependence of flares on the rotational phase for each group of stars.

4.8.3.1 Flare-rotational phase correlation in three double dip stars

We selected three DD stars for our study on the correlation between flare counts and rotational phase: G 173-039 (J02088+494, TIC 250602194), EV Lac (J22468+443, TIC 154101678), and G 208-042 (J19511+464, TIC 273589987). G 173-039 is an M3.5 V dwarf with a rotational velocity of $v, \sin, i = 24.1 \pm 2.4$ and a $P_{\rm rot}$ of approximately 0.75 days. It belongs to the Local Association moving group, indicating an age range of 20 to 150 million years (Cortés-Contreras, 2016). EV Lac, also an M3.5 V dwarf, is identified as a member of the Ursa Major moving group (Cortés-Contreras, 2016). With an estimated age of 300–500 Ma, it rotates at a slower rate than G 173-039, with a rotational velocity of $v, \sin, i = 3.5 \pm 1.5$ and a $P_{\rm rot}$=4.35. G 208-042, an M4.0 V star, has a rotational velocity of $v, \sin, i = 22.1 \pm 0.9$ and a period of 0.59 days. It is a member of the nearby young open cluster IC2391 (Cortés-Contreras, 2016), which is estimated to have an age of 50±5 Ma (Navascues et al. 2004).

The phase-folded light curves of these stars are shown in the top panels (a, b, c) of Figure 4.11. For G 208-042, we conducted the flare analysis using data from both sectors 14 and 15. However, for the purpose of this comparison, we specifically focused on the data from sector 14 due to the observed instability of the double dip (DD) structure in sector 15.

The range of variations in G 173-039 and EV Lac is greater, with magnitudes of 0.020% and 0.029% respectively, compared to $R_{\rm var}$=0.016% for G 208-042. Furthermore, G 173-039 and EV Lac exhibited a higher frequency of energetic flares. Therefore, we considered the bolometric energy with $\log E > 32$ erg for G 173-039 and EV Lac, and $\log E > 31$ erg for G 208-042.

To examine the range of the secondary active regions, we applied a fitting procedure to the primary modulation and subtracted it from the light curve, as demonstrated in the middle panels (d, e, f) of Figure 4.11. In the bottom panels (g, h, i), the distribution of high-energy flares with bolometric energy exceeding the indicated threshold (as shown on the plots) is illustrated, normalised by the stellar rotation period, and plotted against rotation phase bins.

A notable pattern appears in the results, indicating that the emergence of both primary and secondary active regions coincides with a lower occurrence of less energetic flares, as

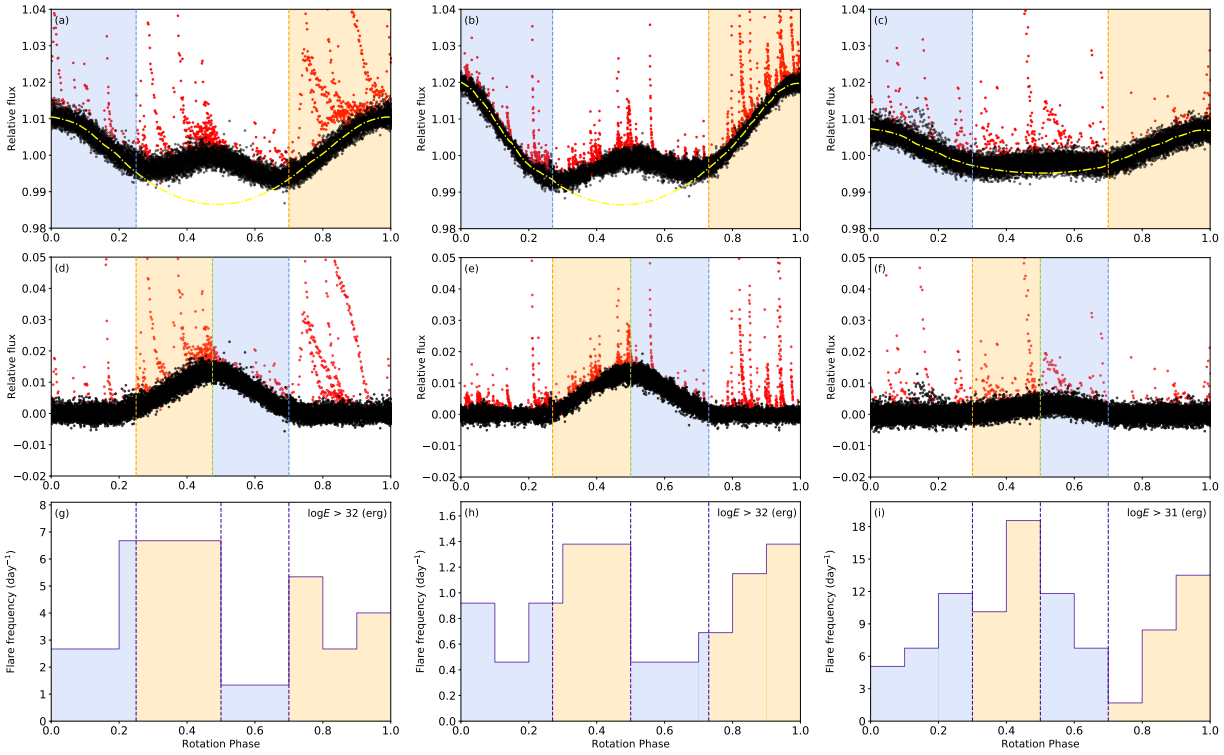

FIGURE 4.11: Phase-folded light curves of double dip stars G 173-039, EV Lac, and G 208-042 are shown in panels a, b, and c, respectively, with yellow dotted lines representing the fitted primary active regions. Panels d, e, and f display the enhanced secondary active regions obtained by subtracting the fit for the primary active regions. Flare frequency (normalised by the stellar rotation period) is plotted against the rotation phase in panels g, h, and i. Blue shading indicates fewer energetic flares as the primary and secondary active regions become visible, while orange shading represents more energetic flares as they disappear.

denoted by the blue shaded areas in the figure's panels. Conversely, the disappearance of the primary and secondary active regions corresponds to an increased number of energetic flares, as represented by the orange shaded areas.

4.8.3.2 Flare-rotational phase correlation in 12 single dip stars

To investigate the correlation between flare counts and rotational phase for SD stars, we carefully selected 12 stars with distinct SD light curves and R_{var} values greater than 0.02%. These stars, along with their Karmn, TIC designations, and references to their individual flare analysis plots, are listed in Table 4.2. The light curves of these stars were phase-folded, aligning their minima (which correspond to the highest coverage of active regions) to the phase interval of $\phi = 0.4 - 0.6$, positioned at the centre of the plot. Flares were categorised into high and low energy groups based on a cut-off of 10^{32} erg. The phase bin of each flare was determined based on its peak location.

Figure 4.12 illustrates the distribution of low-energy, high-energy, and total flares from the 12 stars across the rotational phase. An interesting observation is that the number

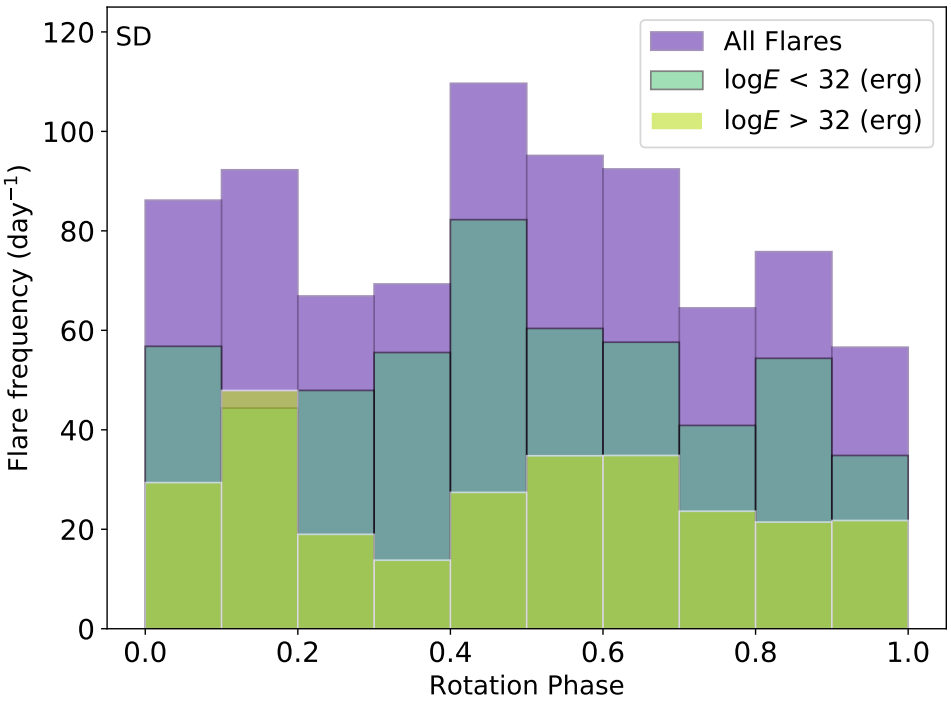

FIGURE 4.12: Flare count distribution across rotation phase for 12 stars with single dip (SD) light curves. Low-energy, high-energy, and total flare distributions are represented by distinct colours.

of low-energy flares appears to be higher in proximity to the minimum brightness phase ($\sim \phi = 0.4 - 0.5$), while high-energy flares are more prevalent during the emergence of active regions ($\sim \phi = 0.1 - 0.2$). However, the presence of any significant phase dependence does not appear statistically significant. It is important to note that the flare counts in this plot are normalised to the stellar rotation period for each star, which gives relatively more weight to the flare counts of faster rotators.

4.8.4 Longest observed target: LP 071-082

LP 071-082 (J18022+642, TIC 233068870) holds the record for the longest monitoring duration within our sample, spanning 11 months (precisely 267.47 days) of TESS observations from July 2019 to June 2020. Figure B.32 displays the light curves captured for this fully convective M5.0 V dwarf. LP 071-082 belongs to the Galactic thin disc population (Cortés-Contreras, 2016), and based on our kinematic data, it is likely a member of the Ursa Major group (Cortés-Contreras, 2016). The Ursa Major group is estimated to have an age of approximately 300–500 Ma (King et al., 2003). This rapidly rotating M dwarf exhibits a $v, \sin, i$ value of 11.3 ± 1.5 km,s^{-1} and maintains a period of 0.28 d throughout the 11-month TESS observation period. Notably, this star demonstrates a flare amplitude of approximately 1.346 in fractional flux units (peaking at BJD 2458889.22 in sector 21), representing the highest amplitude within our sample (refer to panel d, sector 21).

We have observed an intriguing phenomenon of increased brightness in LP 071-082 between two flare events occurring at BJD 2458811.5 and 2458812.2 in sector 18. This elevated

TABLE 4.2: List of 12 stars exhibiting a single dip light curve and $R_{var} > 0.02\%$

Karmn	Name	TIC	Fig.
J05019+011	1RXS J050156.7+010845	269077806	B.8
J06318+414	LP 205-044	144282456	B.13
J07446+035	YZ CMi	266744225	B.14
J07558+833	GJ 1101	289972535	B.16
J09449-123	G 161-071	289706625	B.19
J11474+667	1RXS J114728.8+664405	142878895	B.22
J13536+776	RX J1353.6	219463771	B.25
J15218+209	OT Ser	355793860	B.28
J17338+169	1RXS J173353.5+165515	400361232	B.31
J18131+260	LP 390-16	313988572	B.33
J22012+283	V374 Peg	283410775	B.37
J23548+385	RX J2354.8+3831	291689873	B.39

brightness persists for approximately 17 hours (refer to panel b, sector 18). A similar occurrence is evident between two larger flares at BJD 2458989.48 and 2458990.3 in sector 25, lasting for approximately 20 hours (panel a, sector 25).

The observed increase in stellar brightness between flare events can be attributed to the heating of the stellar corona. Flares release significant amounts of energy, with a portion of that energy being deposited in the corona. This energy input results in the heating of the coronal plasma, causing it to emit additional photons that contribute to the overall brightness of the star. This finding is consistent with the observation that the value of α, representing the slope of the power law fit to the FFD diagram, is measured as 2.02 for this specific star. α values exceeding 2 indicate a more pronounced heating of the corona during flares, which subsequently leads to an increase in stellar brightness. Hence, the observed correlation between the elevation in stellar brightness and the higher α value supports the hypothesis that the heating of the corona during flares contributes to the observed rise in brightness between these events.

4.8.5 Highest flare rate: YZ CMi

The star YZ CMi (J07446+035, TIC 266744225) exhibits the highest frequency of flares within our sample. This activity-saturated star has a spectral type of M4.5 V and a rotation period of 2.77 days. YZ CMi is a potential member of the Beta Pictoris moving group (Nakajima and Morino, 2012), estimated to have an age of 20–26 Ma (Mamajek and Bell, 2014). Flare studies on this UV Cet-type flare star date back to 1967 (Gershberg, 1972). Recently, Maehara et al. (2021) utilised simultaneous TESS photometry and OISTER spectroscopy to study and analyse flare events on YZ CMi. While Maehara et al. (2021) reported 145 flares from the TESS light curve, we identified a total of 143 flare events over 22.79 days of observations, resulting in a flare rate of approximately $\sim 6.3\ d^{-1}$. The light curve of the star is displayed in Fig. B.14.

The light curve exhibits a sinusoidal modulation, indicating the presence of a group of active regions in relatively close proximity to each other. There is a weak correlation between

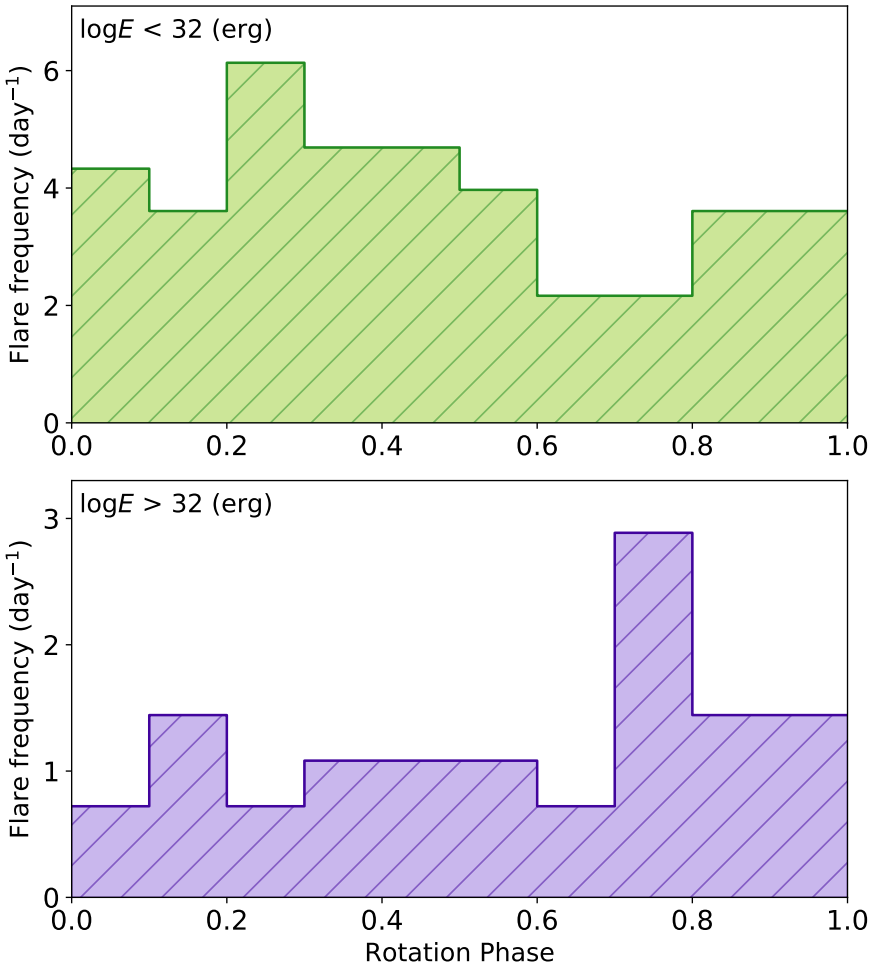

FIGURE 4.13: Frequency of flares of YZ CMi (J07446+035, TIC 266744225) with the bolometric energy lower than 10^{32} erg in the top panel and larger than 10^{32} erg in bottom panel as a function of rotation phase.

rotation phase and flare frequency and energy, as depicted in panels e and g. This suggests that flares may originate from either a single active region consistently in view (nearly pole-on) or from multiple regions distributed at different longitudes. We estimated the inclination of the star to be $i = 36^{+17}_{-14}$ degrees, providing more support for the latter scenario. Despite YZ CMi having the highest flare rate in our sample, only 24.5% of its flares have energies exceeding 10^{32} erg. The consistent flare rate over time, coupled with the lower range of flare energies, prevents the occurrence of very high-energy flares in the same region of this star. This finding confirms that the wait time between a flare and the subsequent one is proportional to the flare energy. Similar to the occurrence of earthquakes on Earth, the consistent and frequent appearance of smaller flares may lead to a delay or absence of large flares.

Considering YZ CMi's relatively stable modulation, such phenomena should be observable in the phase-fold diagram of the star when comparing the phase distribution of low- and high-energy flares. Indeed, this is confirmed by our findings displayed in Fig. 4.13, where flares are divided into two groups based on their energy levels: low-energy ($< 10^{32}$ erg) and high-energy ($> 10^{32}$ erg). Notably, the number of low-energy flares decreases in the phase

interval of $\phi = 0.6 - 0.8$, coinciding with the generation of more energetic flares in a similar phase range of $\phi = 0.7 - 0.8$.

Furthermore, the consistent flare rate observed throughout the phase is indicative of the presence of an asymmetric polar spot, or possibly a group of spots, covering a substantial portion of the pole. This finding aligns with the conclusions of Morin et al. (2008), who employed Zeeman-Doppler imaging to study similar phenomena, as well as the simulations conducted by Baroch et al. (2020).

4.8.6 Longest flare duration and highest flare energy: 1RXS J114728.8+664405

The longest flare was observed in 1RXS J114728.8+664405 (J11474+667, TIC 142878895), an M5.0 V dwarf with the period of 13.35 d that belongs to the Castor Moving Group (Cortés-Contreras, 2016) with an age estimate of ~ 200 Ma (Caballero, 2010). TESS observed this star at sectors 14, 15, and 21. The light curve of the star is shown in Fig. B.22. This complex flare peaked at BJD 2458694.699 in sector 14, lasted for 23 hours, reached an amplitude of 0.495 in fractional flux units, and released energy equal to 3.8×10^{34} erg, which is also the highest flare energy in our sample. The morphology of the flare is shown in Fig. 4.14. A second energetic flare was peaked at a similar phase after two rotations at BJD 2458721.525 in sector 15. The second flare reached a higher amplitude of 0.6559 but lasted only for 4.3 hours and emitted an energy of 7.7×10^{33} erg.

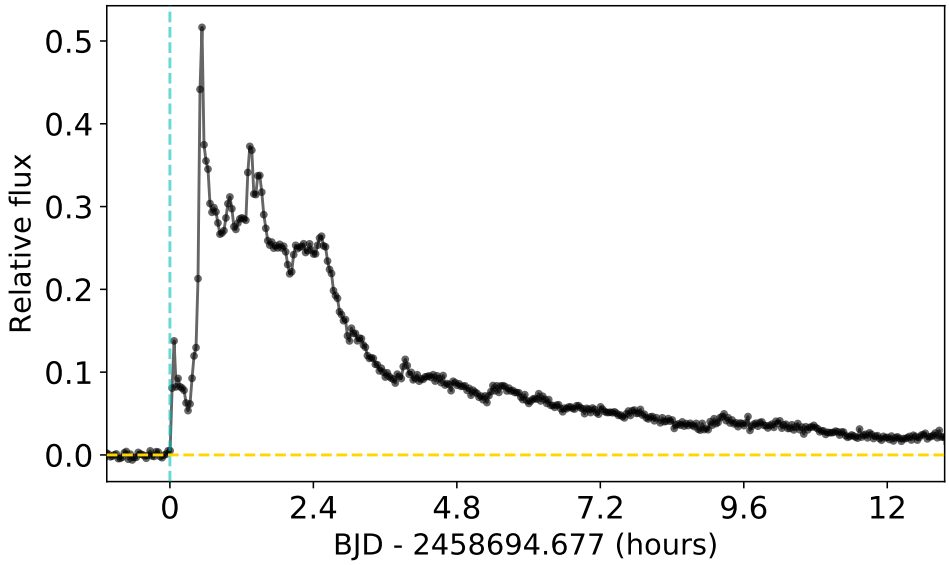

FIGURE 4.14: The morphology of the longest flare in our sample, belonging to 1RXS J114728.8+664405 (J11474+667, TIC 142878895). This complex flare lasted for 23 hours, emitted an energy of 3.8×10^{34} erg, and reached an amplitude of $\sim 50\%$. For visual clarity, we do not show the full duration of the flare.

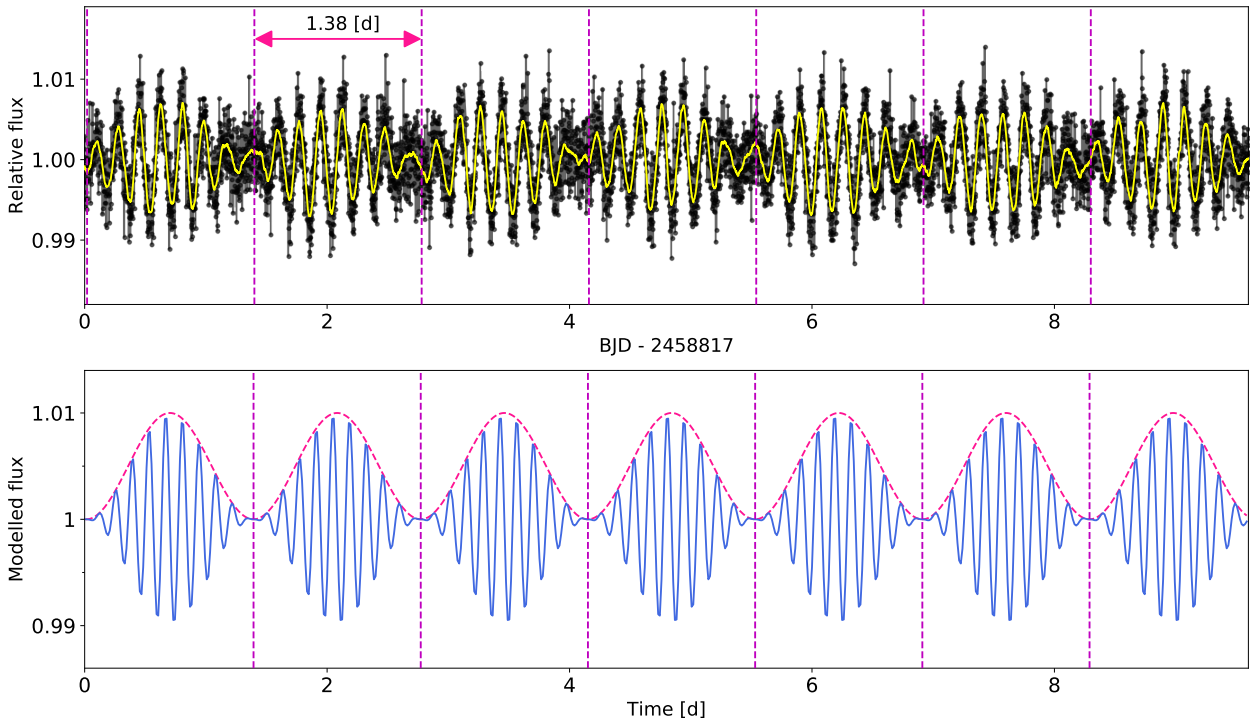

FIGURE 4.15: The top panel shows the TESS light curve of LP 022-420 (J15499+796, TIC 159398282) from sector 19, together with a version of the same curve from which the flares were removed, and which has been smoothed by applying a SavGol filter. The bottom panel shows the modelled light curve consisting of two sinusoidal functions (with 0.188 and 1.38 d periods) multiplied together.

4.8.7 The case of LP 022-420

LP 022-420 (J15499+796, TIC 159398282) is a rapidly rotating ($v \sin i = 26.9 \pm 2.7$ km s^{-1}) M5.0 V star of brightness $J = 9.721 \pm 0.021$ mag (Skrutskie et al., 2006), Gaia DR2 $G_{\rm RP}$ of 11.700 ± 0.0021 mag (Gaia Collaboration et al., 2018b). With an emission index of $\log \mathrm{H}\alpha / L_{\rm bol} = -3.81$, this star displays significant activity and is considered one of the most active stars in our sample. LP 022-420 is a remarkably young star. Its classification as either a young disc star or a member of the Local Association suggests that its age falls within the range of 20 to 150 Ma (Cortes-Contreras et al., 2016). TESS observed it in sectors 14, 15, 19, 20, 21, 25, and 26 over a period of one year. Figures B.29 show the light curve of the star, and the TPFs are shown in Fig. B.1. There is only one other source in the TPF of this star, with a G-band flux less than 0.5% that of LP 022-420 (see Table B.1). The GLS periodogram analysis reveals a significant peak at 0.188 ± 0.000010 d, consistently observed throughout all seven sectors of data. The star's light curve exhibits a secondary modulation with a period of ∼ 1.35 d. This secondary modulation can be attributed to a second group of active regions, characterised by a different pattern of differential rotation that amplifies or reduces the impact of the primary group of active regions.An alternative explanation, taking into account the stellar inclination of approximately $i \sim 21^\circ \pm 2$, is that the star is nearly pole-on in its orientation. This alignment results in the periodic emergence of the second group of active regions into our line of sight, occurring at approximately

intervals of $\sim$ 1.38 days. The observed secondary modulation in the light curve can be attributed to this phenomenon, where the varying visibility of the active regions produces the observed periodic pattern. To gain deeper insights into the surface inhomogeneities of LP 022-420, a comprehensive analysis that incorporates detailed modelling of the active regions is crucial. Advanced modelling tools, such as `StarSim` (Rosich et al., 2020), can be employed to reconstruct the configuration of active regions through the integration of various data sources. These include photometric and radial velocity (RV) data, as well as the incorporation of multi-band photometric observations. However, performing such an in-depth analysis is beyond the scope of the current work.

As a simpler approach, we could retrieve the light curve of LP 022-420 by employing a simple model. This model involves multiplying two sinusoidal functions with periods of 0.188 and 1.35 days, respectively. The upper panel in Figure 4.15 depicts a segment of the stellar light curve, displaying both the original data and a smoothed version obtained by applying a SavGol filter. The lower panel of the figure showcases the simulated light curve that was obtained from our simple model. This simplified approach suggests an alternative scenario that offers a potential explanation for the observed photometric variations within the TESS data.

Using the product-to-sum formula in trigonometry, we know that the multiplication of two sinusoidal signals can be expressed as a combination of cosine values, equal to half the difference between the cosine of the signal difference and the cosine of the signal sum. This suggests a plausible scenario: the observed variations could originate from two periods associated with two spotted stars in a binary system.

Supporting this hypothesis, a study by Schweitzer et al. (2019) utilised CARMENES data to determine the radii and masses of stars in this survey. Their analysis, incorporating effective temperatures ($T_{\rm eff}$) from spectral analysis and luminosities derived from integrated broadband photometry and *Gaia* DR2 parallaxes, generated a Hertzsprung-Russell diagram for CARMENES stars. In this diagram, LP 022-420 stood out as an outlier located above the average Schweitzer et al. (see Figure 10 in 2019). In that study, the elevated luminosity observed in LP 022-420 was attributed to the age of the star. However, it is important to consider that this discrepancy in luminosity could also be attributed to LP 022-420 being a binary system.

Further evidence supporting the binary system hypothesis comes from astrometric observations, specifically the Renormalized Unit Weight Error (RUWE) value provided by *Gaia* for its observed sources. The RUWE, expected to be around 1.0 for single-star models that fit well with astrometric observations, may exceed 1.4 for non-single or problematic sources. In the case of LP 022-420 (Gaia DR2 1708693055848054912), its RUWE value is recorded as 9.44, significantly exceeding the value typically associated with resolved double stars. This substantial deviation from the expected RUWE range further supports the idea that LP 022-420 is a binary system rather than a single star.

4.9 Discussion and future work

We conducted a comprehensive analysis of flaring activity in a sample of 38 active M dwarfs observed by TESS during its primary mission. Our analysis involved determining 11 new rotation periods and confirming the existing rotation periods (P_{rot}) for the remaining 27

stars using the TESS light curves. Within this sample, we identified and carefully analysed a total of 2,434 flares.

To compare flare activity across the stars, we employed flare frequency distribution (FFD) diagrams. Utilising FFD, we estimated the flare energies at a specific rate of 0.1 per day and discovered a noteworthy correlation between the flare energies and stellar mass. The most energetic flares were found to be produced by stars located at the boundary where complete convection occurs (around 0.35 solar masses). Moreover, the correlation between flare rates at an energy of 10^{32} erg and the normalised Hα luminosity exhibited a clear distinction between stars with masses above and below 0.35 solar masses. Interestingly, within both mass groups, the stars with the highest flare rates also displayed the highest Hα emission.

An additional intriguing finding was the correlation between flare rates and the rotational phase. Among the stars in our sample, three with double-dip light curves demonstrated a similar pattern in their flare frequency. Specifically, it appears that the emergence of both primary and secondary active regions coincided with a lower occurrence of energetic flares, while the disappearance of these active regions corresponded to an increased number of energetic flares.

Within our sample, we identified five stars that are likely associated with a significant number of microflares, which may contribute to coronal heating. The selection of these targets was based on their α values, which represent the slope of the power law fitted to the flare frequency distributions (FFDs). In one case the increase in the brightness of the photometric light curve between the flare events provided extra evidence for coronal heating. In one particular case, the noticeable increase in brightness observed in the photometric light curve between the flare events provided additional supporting evidence for the occurrence of coronal heating.

Additionally, within our sample, we investigated the potential binary status of LP 022-420, an active M5.0 V star displaying significant activity, as indicated by its emission index. The light curve of the star exhibits a dominant periodicity with a period of 0.188 days and a secondary modulation with a period of approximately 1.35 days. To provide a potential explanation for the observed photometric variations, we employed a simplified model to analyse the light curve. Our investigations strongly suggest that LP 022-420 is likely a binary system, supported by multiple lines of evidence. These include the secondary modulation observed in the light curve, the anomalous luminosity of the star in the Hertzsprung-Russell diagram, and the elevated Renormalized Unit Weight Error (RUWE) value. Collectively, these indications provide compelling evidence for the binary nature of LP 022-420.

To further improve this study in future research, several steps can be taken. Firstly, it is crucial to address the assumption of 9000$\pm$500 K black-body radiation for flares, as this approximation primarily holds for very strong flares. Investigating this bias in more detail and developing a more accurate model for estimating flare energy should be a priority. By refining the estimation methodology, a better understanding of the true energy release during flares can be achieved.

Moreover, the extended mission of TESS provides an excellent opportunity to gather additional data, enabling us to further investigate the changes in flare rates, rotation periods, and the characteristics of modulations caused by active regions in these young and active stars. This extended data will offer a deeper understanding of the long-term behaviour of surface magnetic activity in partly- and fully-convective M dwarfs.

In addition, conducting complementary spectroscopic observations of these stars in the future will help address the remaining questions and uncertainties that have emerged from this study. By combining photometric and spectroscopic data, a more comprehensive analysis can be performed, providing valuable insights into the physical processes underlying stellar activity.

By incorporating these advancements, future research can enhance our understanding of flare energetics, long-term magnetic activity, and the overall behaviour of M dwarfs. This knowledge will contribute to our broader understanding of stellar astrophysics and the impact of stellar activity on exoplanetary environments.

Chapter 5

The case of V388 Cas

Details of authorship: *This chapter will be submitted to the A&A journal. I am the lead author of this paper and have conducted the scientific research, performed calculations, analysis, and interpretation of the results. The section involving* `StarSim` *was a collaborative effort with David Baroch. I have personally written the text and created the figures presented in this work.*

5.1 Motivation

V388 Cas is a fast-rotating, presumed fully convective M5.0 V dwarf that exhibits significant wavelength dependency in its RV measurements. We have found that this star is a suitable candidate for conducting a comprehensive modelling of its spot configuration, serving as an observable proxy for the stellar magnetic field. This investigation forms an integral part of our ongoing research into the impact of active regions on order-wise RV variations. In order to achieve this, we utilised contemporaneous CARMENES RV data alongside TESS observations to input into the inverse method of the modelling tool, `StarSim`, allowing us to reconstruct the stellar photosphere of the star and determine the potential positions of its active regions. Subsequently, employing the `StarSim` forward model, we simulated RV variations based on a generated active region map within wavelength ranges specifically tailored to align with the CARMENES visual channel's échelle orders. This facilitated a meaningful comparison between the actual and synthetic RV variations. The data we utilised for the in-depth modelling was obtained in November 2019; however, TESS subsequently revisited this target on two occasions. The first revisit occurred after a span of 5 months in April-May 2020, followed by the second visit during the extension program after 2 years and 6 months in November 2022. Notably, the photometric light curve of the star exhibits subtle changes and evolves over this period. Consequently, we measured the range of variation in the photometric light curve and investigated the occurrence rate of flares to explore the relationship between these two indicators of activity for this particular target. Additionally, during one of the CARMENES observations, we serendipitously captured a coronal mass ejection (CME) event that caused blue asymmetry in chromospheric lines. Recognizing this opportunity, we conducted a thorough investigation of this event.

5.2 Context

Late M dwarfs, a subset of M-type stars, have garnered substantial attention in recent years due to their intriguing properties and potential implications for exoplanet habitability. These stars, with masses below $\sim 0.35\ M_\odot$ and spectral types M4.0 V and beyond, are characterised by their fully convective internal structures and distinct magnetic field generation mechanisms that set them apart from earlier M dwarf counterparts. Investigating the internal dynamo processes and activity phenomena in late M dwarfs is of utmost importance for advancing our understanding of stellar physics and its implications on exoplanetary habitability.

One prominent manifestation of stellar magnetic activity is the emergence of photospheric features, including dark spots and bright faculae, which are collectively referred to as active regions. Fast-rotating late-type stars often exhibit long-lasting spot groups that persist on the stellar surface for multiple rotations (Barnes et al., 2001). These persistent features introduce signals associated with the rotation period, posing challenges for precise exoplanet detection (Benedict et al., 1993). Numerous studies have addressed the issue of controversial exoplanet detections arising from stellar intrinsic jitter or spurious signals present in RV curves due to data treatment (see, for instance, Robertson et al., 2014; Robertson, Roy, and Mahadevan, 2015; Sarkis et al., 2018). This underscores the inherent complexity in disentangling genuine exoplanet signals from stellar jitter, even with the utilisation of stellar activity indices derived from spectroscopic data.

One promising approach to mitigate and correct for the impact of stellar activity on RV variations involves precise modelling of spot properties. Previous studies have demonstrated that RV variability induced by active regions exhibits wavelength dependence due to the reduced flux contrast of cold spots and hot faculae in the infrared range (Desort et al., 2007; Reiners et al., 2010; Andersen and Korhonen, 2015). However, the true nature of the situation may be significantly more complex, primarily because spectral lines formed at different atmospheric heights exhibit varying levels of temperature sensitivity (Afram and Berdyugina, 2019). Consequently, certain lines prove to be more effective in probing the temperature contrast between cool spots and the hotter photosphere, resulting in larger RV variations. Numerous efforts have been undertaken to classify spectral lines based on their responsiveness to stellar activity in bright solar-type stars, aiming to exclusively utilise less sensitive lines for precise measurements of RV variations. This approach has demonstrated success in mitigating the stellar activity signal of αCen B by a factor of two (Dumusque, 2018; Cretignier et al., 2020). Unfortunately, the line-by-line selection method faces challenges when applied to M dwarfs. A significant complication arises from the fact that the spectra of cool stars consist of a dense multitude of spectral lines, which are further complicated by the blending of atomic lines with molecular bands. Consequently, identifying individual absorption lines becomes exceedingly difficult. Additionally, the inherent faintness of M dwarfs amplifies the impact of photon noise, making the measurement of RVs for selected individual lines impractical using the line selection technique.

The CARMENES survey employs the `serval` pipeline for the measurement of high-precision RVs from the obtained spectra (Zechmeister et al., 2018). This algorithm utilises a least-squares fitting approach, comparing the spectra against a high signal-to-noise ratio (SNR) template that is generated by co-adding all available spectra of the target (Anglada-Escudé and Butler, 2012). By applying `serval`, RVs are derived for each échelle order of

the spectrograph, enabling further analysis of the contributions of specific spectral sections to the overall averaged RV measurements. One of the valuable by-products of measuring radial velocity per order is the activity indicator known as the chromatic index (CRX), which quantifies the wavelength dependence of RV variations (Zechmeister et al., 2018). However, as demonstrated in Chapter 3, the effectiveness of CRX can be compromised or result in inaccurate outcomes due to the influence of external sources of noise, such as telluric contaminations. In this study, our aim is to investigate the isolated effect of active regions on order-by-order radial velocity variations using synthetic spectra. To ensure a meaningful comparison with real observations, it is crucial to generate a spot map that closely resembles the inhomogeneities present on the stellar photosphere. To accomplish this, we employ the inverse model of the sophisticated model, `StarSim`, to reconstruct a detailed map of the star's spotted surface. Breaking the degeneracy of the inverse model requires simultaneous light and radial velocity curves. Subsequently, we demonstrate the discrepancies between the RV values obtained from a reconstructed spot map of the star and synthetic spectra, as generated by the forward model of `StarSim`, and the corresponding observations for each échelle order.

Flares are another manifestations of magnetic activity frequently observed in low-mass stars with outer convective zones. These events, driven by magnetic reconnection, occur in a stochastic manner. When a magnetic reconnection event takes place in the upper atmosphere, a stream of charged particles is generated, tracing the magnetic field lines and penetrating into the chromosphere and photosphere (Benz and Güdel, 2010). During flare events, X-ray emissions are generated in the chromosphere. Additionally, there can be upward flows of chromospheric material as heated material rises into the upper atmosphere. This phenomenon is commonly known as chromospheric evaporation (Fisher, Canfield, and McClymont, 1985; Abbett and Hawley, 1999). In the photosphere, the collision of charged particles initiates a rapid heating process, causing an increase in brightness in the affected region, which is known as the impulsive phase. Following the subsiding of electron bombardment, the brightness undergoes an exponential decay back to pre-flare levels, referred to as the decay phase (Segura et al., 2010). The duration of the decay phase can vary from minutes to hours and, in extremely rare cases, even extend to days (Osten et al., 2016). In spectral observations, flares are commonly recognised through the enhancement of chromospheric lines, particularly the Balmer lines. Furthermore, as a response to a flare, chromospheric line profiles can undergo broadening and exhibit both red and blue asymmetries (Fuhrmeister et al., 2008; Fuhrmeister et al., 2018). In the case of the Sun, reconnection events typically occur in close proximity to a pair of sunspots or within a cluster of spots. As a result, during the peak of the solar activity cycle when the number and complexity of sunspots rise, the likelihood of flare activity also increases.

Space-based exoplanet transit missions, such as Kepler (Borucki et al., 2010) and TESS (Ricker et al., 2015), have provided a revolutionary data set for statistical studies of flare stars, particularly for low-mass stars. Such missions are well-suited for large-scale studies of flares, as they provide high-precision, continuous light curves that span from months to years. The unique and expansive datasets obtained not only enable comprehensive studies on flares but also facilitate explorations into the long-term variability exhibited by interesting targets. A notable example is the comprehensive analysis conducted by Davenport, Mendoza, and Hawley (2020), who leveraged over 10 years of data from Kepler and TESS to investigate the evolution of flares and starspots in GJ 1243. The objective of this study was to unravel

the evolution of the star's activity over the course of several years. Despite the absence of discernible solar-like activity cycles in this particularly active M4.0 V star, the research underscores the exceptional capabilities of instruments like Kepler and TESS. These missions enable the utilisation of flare rates as a means to detect activity cycles spanning numerous years into the future.

The largest and most long-lasting solar flares are often accompanied by coronal mass ejections (CMEs). These ejections can reach velocities ranging from 60 to 3200 $\mathrm{km\,s^{-1}}$, carrying masses on the order of 10^{12} kg (Benz and Güdel, 2010). It is plausible that a similar association between flares and CMEs exists in other stars as well (Yashiro et al., 2006). Understanding the frequency and estimating the energy released by CMEs is crucial, as they can significantly impact the atmospheres of exoplanets. If these events occur frequently and possess sufficient energy, they can continuously modify planetary atmospheres, which is unfavourable for supporting life (see Vida et al., 2017, and references therein). However, detecting CMEs on other stars is challenging, unlike on our Sun where they are relatively easier to observe, especially if they directly affect Earth. So far, no conclusive identification of CMEs has been made on other stars (Vida et al., 2019a; Leitzinger et al., 2020).

One method of detecting CMEs on other stars involves observing their Doppler signature, primarily observed in Balmer lines. The ejected material manifests as a blue-wing enhancement of the chromospheric lines. In the case of faster events, a distinct emission bump (or absorption, if observed against the stellar background) may be observed (see, e.g. Flores Soriano and Strassmeier, 2017).

The majority of CME detections reported in the literature are isolated events discovered serendipitously, limiting their suitability for statistical analysis. Nevertheless, there are notable examples worth mentioning. For instance, one of the fastest recorded events occurred on AD Leo, reaching a maximum projected velocity of approximately 5800 $\mathrm{km\,s^{-1}}$(Houdebine, Foing, and Rodono, 1990). In a separate study, Vida et al. (2016) conducted a comprehensive analysis of a complex CME event on V374 Peg. They successfully identified an eruption that exceeded the escape velocity with a maximum projected speed. Additionally, efforts have been made to search for CME events using archival data. Vida et al. (2019b) conducted an investigation involving over 5500 spectra extracted from archival spectral data. Their focus was on identifying asymmetric features in Balmer lines, which serve as a signature of ejected material. Through their analysis, they successfully identified 478 events exhibiting line asymmetries, including nine larger-scale events in terms of velocity and mass, observed across 25 objects. The statistical analysis of these events suggests a higher frequency of CME occurrence in cooler stars with stronger chromospheric activity.

In this chapter, we delve into the study of V388 Cassiopeia, a UV Cet-type flare star located at a distance of approximately 10 pc from the Sun. Our objective is to gain a comprehensive understanding of the star's magnetic activity and its manifestations through a thorough analysis of available data from various perspectives. The observational details and data reduction procedures are explained in Section 5.3. In Section 5.4, we provide an introduction to the star itself. Section 5.5 encompasses the results of our multi-aspect analyses. Here, we expound upon the intricacies of reconstructing surface inhomogeneities through simulations in Subsection 5.5.1. Additionally, we present the analysis of a series of flare events observed by TESS in Subsection 5.5.2, as well as an investigation of a CME event using spectroscopic observations from CARMENES in Subsection 5.5.5. Lastly, in Section 5.6, we present a discussion and summary of our results.

5.3 Observations and data reduction

In this section, we provide a detailed description of the instruments and data reduction methods used in this study. We first present the CARMENES spectroscopic data and then the TESS photometric data.

5.3.1 CARMENES spectroscopy

V388 Cassiopeiae, also known as GJ 51, was one of the 345 stars originally chosen to be monitored in the CARMENES Guaranteed Time Observation program, which seeks to identify exoplanets orbiting M dwarfs. The first set of observations were carried out between August 21, 2016 and March 9, 2017, and based on its classification as an active RV loud target (std(RV) > 10 ms^{-1} and $v \sin i > 2$kms^{-1}), the RV modulation of V388 Cas was attributed to stellar activity (further details can be found in Chapter 3 or Tal-Or et al., 2018). Additionally, RV values for V388 Cas showed a significant correlation with the chromatic index, indicating that the RV variations were likely caused by active regions, such as dark spots and/or bright faculae, on the star's surface. As a result, we expected to observe significant rotation modulation in the star's photometric light curve. Given that V388 Cas was scheduled to be observed with TESS, we decided to collect additional RV measurements using the CARMENES spectrograph concurrently with TESS's first observation of the target in Sector 18. These new RV data would enable us to create a more accurate spot map of the star and simulate the effect of stellar activity on RV measurements (details are provided in Subsection 5.5.1). To this end, a second round of CARMENES observations of V388 Cas was conducted from November 4 to December 16, 2019. During this period, we obtained 14 exposures, 7 of which were conducted simultaneously with TESS photometry.

To process the spectra, we utilised the `caracal` pipeline, which applies flat-relative optimal extraction (Zechmeister, Anglada-Escudé, and Reiners, 2014). In addition, the Template Division Telluric Modelling (TDTM) technique was applied to clean all spectra from telluric contamination (Nagel, 2019). The radial velocities of the spectra were derived using the `serval` (SpEctrum Radial Velocity AnaLyser; Zechmeister et al., 2018) pipeline. Prior to deriving RVs, each spectrum was corrected for barycentric motion (Wright and Eastman, 2014), secular acceleration (Zechmeister, Kürster, and Endl, 2009), and instrumental drift. The corrected spectra were then co-added to construct a high signal-to-noise ratio (S/N) template spectrum for each target star. Finally, the RVs of each individual spectrum were

Table 5.1: Summary of the spectroscopic data for V388 Cas

Instrument	CARMENES VIS		CARMENES NIR	
$\Delta\lambda$ (nm)	520–960		960–1710	
R	94 600		80 400	
Subset	VIS1	VIS2	NIR1	NIR2
# of spectra	12	14	9	13
std(RV) [m s^{-1}]	202.59 ± 41.35	206.00 ± 38.93	251.97 ± 59.39	153.00 ± 30.01
$\overline{\delta \mathrm{RV}}$ [m s^{-1}]	17.47	17.91	28.59	30.23
Start date	Aug 2016	Nov 2019	Aug 2016	Nov 2019
End date	Mar 2017	Dec 2019	Mar 2017	Dec 2019

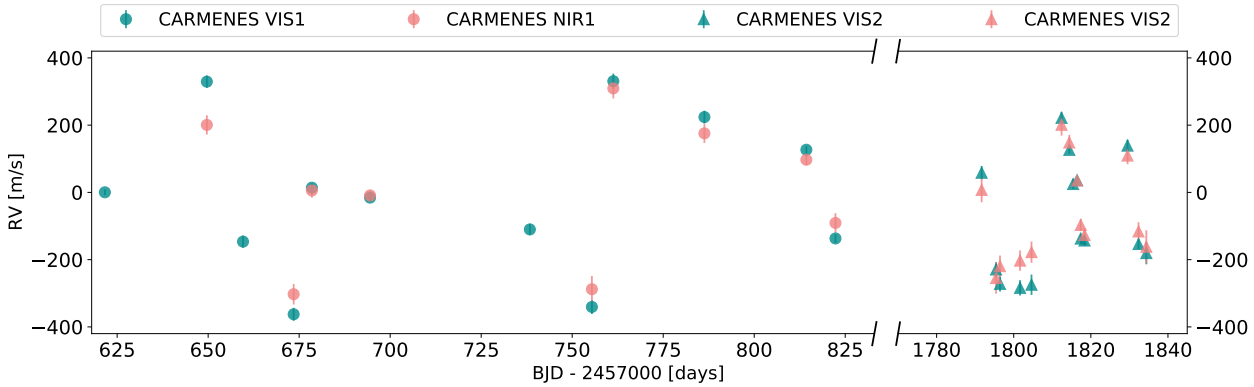

FIGURE 5.1: Time series of RVs for the CARMENES VIS and NIR data. The first observation set spans over 7 months, while the second set covers a period of one month. The time axis is interrupted for a gap of 2 years and 8 months between the two sets of observations.

calculated through least-squares fitting against the template spectrum. We applied nightly zero-points correction to the final RVs (Tal-Or et al., 2019).

The instrument specifications for CARMENES' visual (VIS) and near-infrared (NIR) channels, along with information on the number of observations, the standard deviation of radial velocities (std(RV)), and median radial velocity uncertainties ($\overline{\delta \mathrm{RV}}$) for each observation subset, are provided in Table 5.1. Figure 5.1 displays the RV time series for the VIS and NIR channels, and the data are presented in Table C.1.

5.3.2 TESS photometry

The star V388 Cas was observed in three of the TESS sectors: Sector 18 (Camera #2, CCD #2; 3 November 2019 to 27 November 2019), Sector 24 (Camera #4, CCD #4; 16 April 2020 to 12 May 2020), and Sector 58 (Camera #2, CCD #2; 29 October 2022 to 26 November 2022). While sectors 18 and 24 only have 2-minute integrations available, sector 58 provides both 20-second and 2-minute cadence modes. We obtained calibrated short-cadence data from the Mikulski Archive for Space Telescopes [1] (MAST) website. We used data from Sector 18, which overlaps with part of the radial velocity data from CARMENES, to simulate the surface features of the star (see Section 5.5.1 for details). Data from Sectors 24 and 58 were used to verify the stability of the stellar rotation period over time (see Figure 5.4), as well as to study the evolution of flares on the star (see Section 5.5.2).

We evaluated the light curves of each sector by comparing two methods: Simple Aperture Photometry (SAP; Twicken et al., 2010; Morris et al., 2017) and Pre-search Data Conditioning (PDC; Smith et al., 2012; Stumpe et al., 2012; Stumpe et al., 2014). We chose light curves that exhibited minimal influence from systematics and trends while preserving the astrophysical signatures. Figure 5.2 illustrates the TESS light curves for three sectors, with sector 18 including timestamps indicating the dates of CARMENES observations.

During the initial stages of Sector 18, the spacecraft passed through the Earth's shadow, leading to the temporary shutdown of the instrument. This eclipse period, which lasted from BJD = 2458791.11 to BJD = 2458791.37, resulted in a gap in the data. The thermal

[1] https://mast.stsci.edu/portal/Mashup/Clients/Mast/Portal.html

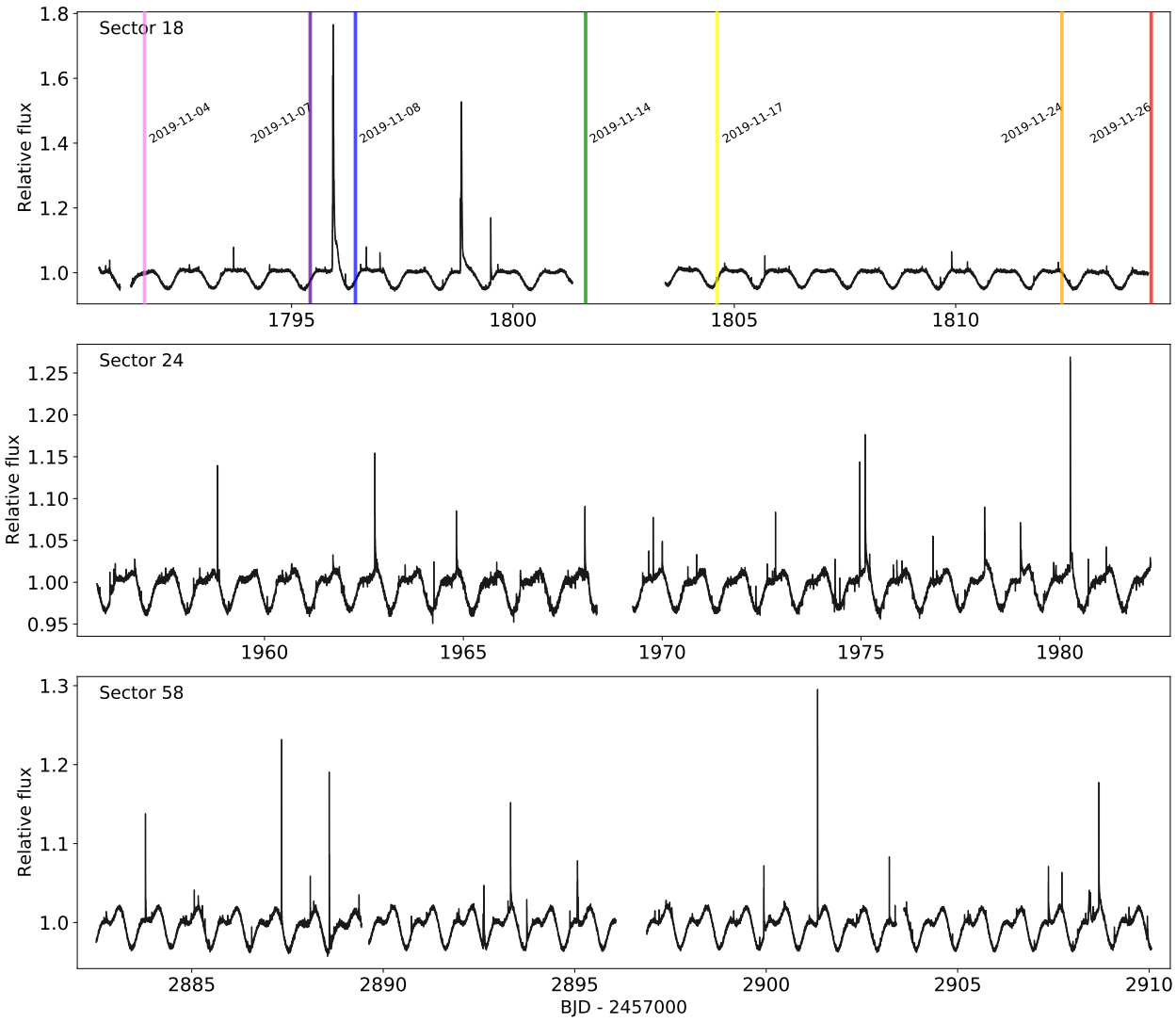

FIGURE 5.2: TESS light curves of V388 Cas in sectors 18, 24, and 58, spanning November 2019, April-May 2020, and November 2022, respectively. The light curve of sector 18 includes timestamps for CARMENES observations. Over the course of three years, subtle changes in the star's light curve reveal the evolution of active regions on its photosphere.

variations experienced by the spacecraft during this interval caused noticeable trends in the raw photometry and SAP data. However, when considering the time of CARMENES observation, the data stability improved sufficiently to be included in our analysis.

5.3.2.1 Flux contamination possibility

TESS has an exceptionally large pixel size of $21'' \, \mathrm{px}^{-1}$, which can result in contamination flux from nearby stars. The contamination flux occurs when the light from neighbouring stars falls within the same pixel as the target star, resulting in a mixed or blended signal in the observations. Such contamination can have several significant implications. Firstly, it can lead to the dilution of the true stellar flux, causing the underestimation of flare energies

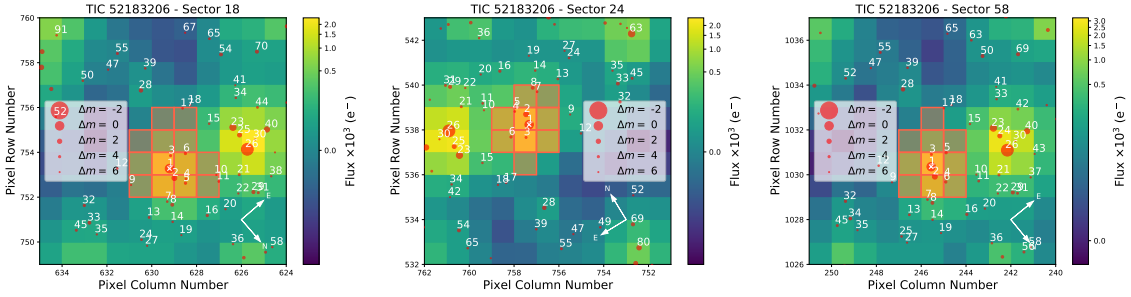

FIGURE 5.3: TESS Target Pixel File (TPF) of V388 Cas, showcasing the fixed aperture mask represented by red-shaded blocks. The position of V388 Cas is denoted by a red circle with a white cross at its centre. Nearby stars, with a maximum magnitude contrast of 6 from the *Gaia* DR2 catalogue, are superimposed on the plot, with circle sizes indicating the magnitude contrast.

and hindering the detection of low-energy flares. Additionally, the presence of contamination introduces the possibility of misattributing variability to an incorrect source or erroneously identifying flares that actually originate from nearby stars. Therefore, it is crucial to address and account for contamination effects when analysing TESS data to ensure accurate and reliable results.

We obtained the TESS target pixel file (TPF) from MAST and determined the stellar positions in the area using the *Gaia* DR2 catalogue (Gaia Collaboration et al., 2018b). Figure 5.3 displays the TPFs created with `tpfplotter` [2], with V388 Cas (marked as number 1) indicated by a red circle with a white cross within the aperture mask. The field surrounding V388 Cas is densely populated, as evident in the figure, with six neighbouring stars located within the aperture mask. Consequently, the flux of V388 Cas (*Gaia* DR2 5228642720376535 04, $G_{\rm RP}$ magnitude of 10.603) is contaminated by the nearby stars, which can present some obstacles in our data analysis. Notably, within the same or adjacent pixel of our target, two nearby stars with relatively low magnitudes (star number 2: *Gaia* DR2 5228642720376517 12, $G_{\rm RP}$ magnitude 12.612; star number 3: *Gaia* DR2 5228642720376559 36, $G_{\rm RP}$ magnitude 15.334) pose potential challenges.

To ensure that the observed variability in our target is not caused by neighbouring stars, we conducted several tests. Firstly, we constructed a Hertzsprung–Russell diagram (HRD) by calculating the absolute *Gaia* G-band magnitude (M_G) for the targets within the TESS aperture mask. This was achieved using trigonometric parallax (ϖ), along with the G, $G_{\rm BP}$, and $G_{\rm RP}$ broad-band magnitudes provided by *Gaia* DR2. Figure C.1 illustrates the overlaid positions of these targets on the background stars in the *Gaia* HRD, (adopted from Figure 5 of Gaia Collaboration et al., 2018a).

To assess variability, we calculated the standard deviation of the blue and red magnitudes (BP and RP) by multiplying their mean error by the square root of the number of observations contributing to their determination. By analysing the values of std(BP) and std(RP) in conjunction with the positions of these targets in the *Gaia* HR diagram, we concluded that none of them exhibited variability. Table C.2 lists the astrometric parameters (coordinates and parallax) and photometric parameters (G, $G_{\rm BP}$, and $G_{\rm RP}$) of targets within the TESS aperture mask, including our calculated values of M_G, std(BP), and std(RP).

[2] https://github.com/jlillo/tpfplotter

As a second test to pinpoint the origin of the observed variability in V388 Cas, we employed the open-source Python package `TESS_localize`[3], developed by Higgins and Bell (2023). The analysis involved providing a list of frequencies obtained from periodogram analysis of V388 Cas light curves, including its rotation frequency and harmonics, along with the TPF data to `TESS_localize`. The software autonomously determined the optimal number of principal components to remove from the light curve, effectively eliminating systematic trends. Subsequently, `TESS_localize` accurately localised the variation to a resolution better than one-fifth of a pixel. For a more comprehensive understanding of the software's methodology, please refer to Higgins and Bell (2023). Under the assumption that nearby stars do not exhibit variability at the same frequencies as V388 Cas, `TESS_localize` verified that the observed variability predominantly originates from V388 Cas itself.

5.4 Stellar parameters

V388 Cas is a UV Cet-type flare star, as reported by Gershberg et al. (1999), located at a distance of slightly less than 10 parsecs from the Sun. It is considered a relatively bright M dwarf, with a magnitude of ≈ 8.6 mag. Table 5.2 presents the stellar properties of V388 Cas, including equatorial coordinates, proper motions, and parallax obtained from the *Gaia* Early Data Release 3 (EDR3; Gaia Collaboration et al., 2021).

The stellar atmospheric parameters (i.e. effective temperature, surface gravity, and metallicity) were derived using the spectral synthesis technique following Marfil et al. (2021), which employs Bayesian spectral synthesis and an MCMC approach. The analysis used the BT-Settl model atmospheres and the radiative transfer code turbospectrum to generate a grid of synthetic spectra for a set of carefully selected magnetically insensitive spectral lines and molecular bands. The procedure is described in detail in Marfil et al. (2021). The final results are in good agreement with the previously reported values by Passegger et al. (2019), with the exception of the [Fe/H] value. As a precautionary measure, we selected a PHOENIX model spectrum (Husser et al., 2013) with $T_{\rm eff} = 3000 \pm 50$, $\log g = 5.020 \pm 0.046$, and solar metallicity as our template for modelling the stellar photosphere (refer to Section 5.5.1 for details on the modelling).

To estimate the radius and mass of the stars, we used the effective temperature of 3000 K and the bolometric luminosity estimated by Cifuentes et al. (2020). The stellar radius was derived using the Stefan-Boltzmann law, $L = 4\pi R^2 \sigma T_{\rm eff}^4$, and propagating the uncertainties in L and $T_{\rm eff}$. The stellar mass was calculated using the radius-mass relation of Schweitzer et al. (2019). Our results are consistent with those reported by Cifuentes et al. (2020). Further details on the methodology can be found in the cited references.

A rotation period of 1.0219 d was reported for V388 Cas by Díez Alonso et al. (2019) based on photometric time series from MEarth data taken in 2011 (Charbonneau et al., 2009; Irwin et al., 2011). To obtain a more recent estimation, we searched for periodic signals in the TESS data using the generalised Lomb-Scargle periodogram (GLS; Zechmeister and Kürster, 2009). Fig. 5.4 displays the resulting power spectrum of TESS data for each sector, as well as the combined sectors. The periodograms are zoomed in around the signal of interest, i.e. the star's rotation period, to reveal nuanced differences between the derived signal for each sector and the combined data, enabling a comprehensive analysis. The highest peaks in the

[3] https://github.com/Higgins00/TESS-Localize

TABLE 5.2: Stellar parameters of V388 Cas.

Parameter	Value	Reference
	Name and identifiers	
Name	V388 Cas	
GJ	51	Gliese (1957)
Karmn	J01033+623	Alonso-Floriano et al. (2015b)
TIC ID	52183206	Stassun et al. (2018)
	Astrometry and kinematics	
α (epoch J2016.0)	01:03:21.52	Gaia Collaboration et al. (2021)
δ (epoch J2016.0)	62:21:57.21	Gaia Collaboration et al. (2021)
$\mu_\alpha \cos\delta$ [mas yr^{-1}]	730.40 ± 0.04	Gaia Collaboration et al. (2021)
μ_δ [mas yr^{-1}]	85.97 ± 0.05	Gaia Collaboration et al. (2021)
π [mas]	101.37 ± 0.05	Gaia Collaboration et al. (2021)
d [pc]	9.86 ± 0.005	Gaia Collaboration et al. (2021)
Galactic population	Young disk	Cortés-Contreras (2016)
	Key photometry	
G [mag]	11.93 ± 0.003	Gaia Collaboration et al. (2021)
J [mag]	8.611 ± 0.027	Skrutskie et al. (2006)
	Photospheric parameters	
Spectral type	M5.0 V	Alonso-Floriano et al. (2015b)
$T_{\rm eff}$ [K]	3057 ± 49	Marfil et al. (2021)
$\log g$ [cgs]	5.12 ± 0.18	Marfil et al. (2021)
[Fe/H] [dex]	-0.24 ± 0.24	Marfil et al. (2021)
	Activity	
$v \sin i$ [km s^{-1}]	10.5 ± 1.5	Reiners et al. (2018)
$P_{\rm rot}$ [d]	1.0241 ± 0.0004	This work
pEW(Hα) [Å]	-9.77 ± 0.04	Schöfer et al. (2019)
$\log L_{\rm H\alpha}/L_{\rm bol}$	-3.534 ± 0.002	Schöfer et al. (2019)
$\log L_{\rm X}/L_{\rm J}$	–2.04	Voges et al. (1999)
	Physical parameters	
$L_\star$ [$10^{-5}\,L_\odot$]	458.14 ± 6.39	Cifuentes et al. (2020)
$R_\star$ [$R_\odot$]	0.2506 ± 0.0085	Cifuentes et al. (2020)
$M_\star$ [$M_\odot$]	0.2404 ± 0.0125	Cifuentes et al. (2020)
i [deg]	$55.96^{+12.46}_{-10.45}$	This work

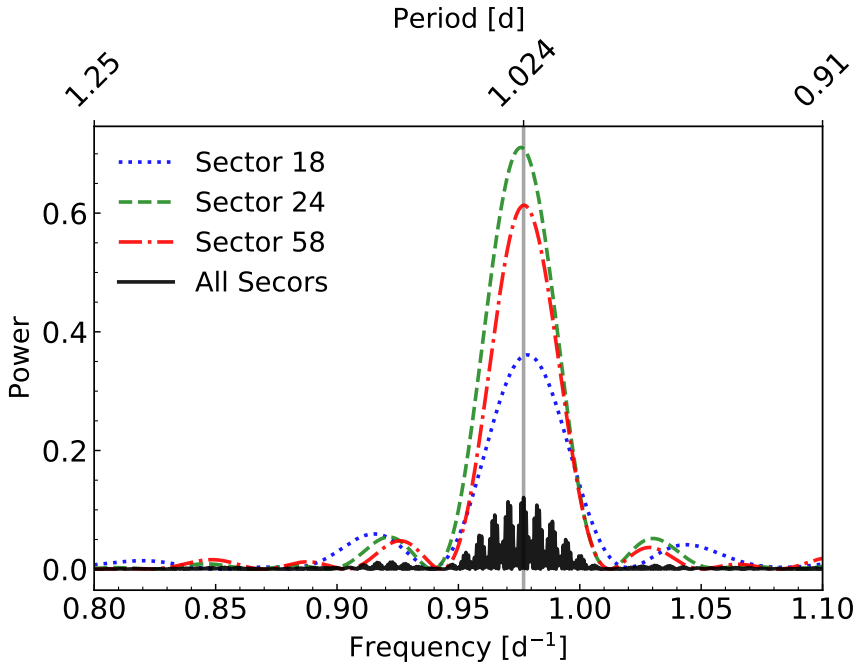

FIGURE 5.4: Zoomed-in GLS periodograms centred around the rotation period of V388 Cas derived for the TESS observations from sectors 18, 24, and 58, as well as the combined data. The solid grey line indicates the rotational period of 1.024 d derived from the combined data.

periodograms of sectors 18, 24, and 58 occur at periods of 1.0220, 1.0247, and 1.0236 d, respectively. The vertical grey line marks the peak period of 1.024 d in the combined data periodogram. The slight shift in the dominant periodicity over time can be attributed to the evolution of active regions on the stellar surface, which is also reflected in the stellar light curve (see Fig. 5.2).

V388 Cas is kinematically associated with the Galactic young disc, as reported by Cortés-Contreras (2016). Although it exhibits considerable X-ray emission as measured by the *ROSAT* All Sky Survey (Voges et al., 1999), its Hα emission is relatively weak for its spectral type. Considering its moderately short rotation period and projected rotational velocity $v \sin i$ of 10.5 km s^{-1} (Reiners et al., 2018), we estimate its age to be less than 0.6 Ga or possibly less than 1.0 Ga. This fairly young age can explain the frequent occurrence of flares observed in V388 Cas (Section 5.5.2).

Large and quasi-sinusoidal variations observed in the light curve of M dwarfs is generally attributed to starspots coming in and out of view as the star rotates (Basri et al., 2011).

5.5 Analyses and results

5.5.1 Spots Modeling with `StarSim`

`StarSim` is a powerful tool designed to model a rotating photosphere of a star with spotted regions, thereby enabling the generation of precise synthetic photometric and spectrometric time series. When provided with a spot map, `StarSim` not only generates photometric or

RV light curves, but also offers additional cross-correlation function (CCF) products such as BIS, FWHM, and Contrast, and even the CRX (see, e.g., Baroch et al., 2020). While we provide a brief overview of the key aspects of the model here, for a more comprehensive understanding, we direct the reader to the detailed descriptions provided by (Herrero et al., 2016) and (Rosich et al., 2020).

The model considers a finely-gridded set of surface elements and utilises synthetic PHOENIX spectra of varying temperatures (Husser et al., 2013). These spectra are assigned to each surface element based on the specific properties of the region it represents, such as the immaculate photosphere, spots, or faculae. Furthermore, the spectra are Doppler-shifted according to the projected velocity of each surface element and are further corrected for limb darkening using the Kurucz ATLAS9 models (Kurucz, 2017). By integrating the contributions from all surface elements, the model calculates photometric light curves or radial velocities. To optimise computational efficiency in the calculation of RVs and other spectral indices associated with the CCF, `StarSim` first generates CCFs using the spectra of individual photosphere, spot, and facular elements. These CCFs are then used to integrate the entire visible surface, thereby eliminating the need for individual spectra. StarSim allows for the specification of various stellar input parameters, including the effective temperature of the star, spot temperature, position, size, and number of active regions, convective shift, stellar rotation period, star radius, surface gravity, and inclination of the stellar spin axis relative to the line of sight. Additionally, it is possible to select the desired wavelength range and compute time-series data for photometry, radial velocity (RV), and cross-correlation function (CCF) parameters.

`StarSim` also has the ability to solve the inverse problem. It can derive the properties of stars and their active regions map by utilising the available photometric or spectrometric time series, or even a combination of both (Rosich et al., 2020). The inversion model starts with a randomised distribution of a fixed number of active elements, each characterised by five adjustable parameters: time of appearance, lifetime, latitude, longitude, and angular radius. The appearance and disappearance of active elements are not sudden; rather, they are assumed to grow or shrink linearly in radius at a rate of 0.5 degrees per day. The total number of active regions is a customisable parameter, defined by the user. The objective is to optimise the surface map using a Monte Carlo Simulated Annealing (MCSA) optimisation algorithm (Kirkpatrick, Gelatt, and Vecchi, 1983). The optimisation process involves successive iterations in which the algorithm randomly selects one of the adjustable parameters from a randomly-selected active element and makes slight modifications to it. Subsequently, the forward problem is recomputed using this updated map, and the log-likelihood ($\ln \mathscr{L}$) is evaluated for each time-series dataset. If the modified map leads to an improvement in the fit quality, the change is accepted. Otherwise, it is accepted with a certain probability. This strategy enables the optimiser to avoid becoming trapped in local maxima, enhancing the effectiveness of the optimisation process. For a more detailed explanation of the implementation of MCSA in StarSim, please refer to Herrero et al. (2016) and Rosich et al. (2020). However, when utilising only a single light curve, the derived spot map becomes highly degenerate due to the large number of parameters and potential correlations among them. This degeneracy implies that different combinations of filling factors and spot distributions can result in the same photometric signal (Rosich et al., 2020). To overcome this, it is necessary to model the photometry in conjunction with radial velocities or light curves obtained using other filters. By incorporating these additional observations, we can break

the degeneracy. When working with observations from a single photometric band, only the active longitudes of the star can be constrained.

5.5.1.1 Implementation of Inverse Model on V388 Cas

We employed the inverse mode of `StarSim` to estimate the distribution of active regions on the stellar photosphere, in particular their latitude. We utilised the TESS photometric data, and since light curves are not strongly sensitive to the latitude of active regions, we incorporated the seven RV data points obtained by CARMENES, which were acquired simultaneously with the TESS observations. To optimise computational efficiency and reduce noise in the model, we performed preprocessing on the TESS data. This involved removing flare events and employing a 30-minute binning technique. We established fixed values for the stellar parameters $R_\star$, $v \sin i$, and $P_{\rm rot}$ based on the information provided in Table 5.2. Additionally, we carefully selected atmospheric models that closely matched the atmospheric parameters of V388Cas, including $T_{\rm eff} = 3000$ K, $\log g = 5.0$ cgs, and [Fe/H]=0.0 dex.

The initial step in modelling the stellar surface involves selecting the number of active elements to be utilised by `StarSim`. To accomplish this, we followed the subsequent steps: firstly, we utilised spot-to-photosphere temperature contrasts of 200 K based on empirical studies (Andersen and Korhonen, 2015). Given the short time span of the data, covering only a few rotation periods, we assumed that the active element map of the star would remain relatively stable. As a result, in the second step, we fixed the time of spot creation and lifespan to ensure the consistent presence of the active regions throughout the simulation. This approach allowed us to minimise only three parameters for each active region: longitude, latitude, and radius. Finally, we simulated the stellar surface using different numbers of active elements, ranging from one to twenty. The model resulting in the lowest Bayesian Information Criterion (BIC; Schwarz, 1978) was selected as the optimal choice. The BIC takes into account both the goodness of fit of the model to the data and the complexity of the model. It balances the trade-off between model complexity and model fit by penalising more complex models that may overfit the data. The BIC is calculated as:

$$BIC = -2\ln(\mathscr{L}) + k\ln(n). \tag{5.1}$$

Here, $\mathscr{L}$ represents the maximised value of the likelihood function of the model, k denotes the number of parameters estimated by the model (in this case, the spot parameters of latitude, longitude, and radius multiplied by the number of active regions), and n corresponds to the number of data points (specifically, the combined binned TESS data and CARMENES RVs).

Figure 5.5 shows the BIC statistic as a function of the number of active elements used for the simulation. There is a rapid decrease in the BIC until reaching $N = 5$, where the BIC starts to slightly increase since the slight improvement on the $\ln \mathscr{L}$ does not compensate for the addition of more free parameters anymore. Thus, we selected $N = 5$ as the optimal number of active elements used in the simulations.

Additionally, to avoid an overweight in the $\ln \mathscr{L}$ of the photometric points for deviations from the models due to flare residuals or TESS systematics, we added quadratically a jitter term to the TESS uncertainties. In order to do that, we computed the dispersion of the residuals when fitting the best model with five active regions, and increased the error bars so their mean value was equal to the dispersion of the residuals. As a result, a jitter of 0.003 was added quadratically to the error bars.

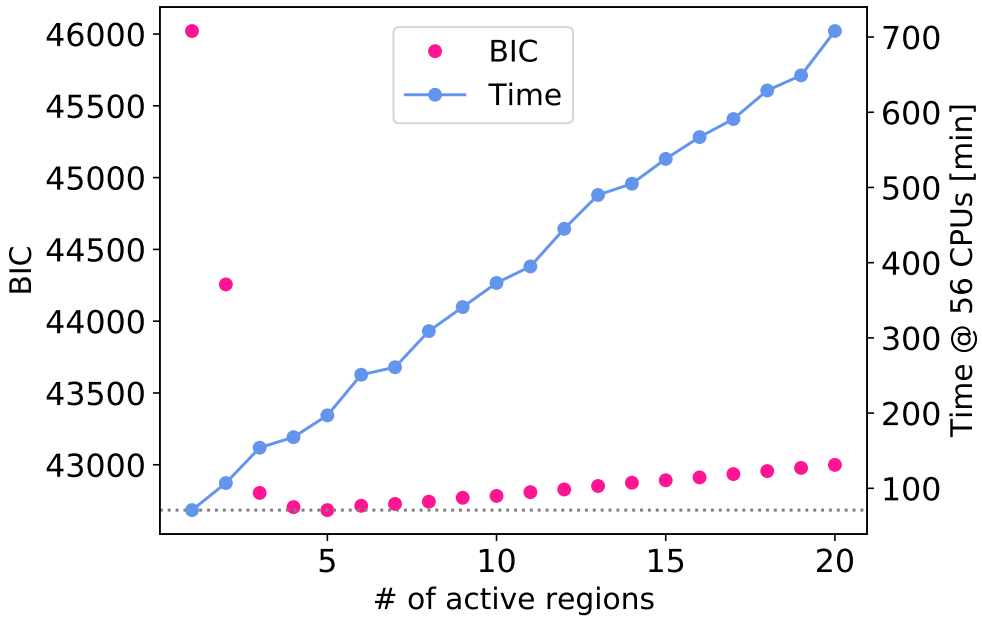

FIGURE 5.5: BIC values correspond to the number of active surface elements (depicted in pink), along with the corresponding simulation times (shown in blue).

Similarly to the optimisation of the number and properties of the active elements of the star, we can also use the `StarSim` inverse modelling to optimise a set of stellar parameters. However, the minimisation procedure is not straightforward due to the high number of free parameters, producing noisy outputs of the evaluation function. To overcome this problem, we followed the procedure outlined by Rosich et al., 2020, in which considered a large number of randomly-generated sets of parameters drawn from the desired prior distribution, and used the best statistically-equivalent solutions (those enclosed within $\Delta\mathscr{L}<15$ from the best-solution) to compute optimal parameters and uncertainties. We refer the reader to Rosich et al., 2020 for a more detailed explanation of the minimisation and optimisation process. In this work, the stellar parameters that are optimised simultaneously are the rotation period, $P_{\rm rot}$, the facula-to-spot area ratio, Q, the temperature contrast between spots and photosphere, ΔT, and the inclination of the star i. Also, we optimised the radial velocity offset of the observations, γRV, since they have no information of the zero-point, while the `StarSim` simulation does.

We adopted uniform priors with ranges specified in Table,5.3. Notably, the prior range for ΔT is limited to 400 K, as `StarSim` does not offer cooler models. Following a similar approach as in Rosich et al., 2020, we narrowed down these ranges based on a significant number of realisations that met the likelihood criterion. Specifically, we included only the ranges defined by this subsample to prevent sampling irrelevant parameter space. We generated a large number of parameter sets by random sampling from the prior distribution. Approximately 6000 realisations were performed, and from these, we selected the statistically equivalent solutions that were within 3σ of the best likelihood value. The median, along with the 68% confidence interval, was then employed to determine the best estimates for the stellar parameters and their respective uncertainties. The obtained parameters and

TABLE 5.3: Best fitting parameters and ranges introduced by the uncertainties on stellar parameters and RV dataset.

Parameter	Prior	Values
$P_{\rm rot}$ [d]	$\mathscr{U}(1.021,1.025)$	$1.02355^{+0.00021}_{-0.00020}$
ΔT [K]	$\mathscr{U}(0,400)$	270^{+90}_{-100}
$\gamma_{\rm RV}$ [m s^{-1}]	$\mathscr{U}(-400,400)$	$68.61^{+102.17}_{-74.54}$
Q	$\mathscr{U}(0,3)$	$0.72^{+0.81}_{-0.48}$
i [deg]	$\mathscr{U}(10,90)$	$50.67^{+17.18}_{-13.02}$

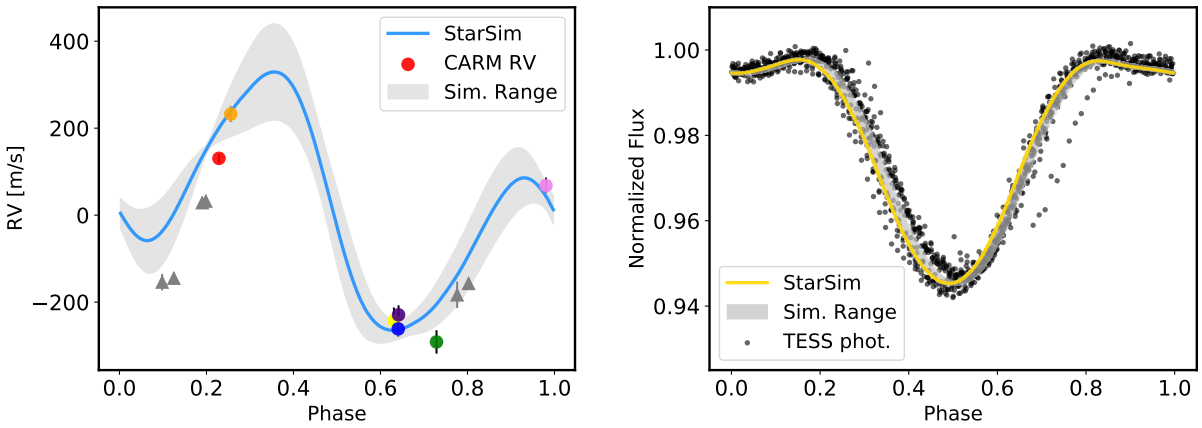

FIGURE 5.6: Inverse model fit of `StarSim` to RVs (left) and photometric light curve data (right). The colours of the RV data points correspond to those used in Figure 5.2.

their corresponding uncertainties are presented in Table,5.3, while Figure C.2 displays a comprehensive corner plot depicting the posterior distribution and the correlation among the parameters. We derived a period of $1.02355^{+0.00021}_{-0.00020}$ days, which exhibits a close proximity to, but is not statistically compatible with, the period of 1.0241 ± 0.0004 days detected by the GLS periodogram. This discrepancy can be attributed to the significant deviation of the light curve from a sinusoidal modulation, which is the underlying assumption of the GLS periodogram's base model.

Figure 5.6 presents the best-fit model to the test photometry in the right panel and radial velocity in the left panel, plotted over the stellar phase. The mean value of 40 inversions is depicted in gold for the photometry and in blue for the radial velocity, while the shaded grey regions represent the corresponding standard deviations in both panels. The photometric data exhibits robust constraints throughout the stellar phase, demonstrating a well-constrained fit. However, due to incomplete coverage during the test observations, certain regions in the radial velocity data have lower constraints. Notably, additional radial velocity data from CARMENES, depicted as grey triangles in the plot, were obtained shortly after the test observations. These data closely follow the fitted light curve, and if acquired simultaneously, could have provided enhanced constraints for those specific regions.

5.5.1.2 Forward Model for V388 Cas simulated spotmap

Finally, we employed the `StarSim` forward model and utilised the obtained surface map from the inverse model's best solution to conduct simulations of radial velocities across the spectral range comparable to the orders of the CARMENES VIS spectrograph. These simulations spanned the complete phase of the star with a cadence of 30 minutes, ensuring a comprehensive representation of the radial velocity data.

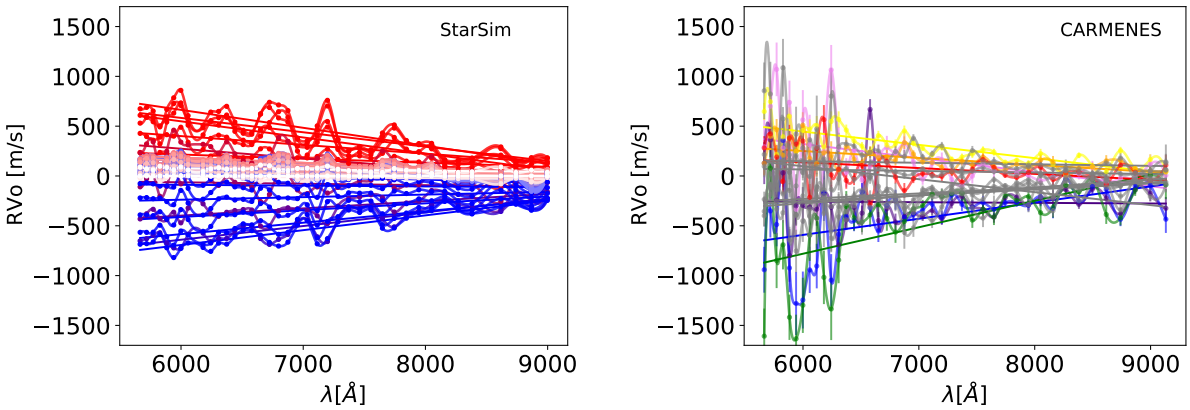

FIGURE 5.7: Comparison of simulated and observed RV data over wavelength. *Left panel*: Simulated RV data over spectral orders. *Right panel*: Observed RV data over spectral orders for V388Cas. The colours of the RV data points correspond to those used in Figure 5.2 and the left panel of Figure 5.6, along with additional observations taken shortly after TESS observations (depicted in grey).

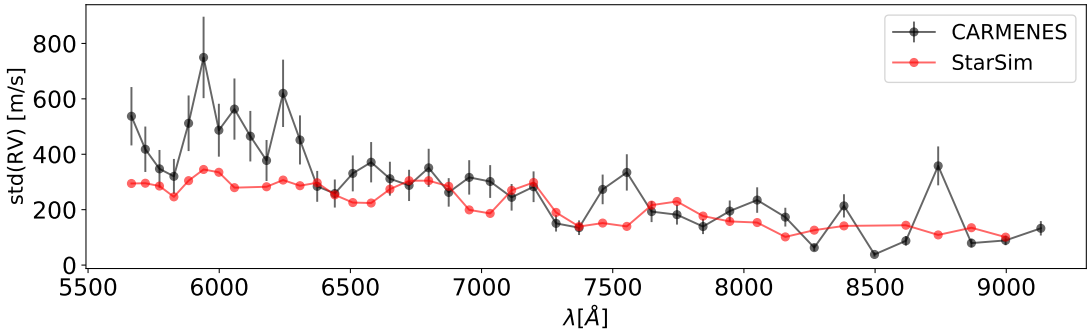

FIGURE 5.8: Comparison of std(RV) over orders between the real and simulated radial velocity data.

In Figure 5.7, the left panel showcases the results of our simulated radial velocity data over spectral orders. The right panel illustrates the RV data obtained from simultaneous observations with TESS (displayed in the same colours as in Figure 5.2 and the left panel of Figure 5.6), along with additional observations taken shortly after TESS observations (depicted in grey). A comparison between the two plots reveals that the simulated data

effectively captures the effect of flux contrast on RV variations across wavelengths. The amplitude of RVs not only decreases towards longer wavelengths but also exhibits an additional squiggle pattern, which is also present in the real data and represents segments of the spectra with different sensitivities to spot-to-photosphere temperature contrast.

To closely examine these squiggle patterns, we calculated the standard deviation of radial velocity over orders, std(RVO), for both the real and simulated radial velocity data. The comparison results are presented in Figure 5.8. However, it is evident that the variations in the simulated data do not entirely match those observed in the real data. Specifically, the real observations demonstrate a much larger excursion, particularly in bluer orders around 580-640 nm. Additionally, areas around λ= 650, 700, 750, and 870 nm exhibit greater variations in the real data. This suggests that our simulation, unfortunately, could not fully capture the effect of the active region on radial velocity variations. The limited number of radial velocity observations could be a contributing factor. Nevertheless, this simulation represents an initial step towards detecting activity-sensitive regions in stellar spectra, and its limitations should be further investigated, possibly with a more comprehensive set of observations.

5.5.2 Flaring activity of V388 Cas

To identify flares, we implemented a robust flare-detection approach outlined in Subection 4.7.1. As the comprehensive methodology is provided in 4.7.1, we present a concise summary of the algorithm here. Each TESS sector underwent independent analysis, accounting for data gaps due to spacecraft re-orientation and data downlink. A trend removal process, employing a smoothing algorithm, effectively mitigated variations caused by factors like stellar rotation. Next, we computed the local median and standard deviation (σ) of the flux at each time sample. Potential flares were identified by flagging any two or more consecutive points that exceeded the local median flux by more than 2.5 σ. We only considered flare candidates with a rise time shorter than the decay time. Additionally, during the inspection phase, we carefully examined and, if necessary, adjusted the start and end times for each flare. After identifying flare candidates, we computed various statistics, such as flare amplitudes, equivalent duration (ED), and flare bolometric energy ($E_{\rm flare}$), following the methodology described in Subsection 4.7.2.

We detected a total of 211 flares in the TESS light curves, with 45 flares identified in Sector 18, 86 flares in Sector 24, and 80 flares in Sector 58. The observed flares exhibited a wide range of bolometric energy release, spanning from 6.2×10^{30} erg to 1.3×10^{34} erg. Notably, the median flare energy for each sector was found to be approximately $\sim 3 \times 10^{31}$ erg. However, the maximum flare energies released across the sectors exhibited a decreasing trend by one order of magnitude, with values of 1.3×10^{34} erg, 1.0×10^{33} erg, and 6.7×10^{32} erg for Sectors 18, 24, and 58, respectively.

To facilitate a robust comparison of flare energies, we constructed flare frequency distribution (FFD) diagrams for both the overall detected flares of V 388Cas and the flares detected in each individual sector. The FFD diagrams serve as informative visual representations, illustrating the occurrence rate of flares from the stars as a function of energy. These diagrams have been widely utilised to compare flare activity levels across different stars and to make comparisons between observations of varying durations (e.g., Lacy, Moffett, and

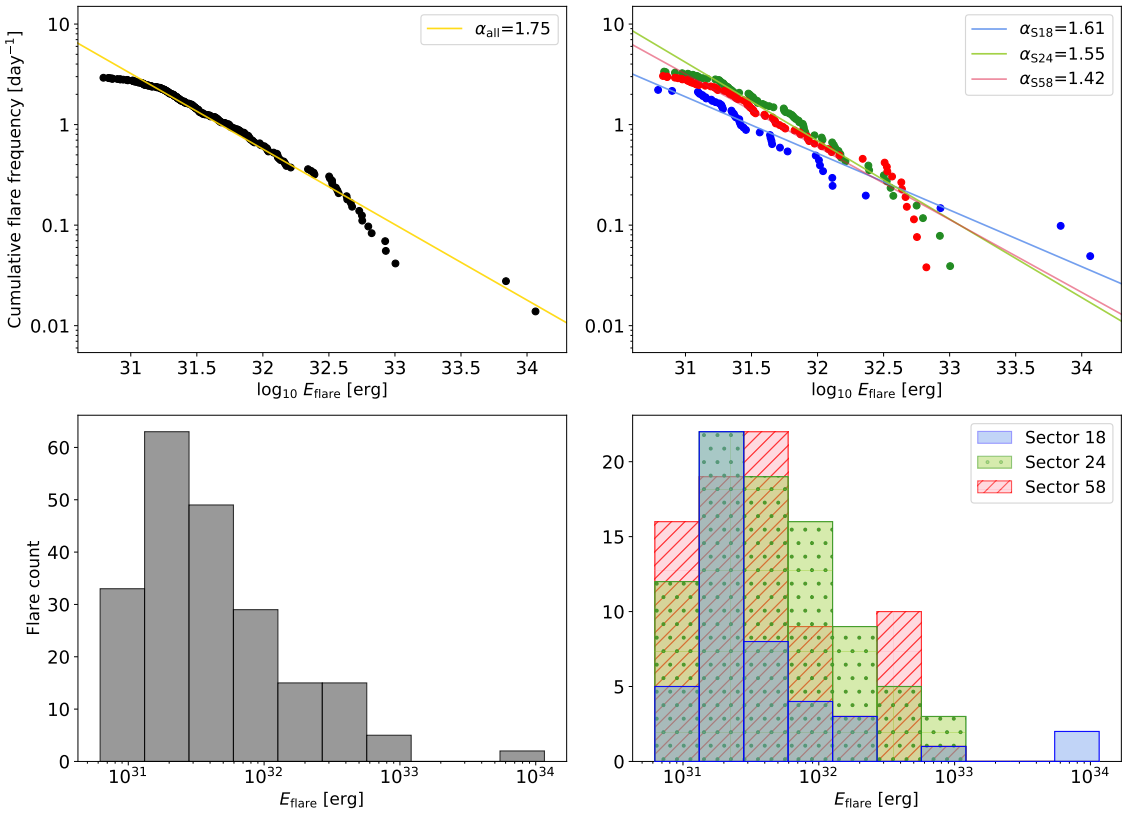

FIGURE 5.9: *Top panel*: The Flare Frequency Distributions (FFDs) of V388 Cas presenting the overall detected flares (on the left) and distinctive sectors (on the right). The fitted lines represent a power-law fit to the data, with the power-law index α indicated for each fit shown in the plot. *Bottom panel*: The corresponding distributions of flare energies.

Evans, 1976; Shibayama et al., 2013; Maehara et al., 2021; Davenport et al., 2019; Davenport, Mendoza, and Hawley, 2020, among other referenced works). Figure 5.9 illustrates the FFDs in the top panels, along with the corresponding distributions of flare energies in the bottom panels. These representations showcase both the overall detected flares (on the left) and the flares detected in each individual sector (on the right) for V388 Cas. The FFDs are modelled using a power-law distribution described by the equation: $dN/dE \propto E^{-\alpha}$. Significant variations in the power-law slope (α) have been established as reliable indicators of changes in flare activity levels (Scoggins, Davenport, and Covey, 2019). If a star undergoes noticeable fluctuations in its flare activity over the course of a few years, it is likely experiencing activity cycles. Notably, several studies consistently report an approximate value of $\alpha \approx 2$ for M stars (e.g., Lacy, Moffett, and Evans, 1976; Hawley et al., 2014; Ilin et al., 2019; Maehara et al., 2021). When the power law has a value of 2 or greater, it suggests the presence of a sufficient number of lower-energy flares capable of depositing enough energy to heat the corona (Audard et al., 2000; Güdel et al., 2002). Conversely, when $\alpha < 2$, it indicates that the energy delivered to the corona primarily relies on the most energetic events, with low-energy flares occurring infrequently and being insufficient to account for coronal heating (Hudson, 1991).

The power-law index obtained from fitting the overall detected flares, spanning a range

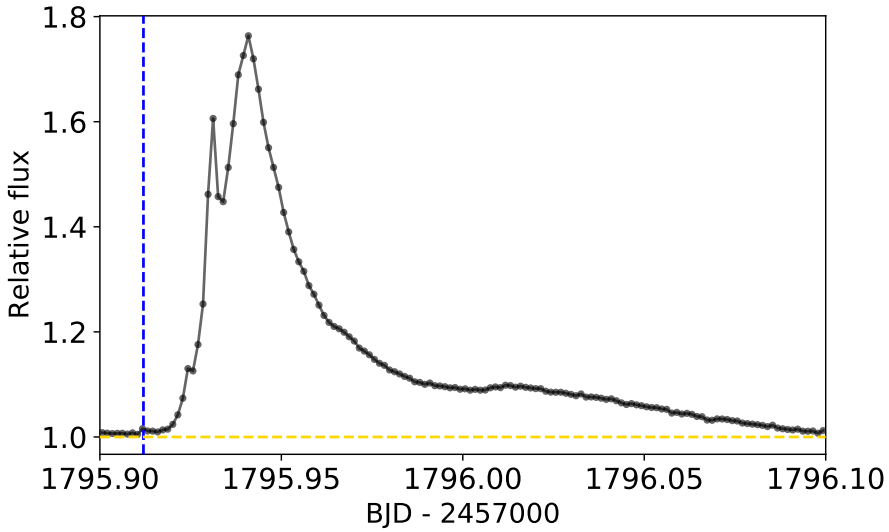

FIGURE 5.10: The morphology of the longest white flare observed in V388 Cas. This superflare lasted for 6 hours and 28 minutes, releasing an energy of 1.3×10^{34} erg, and achieving an amplitude of approximately $\sim 76\%$ relative to the averaged flux during the quiescence phase. The onset of the flare is indicated by the blue vertical dashed line, while the gold horizontal dashed line represents the quiescence level of flux.

of flare energies from the median energy of 10^{31} to the maximum energy of 10^{34} erg, is determined to be $\alpha = 1.75 \pm 0.08$. In specific sectors (18, 24, and 58), the power-law fits yield α values of 1.61 ± 0.21, 1.55 ± 0.15, and 1.42 ± 0.19, respectively. These results indicate no significant variation in the flare rate between different sectors.

Figure 5.10 showcases the largest flare event detected for V388 Cas. This white light flare exhibits a $\sim 76\%$ increase relative to the averaged flux of the quiescence phase and persists for a duration of 6 hours and 28 minutes. With a released bolometric energy of 1.3×10^{34} erg, this flare falls into the classification of a superflare. In solar observations, it is well-established that large and long-lasting flares are often accompanied by CMEs. To explore this possibility, we used a spectroscopic observation by CARMENES, which was obtained 12 hours after the flare onset (refer to Figure 5.2). The findings of this investigation are presented in detail in Subsection 5.5.5.

5.5.3 Comparing light curves

The TESS light curves of V388 Cas reveal a distinctive double dip pattern per rotation that exhibits slow evolution. To conduct a detailed analysis, we first removed the detected flare events and then phase-folded the light curves, as shown in Figure 5.11. The variability range ($R_{\rm var}$) was determined as the difference between the 1^{st} and 99^{th} flux percentiles, following the methodology described in Subsection 4.7.4. The primary and secondary dips appear to remain relatively stable in phase, but their amplitude of variations changes over time. Notably, the primary starspot feature is prominently visible in the light curve of sector 18 (depicted in blue), but it gradually diminishes in subsequent observations of sectors

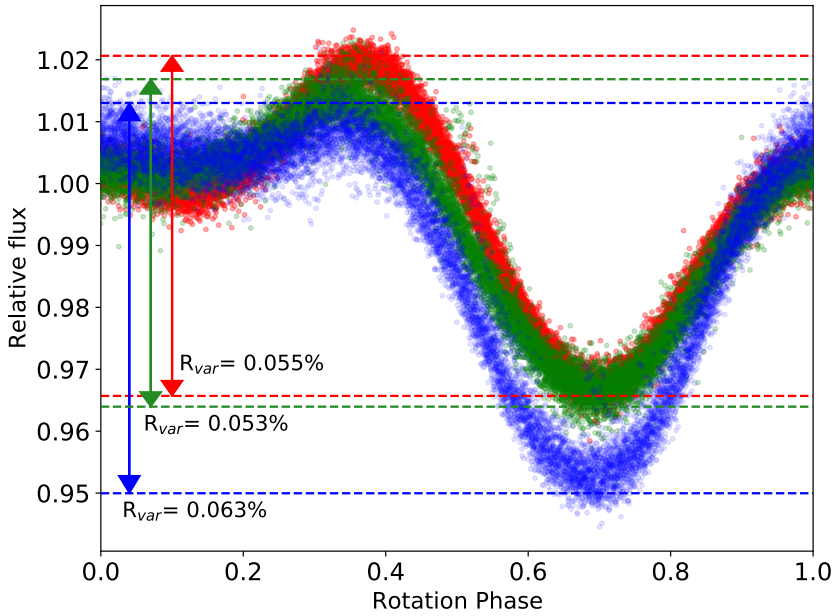

FIGURE 5.11: Phase-folded TESS light curve of V388 Cas for sectors 18 (blue), 24 (green), and 58 (red), illustrating the stellar rotation period. The variability ranges ($R_{\rm var}$) are indicated with corresponding colours for each sector.

24 and 58 (shown in green and red, respectively). In contrast, the secondary spot group becomes more pronounced over time. Simultaneously, the variability range decreases from 0.063% in sector 18 to 0.053% in sector 24 and then shows a slight increase to 0.055% in sector 58. This increase is mainly due to the enhancement of the relative flux maxima in sector 58. Furthermore, there is an observed increasing trend in the overall relative flux minima and maxima as time progresses. This trend implies a potential reduction in either the spot-to-photosphere temperature contrast or the spot filling factor. It is intriguing to highlight this observation, particularly when considering the concurrent decreasing trend in the maximum flare energies released across the sectors over time, as previously mentioned in Subsection 5.5.2.

5.5.4 Correlation between flares and rotation phase

To investigate the relationship between flare count, energy, and the rotation phase of V388 Cas across different observation sectors, we conducted a detailed analysis. In Figure 5.12, we provide a comprehensive view of this behaviour by presenting the phase-folded light curves of V388 Cas in each sector, accompanied by the distribution of flare count and energy across the rotation phase. This analysis allows us to examine the temporal evolution of flares and their dependence on the rotational phase of the star. While the total number of flares in sector 18 is lower compared to sectors 24 and 58, we observe the occurrence of two superflares with bolometric energies exceeding 10^{34} erg in this sector. This finding aligns with the notion that the frequent appearance of low-energy flares can delay or prevent the occurrence of large flares. Specifically, in the phase bins of sector 18 (panel g in the figure),

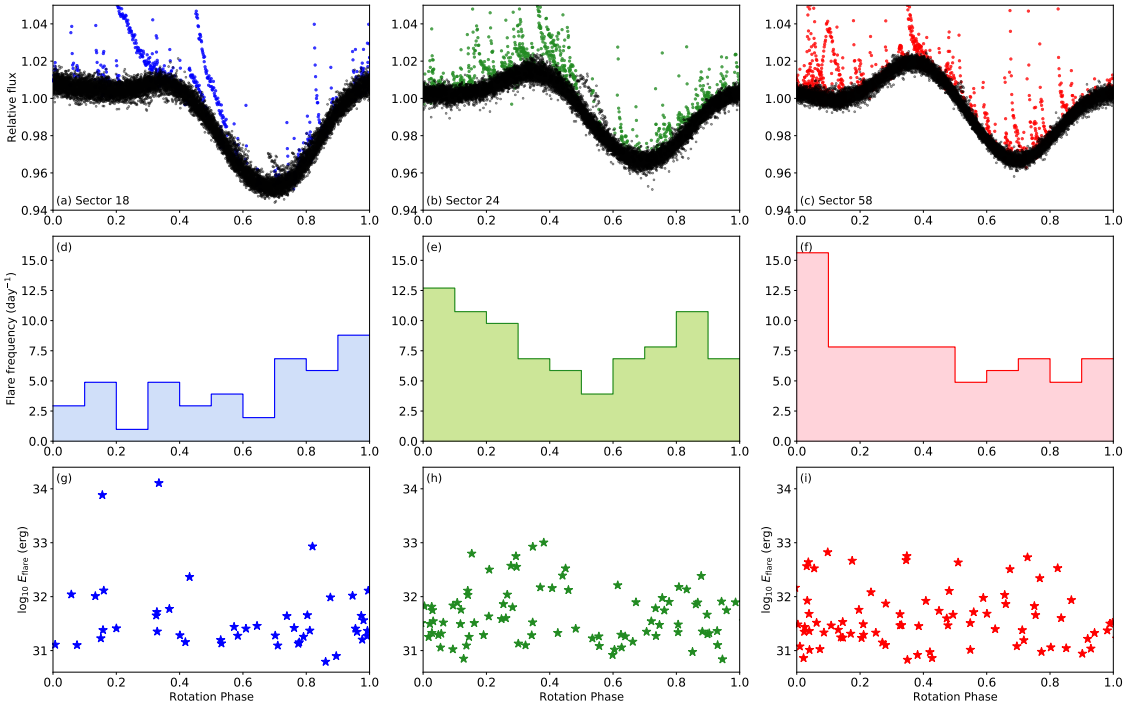

FIGURE 5.12: Distribution of flare count and energy across rotation phase in V388 Cas: Sectors 18 (blue), 24 (green), and 58 (red)

we clearly observe a decrease in the number of flares in the $\phi = 0.2 - 0.3$ range, just before the emergence of the superflare. Interestingly, in sectors 24 and 58, we observe an increase in the number of flares in the secondary spot group as the secondary dip becomes more prominent compared to sector 18. In addition, we observe a pattern pretty similar to what was reported in Subsection 4.8.3.1 for the three double dip stars G 173-039, EV Lac, and G 208-042. Specifically, we observe a lower flare count as the primary dip emerges and a higher count as it disappears in sectors 18 and 24. However, this trend does not persist in sector 58.

5.5.5 Hα wing enhancements

Asymmetries observed in the Hα region are indicative of material motion within the chromospheres. Notably, blue asymmetries are associated with ejected material, while red asymmetries suggest downward motions, commonly referred to as coronal rain or chromospheric condensation. In order to investigate the occurrence of these events, we analysed the chromospheric activity indicators present in the CARMENES spectra, which were taken alongside TESS observations.

During two observations on 08.11.2019 and 17.11.2019, we detected wing enhancements in the Hα (λ6564.6 Å) emission lines. The behaviour of the Hα emissions is depicted in Figure 5.13. On 17.11.2019, we observed a red-wing enhancement, likely resulting from the downward flow of cool plasma along magnetic field lines in the atmosphere. The observation made on 08.11.2019, which exhibited a blue-wing enhancement, took place 12 hours after the onset of the largest flare event in sector 18 (refer to Figure 5.2 and Figure 5.10).

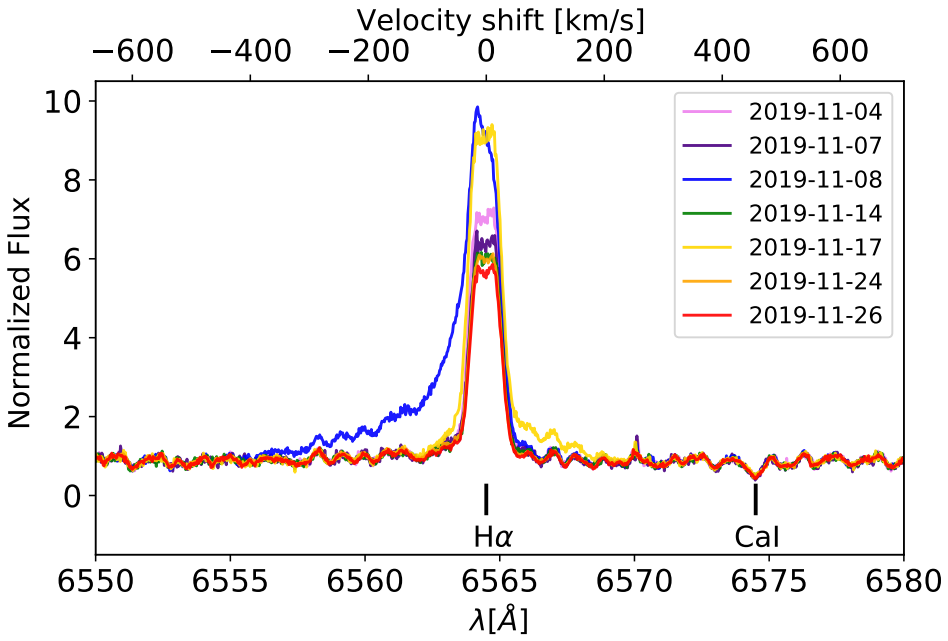

FIGURE 5.13: Normalised Hα line profiles of V388 Cas obtained by CARMENES during TESS observations. The blue spectrum corresponds to the observation on 08.11.2019, showing a strong blue asymmetry. The yellow spectrum represents the observation on 17.11.2019, exhibiting a weaker red asymmetry. The red spectrum corresponds to the quasi-quiescent state of the star, observed on 26.11.2019.

To determine whether the blue-wing enhancement is associated with a CME, we proceeded to calculate the escape velocity for V388 Cas. Using the mass value of approximately 0.2404 $M_\odot$ and a radius of about 0.2506 $R_\odot$ from Table 5.2, we determined an escape velocity of $v_e \approx 604.97$ km s^{-1}.

To accurately estimate the shift in the Hα line profile and determine the corresponding line-of-sight velocity of the blue asymmetry, it is crucial to establish the quiescent state of the star. However, due to the active nature of V388 Cas, we followed the common approach of constructing residual spectra by subtracting the spectrum obtained during minimum activity on 26.11.2019 from the "active" spectra. These residual spectra were then fitted with a Gaussian profile to determine the Doppler displacement from the line core. The upper plot of Figure 5.14 showcases the Hα emissions for both the active and quasi-quiescent states, represented by blue and red, respectively. In the lower panel, the residual spectrum is presented, with the overlaid Gaussian fit capturing the features of the residual spectrum. If the observed asymmetry shift corresponds to a velocity equal to or greater than 10% of the stellar escape velocity, we can have a reasonable level of confidence in the occurrence of a CME (Johnson et al., 2021). In this case, the measured Doppler shift is 39.22 km/s, accounting for only about 6.5% of the stellar escape velocity. However, given that this observation was taken 12 hours after the flare incident, it is unlikely that the plasma material remains immediately above the stellar surface. Instead, a significant portion of it would have already travelled approximately 20 million km away from the star's potential well. This compelling evidence strongly supports the occurrence of a CME event.

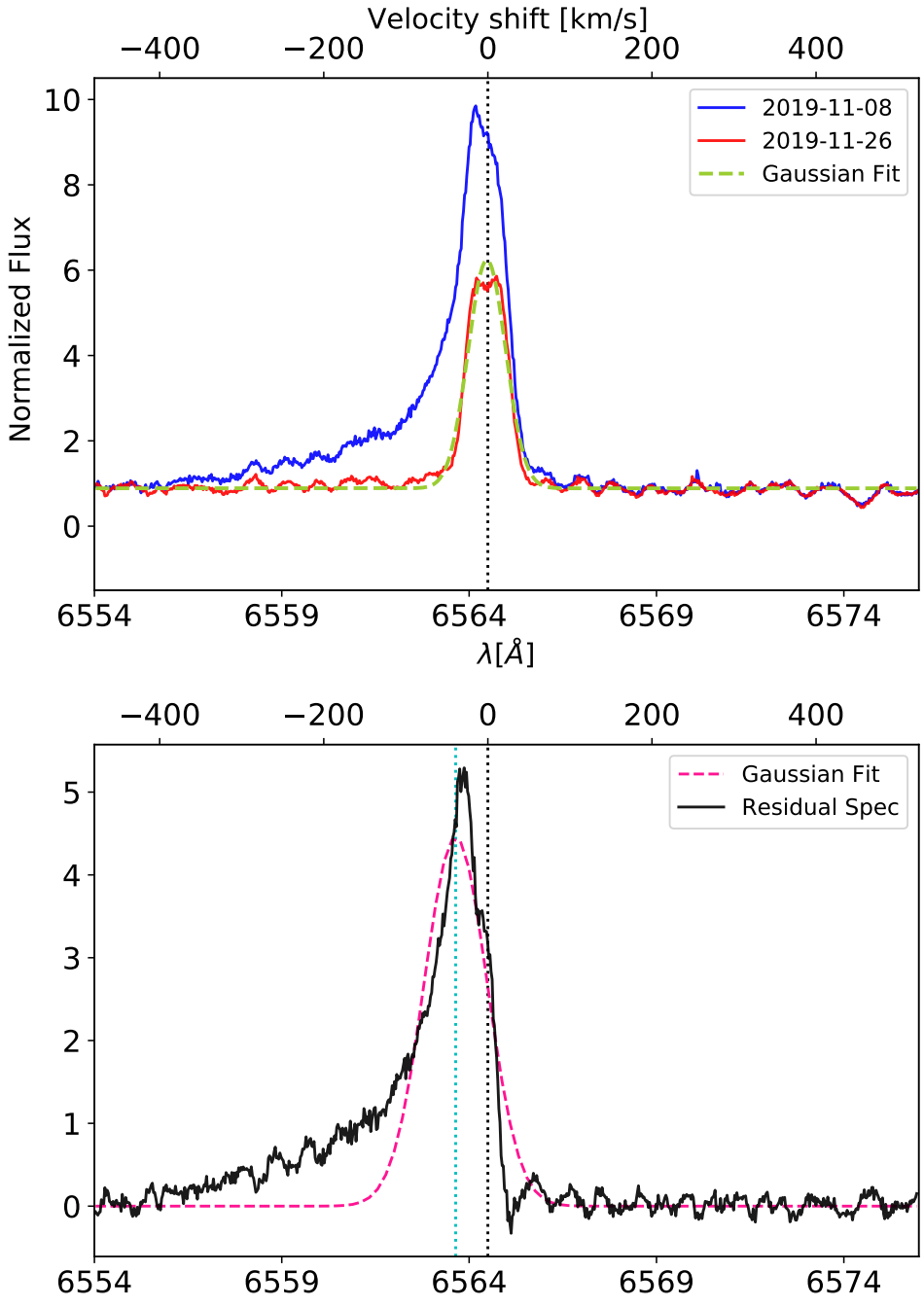

FIGURE 5.14: *Top panel*: Normalised Hα line profiles of V388 in the active state (blue) and quiescent state (red), with a dashed green line indicating the Gaussian fit to the quiescent state. *Bottom panel*: Residual Hα line profile, with a dashed pink line representing the best-fit Gaussian model.

5.6 Summary and discussion

Recovery of photospheric active regions

For the study presented in this chapter, we utilised photometry and radial velocity data from the highly active M5.0 V star, V388 Cas, to reconstruct its surface map and constrain critical stellar parameters susceptible to model degeneracy, namely $P_{\rm rot}$, Q, ΔT, i, and γRV. Our analysis indicates a heterogeneous surface dominated by dark spots with a temperature contrast of 270 K. However, it is worth noting that the available RV data did not provide sufficient constraints for all areas across the rotational phase. To further investigate, we employed the recovered surface map to simulate radial velocity values as a function of wavelength. This allowed us to explore the wavelength dependency of activity-induced radial velocity variations in the absence of systematic effects. While the simulated data successfully captures the influence of flux contrast on radial velocity variations across wavelengths, including the decrease in amplitude towards longer wavelengths and the presence of additional squiggle patterns, a comparison of the std(RV) over orders between the real and simulated radial velocity data demonstrates that the simulation does not perfectly align with the observations. The limited number of radial velocity observations may be the primary factor contributing to this discrepancy. Nonetheless, this type of analysis holds promise for identifying activity-sensitive regions on the stellar spectra of M dwarfs.

Flare activity evolution

Furthermore, we performed an analysis to investigate the evolution of V388 Cas's photometric light curves and flare events using TESS observations from three separate sectors. The first and last sectors were taken three years apart. In our analysis, we employed the flare frequency distribution (FFD) as a primary tool to examine variations in flare rates. We observed that the star displays fewer but more energetic flares during periods when its light curve exhibits a wider range of variability ($R_{\rm var}$). This indicates the presence of active regions with higher temperature contrast to the photosphere or larger filling factors. Moreover, we noticed that over time, the range of variation for the primary active region diminishes, while a secondary active region emerges. This transition leads to a more prominent double-dip light curve for the star. Additionally, we noted a substantial increase in the occurrence of low-energy flares within the secondary region. However, the power law index α remains below 2, indicating an insufficient number of lower energy flares to provide the necessary energy deposition for coronal heating for this star.

Coronal mass ejection (CME) event

Furthermore, by chance, we captured a serendipitous coronal mass ejection (CME) event during one of the CARMENES observations, resulting in a distinctive blue asymmetry in chromospheric lines. Recognising the significance of this occurrence, we proceeded to conduct a comprehensive investigation of this event.

To explore the association between the blue-wing enhancement and the CME in V388 Cas, we calculated the star's escape velocity to be approximately 604.97 km/s. We then applied a Gaussian fit to the residual Hα line profile obtained by subtracting the spectrum from the minimum activity state. The measured Doppler shift was found to be 39.22 $\mathrm{km\,s^{-1}}$,

accounting for only approximately 6.5% of the stellar escape velocity. It is worth noting that for a CME event to occur, the observed asymmetry shift must be equal to or greater than 10% of the stellar escape velocity. However, considering that the observation was made 12 hours after the flare incident, it is reasonable to conclude that the plasma material had already travelled a distance of approximately 20 million km away from the star's potential well. This compelling evidence strongly supports the occurrence of a CME event.

Chapter 6

Conclusions and future Prospects

During my PhD research, I focused on the activity of M dwarfs - a type of star that was once considered uninteresting from a traditional observational standpoint. M dwarfs are smaller and cooler than other stars, resulting in them being fainter and redder. Because they are not visible to the naked eye, they were previously disregarded and not considered as interesting targets for observational studies. Additionally, M dwarfs were thought to be unsuitable for hosting habitable planets due to the proximity of their habitable zones (HZ) to the star, which would expose any planets to high levels of radiation and potentially strong gravitational forces.

In recent years, the emergence of exoplanetary missions has shifted the scientific focus towards M dwarfs, as planetary scientists have realised that these stars are in fact ideal targets for exoplanetary studies, especially in the search for exo-Earths. The abundance of M dwarfs in the galaxy, comprising up to $\sim$70% of all stars, provides ample targets for exoplanetary investigations. However, the most significant advantage of M dwarfs is their smaller size and lower luminosity. These properties make it easier to detect the subtle changes in brightness that occur when a planet transits in front of the star. Since the transit depth is proportional to the area of the star eclipsed by the transiting planet, the larger planet-to-star ratio in M dwarfs results in larger transit depths in the stellar light curve. Additionally, there is a higher likelihood of detecting small planets orbiting within the HZ of M dwarfs. The proximity of the HZ to the star increases the range of inclination angles at which a planet can transit and be visible from Earth, providing more opportunities to detect exoplanets. The lower mass of M dwarfs, coupled with their close-in HZ, offers a unique advantage for the RV method as well. The reduced mass ratio of the M dwarf planetary systems allow for easier detection of planets with a given mass around M dwarfs, compared to larger stars. Moreover, the shorter orbital periods of planets around M dwarfs result in a higher frequency of detections over a given period of time, making them attractive targets for exoplanet studies using the RV method.

Despite their advantages, M dwarf stars present a challenge for exoplanetary research due to their high levels of magnetic activity, which can introduce noise into observations. To address this issue, we can consider two aspects of the problem: interference with the detection of orbiting planets and the direct impact of the activity manifestations, such as flares and coronal mass ejections (CMEs), on exoplanets themselves. Interference with the detection of orbiting planets is often caused by active regions, particularly dark spots on the stellar surface. These surface features may introduce radial velocity (RV) jitter, which can mimic or drown out planetary signatures, or even result in inaccurate estimates of the planetary parameters. The direct impact of activity on exoplanets in close orbits is also an important consideration when studying habitability. Explosive stellar flaring and CMEs are

a double-edged sword. While they can provide the trigger energy for prebiotic chemistry and potentially initiate life, they can also render even a planet within the HZ inhospitable to life by dramatically affecting its atmosphere, possibly stripping it off completely. Therefore, it is important to have a better understanding of the magnitude of activity on M dwarf stars and how it influences data. By understanding the impact of activity on data, we can make informed decisions about which planets should be prioritised for follow-up studies and how to effectively analyse the data to mitigate the potential effects of activity on precise measurements.

Fortunately, exoplanet surveys are providing an ample amount of data that can be used not only to detect exoplanets but also to study the properties of stellar activity and its impact on the observed data. In this work, I took advantage of the data provided by the CARMENES survey to investigate the effect of active regions on radial velocity (RV) measurements.

The presence of active regions induces RV modulation, which can be distinguished from planetary signals based on two main characteristics.

Firstly, the strength of spot-induced variations decreases as the wavelength shifts from blue to near-infrared (NIR) regions. This phenomenon was examined using the chromatic index (CRX) in Chapter 3. This analysis was conducted using the chromatic index (CRX) and focused on a sample of 56 highly active M dwarfs observed by CARMENES in the solar neighbourhood. Through this study, it became apparent that these stars displayed varying degrees of correlation between CRX and RV. Consequently, I categorised the sample based on the significance of their CRX-RV correlation and examined the slope of the CRX-RV linear regression fit in relation to their key stellar properties. The results revealed that rotation plays a crucial role in influencing the observed chromatic behaviour of these stars. In moderately rotating stars, the dominant factor contributing to the negative CRX-RV slope is the effect of active regions. On the other hand, fast rotators exhibit a positive CRX-RV slope, which can be attributed to different physical phenomena such as the Zeeman effect or the presence of telluric contamination and other systematics in the data.

Secondly, the spot-induced RV modulations are typically associated with the rotation period of the star, its harmonics, or aliases of it. This effect was also investigated in Chapter 3. I focused on six early-to-mid-type M dwarfs with well-established rotation periods, ample data coverage, and prominent peaks in the GLS periodogram. The primary aim was to identify rotation period signals (or harmonics) across the orders of the CARMENES spectrograph and compare the significance and amplitude of the variation between these stars. This analysis revealed that highly active stars exhibit rotation signals across almost all orders of the VIS channel and orders in the NIR that are not affected by telluric contamination. In contrast, less active stars predominantly show significant signals in the bluer orders up to $\lambda \sim 759$ nm, while the signals in the redder region either do not manifest or fail to reach the significance threshold. Furthermore, the amplitude of the RV variations appears to be influenced by the presence of titanium oxide (TiO) absorption bands in the spectra, with later-type stars demonstrating larger variations in the semi-amplitude (K) of the rotation signals.

To further investigate the RV variations across different wavelengths, particularly focusing on the observed squiggles, an additional study was conducted using simulation techniques. This study utilised a modelling tool to reconstruct the active regions on the stellar photosphere of a specific star, V388 Cas, which was observed simultaneously by both the

CARMENES and TESS instruments. The results and analysis of this investigation can be found in Chapter 5. In this study, photometry and radial velocity data of the star were utilised to reconstruct the stellar surface map and constrain certain stellar parameters that are prone to cause degeneracy in the modelling. The analysis favoured a heterogeneous surface dominated by dark spots with a temperature contrast of 270 K. However, the available radial velocity data did not provide sufficient constraints for all areas of the rotational phase. Furthermore, the recovered surface map was used to simulate radial velocity values as a function of wavelength, allowing for an investigation of activity-induced radial velocity variations in the absence of systematic effects. The simulated data successfully captured the influence of flux contrast on radial velocity variations across wavelengths, including the decreasing amplitude towards longer wavelengths and the presence of additional squiggle patterns. However, a comparison of the standard deviation of radial velocity over orders between the real and simulated data showed discrepancies, likely due to the limited number of radial velocity observations.

The observation and characterisation of flares are pivotal in understanding the evolution of magnetic fields and their influence on the habitability of planets. In light of this, I conducted a comprehensive analysis of flares in 38 active M dwarfs from the CARMENES sample, which were also observed by TESS. The findings and outcomes of my investigations are presented and discussed in Chapter 4 and Chapter 5 of this thesis. One key finding from this analysis is the strong correlation between flare energies and stellar mass. Notably, we observed that stars near the boundary of complete convection, with a mass around 0.35 $M_{\odot}$, produce the most energetic flares. As we move towards larger or smaller mass ranges, the rate of energetic flares decreases. This finding holds significant implications for the search for habitable exoplanets around these stars. Understanding the relationship between flare activity and stellar mass helps guide our selection of target stars in the quest for potentially habitable worlds. Another significant finding of our study is the close connection between flares and normalised Hα luminosity. Flares being stochastic events, the likelihood of detecting a flare on a faint mid- to late-M dwarf during a regular nightly observation, particularly from ground-based observations, is low. This poses challenges in determining the flare rate for these stars. However, our understanding of the relationship between flares and Hα luminosity provides valuable insights for identifying the optimal targets to monitor in exoplanet research. By leveraging this relationship, we can make more informed decisions about which stars should be prioritised for comprehensive monitoring and investigation. Furthermore, by analysing flares, we can identify stars that may be experiencing coronal heating. It is advisable to avoid these targets in the search for exoplanets, as intense coronal heating can lead to the evaporation of the exoplanet's atmosphere. This process can significantly impact the exoplanet's surface temperature, climate, and overall environmental conditions. The elevated temperatures caused by coronal heating may result in the loss of volatile compounds, including vital elements like water vapour, which are crucial for maintaining habitable conditions on the planet's surface. Additionally, the intense activity and energy release in the stellar corona can generate powerful stellar winds and magnetic fields. These dynamic interactions have the potential to influence the structure and behaviour of the exoplanet's magnetosphere, which in turn can impact its ability to shield the planet from harmful stellar radiation and charged particles. Consequently, understanding and considering the implications of coronal heating in stellar systems is vital for accurately assessing the habitability potential of exoplanets.

Appendix A

A.1 Tables for Chapter 3

TABLE A.1: CARMENES designations, stellar names, spectral types, masses, apparent magnitudes in J band, projected rotational velocities, rotation periods, and normalised Hα luminosities of the active RV-loud sample

Karmn	Name	SpT	Ref.SpT [a]	Mass [b] [$M_\odot$]	J [c] [mag]	$v \sin i$ [d] [km s^{-1}]	P$_{rot}$ [e] [d]	$\log L_{\mathrm{H}\alpha}/L_{\mathrm{bol}}$ [f]
J01019+541	G 218-020	M5.0 V	PMSU	0.141 ± 0.008	9.778 ± 0.022	30.6 ± 3.1	0.139 ± 3.74e-06	-3.764 ± 0.004
J01033+623	V388 Cas	M5.0 V	AF15	0.233 ± 0.012	8.611 ± 0.027	10.5 ± 1.5	1.024 ± 1.01e-05	-3.534 ± 0.002
J01352-072	Barta 161 12	M4.0 V	Ria06	0.376 ± 0.019	8.964 ± 0.021	59.8 ± 6.9	0.704 ± 5.37e-05	-3.495 ± 0.003
J02088+494	G 173-039	M3.5 V	PMSU	0.370 ± 0.050	8.423 ± 0.023	24.1 ± 2.4	0.748 ± 1.53e-04	-3.542 ± 0.003
J02519+224	RBS 365	M4.0 V	Ria06	0.254 ± 0.012	8.919 ± 0.024	27.2 ± 2.7	0.858 ± 3.00e-05	-3.613 ± 0.002
J03473-019	G 80-021	M3.0 V	AF15	0.469 ± 0.029	7.804 ± 0.026	5.2 ± 1.5	3.879 ± 1.92e-03	-3.673 ± 0.002
J04198+425	LSR J0419+4233	M8.5 V	Lep03	0.111 ± 0.009	11.094 ± 0.022	3.6 ± 2.3	0.987 ± 4.83e-04	-4.239 ± 0.011
J04472+206	RX J0447.2+2038	M5.0 V	AF15	0.208 ± 0.033	9.380 ± 0.022	47.6 ± 26.8	0.343 ± 3.00e-04	-3.531 ± 0.002
J05019+011	1RXS J050156.7+010845	M4.0 V	AF15	0.297 ± 0.015	8.526 ± 0.026	6.5 ± 1.5	2.079 ± 3.46e-04	-3.580 ± 0.001
J05062+046	RX J0506.2+0439	M4.0 V	AF15	0.262 ± 0.013	8.909 ± 0.020	24.9 ± 2.5	0.887 ± 1.33e-04	-3.528 ± 0.002
J05084-210	2MASS J05082729-2101444	M5.0 V	Ria06	0.327 ± 0.017	9.716 ± 0.024	25.2 ± 2.5	0.280 ± 1.00e-05	-3.284 ± 0.002
J05365+113	V2689 Ori	M0.0 V	Lep13	0.575 ± 0.013	6.126 ± 0.023	3.8 ± 1.5	11.760 ± 1.93e-02	-4.544 ± 0.012
J05394+406	LSR J0539+4038	M8.0 V	Lep03	0.100 ± 0.009	11.109 ± 0.021	4.1 ± 1.5	...	-4.439 ± 0.013
J06000+027	G 99-049	M4.0 V	PMSU	0.233 ± 0.009	6.905 ± 0.011	4.9 ± 1.5	1.814 ± 1.70e-03	-3.953 ± 0.003
J06318+414	LP 205-044	M5.0 V	PMSU	0.347 ± 0.111	9.680 ± 0.019	58.4 ± 26.1	0.299 ± 8.63e-06	-3.475 ± 0.003
J06574+740	2MASS J06572616+7405265	M4.0 V	Lep13	0.269 ± 0.007	8.926 ± 0.024	27.1 ± 2.7	...	-3.648 ± 0.004
J07446+035	YZ CMi	M4.5 V	PMSU	0.192 ± 0.031	6.581 ± 0.024	4.0 ± 1.5	2.774 ± 5.47e-04	-3.610 ± 0.001
J07472+503	2MASS J07471385+5020386	M4.0 V	Lep13	0.272 ± 0.014	8.855 ± 0.023	10.1 ± 1.5	1.316 ± 3.45e-04	-3.807 ± 0.003
J07558+833	GJ 1101	M4.5 V	AF15	0.264 ± 0.013	8.744 ± 0.026	12.1 ± 1.5	1.107 ± 4.09e-06	-3.756 ± 0.002
J08298+267	DX Cnc	M6.5 V	AF15	0.089 ± 0.009	8.235 ± 0.021	10.5 ± 1.5	0.459 ± 1.00e-05	-4.328 ± 0.007
J08536-034	LP 666-009	M9.0 V	Jen09	0.078 ± 0.008	11.212 ± 0.026	9.3 ± 2.8	0.464 ± 2.03e-04	...
J09003+218	LP 368-128	M6.5 V	AF15	0.082 ± 0.008	9.436 ± 0.020	14.3 ± 1.5	0.439 ± 0.00	-4.180 ± 0.007
J09033+056	NLTT 20861	M7.0 V	New14	0.139 ± 0.051	10.766 ± 0.024	9.7 ± 1.5	...	-4.482 ± 0.010
J09449-123	G 161-071	M5.0 V	AF15	0.167 ± 0.026	8.496 ± 0.024	31.2 ± 3.1	0.442 ± 1.88e-05	-3.378 ± 0.002

TABLE A.1: continued.

Karmn	Name	SpT	Ref.SpT [a]	Mass [b] [$M_\odot$]	J [c] [mag]	$v \sin i$ [d] [km s^{-1}]	P$_{rot}$ [e] [d]	$\log L_{\mathrm{H}\alpha}/L_{\mathrm{bol}}$ [f]
J10196+198	AD Leo	M3.0 V	AF15	0.446 ± 0.005	5.449 ± 0.027	4.35 ± 0.03*	2.240 ± 6.00e-04	-3.614 ± 0.003
J10584-107	LP 731-076	M5.0 V	AF15	0.193 ± 0.009	9.512 ± 0.023	3.2 ± 1.5	...	-4.730 ± 0.040
J11026+219	DS Leo	M1.0 V	Lep13	0.541 ± 0.027	6.522 ± 0.020	2.6 ± 1.5	13.774 ± 1.38e-02	-4.530 ± 0.012
J11201-104	LP 733-099	M2.0 V	Ria06	0.527 ± 0.004	7.814 ± 0.026	3.6 ± 1.5	5.643 ± 5.37e-03	-3.958 ± 0.004
J12156+526	StKM 2-809	M4.0 V	Lep13	0.494 ± 0.005	8.588 ± 0.024	35.3 ± 3.5	0.725 ± 1.13e-04	-3.641 ± 0.005
J12189+111	GL Vir	M5.0 V	PMSU	0.147 ± 0.009	8.525 ± 0.027	15.5 ± 1.6	0.491 ± 3.00e-05	-3.757 ± 0.004
J13005+056	FN Vir	M4.5 V	PMSU	0.196 ± 0.010	8.553 ± 0.035	16.4 ± 1.6	0.601 ± 7.44e-05	-3.762 ± 0.003
J13536+776	RX J1353.6+7737	M4.0 V	Lep13	0.295 ± 0.019	8.635 ± 0.019	8.9 ± 1.5	1.231 ± 4.77e-06	-3.808 ± 0.003
J13591-198	LP 799-007	M4.0 V	PMSU	0.262 ± 0.010	8.334 ± 0.037	3.2 ± 1.5	3.325 ± 2.88e-03	-3.897 ± 0.003
J14173+454	RX J1417.3+4525	M5.0 V	Gig10	0.272 ± 0.010	9.467 ± 0.019	15.9 ± 1.6	0.366 ± 3.32e-06	-3.934 ± 0.006
J14321+081	LP 560-035	M6.0 V	New14	0.126 ± 0.011	10.108 ± 0.024	6.3 ± 1.5	...	-4.132 ± 0.006
J15218+209	OT Ser	M1.5 V	PMSU	0.524 ± 0.108	6.610 ± 0.021	4.3 ± 1.5**	3.380 ± 1.84e-03	-3.766 ± 0.003
J15305+094	NLTT 40406	M5.5 V	AF15	0.110 ± 0.008	9.569 ± 0.025	16.3 ± 1.6	0.305 ± 6.00e-04	-3.957 ± 0.005
J15499+796	LP 022-420	M5.0 V	AF15	0.291 ± 0.010	9.721 ± 0.021	26.9 ± 2.7	0.188 ± 2.89e-07	-3.810 ± 0.005
J16313+408	G 180-060	M5.0 V	PMSU	0.158 ± 0.009	9.461 ± 0.023	7.1 ± 1.5	0.512 ± 1.83e-05	-3.651 ± 0.002
J16555-083	VB 8	M7.0 V	AF15	0.070 ± 0.008	9.776 ± 0.029	5.4 ± 1.5	**1.097 ± 2.98e-04**§	-4.404 ± 0.006
J16570-043	LP 686-027	M3.5 V	PMSU	0.254 ± 0.009	7.971 ± 0.023	10.1 ± 1.5	0.547 ± 1.00e-03	-3.691 ± 0.001
J17338+169	1RXS J173353.5+165515	M5.5 V	Lep13	0.292 ± 0.101	8.895 ± 0.027	41.5 ± 7.7	0.266 ± 4.51e-06	-3.498 ± 0.002
J18022+642	LP 071-082	M5.0 V	AF15	0.164 ± 0.010	8.541 ± 0.024	11.3 ± 1.5	0.280 ± 4.97e-07	-3.814 ± 0.005
J18131+260	LP 390-16	M4.0 V	AF15	0.333 ± 0.017	8.899 ± 0.020	5.9 ± 1.5	2.281 ± 3.69e-04	-3.616 ± 0.002
J18174+483	TYC 3529-1437-1	M2.0 V	Ria06	0.522 ± 0.108	7.770 ± 0.017	3.1 ± 1.0†	15.923 ± 4.66e-04	-4.034 ± 0.004
J18189+661	LP 71-165	M4.5 V	PMSU	0.146 ± 0.009	8.740 ± 0.021	15.3 ± 1.5	0.523 ± 1.42e-06	-4.063 ± 0.008
J18498-238	V1216 Sgr	M3.5 V	Ria06	0.176 ± 0.009	6.222 ± 0.018	3.0 ± 1.5	2.850 ± 1.00e-02	-4.001 ± 0.004
J19169+051S	V1298 Aql	M8.0 V	AF15	0.084 ± 0.009	9.908 ± 0.025	2.7 ± 2.7	23.600 ± 3.00e-01	-4.463 ± 0.008
J19255+096	LSPM J1925+0938	M8.0 V	New14	0.161 ± 0.011	11.214 ± 0.026	34.7 ± 3.5	...	-4.980 ± 0.040

TABLE A.1: continued.

Karmn	Name	SpT	Ref.SpT [a]	Mass [b] [$M_\odot$]	J [c] [mag]	$v \sin i$ [d] [km s^{-1}]	P_{rot} [e] [d]	$\log L_{H\alpha}/L_{bol}$ [f]
J19422-207	2MASS J19421282-2045477	M5.1 V	Shk09	0.209 ± 0.011	9.598 ± 0.024	6.2 ± 1.5	...	-3.760 ± 0.004
J19511+464	G 208-042	M4.0 V	PMSU	0.269 ± 0.011	8.586 ± 0.023	22.1 ± 0.9	0.593 ± 1.98e-05	-3.735 ± 0.003
J20093-012	2MASS J20091824-0113377	M5.0 V	AF15	0.144 ± 0.012	9.403 ± 0.026	4.3 ± 1.5	**3.6535 ± 1.90e-03**[§]	-3.812 ± 0.002
J22012+283	V374 Peg	M4.0 V	PMSU	0.318 ± 0.011	7.635 ± 0.026	36.9 ± 0.7	0.446 ± 1.46e-05	-3.733 ± 0.004
J22468+443	EV Lac	M3.5 V	PMSU	0.336 ± 0.012	6.106 ± 0.030	3.5 ± 1.5	4.349 ± 4.31e-03	-3.650 ± 0.002
J22518+317	GT Peg	M3.0 V	PMSU	0.346 ± 0.053	7.697 ± 0.020	13.2 ± 0.9[‡]	1.630 ± 1.00e-02	-3.555 ± 0.002
J23548+385	RX J2354.8+3831	M4.0 V	Lep13	0.313 ± 0.010	8.937 ± 0.034	3.6 ± 1.5	4.798 ± 1.46e-03	-3.859 ± 0.006

[a] **Spectral type reference codes**: AF15: Alonso-Floriano et al. (2015a), Gig10: Gigoyan et al. (2010), Jen09: Jenkins et al. (2009), Lep03: Lépine, Rich, and Shara (2003), Lep13: Lépine et al. (2013), New14: Newton et al. (2014), PMSU: Palomar/Michigan State University survey (Hawley, Gizis, and Reid, 1996), Ria06: Riaz, Gizis, and Harvin (2006), Shk09: Shkolnik, Liu, and Reid (2009);
[b] **Masses** are from: Schweitzer et al. (2019);
[c] **Magnitudes** are from: Gaia Collaboration et al. (2021);
[d] **Projected rotational velocities ($v \sin i$)** are from Reiners et al. (2018), except
[e] This work
[f] **Normalised Hα luminosities** are from Schöfer et al. (2019).

TABLE A.2: Statistical analysis results of the active RV-loud sample using the VIS data

Karmn	n_{obs} (n_{RV})	$\overline{S/N}$	T_{span}	std(RV)	$\overline{\delta RV}$		CRX-RV				P_{RV}		P_{CRX}		P_{rot}	Cat.
		@Ord82	[y]	[m s^{-1}]	[m s^{-1}]	log(p-value)	$\mathscr{R}$	m	$\lvert m/\sigma_m \rvert$	χ^2_m	P [d]	FAP [%]	P [d]	FAP [%]	[d]	
J01019+541	20 (20)	56.8	1.6	122.25 ± 19.33	48.69	-1.15	-0.25	-7.21 ± 2.59	2.79	3.78	...	...	...	...	0.14	Achrom
J01033+623	26 (26)	71.8	3.3	220.23 ± 30.54	17.62	-4.57	-0.92	-2.91 ± 0.26	11.33	2.71	1.08	11.21	1.06*	0.40	1.02	Chrom
J01352-072	11 (11)	87.4	0.4	450.50 ± 96.05	112.75	-3.06	-0.57	-5.96 ± 1.44	4.14	2.31	...	...	...	...	0.70	Chrom
J02088+494	17 (15)	108.2	1.0	87.07 ± 15.90	33.44	-1.05	0.19	5.23 ± 2.38	2.19	9.42	...	...	...	...	0.75	Achrom
J02519+224	14 (14)	96.4	1.1	369.10 ± 69.75	48.52	-0.43	0.49	1.05 ± 1.26	0.83	7.26	...	...	...	...	0.86	Achrom
J03473-019	11 (11)	115.3	0.4	26.34 ± 5.62	3.01	-0.30	-0.33	-0.16 ± 1.04	0.15	5.11	...	...	...	...	3.88	Achrom
J04198+425	35 (34)	10.3	3.8	153.39 ± 18.60	15.20	-3.59	-0.90	-3.14 ± 0.33	9.49	4.40	...	...	...	...	0.99	Chrom
J04472+206	11 (10)	56.8	0.6	137.20 ± 30.68	172.81	-0.59	-0.41	-11.14 ± 9.15	1.22	0.45	...	...	...	...	0.34	Achrom
J05019+011	29 (29)	72.7	3.4	100.52 ± 13.20	6.60	-6.21	-0.97	-3.00 ± 0.17	17.97	1.76	2.09	≤ 0.1	2.09	≤ 0.1	2.08	Chrom
J05062+046	13 (12)	80.5	1.4	94.49 ± 19.29	56.44	-1.24	0.34	3.24 ± 1.47	2.20	2.21	...	...	...	...	0.89	Achrom
J05084-210	33 (30)	44.8	5.1	512.09 ± 66.11	70.60	-0.33	-0.09	0.10 ± 0.27	0.36	3.29	...	...	...	...	0.28	Achrom
J05365+113	128 (123)	181.1	3.0	13.43 ± 0.86	1.89	-0.40	-0.25	-0.46 ± 0.18	2.58	1.95	11.76	≤ 0.1	...	...	11.51	Achrom
J05394+406	20 (15)	15.1	3.9	23.06 ± 4.21	19.44	-0.19	-0.13	-4.23 ± 9.04	0.47	2.08	...	...	...	...	...	Achrom
J06000+027	14 (14)	100.8	0.9	22.15 ± 4.19	3.18	-3.53	-0.89	-2.96 ± 0.50	5.90	1.09	...	...	...	...	1.81	Chrom
J06318+414	37 (34)	52.6	4.0	304.30 ± 36.90	85.68	-1.90	-0.53	-6.01 ± 1.14	5.27	2.53	0.30‡	1.09	0.30	≤ 0.1	0.30	Sugg
J06574+740	11 (11)	93.7	1.2	224.37 ± 47.83	41.47	-0.62	0.19	0.91 ± 0.81	1.14	1.82	...	...	...	...	...	Achrom
J07446+035	49 (49)	105.1	2.0	95.22 ± 9.62	4.69	-4.99	-0.96	-2.92 ± 0.18	16.48	4.90	2.78	≤ 0.1	2.78	≤ 0.1	2.78	Chrom
J07472+503	16 (16)	99.8	3.4	26.42 ± 4.67	6.94	-0.70	-0.33	-1.91 ± 1.10	1.75	2.22	...	...	...	...	1.32	Achrom
J07558+833	12 (12)	86.4	1.2	80.14 ± 16.36	14.37	-1.52	-0.43	-2.53 ± 0.93	2.71	3.36	...	...	...	...	1.11	Sugg
J08298+267	34 (32)	75.8	4.8	47.62 ± 5.95	6.98	-0.33	0.01	-0.14 ± 0.37	0.38	1.79	0.46	≤ 0.1	...	...	0.46	Achrom
J08536-034	45 (29)	6.8	5.1	149.51 ± 19.63	41.29	-0.37	-0.25	-1.07 ± 1.15	0.93	1.59	...	...	...	...	0.46	Achrom
J09003+218	23 (23)	40.6	4.8	26.59 ± 3.92	20.50	-0.49	-0.06	-1.92 ± 1.89	1.01	1.46	...	...	...	...	0.44	Achrom
J09033+056	32 (31)	22.2	4.0	69.85 ± 8.87	14.79	-2.52	-0.87	-2.44 ± 0.36	6.71	1.66	...	...	...	...	...	Chrom
J09449-123	11 (11)	69.0	0.5	368.39 ± 78.54	61.13	-0.39	-0.07	-0.69 ± 0.84	0.83	5.24	...	...	...	...	0.44	Achrom
J10196+198	46 (43)	88.5	1.9	23.69 ± 2.55	2.30	-3.35	-0.84	-2.81 ± 0.27	10.37	2.21	2.24	≤ 0.1	2.21	≤ 0.1	2.24	Chrom
J10584-107	50 (48)	52.6	3.2	14.00 ± 1.43	3.01	-1.97	-0.69	-3.11 ± 0.47	6.66	1.24	4.62†	≤ 0.1	4.68†	0.37	...	Sugg
J11026+219	53 (50)	151.2	2.3	13.23 ± 1.32	1.89	-1.88	-0.74	-1.48 ± 0.22	6.57	1.44	13.97	0.59	13.72	0.36	13.77	Sugg
J11201-104	28 (26)	135.7	3.9	12.91 ± 1.79	2.93	-0.98	-0.54	-1.75 ± 0.60	2.91	2.39	...	...	...	...	5.64	Achrom
J12156+526	12 (12)	93.7	1.0	316.58 ± 64.62	85.60	-4.00	0.83	6.34 ± 1.20	5.29	2.07	...	...	...	...	0.73	Chrom
J12189+111	12 (12)	82.0	1.0	46.30 ± 9.45	13.67	-1.44	-0.54	-3.45 ± 1.41	2.45	1.86	...	...	...	...	0.49	Sugg
J13005+056	12 (12)	85.0	2.4	128.15 ± 26.16	23.62	-2.51	0.89	3.52 ± 0.94	3.74	1.69	...	...	...	...	0.60	Chrom
J13536+776	24 (23)	94.5	3.9	78.84 ± 11.62	8.97	-0.36	-0.08	-0.67 ± 0.64	1.04	5.11	1.23§	≤ 0.1	...	...	1.23	Achrom
J13591-198	17 (17)	63.2	3.9	12.15 ± 2.08	3.24	-1.77	-0.58	-3.33 ± 0.95	3.49	2.59	...	...	...	...	3.32	Sugg

TABLE A.2: continued.

Karmn	$n_{\rm obs}$ ($n_{\rm RV}$)	$\overline{\rm S/N}$	$T_{\rm span}$	std(RV)	$\overline{\delta \rm RV}$	CRX-RV					$P_{\rm RV}$		$P_{\rm CRX}$		$P_{\rm rot}$	Cat.
		@Ord82	[y]	[m s^{-1}]	[m s^{-1}]	log(p-value)	$\mathscr{R}$	m	$\lvert m/\sigma_m \rvert$	χ^2_m	P [d]	FAP [%]	P [d]	FAP [%]	[d]	
J14173+454	12 (12)	56.8	1.1	103.36 ± 21.10	20.63	-0.22	-0.02	-0.26 ± 0.70	0.37	3.05	...	...	...	...	0.37	Achrom
J14321+081	58 (52)	33.7	2.4	61.40 ± 6.02	10.74	-1.99	-0.71	-4.03 ± 0.59	6.81	4.27	1.46	0.60	...	...	...	Sugg
J15218+209	52 (52)	138.4	2.8	35.75 ± 3.51	5.02	-2.71	-0.77	-3.71 ± 0.40	9.19	3.71	3.37	≤ 0.1	3.37	2.15	3.38	Chrom
J15305+094	14 (14)	52.0	1.5	143.28 ± 27.08	23.48	-3.03	0.85	2.86 ± 0.60	4.81	1.00	...	...	...	...	0.30	Chrom
J15499+796	14 (14)	50.7	0.5	521.15 ± 98.49	64.68	-1.80	0.74	2.03 ± 0.64	3.17	2.19	...	...	...	...	0.19	Sugg
J16313+408	12 (12)	54.7	1.0	60.98 ± 12.45	8.65	-2.14	-0.66	-1.89 ± 0.54	3.50	8.35	...	...	...	...	0.51	Sugg
J16555-083	122 (121)	24.8	2.5	23.91 ± 1.54	8.89	-0.40	0.07	0.64 ± 0.52	1.21	0.83	1.09	≤ 0.1	...	...	**1.1**	Achrom
J16570-043	13 (11)	121.0	1.0	22.81 ± 4.86	6.42	-0.34	-0.09	-0.08 ± 1.34	0.06	1.96	...	...	...	...	0.55	Achrom
J17338+169	12 (12)	64.2	0.9	510.09 ± 104.12	93.55	-2.03	-0.61	-2.83 ± 0.86	3.30	5.30	...	...	...	...	0.27	Sugg
J18022+642	26 (26)	83.8	2.4	53.43 ± 7.41	10.36	-0.46	-0.14	-1.22 ± 0.80	1.52	3.44	...	...	...	...	0.28	Achrom
J18131+260	16 (15)	88.0	3.8	133.53 ± 24.38	8.28	-4.40	-0.92	-2.10 ± 0.26	8.14	2.21	...	...	...	...	2.28	Chrom
J18174+483	71 (69)	143.5	2.7	11.04 ± 0.94	1.91	-2.30	-0.72	-3.38 ± 0.38	9.00	4.24	16.04	0.23	7.96	1.31	16.03	Chrom
J18189+661	12 (11)	92.8	0.8	43.46 ± 9.26	12.56	-1.25	0.51	3.11 ± 1.39	2.24	1.91	...	...	...	...	0.52	Achrom
J18498-238	53 (49)	134.4	1.0	13.35 ± 1.35	2.67	-1.45	-0.59	-2.28 ± 0.41	5.51	1.33	2.86	0.34	1.43	18.19	2.85	Sugg
J19169+051S	50 (49)	22.0	4.2	11.22 ± 1.13	5.68	-0.79	-0.17	-1.15 ± 1.37	0.84	2.56	...	...	...	...	23.60	Achrom
J19255+096	101 (84)	9.1	2.9	219.54 ± 16.94	140.30	-0.79	0.28	4.40 ± 1.15	3.83	0.85	...	...	...	...	...	Achrom
J19422-207	26 (22)	49.3	3.2	118.92 ± 17.93	9.81	-3.10	-0.83	-1.95 ± 0.30	6.48	2.20	1.34[¶]	≤ 0.1	1.34[ℑ]	13.0	...	Chrom
J19511+464	13 (13)	91.7	0.9	111.43 ± 21.85	32.70	-2.94	0.80	7.40 ± 1.84	4.02	2.38	...	...	...	...	0.59	Chrom
J20093-012	12 (12)	67.4	0.9	45.65 ± 9.32	4.47	-5.67	-0.94	-3.38 ± 0.34	10.03	0.89	...	...	...	...	**3.65**	Chrom
J22012+283	12 (11)	111.3	0.6	172.27 ± 36.73	43.56	-0.67	0.57	2.04 ± 1.60	1.27	3.06	...	...	...	...	0.45	Achrom
J22468+443	107 (106)	134.8	1.9	58.75 ± 4.04	3.80	-4.81	-0.94	-2.99 ± 0.12	24.68	2.75	2.19	≤ 0.1	2.19	≤ 0.1	4.35	Chrom
J22518+317	12 (11)	114.9	0.5	45.67 ± 9.74	13.54	-0.84	-0.22	-1.50 ± 2.36	0.64	5.14	...	...	...	...	1.63	Achrom
J23548+385	13 (13)	87.9	0.5	43.70 ± 8.57	3.11	-4.51	-0.91	-2.73 ± 0.35	7.71	2.42	...	...	...	...	4.80	Chrom

Note: Category (Cat.) refers to the classification of the CRX-RV correlation, where Achromatic (Achrom) denotes no significant correlation, Chromatic (Chrom) denotes significant correlation, and Suggestive (Sugg) denotes hints of correlation. For more details on the methodology and criteria used to classify the RV variations, please refer to Section 3.4.

(*) 1 d alias of 16.59 d with FAP $\leq 0.1\%$

(‡) Third significant signal

(†) 1 d alias of 1.27 with FAP $\leq 0.1\%$

(§) 1 d alias of 5.36 with FAP $\leq 0.1\%$

(¶) 1 d alias of 3.88 with FAP $\leq 0.1\%$

(ℑ) Most significant peak at 6.9 with FAP $\sim 3.9\%$

TABLE A.3: Statistical analysis results of the active RV-loud sample using the NIR data

Karmn	n_{obs} (n_{RV})	$\overline{S/N}$	T_{span}	std(RV)	$\overline{\delta RV}$		CRX-RV				P_{RV}		P_{CRX}		P_{rot}	Cat.
		@Ord82	[y]	[m s^{-1}]	[m s^{-1}]	log(p-value)	$\mathscr{R}$	m	$\lvert m/\sigma_m \rvert$	χ^2_m	P [d]	FAP [%]	P [d]	FAP [%]	[d]	
J01019+541	19 (18)	120.8	1.6	158.00 ± 26.33	83.23	-0.61	0.28	1.29 ± 0.91	1.42	1.63	...	...	...	...	0.14	Achrom
J01033+623	23 (20)	154.5	3.1	213.10 ± 33.69	30.42	-3.10	-0.78	-1.69 ± 0.27	6.26	1.22	1.08	13.66	1.08	0.22	1.02	Chrom
J01352-072	10 (6)	161.5	0.2	95.89 ± 27.68	177.94	-1.10	-0.35	-4.77 ± 3.50	1.36	0.67	...	...	...	...	0.70	Achrom
J02088+494	16 (12)	163.9	0.1	217.30 ± 44.36	32.98	-0.30	0.29	0.11 ± 0.17	0.65	0.65	...	...	...	...	0.75	Achrom
J02519+224	14 (11)	140.2	0.9	785.41 ± 167.45	88.29	-3.46	0.87	1.37 ± 0.28	4.96	2.10	...	...	...	...	0.86	Chrom
J03473-019	11 (7)	159.6	0.2	13.48 ± 3.60	10.19	-2.07	-0.60	-3.97 ± 1.87	2.13	1.66	...	...	...	...	3.88	Sugg
J04198+425	46 (37)	48.3	3.8	58.25 ± 6.77	17.87	-0.54	-0.30	-0.53 ± 0.38	1.40	1.97	...	...	...	...	0.99	Achrom
J04472+206	12 (5)	151.7	0.4	540.54 ± 170.93	116.38	-2.02	0.05	-3.16 ± 1.67	1.89	1.21	...	...	...	...	0.34	Sugg
J05019+011	30 (25)	136.5	**2.4**	82.02 ± 11.60	16.67	-3.23	-0.83	-1.90 ± 0.30	6.27	1.02	2.09	≤ 0.1	2.09*	0.68	2.08	Chrom
J05062+046	13 (12)	116.3	1.4	174.60 ± 35.64	98.64	-1.16	-0.15	4.38 ± 1.98	2.21	1.48	...	...	...	...	0.89	Achrom
J05084-210	32 (31)	77.6	5.1	905.75 ± 115.03	157.88	-1.17	0.50	1.29 ± 0.41	3.18	4.19	...	...	...	...	0.28	Achrom
J05365+113	119 (106)	236.7	2.2	20.10 ± 1.38	7.07	-0.43	-0.01	-0.24 ± 0.26	0.89	1.14	11.79	≤ 0.1	**19.53**	≤ 0.1	11.51	Achrom
J05394+406	33 (30)	55.2	3.9	47.36 ± 6.11	13.95	-1.17	-0.52	-1.23 ± 0.34	3.58	1.19	...	...	...	...	...	Achrom
J06000+027	13 (7)	195.8	0.1	22.69 ± 6.06	8.31	-0.60	0.09	-1.69 ± 1.73	0.98	1.99	...	...	...	...	1.81	Achrom
J06318+414	38 (36)	115.6	4.0	197.37 ± 23.26	150.72	-1.04	-0.23	-2.54 ± 0.71	3.56	1.07	...	...	...	...	0.30	Achrom
J06574+740	11 (10)	152.3	1.2	124.91 ± 27.93	84.30	-3.58	0.72	3.36 ± 0.83	4.04	2.68	...	...	...	...	...	Chrom
J07446+035	43 (28)	192.6	1.2	61.72 ± 8.25	11.07	-5.08	-0.94	-2.12 ± 0.17	12.71	0.76	2.78	≤ 0.1	2.78	≤ 0.1	2.78	Chrom
J07472+503	17 (14)	185.4	2.4	31.72 ± 5.99	17.48	-0.97	0.52	2.00 ± 1.04	1.91	1.30	...	...	...	...	1.32	Achrom
J07558+833	14 (13)	150.6	1.2	130.32 ± 25.56	40.04	-2.10	0.71	3.88 ± 1.09	3.57	3.16	...	...	...	...	1.11	Sugg
J08298+267	32 (29)	191.4	4.0	68.36 ± 8.98	12.69	-2.97	-0.81	-1.28 ± 0.17	7.73	0.54	0.46	≤ 0.1	0.46	≤ 0.1	0.46	Chrom
J08536-034	45 (43)	38.5	5.3	190.80 ± 20.57	39.20	-0.68	-0.20	-0.52 ± 0.18	2.98	1.18	0.46	10.76	...	...	0.46	Achrom
J09003+218	23 (22)	107.6	3.9	37.26 ± 5.62	26.76	-0.39	0.07	0.76 ± 0.96	0.79	0.67	...	...	...	...	0.44	Achrom
J09033+056	33 (33)	48.0	4.0	107.49 ± 13.23	82.98	-2.07	0.54	3.75 ± 1.17	3.21	1.92	...	...	...	...	...	Sugg
J09449-123	11 (11)	144.9	0.5	328.35 ± 7...	99.25	-0.65	0.37	1.17 ± 0.94	1.25	0.98	...	...	...	...	0.44	Achrom
J10196+198	46 (42)	156.4	1.9	15.70 ± 1.71	7.64	-1.00	-0.33	-1.56 ± 0.42	3.71	1.39	2.24	≤ 0.1	2.18‡	0.24	2.24	**Achrom**
J10584-107	50 (48)	99.5	3.2	13.31 ± 1.36	10.50	-0.86	-0.11	-1.77 ± 0.67	2.63	1.29	...	...	...	...	...	Achrom
J11026+219	42 (30)	219.3	1.3	12.81 ± 1.65	6.56	-1.80	-0.61	-3.15 ± 0.76	4.12	2.28	13.88	≤ 0.1	13.32	12.78	13.77	Sugg
J11201-104	28 (26)	181.7	2.2	26.02 ± 3.61	11.57	-0.62	0.29	0.04 ± 0.47	0.09	1.65	...	...	...	...	5.64	Achrom
J12156+526	12 (7)	169.8	0.2	337.71 ± 90.26	213.81	-2.32	0.66	6.48 ± 3.14	2.06	1.34	...	...	...	...	0.73	Chrom
J12189+111	11 (7)	160.0	0.2	116.32 ± 31.09	26.49	-1.76	0.85	3.52 ± 1.28	2.76	1.10	...	...	...	...	0.49	Sugg
J13005+056	9 (8)	115.3	1.0	72.87 ± 18.22	39.36	-1.35	0.69	2.38 ± 1.31	1.81	0.44	...	...	...	...	0.60	Sugg
J13536+776	25 (20)	175.2	2.8	99.43 ± 15.72	20.45	-0.78	0.38	0.88 ± 0.42	2.12	1.89	1.23§	15.24	...	...	1.23	Achrom
J13591-198	17 (14)	141.3	2.1	32.52 ± 6.15	8.84	-0.65	-0.14	-1.44 ± 0.99	1.46	2.67	...	...	...	...	3.32	Achrom

TABLE A.3: continued.

Karmn	$n_{\rm obs}$ ($n_{\rm RV}$)	$\overline{\rm S/N}$	$T_{\rm span}$	std(RV)	$\overline{\delta \rm RV}$	CRX-RV					$P_{\rm RV}$		$P_{\rm CRX}$		$P_{\rm rot}$	Cat.
		@Ord82	[y]	[m s^{-1}]	[m s^{-1}]	log(p-value)	$\mathscr{R}$	m	$\lvert m/\sigma_m \rvert$	χ^2_m	P [d]	FAP [%]	P [d]	FAP [%]	[d]	
J14173+454	10 (6)	151.4	0.1	169.26 ± 48.86	24.11	-0.87	-0.68	-0.75 ± 0.54	1.38	0.85	...	...	...	...	0.37	Achrom
J14321+081	61 (58)	71.9	2.5	37.83 ± 3.51	19.58	-0.59	0.02	-1.39 ± 0.60	2.33	2.17	1.46†	0.18	**2.03**	0.11	...	Achrom
J15218+209	52 (41)	165.6	2.2	58.17 ± 6.42	17.08	-0.34	0.09	0.35 ± 0.36	0.95	2.60	18.50	≤ 0.1	...	...	3.38	Achrom
J15305+094	14 (14)	104.4	1.5	84.68 ± 16.00	34.68	-3.21	0.76	4.14 ± 0.86	4.83	1.82	...	...	...	...	0.30	Chrom
J15499+796	16 (16)	95.9	0.5	459.11 ± 81.16	91.83	-4.70	0.92	3.20 ± 0.42	7.69	1.28	...	...	...	...	0.19	Chrom
J16313+408	9 (5)	145.1	0.2	51.09 ± 16.16	11.98	-2.22	-0.88	-1.04 ± 0.15	6.89	0.11	...	...	...	...	0.51	Sugg
J16555-083	122 (62)	90.4	1.4	22.30 ± 2.00	11.37	-1.07	-0.48	-1.51 ± 0.30	5.06	0.95	1.09¶	≤ 0.1	...	...	**1.1**	Achrom
J16570-043	13 (7)	252.0	0.1	18.15 ± 4.85	14.45	-0.99	0.43	2.90 ± 2.84	1.02	0.85	...	...	...	...	0.55	Achrom
J17338+169	12 (5)	167.1	0.1	330.75 ± 104.59	62.82	-0.47	0.03	-0.93 ± 1.46	0.64	1.19	...	...	...	...	0.27	Achrom
J18022+642	28 (20)	164.2	1.8	95.84 ± 15.15	23.54	-0.53	-0.05	-0.92 ± 0.64	1.43	2.47	...	...	...	...	0.28	Achrom
J18131+260	15 (13)	136.8	3.2	63.28 ± 12.41	18.38	-2.96	-0.74	-2.04 ± 0.43	4.74	0.85	...	...	...	...	2.28	Chrom
J18174+483	71 (60)	225.2	2.2	17.27 ± 1.58	7.60	-0.88	-0.20	-2.06 ± 0.52	3.95	1.96	16.13	5.62	...	...	16.03	Achrom
J18189+661	12 (6)	161.7	0.4	40.13 ± 11.58	32.83	-0.72	0.64	10.76 ± 6.80	1.58	0.73	...	...	...	...	0.52	Achrom
J18498-238	53 (48)	148.8	1.0	23.10 ± 2.36	10.46	-1.45	-0.53	-2.04 ± 0.38	5.34	0.71	**21.03**	3.82	...	...	2.85	**Sugg**
J19169+051S	50 (32)	92.8	3.4	12.31 ± 1.54	7.95	-0.79	-0.06	-0.54 ± 0.68	0.80	1.80	...	...	...	...	23.60	Achrom
J19255+096	104 (96)	43.3	2.9	263.27 ± 19.00	133.19	-1.48	0.61	2.94 ± 0.39	7.45	1.00	...	...	...	...	...	Sugg
J19422-207	24 (22)	89.2	3.2	72.34 ± 10.91	22.77	-0.60	-0.28	-0.79 ± 0.44	1.79	1.89	1.34	3.11	...	...	...	Achrom
J19511+464	13 (7)	110.9	0.1	328.50 ± 87.80	90.55	-5.64	0.85	6.81 ± 1.40	4.86	0.83	...	...	...	...	0.59	Chrom
J20093-012	13 (6)	148.8	0.6	17.15 ± 4.95	9.12	-5.73	-0.89	-6.21 ± 1.45	4.28	0.58	...	...	...	...	**3.65**	Chrom
J22012+283	12 (5)	177.9	0.0	126.38 ± 39.97	73.75	-0.53	0.00	1.37 ± 3.59	0.38	2.19	...	...	...	...	0.45	Achrom
J22468+443	109 (74)	177.1	1.1	41.08 ± 3.38	12.60	-2.36	-0.74	-2.13 ± 0.21	9.94	0.83	2.19	≤ 0.1	2.19	≤ 0.1	4.35	Chrom
J22518+317	11 (4)	192.9	0.2	9.54 ± 3.37	27.15	-0.73	-0.07	-0.54 ± 3.56	0.15	1.10	...	...	...	...	1.63	Achrom
J23548+385	11 (4)	172.7	0.1	18.39 ± 6.50	8.69	-5.26	-0.96	-3.21 ± 0.87	3.69	1.01	...	...	...	...	4.80	Chrom

Note: The classifications are similar to those in Table A.2.

TABLE A.4: Periods and FAPs of the best signals for individual VIS orders, with FAPs at $P_{\rm rot}$ and $\frac{1}{2}P_{\rm rot}$ for EV Lac (J22468+443)

Order #	Best Signal		$P_{\rm rot} = 4.362$	$\frac{1}{2}P_{\rm rot} = 2.188$
	P [d]	FAP	FAP	FAP
108	2.188	5.6e-21	2.1e-01	5.8e-21
107	2.188	4.3e-17	3.4e-02	4.3e-17
106	2.188	1.1e-14	1.1e-02	1.2e-14
105	2.188	2.1e-20	2.1e-01	2.1e-20
104	2.188	5.4e-22	7.2e-01	5.7e-22
103	2.188	2.2e-24	1.0e+00	2.3e-24
102	2.188	2.5e-25	9.7e-01	2.5e-25
101	2.188	2.3e-18	2.2e-01	2.8e-18
100	2.188	2.0e-19	6.4e-02	3.1e-19
99	2.188	2.1e-23	3.0e-01	2.1e-23
98	2.188	2.9e-24	9.3e-01	2.9e-24
97	2.188	3.9e-24	7.5e-01	4.3e-24
96	2.188	1.5e-23	1.5e-01	1.5e-23
95	2.188	4.9e-18	1.5e-03	5.1e-18
94	2.188	4.5e-15	9.0e-04	4.8e-15
93	2.188	1.4e-16	2.2e-03	1.4e-16
92	2.188	2.0e-22	4.5e-02	2.1e-22
91	2.188	7.2e-23	6.2e-02	7.2e-23
90	2.188	2.4e-23	5.2e-02	2.7e-23
89	2.188	3.2e-23	4.9e-02	3.3e-23
88	2.188	8.6e-20	1.6e-02	9.0e-20
87	2.188	1.1e-19	2.9e-02	1.1e-19
86	2.188	2.6e-22	1.8e-02	2.6e-22
85	2.188	5.2e-21	4.3e-02	5.2e-21
84	2.188	7.5e-13	1.1e-02	7.9e-13
83	2.188	2.9e-11	1.5e-04	2.9e-11
82	2.188	5.0e-10	6.2e-08	5.4e-10
81	4.355	4.4e-11	3.6e-10	8.7e-09
80	2.188	1.2e-15	1.5e-05	1.9e-15
79	2.188	4.8e-14	7.2e-06	4.8e-14
78	2.188	1.6e-10	3.6e-06	1.6e-10
77	2.188	8.9e-09	1.4e-03	9.8e-09
76	4.359	8.5e-04	9.3e-04	5.2e-01
75	59.446	6.3e-04	4.1e-01	1.1e-02
74	52.579	1.8e-07	1.0e+00	1.0e+00
73	2.188	8.5e-09	7.4e-05	8.5e-09
72	4.357	2.2e-04	5.5e-04	2.9e-02
71	2.188	1.0e-05	5.0e-05	1.1e-05
70	2.189	3.8e-13	9.9e-04	5.1e-13
69	2.190	3.3e-03	8.3e-01	9.4e-03
68	52.816	1.8e-03	1.0e+00	1.0e+00
67	25.759	4.7e-05	1.0e+00	1.0e+00

TABLE A.5: Same as Table A.4, but for the near-IR spectral orders of EV Lac

Order #	Best Signal		$P_{\rm rot} = 4.362$	$\frac{1}{2}P_{\rm rot} = 2.188$
	P [d]	FAP	FAP	FAP
63 L	325.721	1.5e-08	1.0e+00	1.0e+00
62 R	2.189	1.6e-08	1.0e+00	1.6e-08
61 L	2.190	1.4e-03	2.0e-01	1.6e-03
61 R	2.186	7.0e-04	1.6e-01	1.4e-03
60 L	2.191	5.9e-04	1.3e-02	8.3e-04
60 R	2.188	2.8e-05	5.3e-02	3.3e-05
59 L	2.189	2.3e-06	9.8e-01	2.4e-06
59 R	2.190	4.8e-05	9.3e-01	6.0e-05
58 L	32.190	1.0e-02	9.9e-01	2.4e-02
58 R	2.1882	1.3e-03	1.0e+00	1.5e-03
56 L	32.499	3.4e-06	1.0e+00	1.0e+00
56 R	62.371	2.2e-05	1.0e+00	1.0e+00
49 L	...	...	...	...
49 R	...	...	...	...
48 L	33.190	6.8e-05	1.0e+00	3.4e-01
40 R	239.286	4.8e-05	1.0e+00	1.0e+00
39 L	50.685	1.6e-09	1.0e+00	1.0e+00
38 R	219.840	3.8e-07	1.0e+00	1.0e+00
37 L	10.123	2.2e-02	8.4e-01	1.0e+00

TABLE A.6: Activity-related periods and FAPs for the activity indicators of EV Lac

Indicator	Order	Best Signal		$P_{\rm rot}$∼4.36	$\frac{1}{2}P_{\rm rot}$∼2.19
	#	P [d]	FAP[%]	FAP[%]	FAP[%]
He I D_3 [Å]	104	...	...	...	...
Na I D_2 [Å]	104/ 103	...	...	...	...
Na I D_1 [Å]	104/ 103	...	...	...	...
Hα [Å]	93	3.709	4.78	11.45	...
Ca II IRT-a [Å]	72	3.742	15.58	49.52	...
Ca II IRT-b [Å]	72/ 71	3.742	15.76	41.46	...
Ca II IRT-c [Å]	71/ 70	3.742	13.53	43.93	...
Fe 8691 [Å]	70	...	...	...	...
He 10833 [Å]	56 L	2.191	0.74	...	...
Paβ^* [Å]	48 R	2.336	18.86	...	...
CaH 2	90/ 89	...	...	...	...
CaH 3	88/ 87	2.192	0.39	1.37	0.39
TiO 7050	87/ 86	4.360	1.21e-06	1.21e-06	5.87e-03
TiO 8430	73/ 72	4.362	0.61	0.61	...
TiO 8860	69	9.386	0.84	...	...
VO 7436	82	...	...	...	...
VO 7942	77	...	...	...	...
FeH WFB	62 R	9.377	0.78	...	...

TABLE A.7: Same as Table A.4, but for the full dataset of TYC 3529-1437-1 (J18174+483).

Order #	Best Signal		$P_{\rm rot} = 16.037$	$\frac{1}{2}P_{\rm rot} = 8.104$
	P [d]	FAP	FAP	FAP
108	15.958	2.3e-01	8.6e-01	5.4e-01
107	1.534	1.4e-02	1.0e+00	1.0e+00
106	...	...	...	...
105	7.952	3.4e-02	1.0e+00	1.0e+00
104	2.588	1.6e-02	2.0e-01	1.0e+00
103	2.175	7.8e-02	7.2e-01	1.0e+00
102	...	...	...	...
101	7.955	1.7e-02	4.3e-01	1.0e+00
100	15.994	1.1e-03	2.9e-03	1.0e+00
99	7.959	5.5e-03	1.4e-01	4.4e-02
98	16.001	1.0e-02	1.6e-02	9.7e-01
97	7.955	2.0e-04	3.4e-01	6.1e-01
96	15.976	1.6e-02	3.2e-02	7.6e-01
95	1.196	5.8e-02	4.0e-01	7.5e-01
94	1.141	8.0e-03	7.8e-01	2.1e-01
93	16.133	2.3e-02	3.0e-01	9.1e-01
92	15.984	6.5e-03	1.5e-02	9.7e-01
91	...	...	...	...
90	7.954	5.7e-02	1.3e-01	1.7e-01
89	8.094	7.3e-02	1.3e-01	1.0e-01
88	15.996	9.3e-03	1.5e-02	1.4e-01
87	16.094	3.0e-02	7.4e-02	8.6e-02
86	16.063	2.3e-04	3.1e-04	9.7e-03
85	16.032	6.5e-02	6.5e-02	1.7e-01
84	...	...	...	...
83	...	...	...	...
82	1.063	3.5e-02	5.9e-01	5.7e-01
81	16.060	2.1e-03	2.7e-03	1.0e+00
80	...	...	...	...
79	8.093	4.8e-03	9.5e-01	9.5e-03
78	1.059	5.3e-02	1.0e-01	1.0e+00
77	...	...	...	...
76	1.003	2.6e-02	1.0e+00	1.0e+00
75	...	...	...	...
74	1.000	2.7e-06	1.0e+00	1.0e+00
73	2.404	6.2e-02	1.0e+00	9.8e-01
72	1.621	6.0e-02	1.0e+00	1.0e+00
71	...	...	...	...
70	16.050	5.6e-02	5.7e-02	2.2e-01
69	...	...	...	...
68	330.268	1.1e-04	1.0e+00	1.0e+00
67	1.005	5.9e-08	1.0e+00	1.0e+00

TABLE A.8: Same as Table A.4, but for the full dataset of TYC 3529-1437-1 (J18174+483).

Indicator	Order #	Best Signal P [d]	FAP[%]	$P_{\rm rot} = 16.037$ FAP[%]	$\frac{1}{2}P_{\rm rot} = 8.104$ FAP[%]
He I D_3 [Å]	104	...	...	...	...
Na I D_2 [Å]	104/ 103	...	...	...	...
Na I D_1 [Å]	104/ 103	...	...	...	...
Hα [Å]	93	2.049	0.62	8.34	...
Ca II IRT-a [Å]	72	1.067	3.62	43.61	...
Ca II IRT-b [Å]	72/ 71	1.067	2.34	27.31	...
Ca II IRT-c [Å]	71/ 70	1.067	2.93	30.18	...
Fe 8691 [Å]	70	1.41	1.00	...	...
He 10833 [Å]	56 L	...	...	...	...
Paβ [Å]	48 R	...	...	...	...
CaH 2	90/ 89	...	...	...	...
CaH 3	88/ 87	4.641	1.88	...	39.27
TiO 7050	87/ 86	...	...	...	...
TiO 8430	73/ 72	...	...	...	...
TiO 8860	69	...	...	...	...
VO 7436	82	...	...	...	...
VO 7942	77	1.357	0.13	...	...
FeH WFB	62 R	...	...	...	...

TABLE A.9: Same as Table A.4, but for the first subset of TYC 3529-1437-1 (J18174+483).

Order #	Best Signal		$P_{\rm rot} = 15.962$
	P [d]	FAP	FAP
108	...	...	...
107	1.027	2.7e-02	1.0e+00
106	15.912	3.8e-02	9.6e-02
105	15.924	1.1e-02	2.2e-02
104	...	...	3.4e-01
103	15.941	1.0e-02	1.2e-02
102	...	...	...
101	15.921	1.3e-01	2.3e-01
100	15.962	5.1e-03	5.1e-03
99	15.927	4.3e-03	7.0e-03
98	15.959	4.7e-03	4.8e-03
97	15.941	2.9e-03	3.7e-03
96	15.944	5.8e-04	6.9e-04
95	15.977	5.8e-03	6.6e-03
94	15.965	3.9e-03	4.0e-03
93	15.965	9.8e-04	9.9e-04
92	15.935	5.6e-05	9.6e-05
91	15.959	1.6e-02	1.6e-02
90	15.938	2.6e-03	3.3e-03
89	15.935	1.4e-02	1.8e-02
88	15.953	1.2e-04	1.3e-04
87	15.974	1.4e-02	1.5e-02
86	15.962	2.8e-04	2.8e-04
85	15.986	3.2e-02	3.7e-02
84	...	...	...
83	...	...	...
82	16.977	4.0e-02	2.1e-01
81	16.121	1.3e-03	1.0e-01
80	15.980	7.8e-02	8.5e-02
79	16.221	3.9e-01	9.5e-01
78	16.184	8.5e-02	9.9e-01
77	...	...	...
76	2.177	3.3e-02	1.0e+00
75	2.489	6.3e-02	1.0e+00
74	1.005	8.1e-02	1.0e+00
73	...	...	...
72	1.356	6.9e-02	1.0e+00
71	1.801	5.8e-03	1.0e+00
70	15.950	1.2e-03	1.3e-03
69	...	...	...
68	...	...	...
67	3.789	5.1e-02	1.0e+00

TABLE A.10: Same as Table A.6, but for the first subset of TYC 3529-1437-1 (J18174+483).

Indicator	Order	Best Signal		$P_{\rm rot} = 15.962$
	#	P [d]	FAP[%]	FAP[%]
He I D_3 [Å]	104	16.034	1.7	6.5
Na I D_2 [Å]	104/ 103	...	...	...
Na I D_1 [Å]	104/ 103	...	...	...
Hα [Å]	93	16.031	3.6e-03	1.6e-02
Ca II IRT-a [Å]	72	15.921	0.83	0.97
Ca II IRT-b [Å]	72/ 71	15.912	0.20	0.25
Ca II IRT-c [Å]	71/ 70	15.897	0.30	0.50
Fe 8691 [Å]	70	...	...	...
He 10833 [Å]	56 L	...	...	...
Paβ [Å]	48 R	...	...	...
CaH 2	90/ 89	...	...	...
CaH 3	88/ 87	...	...	...
TiO 7050	87/ 86	16.069	1.4e-05	0.36
TiO 8430	73/ 72	...	...	...
TiO 8860	69	...	...	...
VO 7436	82	...	...	...
VO 7942	77	...	...	...
FeH WFB	62 R	...	...	...

TABLE A.11: Same as Table A.4, but for the second subset of TYC 3529-1437-1 (J18174+483).

Order #	Best Signal		$P_{\rm rot} = 8.043$
	P [d]	FAP	FAP
108	1.559	1.0e-02	3.4e-01
107	7.933	1.7e-03	2.4e-02
106	8.024	2.1e-02	2.3e-02
105	7.978	3.5e-02	4.6e-02
104	7.974	5.3e-04	1.7e-03
103	8.029	9.1e-02	9.4e-02
102	7.938	6.3e-03	2.6e-02
101	8.024	1.4e-03	1.5e-03
100	7.956	2.7e-02	7.1e-02
99	7.969	1.5e-07	5.3e-06
98	7.988	1.9e-05	6.3e-05
97	8.001	3.8e-05	8.6e-05
96	8.001	1.2e-06	3.0e-06
95	8.011	1.6e-02	1.9e-02
94	8.123	1.3e-03	3.8e-03
93	7.974	3.8e-01	5.0e-01
92	7.988	1.0e-05	3.7e-05
91	8.024	3.4e-05	4.1e-05
90	8.057	2.1e-07	2.5e-07
89	8.024	3.9e-07	4.5e-07
88	8.034	8.6e-07	9.1e-07
87	8.048	1.6e-06	1.6e-06
86	8.066	7.5e-08	1.2e-07
85	8.015	5.2e-05	7.6e-05
84	8.076	2.1e-01	2.3e-01
83	...	...	...
82	8.020	1.7e-02	1.9e-02
81	8.029	9.1e-02	9.5e-02
80	8.146	2.1e-01	5.5e-01
79	1.144	9.4e-02	9.1e-01
78	...	...	...
77	...	...	...
76	78.773	3.0e-02	1.0e+00
75	3.696	2.2e-02	1.0e+00
74	1.003	2.0e-02	1.0e+00
73	1.145	2.3e-02	5.7e-01
72	1.625	8.9e-03	1.0e+00
71	...	...	...
70	1.135	3.5e-03	1.8e-02
69	1.546	1.0e-02	1.0e+00
68	...	...	..
67	72.997	2.7e-06	1.0e+00

TABLE A.12: Activity-related periods and FAPs for the near-IR spectral orders of TYC 3529-1437-1 (Subset 2)

Order #	Best Signal		$P_{\rm rot}$ = 8.029
	P [d]	FAP	FAP
63 L	...	...	...
62 R	36.208	5.6e-02	1.8e-01
61 L	...	...	...
61 R	...	...	...
60 L	...	...	...
60 R	...	...	...
59 L	1.146	8.5e-04	1.5e-02
59 R	...	...	...
58 L	8.123	2.0e-03	2.7e-02
58 R	...	...	...
56 L	5.294	8.2e-02	1.0e+00
56 R	170.103	7.6e-03	1.0e+00
49 L	...	...	...
49 R	4.462	1.3e-02	9.9e-01
48 L	...	...	...
40 R	...	...	...
39 L	...	...	...
38 R	...	...	...
37 L	1.019	4.4e-02	1.0e+00

TABLE A.13: Same as Table A.6, but for the second subset of TYC 3529-1437-1 (J18174+483).

Indicator	Order	Best Signal		$P_{\rm rot}$ = 8.043
	#	P [d]	FAP[%]	FAP[%]
He I D_3 [Å]	104	...	...	...
Na I D_2 [Å]	104/ 103	...	...	...
Na I D_1 [Å]	104/ 103	...	...	...
Hα [Å]	93	...	...	...
Ca II IRT-a [Å]	72	...	...	...
Ca II IRT-b [Å]	72/ 71	...	...	...
Ca II IRT-c [Å]	71/ 70	...	...	...
Fe 8691 [Å]	70	...	...	...
He 10833 [Å]	56 L	...	...	...
Paβ [Å]	48 R	...	...	...
CaH 2	90/ 89	...	...	...
CaH 3	88/ 87	...	...	...
TiO 7050	87/ 86	7.835	5.0	...
TiO 8430	73/ 72	...	...	...
TiO 8860	69	...	...	...
VO 7436	82	...	...	...
VO 7942	77	...	...	...
FeH WFB	62 R	...	...	...

TABLE A.14: Same as Table A.4, but for OT Ser (J15218+209).

Order #	Best Signal		$P_{\rm rot} = 3.372$
	P [d]	FAP	FAP
108	3.374	1.9e-08	1.8e-07
107	3.374	3.6e-08	8.5e-07
106	3.374	3.9e-08	6.2e-06
105	3.371	9.7e-10	3.7e-09
104	3.373	2.1e-08	2.4e-07
103	3.374	5.7e-08	1.7e-06
102	3.373	6.8e-09	5.7e-08
101	3.374	6.8e-09	3.0e-07
100	3.373	8.4e-09	6.2e-08
99	3.374	9.5e-08	1.1e-06
98	3.374	1.5e-08	6.8e-07
97	3.374	7.7e-10	4.0e-08
96	3.373	1.5e-08	1.4e-07
95	3.373	1.6e-08	3.3e-08
94	3.373	7.4e-05	2.4e-04
93	3.374	1.4e-08	3.5e-06
92	3.372	1.2e-07	1.7e-07
91	3.374	1.7e-09	4.1e-08
90	3.373	2.2e-08	1.0e-07
89	3.373	3.0e-09	1.2e-08
88	3.373	3.2e-09	9.8e-09
87	3.373	1.5e-07	2.6e-07
86	3.373	1.2e-07	2.4e-07
85	3.373	1.2e-08	1.0e-07
84	1.058	3.8e-02	8.2e-02
83	3.550	1.4e-03	2.7e-02
82	3.372	6.5e-10	7.2e-10
81	3.409	1.6e-04	1.8e-03
80	1.000	2.5e-01	1.0e+00
79	1.718	2.6e-01	1.0e+00
78	1.082	7.9e-01	1.0e+00
77	35.146	6.8e-04	9.6e-01
76	18.383	3.9e-04	1.0e+00
75	19.356	1.2e-03	1.0e+00
74	12.625	5.1e-04	1.0e+00
73	3.374	1.0e-07	2.4e-06
72	1.421	4.4e-03	3.0e-01
71	1.486	1.0e-03	1.4e-02
70	3.373	8.5e-10	1.6e-08
69	2.994	9.6e-02	8.7e-01
68	73.780	1.6e-05	1.0e+00
67	73.672	1.9e-06	1.0e+00

TABLE A.15: Same as Table A.6, but for OT Ser (J15218+209).

Indicator	Order #	Best Signal P [d]	Best Signal FAP[%]	$P_{\rm rot}$∼3.372 FAP[%]	
He I D_3 [Å]	104	...	...	...	
Na I D_2 [Å]	104/ 103	...	...	...	
Na I D_1 [Å]	104/ 103	...	...	...	
Hα [Å]	93	...	...	...	
Ca II IRT-a [Å]	72	...	...	...	
Ca II IRT-b [Å]	72/ 71	...	...	...	
Ca II IRT-c [Å]	71/ 70	...	...	...	
Fe 8691 [Å]	70	...	...	...	
He 10833 [Å]	56 L	...	...	...	
Paβ [Å]	48 R	...	...	...	
CaH 2	90/ 89	...	...	...	
CaH 3	88/ 87	1.375	1.1e-02	...	
TiO 7050	87/ 86	1.415	6.4e-02	...	
TiO 8430	73/ 72	1.415	6.1	...	
TiO 8860	69	...	...	...	
VO 7436	82	...	...	...	...
VO 7942	77	1.415	1.8	...	
FeH WFB	62 R	...	...	...	

TABLE A.16: Same as Table A.4, but for DS Leo (J11026+219).

Order #	Best Signal		$P_{\rm rot}$ = 13.970	$P_{\rm rot}$ = 13.723
	P [d]	FAP	FAP	FAP
108	13.746	3.3e-02	1.6e-01	5.7e-02
107	13.984	1.2e-02	1.4e-02	1.5e-02
106	13.995	2.0e-03	4.5e-03	1.7e-01
105	...	...	...	...
104	13.993	1.5e-01	2.2e-01	4.2e-01
103	13.910	2.4e-04	3.6e-02	8.5e-01
102	14.004	3.6e-03	1.4e-02	8.9e-03
101	13.719	4.7e-03	6.8e-01	4.8e-03
100	13.726	7.4e-03	1.1e-02	7.4e-03
99	13.974	1.6e-03	1.6e-03	3.2e-03
98	13.984	8.9e-04	1.0e-03	1.7e-02
97	14.016	3.6e-04	9.0e-03	2.8e-03
96	13.721	7.9e-04	1.5e-03	7.9e-04
95	14.002	9.3e-03	2.5e-02	2.6e-02
94	13.755	8.8e-02	6.4e-01	2.3e-01
93	14.011	2.6e-02	1.1e-01	1.5e-01
92	6.886	2.1e-03	1.0e+00	7.5e-02
91	13.968	3.5e-02	3.5e-02	1.0e-01
90	13.984	2.2e-04	2.8e-04	8.3e-04
89	13.974	1.2e-03	1.2e-03	7.1e-03
88	13.963	1.1e-02	1.2e-02	1.6e-01
87	13.149	5.6e-02	2.4e-01	6.5e-02
86	13.732	1.6e-03	8.3e-02	1.8e-03
85	1.077	5.6e-03	1.0e+00	6.7e-01
84	45.726	4.1e-02	1.0e+00	1.0e+00
83	2.197	4.5e-02	5.3e-01	1.6e-01
82	1.077	9.0e-03	7.9e-02	6.9e-01
81	1.136	2.3e-02	2.0e-01	9.8e-01
80	1.707	2.8e-02	1.0e+00	1.0e+00
79	1.708	2.3e-02	1.0e+00	1.0e+00
78	1.254	1.9e-02	1.0e+00	1.0e+00
77	...	...	...	...
76	11.678	2.0e-02	9.5e-01	1.0e+00
75	1.008	9.0e-02	8.8e-01	1.0e+00
74	...	...	...	...
73	1.075	2.2e-02	6.7e-01	9.2e-02
72	1.770	2.6e-02	1.0e+00	1.0e+00
71	13.986	2.9e-02	3.2e-02	1.5e-01
70	13.737	3.8e-03	6.8e-02	5.3e-03
69	...	...	...	...
68	1.614	5.3e-02	1.0e+00	1.0e+00
67	...	...	...	...

TABLE A.17: Same as Table A.5, but for the near-IR spectral orders of DS Leo (J11026+219).

Order #	Best Signal P [d]	FAP	$P_{\rm rot}$ = 13.883 FAP
63 L	6.134	4.8e-02	9.8e-01
62 R	...	...	...
61 L	1.077	4.9e-02	5.8e-01
61 R	...	...	...
60 L	...	...	...
60 R	...	...	...
59 L	13.848	8.0e-04	1.4e-03
59 R	13.723	1.4e-02	8.3e-01
58 L	13.867	2.9e-04	3.4e-04
58 R	13.855	3.0e-03	4.0e-03
56 L	13.859	1.2e-02	1.6e-02
56 R	...	...	...
49 L	6.920	5.2e-02	1.0e+00
49 R	4.593	2.9e-02	1.0e+00
48 L	...	...	...
40 R	...	...	...
39 L	...	...	...
38 R	...	...	...
37 L	...	...	...

TABLE A.18: Same as Table A.6, but for DS Leo (J11026+219).

Indicator	Order #	Best Signal P [d]	FAP[%]	$P_{\rm rot}$∼13.723 FAP[%]
He I D_3 [Å]	104	...	...	...
Na I D_2 [Å]	104/ 103	...	...	...
Na I D_1 [Å]	104/ 103	...	...	...
Hα [Å]	93	6.867	2.9	...
Ca II IRT-a [Å]	72	6.867	4.3	...
Ca II IRT-b [Å]	72/ 71	6.865	0.4	...
Ca II IRT-c [Å]	71/ 70	6.868	3.18	...
Fe 8691 [Å]	70	...	...	...
He 10833 [Å]	56 L	...	...	...
Paβ [Å]	48 R	6.814	6.9	...
CaH 2	90/ 89	...	...	...
CaH 3	88/ 87	14.67	5.4	...
TiO 7050	87/ 86	13.974	0.6	0.63
		6.898	1.1	0.63
TiO 8430	73/ 72	...	...	...
TiO 8860	69	...	...	...
VO 7436	82	...	...	...
VO 7942	77	...	...	...
FeH WFB	62 R	...	...	...

TABLE A.19: Same as Table A.4, but for YZ CMi (J07446+035).

Order #	Best Signal		$P_{\rm rot} = 2.776$
	P [d]	FAP	FAP
108	2.776	2.8e-14	2.9e-14
107	2.776	2.2e-14	2.3e-14
106	2.776	9.4e-11	1.1e-10
105	2.776	2.5e-15	3.2e-15
104	2.776	7.5e-08	7.5e-08
103	2.776	1.2e-16	1.2e-16
102	2.776	3.1e-16	3.8e-16
101	2.776	4.3e-16	6.0e-16
100	2.776	4.1e-14	5.5e-14
99	2.776	2.5e-15	2.8e-15
98	2.776	2.5e-15	2.6e-15
97	2.776	6.7e-18	7.7e-18
96	2.776	1.4e-17	1.4e-17
95	2.776	2.6e-17	3.0e-17
94	2.777	5.8e-16	1.3e-15
93	2.776	3.2e-16	3.3e-16
92	2.776	8.9e-19	9.3e-19
91	2.776	9.3e-18	9.3e-18
90	2.776	1.3e-20	1.7e-20
89	2.776	1.3e-18	1.3e-18
88	2.776	6.8e-19	8.1e-19
87	2.776	4.6e-21	4.9e-21
86	2.776	3.9e-19	4.1e-19
85	2.776	7.6e-19	1.2e-18
84	2.777	8.5e-20	1.8e-19
83	2.776	3.8e-20	3.8e-20
82	2.776	7.7e-21	8.2e-21
81	2.777	2.5e-21	9.9e-21
80	2.776	1.5e-19	2.5e-19
79	2.777	2.0e-21	4.9e-21
78	2.777	3.4e-20	1.3e-19
77	2.776	5.3e-19	9.0e-19
76	2.776	1.6e-13	1.6e-13
75	2.777	2.8e-11	6.4e-11
74	2.777	1.6e-03	3.0e-03
73	2.776	2.6e-13	2.8e-13
72	2.777	9.6e-12	3.4e-11
71	2.777	1.3e-14	6.9e-14
70	2.776	2.5e-19	2.6e-19
69	2.777	8.4e-12	2.2e-10
68	1.718	5.4e-02	4.2e-01
67	...	...	...

TABLE A.20: Same as Table A.5, but for the near-IR spectral orders of YZ CMi (J07446+035).

Order #	Best Signal P [d]	FAP	$P_{\rm rot} = 2.776$ FAP
63 L	...	...	...
62 R	2.776	2.9e-12	3.6e-12
61 L	2.776	6.0e-11	6.0e-11
61 R	2.777	1.8e-09	5.6e-09
60 L	2.777	3.4e-10	7.7e-10
60 R	2.776	2.0e-06	2.2e-06
59 L	2.776	1.7e-10	1.7e-10
59 R	2.776	1.1e-11	1.1e-11
58 L	2.777	7.2e-06	9.9e-06
58 R	2.778	2.3e-06	2.4e-05
56 L	2.775	1.2e-03	1.6e-03
56 R	...	...	...
49 L	2.780	7.7e-03	3.7e-02
49 R	2.772	3.0e-02	4.7e-01
48 L	1.556	5.1e-02	4.0e-01
40 R	...	...	...
39 L	...	...	...
38 R	1.557	2.5e-03	3.8e-02
37 L	2.759	3.1e-03	1.2e-01

TABLE A.21: Same as Table A.6, but for YZ CMi (J07446+035).

Indicator	Order #	Best Signal P [d]	FAP[%]	$P_{\rm rot}\sim2.776$ FAP[%]
He I D_3 [Å]	104	...	...	...
Na I D_2 [Å]	104/ 103	...	...	...
Na I D_1 [Å]	104/ 103	...	...	...
Hα [Å]	93	...	...	...
Ca II IRT-a [Å]	72	...	...	...
Ca II IRT-b [Å]	72/ 71	...	...	...
Ca II IRT-c [Å]	71/ 70	...	...	...
Fe 8691 [Å]	70	...	...	...
He 10833 [Å]	56 L	...	...	...
Paβ [Å]	48 R	...	...	...
CaH 2	90/ 89	...	...	...
CaH 3	88/ 87	2.774	2.5e-05	5.12e-04
TiO 7050	87/ 86	2.775	6.1e-16	5.11e-14
TiO 8430	73/ 72	2.775	1.3e-09	1.80e-8
TiO 8860	69	2.799	6.85	...
VO 7436	82	2.778	6.5e-04	8.17e-03
VO 7942	77	...	...	...
FeH WFB	62 R	2.806	5.1	...

TABLE A.22: Same as Table A.4, but for V2689 Ori (J05365+113).

Order #	Best Signal		$P_{\rm rot} = 11.761$
	P [d]	FAP[%]	FAP[%]
108	11.890	7.6e-04	1.4e-03
107	11.886	1.9e-05	7.4e-03
106	11.772	1.3e-04	2.0e-04
105	...	...	...
104	11.753	3.7e-03	4.2e-03
103	11.767	1.3e-04	1.5e-04
102	11.760	...	2.3e-04
101	11.758	...	4.5e-05
100	11.750	5.0e-07	1.2e-06
99	11.774	4.1e-06	5.6e-06
98	11.753	4.4e-12	6.6e-12
97	11.877	2.4e-06	6.3e-05
96	11.745	1.1e-05	4.3e-05
95	11.776	4.8e-07	1.1e-06
94	11.880	4.4e-08	1.4e-04
93	11.746	5.4e-05	1.0e-04
92	11.745	3.6e-07	1.7e-06
91	11.871	6.9e-04	1.1e-03
90	11.757	1.1e-08	1.2e-08
89	11.765	5.2e-08	5.4e-08
88	11.766	3.7e-05	4.1e-05
87	11.767	...	8.5e-02
86	11.762	4.9e-05	4.9e-05
85	11.784	9.4e-05	4.7e-04
84	120.294	7.8e-06	1.0e+00
83	11.771	7.7e-07	1.2e-06
82	11.755	1.2e-05	1.3e-05
81	11.753	...e-04	3.8e-04
80	345.829	1.1e-03	1.0e+00
79	...	...	...
78	119.384	2.3e-05	1.0e+00
77	120.294	3.2e-03	5.0e-01
76	72.810	1.1e-04	6.5e-01
75	120.556	1.0e-06	1.0e+00
74	36.220	3.0e-02	1.0e+00
73	11.785	1.3e-03	5.3e-03
72	11.886	1.7e-05	1.2e-03
71	11.893	...	8.7e-02
70	11.765	7.0e-08	7.4e-08
69	24.972	3.9e-02	2.6e-01
68	60.658	1.5e-03	1.0e+00
67	90.751	1.1e-05	1.0e+00

TABLE A.23: Same as Table A.5, but for the near-IR spectral orders of V2689 Ori (J05365+113).

Order #	Best Signal		$P_{\rm rot}$ = 11.790
	P [d]	FAP	FAP
63 L	121.318	9.6e-06	1.0e+00
62 R	12.490	1.7e-02	1.0e+00
61 L	33.214	2.6e-02	1.0e+00
61 R	1.105	7.1e-03	3.3e-01
60 L	70.990	7.2e-03	6.7e-01
60 R	...	...	...
59 L	11.757	4.3e-03	9.0e-03
59 R	1.091	3.7e-02	2.2e-01
58 L	11.759	9.8e-04	4.4e-03
58 R	11.863	1.0e-03	9.5e-02
56 L	11.838	...	1.6e-02
56 R	181.599	3.0e-05	1.0e+00
49 L	335.465	1.1e-02	1.0e+00
49 R	11.901	...	1.0e+00
48 L	11.847	3.6e-03	3.6e-02
40 R	357.753	2.8e-02	1.0e+00
39 L	344.038	7.7e-02	3.4e-01
38 R	...	...	...
37 L	...	...	...

TABLE A.24: Same as Table A.6, but for V2689 Ori (J05365+113).

Indicator	Order	Best Signal		$P_{\rm rot}$~11.761
	#	P [d]	FAP[%]	FAP[%]
He I D_3 [Å]	104	12.298	4.98	...
Na I D_2 [Å]	104/ 103	...	...	...
Na I D_1 [Å]	104/ 103	...	...	...
Hα [Å]	93	11.799	4.89e-08	2.52e-04
Ca II IRT-a [Å]	72	11.796	1.72e-08	3.77e-05
Ca II IRT-b [Å]	72/ 71	11.796	1.34e-07	1.15e-04
Ca II IRT-c [Å]	71/ 70	11.796	2.04e-07	1.62e-04
Fe 8691 [Å]	70	...	...	...
He 10833 [Å]	56 L	...	...	...
Paβ [Å]	48 R	...	...	...
CaH 2	90/ 89	...	...	...
CaH 3	88/ 87	11.895	2.94e-02	...
TiO 7050	87/ 86	11.823	1.12e-04	...
TiO 8430	73/ 72	11.838	...	...
TiO 8860	69	...	...	...
VO 7436	82	...	...	...
VO 7942	77	...	...	...
FeH WFB	62 R	...	...	...

A.2 RV over wavelength and CRX-RV plots

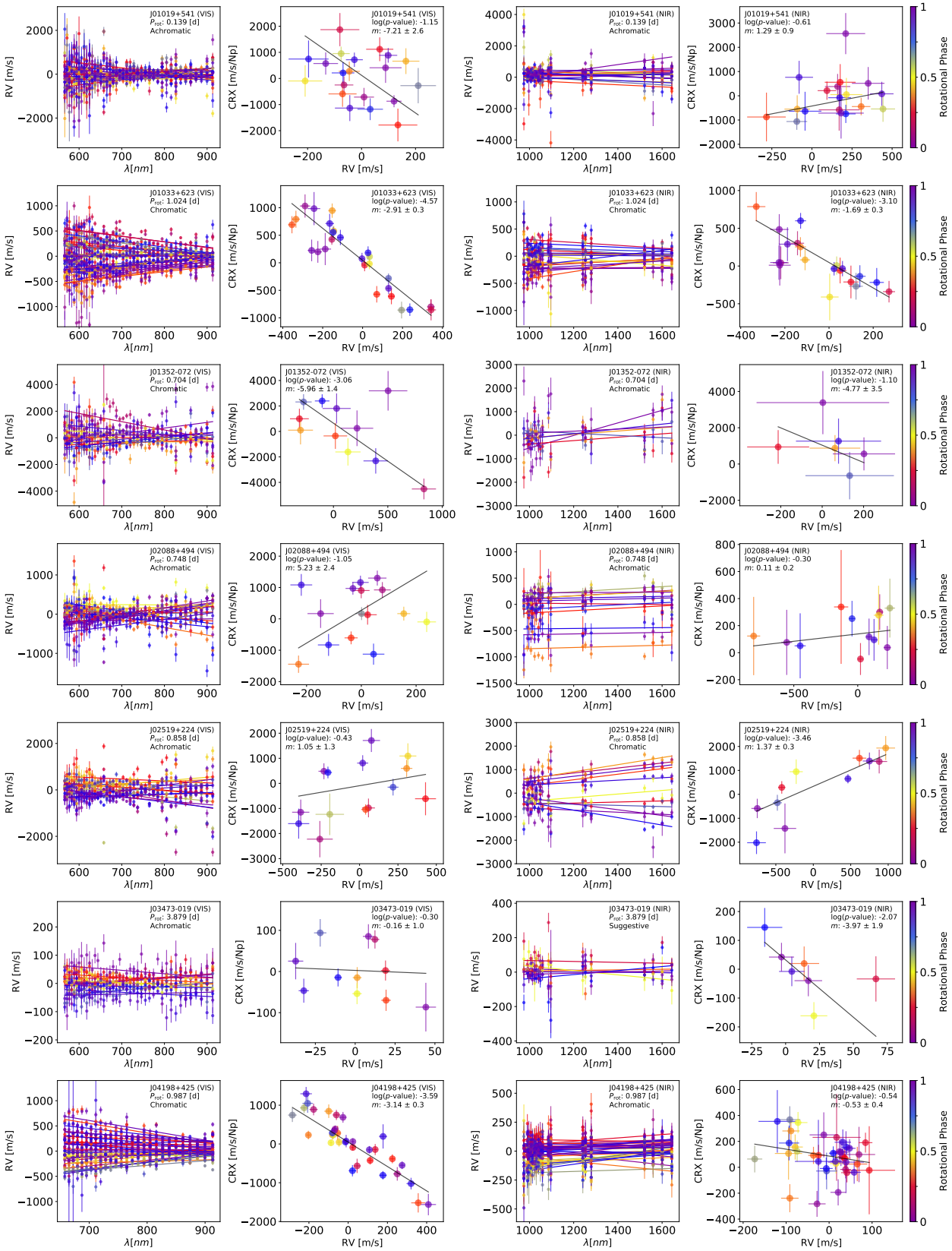

FIGURE A.1: RV measurements per order over wavelength range and their corresponding CRX-RV correlation for the active RV-loud sample using VIS and NIR data. Plots are colour-coded by rotation phase, and targets with unknown rotation periods are colour-coded by the number of observations.

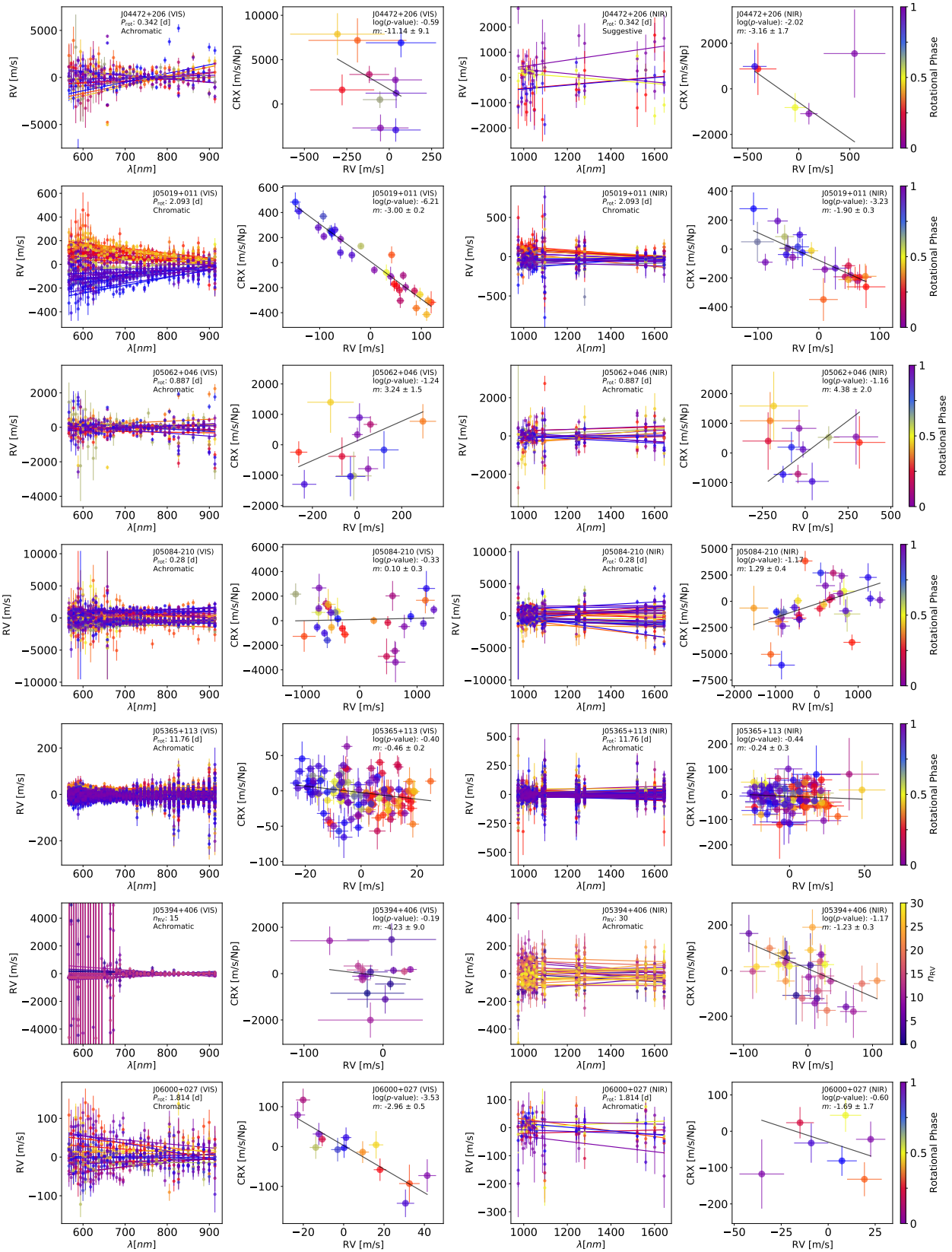
J04472+206 (VIS)
P_{rot}: 0.342 [d]
Achromatic
J04472+206 (VIS)
log(p-value): -0.59
m: -11.14 ± 9.1
J04472+206 (NIR)
P_{rot}: 0.342 [d]
Suggestive
J04472+206 (NIR)
log(p-value): -2.02
m: -3.16 ± 1.7
J05019+011 (VIS)
P_{rot}: 2.093 [d]
Chromatic
J05019+011 (VIS)
log(p-value): -6.21
m: -3.00 ± 0.2
J05019+011 (NIR)
P_{rot}: 2.093 [d]
Chromatic
J05019+011 (NIR)
log(p-value): -3.23
m: -1.90 ± 0.3
J05062+046 (VIS)
P_{rot}: 0.887 [d]
Achromatic
J05062+046 (VIS)
log(p-value): -1.24
m: 3.24 ± 1.5
J05062+046 (NIR)
P_{rot}: 0.887 [d]
Achromatic
J05062+046 (NIR)
log(p-value): -1.16
m: 4.38 ± 2.0
J05084-210 (VIS)
P_{rot}: 0.28 [d]
Achromatic
J05084-210 (VIS)
log(p-value): -0.33
m: 0.10 ± 0.3
J05084-210 (NIR)
P_{rot}: 0.28 [d]
Achromatic
J05084-210 (NIR)
log(p-value): -1.17
m: 1.29 ± 0.4
J05365+113 (VIS)
P_{rot}: 11.76 [d]
Achromatic
J05365+113 (VIS)
log(p-value): -0.40
m: -0.46 ± 0.2
J05365+113 (NIR)
P_{rot}: 11.76 [d]
Achromatic
J05365+113 (NIR)
log(p-value): -0.44
m: -0.24 ± 0.3
J05394+406 (VIS)
n_{RV}: 15
Achromatic
J05394+406 (VIS)
log(p-value): -0.19
m: -4.23 ± 9.0
J05394+406 (NIR)
n_{RV}: 30
Achromatic
J05394+406 (NIR)
log(p-value): -1.17
m: -1.23 ± 0.3
J06000+027 (VIS)
P_{rot}: 1.814 [d]
Chromatic
J06000+027 (VIS)
log(p-value): -3.53
m: -2.96 ± 0.5
J06000+027 (NIR)
P_{rot}: 1.814 [d]
Achromatic
J06000+027 (NIR)
log(p-value): -0.60
m: -1.69 ± 1.7
RV [m/s]
CRX [m/s/Np]
λ[nm]
Rotational Phase
n_{RV}

continued.

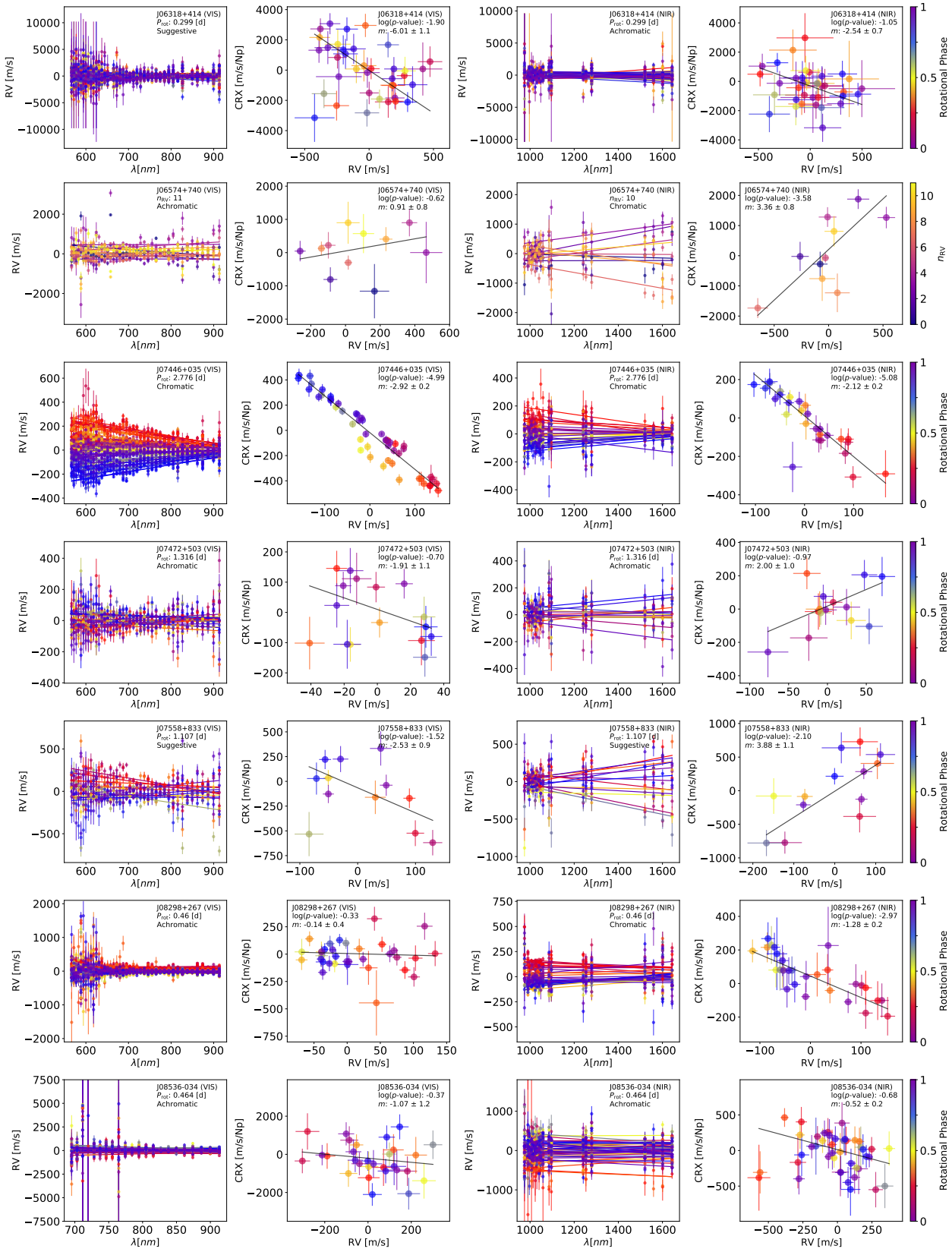
J06318+414 (VIS)
P_{rot}: 0.299 [d]
Suggestive
J06318+414 (VIS)
log(p-value): -1.90
m: -6.01 ± 1.1
J06318+414 (NIR)
P_{rot}: 0.299 [d]
Achromatic
J06318+414 (NIR)
log(p-value): -1.05
m: -2.54 ± 0.7
J06574+740 (VIS)
n_{RV}: 11
Achromatic
J06574+740 (VIS)
log(p-value): -0.62
m: 0.91 ± 0.8
J06574+740 (NIR)
n_{RV}: 10
Chromatic
J06574+740 (NIR)
log(p-value): -3.58
m: 3.36 ± 0.8
J07446+035 (VIS)
P_{rot}: 2.776 [d]
Chromatic
J07446+035 (VIS)
log(p-value): -4.99
m: -2.92 ± 0.2
J07446+035 (NIR)
P_{rot}: 2.776 [d]
Chromatic
J07446+035 (NIR)
log(p-value): -5.08
m: -2.12 ± 0.2
J07472+503 (VIS)
P_{rot}: 1.316 [d]
Achromatic
J07472+503 (VIS)
log(p-value): -0.70
m: -1.91 ± 1.1
J07472+503 (NIR)
P_{rot}: 1.316 [d]
Achromatic
J07472+503 (NIR)
log(p-value): -0.97
m: 2.00 ± 1.0
J07558+833 (VIS)
P_{rot}: 1.107 [d]
Suggestive
J07558+833 (VIS)
log(p-value): -1.52
m: -2.53 ± 0.9
J07558+833 (NIR)
P_{rot}: 1.107 [d]
Suggestive
J07558+833 (NIR)
log(p-value): -2.10
m: 3.88 ± 1.1
J08298+267 (VIS)
P_{rot}: 0.46 [d]
Achromatic
J08298+267 (VIS)
log(p-value): -0.33
m: -0.14 ± 0.4
J08298+267 (NIR)
P_{rot}: 0.46 [d]
Chromatic
J08298+267 (NIR)
log(p-value): -2.97
m: -1.28 ± 0.2
J08536-034 (VIS)
P_{rot}: 0.464 [d]
Achromatic
J08536-034 (VIS)
log(p-value): -0.37
m: -1.07 ± 1.2
J08536-034 (NIR)
P_{rot}: 0.464 [d]
Achromatic
J08536-034 (NIR)
log(p-value): -0.68
m: -0.52 ± 0.2
RV [m/s]
CRX [m/s/Np]
λ[nm]
Rotational Phase
n_{RV}

continued.

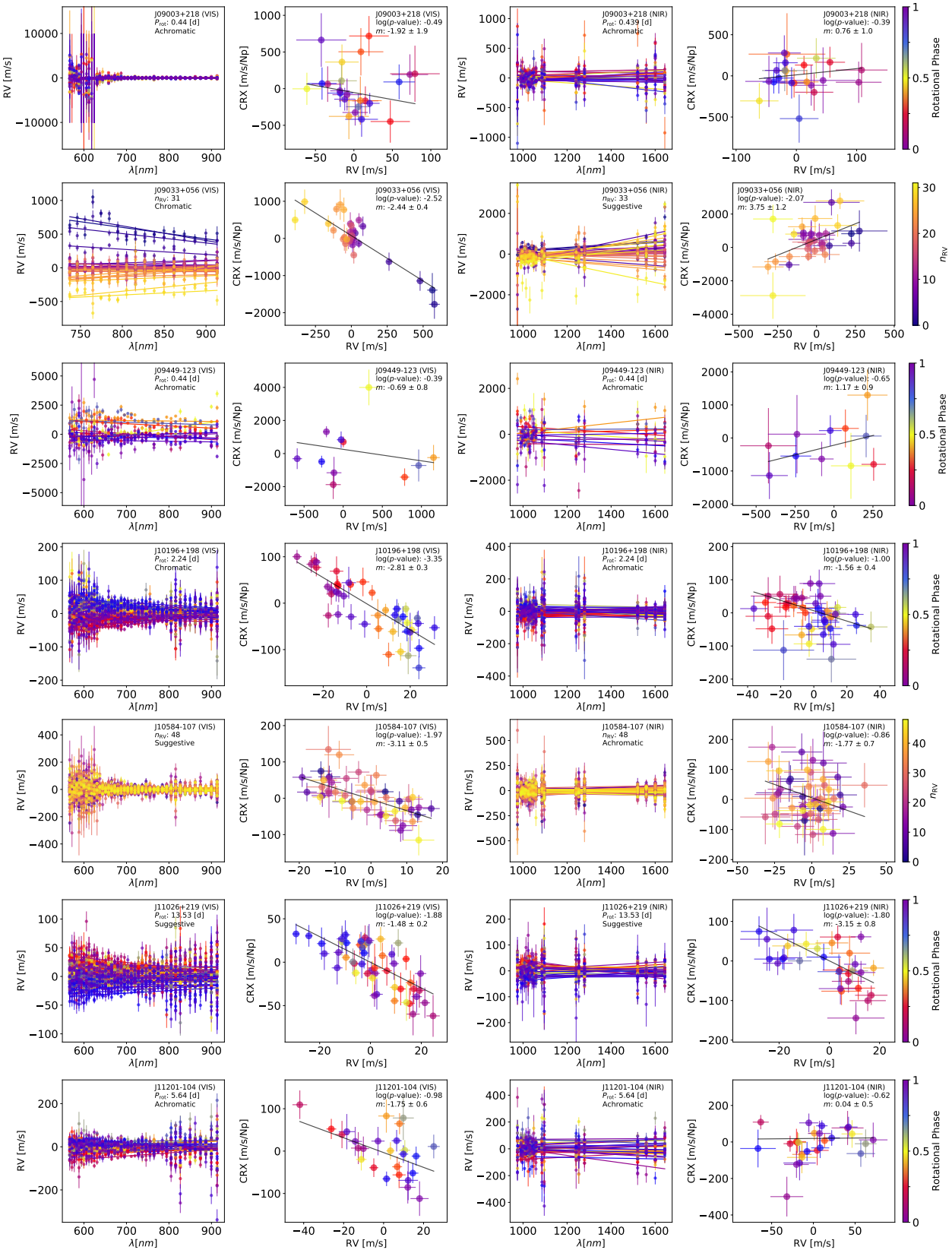
J09003+218 (VIS)
P_{rot}: 0.44 [d]
Achromatic
J09003+218 (VIS)
log(p-value): -0.49
m: -1.92 ± 1.9
J09003+218 (NIR)
P_{rot}: 0.439 [d]
Achromatic
J09003+218 (NIR)
log(p-value): -0.39
m: 0.76 ± 1.0
J09033+056 (VIS)
n_{RV}: 31
Chromatic
J09033+056 (VIS)
log(p-value): -2.52
m: -2.44 ± 0.4
J09033+056 (NIR)
n_{RV}: 33
Suggestive
J09033+056 (NIR)
log(p-value): -2.07
m: 3.75 ± 1.2
J09449-123 (VIS)
P_{rot}: 0.44 [d]
Achromatic
J09449-123 (VIS)
log(p-value): -0.39
m: -0.69 ± 0.8
J09449-123 (NIR)
P_{rot}: 0.44 [d]
Achromatic
J09449-123 (NIR)
log(p-value): -0.65
m: 1.17 ± 0.9
J10196+198 (VIS)
P_{rot}: 2.24 [d]
Chromatic
J10196+198 (VIS)
log(p-value): -3.35
m: -2.81 ± 0.3
J10196+198 (NIR)
P_{rot}: 2.24 [d]
Achromatic
J10196+198 (NIR)
log(p-value): -1.00
m: -1.56 ± 0.4
J10584-107 (VIS)
n_{RV}: 48
Suggestive
J10584-107 (VIS)
log(p-value): -1.97
m: -3.11 ± 0.5
J10584-107 (NIR)
n_{RV}: 48
Achromatic
J10584-107 (NIR)
log(p-value): -0.86
m: -1.77 ± 0.7
J11026+219 (VIS)
P_{rot}: 13.53 [d]
Suggestive
J11026+219 (VIS)
log(p-value): -1.88
m: -1.48 ± 0.2
J11026+219 (NIR)
P_{rot}: 13.53 [d]
Suggestive
J11026+219 (NIR)
log(p-value): -1.80
m: -3.15 ± 0.8
J11201-104 (VIS)
P_{rot}: 5.64 [d]
Achromatic
J11201-104 (VIS)
log(p-value): -0.98
m: -1.75 ± 0.6
J11201-104 (NIR)
P_{rot}: 5.64 [d]
Achromatic
J11201-104 (NIR)
log(p-value): -0.62
m: 0.04 ± 0.5
RV [m/s]
CRX [m/s/Np]
λ[nm]
RV [m/s]
Rotational Phase
n_{RV}

continued.

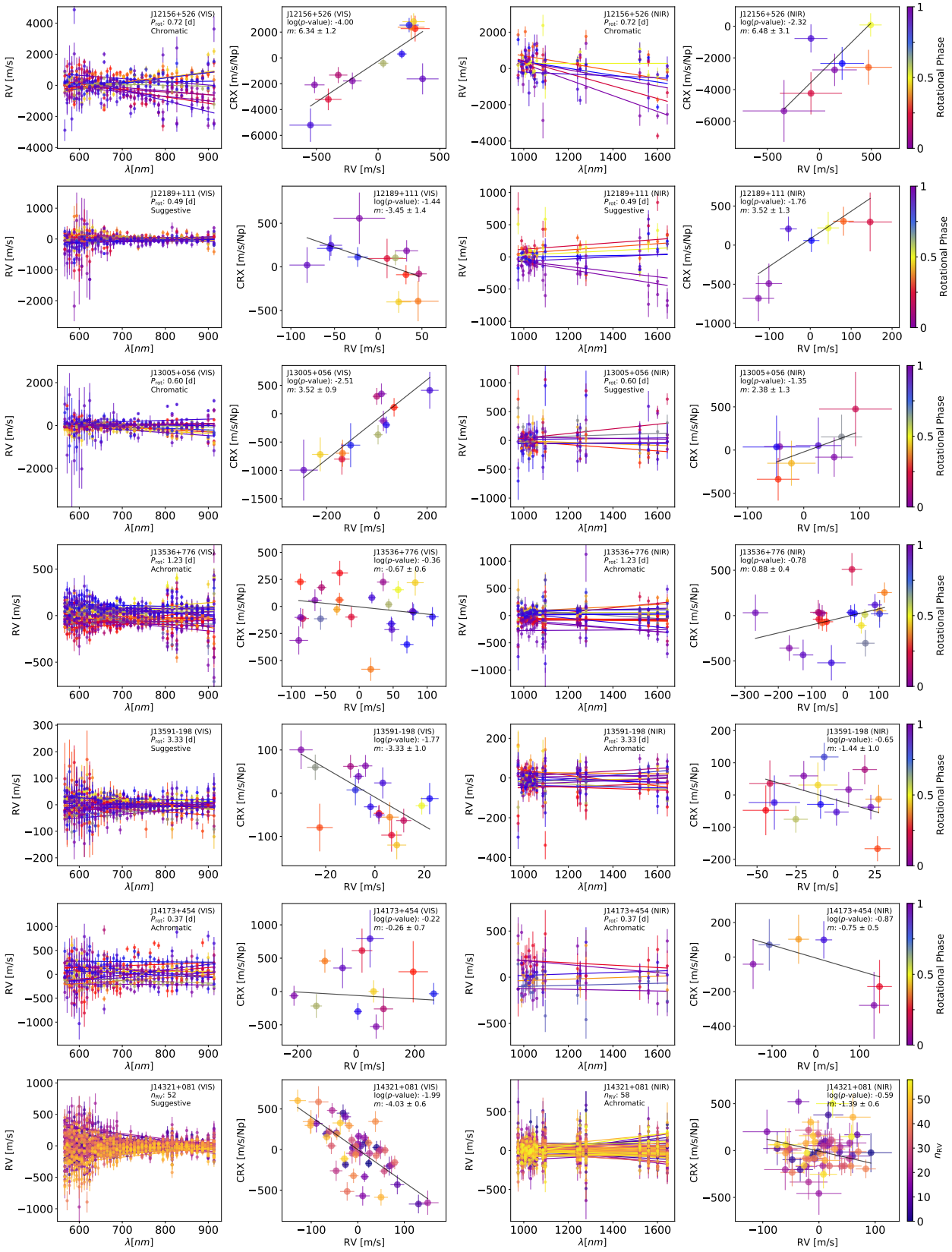
J12156+526 (VIS)
P_{rot}: 0.72 [d]
Chromatic
J12156+526 (VIS)
log(p-value): -4.00
m: 6.34 ± 1.2
J12156+526 (NIR)
P_{rot}: 0.72 [d]
Chromatic
J12156+526 (NIR)
log(p-value): -2.32
m: 6.48 ± 3.1
J12189+111 (VIS)
P_{rot}: 0.49 [d]
Suggestive
J12189+111 (VIS)
log(p-value): -1.44
m: -3.45 ± 1.4
J12189+111 (NIR)
P_{rot}: 0.49 [d]
Suggestive
J12189+111 (NIR)
log(p-value): -1.76
m: 3.52 ± 1.3
J13005+056 (VIS)
P_{rot}: 0.60 [d]
Chromatic
J13005+056 (VIS)
log(p-value): -2.51
m: 3.52 ± 0.9
J13005+056 (NIR)
P_{rot}: 0.60 [d]
Suggestive
J13005+056 (NIR)
log(p-value): -1.35
m: 2.38 ± 1.3
J13536+776 (VIS)
P_{rot}: 1.23 [d]
Achromatic
J13536+776 (VIS)
log(p-value): -0.36
m: -0.67 ± 0.6
J13536+776 (NIR)
P_{rot}: 1.23 [d]
Achromatic
J13536+776 (NIR)
log(p-value): -0.78
m: 0.88 ± 0.4
J13591-198 (VIS)
P_{rot}: 3.33 [d]
Suggestive
J13591-198 (VIS)
log(p-value): -1.77
m: -3.33 ± 1.0
J13591-198 (NIR)
P_{rot}: 3.33 [d]
Achromatic
J13591-198 (NIR)
log(p-value): -0.65
m: -1.44 ± 1.0
J14173+454 (VIS)
P_{rot}: 0.37 [d]
Achromatic
J14173+454 (VIS)
log(p-value): -0.22
m: -0.26 ± 0.7
J14173+454 (NIR)
P_{rot}: 0.37 [d]
Achromatic
J14173+454 (NIR)
log(p-value): -0.87
m: -0.75 ± 0.5
J14321+081 (VIS)
n_{RV}: 52
Suggestive
J14321+081 (VIS)
log(p-value): -1.99
m: -4.03 ± 0.6
J14321+081 (NIR)
n_{RV}: 58
Achromatic
J14321+081 (NIR)
log(p-value): -0.59
m: -1.39 ± 0.6
RV [m/s]
CRX [m/s/Np]
λ[nm]
Rotational Phase
n_{RV}

continued.

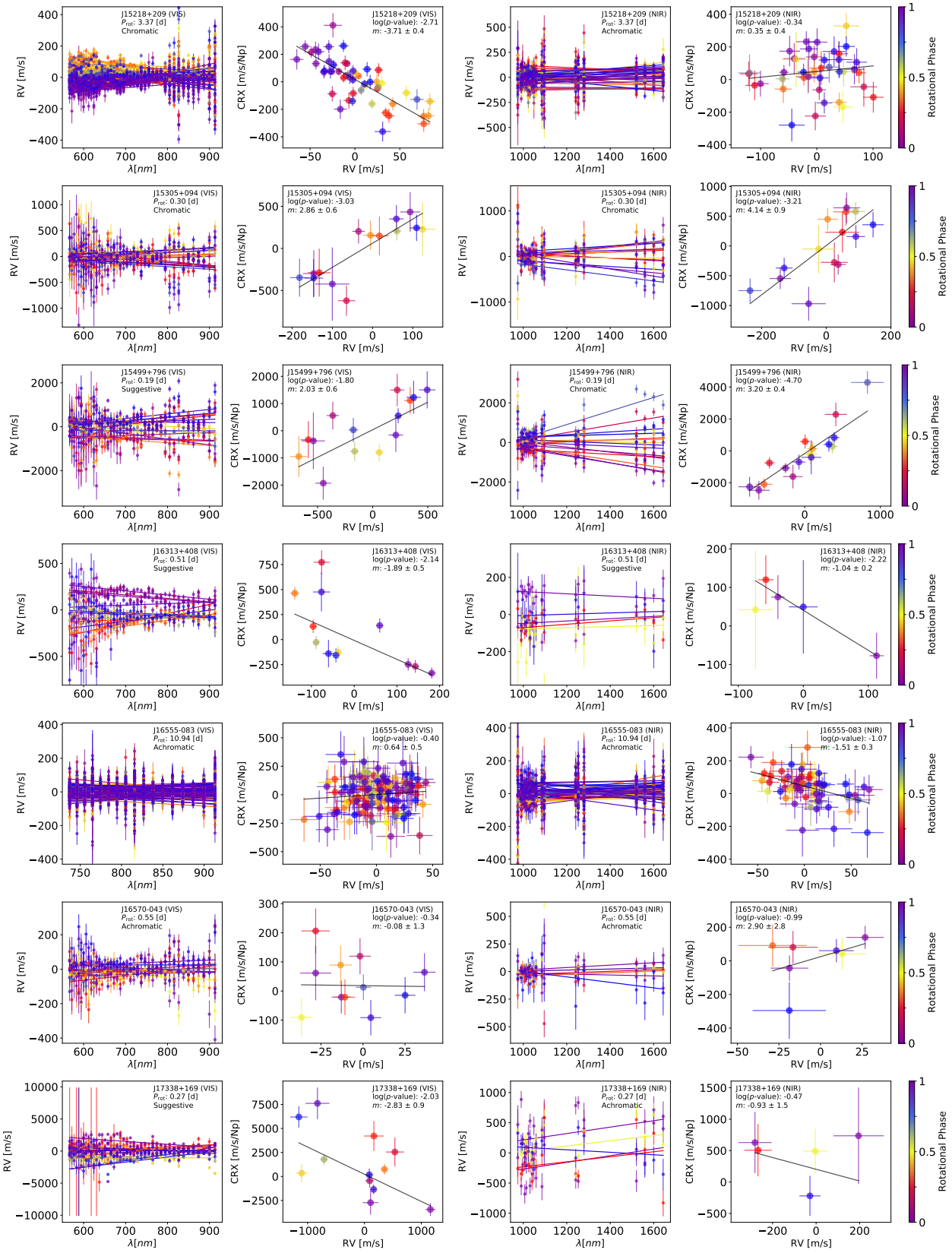
J15218+209 (VIS)
P_{rot}: 3.37 [d]
Chromatic
J15218+209 (VIS)
log(p-value): -2.71
m: -3.71 ± 0.4
J15218+209 (NIR)
P_{rot}: 3.37 [d]
Achromatic
J15218+209 (NIR)
log(p-value): -0.34
m: 0.35 ± 0.4
J15305+094 (VIS)
P_{rot}: 0.30 [d]
Chromatic
J15305+094 (VIS)
log(p-value): -3.03
m: 2.86 ± 0.6
J15305+094 (NIR)
P_{rot}: 0.30 [d]
Chromatic
J15305+094 (NIR)
log(p-value): -3.21
m: 4.14 ± 0.9
J15499+796 (VIS)
P_{rot}: 0.19 [d]
Suggestive
J15499+796 (VIS)
log(p-value): -1.80
m: 2.03 ± 0.6
J15499+796 (NIR)
P_{rot}: 0.19 [d]
Chromatic
J15499+796 (NIR)
log(p-value): -4.70
m: 3.20 ± 0.4
J16313+408 (VIS)
P_{rot}: 0.51 [d]
Suggestive
J16313+408 (VIS)
log(p-value): -2.14
m: -1.89 ± 0.5
J16313+408 (NIR)
P_{rot}: 0.51 [d]
Suggestive
J16313+408 (NIR)
log(p-value): -2.22
m: -1.04 ± 0.2
J16555-083 (VIS)
P_{rot}: 10.94 [d]
Achromatic
J16555-083 (VIS)
log(p-value): -0.40
m: 0.64 ± 0.5
J16555-083 (NIR)
P_{rot}: 10.94 [d]
Achromatic
J16555-083 (NIR)
log(p-value): -1.07
m: -1.51 ± 0.3
J16570-043 (VIS)
P_{rot}: 0.55 [d]
Achromatic
J16570-043 (VIS)
log(p-value): -0.34
m: -0.08 ± 1.3
J16570-043 (NIR)
P_{rot}: 0.55 [d]
Achromatic
J16570-043 (NIR)
log(p-value): -0.99
m: 2.90 ± 2.8
J17338+169 (VIS)
P_{rot}: 0.27 [d]
Suggestive
J17338+169 (VIS)
log(p-value): -2.03
m: -2.83 ± 0.9
J17338+169 (NIR)
P_{rot}: 0.27 [d]
Achromatic
J17338+169 (NIR)
log(p-value): -0.47
m: -0.93 ± 1.5
RV [m/s]
CRX [m/s/Np]
λ[nm]
Rotational Phase

continued.

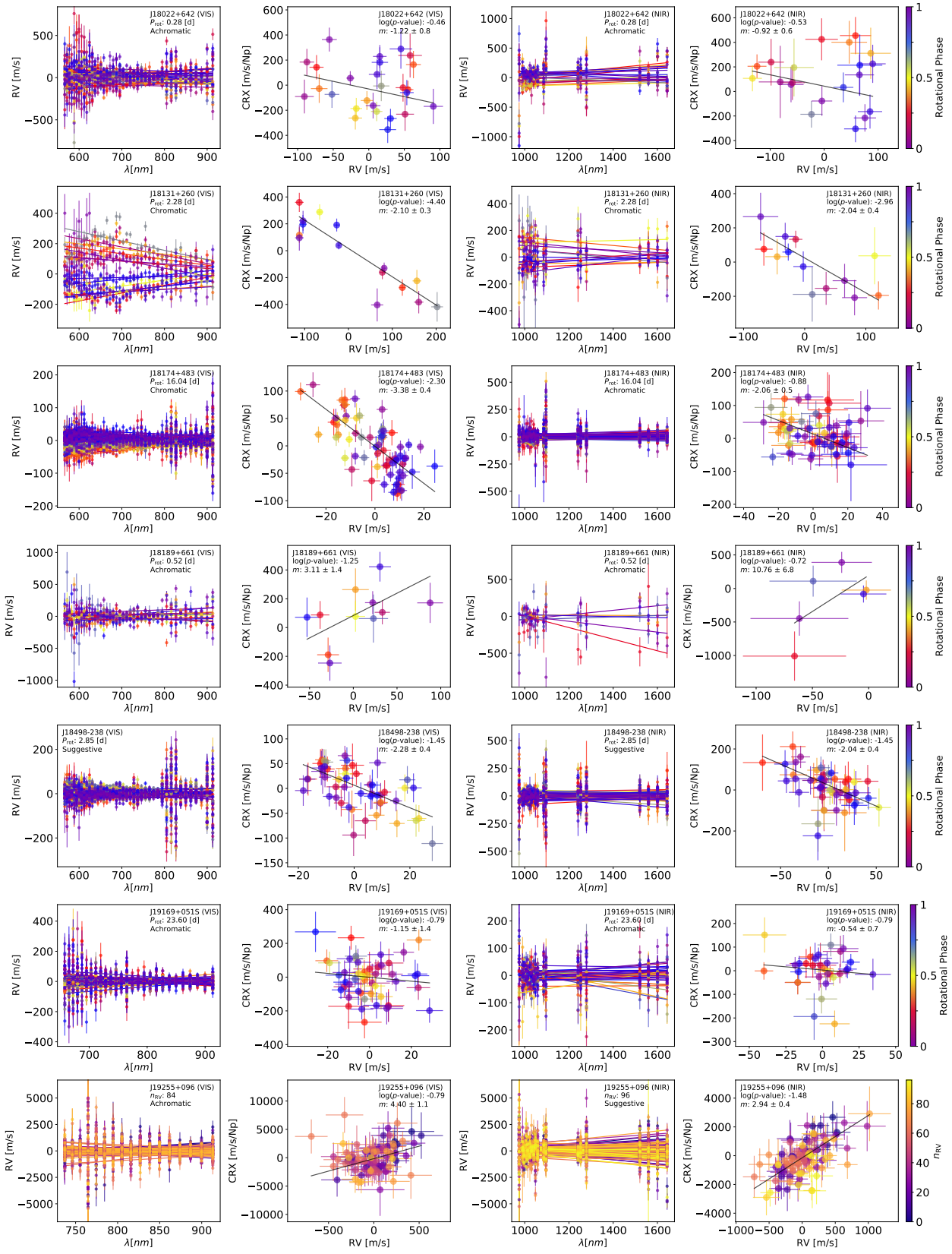
J18022+642 (VIS)
P_{rot}: 0.28 [d]
Achromatic
J18022+642 (VIS)
log(p-value): -0.46
m: -1.22 ± 0.8
J18022+642 (NIR)
P_{rot}: 0.28 [d]
Achromatic
J18022+642 (NIR)
log(p-value): -0.53
m: -0.92 ± 0.6
J18131+260 (VIS)
P_{rot}: 2.28 [d]
Chromatic
J18131+260 (VIS)
log(p-value): -4.40
m: -2.10 ± 0.3
J18131+260 (NIR)
P_{rot}: 2.28 [d]
Chromatic
J18131+260 (NIR)
log(p-value): -2.96
m: -2.04 ± 0.4
J18174+483 (VIS)
P_{rot}: 16.04 [d]
Chromatic
J18174+483 (VIS)
log(p-value): -2.30
m: -3.38 ± 0.4
J18174+483 (NIR)
P_{rot}: 16.04 [d]
Achromatic
J18174+483 (NIR)
log(p-value): -0.88
m: -2.06 ± 0.5
J18189+661 (VIS)
P_{rot}: 0.52 [d]
Achromatic
J18189+661 (VIS)
log(p-value): -1.25
m: 3.11 ± 1.4
J18189+661 (NIR)
P_{rot}: 0.52 [d]
Achromatic
J18189+661 (NIR)
log(p-value): -0.72
m: 10.76 ± 6.8
J18498-238 (VIS)
P_{rot}: 2.85 [d]
Suggestive
J18498-238 (VIS)
log(p-value): -1.45
m: -2.28 ± 0.4
J18498-238 (NIR)
P_{rot}: 2.85 [d]
Suggestive
J18498-238 (NIR)
log(p-value): -1.45
m: -2.04 ± 0.4
J19169+051S (VIS)
P_{rot}: 23.60 [d]
Achromatic
J19169+051S (VIS)
log(p-value): -0.79
m: -1.15 ± 1.4
J19169+051S (NIR)
P_{rot}: 23.60 [d]
Achromatic
J19169+051S (NIR)
log(p-value): -0.79
m: -0.54 ± 0.7
J19255+096 (VIS)
n_{RV}: 84
Achromatic
J19255+096 (VIS)
log(p-value): -0.79
m: 4.40 ± 1.1
J19255+096 (NIR)
n_{RV}: 96
Suggestive
J19255+096 (NIR)
log(p-value): -1.48
m: 2.94 ± 0.4
RV [m/s]
CRX [m/s/Np]
λ[nm]
RV [m/s]
Rotational Phase
n_{RV}

continued.

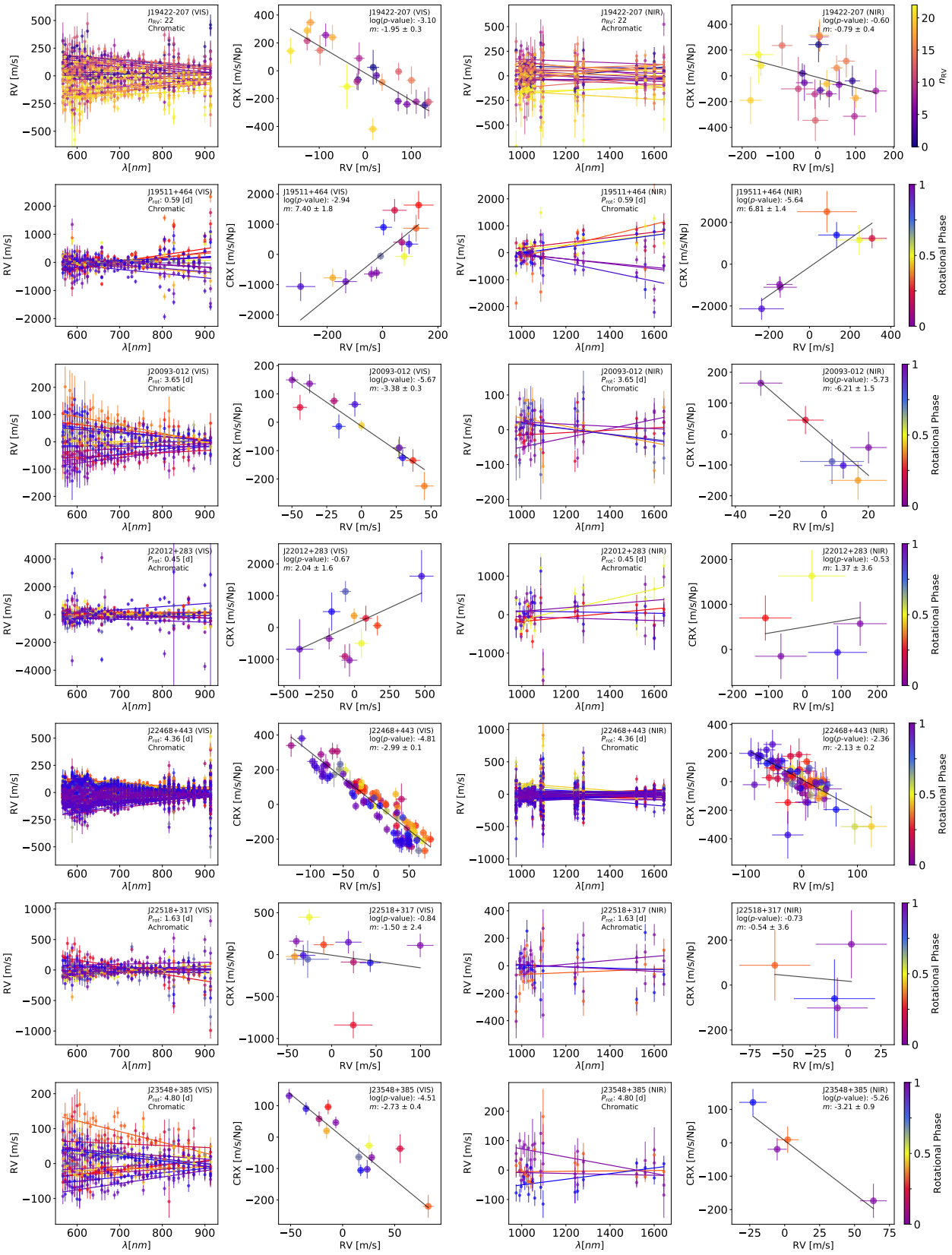
J19422-207 (VIS)
n_{RV}: 22
Chromatic
J19422-207 (VIS)
log(p-value): -3.10
m: -1.95 ± 0.3
J19422-207 (NIR)
n_{RV}: 22
Achromatic
J19422-207 (NIR)
log(p-value): -0.60
m: -0.79 ± 0.4
J19511+464 (VIS)
P_{rot}: 0.59 [d]
Chromatic
J19511+464 (VIS)
log(p-value): -2.94
m: 7.40 ± 1.8
J19511+464 (NIR)
P_{rot}: 0.59 [d]
Chromatic
J19511+464 (NIR)
log(p-value): -5.64
m: 6.81 ± 1.4
J20093-012 (VIS)
P_{rot}: 3.65 [d]
Chromatic
J20093-012 (VIS)
log(p-value): -5.67
m: -3.38 ± 0.3
J20093-012 (NIR)
P_{rot}: 3.65 [d]
Chromatic
J20093-012 (NIR)
log(p-value): -5.73
m: -6.21 ± 1.5
J22012+283 (VIS)
P_{rot}: 0.45 [d]
Achromatic
J22012+283 (VIS)
log(p-value): -0.67
m: 2.04 ± 1.6
J22012+283 (NIR)
P_{rot}: 0.45 [d]
Achromatic
J22012+283 (NIR)
log(p-value): -0.53
m: 1.37 ± 3.6
J22468+443 (VIS)
P_{rot}: 4.36 [d]
Chromatic
J22468+443 (VIS)
log(p-value): -4.81
m: -2.99 ± 0.1
J22468+443 (NIR)
P_{rot}: 4.36 [d]
Chromatic
J22468+443 (NIR)
log(p-value): -2.36
m: -2.13 ± 0.2
J22518+317 (VIS)
P_{rot}: 1.63 [d]
Achromatic
J22518+317 (VIS)
log(p-value): -0.84
m: -1.50 ± 2.4
J22518+317 (NIR)
P_{rot}: 1.63 [d]
Achromatic
J22518+317 (NIR)
log(p-value): -0.73
m: -0.54 ± 3.6
J23548+385 (VIS)
P_{rot}: 4.80 [d]
Chromatic
J23548+385 (VIS)
log(p-value): -4.51
m: -2.73 ± 0.4
J23548+385 (NIR)
P_{rot}: 4.80 [d]
Chromatic
J23548+385 (NIR)
log(p-value): -5.26
m: -3.21 ± 0.9
RV [m/s]
CRX [m/s/Np]
λ[nm]
RV [m/s]
n_{RV}
Rotational Phase

continued.

A.3 Slopes of CRX-RV Regression across Stellar Properties

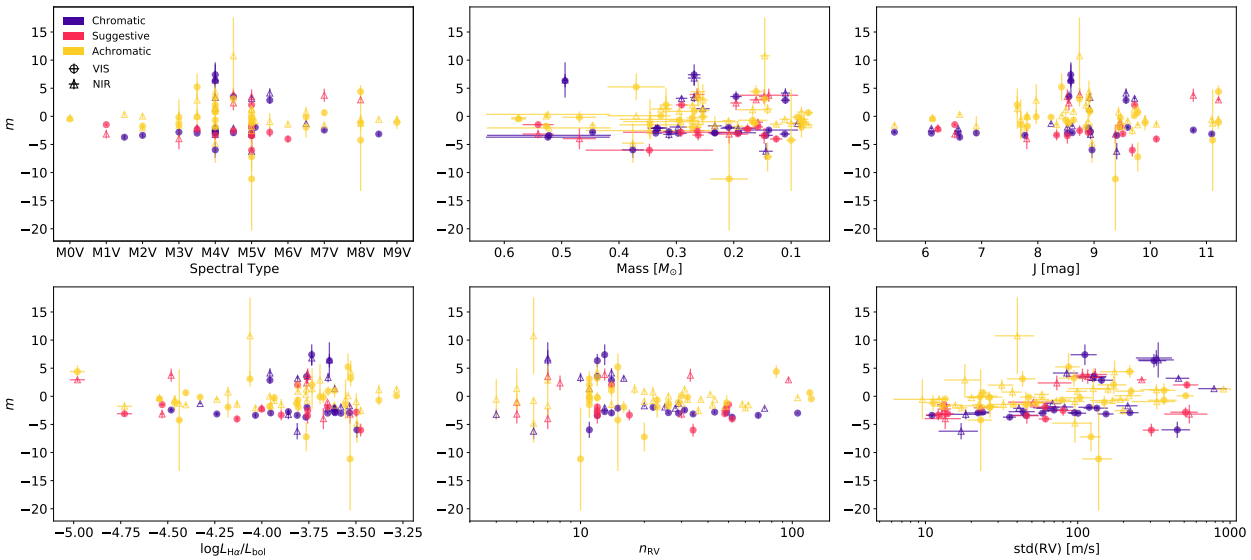

FIGURE A.2: The CRX-RV regression slopes as a function of the spectral type (*top left*), stellar mass (*top middle*), J magnitude (*top right*), Hα activity ($\log L_{H\alpha}/L_{bol}$, *bottom left*), number of RV data points (n_{RV}, *bottom middle*), and RV scatter (std(RV), *bottom right*). Symbols are the same as in Fig. 3.3.

A.4 Phase-folded plots

A.4.1 EV Lac (J22468+443)

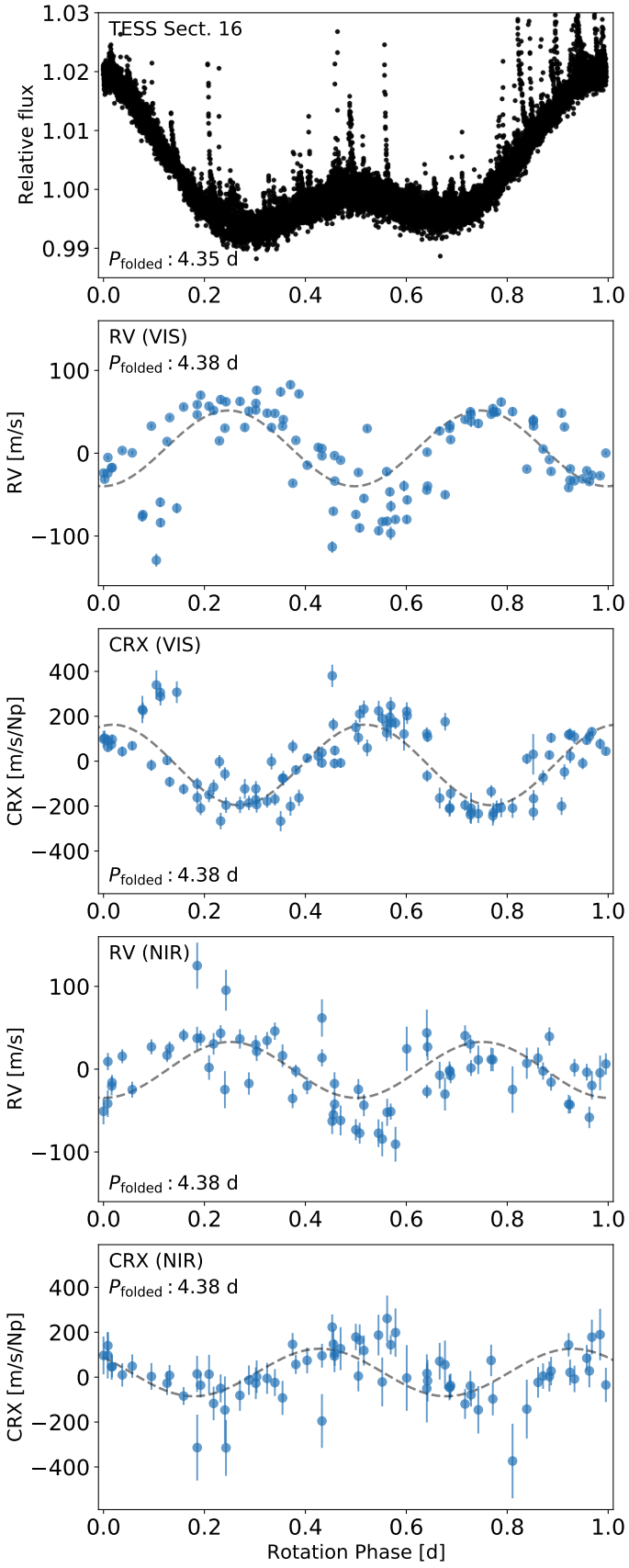

FIGURE A.3: Phase-folded plots of EV Lac: TESS Light Curve, Radial Velocities (VIS and NIR), and CRXs (VIS and NIR)

.

A.4.2 TYC 3529-1437-1 (J18174+483)

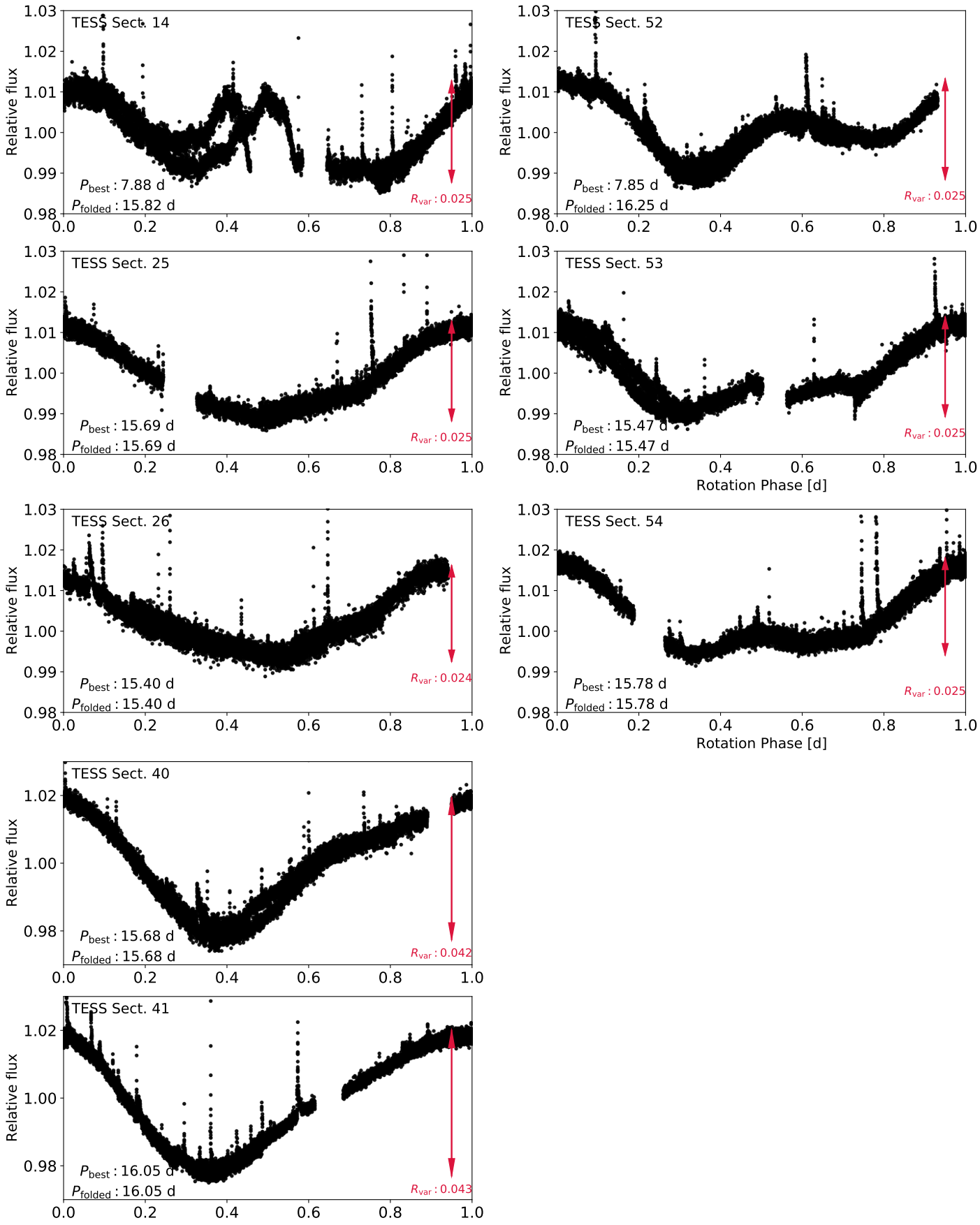

FIGURE A.4: Phase-folded plots of TYC 3529-1437-1: TESS Light Curves

.

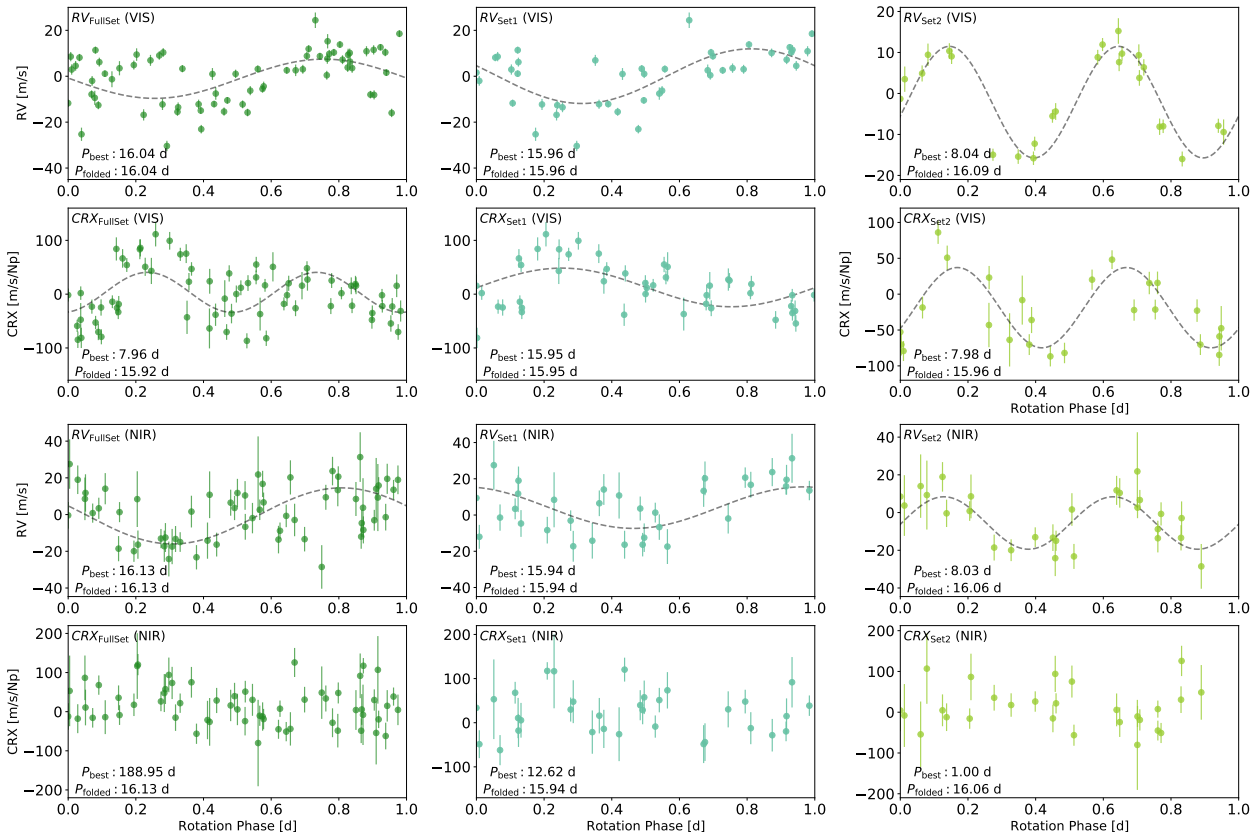

FIGURE A.5: Phase-folded plots of TYC 3529-1437-1: Radial Velocities (VIS and NIR) and CRXs (VIS and NIR). *Left*: Full dataset with 69 data points. *Middle*: First subset with 44 data points. *Right*: Second subset with 25 data points.

.

A.4.3 OT Ser (J15218+209)

A.4.4 J11026+219 (DS Leo)

A.4.5 YZ CMi (J07446+035)

A.4.6 V2689 Ori (J05365+113)

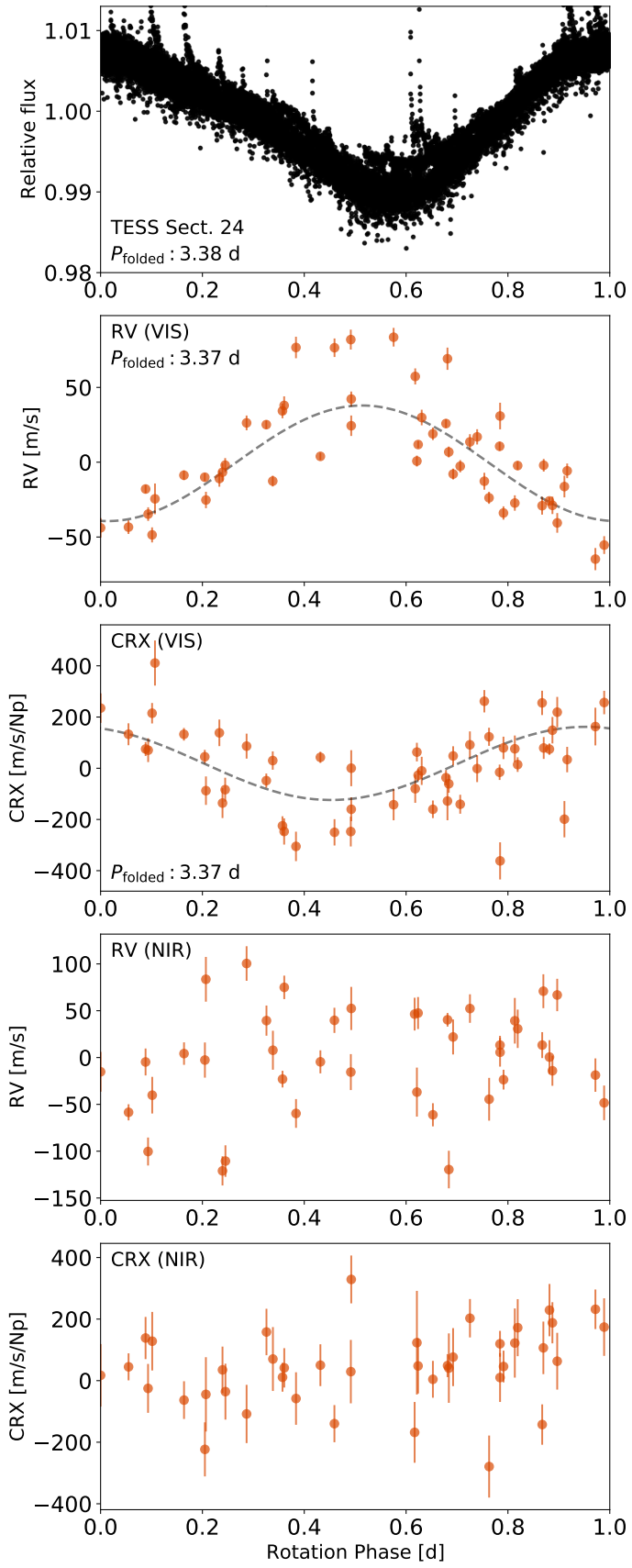

FIGURE A.6: Phase-folded plots of OT Ser: TESS Light Curve, Radial Velocities (VIS and NIR), and CRXs (VIS and NIR)

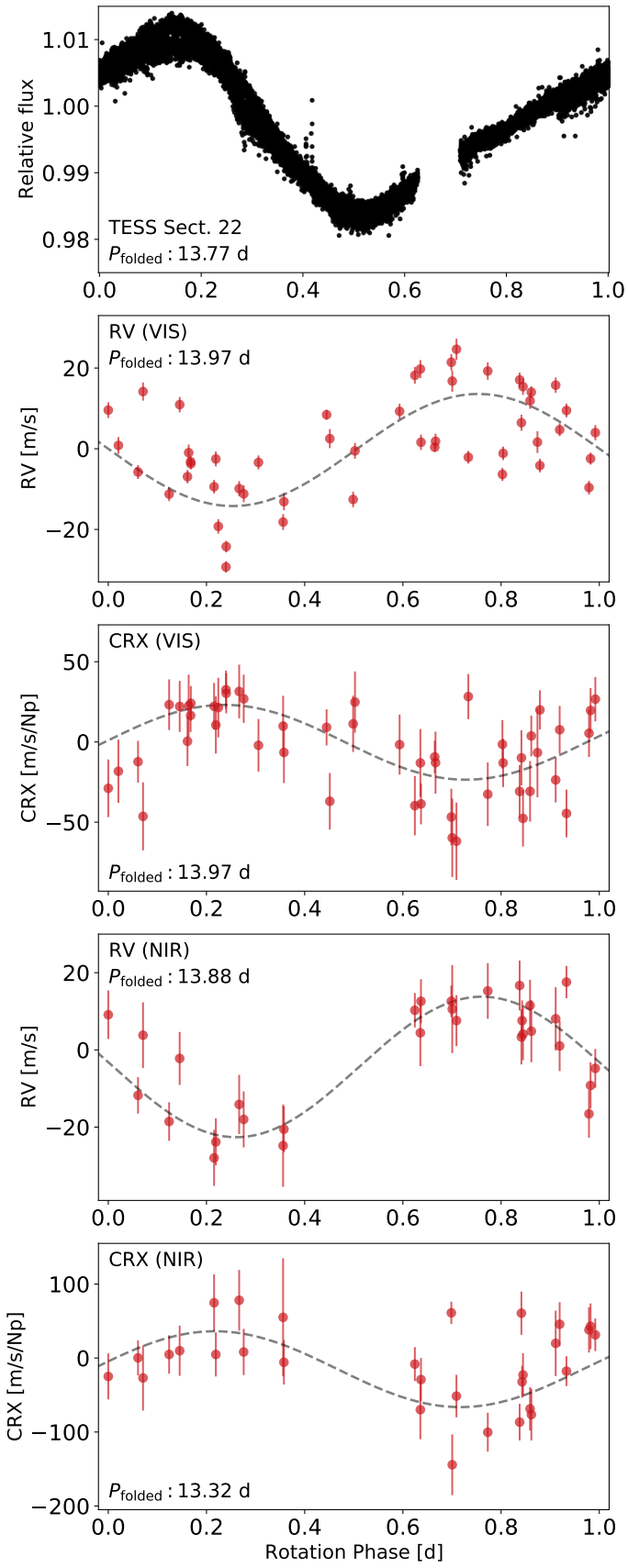

FIGURE A.7: Phase-folded plots of DS Leo: TESS Light Curve, Radial Velocities (VIS and NIR), and CRXs (VIS and NIR)

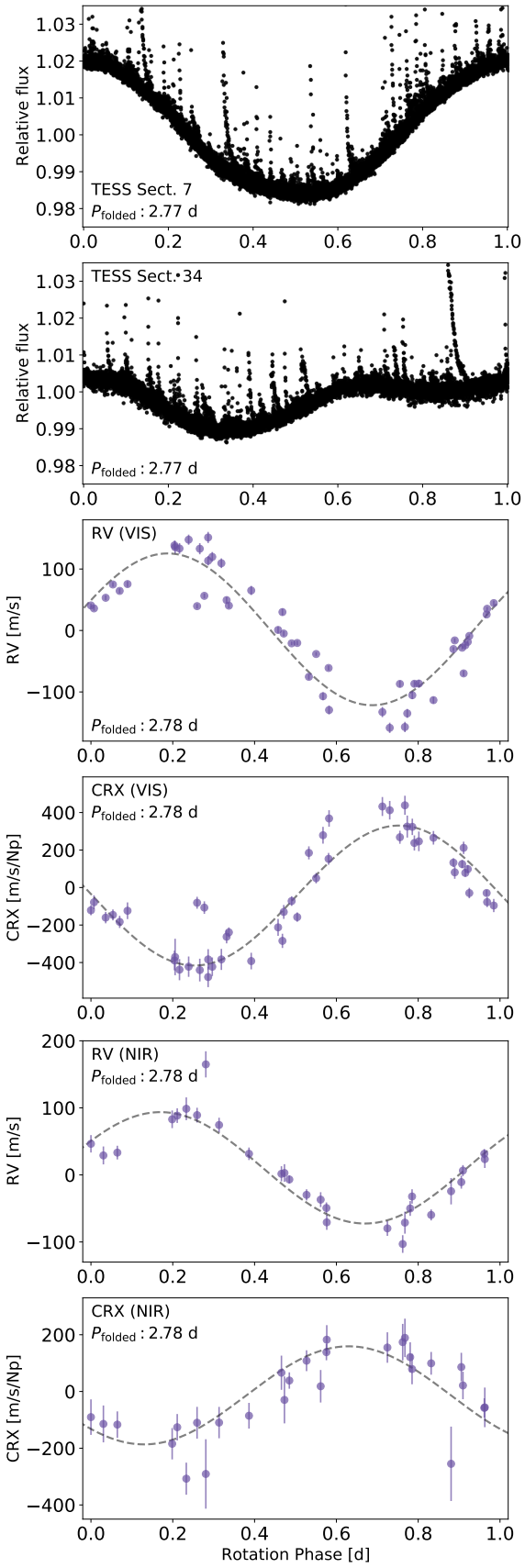

FIGURE A.8: Phase-folded plots of YZ CMi: TESS Light Curve, Radial Velocities (VIS and NIR), and CRXs (VIS and NIR)

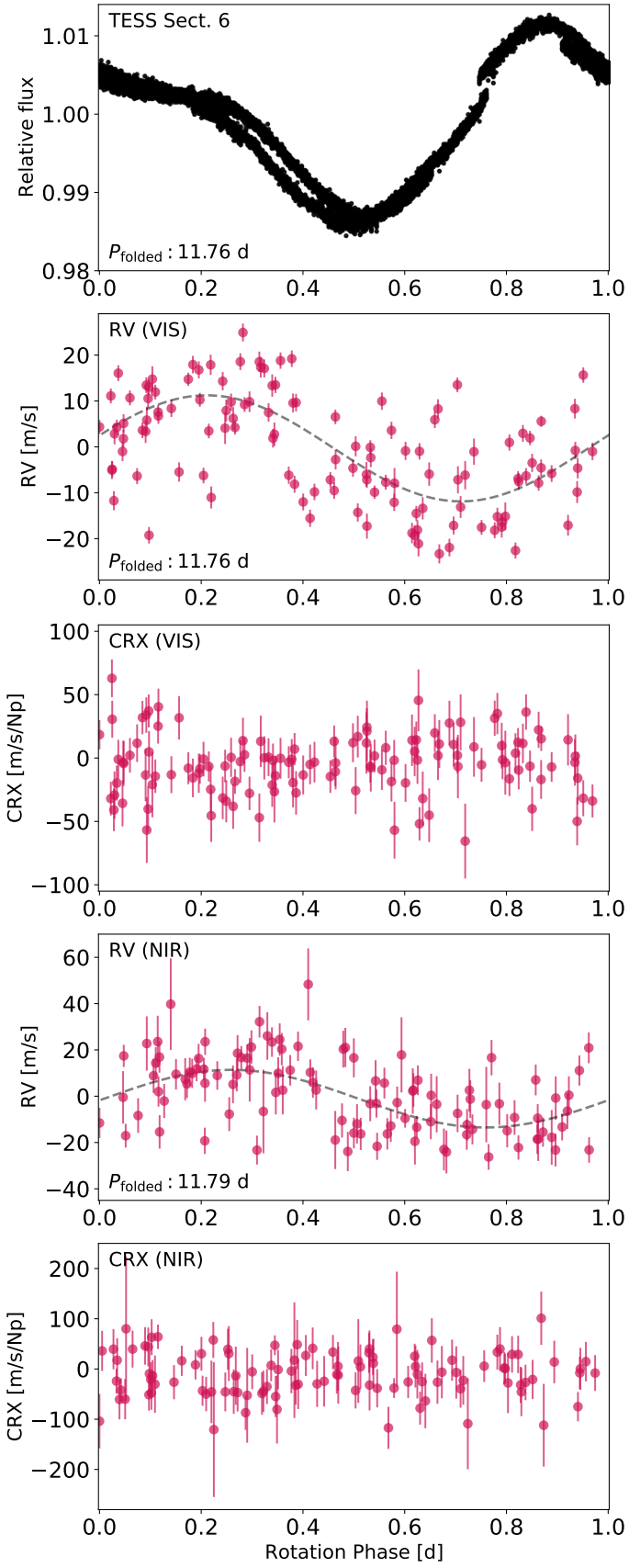

FIGURE A.9: Phase-folded plots of V2689 Ori: TESS Light Curve, Radial Velocities (VIS and NIR), and CRXs (VIS and NIR)

Appendix B

B.1 Tables for Chapter 4

TABLE B.1: Summary of TESS Observations: Sectors, Cameras, CCDs, Star Counts, Contamination Percentage, and Light Curve Types

TIC	Sector	Camera	CCD	In Aper.[a]	In cont.[b] %	Out Aper.[c]	LC Type
29853348	3	1	3	1	0	0	SAP
146539195	5	2	2	2	4.15	0	SAP
269077806	5	1	2	2	0.86	0	SAP
333680372	5	1	1	1	0	0	SAP
455029978	5	1	2	4	40.29	0	PDCSAP
282501711	6	1	1	2	0.61	0	PDCSAP
436248822	6	1	4	1	0	0	SAP
266744225	7	1	4	2	0.63	0	SAP
7975441	8	1	1	1	0	2	PDCSAP
270511002	8	1	4	1	0	0	–
289706625	8	1	2	2	17.21	0	SAP
148563078	9	1	4	2	5.20	1	–
453465810	9	1	3	1	0	0	–
125421413	11	1	4	2	8.70	1	SAP
142878895	14	4	4	1	0	0	SAP
142878895	15	4	3	1	0	0	SAP
142878895	21	3	2	1	0	0	SAP
159398282	14	3	3	2	0.43	0	PDCSAP
159398282	15	3	3	2	0.43	0	PDCSAP
159398282	19	3	3	2	0.43	0	PDCSAP
159398282	20	3	3	2	0.43	0	PDCSAP
159398282	21	3	4	2	0.43	0	PDCSAP
159398282	25	3	4	2	0.43	0	PDCSAP
159398282	26	3	4	2	0.43	0	PDCSAP
219463771	14	4	2	1	0	0	SAP
219463771	15	3	3	1	0	0	SAP
219463771	20	3	3	1	0	0	SAP
219463771	21	3	4	1	0	0	SAP
219463771	26	3	4	1	0	0	SAP
233068870	14	3	1	1	0	0	SAP
233068870	15	3	1	1	0	0	SAP
233068870	16	3	1	2	0.74	0	PDCSAP
233068870	17	4	4	1	0	0	SAP
233068870	18	4	4	2	0.74	0	PDCSAP
233068870	19	4	4	1	0	0	PDCSAP
233068870	20	4	3	2	0.74	0	PDCSAP
233068870	21	4	3	2	0.74	0	SAP
233068870	22	4	3	1	0	0	SAP
233068870	24	3	2	3	10.06	0	PDCSAP
233068870	25	3	2	3	10.06	0	SAP
273589987	14	2	4	9	11.84	0	PDCSAP
273589987	15	2	3	8	8.07	2	PDCSAP
289726188	14	2	2	2	0.83	0	SAP
289726188	25	2	1	2	0.83	0	SAP
289726188	26	2	4	2	0.83	0	SAP
406857100	14	3	2	2	1.98	0	SAP

continued.

TIC	Sector	Camera	CCD	In Aper.[a]	In cont.[b] %	Out Aper.[c]	LC Type
406857100	15	3	2	3	2.85	0	SAP
406857100	17	4	1	2	1.98	0	PDCSAP
406857100	18	4	1	2	1.98	0	PDCSAP
406857100	20	4	4	2	1.98	0	PDCSAP
406857100	21	4	4	2	1.98	0	PDCSAP
406857100	23	4	3	3	2.85	0	PDCSAP
406857100	24	3	2	2	1.98	0	PDCSAP
406857100	25	3	2	2	1.98	0	PDCSAP
406857100	26	3	2	2	1.98	0	PDCSAP
283410775	15	1	4	3	5.67	0	PDCSAP
154101678	16	1	4	1	0	0	SAP
168747450	16	4	4	1	0	0	PDCSAP
168747450	23	3	1	1	0	0	PDCSAP
252110114	17	2	1	4	4.48	5	PDCSAP
252110114	18	2	2	6	7.20	4	PDCSAP
291689873	17	2	3	3	1.54	0	SAP
52183206	18	2	2	7	31.38	2	SAP
52183206	24	4	4	8	37.27	1	SAP
250602194	18	2	3	4	1.98	2	PDCSAP
141476700	19	2	1	3	–	6	–
141476700	20	2	2	5	–	6	–
141476700	26	4	4	5	–	6	–
239097694	19	1	4	11	39.78	9	–
289972535	19	3	2	1	0	0	SAP
289972535	20	3	1	1	0	1	SAP
289972535	26	4	1	1	0	1	SAP
347994537	19	1	2	3	93.84	11	PDCSAP
144282456	20	1	2	3	2.31	2	SAP
309661100	20	1	1	1	0	0	SAP
3664898	21	1	3	3	53.19	0	PDCSAP
97488127	22	1	3	1	0	0	SAP
416538839	22	2	2	1	0	0	SAP
411248800	23	1	3	1	0	0	PDCSAP
255932726	24	2	4	1	0	0	SAP
255932726	25	2	3	1	0	0	PDCSAP
355793860	24	1	4	1	0	0	SAP
313988572	26	1	1	2	0.50	0	SAP
400361232	26	1	3	4	4.57	0	SAP

[a:] Number of stars within the aperture mask, including the main target;
[b:] Contamination of flux by neighbouring stars within the aperture mask;
[c:] Number of stars located outside the aperture mask within a 42 ″distance.

TABLE B.2: Stellar properties of the sample

Karmn *	Name	TIC	$G_{\rm RP}$ [a] [mag]	SpT [b]	$v \sin i$ [c] [km s^{-1}]	$R_\star$ $R_\odot$	$M_\star$ $M_\odot$	i (deg)
J01019+541	G 218-020	252110114	11.82	M5.0 V	30.6 ± 3.1	0.177 ± 0.006	0.163 ± 0.010	28 ± 3
J01033+623	V388 Cas	52183206	10.60	M5.0 V	10.5 ± 1.5	0.251 ± 0.008	0.241 ± 0.013	56^{+12}_{-10}
J01352-072	Barta 161 12	29853348	10.76	M4.0 V	59.8 ± 6.9	0.713 ± 0.023	0.729 ± 0.028	72^{+9}_{-10}
J02088+494	G 173-039	250602194	10.10	M3.5 V	24.1 ± 2.4	0.401 ± 0.013	0.399 ± 0.017	61^{+11}_{-9}
J03473-019	G 80-021	333680372	9.37	M3.0 V	5.2 ± 1.5	0.510 ± 0.016	0.514 ± 0.020	47^{+17}_{-15}
J04198+425	LSR J0419+4233	347994537	14.01	M8.5 V	3.6 ± 2.3	0.122 ± 0.004	0.105 ± 0.009	35 ±
J05019+011	1RXS J050156.7+010845	269077806	10.29	M4.0 V	6.5 ± 1.5	0.589 ± 0.019	0.598 ± 0.024	27 ± 7
J05062+046	RX J0506.2+0439	455029978	10.76	M4.0 V	24.9 ± 2.5	0.496 ± 0.016	0.499 ± 0.020	60^{+11}_{-9}
J05084-210	2MASS J05082729-2101444	146539195	11.74	M5.0 V	25.2 ± 2.5	0.729 ± 0.026	0.745 ± 0.031	11 ± 1
J05365+113	V2689 Ori	436248822	7.30	M0.0 V	3.8 ± 1.5	0.573 ± 0.016	0.581 ± 0.021	
(J05394+406)	LSR J0539+4038	239097694	13.75	M8.0 V	4.1 ± 1.5	0.115 ± 0.005	0.098 ± 0.009	
J06000+027	G 99-049	282501711	8.67	M4.0 V	4.9 ± 1.5	0.246 ± 0.008	0.235 ± 0.012	43^{+17}_{-15}
J06318+414	LP 205-044	144282456	11.73	M5.0 V	58.4 ± 26.1	0.420 ± 0.014	0.420 ± 0.018	42 ± 21
(J06574+740)	2MASS J06572616+7405265	141476700	10.59	M4.0 V	27.1 ± 2.7	0.495 ± 0.058	0.499 ± 0.062	
J07446+035	YZ CMi	266744225	8.44	M4.5 V	4.0 ± 1.5	0.368 ± 0.013	0.364 ± 0.017	36^{+17}_{-14}
J07472+503	2MASS J07471385+5020386	309661100	10.58	M4.0 V	10.1 ± 1.5	0.272 ± 0.009	0.263 ± 0.013	62 ± 12
J07558+833	GJ 1101	289972535	10.52	M4.5 V	12.1 ± 1.5	0.270 ± 0.009	0.261 ± 0.013	65 ± 11
J08298+267	DX Cnc	3664898	10.70	M6.5 V	10.5 ± 1.5	0.142 ± 0.005	0.126 ± 0.010	42^{+8}_{-7}
J08536-034	LP 666-009	7975441	14.33	M9.0 V	9.3 ± 2.8	0.083 ± 0.003	0.064 ± 0.009	53^{+17}_{-18}
(J09033+056)	NLTT 20861	270511002	13.05	M7.0 V	9.7 ± 1.5	0.164 ± 0.006	0.149 ± 0.010	

TABLE B.2: continued.

Karmn	Name	TIC	$G_{\rm RP}$ [a] [mag]	SpT [b]	$v \sin i$ [c] [km s^{-1}]	$R_\star$ $R_\odot$	$M_\star$ $M_\odot$	i (deg)
J09449-123	G 161-071	289706625	10.55	M5.0 V	31.2 ± 3.1	0.342 ± 0.012	0.337 ± 0.016	53^{+9}_{-7}
(J10584-107)	LP 731-076	148563078	11.47	M5.0 V	3.2 ± 1.5	0.220 ± 0.007	0.208 ± 0.011	
J11026+219	DS Leo	97488127	7.83	M1.0 V	2.6 ± 1.5	0.531 ± 0.014	0.536 ± 0.019	
J11201-104	LP 733-099	453465810	9.24	M2.0 V	3.6 ± 1.5	0.539 ± 0.016	0.545 ± 0.021	42^{+20}_{-19}
J11474+667	1RXS J114728.8+664405	142878895	11.65	M5.0 V	2.7 ± 1.5	0.329 ± 0.011	0.323 ± 0.015	
J12156+526	StKM 2-809	416538839	10.21	M4.0 V	35.3 ± 3.5	0.556 ± 0.018	0.562 ± 0.023	63^{+11}_{-9}
J13005+056	FN Vir	411248800	10.48	M4.5 V	16.4 ± 1.6	0.202 ± 0.007	0.189 ± 0.011	67 ± 10
J13536+776	RX J1353.6+7737	219463771	10.34	M4.0 V	8.9 ± 1.5	0.280 ± 0.009	0.272 ± 0.013	50^{+13}_{-10}
J13591-198	LP 799-007	125421413	10.15	M4.0 V	3.2 ± 1.5	0.269 ± 0.009	0.260 ± 0.013	
J14173+454	RX J1417.3+4525	168747450	11.34	M5.0 V	15.9 ± 1.6	0.290 ± 0.009	0.282 ± 0.013	23 ± 3
J15218+209	OT Ser	355793860	8.06	M1.5 V	4.3 ± 1.5	0.585 ± 0.018	0.593 ± 0.022	29^{+12}_{-11}
J15499+796	LP 022-420	159398282	11.70	M5.0 V	26.9 ± 2.7	0.283 ± 0.010	0.275 ± 0.014	21 ± 2
J16313+408	G 180-060	255932726	11.59	M5.0 V	7.1 ± 1.5	0.203 ± 0.007	0.191 ± 0.011	21 ± 5
J17338+169	1RXS J173353.5+165515	400361232	11.03	M5.5 V	41.5 ± 7.7	0.374 ± 0.014	0.370 ± 0.018	36^{+8}_{-7}
J18022+642	LP 071-082	233068870	10.46	M5.0 V	11.3 ± 1.5	0.193 ± 0.007	0.179 ± 0.011	19 ± 3
J18131+260	LP 390-16	313988572	10.69	M4.0 V	5.9 ± 1.5	0.348 ± 0.011	0.343 ± 0.015	47^{+16}_{-14}
J18174+483	TYC 3529-1437-1	289726188	9.30	M2.0 V	3.1 ± 1.0 [d]	0.579 ± 0.018	0.587 ± 0.022	53^{+18}_{-21}
J18189+661	LP 71-165	406857100	10.64	M4.5 V	15.3 ± 1.5	0.161 ± 0.005	0.145 ± 0.010	68 ± 10
J19511+464	G 208-042	273589987	10.33	M4.0 V	22.1 ± 0.9	0.263 ± 0.008	0.253 ± 0.013	74 ± 7
J22012+283	V374 Peg	283410775	9.42	M4.0 V	36.9 ± 0.7	0.312 ± 0.010	0.305 ± 0.014	80 ± 5

TABLE B.2: continued.

Karmn	Name	TIC	$G_{\rm RP}$ [a] [mag]	SpT [b]	$v \sin i$ [c] [km s^{-1}]	$R_\star$ $R_\odot$	$M_\star$ $M_\odot$	i (deg)
J22468+443	EV Lac	154101678	7.81	M3.5 V	3.5 ± 1.5	0.344 ± 0.011	0.339 ± 0.015	44 ± 21
J23548+385	RX J2354.8+3831	291689873	10.67	M4.0 V	3.6 ± 1.5	0.334 ± 0.011	0.329 ± 0.015	46^{+20}_{-22}

* Stars marked with a Karmn designation in parentheses have been excluded from the study (for further details, refer to Section 4.5.1).

a: Gaia DR2: Gaia Collaboration et al. (2018b);

b: Spectral types obtained from the CARMENES Input Catalogue (Jeffers et al., 2018);

c: Projected rotational velocities ($v \sin i$) obtained from Reiners et al. (2018) unless otherwise specified;

d: Fouqué et al. (2018).

TABLE B.3: Median pEW of activity indices

Karmn	No.	$\log L_{\rm Hff}/L_{\rm bol}$	Hα Å	He D$_3$ Å	Na D$_2$ Å	Na D$_1$ Å	Na D Å	Ca IRT-a Å	Ca IRT-b Å	Ca IRT-c Å	Fe 8691 Å
J01019+541	21	-3.81 ± 0.005	-5.19 ± 0.06	-0.69 ± 0.06	-1.85 ± 0.21	-1.38 ± 0.14	-3.21 ± 0.23	-0.09 ± 0.02	-0.03 ± 0.02	0.08 ± 0.01	0.06 ± 0.017
J01033+623	27	-3.58 ± 0.002	-8.81 ± 0.04	-1.07 ± 0.05	-1.68 ± 0.07	-1.22 ± 0.07	-2.90 ± 0.14	-0.24 ± 0.01	-0.22 ± 0.01	-0.05 ± 0.01	0.07 ± 0.011
J01352-072	11	-3.51 ± 0.002	-7.44 ± 0.03	-0.90 ± 0.05	-1.33 ± 0.07	-1.06 ± 0.06	-2.37 ± 0.14	-0.34 ± 0.02	-0.35 ± 0.01	-0.23 ± 0.01	0.05 ± 0.006
J02088+494	17	-3.55 ± 0.003	-6.26 ± 0.04	-0.70 ± 0.03	-1.00 ± 0.03	-0.81 ± 0.03	-1.80 ± 0.06	-0.24 ± 0.01	-0.31 ± 0.01	-0.20 ± 0.01	0.06 ± 0.007
J03473-019	11	-3.69 ± 0.006	-3.83 ± 0.05	-0.39 ± 0.02	-0.45 ± 0.02	-0.32 ± 0.02	-0.80 ± 0.05	-0.30 ± 0.02	-0.35 ± 0.01	-0.26 ± 0.01	0.06 ± 0.006
J04198+425	35	-4.23 ± 0.021	-11.16 ± 0.54	-0.91 ± 1.32	-5.32 ± 2.41	-3.19 ± 1.62	-8.53 ± 3.53	0.04 ± 0.07	-0.23 ± 0.09	-0.28 ± 0.05	-0.11 ± 0.041
J05019+011	29	-3.57 ± 0.003	-6.51 ± 0.05	-0.55 ± 0.04	-0.87 ± 0.05	-0.76 ± 0.06	-1.62 ± 0.12	-0.13 ± 0.01	-0.12 ± 0.02	-0.06 ± 0.02	0.04 ± 0.010
J05062+046	13	-3.52 ± 0.003	-7.27 ± 0.06	-0.71 ± 0.07	-0.96 ± 0.07	-0.81 ± 0.05	-1.79 ± 0.10	-0.13 ± 0.01	-0.14 ± 0.01	-0.08 ± 0.02	0.03 ± 0.010
J05084-210	25	-3.34 ± 0.003	-15.27 ± 0.12	-1.22 ± 0.11	-2.24 ± 0.23	-1.63 ± 0.18	-3.70 ± 0.39	-0.18 ± 0.03	-0.18 ± 0.02	-0.06 ± 0.02	-0.03 ± 0.017
J05365+113	130	-4.52 ± 0.026	-0.46 ± 0.03	0.00 ± 0.02	-0.04 ± 0.02	-0.09 ± 0.02	-0.13 ± 0.03	-0.14 ± 0.01	-0.18 ± 0.01	-0.16 ± 0.01	0.00 ± 0.005
J06000+027	14	-3.95 ± 0.005	-2.74 ± 0.03	-0.31 ± 0.02	-0.46 ± 0.03	-0.35 ± 0.03	-0.82 ± 0.07	-0.05 ± 0.01	0.02 ± 0.01	0.04 ± 0.01	0.05 ± 0.008
J06318+414	33	-3.52 ± 0.004	-10.07 ± 0.08	-0.94 ± 0.05	-1.28 ± 0.14	-1.06 ± 0.09	-2.34 ± 0.18	-0.11 ± 0.01	-0.11 ± 0.02	-0.01 ± 0.02	0.03 ± 0.011
J07446+035	51	-3.61 ± 0.005	-7.29 ± 0.08	-0.82 ± 0.09	-0.87 ± 0.04	-0.66 ± 0.03	-1.54 ± 0.06	-0.18 ± 0.01	-0.21 ± 0.01	-0.09 ± 0.01	0.06 ± 0.010
J07472+503	16	-3.83 ± 0.003	-3.56 ± 0.02	-0.35 ± 0.02	-0.55 ± 0.03	-0.45 ± 0.03	-1.00 ± 0.06	-0.06 ± 0.01	0.08 ± 0.01	0.08 ± 0.01	0.07 ± 0.007
J07558+833	14	-3.76 ± 0.003	-5.10 ± 0.04	-0.63 ± 0.03	-0.77 ± 0.06	-0.56 ± 0.04	-1.32 ± 0.12	-0.12 ± 0.02	-0.02 ± 0.01	0.03 ± 0.01	0.08 ± 0.010
J08298+267	31	-4.31 ± 0.006	-4.69 ± 0.07	-0.47 ± 0.07	-0.50 ± 0.18	-0.01 ± 0.28	-0.49 ± 0.58	-0.09 ± 0.01	-0.08 ± 0.01	0.07 ± 0.01	-0.00 ± 0.025
J08536-034	42	-4.45 ± 0.054	-8.04 ± 0.73	-0.10 ± 0.29	-3.66 ± 1.37	-2.11 ± 1.18	-6.16 ± 4.37	-0.14 ± 0.07	-0.26 ± 0.09	-0.32 ± 0.09	-0.20 ± 0.061
J09449-123	11	-3.37 ± 0.002	-14.38 ± 0.05	-1.68 ± 0.07	-1.71 ± 0.11	-1.36 ± 0.09	-2.96 ± 0.22	-0.22 ± 0.01	-0.23 ± 0.01	-0.06 ± 0.01	0.02 ± 0.008
J11026+219	54	-4.51 ± 0.020	-0.51 ± 0.02	-0.04 ± 0.01	-0.13 ± 0.02	-0.08 ± 0.02	-0.21 ± 0.03	-0.08 ± 0.01	-0.08 ± 0.01	-0.08 ± 0.01	0.05 ± 0.007
J11201-104	29	-3.97 ± 0.008	-1.84 ± 0.03	-0.17 ± 0.02	-0.25 ± 0.04	-0.20 ± 0.02	-0.47 ± 0.05	-0.25 ± 0.01	-0.30 ± 0.02	-0.23 ± 0.01	0.06 ± 0.005
J11474+667	40	-3.71 ± 0.005	-6.48 ± 0.08	-0.78 ± 0.08	-1.08 ± 0.12	-0.82 ± 0.14	-1.84 ± 0.19	-0.14 ± 0.02	-0.04 ± 0.02	0.05 ± 0.03	0.08 ± 0.017
J12156+526	13	-3.65 ± 0.004	-5.45 ± 0.05	-0.63 ± 0.02	-0.70 ± 0.03	-0.50 ± 0.03	-1.19 ± 0.05	-0.13 ± 0.01	0.04 ± 0.02	0.05 ± 0.01	0.09 ± 0.005
J13005+056	12	-3.76 ± 0.005	-5.21 ± 0.07	-0.66 ± 0.06	-1.24 ± 0.05	-0.99 ± 0.20	-2.19 ± 0.10	-0.14 ± 0.01	-0.23 ± 0.02	-0.11 ± 0.02	0.02 ± 0.011
J13536+776	25	-3.79 ± 0.003	-3.88 ± 0.03	-0.39 ± 0.03	-0.55 ± 0.03	-0.44 ± 0.03	-0.98 ± 0.06	-0.04 ± 0.02	0.10 ± 0.01	0.09 ± 0.01	0.07 ± 0.011
J13591-198	17	-3.89 ± 0.004	-3.14 ± 0.03	-0.29 ± 0.06	-0.65 ± 0.09	-0.54 ± 0.04	-1.21 ± 0.09	-0.03 ± 0.02	-0.09 ± 0.01	-0.06 ± 0.01	0.02 ± 0.011
J14173+454	12	-3.93 ± 0.005	-3.92 ± 0.05	-0.52 ± 0.07	-0.94 ± 0.13	-0.63 ± 0.11	-1.56 ± 0.28	-0.06 ± 0.02	0.23 ± 0.01	0.24 ± 0.02	0.11 ± 0.013
J15218+209	54	-3.76 ± 0.005	-2.92 ± 0.04	-0.21 ± 0.02	-0.63 ± 0.02	-0.55 ± 0.02	-1.18 ± 0.04	-0.34 ± 0.01	-0.45 ± 0.01	-0.35 ± 0.01	0.07 ± 0.005
J15499+796	15	-3.82 ± 0.007	-5.02 ± 0.08	-0.63 ± 0.08	-1.47 ± 0.11	-1.05 ± 0.10	-2.57 ± 0.22	-0.09 ± 0.02	0.05 ± 0.02	0.13 ± 0.01	0.06 ± 0.019
J16313+408	13	-3.68 ± 0.003	-7.05 ± 0.05	-0.96 ± 0.08	-2.43 ± 0.16	-1.93 ± 0.10	-4.39 ± 0.31	-0.14 ± 0.02	-0.24 ± 0.02	-0.05 ± 0.05	0.01 ± 0.016
J17338+169	12	-3.51 ± 0.004	-11.86 ± 0.12	-1.38 ± 0.11	-1.71 ± 0.13	-1.33 ± 0.13	-3.04 ± 0.26	-0.18 ± 0.01	-0.27 ± 0.01	-0.14 ± 0.01	-0.05 ± 0.008
J18022+642	29	-3.84 ± 0.005	-4.87 ± 0.05	-0.60 ± 0.03	-1.29 ± 0.10	-0.93 ± 0.05	-2.23 ± 0.16	-0.07 ± 0.02	0.13 ± 0.01	0.19 ± 0.01	0.10 ± 0.014
J18131+260	16	-3.61 ± 0.003	-5.92 ± 0.04	-0.63 ± 0.04	-0.78 ± 0.05	-0.62 ± 0.04	-1.39 ± 0.10	-0.11 ± 0.01	-0.06 ± 0.01	-0.01 ± 0.01	0.07 ± 0.010

TABLE B.3: continued.

Karmn	No.	$\log L_{\rm Hff}/L_{\rm bol}$	Hα Å	He D_3 Å	Na D_2 Å	Na D_1 Å	Na D Å	Ca IRT-a Å	Ca IRT-b Å	Ca IRT-c Å	Fe 8691 Å
J18174+483	71	-4.00 ± 0.005	-1.70 ± 0.02	-0.12 ± 0.01	-0.19 ± 0.02	-0.15 ± 0.02	-0.34 ± 0.04	-0.17 ± 0.01	-0.22 ± 0.01	-0.17 ± 0.01	0.04 ± 0.005
J18189+661	13	-4.08 ± 0.007	-2.47 ± 0.04	-0.32 ± 0.05	-1.00 ± 0.05	-0.68 ± 0.05	-1.68 ± 0.11	-0.02 ± 0.01	0.07 ± 0.01	0.12 ± 0.01	0.08 ± 0.013
J19511+464	14	-3.73 ± 0.004	-4.52 ± 0.05	-0.53 ± 0.02	-0.73 ± 0.04	-0.52 ± 0.04	-1.25 ± 0.09	-0.08 ± 0.01	0.01 ± 0.01	0.03 ± 0.01	0.07 ± 0.008
J22012+283	12	-3.57 ± 0.002	-6.48 ± 0.04	-0.72 ± 0.02	-0.79 ± 0.03	-0.59 ± 0.04	-1.37 ± 0.06	-0.15 ± 0.01	-0.09 ± 0.01	-0.03 ± 0.01	0.06 ± 0.006
J22468+443	107	-3.64 ± 0.004	-5.04 ± 0.04	-0.50 ± 0.05	-0.76 ± 0.04	-0.66 ± 0.03	-1.42 ± 0.05	-0.16 ± 0.01	-0.23 ± 0.01	-0.13 ± 0.01	0.05 ± 0.008
J23548+385	13	-3.68 ± 0.003	-5.04 ± 0.04	-0.62 ± 0.02	-0.57 ± 0.04	-0.41 ± 0.03	-0.97 ± 0.08	-0.08 ± 0.01	0.03 ± 0.02	0.06 ± 0.01	0.09 ± 0.014

TABLE B.4: Flare analysis results for the stellar sample

Karmn	Name	TIC	Obs. time (d)	Flare freq (d^{-1})	F Duration (min)	Amplitude	ED (sec)	$log(E_{flare})$ (erg)	α	R_{var}	P_{rot} (d)	Ro
J01019+541	G 218-020	252110114	36.80	0.71	8 - 56	0.012 - 0.655	3.88 - 444.04	30.88 - 32.93	1.95	0.021	0.139	0.001 ± 5.7e-05
J01033+623*	V388 Cas	52183206	45.89	2.85	6 - 288	0.003 - 0.592	1.34 - 1825.88	30.81 - 33.94	1.79	0.054	1.024	0.014 ± 0.00058
J01352-072	Barta 161 12	29853348	19.07	1.63	6 - 110	0.003 - 0.151	1.29 - 129.50	31.86 - 33.86	1.51	0.109	0.703	0.031 ± 0.0016
J02088+494	G 173-039	250602194	21.19	2.55	6 - 268	0.003 - 0.497	0.73 - 611.89	31.20 - 34.12	1.50	0.020	0.749	0.016 ± 0.00071
J03473-019	G 80-021	333680372	24.23	2.93	6 - 124	0.002 - 0.145	0.61 - 79.46	31.40 - 33.51	1.56	0.035	3.858	0.110 ± 0.0051
J04198+425*	LSR J0419	347994537	23.33	0.13	10 - 20	0.097 - 0.194	28.48 - 74.34	30.87 - 31.29	2.00	0.083	0.987	0.008 ± 0.00029
J05019+011	1RXS J0501	269077806	24.04	1.87	6 - 130	0.001 - 0.150	0.81 - 154.66	31.51 - 33.79	1.48	0.029	2.088	0.071 ± 0.0035
J05062+046*	RX J0506.2	455029978	24.23	1.49	6 - 104	0.005 - 0.047	1.32 - 100.55	31.65 - 33.53	1.71	0.019	0.889	0.024 ± 0.0011
J05084-210	2MASS J05	146539195	24.15	0.70	8 - 74	0.008 - 0.139	3.08 - 258.92	32.10 - 34.02	1.75	0.052	0.281	0.013 ± 0.00071
J05365+113	V2689 Ori	436248822	20.68	0.82	6 - 68	0.001 - 0.004	0.21 - 3.87	31.42 - 32.69	1.75	0.026	11.45	0.378 ± 2e-05
J06000+027	G 99-049	282501711	20.67	3.29	6 - 108	0.001 - 0.095	0.35 - 32.36	30.43 - 32.40	1.83	0.005	1.814	0.024 ± 0.00098
J06318+414	LP 205-044	144282456	23.08	1.04	6 - 82	0.008 - 0.197	1.85 - 164.46	31.40 - 33.35	1.46	0.034	0.300	0.007 ± 0.00032
J07446+035	YZ CMi	266744225	22.79	6.27	6 - 212	0.001 - 0.146	0.31 - 140.54	30.59 - 33.25	1.75	0.038	2.772	0.054 ± 0.0025
J07472+503	2MASS J07	309661100	23.08	1.08	8 - 70	0.003 - 0.045	1.44 - 26.94	31.16 - 32.43	2.13	0.014	1.314	0.019 ± 0.00079
J07558+833	GJ 1101	289972535	72.21	2.26	6 - 72	0.003 - 0.276	1.00 - 121.82	30.95 - 33.04	2.03	0.040	1.107	0.016 ± 0.00066
J08298+267*	DX Cnc	3664898	23.36	0.94	8 - 78	0.007 - 0.795	2.55 - 222.28	30.19 - 32.13	1.78	0.016	0.459	0.004 ± 0.00016
J08536-034	LP 666-009	7975441	17.67	0.57	6 - 30	0.025 - 0.368	7.30 - 265.38	30.07 - 31.63	1.53	0.080	0.464	0.003 ± 8.2e-05
J09449-123	G 161-071	289706625	19.95	2.81	6 - 254	0.004 - 0.317	1.14 - 781.47	31.01 - 33.84	1.58	0.084	0.442	0.008 ± 0.00036
J11026+219	DS Leo	97488127	22.40	0.54	6 - 50	0.002 - 0.011	0.77 - 7.99	31.84 - 32.85	1.81	0.030	13.703	0.410 ± 0.022
J11201-104	LP 733-099	453465810	22.34	0.72	8 - 144	0.002 - 0.126	1.05 - 74.69	31.77 - 33.62	1.64	0.017	5.704	0.174 ± 0.008
J11474+667	1RXS J1147	142878895	77.12	0.84	6 - 1386	0.009 - 0.697	2.46 - 4649.33	31.31 - 34.58	1.75	0.072	13.347	0.232 ± 0.017
J12156+526	StKM 2-809	416538839	21.91	2.10	8 - 106	0.003 - 0.126	1.19 - 84.73	31.71 - 33.57	1.66	0.024	0.725	0.023 ± 0.0011
J13005+056	FN Vir	411248800	19.20	1.51	6 - 54	0.004 - 0.049	1.45 - 36.54	30.81 - 32.21	1.85	0.014	0.601	0.007 ± 0.00027
J13536+776	RX J1353.6	219463771	125.63	0.71	6 - 200	0.003 - 0.119	0.85 - 251.28	30.94 - 33.41	1.71	0.020	1.231	0.018 ± 0.00077
J13591-198	LP 799-007	125421413	18.34	1.09	6 - 140	0.004 - 0.059	1.12 - 75.91	31.00 - 32.83	1.72	0.013	3.346	0.048 ± 0.002
J14173+454	RX J1417.3	168747450	44.98	1.00	6 - 48	0.006 - 0.310	2.48 - 172.93	31.36 - 33.21	1.99	0.019	0.366	0.006 ± 0.00024
J15218+209	OT Ser	355793860	25.56	2.39	6 - 200	0.001 - 0.302	0.31 - 282.71	31.27 - 34.24	1.58	0.021	3.380	0.114 ± 0.0054
J15499+796	LP 022-420	159398282	172.86	0.27	6 - 134	0.012 - 0.624	3.54 - 657.98	31.46 - 33.73	1.66	0.019	0.188	0.003 ± 0.00013
J16313+408	G 180-060	255932726	49.95	0.66	8 - 70	0.010 - 0.215	3.16 - 170.98	30.91 - 32.64	1.95	0.020	0.512	0.006 ± 0.00024
J17338+169	1RXS J1733	400361232	23.94	1.25	10 - 90	0.008 - 0.326	3.77 - 339.01	31.51 - 33.47	1.78	0.062	0.266	0.005 ± 0.00026
J18022+642	LP 071-082	233068870	267.47	1.73	6 - 218	0.003 - 1.346	1.02 - 1720.54	30.56 - 33.79	2.02	0.011	0.280	0.003 ± 0.00012
J18131+260	LP 390-16	313988572	23.94	1.63	6 - 318	0.005 - 0.388	1.39 - 433.10	31.27 - 33.77	1.48	0.067	2.286	0.042 ± 0.0018

Table B.4: continued.

Karmn	Name	TIC	Obs. time (d)	Flare freq (d^{-1})	F Duration (min)	Amplitude	ED (sec)	$log(E_{flare})$ (erg)	α	R_{var}	P_{rot} (d)	Ro
J18174+483	TYC 3529-1	289726188	74.23	0.81	8 - 256	0.003 - 0.065	0.96 - 115.99	31.77 - 33.85	1.49	0.026	15.188	0.507 ± 0.031
J18189+661	LP 71-165	406857100	236.29	0.63	6 - 82	0.004 - 0.162	1.26 - 78.43	30.54 - 32.34	2.02	0.012	0.523	0.005 ± 0.00019
J19511+464	G 208-042	273589987	50.85	2.32	6 - 88	0.003 - 0.223	0.67 - 74.14	30.77 - 32.81	1.92	0.016	0.593	0.008 ± 0.00034
J22012+283	V374 Peg	283410775	18.35	3.60	6 - 96	0.003 - 0.203	0.79 - 107.94	30.98 - 33.12	2.22	0.025	0.446	0.007 ± 0.00032
J22468+443	EV Lac	154101678	23.37	5.22	6 - 276	0.002 - 0.288	0.36 - 195.52	30.74 - 33.48	1.53	0.029	4.349	0.079 ± 0.0034
J23548+385	RX J2354.8	291689873	18.16	2.20	6 - 200	0.004 - 0.292	1.91 - 164.44	31.37 - 33.31	1.66	0.056	4.743	0.084 ± 0.0036

* Stars with an asterisk next to their designations have more than 25% contamination in their flux (for further details, refer to Section 4.5.1).

B.2 TPF plots

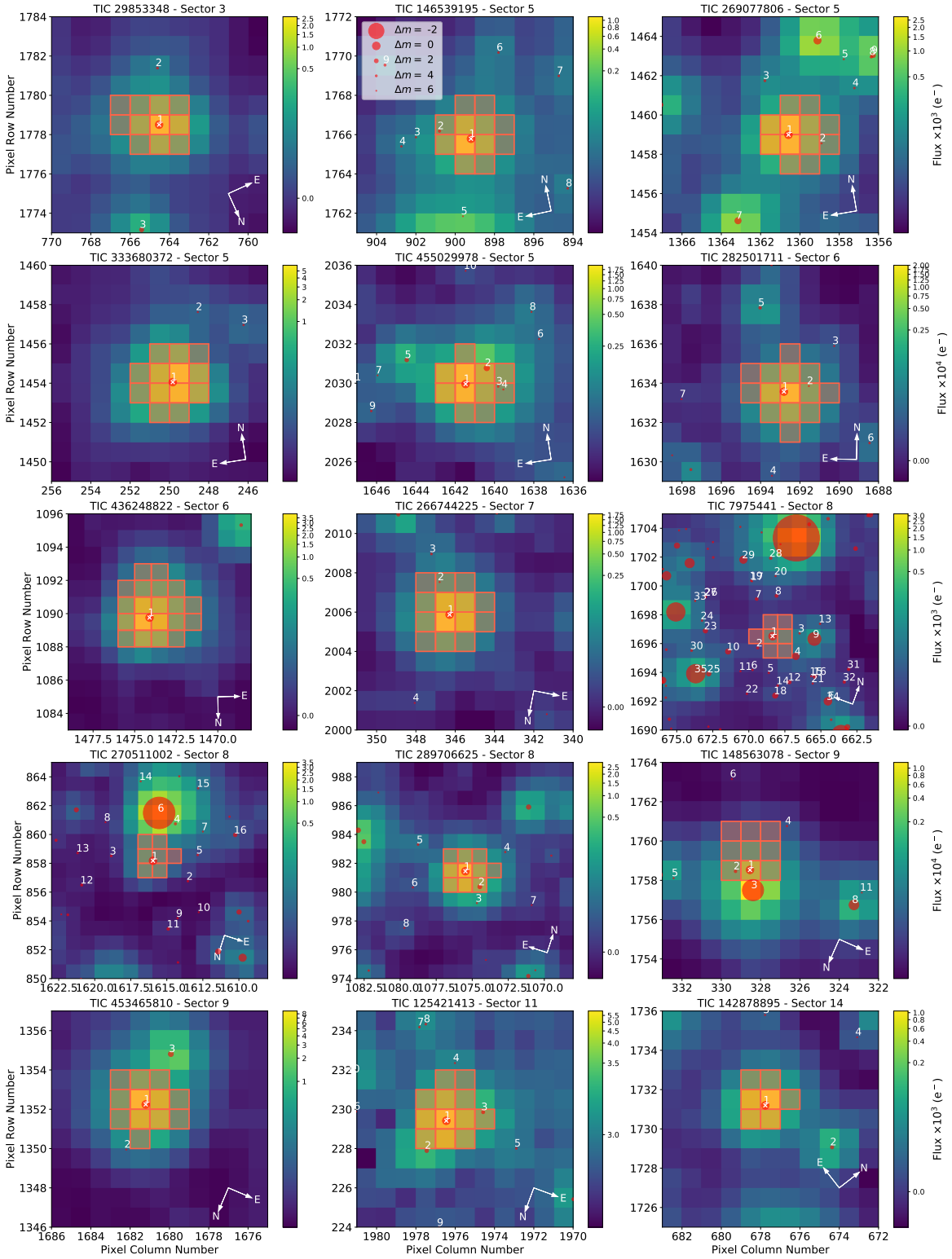

FIGURE B.1: Target pixel files (TPF) of targets in TESS Sectors. The electron counts are color-coded. The red bordered pixels are used in the simple aperture photometry (SAP). The size of the red circles indicates the TESS magnitudes of the main star (circle #1 marked with $\ll \times \gg$) and all stars in its vicinity.

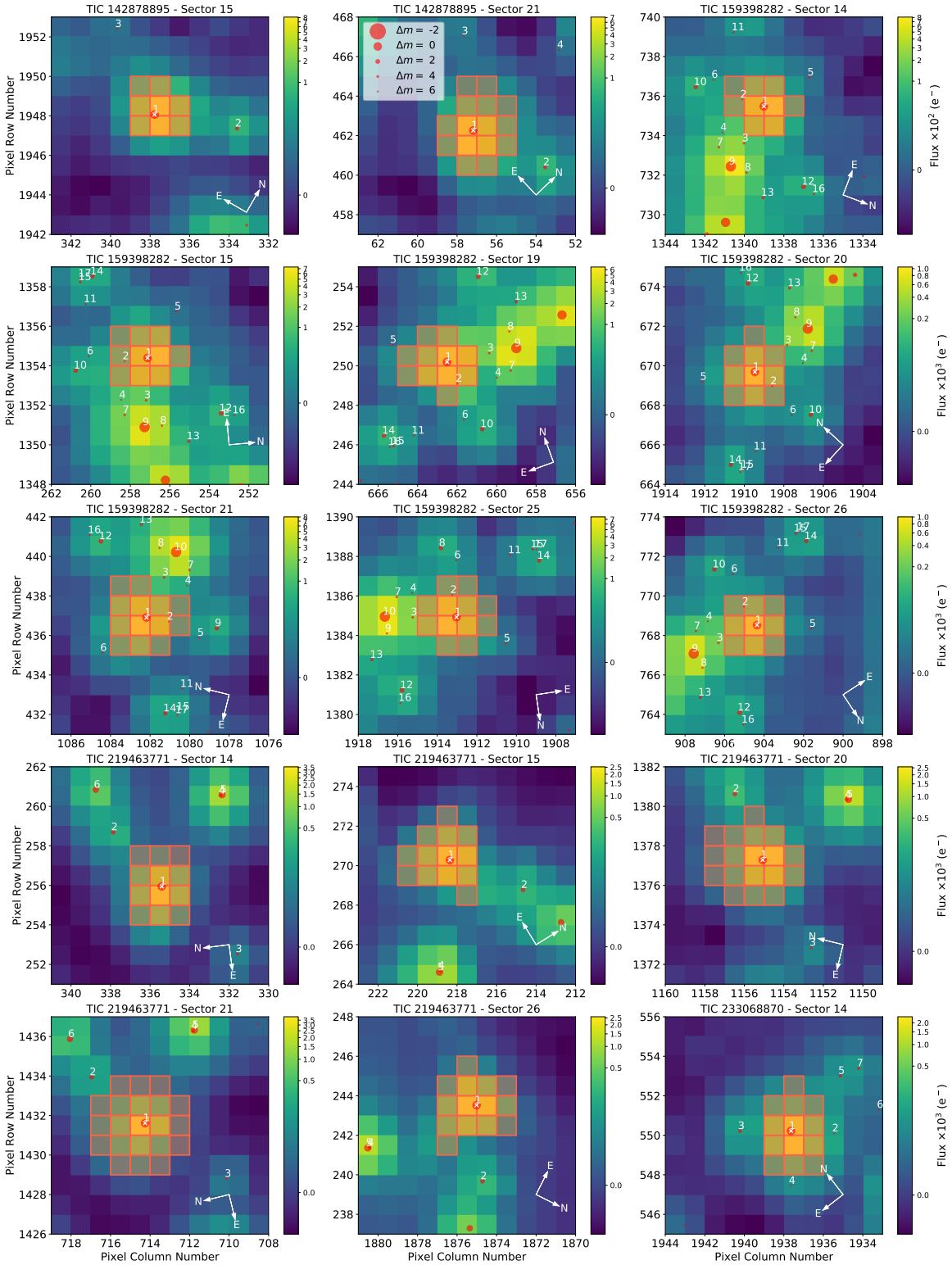
TIC 142878895 - Sector 15
TIC 142878895 - Sector 21
TIC 159398282 - Sector 14
TIC 159398282 - Sector 15
TIC 159398282 - Sector 19
TIC 159398282 - Sector 20
TIC 159398282 - Sector 21
TIC 159398282 - Sector 25
TIC 159398282 - Sector 26
TIC 219463771 - Sector 14
TIC 219463771 - Sector 15
TIC 219463771 - Sector 20
TIC 219463771 - Sector 21
TIC 219463771 - Sector 26
TIC 233068870 - Sector 14
Δm = -2
Δm = 0
Δm = 2
Δm = 4
Δm = 6
Pixel Row Number
Pixel Column Number
Flux ×10² (e⁻)
Flux ×10³ (e⁻)

continued.

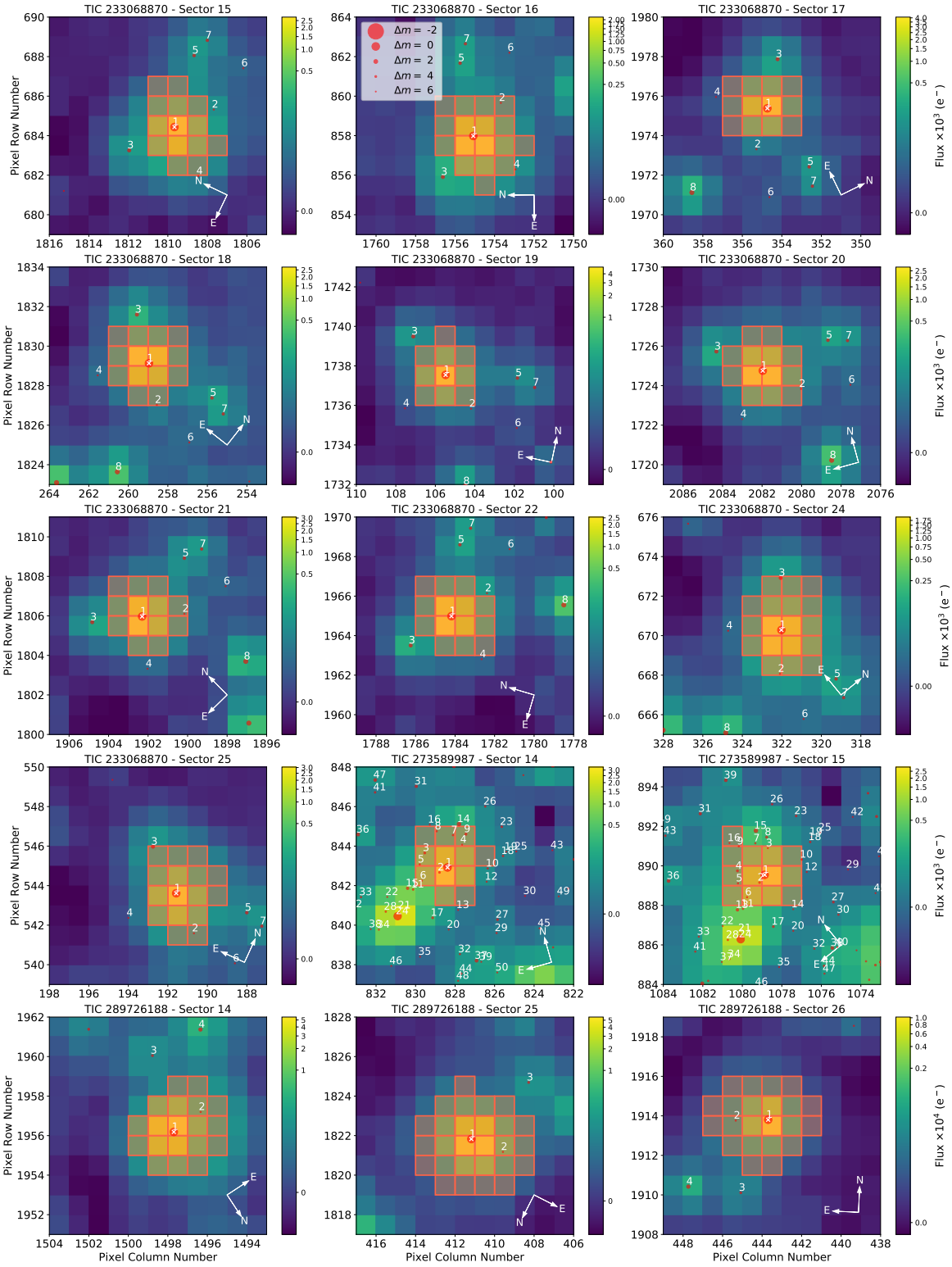
TIC 233068870 - Sector 15
TIC 233068870 - Sector 16
TIC 233068870 - Sector 17
TIC 233068870 - Sector 18
TIC 233068870 - Sector 19
TIC 233068870 - Sector 20
TIC 233068870 - Sector 21
TIC 233068870 - Sector 22
TIC 233068870 - Sector 24
TIC 233068870 - Sector 25
TIC 273589987 - Sector 14
TIC 273589987 - Sector 15
TIC 289726188 - Sector 14
TIC 289726188 - Sector 25
TIC 289726188 - Sector 26
Δm = -2
Δm = 0
Δm = 2
Δm = 4
Δm = 6
Pixel Row Number
Pixel Column Number
Flux ×10³ (e⁻)
Flux ×10⁴ (e⁻)

continued.

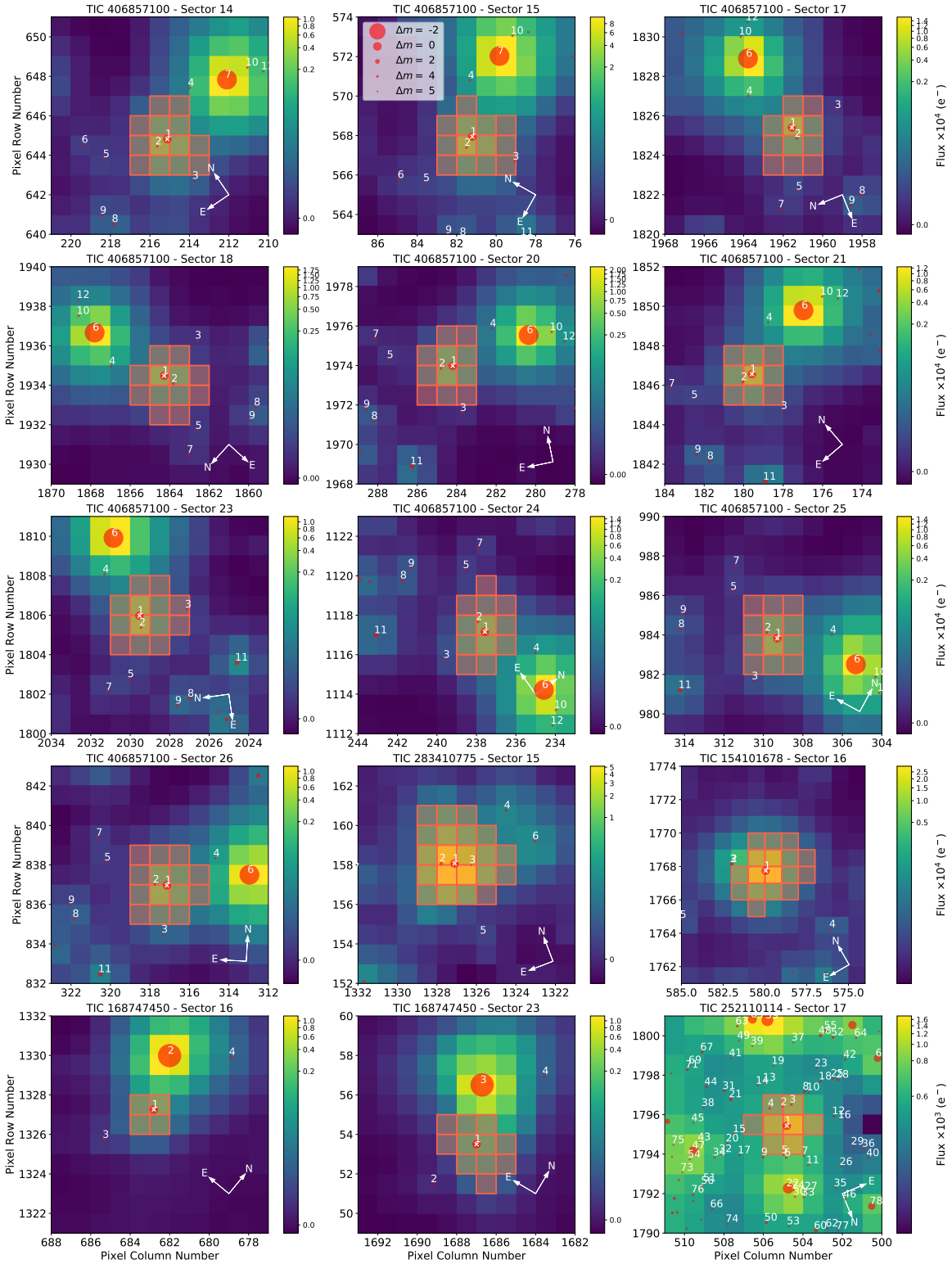
TIC 406857100 - Sector 14
TIC 406857100 - Sector 15
TIC 406857100 - Sector 17
TIC 406857100 - Sector 18
TIC 406857100 - Sector 20
TIC 406857100 - Sector 21
TIC 406857100 - Sector 23
TIC 406857100 - Sector 24
TIC 406857100 - Sector 25
TIC 406857100 - Sector 26
TIC 283410775 - Sector 15
TIC 154101678 - Sector 16
TIC 168747450 - Sector 16
TIC 168747450 - Sector 23
TIC 252110114 - Sector 17
Δm = -2
Δm = 0
Δm = 2
Δm = 4
Δm = 5
Pixel Row Number
Pixel Column Number
Flux ×10⁴ (e⁻)
Flux ×10³ (e⁻)

continued.

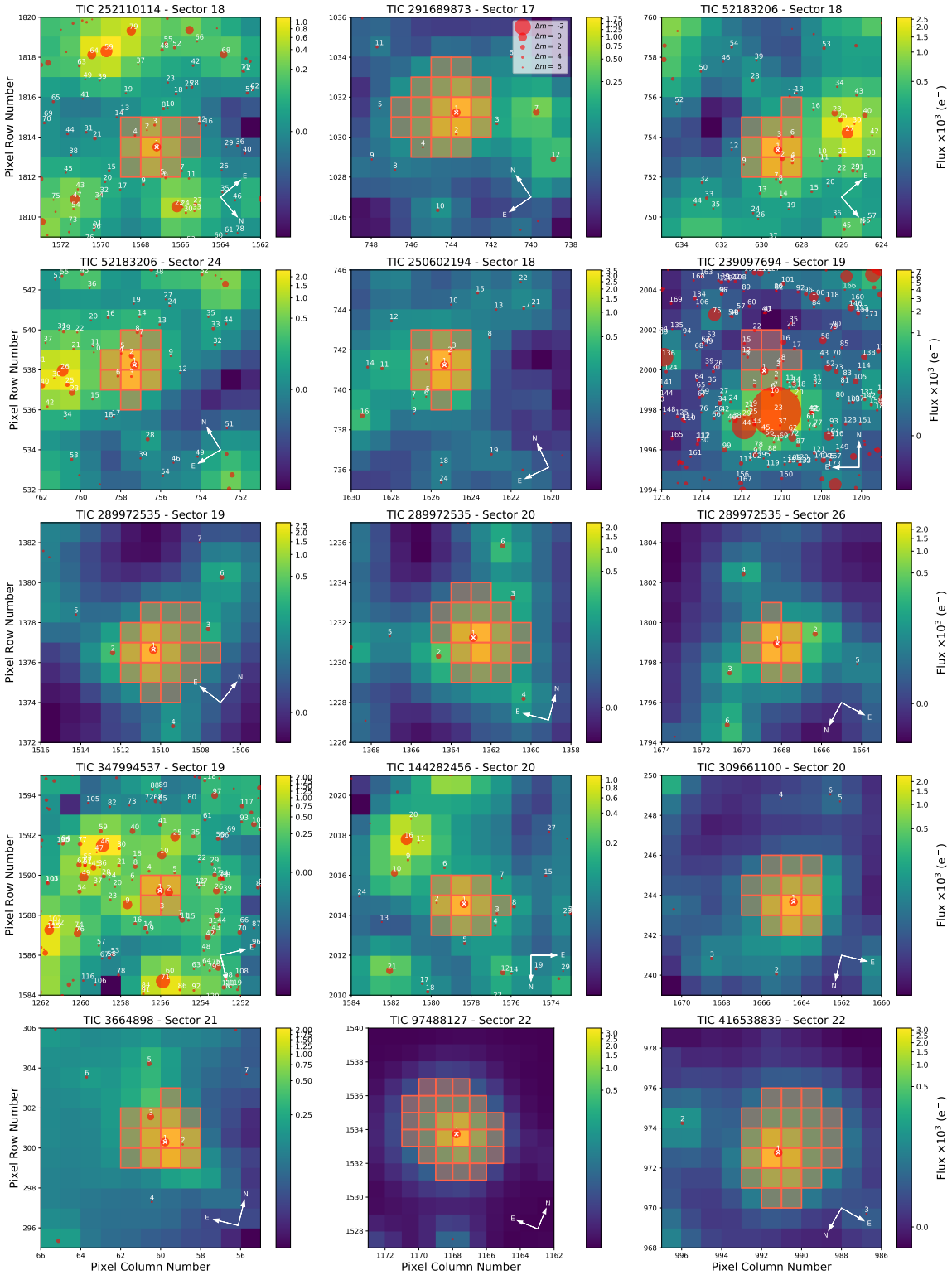
TIC 252110114 - Sector 18
TIC 291689873 - Sector 17
TIC 52183206 - Sector 18
TIC 52183206 - Sector 24
TIC 250602194 - Sector 18
TIC 239097694 - Sector 19
TIC 289972535 - Sector 19
TIC 289972535 - Sector 20
TIC 289972535 - Sector 26
TIC 347994537 - Sector 19
TIC 144282456 - Sector 20
TIC 309661100 - Sector 20
TIC 3664898 - Sector 21
TIC 97488127 - Sector 22
TIC 416538839 - Sector 22
Pixel Row Number
Pixel Column Number
Flux ×10³ (e⁻)

continued.

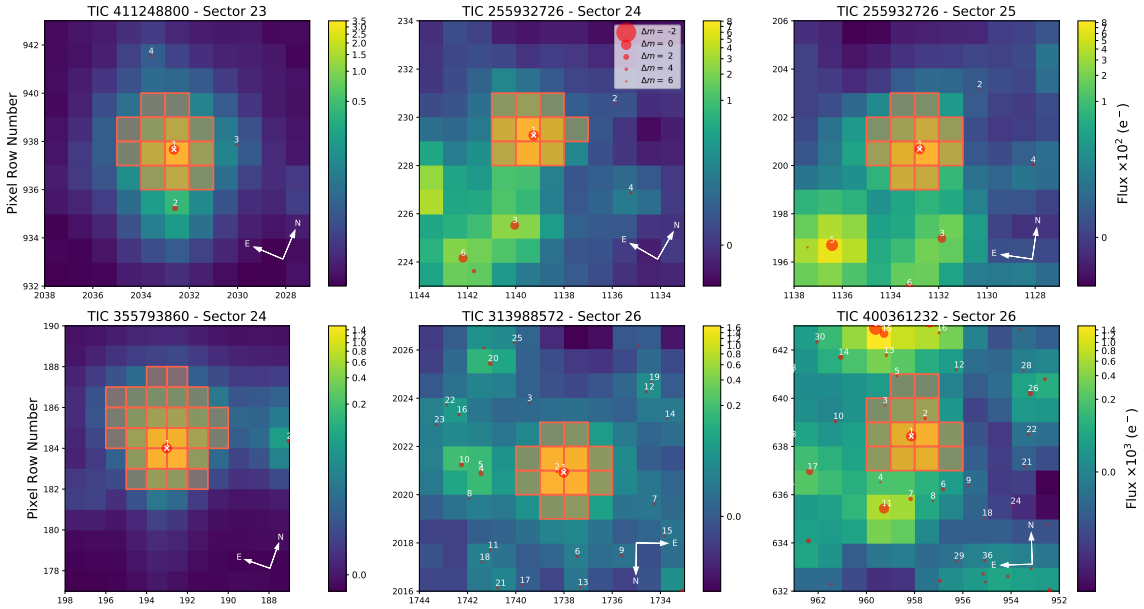
TIC 411248800 - Sector 23
TIC 255932726 - Sector 24
TIC 255932726 - Sector 25
TIC 355793860 - Sector 24
TIC 313988572 - Sector 26
TIC 400361232 - Sector 26
Pixel Row Number
Flux ×10² (e⁻)
Flux ×10³ (e⁻)
Δm = -2
Δm = 0
Δm = 2
Δm = 4
Δm = 6
N
E

continued.

B.3 Comparison of rotation periods: TESS data vs. published values

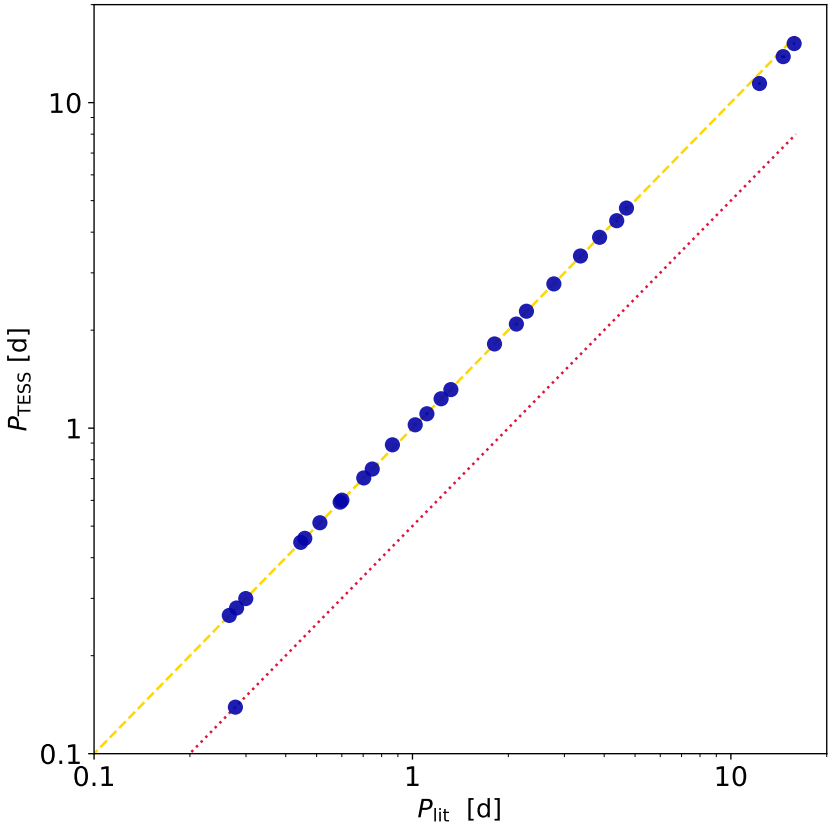

FIGURE B.2: Correlation between P_{rot} derived from TESS data and those previously published by Díez Alonso et al. (2019) and Kiraga (2012). The yellow dashed line represents a one-to-one correlation, while the red dotted line indicates the first harmonics of the rotation periods. The only outlier is G 218-020 (J01019+541, TIC 252110114).

B.4 TESS Light curve and flare analysis plots

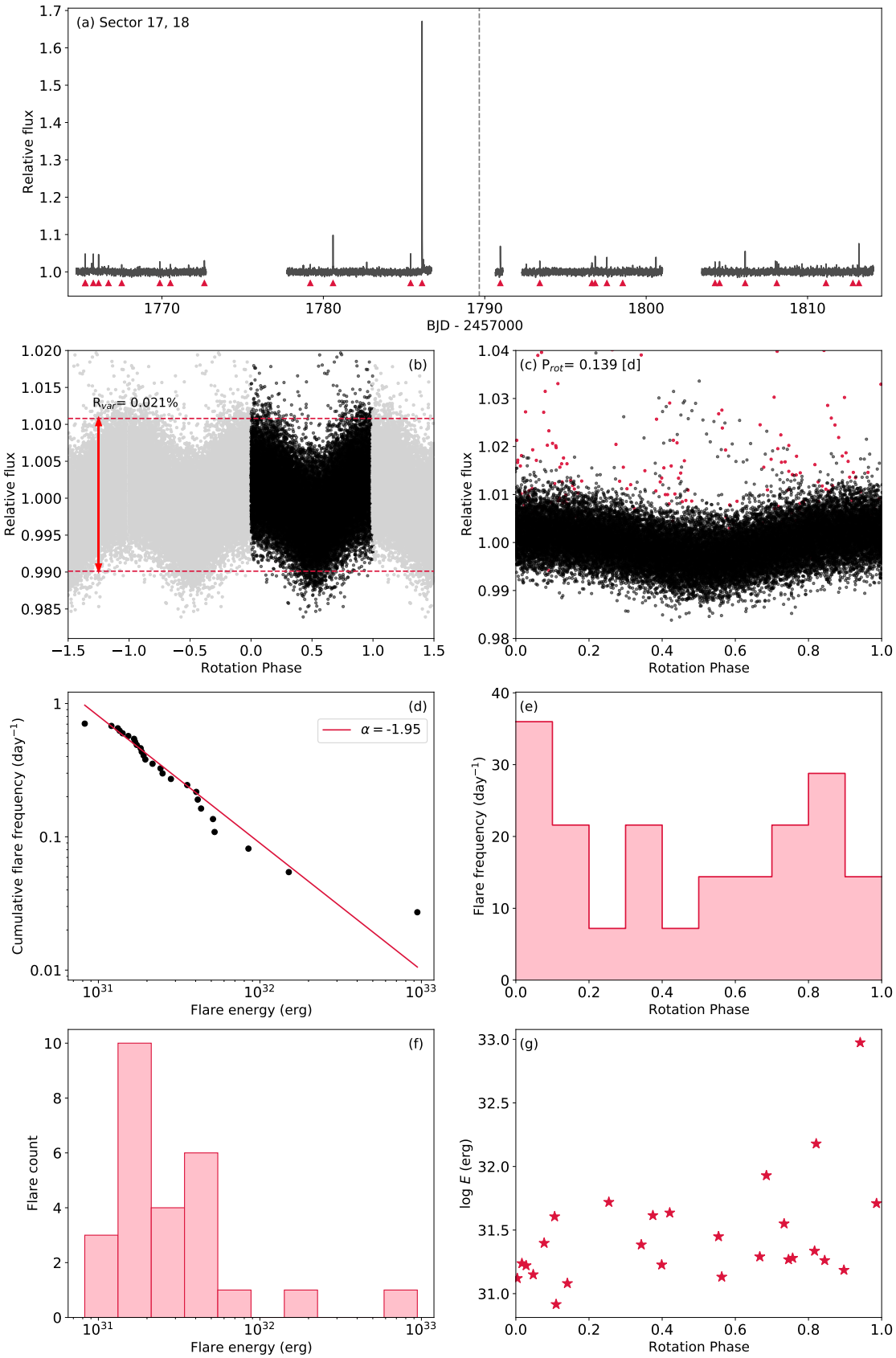

FIGURE B.3: Flare analysis results for G 218-020 (J01019+541, TIC 252110114). (a) TESS light curve displaying the observed variability and detected flares. (b) Variability range of the light curve after removing flares. (c) Phase-folded light curve illustrating rotational variations. (d) Cumulative FFD based on energy. (e) Frequency of flares plotted against rotation phase. (f) Flare count plotted against flare energy. (g) Bolometric energy of each flare plotted against rotation phase.

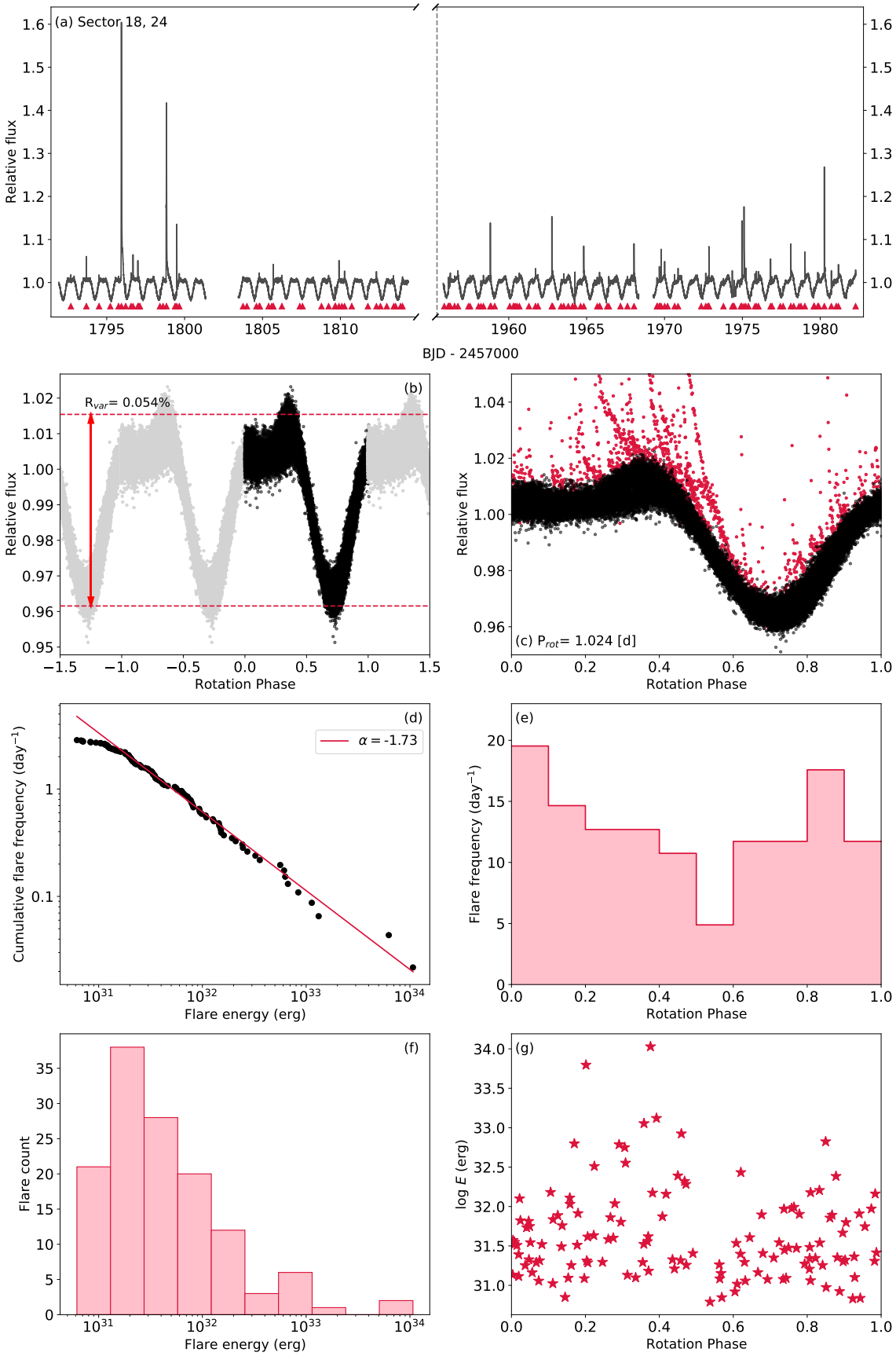

FIGURE B.4: Same as Fig. B.3 but for V388 Cas (J01033+623, TIC 52183206).

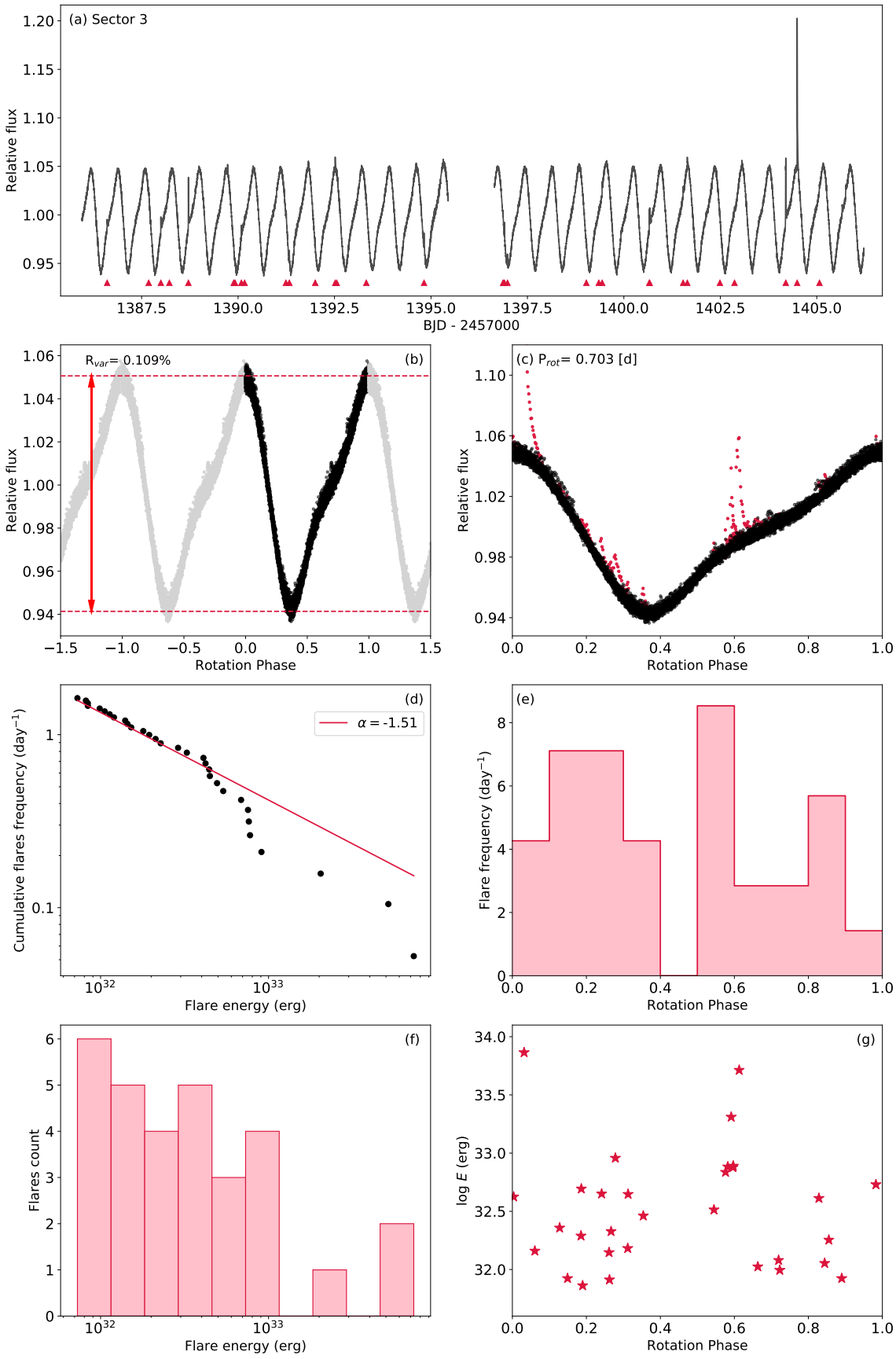

FIGURE B.5: Same as Fig. B.3 but for Barta 161 12 (J01352-072, TIC 29853348).

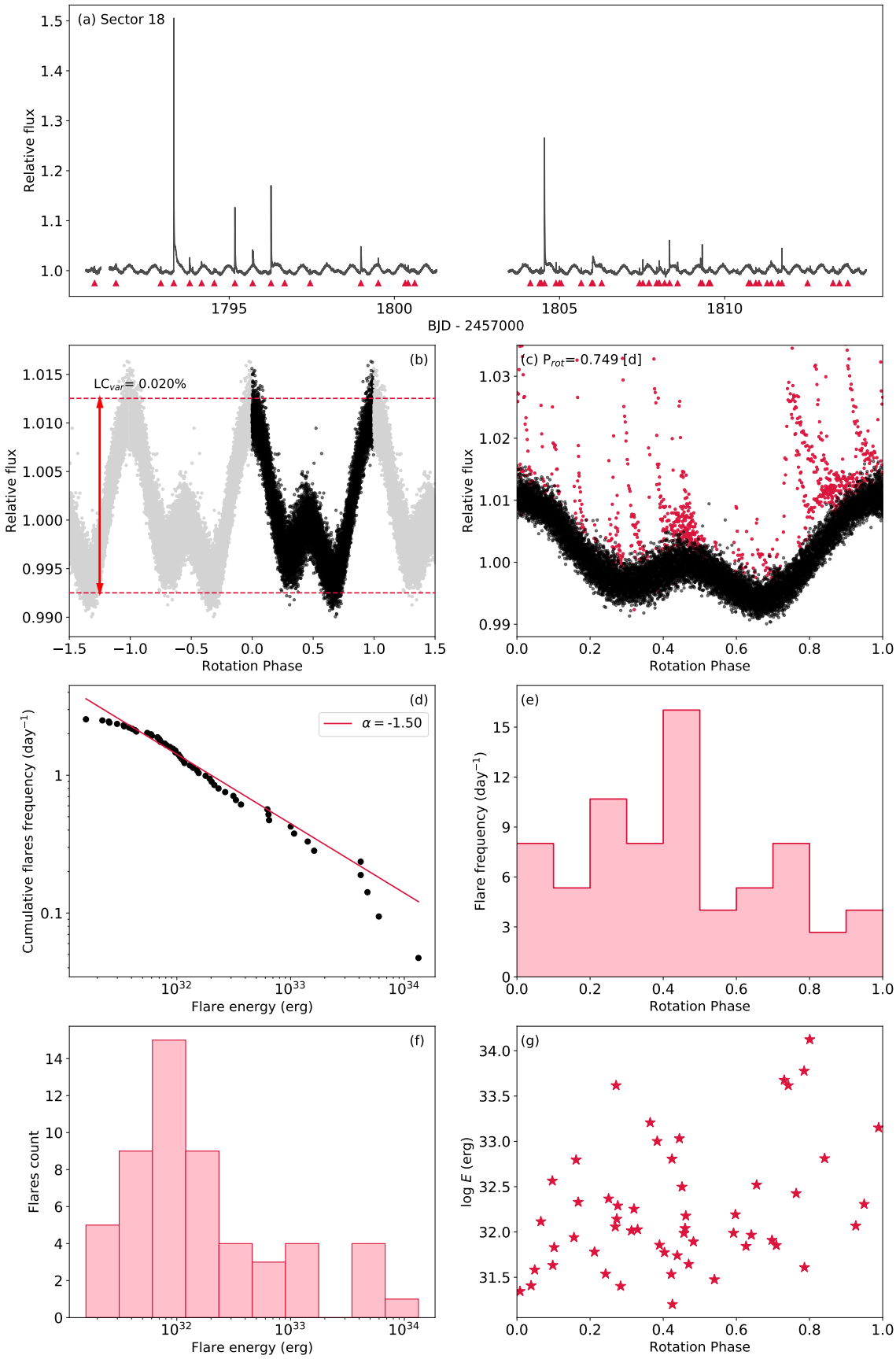

FIGURE B.6: Same as Fig. B.3 but for G 173-039 (J02088+494, TIC 250602194).

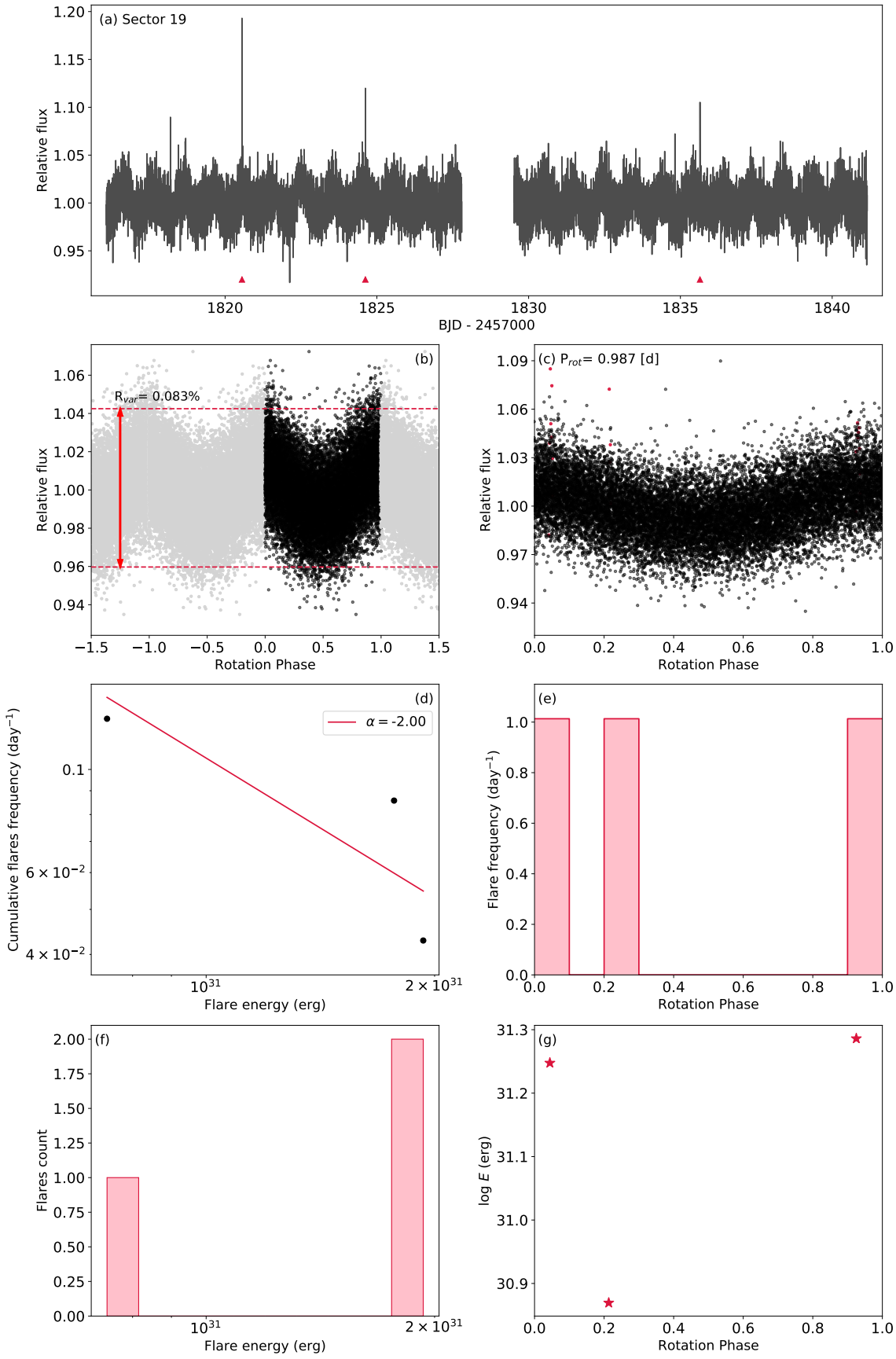

FIGURE B.7: Same as Fig. B.3 but for LSR J0419+4233 (J04198+425, TIC 347994537).

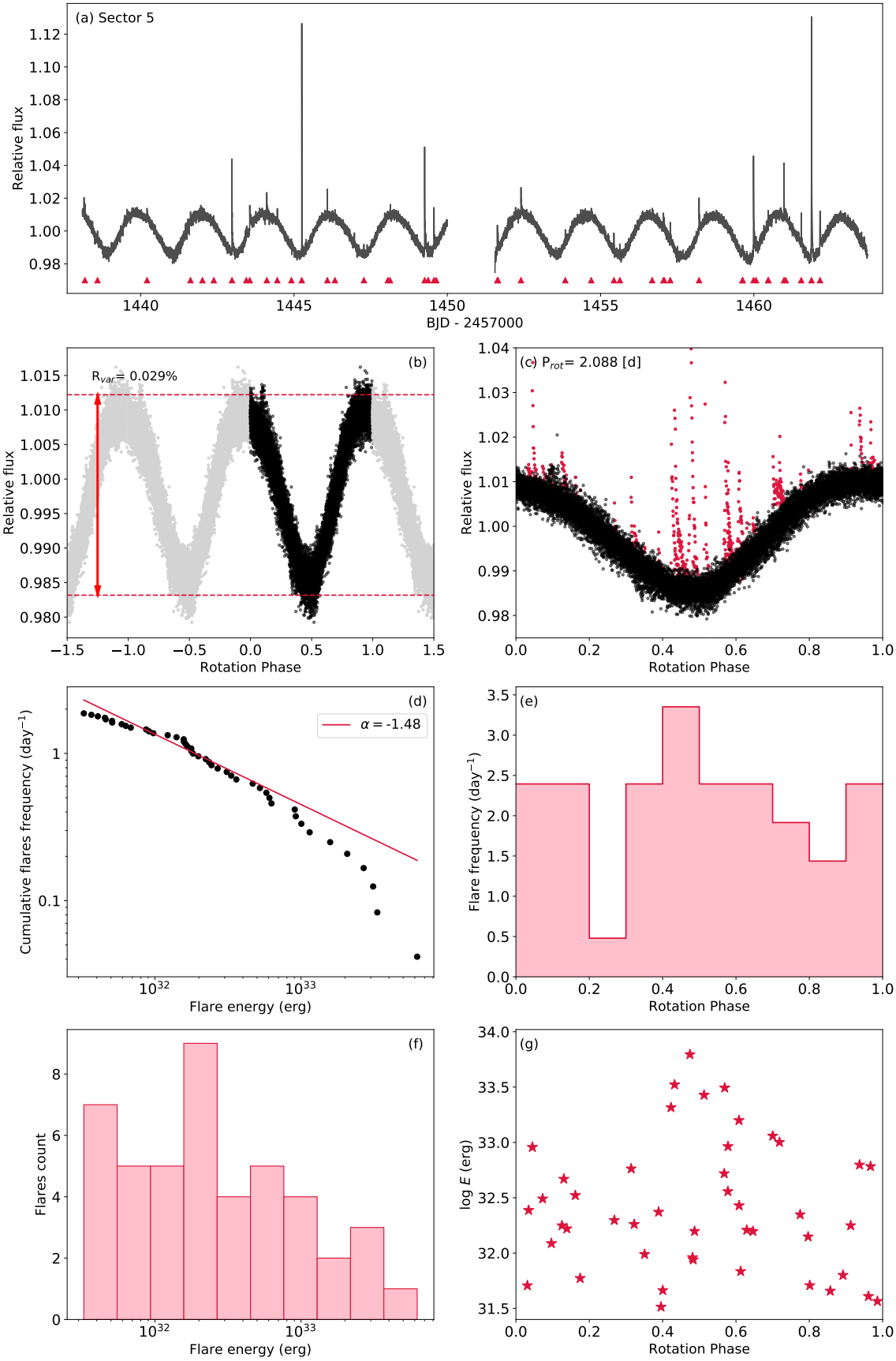

FIGURE B.8: Same as Fig. B.3 but for 1RXS J050156.7+010845 (J05019+011, TIC 269077806).

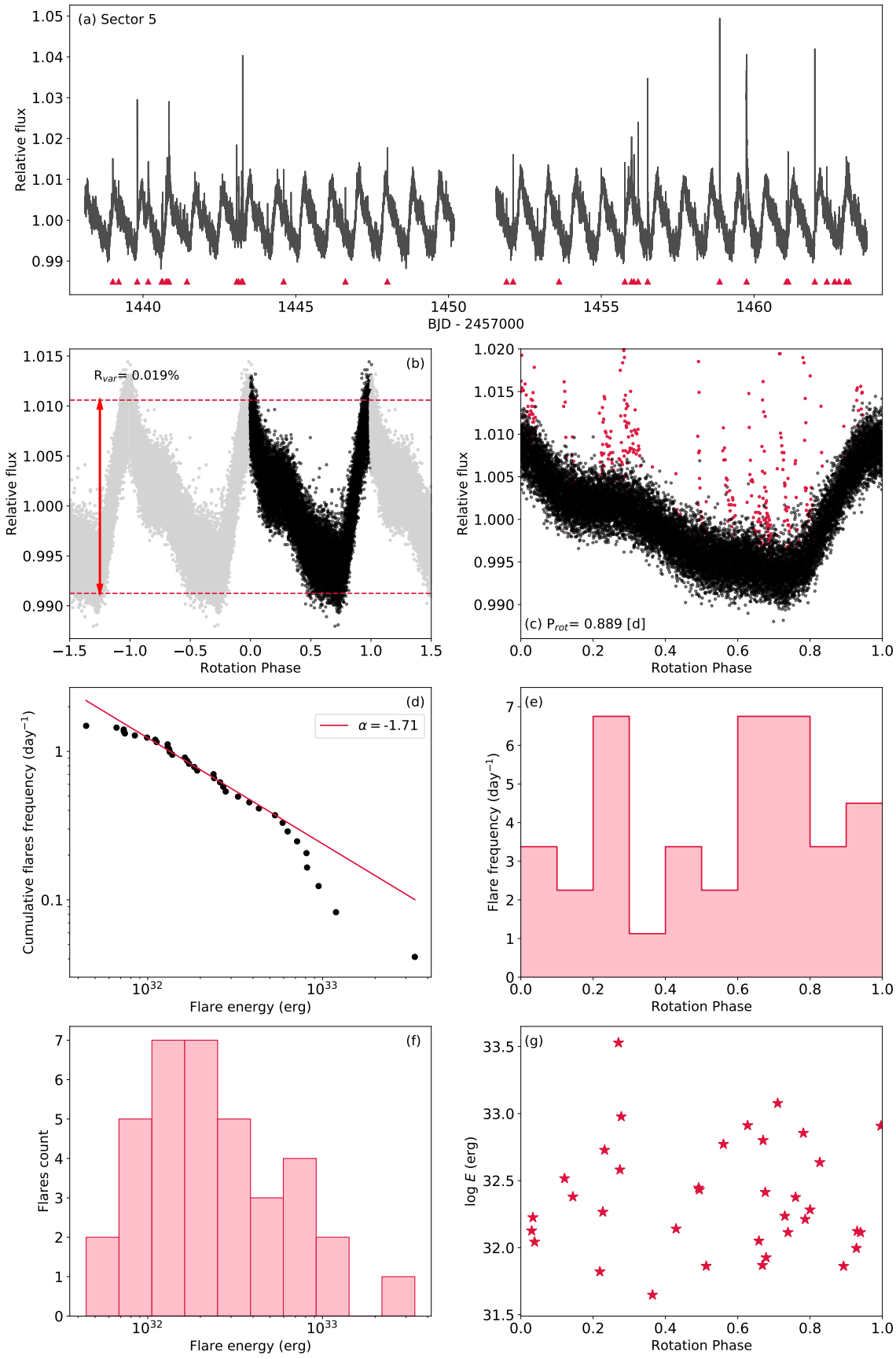

FIGURE B.9: Same as Fig. B.3 but for RX J0506.2+0439 (J05062+046, TIC 455029978).

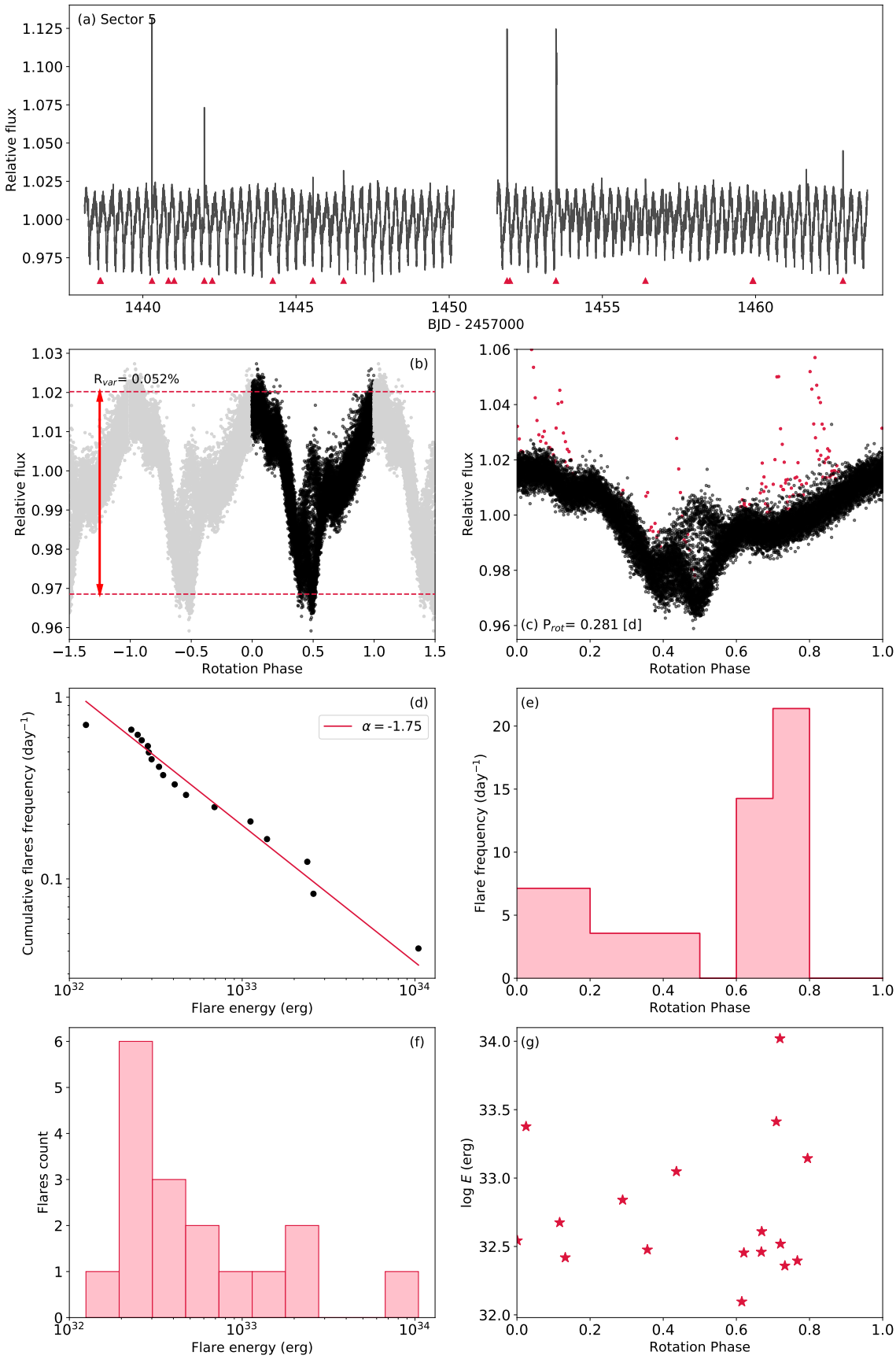

FIGURE B.10: Same as Fig. B.3 but for 2MASS J05082729-2101444 (J05084-210, TIC 146539195).

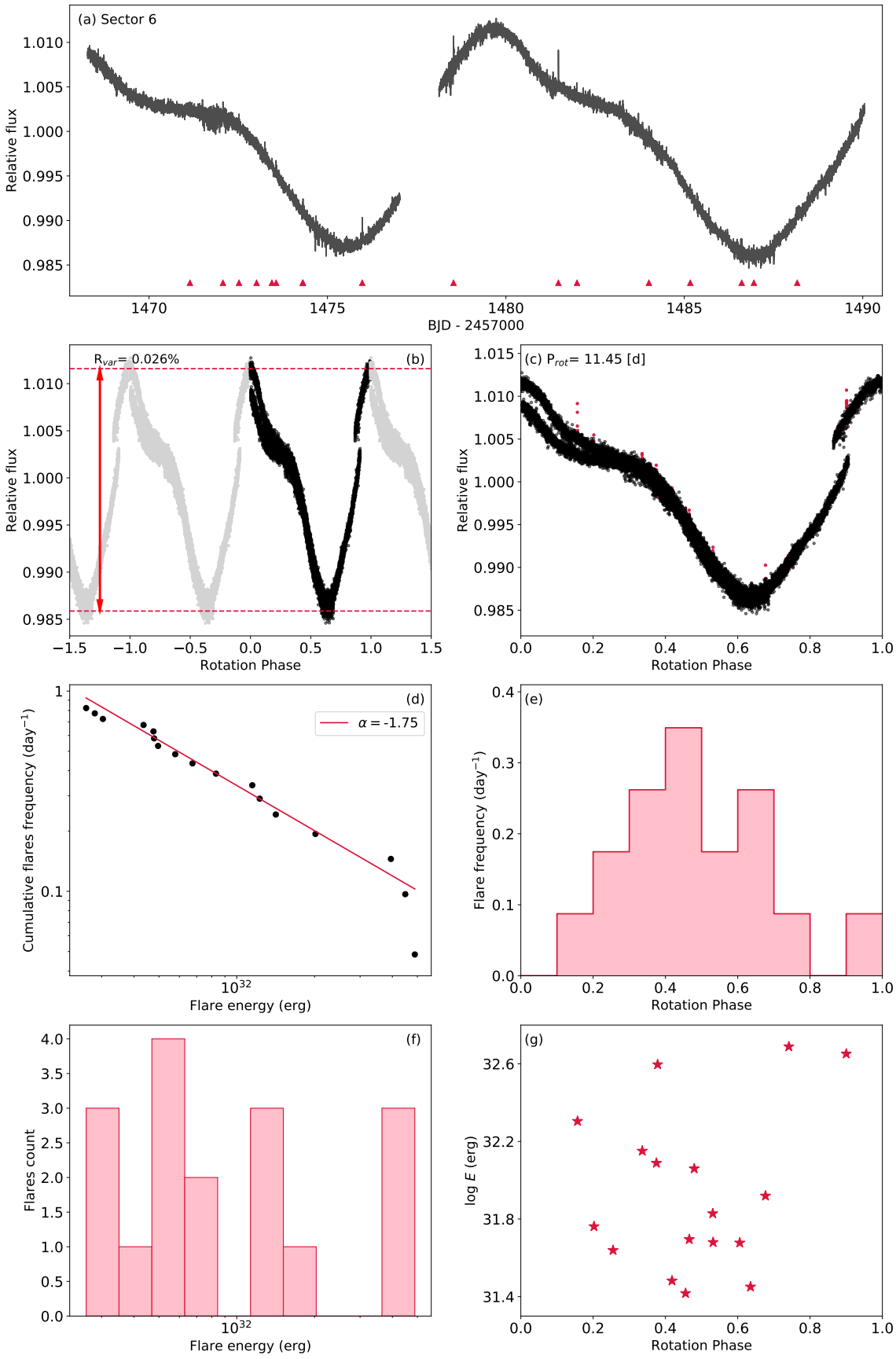

FIGURE B.11: Same as Fig. B.3 but for V2689 Ori (J05365+113, TIC 436248822).

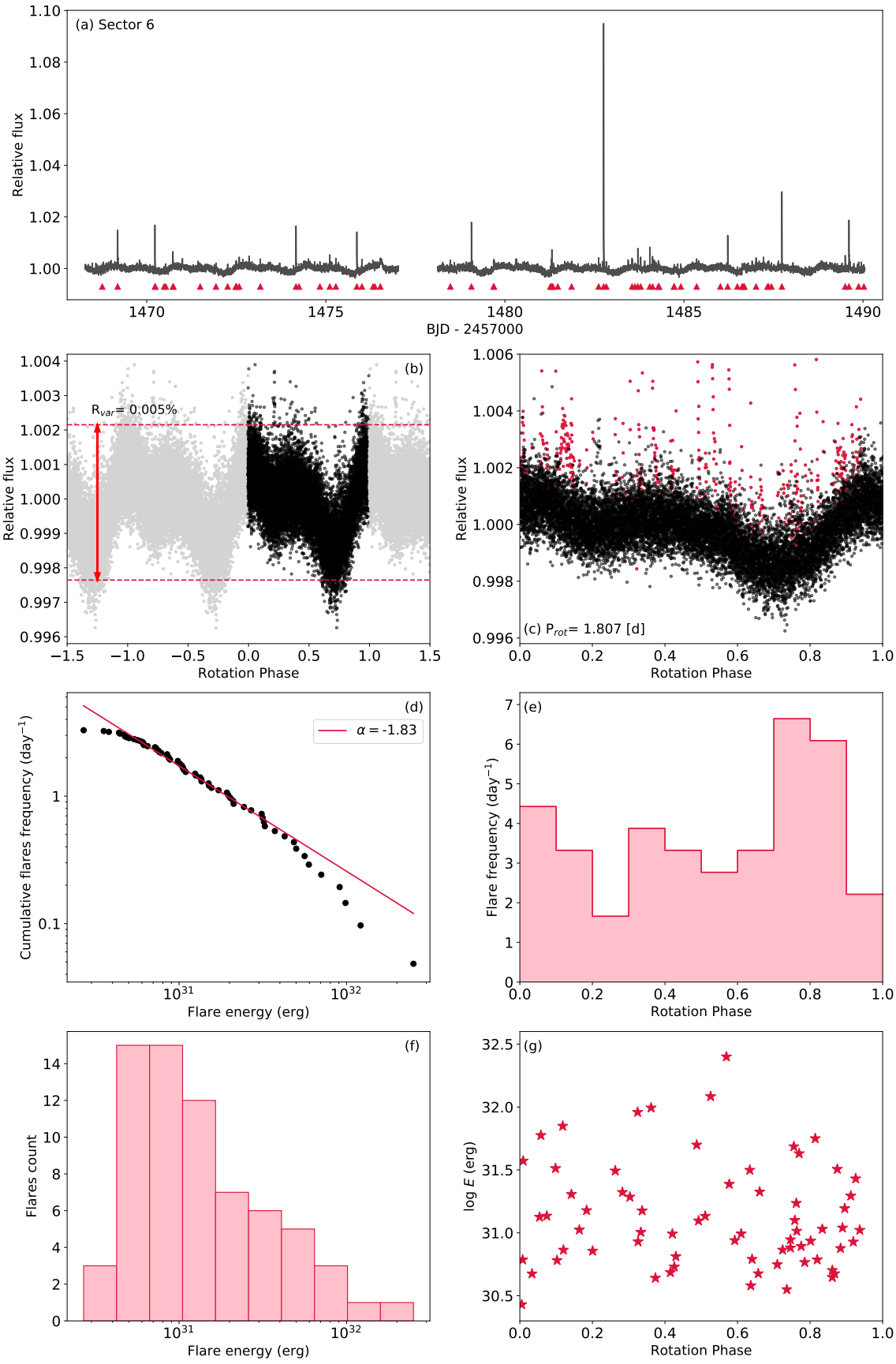

FIGURE B.12: Same as Fig. B.3 but for G 99-049 (J06000+027, TIC 282501711).

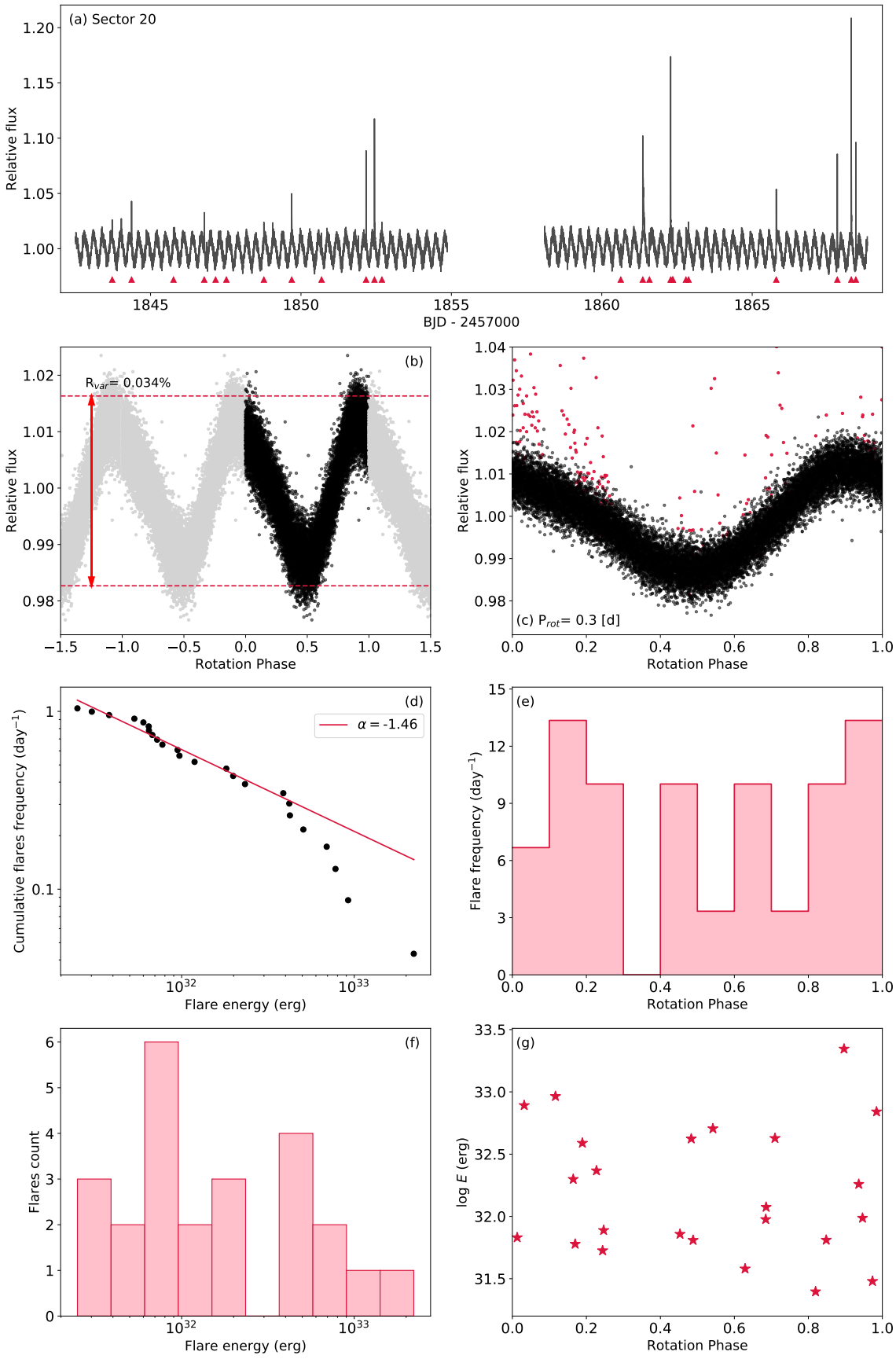

FIGURE B.13: Same as Fig. B.3 but for LP 205-044 (J06318+414, TIC 144282456).

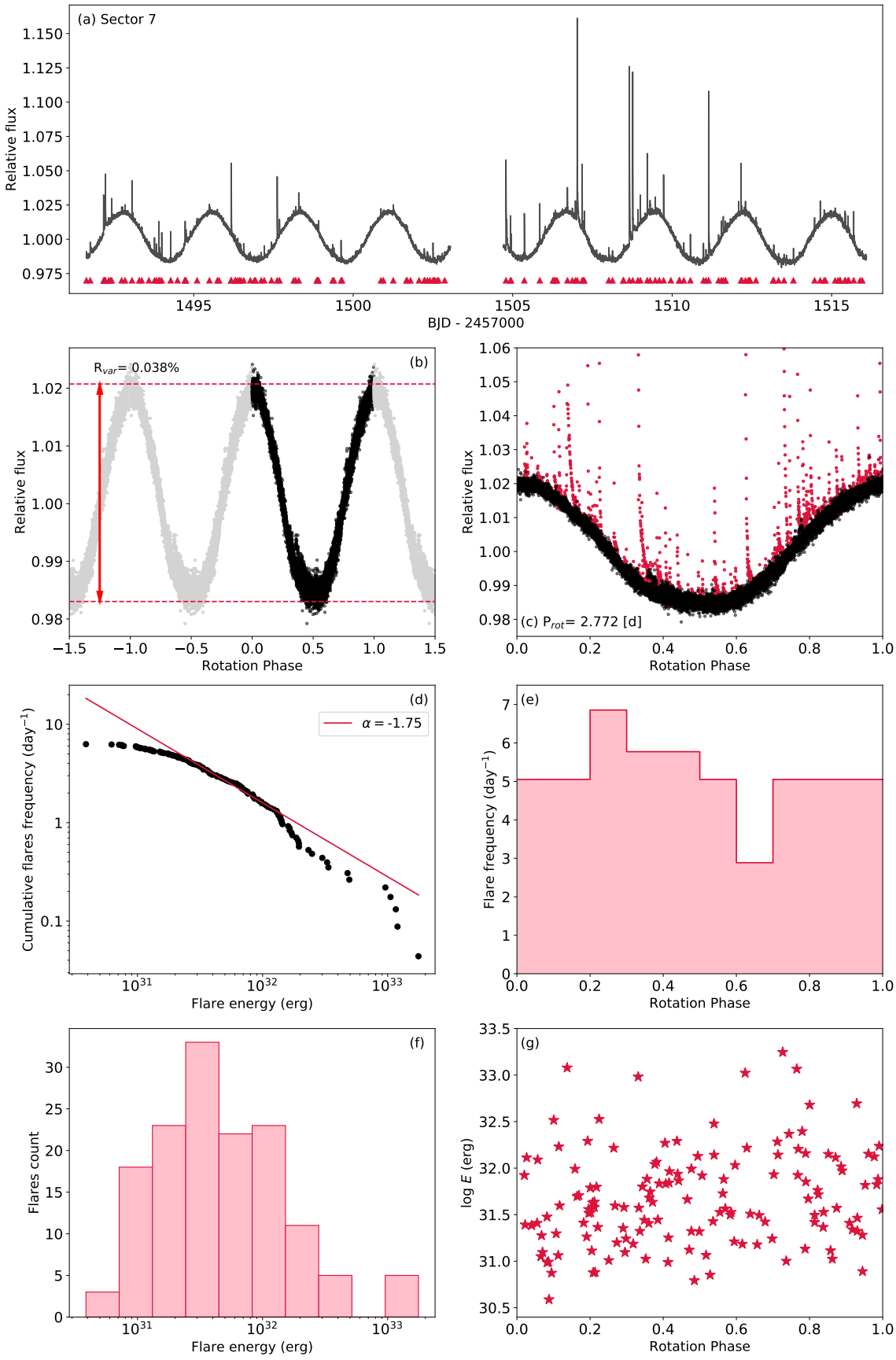

FIGURE B.14: Same as Fig. B.3 but for YZ CMi (J07446+035, TIC 266744225).

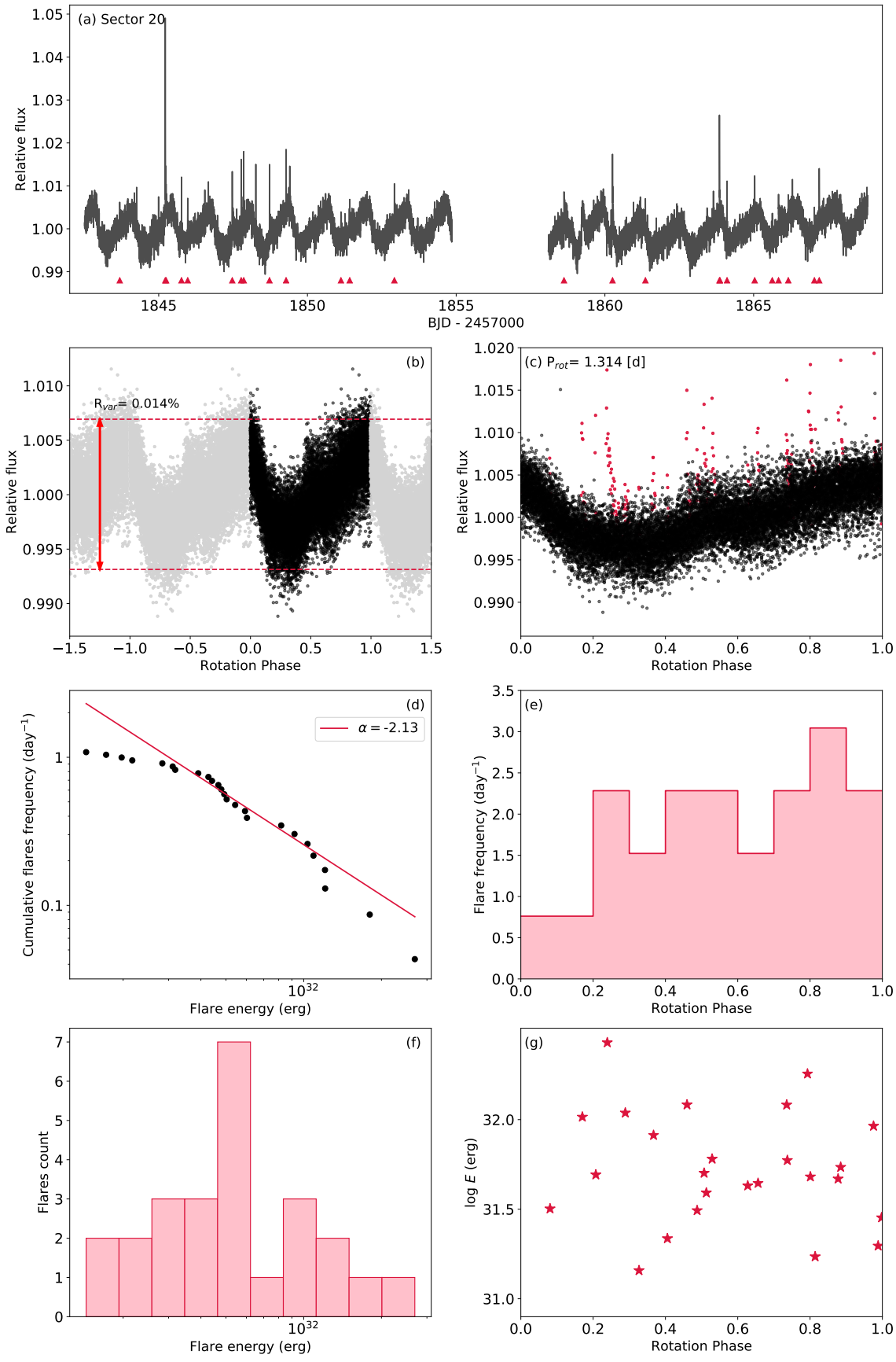

FIGURE B.15: Same as Fig. B.3 but for 2MASS J07471385+5020386 (J07472+503, TIC 309661100).

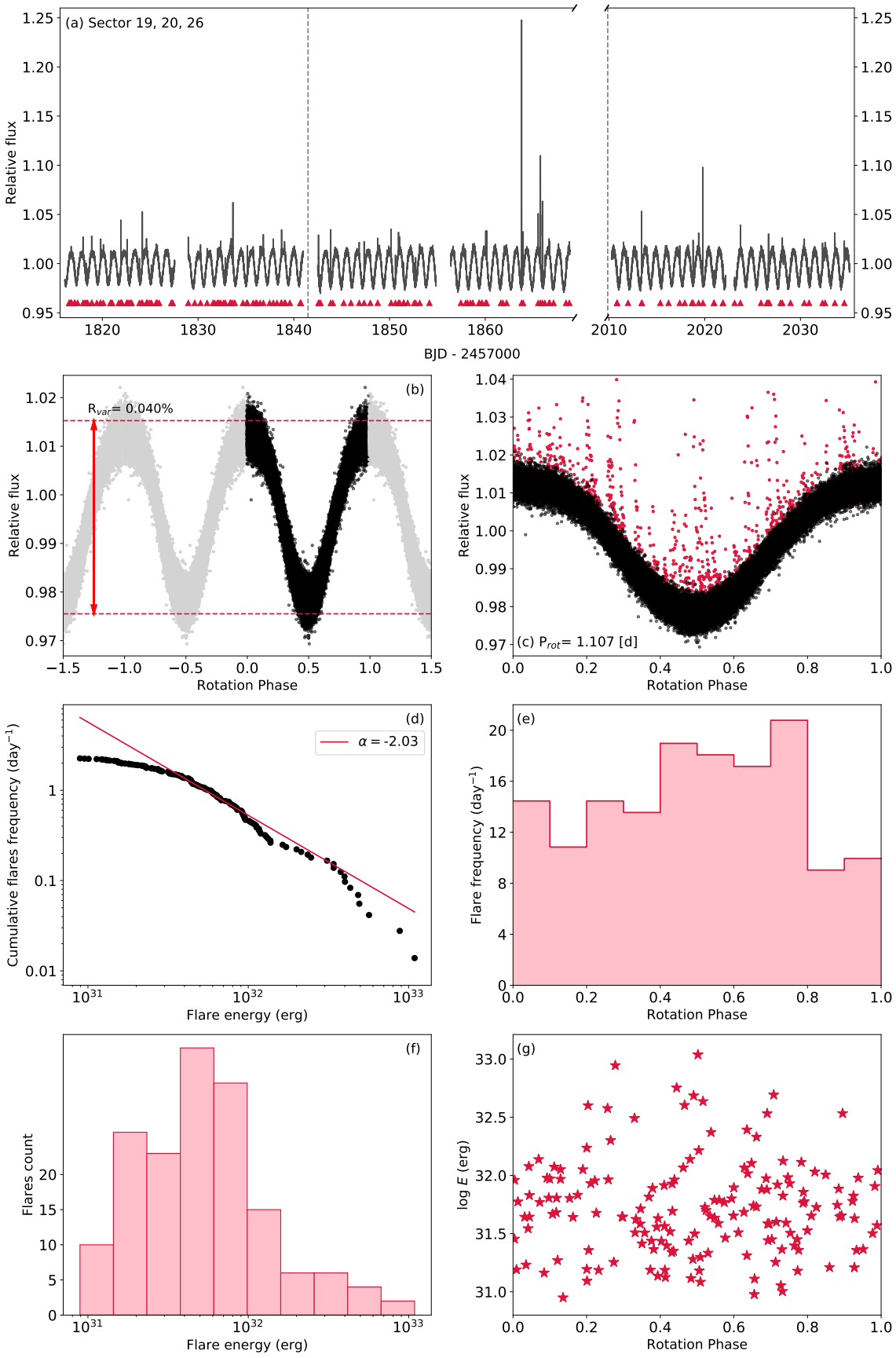

FIGURE B.16: Same as Fig. B.3 but for GJ 1101 (J07558+833, TIC 289972535).

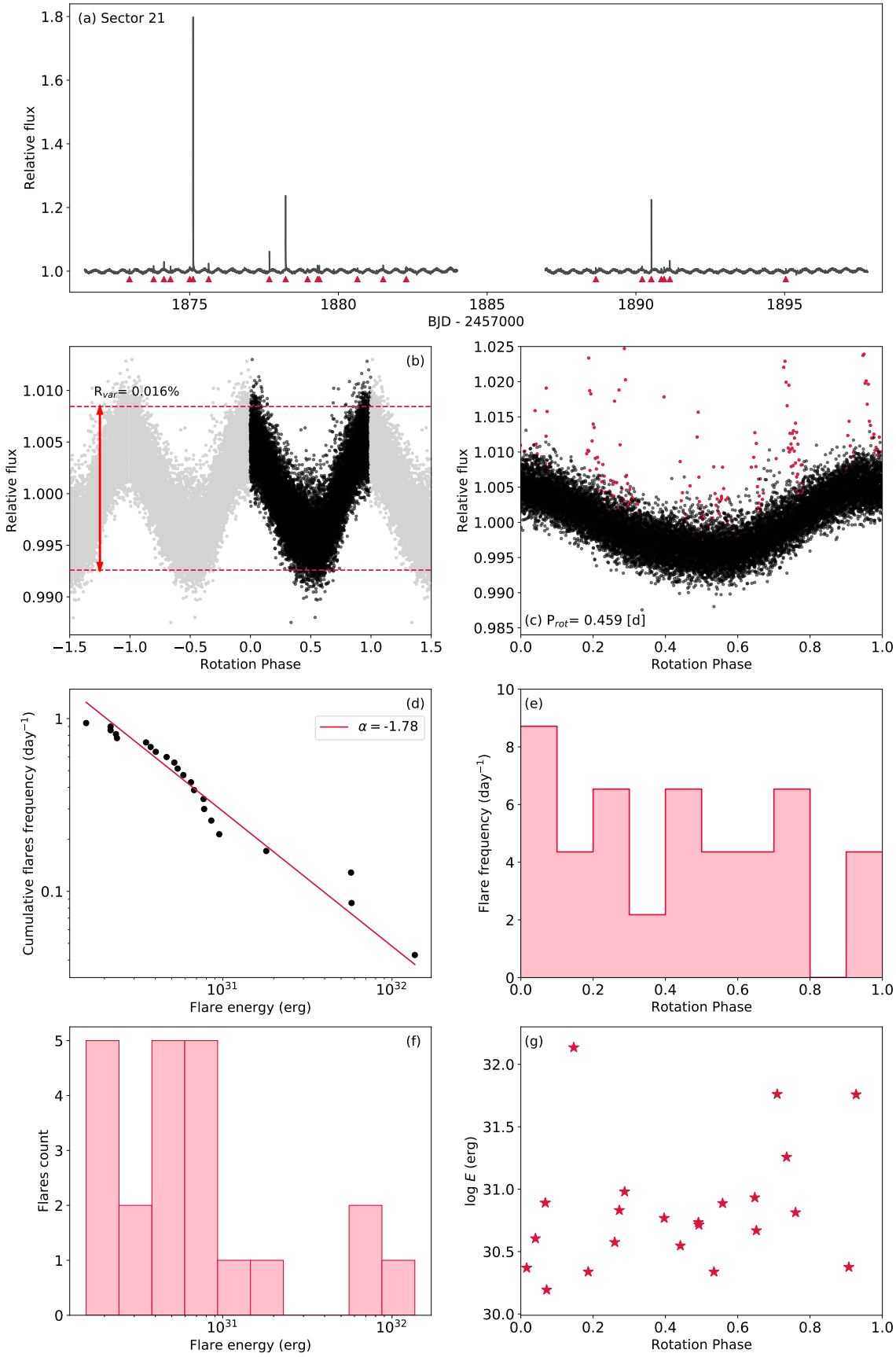

FIGURE B.17: Same as Fig. B.3 but for DX Cnc (J08298+267, TIC 3664898).

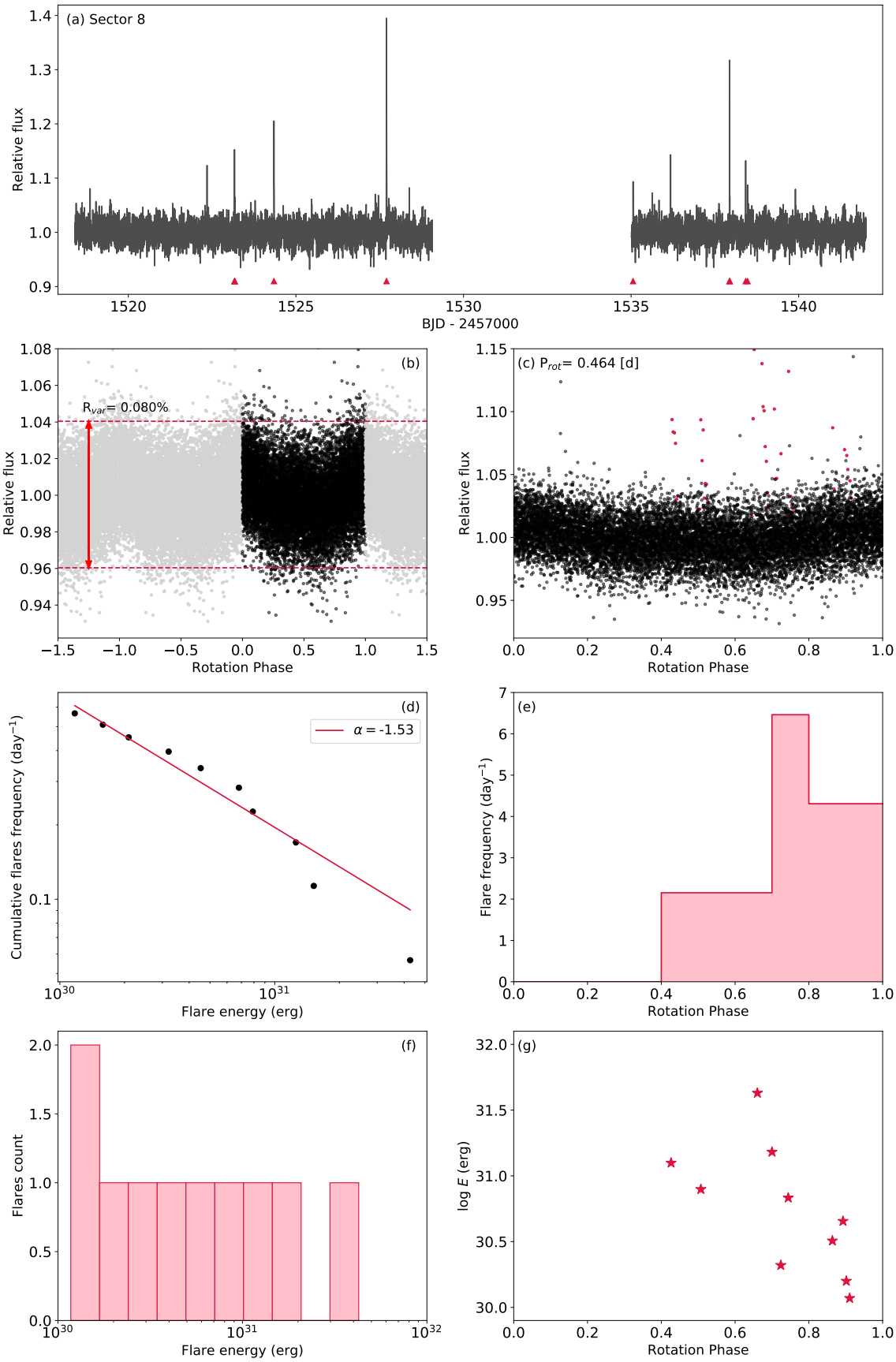

FIGURE B.18: Same as Fig. B.3 but for LP 666-009 (J08536-034, TIC 7975441).

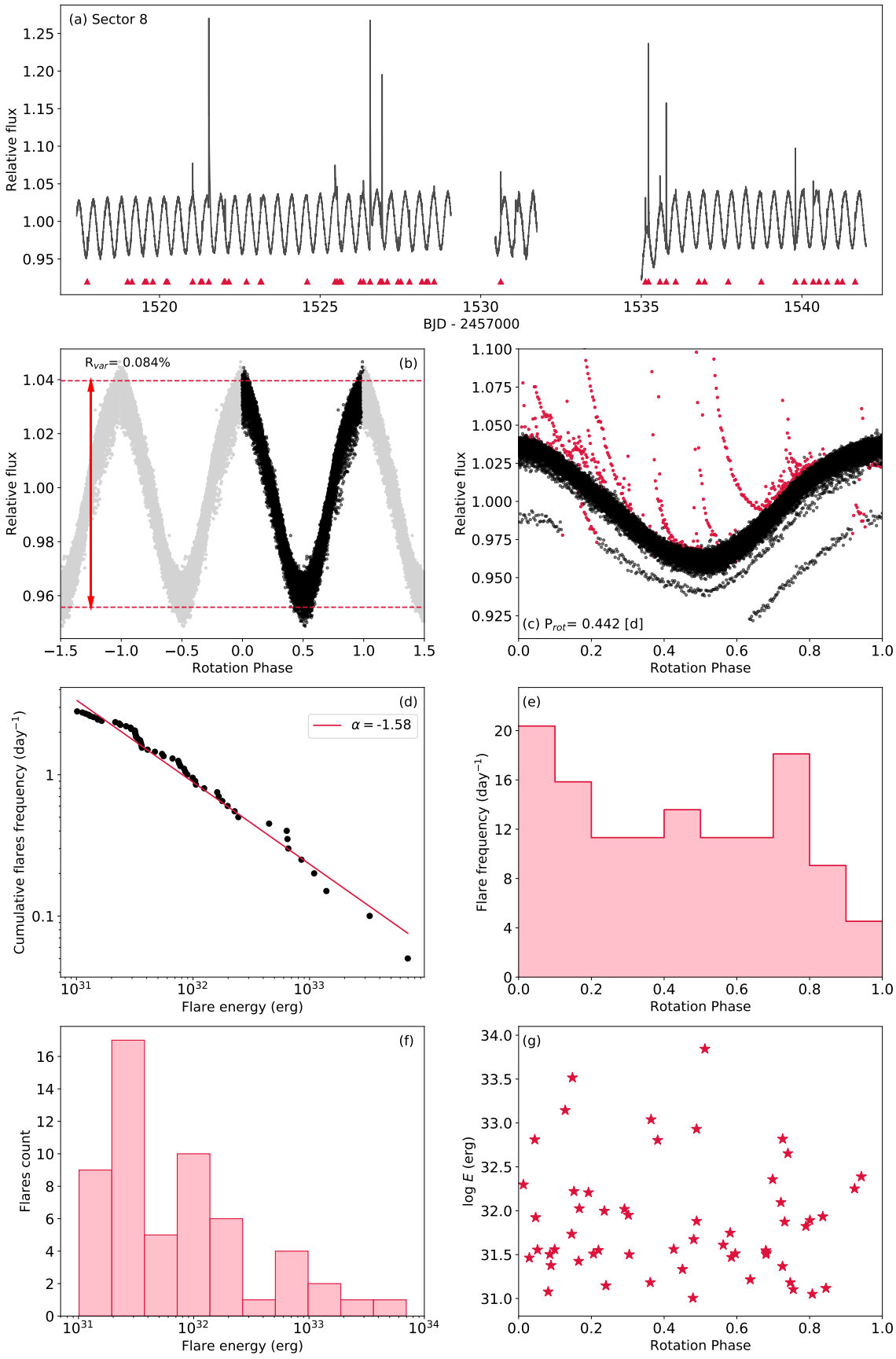

FIGURE B.19: Same as Fig. B.3 but for G 161-071 (J09449-123, TIC 289706625).

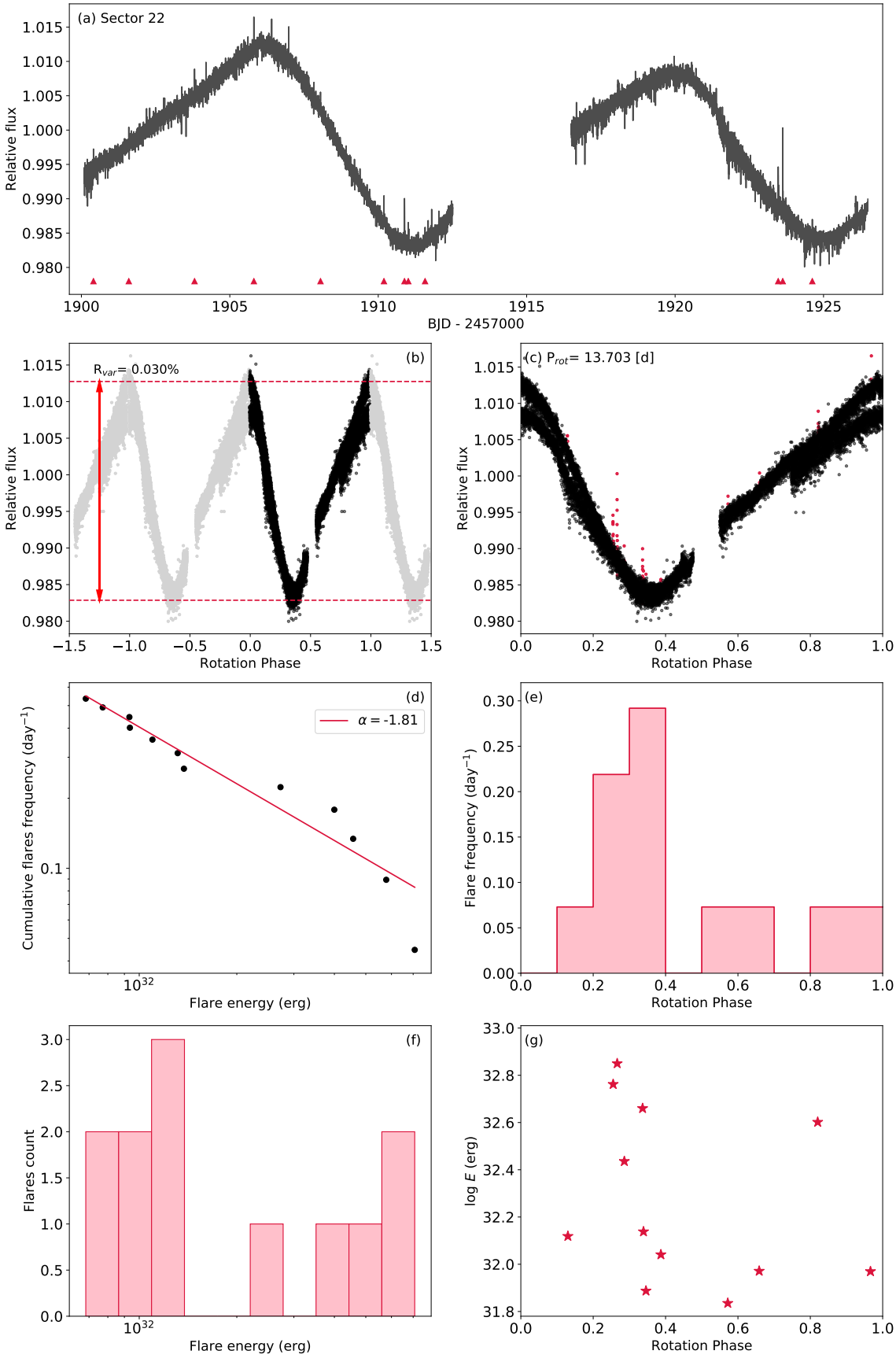

FIGURE B.20: Same as Fig. B.3 but for DS Leo (J11026+219, TIC 97488127).

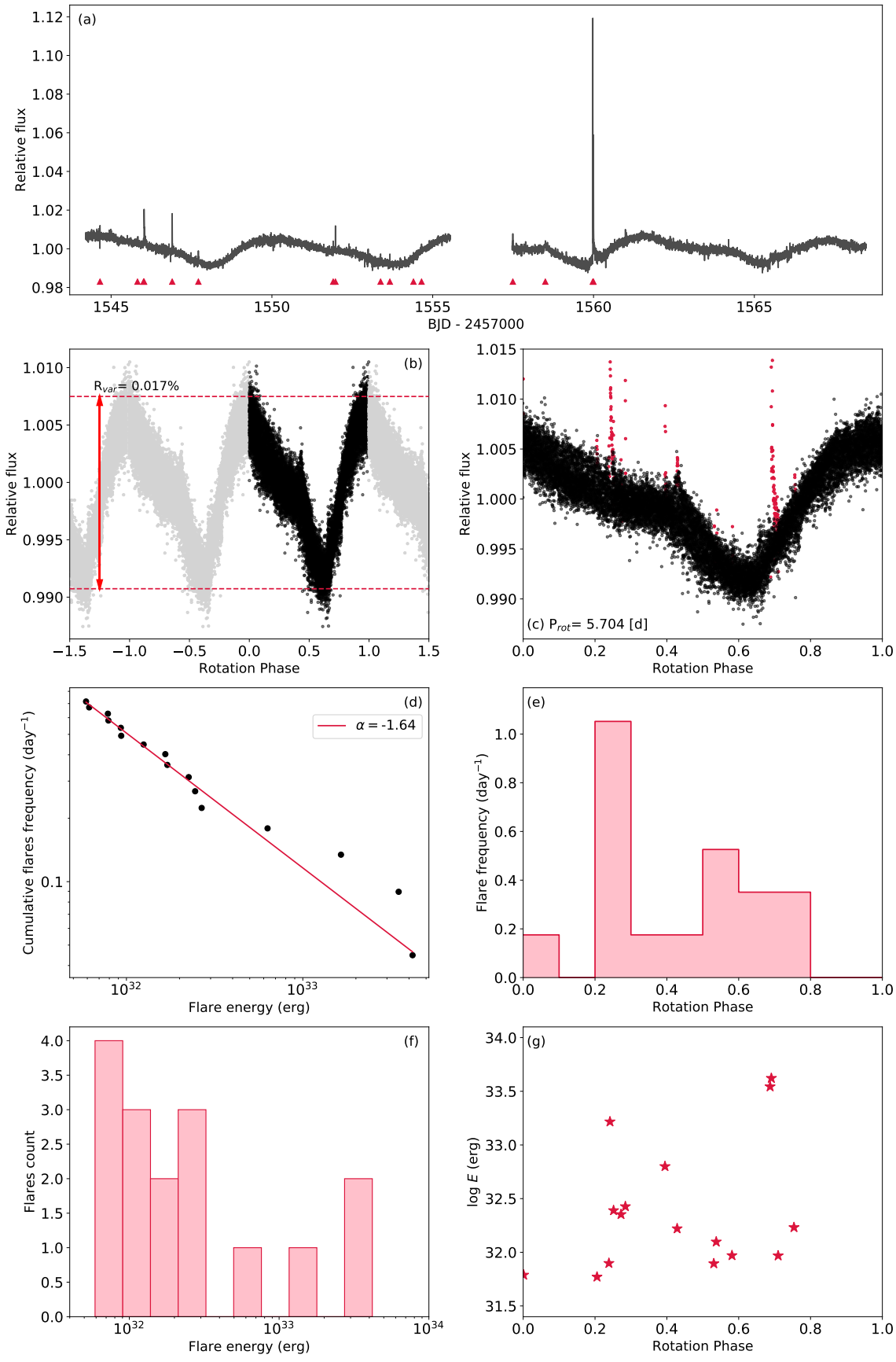

FIGURE B.21: Same as Fig. B.3 but for LP 733-099 (J11201-104, TIC 453465810).

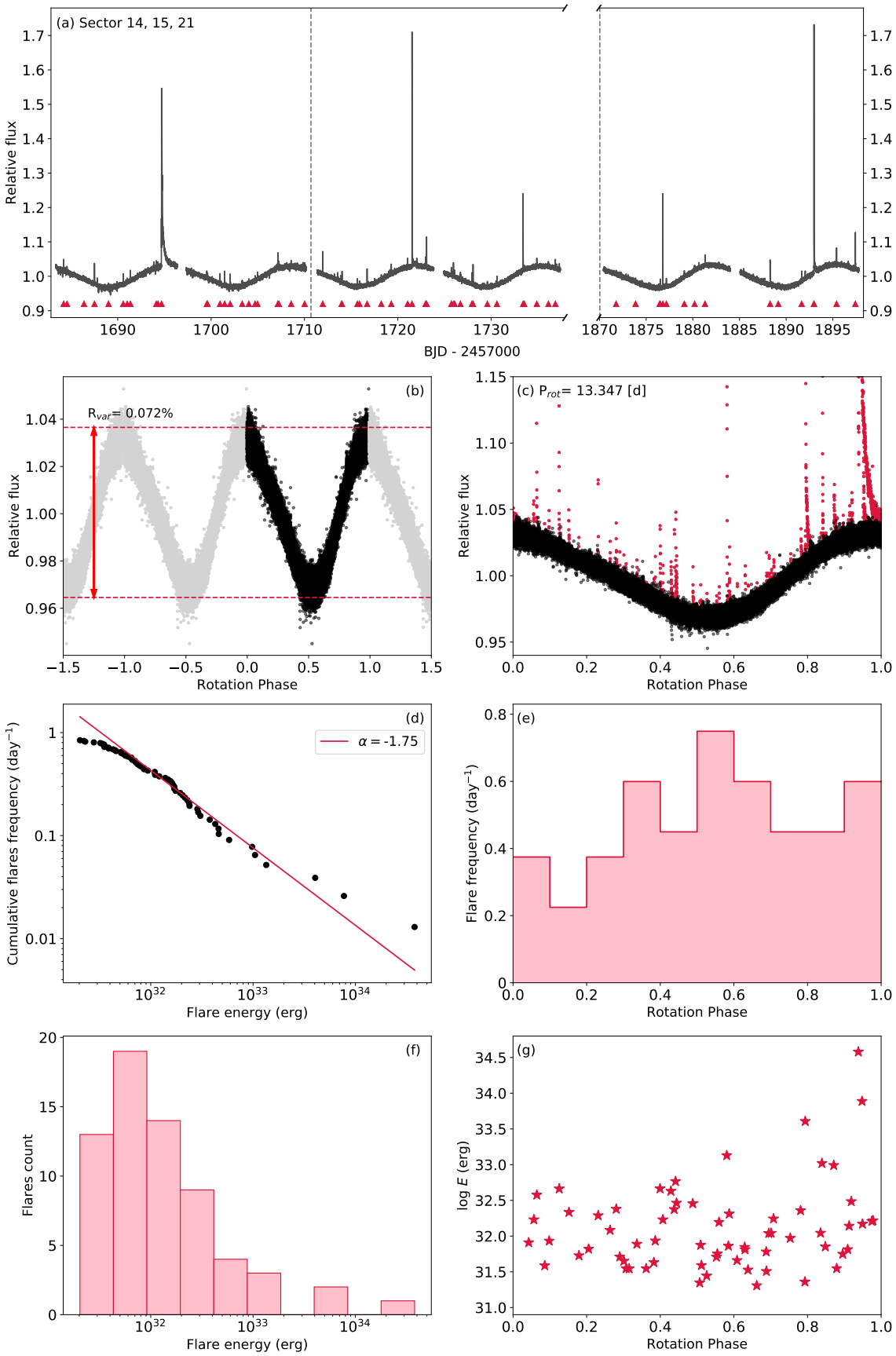

FIGURE B.22: Same as Fig. B.3 but for 1RXS J114728.8+664405 (J11474+667, TIC 142878895).

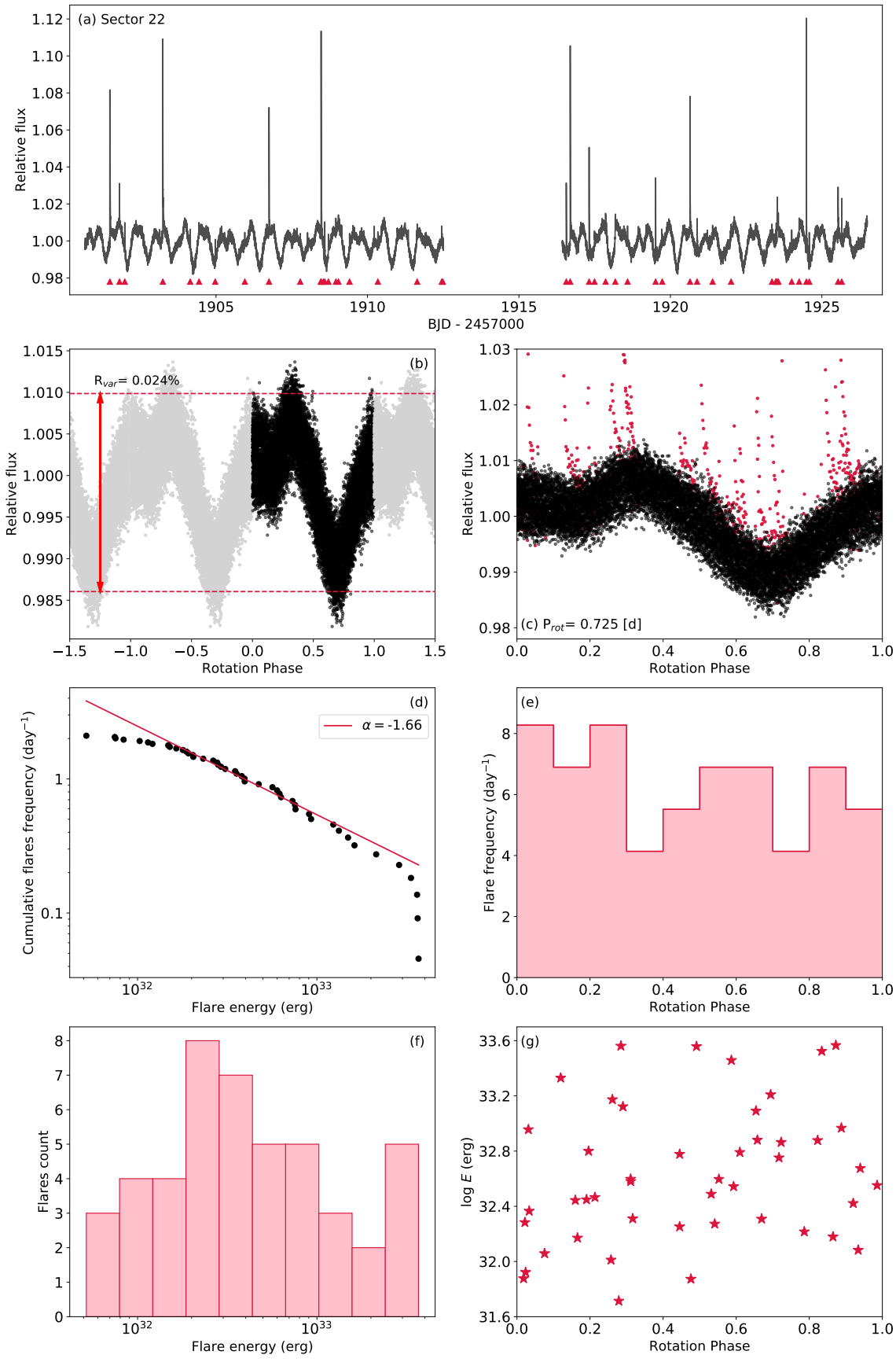

FIGURE B.23: Same as Fig. B.3 but for StKM 2-809 (J12156+526, TIC 416538839).

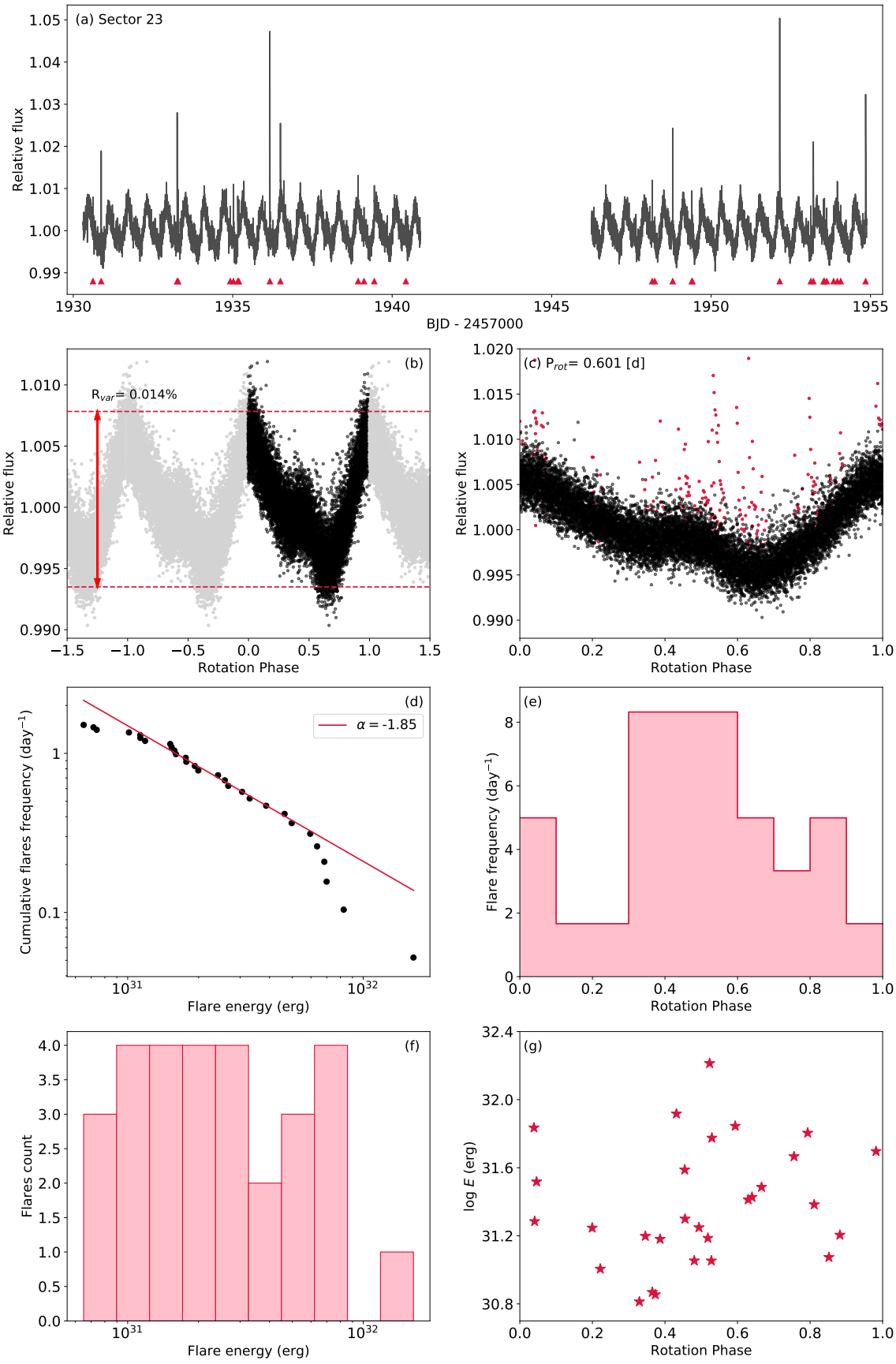

FIGURE B.24: Same as Fig. B.3 but for FN Vir (J13005+056, TIC 411248800).

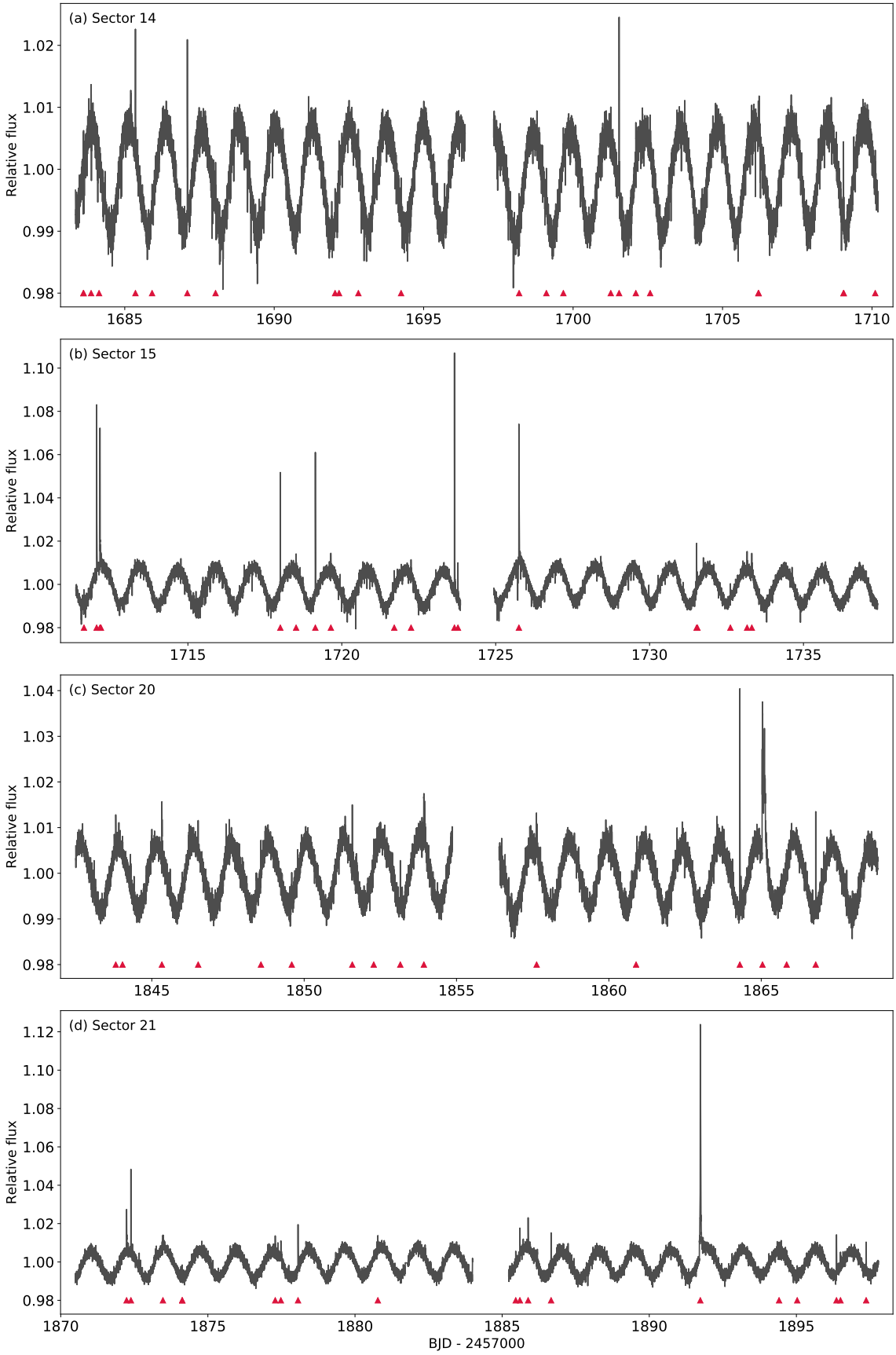

FIGURE B.25: TESS light curve of RX J1353.6+7737 (J13536+776, TIC 219463771) for sectors 14, 15, 20, and 21.

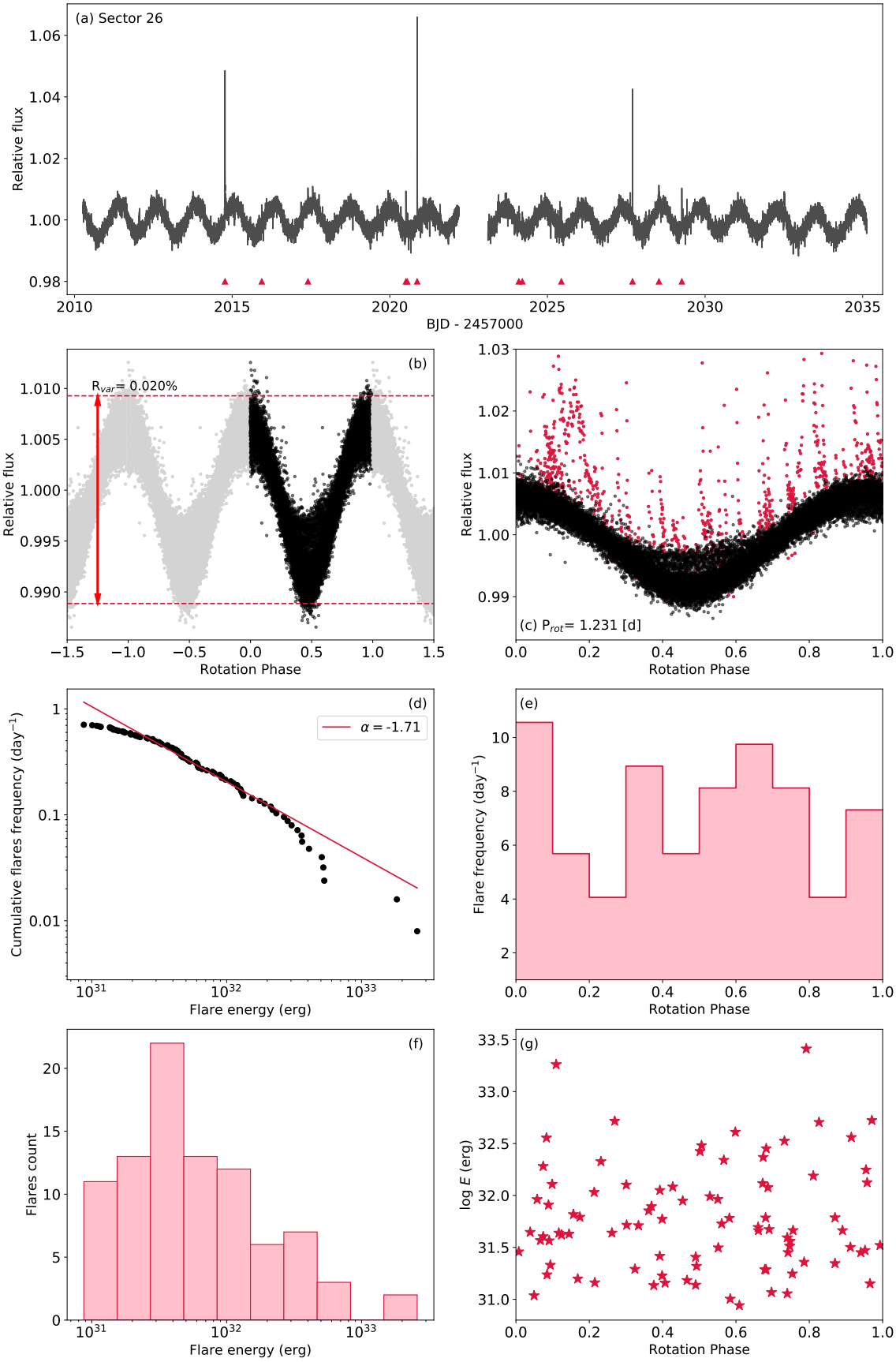

Same as Fig. B.3 but for RX J1353.6+7737 (J13536+776, TIC 219463771).

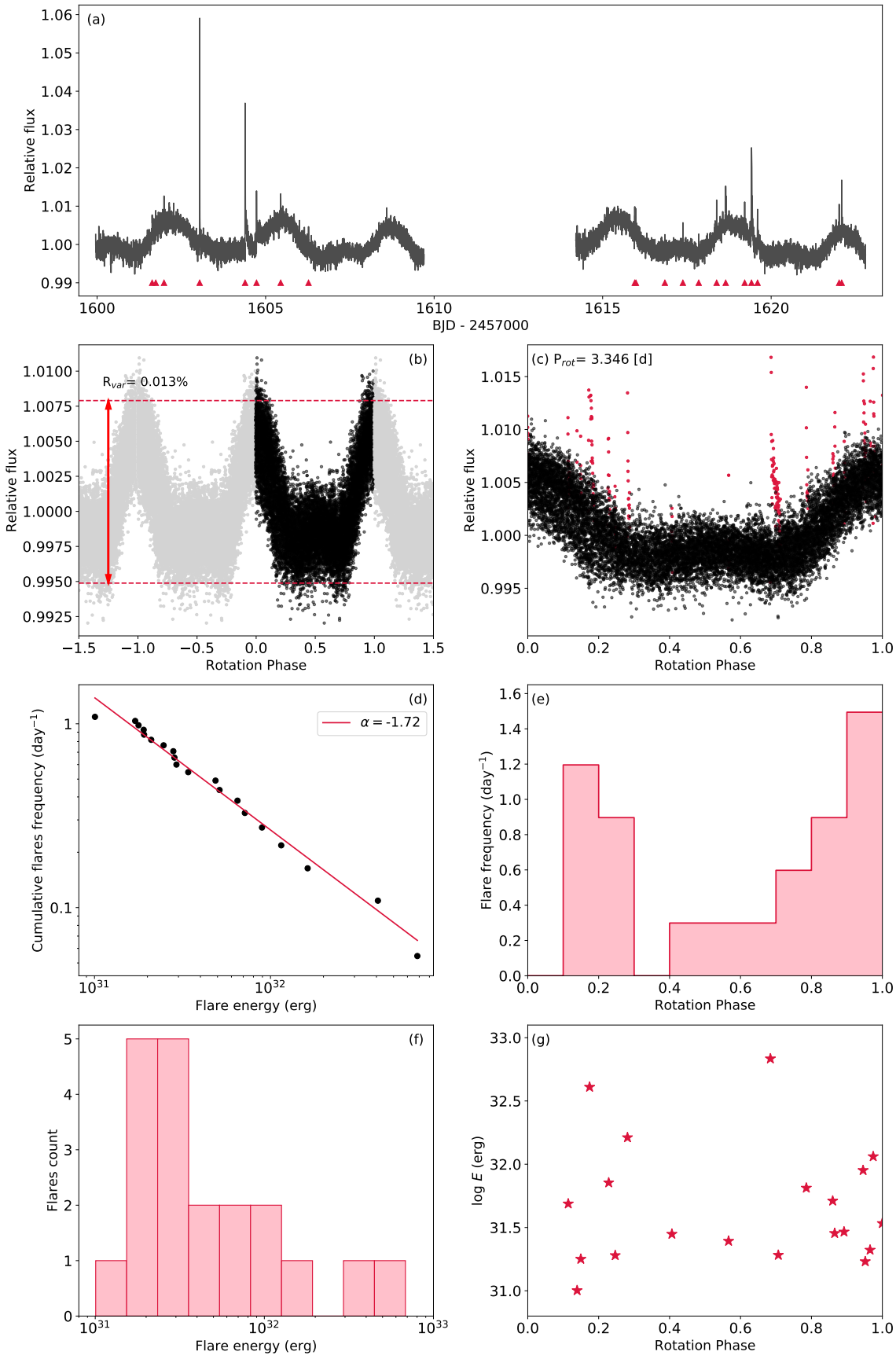

FIGURE B.26: Same as Fig. B.3 but for LP 799-007 (J13591-198, TIC 125421413).

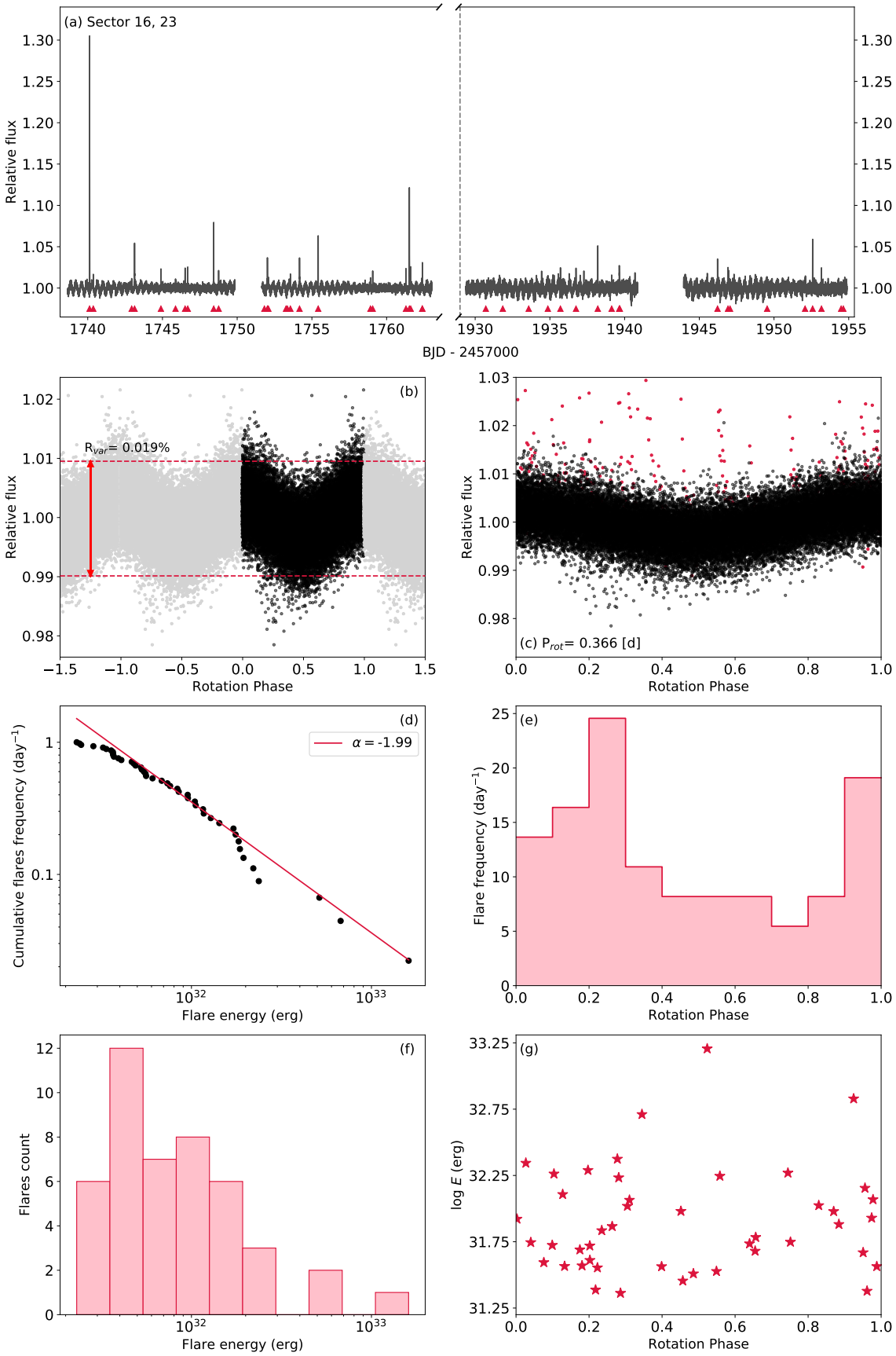

FIGURE B.27: Same as Fig. B.3 but for RX J1417.3+4525 (J14173+454, TIC 168747450).

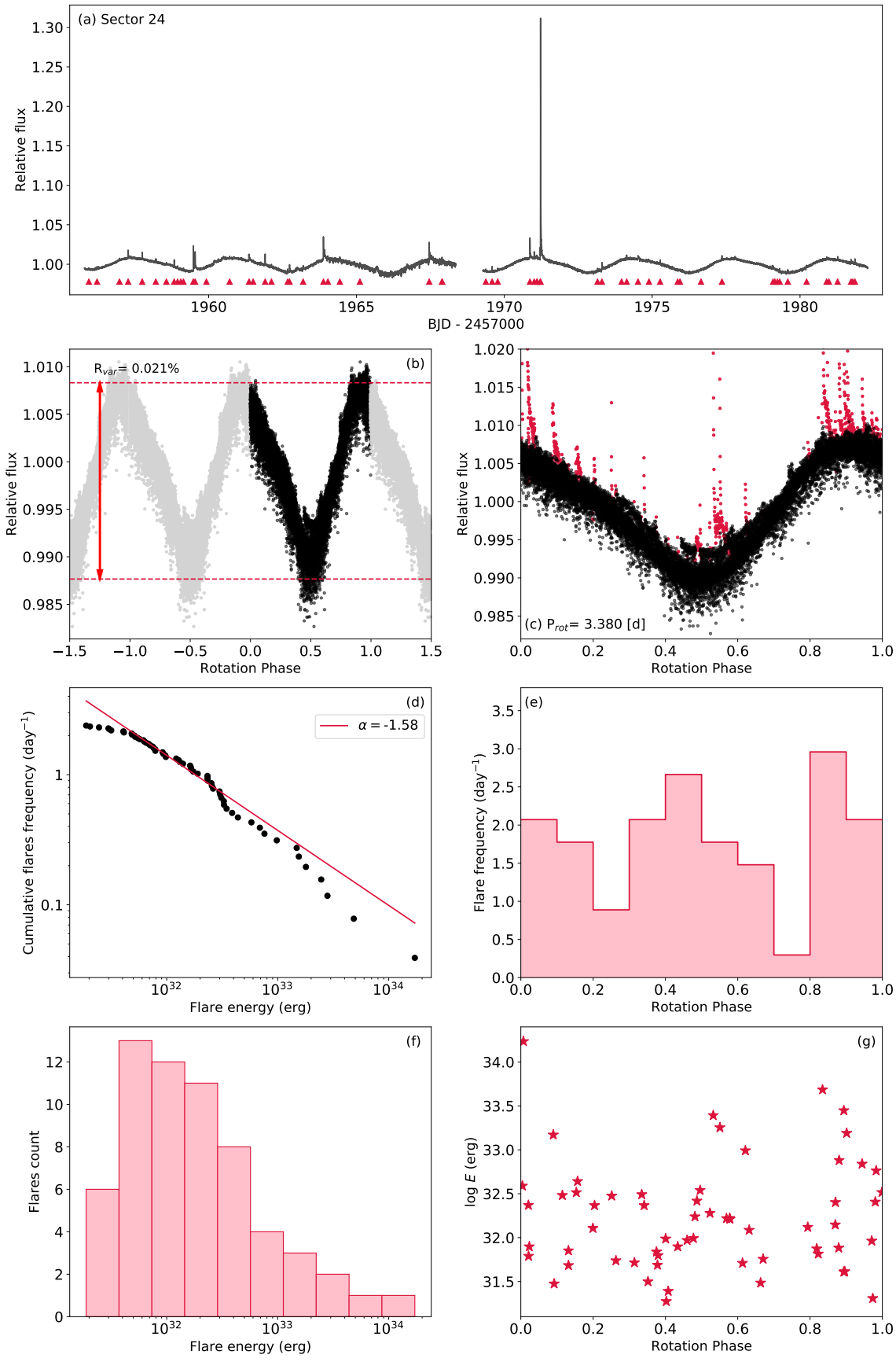

FIGURE B.28: Same as Fig. B.3 but for OT Ser (J15218+209, TIC 355793860).

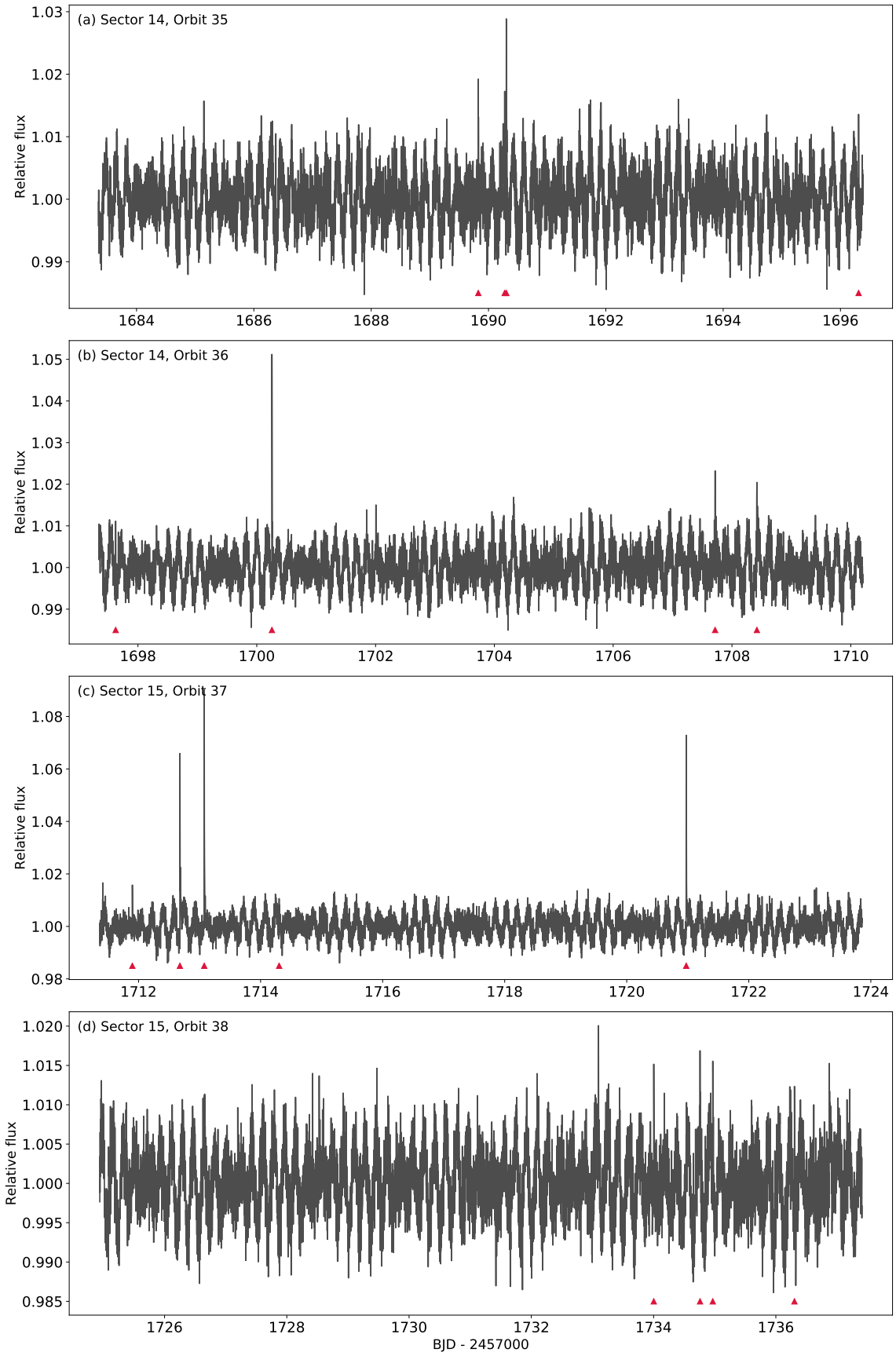

FIGURE B.29: TESS light curve of LP 022-420 (J15499+796, TIC 159398282) for sectors 14 and 15.

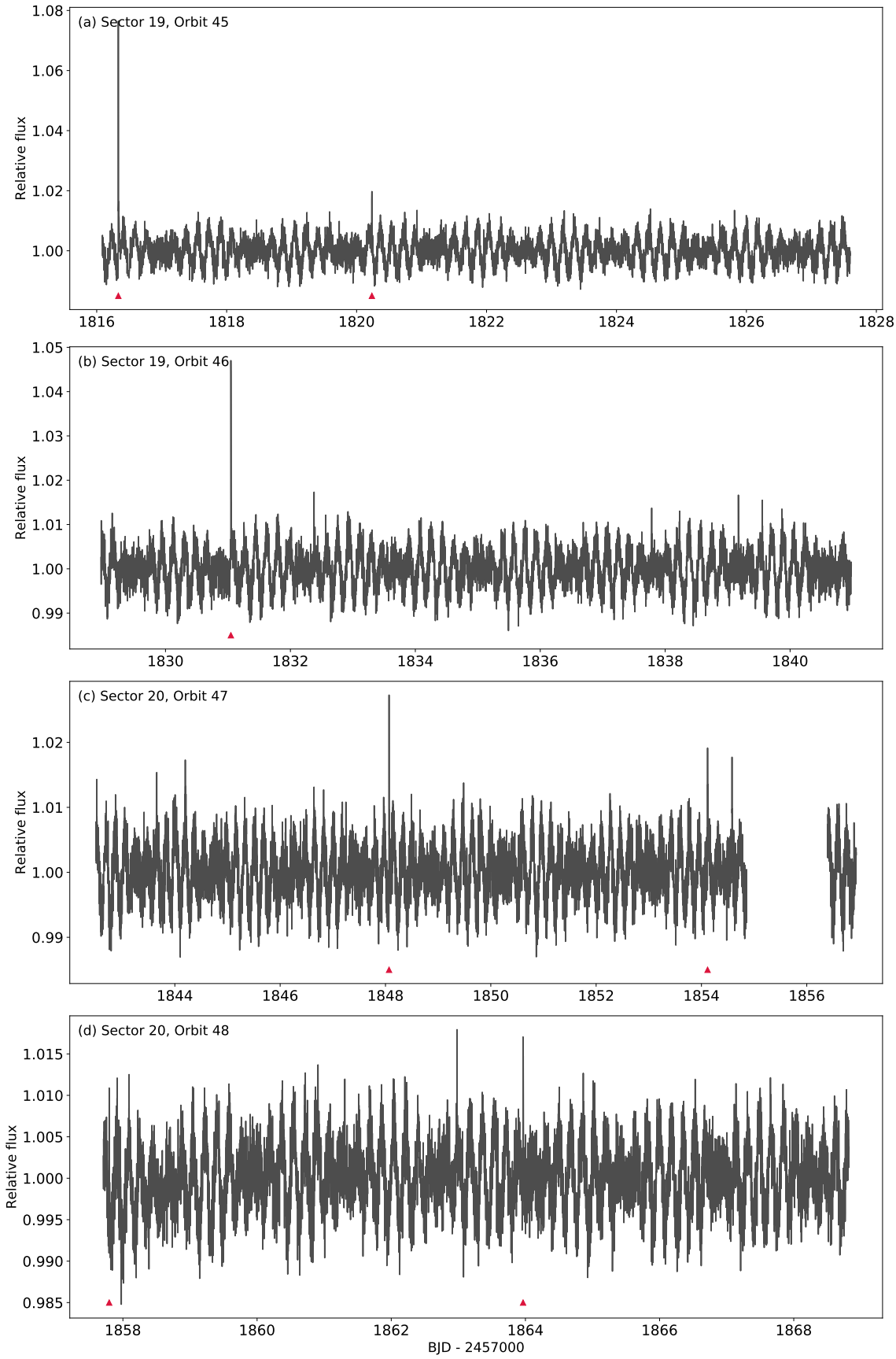

TESS light curve of LP 022-420 (J15499+796, TIC 159398282) for sectors 19 and 20.

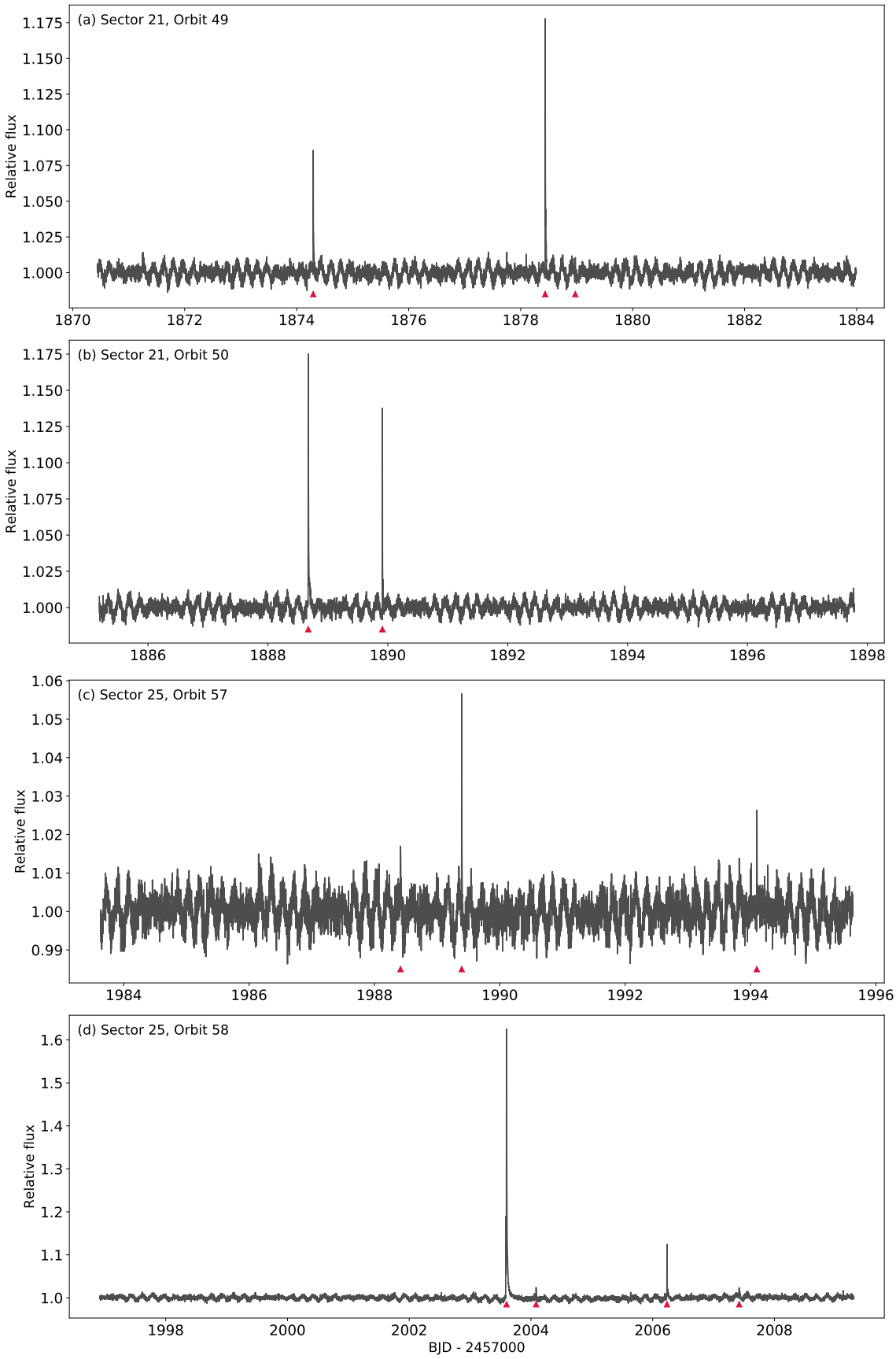

TESS light curve of LP 022-420 (J15499+796, TIC 159398282) for sectors 21 and 25.

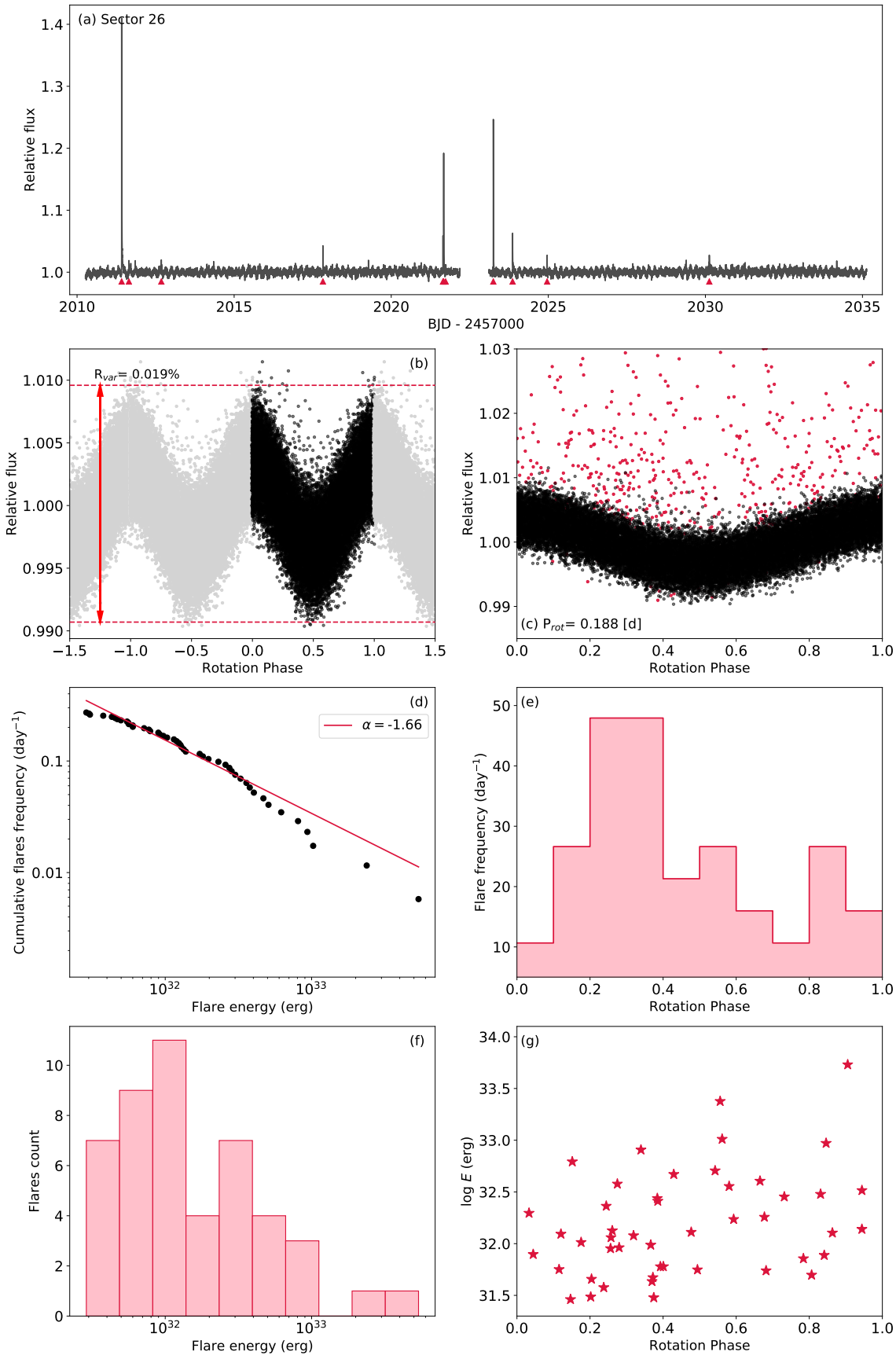

Same as Fig. B.3 but for LP 022-420 (J15499+796, TIC 159398282). Data in panel (b) and (c) is binned but R_{var} is calculated from unbinned data.

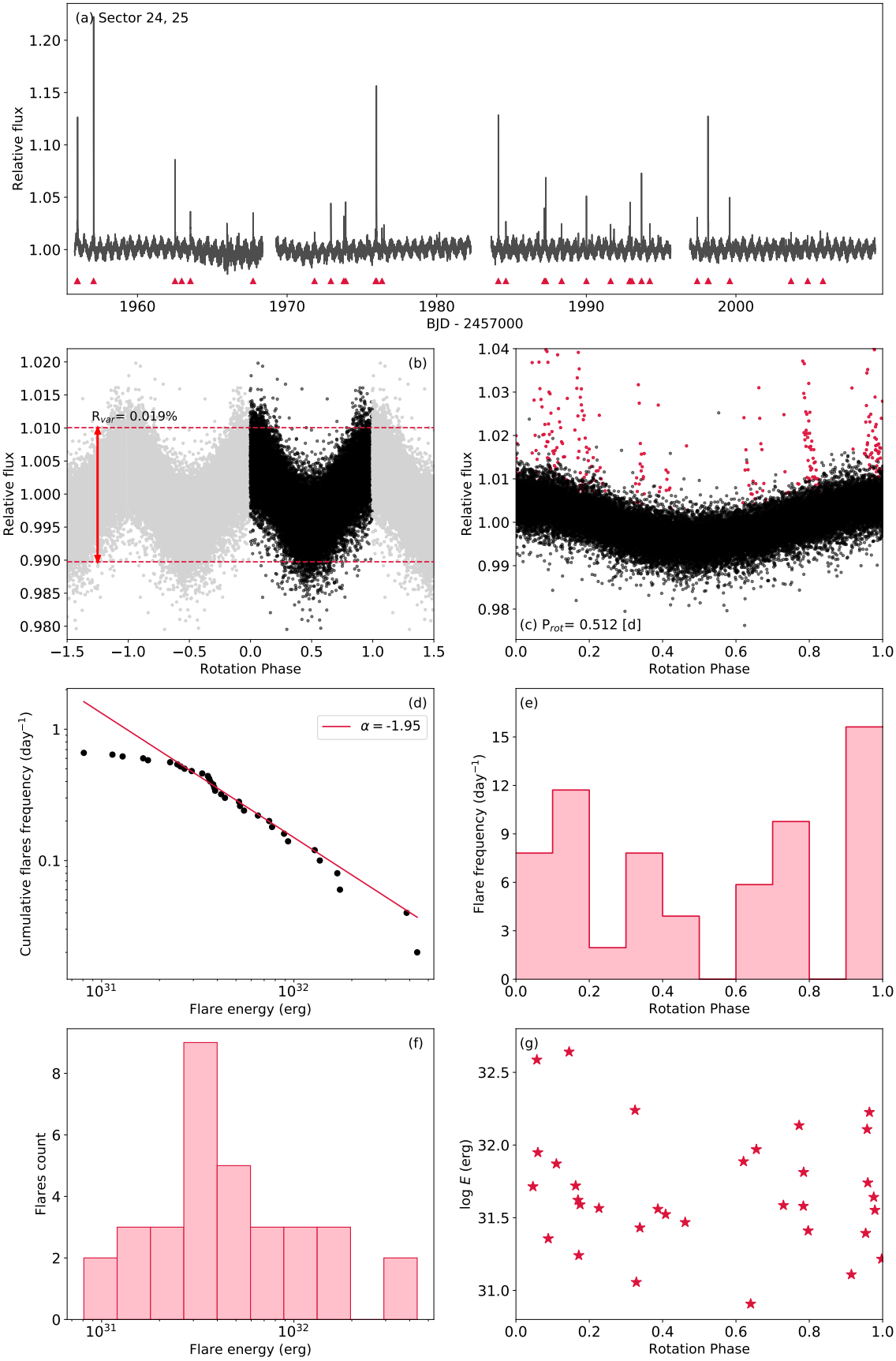

FIGURE B.30: Same as Fig. B.3 but for G 180-060 (J16313+408, TIC 255932726).

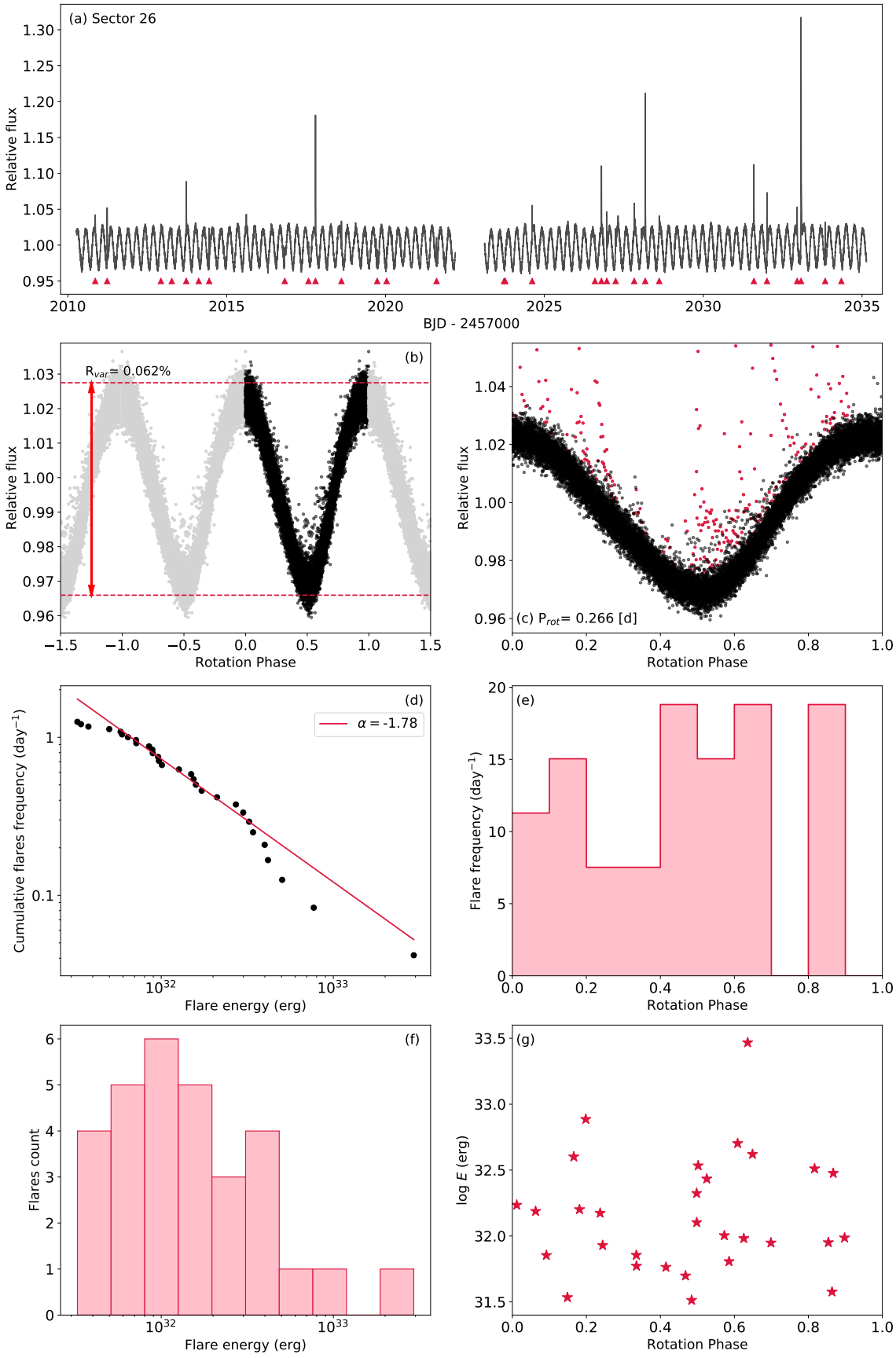

FIGURE B.31: Same as Fig. B.3 but for 1RXS J173353.5+165515 (J17338+169, TIC 400361232).

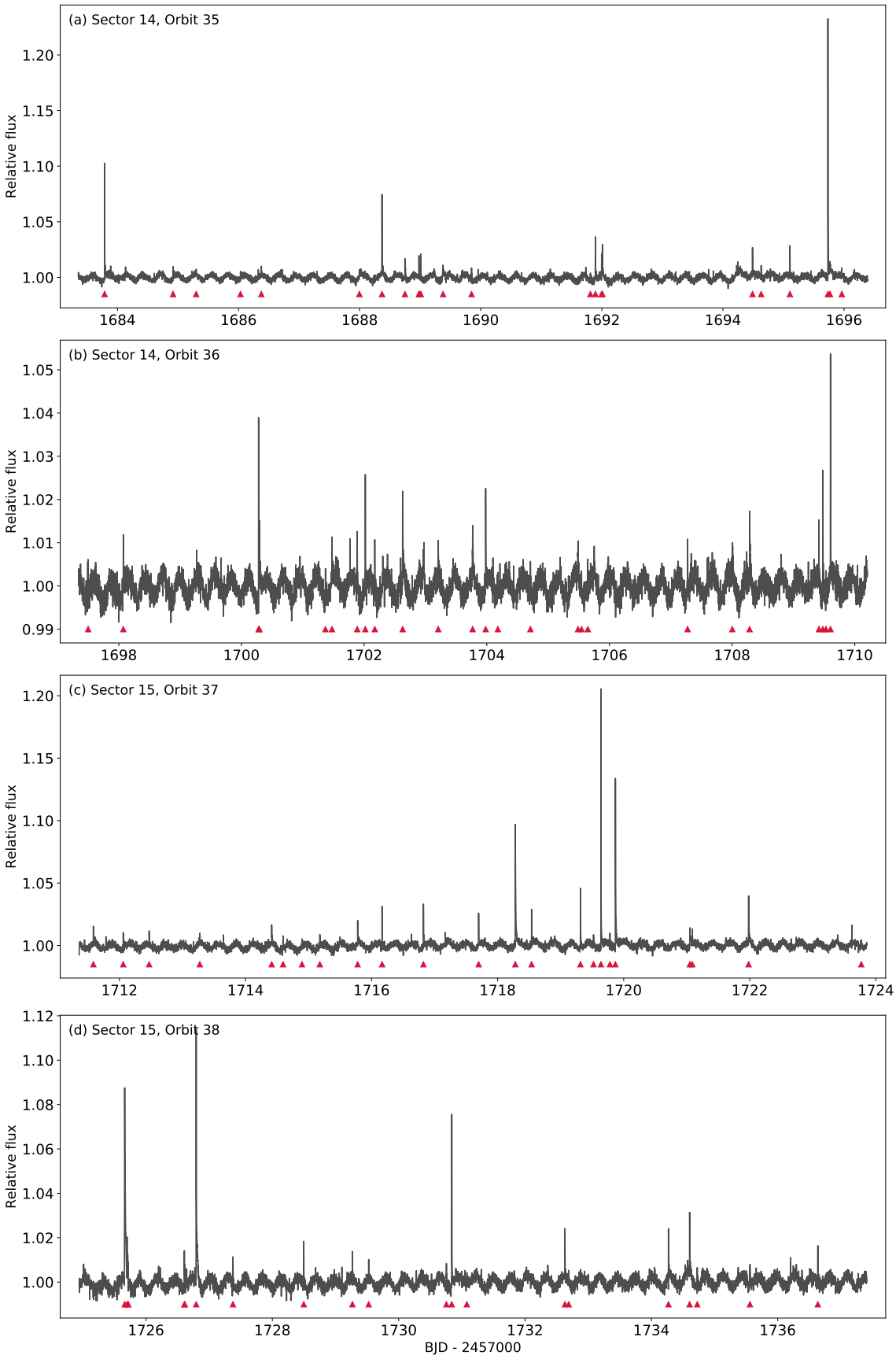

FIGURE B.32: TESS light curve of LP 071-082 (J18022+642, TIC 233068870) for sectors 14 and 15.

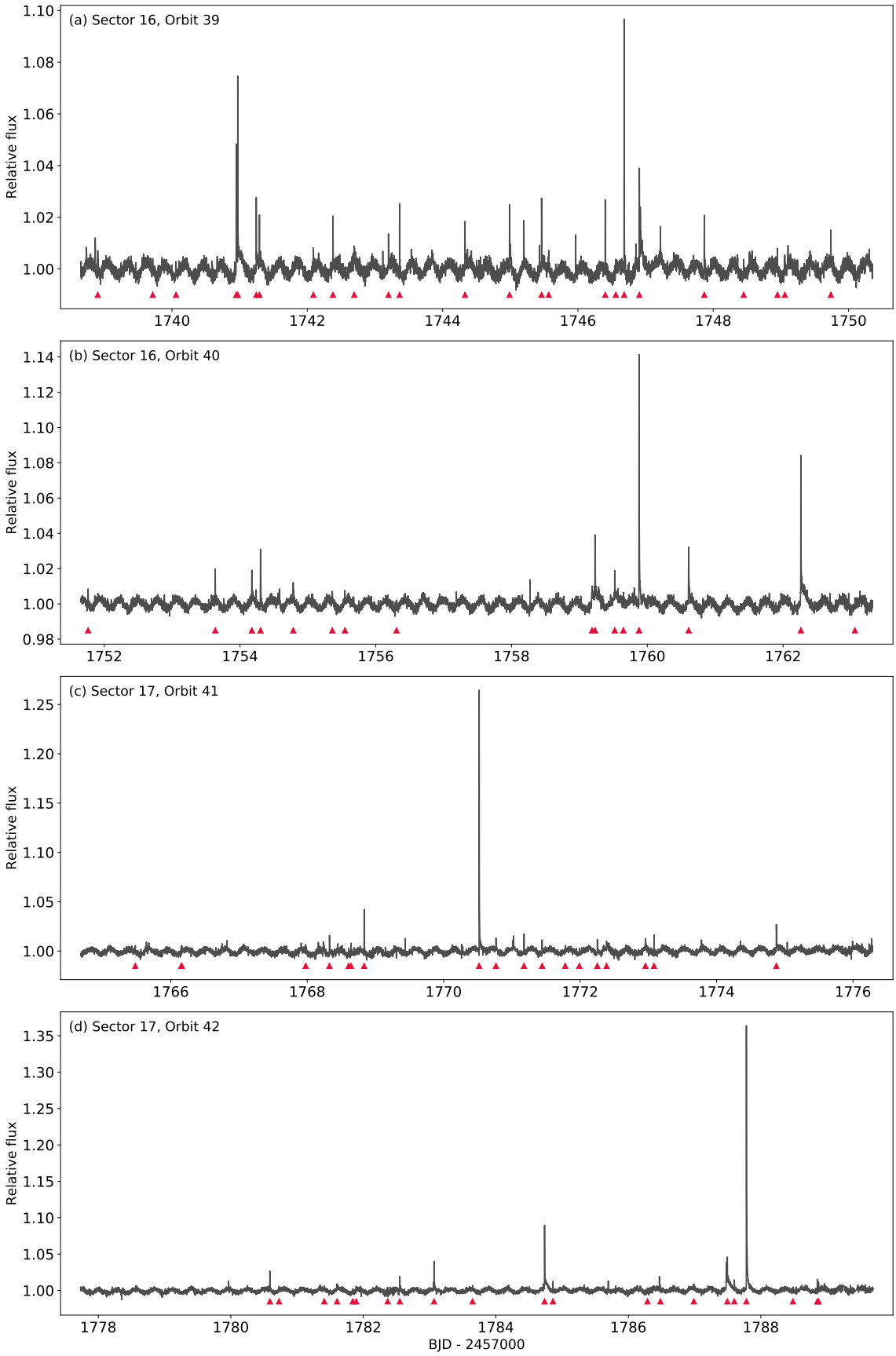

TESS light curve of LP 071-082 (J18022+642, TIC 233068870) for sectors 16 and 17.

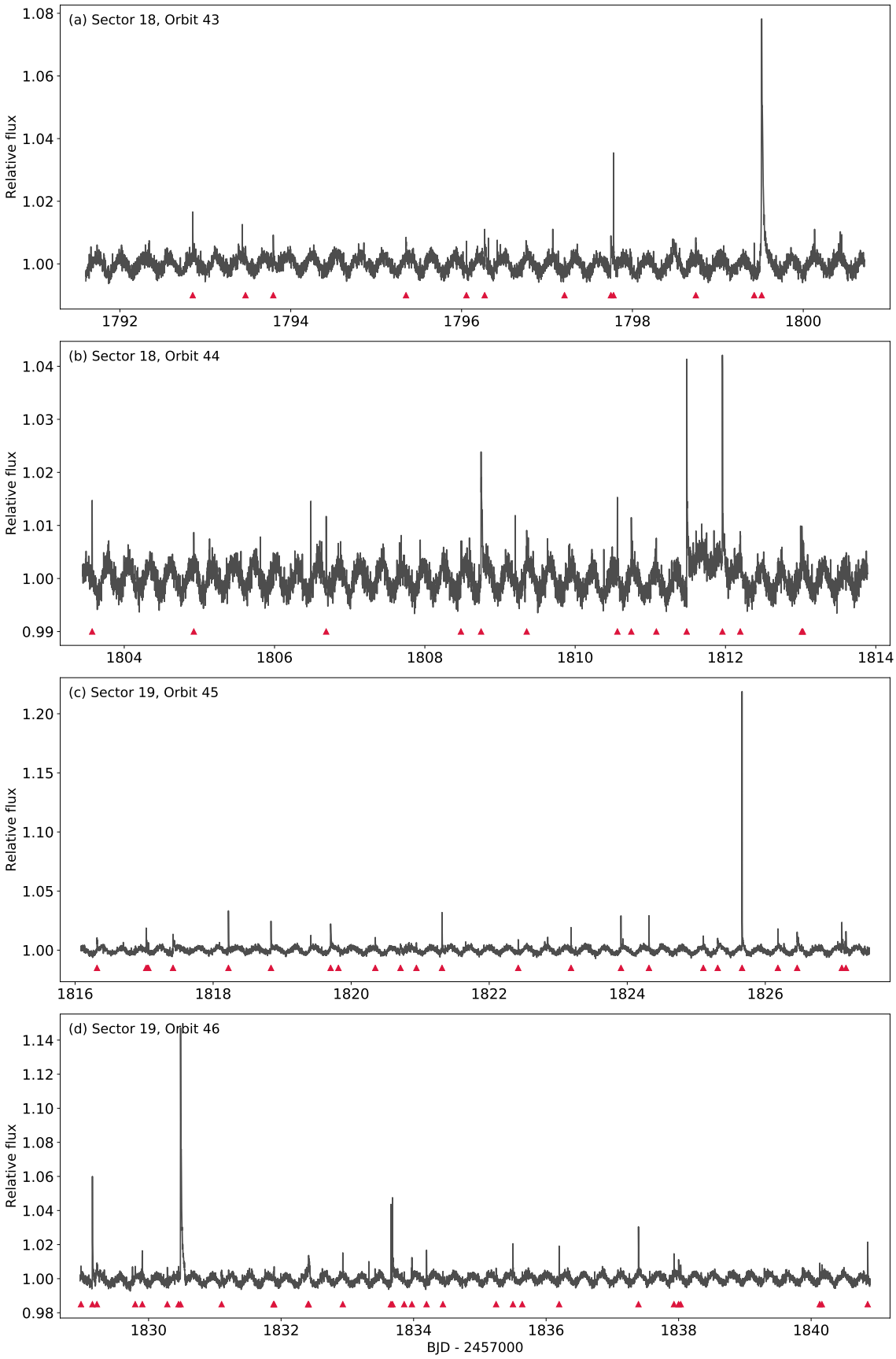

TESS light curve of LP 071-082 (J18022+642, TIC 233068870) for sectors 18 and 19.

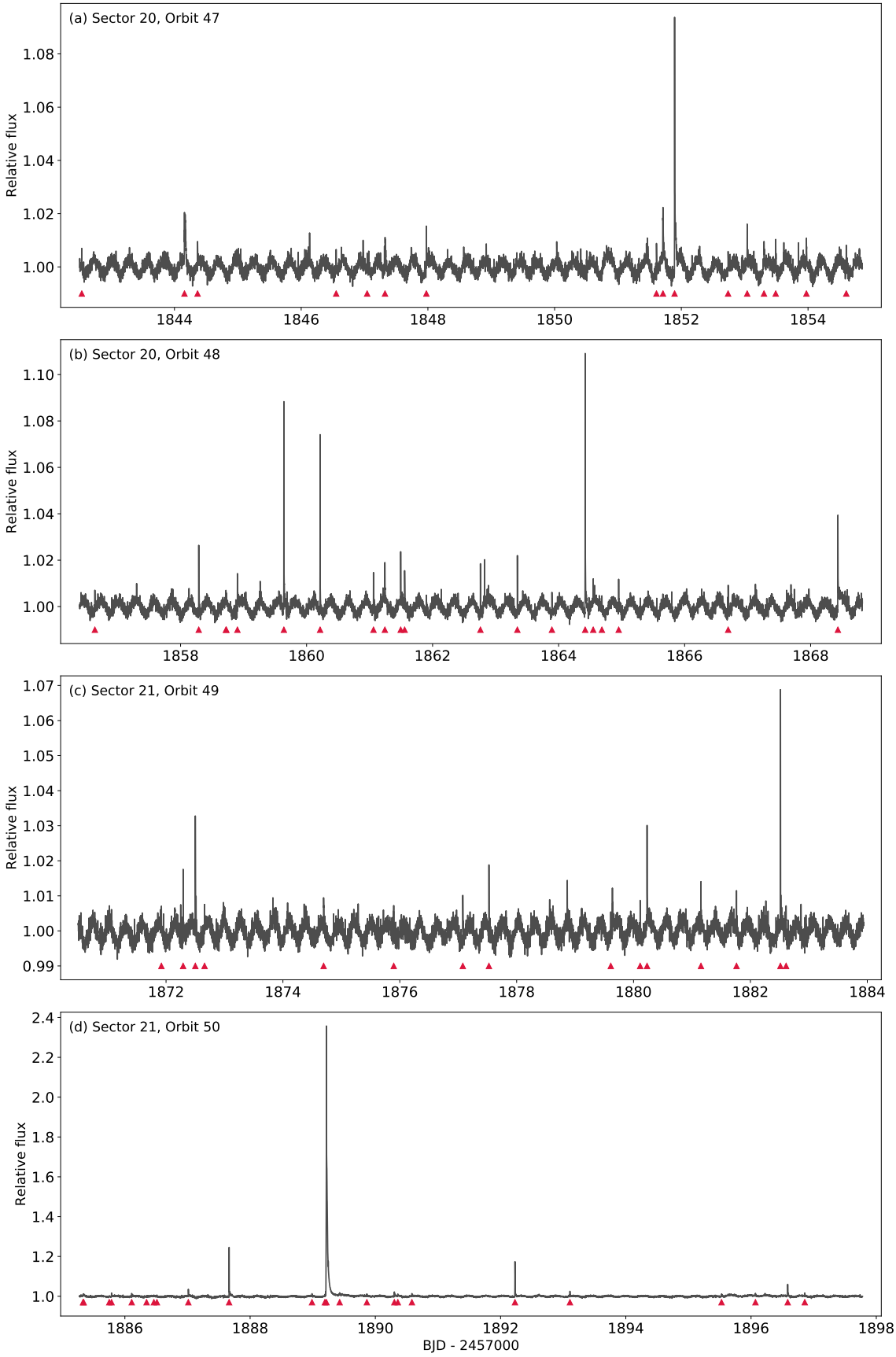

TESS light curve of LP 071-082 (J18022+642, TIC 233068870) for sectors 20 and 21.

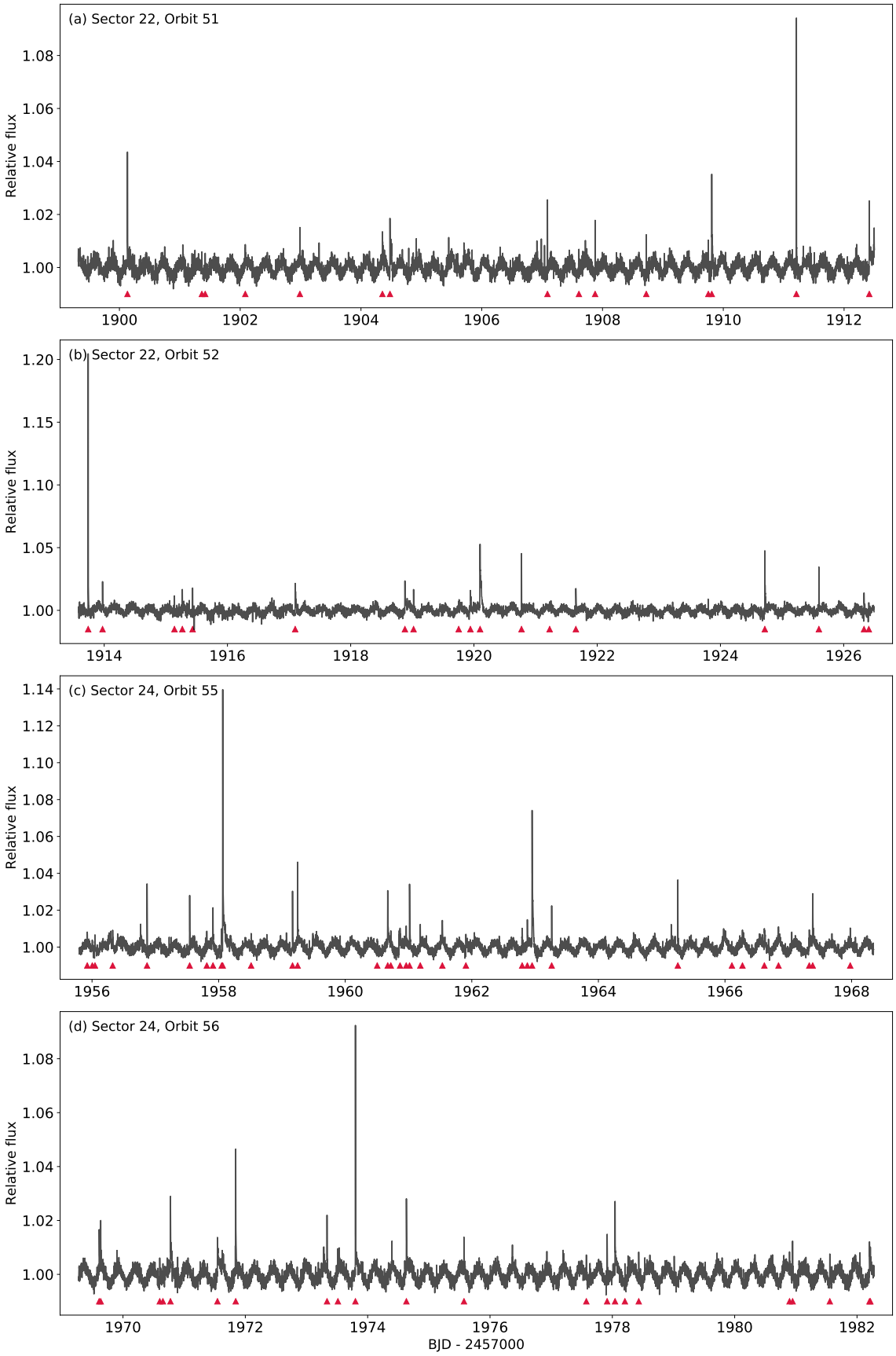

TESS light curve of LP 071-082 (J18022+642, TIC 233068870) for sectors 22 and 24.

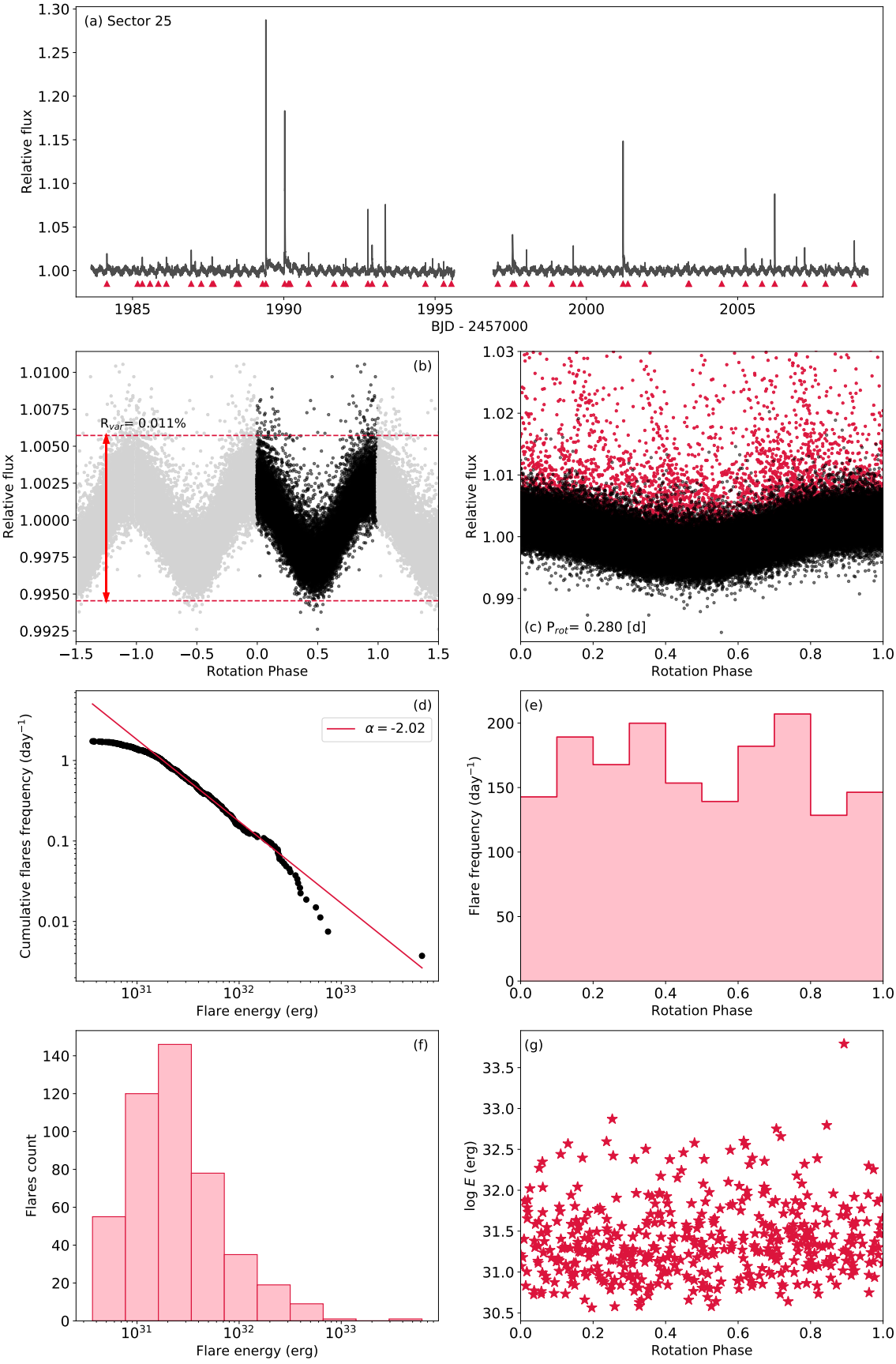

Same as Fig. B.3 but for LP 071-082 (J18022+642, TIC 233068870). Data in panel (b) is binned but R_{var} is calculated from unbinned data.

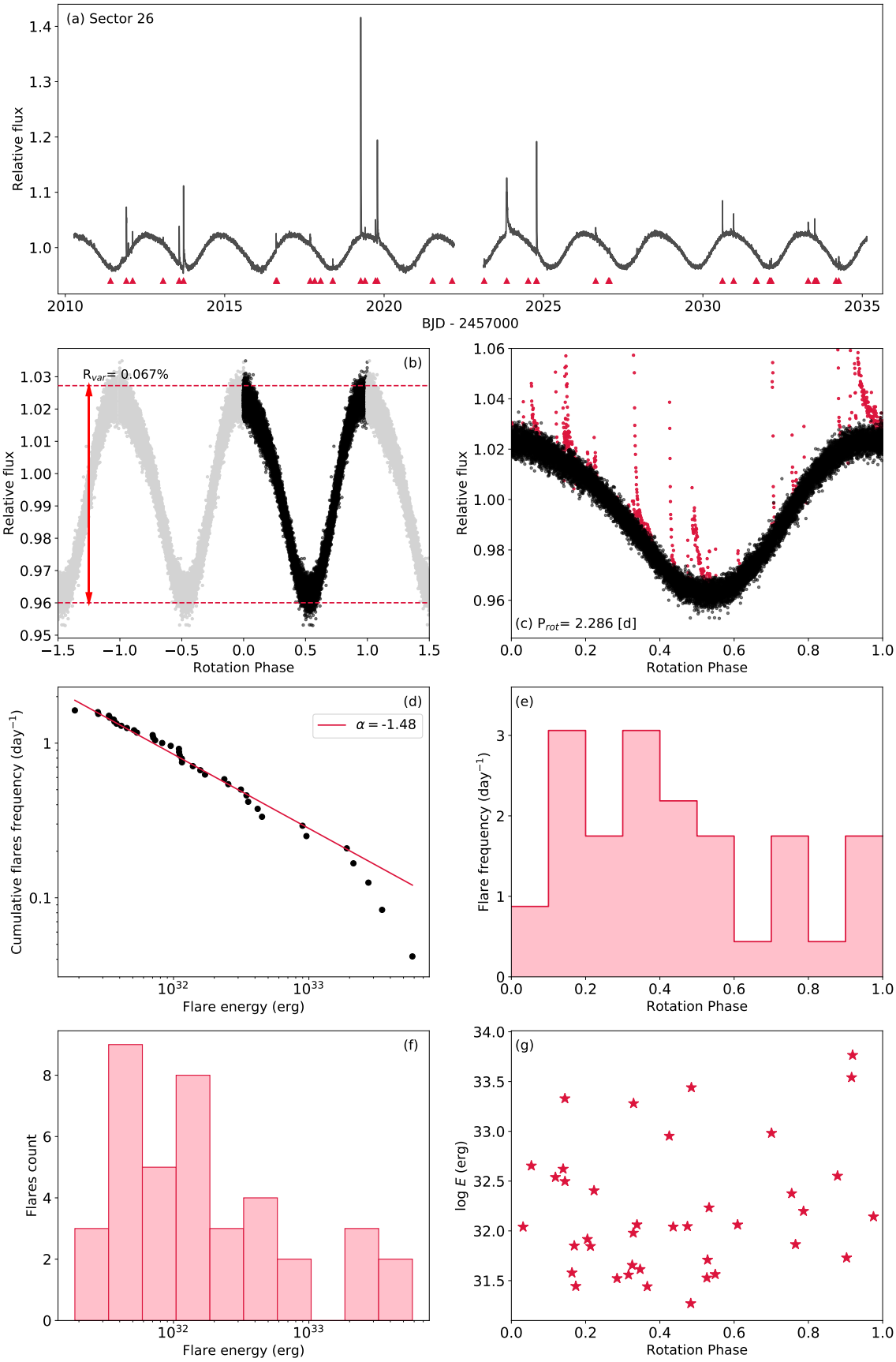

FIGURE B.33: Same as Fig. B.3 but for LP 390-16 (J18131+260, TIC 313988572).

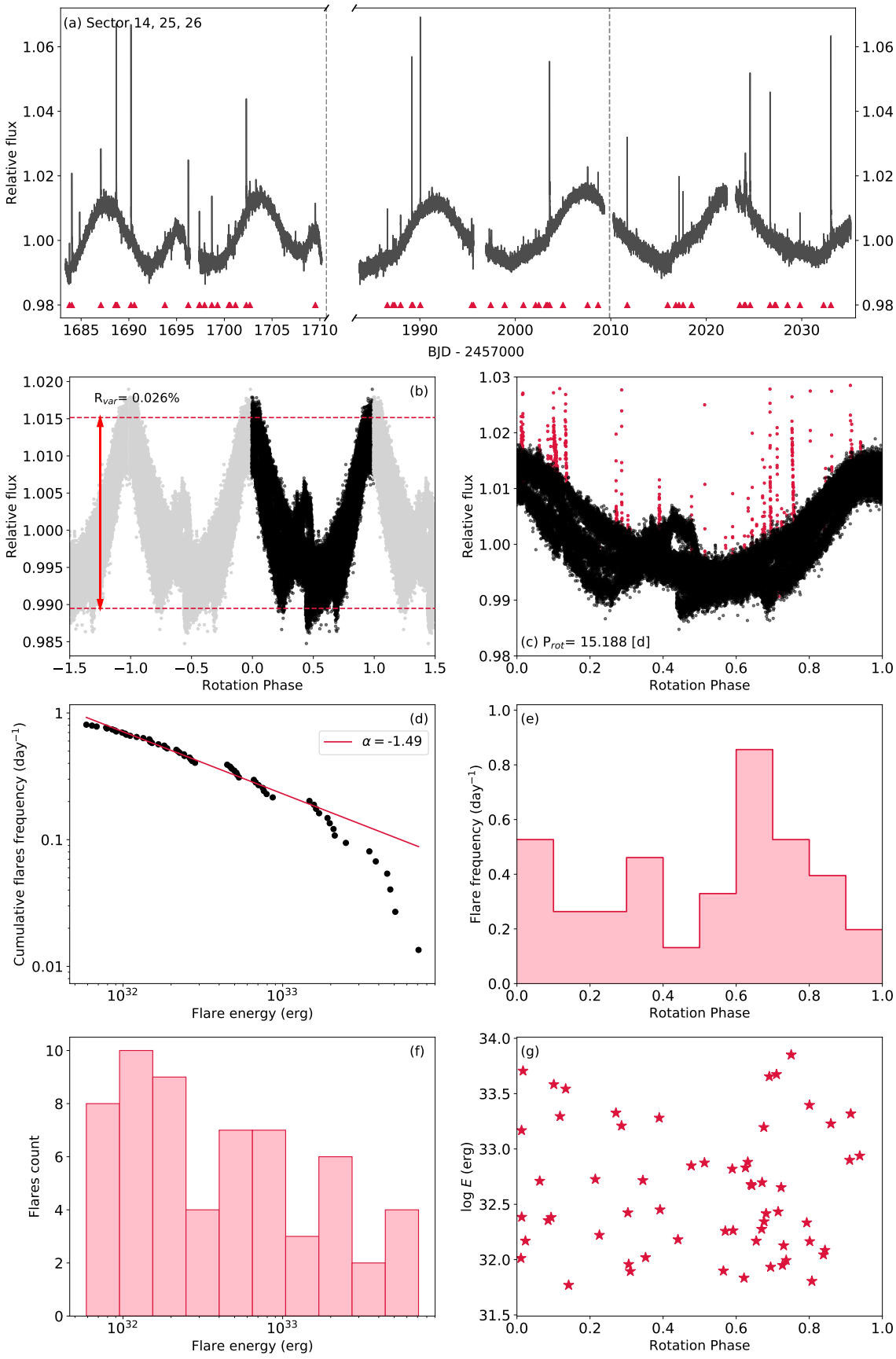

FIGURE B.34: Same as Fig. B.3 but for TYC 3529-1437-1 (J18174+483, TIC 289726188).

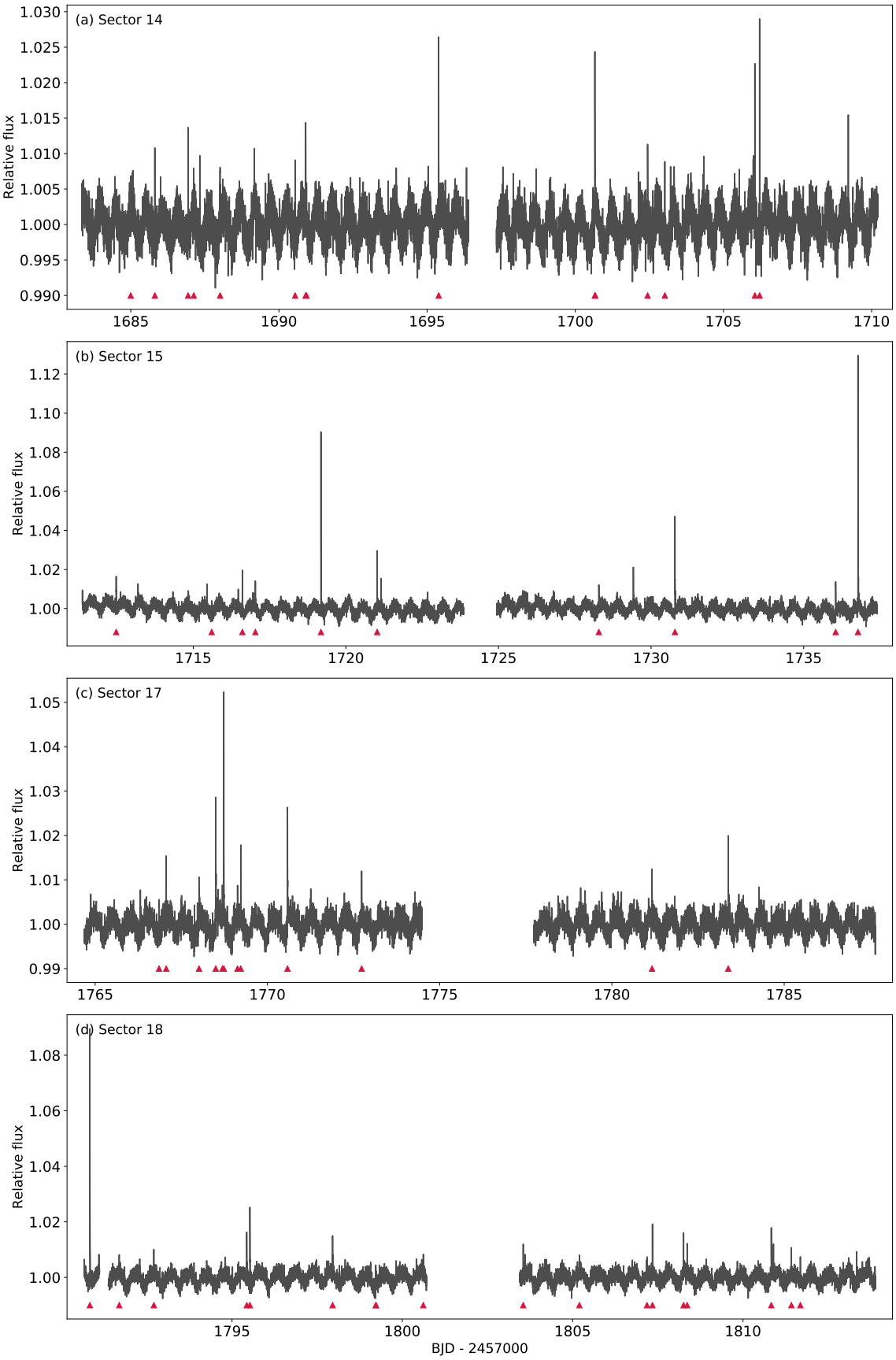

FIGURE B.35: TESS light curve of LP 71-165 (J18189+661, TIC 406857100) for sectors 14, 15, 17, and 18.

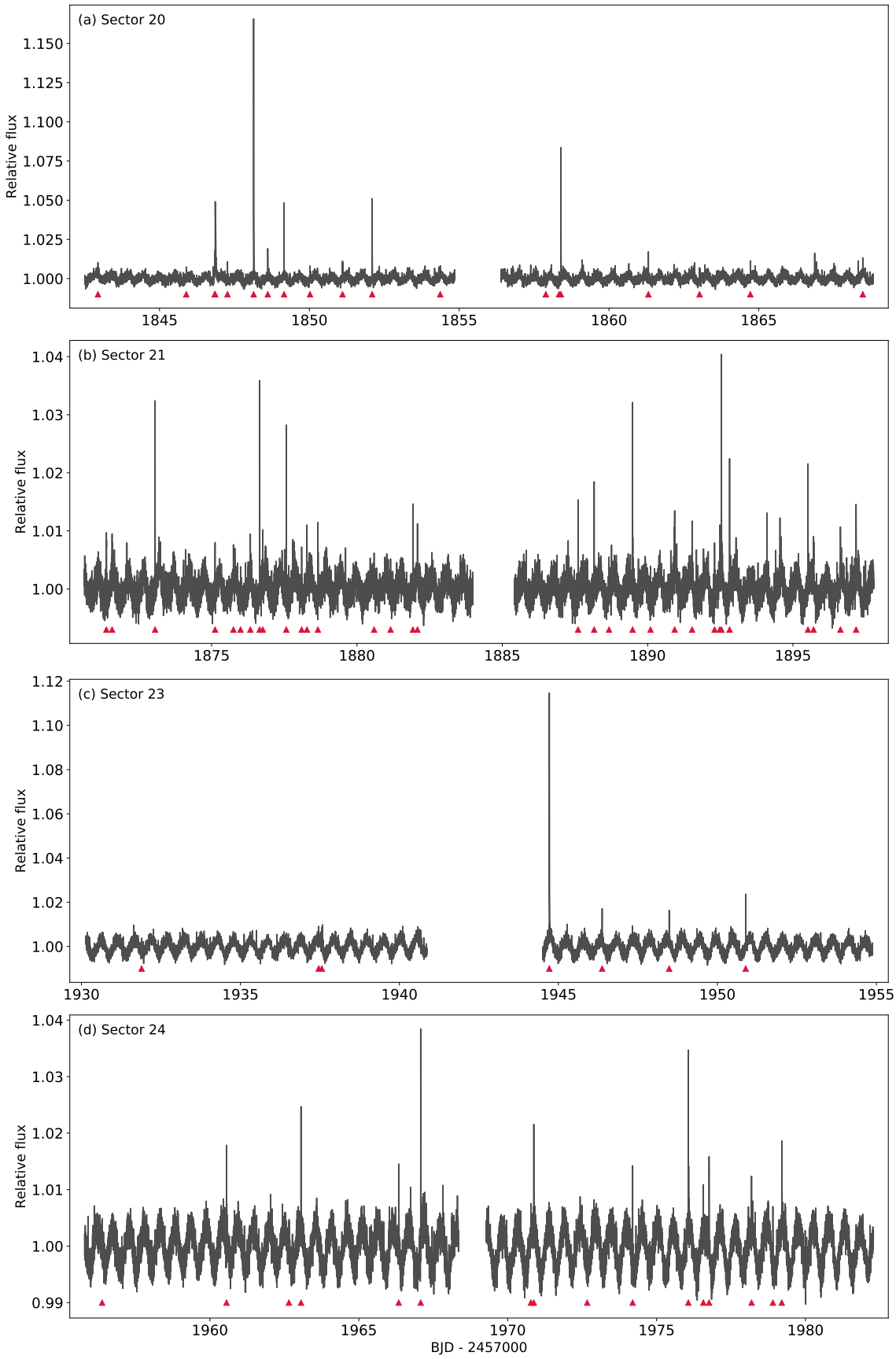

TESS light curve of LP 71-165 (J18189+661, TIC 406857100) for sectors 20, 21, 23, and 24.

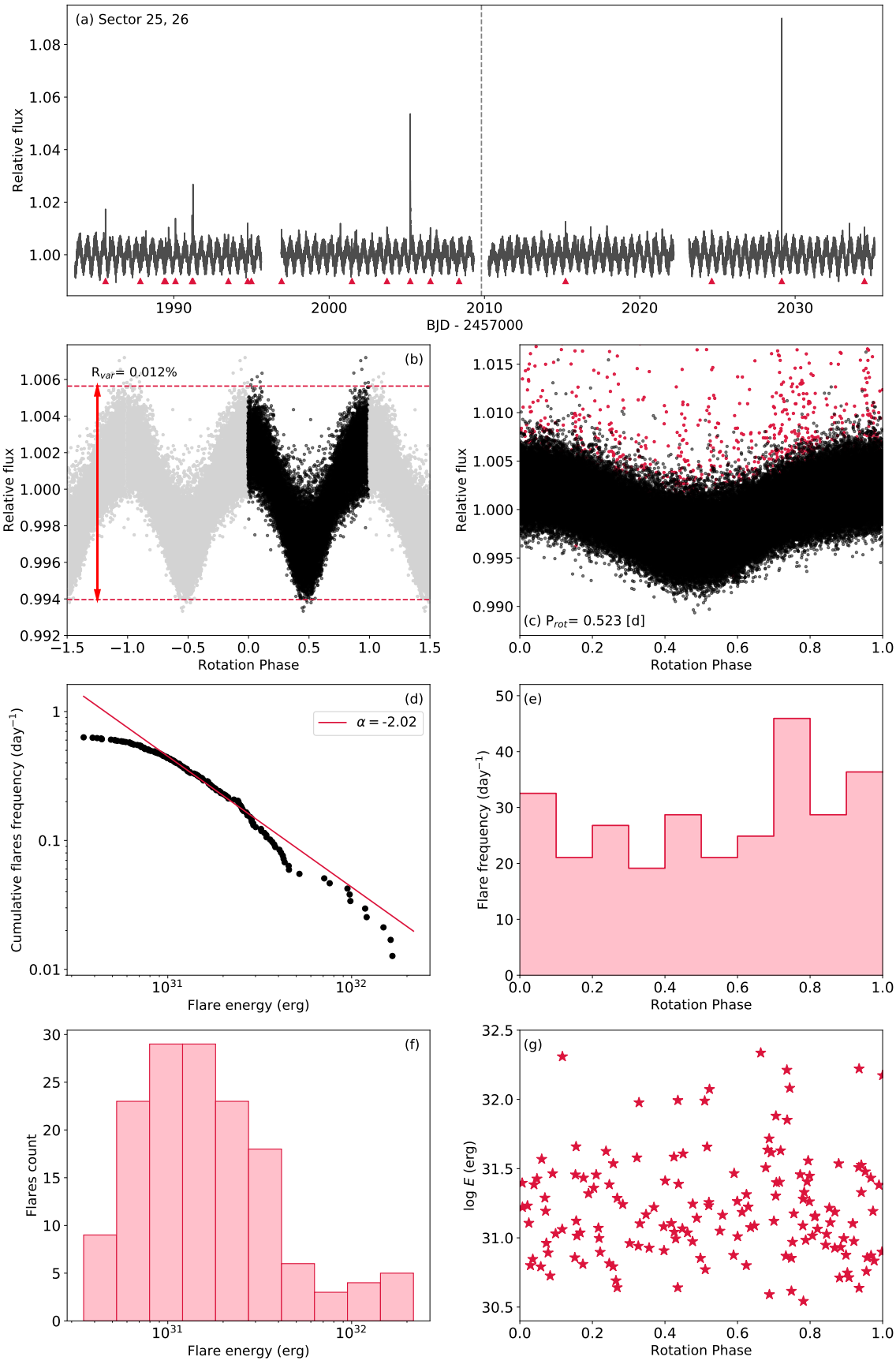

[
]Same as Fig. B.3 but for LP 71-165 (J18189+661, TIC 406857100). Data in panel (b) is binned but R_{var} is calculated from unbinned data.

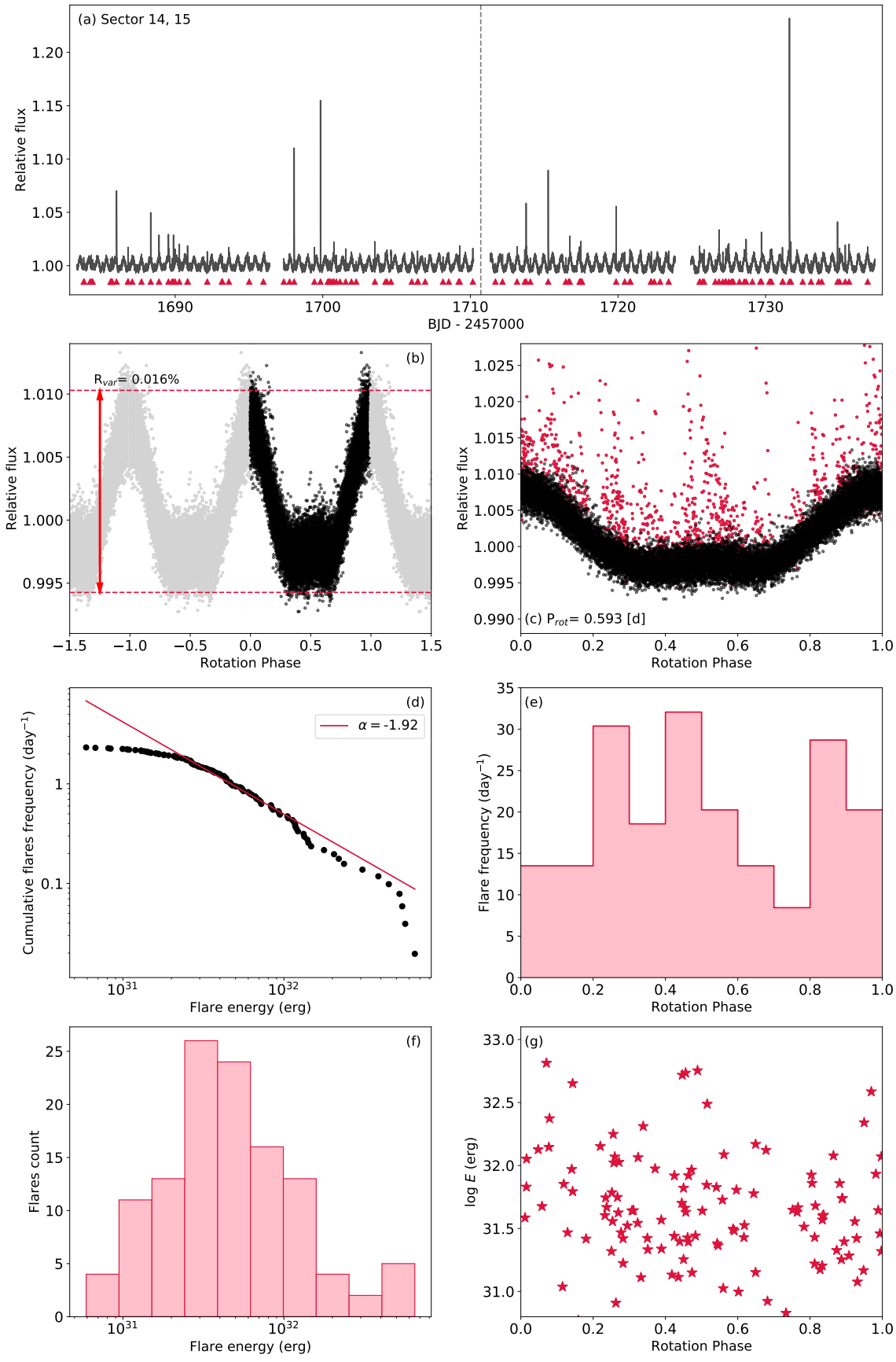

FIGURE B.36: Same as Fig. B.3 but for G 208-042 (J19511+464, TIC 273589987).

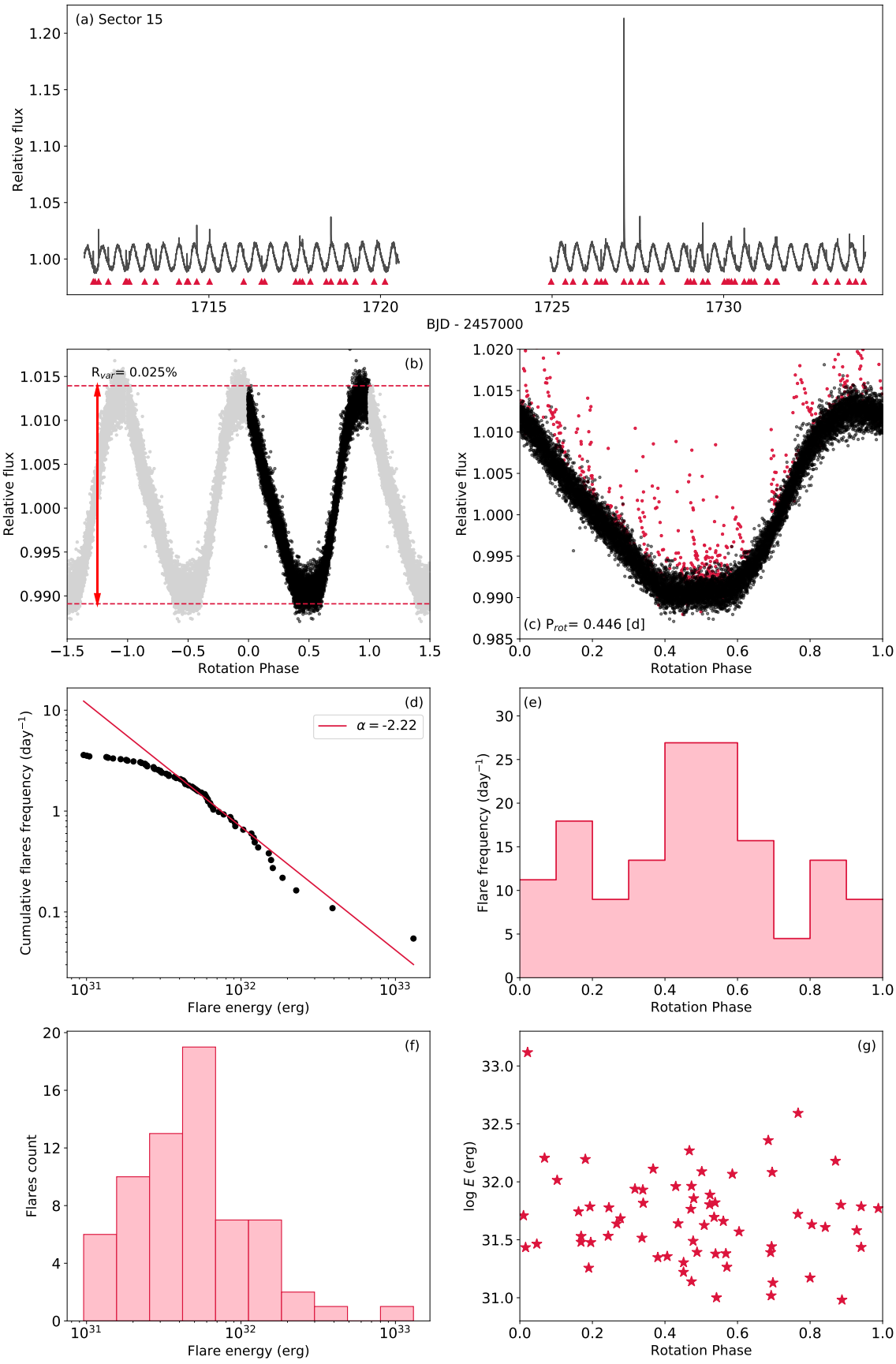

FIGURE B.37: Same as Fig. B.3 but for V374 Peg (J22012+283, TIC 283410775).

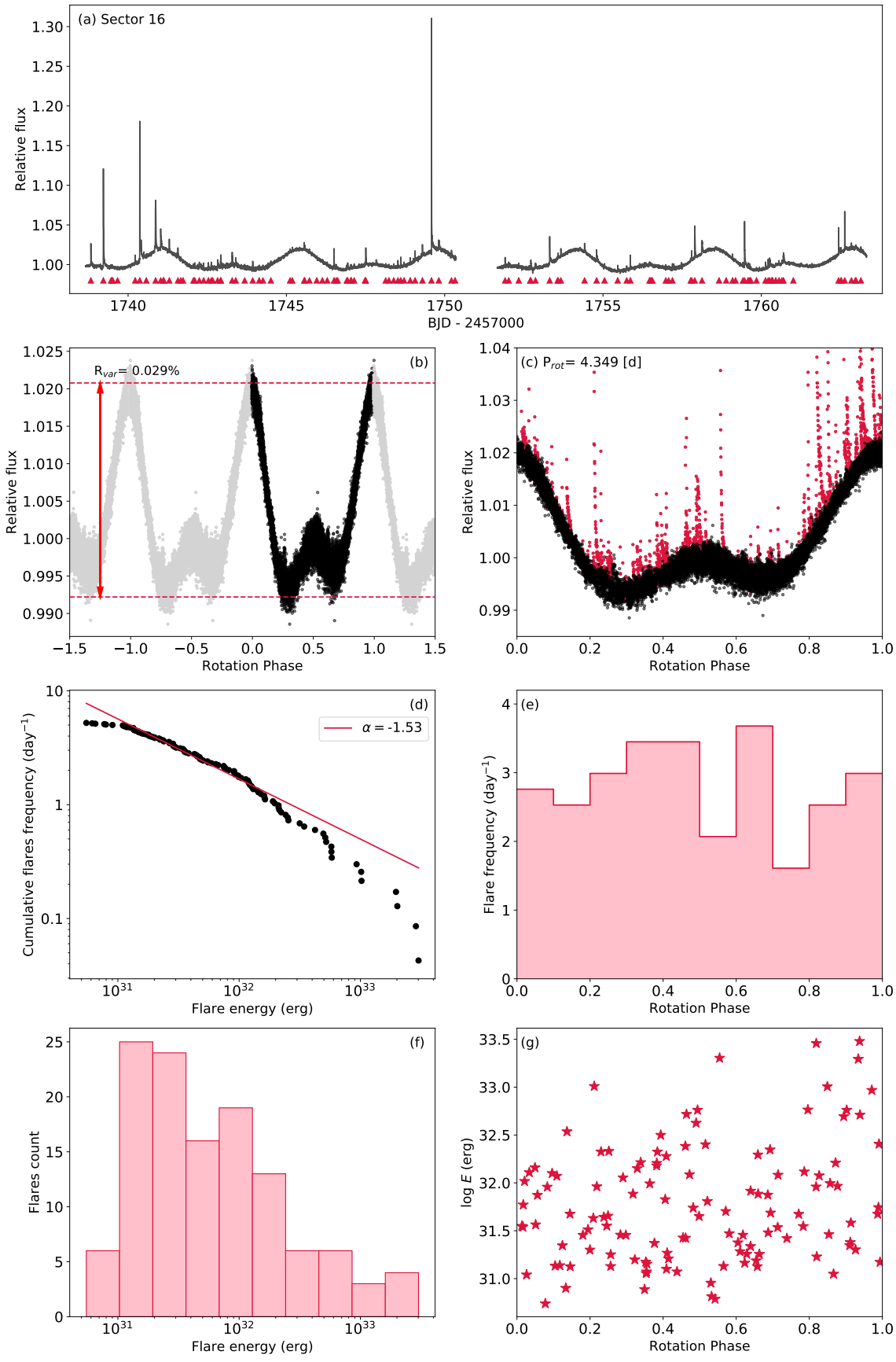

FIGURE B.38: Same as Fig. B.3 but for EV Lac (J22468+443, TIC 154101678).

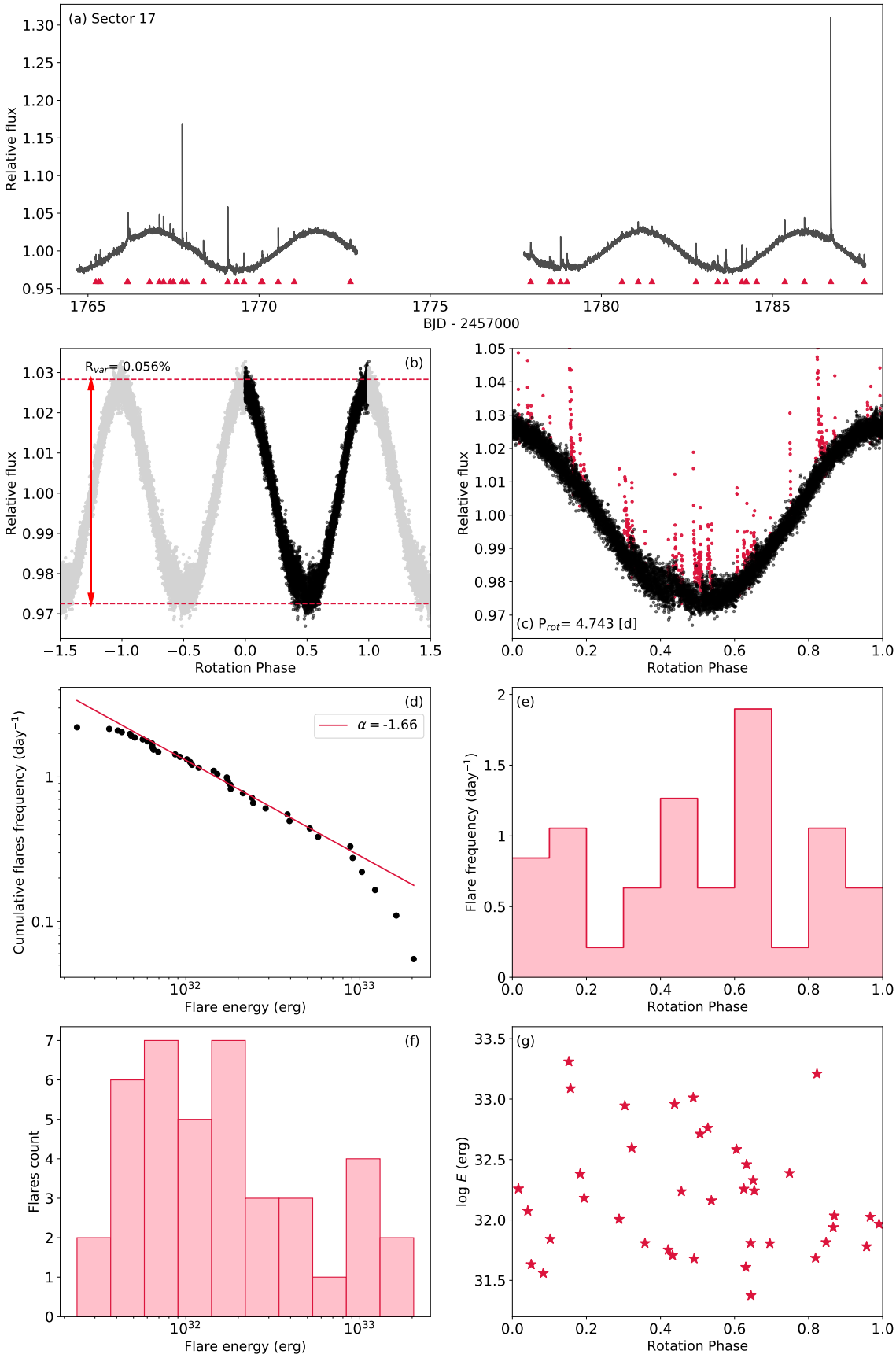

FIGURE B.39: Same as Fig. B.3 but for RX J2354.8+3831 (J23548+385, TIC 291689873).

Appendix C

TABLE C.1: CARMENES RV measurements for V388 Cas

(A) VIS data

BJD	RV [$m\,s^{-1}$]	σ_{RV} [$m\,s^{-1}$]
2457621.63442	0.26	8.41
2457649.64220	329.36	18.36
2457659.57770	−146.40	18.07
2457673.48560	−362.43	19.29
2457678.49347	14.06	11.99
2457694.46972	−15.49	11.00
2457738.37278	−110.12	16.87
2457755.41479	−340.60	21.17
2457761.29962	330.75	22.71
2457786.31823	224.03	19.12
2457814.32416	126.88	11.13
2457822.32022	−136.94	13.46
2458791.67921	58.46	20.12
2458795.42166	−229.23	21.94
2458796.44210	−272.07	22.75
2458801.64200	−283.84	22.78
2458804.60795	−274.59	30.31
2458812.40069	221.61	17.96
2458814.41697	126.45	11.45
2458815.39957	24.89	14.60
2458816.43008	36.17	7.35
2458817.37696	−137.37	12.86
2458818.37145	−143.17	16.08
2458829.51454	139.04	17.87
2458832.37742	−153.61	14.68
2458834.39447	−180.57	33.25

(B) NIR data

BJD	RV [$m\,s^{-1}$]	σ_{RV} [$m\,s^{-1}$]
2457649.64351	200.72	28.59
2457673.48731	−302.76	30.60
2457678.49454	5.65	21.14
2457694.46840	−8.91	14.01
2457755.41363	−287.99	39.15
2457761.29931	309.30	29.98
2457786.31751	175.61	28.50
2457814.32379	97.14	15.64
2457822.31974	−90.80	28.95
2458791.67986	7.47	36.77
2458795.42078	−254.82	46.31
2458796.44210	−219.37	31.50
2458801.64194	−202.86	30.23
2458804.60768	−177.73	31.57
2458812.40077	201.09	32.19
2458814.41622	148.32	22.77
2458816.43057	35.28	14.99
2458817.37934	−96.87	18.22
2458818.37150	−126.91	20.41
2458829.51462	109.46	25.68
2458832.37654	−116.17	27.48
2458834.39396	−161.66	49.24

TABLE C.2: Astrometric and photometric parameters for stars near V388 Cas from *Gaia* DR2. Includes coordinates, parallax, G, $G_{\rm BP}$, $G_{\rm RP}$ magnitudes, along with oBP and oRP values indicating the number of observations contributing to BP and RP magnitudes, respectively. Also includes our calculated values for M_G (absolute Gaia magnitude), std(BP), and std(RP).

Nr.	DR2 Source Id	α	δ	ϖ	G	BP	oBP	RP	oRP	M_G	std(BP)	std(RP)
		σ_α	σ_δ	σ_ϖ	σ_G	σ_{BP}		σ_{RP}		σ_{M_G}		
		(deg)	(deg)	(mas)	(mag)	(mag)		(mag)				
1	522864272037653504	15.839	62.366	101.637	11.924	13.907	17	10.603	19	11.959	0.070	0.027
		0.102	0.126	0.081	0.003	0.017		0.006		0.003		
2	522864272037651712	15.839	62.369	0.328	13.563	14.490	37	12.612	35	1.142	0.016	0.005
		0.013	0.014	0.021	0.000	0.003		0.001		0.027		
3	522864272037655936	15.846	62.364	0.384	16.099	16.696	37	15.334	37	4.020	0.021	0.016
		0.029	0.032	0.047	0.001	0.004		0.003		0.053		
4	522864375116864640	15.844	62.371	0.461	16.717	17.518	29	15.800	29	5.037	0.041	0.022
		0.044	0.055	0.072	0.001	0.008		0.004		0.068		
5	522864375116864256	15.842	62.372	0.042	15.808	17.133	35	14.648	34	-1.081	0.039	0.013
		0.032	0.035	0.053	0.001	0.007		0.002		0.546		
6	522864065879224704	15.852	62.366	0.780	15.847	16.608	38	14.983	37	5.307	0.022	0.012
		0.026	0.028	0.043	0.001	0.004		0.002		0.024		
9	522864233374163712	15.819	62.363	0.484	17.820	18.536	28	16.945	29	6.246	0.120	0.047
		0.083	0.109	0.134	0.001	0.023		0.009		0.120		

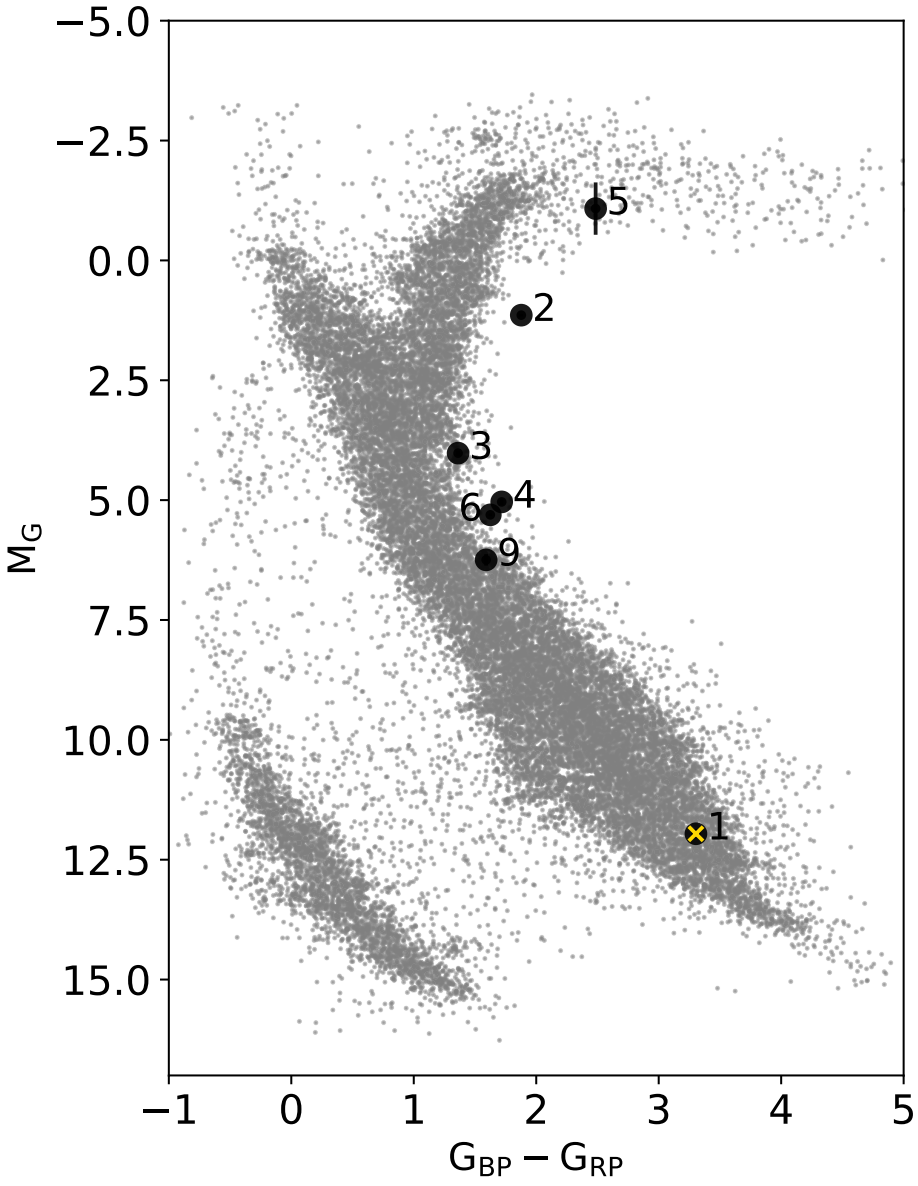

FIGURE C.1: Position of V388 Cas and nearby stars within the TESS aperture mask superimposed on the background stars in the *Gaia* HR diagram (adapted from Figure 5 of Gaia Collaboration et al., 2018a). The target numbers correspond to those in Figure 5.3, with V388 Cas indicated by a black circle with a yellow cross at its centre.

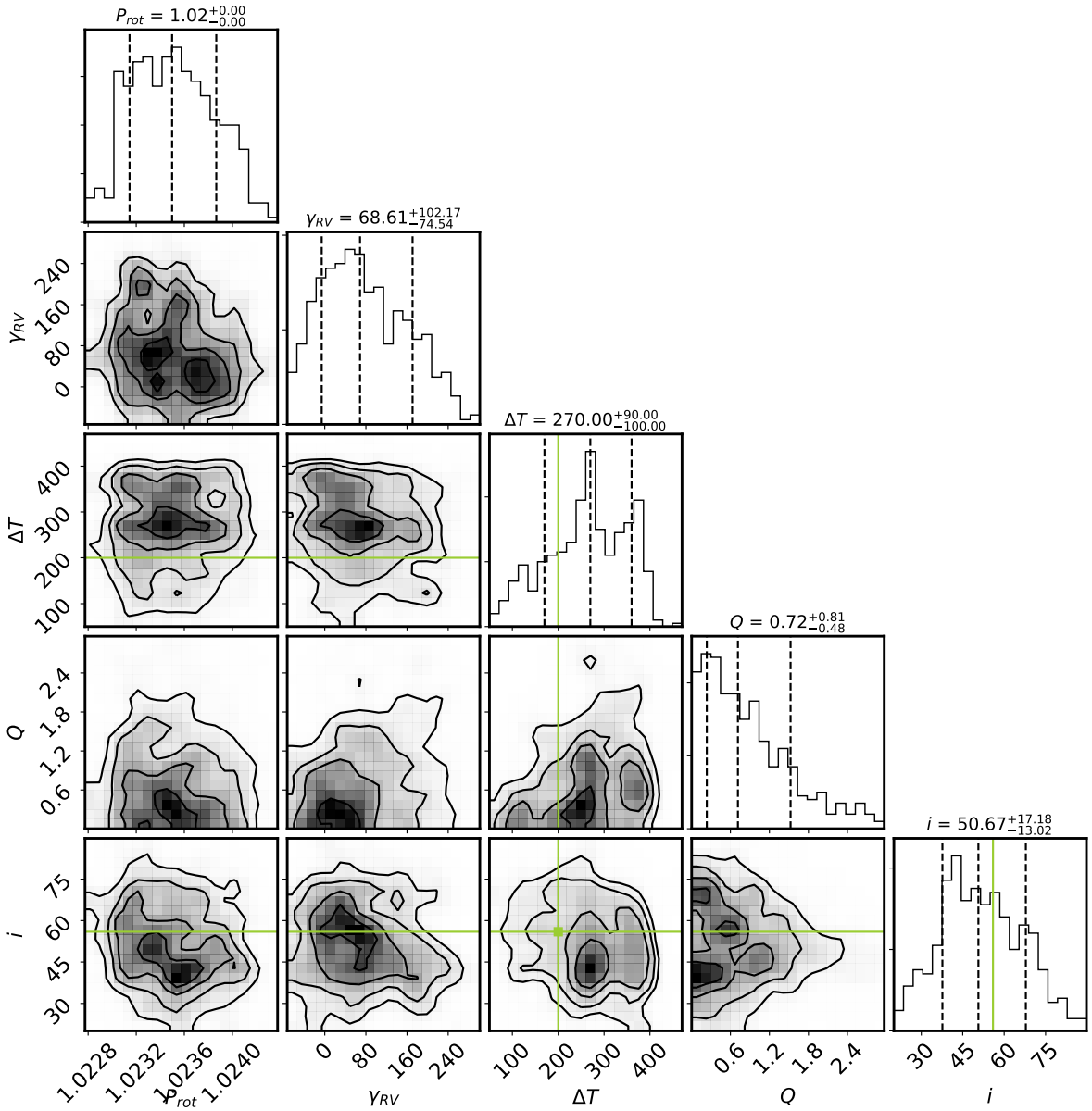

FIGURE C.2: Posterior distribution of parameters for the optimised spot model fit.

Bibliography

Abbett, William P. and Suzanne L. Hawley (Aug. 1999). "Dynamic Models of Optical Emission in Impulsive Solar Flares". In: *ApJ* 521.2, pp. 906–919. DOI: 10.1086/307576.

Afram, N. and S. V. Berdyugina (Sept. 2019). "Complexity of magnetic fields on red dwarfs". In: *A&A* 629, A83, A83. DOI: 10.1051/0004-6361/201935793.

Airapetian, V. S. et al. (June 2016). "Prebiotic chemistry and atmospheric warming of early Earth by an active young Sun". In: *Nature Geoscience* 9.6, pp. 452–455. DOI: 10.1038/ngeo2719.

Alfvén, H. (Oct. 1942). "Existence of Electromagnetic-Hydrodynamic Waves". In: *Nature* 150.3805, pp. 405–406. DOI: 10.1038/150405d0.

Aller, A. et al. (Mar. 2020). "Planetary nebulae seen with TESS: Discovery of new binary central star candidates from Cycle 1". In: *A&A* 635, A128, A128. DOI: 10.1051/0004-6361/201937118.

Alonso-Floriano, F. J. et al. (May 2015a). "CARMENES input catalogue of M dwarfs. I. Low-resolution spectroscopy with CAFOS". In: *A&A* 577, A128, A128. DOI: 10.1051/0004-6361/201525803.

— (May 2015b). "CARMENES input catalogue of M dwarfs. I. Low-resolution spectroscopy with CAFOS". In: *A&A* 577, A128, A128. DOI: 10.1051/0004-6361/201525803.

Amado, P. J. and The Carmenes Consortium (2016). "CARMENES: Commissioning and first scientific results at the telescope. A precursor for HiRES@E-ELT". In: *Proceedings of the XII Scientific Meeting of the Spanish Astronomical Society*. Bilbao, Spain, pp. 18–22.

Andersen, J. M. and H. Korhonen (Apr. 2015). "Stellar activity as noise in exoplanet detection - II. Application to M dwarfs". In: *MNRAS* 448.4, pp. 3053–3069. DOI: 10.1093/mnras/stu2731.

Anglada-Escudé, G. et al. (Sept. 2014). "Two planets around Kapteyn's star: a cold and a temperate super-Earth orbiting the nearest halo red dwarf". In: *MNRAS* 443, pp. L89–L93. DOI: 10.1093/mnrasl/slu076.

Anglada-Escudé, G. et al. (Oct. 2016). "No Evidence for Activity Correlations in the Radial Velocities of Kapteyn's Star". In: *ApJ* 830.2, 74, p. 74. DOI: 10.3847/0004-637X/830/2/74.

Anglada-Escudé, Guillem and R. Paul Butler (June 2012). "The HARPS-TERRA Project. I. Description of the Algorithms, Performance, and New Measurements on a Few Remarkable Stars Observed by HARPS". In: *ApJS* 200.2, 15, p. 15. DOI: 10.1088/0067-0049/200/2/15.

Anglada-Escudé, Guillem and Mikko Tuomi (Mar. 2015). "Comment on "Stellar activity masquerading as planets in the habitable zone of the M dwarf Gliese 581"". In: *Science* 347.6226, pp. 1080–1080. DOI: 10.1126/science.1260796.

Antiochos, S. K. (Aug. 1998). "The Magnetic Topology of Solar Eruptions". In: *ApJ* 502.2, pp. L181–L184. DOI: 10.1086/311507.

Antiochos, S. K., C. R. DeVore, and J. A. Klimchuk (Jan. 1999). "A Model for Solar Coronal Mass Ejections". In: *ApJ* 510.1, pp. 485–493. DOI: 10.1086/306563.

Artigau, Étienne et al. (July 2014). "Telluric-line subtraction in high-accuracy velocimetry: a PCA-based approach". In: *Observatory Operations: Strategies, Processes, and Systems V*. Ed. by Alison B. Peck, Chris R. Benn, and Robert L. Seaman. Vol. 9149. Society of Photo-Optical Instrumentation Engineers (SPIE) Conference Series, 914905, p. 914905. DOI: 10.1117/12.2056385.

Asplund, Martin et al. (Sept. 2009). "The Chemical Composition of the Sun". In: *ARA&A* 47.1, pp. 481–522. DOI: 10.1146/annurev.astro.46.060407.145222.

Audard, Marc et al. (Sept. 2000). "Extreme-Ultraviolet Flare Activity in Late-Type Stars". In: *ApJ* 541.1, pp. 396–409. DOI: 10.1086/309426.

Babcock, H. W. (Mar. 1961). "The Topology of the Sun's Magnetic Field and the 22-YEAR Cycle." In: *ApJ* 133, p. 572. DOI: 10.1086/147060.

Bakker, Frederik (2018). "The End of Epicurean Infinity: Critical Reflections on the Epicurean Infinite Universe". In: *Space, Imagination and the Cosmos from Antiquity to the Early Modern Period*. Ed. by Frederik Bakker, Delphine Bellis, and Carla Rita Palmerino, pp. 41–67.

Baliunas, S. L. et al. (Jan. 1995). "Chromospheric Variations in Main-Sequence Stars. II." In: *ApJ* 438, p. 269. DOI: 10.1086/175072.

Baranne, A. et al. (Oct. 1996). "ELODIE: A spectrograph for accurate radial velocity measurements." In: *A&AS* 119, pp. 373–390.

Barnes, J. R. et al. (Sept. 2001). "Further images of α Persei G dwarfs". In: *MNRAS* 326.3, pp. 1057–1066. DOI: 10.1046/j.1365-8711.2001.04648.x.

Baroch, D. et al. (Sept. 2020). "The CARMENES search for exoplanets around M dwarfs. Convective shift and starspot constraints from chromatic radial velocities". In: *A&A* 641, A69, A69. DOI: 10.1051/0004-6361/202038213.

Barry, Don C. (Nov. 1988). "The Chromospheric Age Dependence of the Birthrate, Composition, Motions, and Rotation of Late F and G Dwarfs within 25 Parsecs of the Sun". In: *ApJ* 334, p. 436. DOI: 10.1086/166848.

Basri, Gibor and Hieu T. Nguyen (Aug. 2018). "Double Dipping: A New Relation between Stellar Rotation and Starspot Activity". In: *ApJ* 863.2, 190, p. 190. DOI: 10.3847/1538-4357/aad3b6.

Basri, Gibor and Riya Shah (Sept. 2020). "The Information Content in Analytic Spot Models of Broadband Precision Light Curves. II. Spot Distributions and Lifetimes and Global and Differential Rotation". In: *ApJ* 901.1, 14, p. 14. DOI: 10.3847/1538-4357/abae5d.

Basri, Gibor et al. (Apr. 2010). "Photometric Variability in Kepler Target Stars: The Sun Among Stars—a First Look". In: *ApJ* 713.2, pp. L155–L159. DOI: 10.1088/2041-8205/713/2/L155.

Basri, Gibor et al. (2011). "Photometric Variability in Kepler Target Stars. II. An Overview of Amplitude, Periodicity, and Rotation in First Quarter Data". In: *AJ* 141.1, 20, p. 20. DOI: 10.1088/0004-6256/141/1/20.

Basu, Sarbani et al. (July 2009). "Fresh Insights on the Structure of the Solar Core". In: *ApJ* 699.2, pp. 1403–1417. DOI: 10.1088/0004-637X/699/2/1403.

Bauer, F. F. et al. (Aug. 2020). "The CARMENES search for exoplanets around M dwarfs. Measuring precise radial velocities in the near infrared: The example of the super-Earth CD Cet b". In: *A&A* 640, A50, A50. DOI: 10.1051/0004-6361/202038031.

Beck, John G. (Jan. 2000). "A comparison of differential rotation measurements - (Invited Review)". In: *Sol. Phys.* 191.1, pp. 47–70. DOI: 10.1023/A:1005226402796.

Bedell, Megan et al. (Oct. 2019). "WOBBLE: A Data-driven Analysis Technique for Time-series Stellar Spectra". In: *AJ* 158.4, 164, p. 164. DOI: 10.3847/1538-3881/ab40a7.

Benedict, G. F. et al. (May 1993). "Periodic Low Amplitude Variations in the Brightness of Proxima Centauri". In: *PASP* 105, p. 487. DOI: 10.1086/133182.

Benz, Arnold O. and Manuel Güdel (Sept. 2010). "Physical Processes in Magnetically Driven Flares on the Sun, Stars, and Young Stellar Objects". In: *ARA&A* 48, pp. 241–287. DOI: 10.1146/annurev-astro-082708-101757.

Berdyugina, S. V. and I. G. Usoskin (July 2003). "Active longitudes in sunspot activity: Century scale persistence". In: *A&A* 405, pp. 1121–1128. DOI: 10.1051/0004-6361:20030748.

Berdyugina, Svetlana V. (Dec. 2005). "Starspots: A Key to the Stellar Dynamo". In: *Living Reviews in Solar Physics* 2.1, 8, p. 8. DOI: 10.12942/lrsp-2005-8.

Berdyugina, Svetlana V. and Ilkka Tuominen (Aug. 1998). "Permanent active longitudes and activity cycles on RS CVn stars". In: *A&A* 336, pp. L25–L28.

Björn, L.O. (ed.) (2015). *Photobiology. The Science of Light and Life*. 3rd ed. Springer-Verlag New York. ISBN: 978-1-4939-1467-8,978-1-4939-1468-5. DOI: 10.1007/978-1-4939-1468-5.

Bogdan, T. J. et al. (Apr. 1988). "Distribution of Sunspot Umbral Areas: 1917–1982". In: *ApJ* 327, p. 451. DOI: 10.1086/166206.

Boisse, I. et al. (Mar. 2009). "Stellar activity of planetary host star HD 189 733". In: *A&A* 495.3, pp. 959–966. DOI: 10.1051/0004-6361:200810648.

Boisse, I. et al. (Apr. 2011). "Disentangling between stellar activity and planetary signals". In: *A&A* 528, A4, A4. DOI: 10.1051/0004-6361/201014354.

Bonfils, X. et al. (Oct. 2007). "The HARPS search for southern extra-solar planets. X. A m sin i = 11 M_⊕ planet around the nearby spotted M dwarf <ASTROBJ>GJ 674</ASTROBJ>". In: *A&A* 474.1, pp. 293–299. DOI: 10.1051/0004-6361:20077068.

Bopp, B. W. and T. J. Moffett (Oct. 1973). "High time resolution studies of UV Ceti." In: *ApJ* 185, p. 239. DOI: 10.1086/152412.

Borucki, W. J. and A. L. Summers (Apr. 1984). "The photometric method of detecting other planetary systems". In: *Icarus* 58.1, pp. 121–134. DOI: 10.1016/0019-1035(84)90102-7.

Borucki, William J. et al. (Feb. 2010). "Kepler Planet-Detection Mission: Introduction and First Results". In: *Science* 327.5968, p. 977. DOI: 10.1126/science.1185402.

Brown, T. M. and J. Christensen-Dalsgaard (June 1998). "Accurate Determination of the Solar Photospheric Radius". In: *ApJ* 500.2, pp. L195–L198. DOI: 10.1086/311416.

Browning, Matthew K. (Apr. 2008). "Simulations of Dynamo Action in Fully Convective Stars". In: *ApJ* 676.2, pp. 1262–1280. DOI: 10.1086/527432.

Browning, Matthew K. et al. (Feb. 2010). "Rotation and Magnetic Activity in a Sample of M-Dwarfs". In: *AJ* 139.2, pp. 504–518. DOI: 10.1088/0004-6256/139/2/504.

Buccino, Andrea P., Guillermo A. Lemarchand, and Pablo J. D. Mauas (Aug. 2006). "Ultraviolet radiation constraints around the circumstellar habitable zones". In: *Icarus* 183.2, pp. 491–503. DOI: 10.1016/j.icarus.2006.03.007.

Caballero, J. A. (May 2010). "Reaching the boundary between stellar kinematic groups and very wide binaries . II. α Librae + KU Librae: a common proper motion system in Castor separated by 1.0 pc". In: *A&A* 514, A98, A98. DOI: 10.1051/0004-6361/200913986.

Caballero, J. A. et al. (Aug. 2016). "Carmencita, The CARMENES Input Catalogue of Bright, Nearby M Dwarfs". In: *19th Cambridge Workshop on Cool Stars, Stellar Systems, and the Sun (CS19)*. Cambridge Workshop on Cool Stars, Stellar Systems, and the Sun, 148, p. 148. DOI: 10.5281/zenodo.60060.

Campbell, Dylan (Oct. 2016). "Aristotle's On the Heavens". In: *World History Encyclopedia* 959.

Candelaresi, S. et al. (Sept. 2014). "Superflare Occurrence and Energies on G-, K-, and M-type Dwarfs". In: *ApJ* 792.1, 67, p. 67. DOI: 10.1088/0004-637X/792/1/67.

Cannon, Annie J. and Edward C. Pickering (Jan. 1901). "Spectra of bright southern stars photographed with the 13-inch Boyden telescope as part of the Henry Draper Memorial". In: *Annals of Harvard College Observatory* 28, 129–P.6.

— (1918–1924). "The Henry Draper catalogue". In: *Annals of Harvard College Observatory*.

Carrington, R.C. (1863). *Observations of the Spots on the Sun from November 9. 1853, to March 24, 1861, Made at Redhill*. Williams and Norgate. URL: https://books.google.de/books?id=GY1DAAAAcAAJ.

Cegla, H. M. et al. (July 2019). "Stellar Surface Magnetoconvection as a Source of Astrophysical Noise. III. Sun-as-a-Star Simulations and Optimal Noise Diagnostics". In: *ApJ* 879.1, 55, p. 55. DOI: 10.3847/1538-4357/ab16d3.

Chabrier, G. and M. Küker (Feb. 2006). "Large-scale $\alpha\hat{2}$-dynamo in low-mass stars and brown dwarfs". In: *A&A* 446.3, pp. 1027–1037. DOI: 10.1051/0004-6361:20042475.

Chabrier, Gilles and Isabelle Baraffe (Nov. 1997). "Structure and evolution of low-mass stars". In: *A&A* 327, pp. 1039–1053.

Chang, S. W., Y. I. Byun, and J. D. Hartman (Nov. 2015). "Photometric Study on Stellar Magnetic Activity. I. Flare Variability of Red Dwarf Stars in the Open Cluster M37". In: *ApJ* 814.1, 35, p. 35. DOI: 10.1088/0004-637X/814/1/35.

Charbonneau, D. (Jan. 2003). "HD 209458 and the Power of the Dark Side". In: *Scientific Frontiers in Research on Extrasolar Planets*. Ed. by Drake Deming and Sara Seager. Vol. 294. Astronomical Society of the Pacific Conference Series, pp. 449–456.

Charbonneau, David et al. (Jan. 2000). "Detection of Planetary Transits Across a Sun-like Star". In: *ApJ* 529.1, pp. L45–L48. DOI: 10.1086/312457.

Charbonneau, David et al. (Dec. 2009). "A super-Earth transiting a nearby low-mass star". In: *Nature* 462.7275, pp. 891–894. DOI: 10.1038/nature08679.

Charbonneau, P. et al. (Dec. 1999). "Helioseismic Constraints on the Structure of the Solar Tachocline". In: *ApJ* 527.1, pp. 445–460. DOI: 10.1086/308050.

Charbonneau, Paul (Aug. 2014). "Solar Dynamo Theory". In: *ARA&A* 52, pp. 251–290. DOI: 10.1146/annurev-astro-081913-040012.

Chaussidon, Marc (2007). "In Lectures in Astrobiology II". In: *Lectures in Astrobiology II*. Ed. by Muriel Gargaud, Hervé Martin, and Philippe Claeys. SpringerVerlag, p. 45.

Chen, J. (2017). "Physics of erupting solar flux ropes: coronal mass ejections (CMEs)—recent advances in theory and observation". In: *Physics of Plasmas* 24.9, p. 090501.

Chen, P. F. (Apr. 2011). "Coronal Mass Ejections: Models and Their Observational Basis". In: *Living Reviews in Solar Physics* 8.1, 1, p. 1. DOI: 10.12942/lrsp-2011-1.

Christensen-Dalsgaard, Jørgen (Nov. 2002). "Helioseismology". In: *Reviews of Modern Physics* 74.4, pp. 1073–1129. DOI: 10.1103/RevModPhys.74.1073.

Cifuentes, C. et al. (Oct. 2020). "CARMENES input catalogue of M dwarfs. V. Luminosities, colours, and spectral energy distributions". In: *A&A* 642, A115, A115. DOI: 10.1051/0004-6361/202038295.

Clough, S. A. et al. (Mar. 2005). "Atmospheric radiative transfer modeling: a summary of the AER codes". In: *J. Quant. Spectr. Rad. Transf.* 91.2, pp. 233–244. DOI: 10.1016/j.jqsrt.2004.05.058.

Coriolis, Gustave Gaspard (1835). *Théorie mathématique des effets du jeu de billard*. Carilian-Goeury.

Cortés-Contreras, M. (2016). "CARMENES-UCM: scientific preparation of the sample. Multiplicity, chromospheric activity and kinematics". PhD thesis. Universidad Complutense de Madrid, Spain.

Cortes-Contreras, M. et al. (Sept. 2016). "VizieR Online Data Catalog: CARMENES input catalogue of M dwarfs II (Cortes-Contreras+ 2017)". In: *VizieR Online Data Catalog* 359.

Cowling, T. G. (Nov. 1933). "The magnetic field of sunspots". In: *MNRAS* 94, pp. 39–48. DOI: 10.1093/mnras/94.1.39.

Cox, Arthur N. (2000). *Allen's astrophysical quantities*.

Cretignier, M. et al. (Jan. 2020). "Measuring precise radial velocities on individual spectral lines. II. Dependance of stellar activity signal on line depth". In: *A&A* 633, A76, A76. DOI: 10.1051/0004-6361/201936548.

Davenport, James R. A. (Sept. 2016). "The Kepler Catalog of Stellar Flares". In: *ApJ* 829.1, 23, p. 23. DOI: 10.3847/0004-637X/829/1/23.

Davenport, James. R. A., Guadalupe Tovar Mendoza, and Suzanne L. Hawley (July 2020). "10 Years of Stellar Activity for GJ 1243". In: *AJ* 160.1, 36, p. 36. DOI: 10.3847/1538-3881/ab9536.

Davenport, James R. A. et al. (Dec. 2014). "Kepler Flares. II. The Temporal Morphology of White-light Flares on GJ 1243". In: *ApJ* 797.2, 122, p. 122. DOI: 10.1088/0004-637X/797/2/122.

Davenport, James R. A. et al. (Feb. 2019). "The Evolution of Flare Activity with Stellar Age". In: *ApJ* 871.2, 241, p. 241. DOI: 10.3847/1538-4357/aafb76.

Davidson, P. A. (2001). *An Introduction to Magnetohydrodynamics*. 1st ed. Cambridge Texts in Applied Mathematics. Cambridge University Press. ISBN: 9780521794879,0521794870.

Davis, Allen B. et al. (Sept. 2017). "Insights on the Spectral Signatures of Stellar Activity and Planets from PCA". In: *ApJ* 846.1, 59, p. 59. DOI: 10.3847/1538-4357/aa8303.

Delfosse, X. et al. (Mar. 1998). "Rotation and chromospheric activity in field M dwarfs". In: *A&A* 331, pp. 581–595.

Desort, M. et al. (Oct. 2007). "Search for exoplanets with the radial-velocity technique: quantitative diagnostics of stellar activity". In: *A&A* 473.3, pp. 983–993. DOI: 10.1051/0004-6361:20078144.

Díez Alonso, E. et al. (Jan. 2019). "CARMENES input catalogue of M dwarfs. IV. New rotation periods from photometric time series". In: *A&A* 621, A126, A126. DOI: 10.1051/0004-6361/201833316.

Dobler, Wolfgang, Michael Stix, and Axel Brandenburg (Feb. 2006). "Magnetic Field Generation in Fully Convective Rotating Spheres". In: *ApJ* 638.1, pp. 336–347. DOI: 10.1086/498634.

Donati, J. F. et al. (Oct. 2008). "Large-scale magnetic topologies of early M dwarfs". In: *MNRAS* 390.2, pp. 545–560. DOI: 10.1111/j.1365-2966.2008.13799.x.

Donati, Jean-François et al. (Feb. 2006). "The Large-Scale Axisymmetric Magnetic Topology of a Very-Low-Mass Fully Convective Star". In: *Science* 311.5761, pp. 633–635. DOI: 10.1126/science.1121102.

Douglas, S. T. et al. (Nov. 2014). "The Factory and the Beehive. II. Activity and Rotation in Praesepe and the Hyades". In: *ApJ* 795.2, 161, p. 161. DOI: 10.1088/0004-637X/795/2/161.

Doyle, L., G. Ramsay, and J. G. Doyle (May 2020). "Superflares and variability in solar-type stars with TESS in the Southern hemisphere". In: *MNRAS* 494.3, pp. 3596–3610. DOI: 10.1093/mnras/staa923.

Doyle, L. et al. (Oct. 2018). "Investigating the rotational phase of stellar flares on M dwarfs using K2 short cadence data". In: *MNRAS* 480.2, pp. 2153–2164. DOI: 10.1093/mnras/sty1963.

Doyle, L. et al. (Oct. 2019). "Probing the origin of stellar flares on M dwarfs using TESS data sectors 1-3". In: *MNRAS* 489.1, pp. 437–445. DOI: 10.1093/mnras/stz2205.

Dumusque, X. (Nov. 2018). "Measuring precise radial velocities on individual spectral lines. I. Validation of the method and application to mitigate stellar activity". In: *A&A* 620, A47, A47. DOI: 10.1051/0004-6361/201833795.

Durney, Bernard R., David S. De Young, and Ian W. Roxburgh (June 1993). "On the Generation of the Largescale and Turbulent Magnetic Fields in the Solar Type Stars". In: *Sol. Phys.* 145.2, pp. 207–225. DOI: 10.1007/BF00690652.

Emilio, M. et al. (May 2012). "Measuring the Solar Radius from Space during the 2003 and 2006 Mercury Transits". In: *ApJ* 750.2, 135, p. 135. DOI: 10.1088/0004-637X/750/2/135.

Engvold, Oddbjørn (Jan. 2015). "Description and Classification of Prominences". In: *Solar Prominences*. Ed. by Jean-Claude Vial and Oddbjørn Engvold. Vol. 415. Astrophysics and Space Science Library, p. 31. DOI: 10.1007/978-3-319-10416-4_2.

Eversberg, Thomas and Klaus Vollmann (2015). *Spectroscopic Instrumentation: Fundamentals and Guidelines for Astronomers*. DOI: 10.1007/978-3-662-44535-8.

Feinstein, Adina D. et al. (Nov. 2020). "Flare Statistics for Young Stars from a Convolutional Neural Network Analysis of TESS Data". In: *AJ* 160.5, 219, p. 219. DOI: 10.3847/1538-3881/abac0a.

Figueira, P. et al. (Sept. 2013). "Line-profile variations in radial-velocity measurements. Two alternative indicators for planetary searches". In: *A&A* 557, A93, A93. DOI: 10.1051/0004-6361/201220779.

Fisher, G. H., R. C. Canfield, and A. N. McClymont (Feb. 1985). "Flare Loop Radiative Hydrodynamics - Part Six - Chromospheric Evaporation due to Heating by Nonthermal Electrons". In: *ApJ* 289, p. 425. DOI: 10.1086/162902.

Fisher, R. A. (1925). "Theory of Statistical Estimation". In: *Proceedings of the Cambridge Philosophical Society* 22, p. 700. DOI: 10.1017/S0305004100009580.

Flores Soriano, M. and K. G. Strassmeier (Jan. 2017). "Short-term evolution and coexistence of spots, plages and flare activity on LQ Hydrae". In: *A&A* 597, A101, A101. DOI: 10.1051/0004-6361/201629338.

Fouqué, Pascal et al. (Apr. 2018). "SPIRou Input Catalogue: global properties of 440 M dwarfs observed with ESPaDOnS at CFHT". In: *MNRAS* 475.2, pp. 1960–1986. DOI: 10.1093/mnras/stx3246.

Fowler, A. and International Astronomical Union (1922). *Transactions of the International Astronomical Union*. Vol. 1. 1st General Assembly Held at Rome 2-10 May. Rome: International Astronomical Union.

Fuhrmeister, B. et al. (Aug. 2008). "Multiwavelength observations of a giant flare on CN Leonis. I. The chromosphere as seen in the optical spectra". In: *A&A* 487.1, pp. 293–306. DOI: 10.1051/0004-6361:200809379.

Fuhrmeister, B. et al. (Oct. 2011). "Multi-wavelength observations of Proxima Centauri". In: *A&A* 534, A133, A133. DOI: 10.1051/0004-6361/201117447.

Fuhrmeister, B. et al. (July 2018). "The CARMENES search for exoplanets around M dwarfs. Wing asymmetries of Hα, Na I D, and He I lines". In: *A&A* 615, A14, A14. DOI: 10.1051/0004-6361/201732204.

Fuhrmeister, B. et al. (Mar. 2019). "The CARMENES search for exoplanets around M dwarfs. Period search in Hα, Na I D, and Ca II IRT lines". In: *A&A* 623, A24, A24. DOI: 10.1051/0004-6361/201834483.

Fuhrmeister, B. et al. (Aug. 2020). "The CARMENES search for exoplanets around M dwarfs. Variability of the He I line at 10 830 Å". In: *A&A* 640, A52, A52. DOI: 10.1051/0004-6361/202038279.

Fuhrmeister, B. et al. (Jan. 2022). "The CARMENES search for exoplanets around M dwarfs. Diagnostic capabilities of strong K I lines for photosphere and chromosphere". In: *A&A* 657, A125, A125. DOI: 10.1051/0004-6361/202141733.

Gaia Collaboration et al. (Aug. 2018a). "Gaia Data Release 2. Observational Hertzsprung-Russell diagrams". In: *A&A* 616, A10, A10. DOI: 10.1051/0004-6361/201832843.

Gaia Collaboration et al. (Aug. 2018b). "Gaia Data Release 2. Summary of the contents and survey properties". In: *A&A* 616, A1, A1. DOI: 10.1051/0004-6361/201833051.

Gaia Collaboration et al. (May 2021). "Gaia Early Data Release 3. The Gaia Catalogue of Nearby Stars". In: *A&A* 649, A6, A6. DOI: 10.1051/0004-6361/202039498.

García, Rafael A. et al. (June 2007). "Tracking Solar Gravity Modes: The Dynamics of the Solar Core". In: *Science* 316.5831, p. 1591. DOI: 10.1126/science.1140598.

Gardner, Jonathan P. et al. (Apr. 2006). "The James Webb Space Telescope". In: *Space Sci. Rev.* 123.4, pp. 485–606. DOI: 10.1007/s11214-006-8315-7.

Gershberg, R. E. (Nov. 1972). "Some results of the cooperative photometric observations of the UV Cet-type flare stars in the years 1967 71". In: *Ap&SS* 19.1, pp. 75–92. DOI: 10.1007/BF00643168.

Gershberg, R. E. and N. I. Shakhovskaia (Sept. 1983). "Characteristics of activity energetics of the UV cet-type flare stars". In: *Ap&SS* 95.2, pp. 235–253. DOI: 10.1007/BF00653631.

Gershberg, R. E. et al. (Nov. 1999). "Catalogue and bibliography of the UV Cet-type flare stars and related objects in the solar vicinity". In: *A&AS* 139, pp. 555–558. DOI: 10.1051/aas:1999407.

Gigoyan, K. S. et al. (Jan. 2010). "Late-type stars found in the DFBS". In: *Astrophysics* 53.1, pp. 123–132. DOI: 10.1007/s10511-010-9105-1.

Giles, Helen A. C., Andrew Collier Cameron, and Raphaëlle D. Haywood (Dec. 2017). "A Kepler study of starspot lifetimes with respect to light-curve amplitude and spectral type". In: *MNRAS* 472.2, pp. 1618–1627. DOI: 10.1093/mnras/stx1931.

Gillon, Michaël et al. (Feb. 2017). "Seven temperate terrestrial planets around the nearby ultracool dwarf star TRAPPIST-1". In: *Nature* 542.7642, pp. 456–460. DOI: 10.1038/nature21360.

Gizis, John E. et al. (Aug. 2000). "New Neighbors from 2MASS: Activity and Kinematics at the Bottom of the Main Sequence". In: *AJ* 120.2, pp. 1085–1099. DOI: 10.1086/301456.

Gliese, W. (1957). "Katalog der Sterne näher ALS 20 Parsek für 1950.0". In: *Astronomisches Rechen-Institut Heidelberg Mitteilungen Serie A* 8, p. 1.

Gordon, Iouli E., Laurence S. Rothman, and Geoffrey C. Toon (Sept. 2011). "Revision of spectral parameters for the B- and γ-bands of oxygen and their validation against atmospheric spectra". In: *J. Quant. Spectr. Rad. Transf.* 112, pp. 2310–2322. DOI: 10.1016/j.jqsrt.2011.05.007.

Gray, David F. (Nov. 1992). "The Inferred Color Index of the Sun". In: *PASP* 104, p. 1035. DOI: 10.1086/133086.

Güdel, M. et al. (Dec. 2002). "Flares and Coronal Heating in Active Stars - A Statistical Investigation". In: *Stellar Coronae in the Chandra and XMM-NEWTON Era*. Ed. by Fabio Favata and Jeremy J. Drake. Vol. 277. Astronomical Society of the Pacific Conference Series, p. 491.

Gullikson, Kevin, Sarah Dodson-Robinson, and Adam Kraus (Sept. 2014). "Correcting for Telluric Absorption: Methods, Case Studies, and Release of the TelFit Code". In: *AJ* 148.3, 53, p. 53. DOI: 10.1088/0004-6256/148/3/53.

Günther, Maximilian N. et al. (Feb. 2020). "Stellar Flares from the First TESS Data Release: Exploring a New Sample of M Dwarfs". In: *AJ* 159.2, 60, p. 60. DOI: 10.3847/1538-3881/ab5d3a.

Haghighipour, Nader et al. (May 2010). "The Lick-Carnegie Exoplanet Survey: A Saturn-Mass Planet in the Habitable Zone of the Nearby M4V Star HIP 57050". In: *ApJ* 715.1, pp. 271–276. DOI: 10.1088/0004-637X/715/1/271.

Hale, George E. (Nov. 1908). "On the Probable Existence of a Magnetic Field in Sun-Spots". In: *ApJ* 28, p. 315. DOI: 10.1086/141602.

— (June 1915). "The Direction of Rotation of Sun-Spot Vortices". In: *Proceedings of the National Academy of Science* 1.6, pp. 382–384. DOI: 10.1073/pnas.1.6.382.

— (Jan. 1924). "Sun-spots as Magnets and the Periodic Reversal of their Polarity". In: *Nature* 113.2829, pp. 105–112. DOI: 10.1038/113105a0.

Hale, George E. et al. (Apr. 1919). "The Magnetic Polarity of Sun-Spots". In: *ApJ* 49, p. 153. DOI: 10.1086/142452.

Hartmann, Lee W. and Robert W. Noyes (Jan. 1987). "Rotation and magnetic activity in main-sequence stars." In: *ARA&A* 25, pp. 271–301. DOI: 10.1146/annurev.aa.25.090187.001415.

Hathaway, David H. (Dec. 2010). "The Solar Cycle". In: *Living Reviews in Solar Physics* 7.1, 1, p. 1. DOI: 10.12942/lrsp-2010-1.

Hauchecorne, A. et al. (Mar. 2014). "Solar Radius Determination from Sodism/Picard and HMI/SDO Observations of the Decrease of the Spectral Solar Radiance during the 2012 June Venus Transit". In: *ApJ* 783.2, 127, p. 127. DOI: 10.1088/0004-637X/783/2/127.

Hawley, S. L., J. E. Gizis, and I. N. Reid (Dec. 1996). "The Palomar/MSU Nearby Star Spectroscopic Survey.II.The Southern M Dwarfs and Investigation of Magnetic Activity". In: *AJ* 112, p. 2799. DOI: 10.1086/118222.

Hawley, Suzanne L. et al. (Dec. 2014). "Kepler Flares. I. Active and Inactive M Dwarfs". In: *ApJ* 797.2, 121, p. 121. DOI: 10.1088/0004-637X/797/2/121.

Heise, J. et al. (Dec. 1975). "Evidence for X-ray emission from flare stars observed by ANS." In: *ApJ* 202, pp. L73–L76. DOI: 10.1086/181984.

Henry, G. W. et al. (Nov. 1999). "HD 209458". In: *IAU Circ.* 7307, p. 1.

Henry, Todd J. et al. (Dec. 2006). "The Solar Neighborhood. XVII. Parallax Results from the CTIOPI 0.9 m Program: 20 New Members of the RECONS 10 Parsec Sample". In: *AJ* 132.6, pp. 2360–2371. DOI: 10.1086/508233.

Henry, Todd J. et al. (June 2018). "The Solar Neighborhood XLIV: RECONS Discoveries within 10 parsecs". In: *AJ* 155.6, 265, p. 265. DOI: 10.3847/1538-3881/aac262.

Herrero, Enrique et al. (2016). "Modelling the photosphere of active stars for planet detection and characterization". In: *A&A* 586, A131, A131. DOI: 10.1051/0004-6361/201425369.

Hertzsprung, Ejnar (July 1905). "Zur Stralung Der Strerne". In: *Zeitschrift Fur Wissenschaftliche Photographie* 3, pp. 442–449.

Hetherington, Barry (1996). *A chronicle of pre-telescopic astronomy.*

Higgins, Michael E. and Keaton J. Bell (Apr. 2023). "Localizing Sources of Variability in Crowded TESS Photometry". In: *AJ* 165.4, 141, p. 141. DOI: 10.3847/1538-3881/acb20c.

Hintz, D. et al. (June 2020). "The CARMENES search for exoplanets around M dwarfs. The He I infrared triplet lines in PHOENIX models of M 2-3 V stars". In: *A&A* 638, A115, A115. DOI: 10.1051/0004-6361/202037596.

Hirayama, T. (Jan. 1978). "A Model of Solar Faculae and Their Lifetime". In: *PASJ* 30, pp. 337–352.

Hornsby, Thomas (Jan. 1771). "The Quantity of the Sun's Parallax, as Deduced from the Observations of the Transit of Venus, on June 3, 1769: By Thomas Hornsby, M. A. Savilian Professor of Astronomy in the University of Oxford, and F. R. S." In: *Philosophical Transactions of the Royal Society of London Series I* 61, pp. 574–579.

Houdebine, E. R., B. H. Foing, and M. Rodono (Nov. 1990). "Dynamics of flares on late-type dMe stars. I. Flare mass ejections and stellar evolution." In: *A&A* 238, p. 249.

Howard, Ward S. et al. (Aug. 2019). "EvryFlare. I. Long-term Evryscope Monitoring of Flares from the Cool Stars across Half the Southern Sky". In: *ApJ* 881.1, 9, p. 9. DOI: 10.3847/1538-4357/ab2767.

Hudson, H. S. (June 1991). "Solar flares, microflares, nanoflares, and coronal heating". In: *Sol. Phys.* 133.2, pp. 357–369. DOI: 10.1007/BF00149894.

Hunt-Walker, Nicholas M. et al. (June 2012). "MOST Observations of the Flare Star AD Leo". In: *PASP* 124.916, p. 545. DOI: 10.1086/666495.

Husser, T. O. et al. (May 2013). "A new extensive library of PHOENIX stellar atmospheres and synthetic spectra". In: *A&A* 553, A6, A6. DOI: 10.1051/0004-6361/201219058.

Iglewicz Boris; Hoaglin, David C. (1993). *How to detect and handle outliers.* ASQC basic references in quality control 16. ASQC Quality Press. ISBN: 9780873892476,087389247X.

Ilin, Ekaterina et al. (Feb. 2019). "Flares in open clusters with K2 . I. M 45 (Pleiades), M 44 (Praesepe), and M 67". In: *A&A* 622, A133, A133. DOI: 10.1051/0004-6361/201834400.

Irwin, Jonathan et al. (Feb. 2009). "The MEarth project: searching for transiting habitable super-Earths around nearby M dwarfs". In: *Transiting Planets.* Ed. by Frédéric Pont, Dimitar Sasselov, and Matthew J. Holman. Vol. 253, pp. 37–43. DOI: 10.1017/S1743921308026215.

Irwin, Jonathan et al. (Jan. 2011). "On the Angular Momentum Evolution of Fully Convective Stars: Rotation Periods for Field M-dwarfs from the MEarth Transit Survey". In: *ApJ* 727.1, 56, p. 56. DOI: 10.1088/0004-637X/727/1/56.

Irwin, Jonathan M. et al. (Jan. 2015). "The MEarth-North and MEarth-South Transit Surveys: Searching for Habitable Super-Earth Exoplanets Around Nearby M-dwarfs". In: *18th Cambridge Workshop on Cool Stars, Stellar Systems, and the Sun*. Vol. 18. Cambridge Workshop on Cool Stars, Stellar Systems, and the Sun, pp. 767–772.

Jackman, James A. G., Evgenya Shkolnik, and R. O. Parke Loyd (Apr. 2021). "Stellar flares from blended and neighbouring stars in Kepler short cadence observations". In: *MNRAS* 502.2, pp. 2033–2042. DOI: 10.1093/mnras/stab166.

Jackson, R. J. and R. D. Jeffries (May 2013). "On the relationship between the size and surface coverage of starspots on magnetically active low-mass stars". In: *MNRAS* 431.2, pp. 1883–1890. DOI: 10.1093/mnras/stt304.

Jeffers, S. V. et al. (June 2018). "CARMENES input catalogue of M dwarfs. III. Rotation and activity from high-resolution spectroscopic observations". In: *A&A* 614, A76, A76. DOI: 10.1051/0004-6361/201629599.

Jeffers, S. V. et al. (July 2022). "The CARMENES search for exoplanets around M dwarfs. Benchmarking the impact of activity in high-precision radial velocity measurements". In: *A&A* 663, A27, A27. DOI: 10.1051/0004-6361/202141880.

Jenkins, J. S. et al. (Oct. 2009). "Rotational Velocities for M Dwarfs". In: *ApJ* 704.2, pp. 975–988. DOI: 10.1088/0004-637X/704/2/975.

Jenkins, Jon M. et al. (Aug. 2016). "The TESS science processing operations center". In: *Software and Cyberinfrastructure for Astronomy IV*. Ed. by Gianluca Chiozzi and Juan C. Guzman. Vol. 9913. Society of Photo-Optical Instrumentation Engineers (SPIE) Conference Series, 99133E, 99133E. DOI: 10.1117/12.2233418.

Johnson, E. N. et al. (July 2021). "Simultaneous photometric and CARMENES spectroscopic monitoring of fast-rotating M dwarf GJ 3270. Discovery of a post-flare corotating feature". In: *A&A* 651, A105, A105. DOI: 10.1051/0004-6361/202040159.

Kane, Stephen R. et al. (Mar. 2016). "Stellar Activity and Exclusion of the Outer Planet in the HD 99492 System". In: *ApJ* 820.1, L5, p. L5. DOI: 10.3847/2041-8205/820/1/L5.

Kapteyn, J. C. (Jan. 1902). "On the Luminosity of the Fixed Stars". In: *Publications of the Kapteyn Astronomical Laboratory Groningen* 11, pp. 1–32.

Kausch, W. et al. (Apr. 2015). "Molecfit: A general tool for telluric absorption correction. II. Quantitative evaluation on ESO-VLT/X-Shooterspectra". In: *A&A* 576, A78, A78. DOI: 10.1051/0004-6361/201423909.

Kepler, J. (1619). *Harmonices Mundi libri v.*

King, Jeremy R. et al. (Apr. 2003). "Stellar Kinematic Groups. II. A Reexamination of the Membership, Activity, and Age of the Ursa Major Group". In: *AJ* 125.4, pp. 1980–2017. DOI: 10.1086/368241.

Kiraga, M. (Mar. 2012). "ASAS Photometry of ROSAT Sources. I. Periodic Variable Stars Coincident with Bright Sources from the ROSAT All Sky Survey". In: *Acta Astron.* 62.1, pp. 67–95.

Kirkpatrick, S., C. D. Gelatt, and M. P. Vecchi (May 1983). "Optimization by Simulated Annealing". In: *Science* 220.4598, pp. 671–680. DOI: 10.1126/science.220.4598.671.

Kjeldsen, H. and T. R. Bedding (Jan. 1995). "Amplitudes of stellar oscillations: the implications for asteroseismology." In: *A&A* 293, pp. 87–106.

Kliem, B. and T. Török (June 2006). "Torus Instability". In: *Phys. Rev. Lett.* 96.25, 255002, p. 255002. DOI: 10.1103/PhysRevLett.96.255002.

Kossakowski, D. et al. (Oct. 2022). "The CARMENES search for exoplanets around M dwarfs. Stable radial-velocity variations at the rotation period of AD Leonis: A test case study of current limitations to treating stellar activity". In: *A&A* 666, A143, A143. DOI: 10.1051/0004-6361/202243773.

Kraft, Robert P. (Nov. 1967). "Studies of Stellar Rotation. V. The Dependence of Rotation on Age among Solar-Type Stars". In: *ApJ* 150, p. 551. DOI: 10.1086/149359.

Kürster, M. et al. (June 2003). "The low-level radial velocity variability in Barnard's star (= GJ 699). Secular acceleration, indications for convective redshift, and planet mass limits". In: *A&A* 403, pp. 1077–1087. DOI: 10.1051/0004-6361:20030396.

Kurucz, Robert L. (2017). *ATLAS9: Model atmosphere program with opacity distribution functions*.

Lacy, C. H., T. J. Moffett, and D. S. Evans (Jan. 1976). "UV Ceti stars: statistical analysis of observational data." In: *ApJS* 30, pp. 85–96. DOI: 10.1086/190358.

Lafarga, M. et al. (Apr. 2020). "The CARMENES search for exoplanets around M dwarfs. Radial velocities and activity indicators from cross-correlation functions with weighted binary masks". In: *A&A* 636, A36, A36. DOI: 10.1051/0004-6361/201937222.

Lafarga, M. et al. (Aug. 2021). "The CARMENES search for exoplanets around M dwarfs. Mapping stellar activity indicators across the M dwarf domain". In: *A&A* 652, A28, A28. DOI: 10.1051/0004-6361/202140605.

Lagrange, A. M. et al. (Apr. 2011). "Using the Sun to estimate Earth-like planets detection capabilities . III. Impact of spots and plages on astrometric detection". In: *A&A* 528, L9, p. L9. DOI: 10.1051/0004-6361/201016354.

Lallement, R. et al. (Apr. 1993). "Correction of spectra for telluric absorption lines with the help of a molecular data bank and high resolution forward modelling: H,O lines around the sodium doublet at 589.5 NM". In: *A&A* 271, p. 734.

Lammer, Helmut et al. (Feb. 2007). "Coronal Mass Ejection (CME) Activity of Low Mass M Stars as An Important Factor for The Habitability of Terrestrial Exoplanets. II. CME-Induced Ion Pick Up of Earth-like Exoplanets in Close-In Habitable Zones". In: *Astrobiology* 7.1, pp. 185–207. DOI: 10.1089/ast.2006.0128.

Lang, Kenneth R. (1999). *Astrophysical formulae. space, time, matter, and cosmology*. 3rd enl. and rev. ed. Vol. Volume 2. Astronomy and astrophysics library. Springer. ISBN: 9783540646648,3540646647,354061267X. URL: http://gen.lib.rus.ec/book/index.php?md5=5acbcbe4db50de39436f39574bc758ed.

Lanza, A. F. et al. (Jan. 2009). "Magnetic activity in the photosphere of CoRoT-Exo-2a. Active longitudes and short-term spot cycle in a young Sun-like star". In: *A&A* 493.1, pp. 193–200. DOI: 10.1051/0004-6361:200810591.

Lanza, A. F. et al. (Sept. 2018). "The GAPS Programme with HARPS-N at TNG. XVII. Line profile indicators and kernel regression as diagnostics of radial-velocity variations due to stellar activity in solar-like stars". In: *A&A* 616, A155, A155. DOI: 10.1051/0004-6361/201731010.

Larmor Joseph, Sir (Dec. 1919). "How Could a Rotating Body Such as the Sun Become a Magnet?" In: *Report of the British Association for the Advancement of Science* , 87th Meeting, pp. 159–160. DOI: 10.4159/harvard.9780674366688.c20.

Leitzinger, M. et al. (Apr. 2020). "A census of coronal mass ejections on solar-like stars". In: *MNRAS* 493.3, pp. 4570–4589. DOI: 10.1093/mnras/staa504.

Lépine, Sébastien, R. Michael Rich, and Michael M. Shara (Mar. 2003). "Spectroscopy of New High Proper Motion Stars in the Northern Sky. I. New Nearby Stars, New High-Velocity Stars, and an Enhanced Classification Scheme for M Dwarfs". In: *AJ* 125.3, pp. 1598–1622. DOI: 10.1086/345972.

Lépine, Sébastien et al. (Apr. 2013). "A Spectroscopic Catalog of the Brightest (J < 9) M Dwarfs in the Northern Sky". In: *AJ* 145.4, 102, p. 102. DOI: 10.1088/0004-6256/145/4/102.

Litvinenko, Yuri E. and M. S. Wheatland (Feb. 2015). "Modeling Sunspot and Starspot Decay by Turbulent Erosion". In: *ApJ* 800.2, 130, p. 130. DOI: 10.1088/0004-637X/800/2/130.

— (Jan. 2017). "Sunspot and Starspot Lifetimes in a Turbulent Erosion Model". In: *ApJ* 834.2, 108, p. 108. DOI: 10.3847/1538-4357/834/2/108.

Lovis, C. et al. (July 2011). "The HARPS search for southern extra-solar planets. XXXI. Magnetic activity cycles in solar-type stars: statistics and impact on precise radial velocities". In: *arXiv e-prints*, arXiv:1107.5325, arXiv:1107.5325.

Maehara, Hiroyuki et al. (Feb. 2021). "Time-resolved spectroscopy and photometry of M dwarf flare star YZ Canis Minoris with OISTER and TESS: Blue asymmetry in the Hα line during the non-white light flare". In: *PASJ* 73.1, pp. 44–65. DOI: 10.1093/pasj/psaa098.

Maggio, A. et al. (Apr. 1987). "Einstein Observatory Survey of X-Ray Emission from Solar-Type Stars: The Late F and G Dwarf Stars". In: *ApJ* 315, p. 687. DOI: 10.1086/165170.

Maiolino, R., G. H. Rieke, and M. J. Rieke (Jan. 1996). "Correction of the Atmospheric Transmission in Infrared Spectroscopy". In: *AJ* 111, p. 537. DOI: 10.1086/117804.

Makarov, V. V. et al. (Dec. 2009). "Starspot Jitter in Photometry, Astrometry, and Radial Velocity Measurements". In: *ApJ* 707.1, pp. L73–L76. DOI: 10.1088/0004-637X/707/1/L73.

Mamajek, Eric E. and Cameron P. M. Bell (Dec. 2014). "On the age of the β Pictoris moving group". In: *MNRAS* 445.3, pp. 2169–2180. DOI: 10.1093/mnras/stu1894.

Marfil, E. et al. (Dec. 2021). "The CARMENES search for exoplanets around M dwarfs. Stellar atmospheric parameters of target stars with SteParSyn". In: *A&A* 656, A162, A162. DOI: 10.1051/0004-6361/202141980.

Mayor, M. and D. Queloz (Nov. 1995). "A Jupiter-mass companion to a solar-type star". In: *Nature* 378, pp. 355–359. DOI: 10.1038/378355a0.

McIntosh, Patrick S. (Sept. 1990). "The Classification of Sunspot Groups". In: *Sol. Phys.* 125.2, pp. 251–267. DOI: 10.1007/BF00158405.

Medina, Amber A. et al. (Dec. 2020). "Flare Rates, Rotation Periods, and Spectroscopic Activity Indicators of a Volume-complete Sample of Mid- to Late-M Dwarfs within 15 pc". In: *ApJ* 905.2, 107, p. 107. DOI: 10.3847/1538-4357/abc686.

Micela, G. et al. (May 1985). "Einstein X-ray survey of the Pleiades : the dependence of X-ray emission on stellar age." In: *ApJ* 292, pp. 172–180. DOI: 10.1086/163143.

Mohanty, Subhanjoy and Gibor Basri (Jan. 2003a). "Rotation and Activity in Mid-M to L Field Dwarfs". In: *ApJ* 583.1, pp. 451–472. DOI: 10.1086/345097.

— (Jan. 2003b). "Rotation and Activity in Mid-M to L Field Dwarfs". In: *ApJ* 583.1, pp. 451–472. DOI: 10.1086/345097.

Moore, Ronald L. et al. (May 2001). "Onset of the Magnetic Explosion in Solar Flares and Coronal Mass Ejections". In: *ApJ* 552.2, pp. 833–848. DOI: 10.1086/320559.

Morin, J. et al. (Oct. 2008). "Large-scale magnetic topologies of mid M dwarfs". In: *MNRAS* 390.2, pp. 567–581. DOI: 10.1111/j.1365-2966.2008.13809.x.

Morris, Robert L. et al. (Jan. 2017). *Kepler Data Processing Handbook: Photometric Analysis*. Kepler Science Document.

Mossman, J. E. (Mar. 1989). "A comprehensive search for sunspots without the aid of a telescope, 1981-1982". In: *QJRAS* 30, pp. 59–64.

Mullan, D. J. and H. P. Bais (Oct. 2018). "Photosynthesis on a Planet Orbiting an M Dwarf: Enhanced Effectiveness during Flares". In: *ApJ* 865.2, 101, p. 101. DOI: 10.3847/1538-4357/aadfd1.

Muslimov, Eduard et al. (Mar. 2023). "Optical Design of a Slitless Astronomical Spectrograph with a Composite Holographic Grism". In: *Photonics for Solar Energy Systems IX* 10.4, p. 385. DOI: 10.3390/photonics10040385.

Nagel, Evangelos (Jan. 2019). "High precision optical and near-infrared velocimetry with CARMENES". PhD thesis. University of Hamburg, Germany.

Nakajima, Tadashi and Jun-Ichi Morino (Jan. 2012). "Potential Members of Stellar Kinematic Groups within 30 pc of the Sun". In: *AJ* 143.1, 2, p. 2. DOI: 10.1088/0004-6256/143/1/2.

Newton, Elisabeth R. et al. (Jan. 2014). "Near-infrared Metallicities, Radial Velocities, and Spectral Types for 447 Nearby M Dwarfs". In: *AJ* 147.1, 20, p. 20. DOI: 10.1088/0004-6256/147/1/20.

Newton, Elisabeth R. et al. (Jan. 2017). "The Hα Emission of Nearby M Dwarfs and its Relation to Stellar Rotation". In: *ApJ* 834.1, 85, p. 85. DOI: 10.3847/1538-4357/834/1/85.

Norton, A. J. et al. (May 2007). "New periodic variable stars coincident with ROSAT sources discovered using SuperWASP". In: *A&A* 467.2, pp. 785–905. DOI: 10.1051/0004-6361:20077084.

Noyes, R. W. et al. (Apr. 1984). "Rotation, convection, and magnetic activity in lower main-sequence stars." In: *ApJ* 279, pp. 763–777. DOI: 10.1086/161945.

Nutzman, Philip and David Charbonneau (Mar. 2008). "Design Considerations for a Ground-Based Transit Search for Habitable Planets Orbiting M Dwarfs". In: *PASP* 120.865, p. 317. DOI: 10.1086/533420.

Olah, K. et al. (July 1989). "Long-lived active longitudes on the spotted RS CVn star sigma Geminorum." In: *A&A* 218, pp. 192–194.

O'Neal, Douglas et al. (Oct. 2004). "Further Results of TiO-Band Observations of Starspots". In: *AJ* 128.4, pp. 1802–1811. DOI: 10.1086/423438.

Osten, Rachel A. et al. (Dec. 2016). "A Very Bright, Very Hot, and Very Long Flaring Event from the M Dwarf Binary System DG CVn". In: *ApJ* 832.2, 174, p. 174. DOI: 10.3847/0004-637X/832/2/174.

Parenti, Susanna (Mar. 2014). "Solar Prominences: Observations". In: *Living Reviews in Solar Physics* 11.1, 1, p. 1. DOI: 10.12942/lrsp-2014-1.

Parker, E. N. (May 1975). "The generation of magnetic fields in astrophysical bodies. X. Magnetic buoyancy and the solar dynamo." In: *ApJ* 198, pp. 205–209. DOI: 10.1086/153593.

Parker, Eugene N. (Sept. 1955a). "Hydromagnetic Dynamo Models." In: *ApJ* 122, p. 293. DOI: 10.1086/146087.

— (Mar. 1955b). "The Formation of Sunspots from the Solar Toroidal Field." In: *ApJ* 121, p. 491. DOI: 10.1086/146010.

Passegger, V. M. et al. (July 2019). "The CARMENES search for exoplanets around M dwarfs. Photospheric parameters of target stars from high-resolution spectroscopy. II. Simultaneous multiwavelength range modeling of activity insensitive lines". In: *A&A* 627, A161, A161. DOI: 10.1051/0004-6361/201935679.

Pepe, Francesco A. et al. (July 2010). "ESPRESSO: the Echelle spectrograph for rocky exoplanets and stable spectroscopic observations". In: *Ground-based and Airborne Instrumentation for Astronomy III*. Ed. by Ian S. McLean, Suzanne K. Ramsay, and Hideki Takami. Vol. 7735. Society of Photo-Optical Instrumentation Engineers (SPIE) Conference Series, 77350F, 77350F. DOI: 10.1117/12.857122.

Perger, M. et al. (Apr. 2019). "Gliese 49: activity evolution and detection of a super-Earth. A HADES and CARMENES collaboration". In: *A&A* 624, A123, A123. DOI: 10.1051/0004-6361/201935192.

Perryman, Michael (2018). *The Exoplanet Handbook, 2nd Edition*. 2nd ed. Cambridge University Press. ISBN: 9781108419772. URL: http://gen.lib.rus.ec/book/index.php?md5=4e2c538aeb60b60e0a28bb093c2ea3bc.

Pickering, Edward C. (Jan. 1890). "The Draper Catalogue of stellar spectra photographed with the 8-inch Bache telescope as a part of the Henry Draper memorial". In: *Annals of Harvard College Observatory* 27, pp. 1–388.

Pickering, Edward C. and M. Fleming (Jan. 1897). "Miscellaneous investigations of the Henry Draper Memorial". In: *Annals of Harvard College Observatory* 26, 193–P.XI.2.

Pipin, V. V. and N. Yokoi (May 2018). "Generation of a Large-scale Magnetic Field in a Convective Full-sphere Cross-helicity Dynamo". In: *ApJ* 859.1, 18, p. 18. DOI: 10.3847/1538-4357/aabae6.

Pizzolato, N. et al. (Jan. 2003). "The stellar activity-rotation relationship revisited: Dependence of saturated and non-saturated X-ray emission regimes on stellar mass for late-type dwarfs". In: *A&A* 397, pp. 147–157. DOI: 10.1051/0004-6361:20021560.

Pogson, Norman (Nov. 1856). "Magnitudes of Thirty-six of the Minor Planets for the first day of each month of the year 1857". In: *MNRAS* 17, pp. 12–15. DOI: 10.1093/mnras/17.1.12.

Pollacco, D. L. et al. (Oct. 2006). "The WASP Project and the SuperWASP Cameras". In: *PASP* 118.848, pp. 1407–1418. DOI: 10.1086/508556.

Prša, Andrej et al. (Aug. 2016). "Nominal Values for Selected Solar and Planetary Quantities: IAU 2015 Resolution B3". In: *AJ* 152.2, 41, p. 41. DOI: 10.3847/0004-6256/152/2/41.

Queloz, D. et al. (Nov. 2001). "No planet for HD 166435". In: *A&A* 379, pp. 279–287. DOI: 10.1051/0004-6361:20011308.

Quintana, Elisa V. et al. (Apr. 2014). "An Earth-Sized Planet in the Habitable Zone of a Cool Star". In: *Science* 344.6181, pp. 277–280. DOI: 10.1126/science.1249403.

Quirrenbach, A. et al. (July 2014). "CARMENES instrument overview". In: *Ground-based and Airborne Instrumentation for Astronomy V*. Ed. by Suzanne K. Ramsay, Ian S. McLean, and Hideki Takami. Vol. 9147. Society of Photo-Optical Instrumentation Engineers (SPIE) Conference Series, 91471F, 91471F. DOI: 10.1117/12.2056453.

Quirrenbach, A. et al. (Aug. 2016). "CARMENES: an overview six months after first light". In: *Ground-based and Airborne Instrumentation for Astronomy VI*. Ed. by Christopher J. Evans, Luc Simard, and Hideki Takami. Vol. 9908. Society of Photo-Optical Instrumentation Engineers (SPIE) Conference Series, 990812, p. 990812. DOI: 10.1117/12.2231880.

Quirrenbach, A. et al. (July 2018). "CARMENES: high-resolution spectra and precise radial velocities in the red and infrared". In: *Ground-based and Airborne Instrumentation for Astronomy VII*. Ed. by Christopher J. Evans, Luc Simard, and Hideki Takami. Vol. 10702. Society of Photo-Optical Instrumentation Engineers (SPIE) Conference Series, 107020W, 107020W. DOI: 10.1117/12.2313689.

Quirrenbach, Andreas et al. (Dec. 2020). "The CARMENES M-dwarf planet survey". In: *Society of Photo-Optical Instrumentation Engineers (SPIE) Conference Series*. Vol. 11447. Society of Photo-Optical Instrumentation Engineers (SPIE) Conference Series, 114473C, p. 114473C. DOI: 10.1117/12.2561380.

Ramsay, Gavin et al. (Sept. 2013). "Short-duration high-amplitude flares detected on the M dwarf star KIC 5474065". In: *MNRAS* 434.3, pp. 2451–2457. DOI: 10.1093/mnras/stt1182.

Randich, S. (Jan. 2000). "Coronal activity among open cluster stars". In: *Stellar Clusters and Associations: Convection, Rotation, and Dynamos*. Ed. by R. Pallavicini, G. Micela, and S. Sciortino. Vol. 198. Astronomical Society of the Pacific Conference Series, p. 401.

Ranjan, Sukrit, Robin Wordsworth, and Dimitar D. Sasselov (July 2017). "The Surface UV Environment on Planets Orbiting M Dwarfs: Implications for Prebiotic Chemistry and the Need for Experimental Follow-up". In: *ApJ* 843.2, 110, p. 110. DOI: 10.3847/1538-4357/aa773e.

Raymond, Sean N. (2011). "Nice Model". In: *Encyclopedia of Astrobiology*. Ed. by Muriel Gargaud et al. Berlin, Heidelberg: Springer Berlin Heidelberg, pp. 1116–1117. ISBN: 978-3-642-11274-4. DOI: 10.1007/978-3-642-11274-4_1058. URL: https://doi.org/10.1007/978-3-642-11274-4_1058.

Reiners, A. (May 2007). "The narrowest M-dwarf line profiles and the rotation-activity connection at very slow rotation". In: *A&A* 467.1, pp. 259–268. DOI: 10.1051/0004-6361:20066991.

— (May 2009). "Activity-induced radial velocity jitter in a flaring M dwarf". In: *A&A* 498.3, pp. 853–861. DOI: 10.1051/0004-6361/200810257.

Reiners, A. and G. Basri (Feb. 2007). "The First Direct Measurements of Surface Magnetic Fields on Very Low Mass Stars". In: *ApJ* 656.2, pp. 1121–1135. DOI: 10.1086/510304.

Reiners, A. et al. (Feb. 2010). "Detecting Planets Around Very Low Mass Stars with the Radial Velocity Method". In: *ApJ* 710.1, pp. 432–443. DOI: 10.1088/0004-637X/710/1/432.

Reiners, A. et al. (Apr. 2013). "Radial velocity signatures of Zeeman broadening". In: *A&A* 552, A103, A103. DOI: 10.1051/0004-6361/201220437.

Reiners, A. et al. (Apr. 2018). "The CARMENES search for exoplanets around M dwarfs. High-resolution optical and near-infrared spectroscopy of 324 survey stars". In: *A&A* 612, A49, A49. DOI: 10.1051/0004-6361/201732054.

Reiners, A. et al. (June 2022). "Magnetism, rotation, and nonthermal emission in cool stars. Average magnetic field measurements in 292 M dwarfs". In: *A&A* 662, A41, A41. DOI: 10.1051/0004-6361/202243251.

Reiners, Ansgar and Subhanjoy Mohanty (Feb. 2012). "Radius-dependent Angular Momentum Evolution in Low-mass Stars. I". In: *ApJ* 746.1, 43, p. 43. DOI: 10.1088/0004-637X/746/1/43.

Riaz, Basmah, John E. Gizis, and James Harvin (Aug. 2006). "Identification of New M Dwarfs in the Solar Neighborhood". In: *AJ* 132.2, pp. 866–872. DOI: 10.1086/505632.

Ricker, George R. et al. (Jan. 2015). "Transiting Exoplanet Survey Satellite (TESS)". In: *Journal of Astronomical Telescopes, Instruments, and Systems* 1, 014003, p. 014003. DOI: 10.1117/1.JATIS.1.1.014003.

Rimmer, Paul B. et al. (Aug. 2018). "The origin of RNA precursors on exoplanets". In: *Science Advances* 4.8, eaar3302. DOI: 10.1126/sciadv.aar3302.

Robertson, P., A. Roy, and S. Mahadevan (June 2015). "Stellar Activity Mimics a Habitable-zone Planet around Kapteyn's Star". In: *ApJ* 805, L22, p. L22. DOI: 10.1088/2041-8205/805/2/L22.

Robertson, P. et al. (July 2014). "Stellar activity masquerading as planets in the habitable zone of the M dwarf Gliese 581". In: *Science* 345, pp. 440–444. DOI: 10.1126/science.1253253.

Roettenbacher, Rachael M. and Krisztián Vida (Nov. 2018). "The Connection between Starspots and Flares on Main-sequence Kepler Stars". In: *ApJ* 868.1, 3, p. 3. DOI: 10.3847/1538-4357/aae77e.

Rosich, A. et al. (Sept. 2020). "Correcting for chromatic stellar activity effects in transits with multiband photometric monitoring: application to WASP-52". In: *A&A* 641, A82, A82. DOI: 10.1051/0004-6361/202037586.

Rothman, L. S. et al. (June 2009). "The HITRAN 2008 molecular spectroscopic database". In: *J. Quant. Spectr. Rad. Transf.* 110.9-10, pp. 533–572. DOI: 10.1016/j.jqsrt.2009.02.013.

Rudolf, N. et al. (Jan. 2016). "Modelling telluric line spectra in the optical and infrared with an application to VLT/X-Shooter spectra". In: *A&A* 585, A113, A113. DOI: 10.1051/0004-6361/201322749.

Rudolf Kippenhahn Alfred Weigert, Achim Weiss (auth.) (2012). *Stellar Structure and Evolution*. 2nd ed. Astronomy and Astrophysics Library. Springer-Verlag Berlin Heidelberg. ISBN: 978-3-642-30255-8,978-3-642-30304-3. URL: http://gen.lib.rus.ec/book/index.php?md5=69d1b45363580880b15aacdff0ca6f63.

Russell, Henry Norris (May 1914). "Relations Between the Spectra and Other Characteristics of the Stars". In: *Popular Astronomy* 22, pp. 275–294.

Saar, Steven H., R. Paul Butler, and Geoffrey W. Marcy (May 1998). "Magnetic Activity-related Radial Velocity Variations in Cool Stars: First Results from the Lick Extrasolar Planet Survey". In: *ApJ* 498.2, pp. L153–L157. DOI: 10.1086/311325.

Salpeter, E. E. (Nov. 1952). "Nuclear Reactions in the Stars. I. Proton-Proton Chain". In: *Physical Review* 88.3, pp. 547–553. DOI: 10.1103/PhysRev.88.547.

Sarkis, P. et al. (June 2018). "The CARMENES Search for Exoplanets around M Dwarfs: A Low-mass Planet in the Temperate Zone of the Nearby K2-18". In: *AJ* 155, 257, p. 257. DOI: 10.3847/1538-3881/aac108.

Schöfer, P. et al. (Mar. 2019). "The CARMENES search for exoplanets around M dwarfs. Activity indicators at visible and near-infrared wavelengths". In: *A&A* 623, A44, A44. DOI: 10.1051/0004-6361/201834114.

Schou, J. et al. (Nov. 1997). "Determination of the Sun's Seismic Radius from the SOHO Michelson Doppler Imager". In: *ApJ* 489, p. L197. DOI: 10.1086/316782.

Schou, J. et al. (Sept. 1998). "Helioseismic Studies of Differential Rotation in the Solar Envelope by the Solar Oscillations Investigation Using the Michelson Doppler Imager". In: *ApJ* 505.1, pp. 390–417. DOI: 10.1086/306146.

Schrijver, C. J. (July 2002). "Solar spots as prototypes for stellar spots". In: *Astronomische Nachrichten* 323, pp. 157–164. DOI: 10.1002/1521-3994(200208)323:3/4<157::AID-ASNA157>3.0.CO;2-Q.

Schrijver, Carolus J. and George L. Siscoe (2011). *Heliophysics: Plasma Physics of the Local Cosmos*.

Schwarz, Gideon (July 1978). "Estimating the Dimension of a Model". In: *Annals of Statistics* 6.2, pp. 461–464.

Schweitzer, A. et al. (May 2019). "The CARMENES search for exoplanets around M dwarfs. Different roads to radii and masses of the target stars". In: *A&A* 625, A68, A68. DOI: 10.1051/0004-6361/201834965.

Scoggins, Matthew T., James. R. A. Davenport, and Kevin R. Covey (Sept. 2019). "Using Flare Rates to Search for Stellar Activity Cycles". In: *Research Notes of the American Astronomical Society* 3.9, 137, p. 137. DOI: 10.3847/2515-5172/ab45a0.

Secchi, Angelo (1868). *Sugli spettri prismatici delle stelle fisse*.

— (1875). *Le Soleil*. DOI: 10.3931/e-rara-14748.

Seehafer, N. (Jan. 1996). "Nature of the α effect in magnetohydrodynamics". In: *Phys. Rev. E* 53.1, pp. 1283–1286. DOI: 10.1103/PhysRevE.53.1283.

Segura, Antígona et al. (Sept. 2010). "The Effect of a Strong Stellar Flare on the Atmospheric Chemistry of an Earth-like Planet Orbiting an M Dwarf". In: *Astrobiology* 10.7, pp. 751–771. DOI: 10.1089/ast.2009.0376.

Seifahrt, A. et al. (Dec. 2010). "Synthesising, using, and correcting for telluric features in high-resolution astronomical spectra . A near-infrared case study using CRIRES". In: *A&A* 524, A11, A11. DOI: 10.1051/0004-6361/200913782.

Shibata, Kazunari and Tetsuya Magara (Dec. 2011). "Solar Flares: Magnetohydrodynamic Processes". In: *Living Reviews in Solar Physics* 8.1, 6, p. 6. DOI: 10.12942/lrsp-2011-6.

Shibayama, Takuya et al. (Nov. 2013). "Superflares on Solar-type Stars Observed with Kepler. I. Statistical Properties of Superflares". In: *ApJS* 209.1, 5, p. 5. DOI: 10.1088/0067-0049/209/1/5.

Shkolnik, Evgenya, Michael C. Liu, and I. Neill Reid (July 2009). "Identifying the Young Low-mass Stars within 25 pc. I. Spectroscopic Observations". In: *ApJ* 699.1, pp. 649–666. DOI: 10.1088/0004-637X/699/1/649.

Shulyak, D. et al. (June 2019). "Magnetic fields in M dwarfs from the CARMENES survey". In: *A&A* 626, A86, A86. DOI: 10.1051/0004-6361/201935315.

Silverberg, Steven M. et al. (Oct. 2016). "Kepler Flares. IV. A Comprehensive Analysis of the Activity of the dM4e Star GJ 1243". In: *ApJ* 829.2, 129, p. 129. DOI: 10.3847/0004-637X/829/2/129.

Simola, U., X. Dumusque, and J. Cisewski-Kehe (Feb. 2019). "Measuring precise radial velocities and cross-correlation function line-profile variations using a Skew Normal density". In: *A&A* 622, A131, A131. DOI: 10.1051/0004-6361/201833895.

Simon, G. W. and R. B. Leighton (Oct. 1964). "Velocity Fields in the Solar Atmosphere. III. Large-Scale Motions, the Chromospheric Network, and Magnetic Fields." In: *ApJ* 140, p. 1120. DOI: 10.1086/148010.

Skrutskie, M. F. et al. (Feb. 2006). "The Two Micron All Sky Survey (2MASS)". In: *AJ* 131.2, pp. 1163–1183. DOI: 10.1086/498708.

Skumanich, A. (Feb. 1972). "Time Scales for Ca II Emission Decay, Rotational Braking, and Lithium Depletion". In: *ApJ* 171, p. 565. DOI: 10.1086/151310.

Smette, A. et al. (Apr. 2015). "Molecfit: A general tool for telluric absorption correction. I. Method and application to ESO instruments". In: *A&A* 576, A77, A77. DOI: 10.1051/0004-6361/201423932.

Smith, Jeffrey C. et al. (Sept. 2012). "Kepler Presearch Data Conditioning II - A Bayesian Approach to Systematic Error Correction". In: *PASP* 124.919, p. 1000. DOI: 10.1086/667697.

Soderblom, David R. (Sept. 2010). "The Ages of Stars". In: *ARA&A* 48, pp. 581–629. DOI: 10.1146/annurev-astro-081309-130806.

Solanki, Sami K. (Jan. 2003). "Sunspots: An overview". In: *A&A Rev.* 11.2-3, pp. 153–286. DOI: 10.1007/s00159-003-0018-4.

Spiegel, E. A. and J. P. Zahn (Nov. 1992). "The solar tachocline." In: *A&A* 265, pp. 106–114.

Spörer, F. W. Gustav (Oct. 1879). "Beobachtung der Sonnenflecken etc." In: *Astronomische Nachrichten* 96.2, p. 23. DOI: 10.1002/asna.18790960205.

Spruit, H. C. (Nov. 1976). "Pressure equilibrium and energy balance of small photospheric fluxtubes." In: *Sol. Phys.* 50.2, pp. 269–295. DOI: 10.1007/BF00155292.

Stassun, Keivan G. et al. (2018). "The TESS Input Catalog and Candidate Target List". In: *AJ* 156.3, 102, p. 102. DOI: 10.3847/1538-3881/aad050.

Stelzer, B. et al. (Dec. 2016). "A path towards understanding the rotation-activity relation of M dwarfs with K2 mission, X-ray and UV data". In: *MNRAS* 463.2, pp. 1844–1864. DOI: 10.1093/mnras/stw1936.

Stephenson, F. R. (Apr. 1990). "Historical Evidence concerning the Sun: Interpretation of Sunspot Records during the Telescopic and Pretelescopic Eras". In: *Philosophical Transactions of the Royal Society of London Series A* 330.1615, pp. 499–512. DOI: 10.1098/rsta.1990.0031.

Stepien, K. (Dec. 1994). "Applicability of the Rossby number in activity-rotation relations for dwarfs and giants." In: *A&A* 292, pp. 191–207.

Stock, S. et al. (Apr. 2020). "The CARMENES search for exoplanets around M dwarfs. Characterization of the nearby ultra-compact multiplanetary system YZ Ceti". In: *A&A* 636, A119, A119. DOI: 10.1051/0004-6361/201936732.

Strassmeier, Klaus G. (Sept. 2009). "Starspots". In: *A&A Rev.* 17.3, pp. 251–308. DOI: 10.1007/s00159-009-0020-6.

Stumpe, Martin C. et al. (Sept. 2012). "Kepler Presearch Data Conditioning I—Architecture and Algorithms for Error Correction in Kepler Light Curves". In: *PASP* 124.919, p. 985. DOI: 10.1086/667698.

Stumpe, Martin C. et al. (Jan. 2014). "Multiscale Systematic Error Correction via Wavelet-Based Bandsplitting in Kepler Data". In: *PASP* 126.935, p. 100. DOI: 10.1086/674989.

Tal-Or, L. et al. (June 2018). "The CARMENES search for exoplanets around M dwarfs. Radial-velocity variations of active stars in visual-channel spectra". In: *A&A* 614, A122, A122. DOI: 10.1051/0004-6361/201732362.

Tal-Or, Lev et al. (Mar. 2019). "Correcting HIRES/Keck radial velocities for small systematic errors". In: *MNRAS* 484.1, pp. L8–L13. DOI: 10.1093/mnrasl/sly227.

Thomas, John H. and Nigel O. Weiss (2008). *Sunspots and Starspots*.

Thompson, A. P. G. et al. (June 2017). "The changing face of α Centauri B: probing plage and stellar activity in K dwarfs". In: *MNRAS* 468.1, pp. L16–L20. DOI: 10.1093/mnrasl/slx018.

Toledo-Padrón, B. et al. (Oct. 2019). "Stellar activity analysis of Barnard's Star: very slow rotation and evidence for long-term activity cycle". In: *MNRAS* 488.4, pp. 5145–5161. DOI: 10.1093/mnras/stz1975.

Török, T. and B. Kliem (Sept. 2005). "Confined and Ejective Eruptions of Kink-unstable Flux Ropes". In: *ApJ* 630.1, pp. L97–L100. DOI: 10.1086/462412.

Torres, Guillermo et al. (Feb. 2015). "Validation of 12 Small Kepler Transiting Planets in the Habitable Zone". In: *ApJ* 800.2, 99, p. 99. DOI: 10.1088/0004-637X/800/2/99.

Trifonov, T. et al. (Feb. 2018). "The CARMENES search for exoplanets around M dwarfs . First visual-channel radial-velocity measurements and orbital parameter updates of seven M-dwarf planetary systems". In: *A&A* 609, A117, A117. DOI: 10.1051/0004-6361/201731442.

Tu, Zuo-Lin et al. (Feb. 2020). "Superflares on Solar-type Stars from the First Year Observation of TESS". In: *ApJ* 890.1, 46, p. 46. DOI: 10.3847/1538-4357/ab6606.

Tuomi, Mikko et al. (May 2018). "AD Leonis: Radial Velocity Signal of Stellar Rotation or Spin-Orbit Resonance?" In: *AJ* 155.5, 192, p. 192. DOI: 10.3847/1538-3881/aab09c.

Twicken, Joseph D. et al. (2010). "Photometric analysis in the Kepler Science Operations Center pipeline". In: *Proc. SPIE*. Vol. 7740. Society of Photo-Optical Instrumentation Engineers (SPIE) Conference Series, 774023, p. 774023. DOI: 10.1117/12.856790.

Vacca, William D., Michael C. Cushing, and John T. Rayner (Mar. 2003). "A Method of Correcting Near-Infrared Spectra for Telluric Absorption". In: *PASP* 115.805, pp. 389–409. DOI: 10.1086/346193.

Valenti, Jeff A., Nikolai Piskunov, and Christopher M. Johns-Krull (May 1998). "Spectral Synthesis of TiO Lines". In: *ApJ* 498.2, pp. 851–862. DOI: 10.1086/305587.

Van Doorsselaere, Tom, Hoda Shariati, and Jonas Debosscher (Oct. 2017). "Stellar Flares Observed in Long-cadence Data from the Kepler Mission". In: *ApJS* 232.2, 26, p. 26. DOI: 10.3847/1538-4365/aa8f9a.

Vaughan, A. H., G. W. Preston, and O. C. Wilson (June 1978). "Flux measurements of Ca II and K emission." In: *PASP* 90, pp. 267–274. DOI: 10.1086/130324.

Venot, Olivia et al. (Oct. 2016). "Influence of Stellar Flares on the Chemical Composition of Exoplanets and Spectra". In: *ApJ* 830.2, 77, p. 77. DOI: 10.3847/0004-637X/830/2/77.

Vernazza, J. E., E. H. Avrett, and R. Loeser (Apr. 1981). "Structure of the solar chromosphere. III. Models of the EUV brightness components of the quiet sun." In: *ApJS* 45, pp. 635–725. DOI: 10.1086/190731.

Vida, K. et al. (May 2016). "Investigating magnetic activity in very stable stellar magnetic fields. Long-term photometric and spectroscopic study of the fully convective M4 dwarf V374 Pegasi". In: *A&A* 590, A11, A11. DOI: 10.1051/0004-6361/201527925.

Vida, K. et al. (June 2017). "Frequent Flaring in the TRAPPIST-1 System—Unsuited for Life?" In: *ApJ* 841.2, 124, p. 124. DOI: 10.3847/1538-4357/aa6f05.

Vida, Krisztián et al. (Oct. 2019a). "Flaring Activity of Proxima Centauri from TESS Observations: Quasiperiodic Oscillations during Flare Decay and Inferences on the Habitability of Proxima b". In: *ApJ* 884.2, 160, p. 160. DOI: 10.3847/1538-4357/ab41f5.

Vida, Krisztián et al. (Mar. 2019b). "The quest for stellar coronal mass ejections in late-type stars. I. Investigating Balmer-line asymmetries of single stars in Virtual Observatory data". In: *A&A* 623, A49, A49. DOI: 10.1051/0004-6361/201834264.

Vilhu, Osmi and Frederick M. Walter (Oct. 1987). "Chromospheric-Coronal Activity at Saturated Levels". In: *ApJ* 321, p. 958. DOI: 10.1086/165689.

Voges, W. et al. (Sept. 1999). "The ROSAT all-sky survey bright source catalogue". In: *A&A* 349, pp. 389–405. DOI: 10.48550/arXiv.astro-ph/9909315.

Walkowicz, Lucianne M. et al. (Feb. 2011). "White-light Flares on Cool Stars in the Kepler Quarter 1 Data". In: *AJ* 141.2, 50, p. 50. DOI: 10.1088/0004-6256/141/2/50.

Wallerstein, George and Peter S. Conti (Jan. 1969). "Lithium and Beryllium in Stars". In: *ARA&A* 7, p. 99. DOI: 10.1146/annurev.aa.07.090169.000531.

West, Andrew A. et al. (July 2004). "Spectroscopic Properties of Cool Stars in the Sloan Digital Sky Survey: An Analysis of Magnetic Activity and a Search for Subdwarfs". In: *AJ* 128.1, pp. 426–436. DOI: 10.1086/421364.

West, Andrew A. et al. (Mar. 2008). "Constraining the Age-Activity Relation for Cool Stars: The Sloan Digital Sky Survey Data Release 5 Low-Mass Star Spectroscopic Sample". In: *AJ* 135.3, pp. 785–795. DOI: 10.1088/0004-6256/135/3/785.

Widemann, T. et al. (Feb. 1994). "High-resolution spectroscopy of cool K and M stars through the telluric water vapor absorption band near 9360 A." In: *A&A* 282, pp. 879–889.

Wilson, O. C. (May 1966). "Stellar Convection Zones, Chromospheres, and Rotation". In: *ApJ* 144, p. 695. DOI: 10.1086/148649.

— (July 1968). "Flux Measurements at the Centers of Stellar H- and K-Lines". In: *ApJ* 153, p. 221. DOI: 10.1086/149652.

Winn, J. N. (2010). "Exoplanet Transits and Occultations". In: *Exoplanets*. Ed. by S. Seager, pp. 55–77.

Winters, Jennifer G. et al. (Jan. 2015). "The Solar Neighborhood. XXXV. Distances to 1404 m Dwarf Systems Within 25 pc in the Southern Sky". In: *AJ* 149.1, 5, p. 5. DOI: 10.1088/0004-6256/149/1/5.

Wise, A. W. et al. (Oct. 2018). "New Methods for Finding Activity-sensitive Spectral Lines: Combined Visual Identification and an Automated Pipeline Find a Set of 40 Activity Indicators". In: *AJ* 156.4, 180, p. 180. DOI: 10.3847/1538-3881/aadd94.

Wolszczan, A. and D. A. Frail (Jan. 1992). "A planetary system around the millisecond pulsar PSR1257 + 12". In: *Nature* 355.6356, pp. 145–147. DOI: 10.1038/355145a0.

Wright, J. T. and J. D. Eastman (Sept. 2014). "Barycentric Corrections at 1 cm s^{-1} for Precise Doppler Velocities". In: *PASP* 126.943, p. 838. DOI: 10.1086/678541.

Wright, J. T. et al. (June 2004). "Chromospheric Ca II Emission in Nearby F, G, K, and M Stars". In: *ApJS* 152.2, pp. 261–295. DOI: 10.1086/386283.

Wright, Nicholas J. and Jeremy J. Drake (July 2016). "Solar-type dynamo behaviour in fully convective stars without a tachocline". In: *Nature* 535.7613, pp. 526–528. DOI: 10.1038/nature18638.

Wright, Nicholas J. et al. (Dec. 2011). "The Stellar-activity-Rotation Relationship and the Evolution of Stellar Dynamos". In: *ApJ* 743.1, 48, p. 48. DOI: 10.1088/0004-637X/743/1/48.

Wright, Nicholas J. et al. (Sept. 2018). "The stellar rotation-activity relationship in fully convective M dwarfs". In: *MNRAS* 479.2, pp. 2351–2360. DOI: 10.1093/mnras/sty1670.

Yashiro, S. et al. (Oct. 2006). "Different Power-Law Indices in the Frequency Distributions of Flares with and without Coronal Mass Ejections". In: *ApJ* 650.2, pp. L143–L146. DOI: 10.1086/508876.

Zechmeister, M., G. Anglada-Escudé, and A. Reiners (Jan. 2014). "Flat-relative optimal extraction. A quick and efficient algorithm for stabilised spectrographs". In: *A&A* 561, A59, A59. DOI: 10.1051/0004-6361/201322746.

Zechmeister, M. and M. Kürster (Mar. 2009). "The generalised Lomb-Scargle periodogram. A new formalism for the floating-mean and Keplerian periodograms". In: *A&A* 496.2, pp. 577–584. DOI: 10.1051/0004-6361:200811296.

Zechmeister, M., M. Kürster, and M. Endl (Oct. 2009). "The M dwarf planet search programme at the ESO VLT + UVES. A search for terrestrial planets in the habitable zone of M dwarfs". In: *A&A* 505.2, pp. 859–871. DOI: 10.1051/0004-6361/200912479.

Zechmeister, M. et al. (Jan. 2018). "Spectrum radial velocity analyser (SERVAL). High-precision radial velocities and two alternative spectral indicators". In: *A&A* 609, A12, A12. DOI: 10.1051/0004-6361/201731483.

Zechmeister, M. et al. (July 2019). "The CARMENES search for exoplanets around M dwarfs. Two temperate Earth-mass planet candidates around Teegarden's Star". In: *A&A* 627, A49, A49. DOI: 10.1051/0004-6361/201935460.

Acknowledgements

The work presented in this dissertation would have been an insurmountable task without the assistance and support of an extensive network of individuals who played crucial roles in various capacities. I would like to express my deepest gratitude to the following individuals whose unwavering support and encouragement have been instrumental in the completion of this thesis:

First and foremost, I extend my heartfelt appreciation to Andreas Quirrenbach. His unwavering support and inspiring words provided me with the strength and determination to take the final steps towards the culmination of my PhD journey.

I am truly thankful to Cornelis Dullemond, who graciously accepted the role of the second referee for this thesis. His understanding of my anxious nature and continuous support were immeasurable assets throughout this journey, providing a profound sense of calm and reassurance. I extend my sincere thanks to Anna Pasquali and Mario Trieloff for their participation in my defense examination panel.

I am deeply grateful to Guido Thimm for his assistance during my most challenging moments. His remarkable compassion and exceptional skills in managing peripheral issues were instrumental in enabling me to maintain a clear focus on my primary task.

I owe a special debt of gratitude to Ansgar Reiners, whose influence on my work has been profound. His invaluable feedback and guidance have significantly shaped my research and academic growth.

I would also like to express my sincere appreciation to Sabine Reffert for her role in helping me commence my journey. Her guidance allowed me to explore various methodologies and develop my skills as a researcher. I extend my thanks to Martin Kürster, the third advisor on my IMPRS thesis committee, for his consistent support.

The completion of my work would not have been possible without the invaluable data provided by CARMENES. I extend my gratitude to all the members of this consortium, with special mention to José Caballero and David Baroch for their contributions.

Being part of the IMPRS program has been an extraordinary experience that has made my exploration of astrophysics even more enjoyable. I am grateful for the opportunity to meet wonderful individuals from diverse backgrounds, and I would like to express my gratitude to all my friends, colleagues, and fellow PhD students. Your presence in my life has added vibrant colours to my journey.

In particular, I want to acknowledge the LSW family, who provided me with a supportive and nurturing environment. I am deeply grateful to Barbara Wright, Stefan, and Thomas Zinser for creating a haven-like atmosphere for me at LSW. I want to wholeheartedly express my deep appreciation to my incredible friends who have been there for me, especially throughout this past year. To Philipp Hottinger, I honestly cannot imagine what I would have done without you, Hotti. From our memorable excursions in the Königstuhl woods, enjoyable shared lunches, and puzzle-solving sessions, to those challenging days where we persevered together, you have consistently stood by my side. To Theodora Xylakis-Dornbusch and her precious little Ion, your presence brought light and joy to my days. To Paul Heeren, you have been more than just an officemate; you have been a true friend. To Dane Späth and Emily Hunt, thank you for the enriching SMART talks and meetings. To Adrian Kaminski, your wise advice and kindness have been deeply appreciated. To all my distant friends whom I haven't heard from in a while, your impact on my life remains cherished. To my Iranian

friends, who provided solace and alleviated my homesickness, I express my sincere gratitude. In particular, I want to extend my deepest appreciation to Sara Khalafinejad and Mohammadreza Kamali, who have embraced me as a cherished family member. Your support and kindness have touched my heart in immeasurable ways.

Finally, I want to dedicate a heartfelt tribute to my family. Maman Parvaneh and Baba Hamid, you are my pillars of strength and everything I hold dear. Words cannot adequately convey the depth of my feelings and the extent of my gratitude for your constant love and support. Maman Parvaneh, thank you for raising me to be a strong, dignified woman who stands up for herself. These qualities have proven invaluable throughout my life's journey. In all my achievements, you have played a pivotal role. Baba Hamid, I am grateful for your open-mindedness, unwavering trust, and belief in me. Your faith has fuelled my determination to overcome challenges and pursue my dreams. To my Uncle Shahab, you have always treated me like your own daughter. Your enthusiasm for science and the universe, combined with your dedication to your work, has served as a constant inspiration. And lastly, I want to pay tribute to the cherished memory of my dear Uncle Hamid. I am certain that reaching this milestone would have brought immense joy to your heart. Your memory continues to shine brightly in my heart, serving as a guiding light as I forge ahead.

Declaration of Authorship

I, Sepideh Sadegi, declare that this thesis titled, "Investigating the Activity of M Dwarfs: Spectroscopic, Photometric, and Modelling Analyses" and the work presented in it are my own. I confirm that:

- This work was done wholly or mainly while in candidature for a research degree at this University.
- Where any part of this thesis has previously been submitted for a degree or any other qualification at this University or any other institution, this has been clearly stated.
- Where I have consulted the published work of others, this is always clearly attributed.
- Where I have quoted from the work of others, the source is always given. With the exception of such quotations, this thesis is entirely my own work.
- I have acknowledged all main sources of help.
- Where the thesis is based on work done by myself jointly with others, I have made clear exactly what was done by others and what I have contributed myself.

Signed:

Date: